This is Volume 62 in the
INTERNATIONAL GEOPHYSICS SERIES
A series of monographs and textbooks
Edited by RENATA DMOWSKA and JAMES R. HOLTON
A complete list of books in this series appears at the end of this volume.

Paleoseismology

Edited by

James P. McCalpin
GEO-HAZ CONSULTING, INC.
ESTES PARK, COLORADO

ACADEMIC PRESS
San Diego New York Boston London
Sydney Tokyo Toronto

This book is printed on acid-free paper. ♾

Academic Press, Inc.
A Division of Harcourt Brace & Company
525 B Street, Suite 1900, San Diego, California 92101-4495

United Kingdom Edition published by
Academic Press Limited
24-28 Oval Road, London NW1 7DX

Library of Congress Cataloging-in-Publication Data

Paleoseismology / edited by James P. McCalpin.
p. cm. -- (International geophysics series: v. 62)
Includes index.
ISBN 0-12-481825-0 (alk. paper)
1. Paleoseismology. I. McCalpin, James. II. Series.
QE539.2.P34P35 1996
551.2.'2---dc20 96-2096
CIP

PRINTED IN THE UNITED STATES OF AMERICA
96 97 98 99 00 01 EB 9 8 7 6 5 4 3 2 1

The rupture trace of the 1983 M_s 7.3 Borah Peak, Idaho earthquake (Lost River fault zone) approximately 50 m north of the Doublesprings Pass Road, is dominated by a 15-m-wide graben. One year after the rupture, a 3-4-m-deep, 45-m-long trench (left and lower center) was excavated across the fault trace to identify and characterize paleoearthquakes; note persons in trench at far left for scale. The sense and amount of 1983 displacements at this location closely mimicked those of the previous earthquake (ca. 5000–6000 years ago), suggesting characteristic earthquake behavior at this location (see Chapter 9). Photograph taken in April 1985, 17 months after the rupture. The log of this trench is shown in Schwartz and Crone, 1985.

Contents

Chapter 1 Introduction to Paleoseismology

James P. McCalpin and Alan R. Nelson

Chapter 2 Field Techniques in Paleoseismology

James P. McCalpin

Chapter 3 Paleoseismology in Extensional Tectonic Environments

James P. McCalpin

Chapter 4 Paleoseismology of Volcanic Environments

William R. Hackett, Suzette M. Jackson, and Richard P. Smith

Chapter 5 Paleoseismology of Compressional Tectonic Environments

Gary A. Carver and James P. McCalpin

Chapter 6 Paleoseismology in Strike-Slip Tectonic Environments

Ray J. Weldon II, James P. McCalpin, and Thomas K. Rockwell

Chapter 7 Using Liquefaction-Induced Features for Paleoseismic Analysis

Stephen F. Obermeier

Chapter 8 Using Landslides for Paleoseismic Analysis

Randall W. Jibson

Chapter 9 Application of Paleoseismic Data to Seismic Hazard Assessment and Neotectonic Research

James P. McCalpin

Contributors

Numbers in parentheses indicate page numbers on which authors' contributions begin.

Gary A. Carver (183) Department of Geology, Humboldt State University, Arcata, California 95521. E-mail: gacl@axe.humboldt.edu
William R. Hackett (147) WRH Associates, 2880 E. Naniloa Circle, Salt Lake City, Utah 84117. E-mail: bhackett@xmission.com
Suzette M. Jackson (147) Lockheed Idaho Technologies Co., P.O. Box 1625, MS 2107, Idaho Falls, Idaho 83415. E-mail: msj@inel.gov
Randall Jibson (397) U.S. Geological Survey, Box 25046, MS 966, Denver Federal Center, Denver, Colorado 80225. E-mail: jibson@gldvxa.cr.usgs.gov
James P. McCalpin (1, 33, 85, 183, 271, 439) GEO-HAZ Consulting, Inc., P.O. Box 1377, 1221 Graves Ave., Estes Park, Colorado 80517. E-mail: mccalpin@geohaz.com.
Alan R. Nelson (1) U.S. Geological Survey, Box 25046, MS 966, Denver Federal Center, Denver, Colorado 80225. E-mail: anelson@gldvxa.cr.usgs.gov
Stephen F. Obermeier (331) U.S. Geological Survey, National Center, Reston, Virginia 20192. E-mail: sobermei@usgs.gov
Thomas K. Rockwell (271) Department of Geological Sciences, San Diego State University, San Diego, California 92182. E-mail: trockwel@geology.sdsu.edu
Richard P. Smith (147) Lockheed Idaho Technologies Company, P.O. Box 1625, MS 2107, Idaho Falls, Idaho 83415. E-mail: rps3@inel.gov
Ray J. Weldon II (271) Department of Geological Sciences, Cascade Hall, University of Oregon, Eugene, Oregon 97403. E-mail: ray@neotec.uoregon.edu

Preface

A clear sign of the youth of paleoseismology has been the lack of a comprehensive book on this rapidly developing field of research. This book is designed to meet this need for an overview volume, one that outlines the concepts behind and techniques used in current investigations. Books by Wallace (1986), Vita-Finzi (1986), and particularly Crone and Omdahl (1987) partly filled this need in the late 1980s. In many ways this book is an outgrowth of Crone and Omdahl's volume, which summarized the "Directions in Paleoseismology" conference convened by the U.S. Geological Survey. The scope of paleoseismology has expanded so rapidly in the past decade, however, that even full-time paleoseismologists have difficulty maintaining an awareness of important developments throughout the specialty. A parallel development is that paleoseismologists, many of whom had previously worked in relative isolation within their respective countries, began to collaborate in the late 1980s. There is also an increasing awareness of the value of collaboration with specialists in structural geology, geodesy, and seismology for solving paleoseismic problems (Wallace, 1986; Weldon, 1991). Such timely collaboration makes it easier for us to provide a broader perspective on many aspects of paleoseismology than would have been possible a decade ago. This book appears at a time in the development of paleoseismology when some techniques have become routine and some concepts widely accepted, but when many other aspects of the field are still rapidly evolving (Vittori *et al.*, 1991).

Much of the emphasis throughout the book is on techniques and case histories, for two reasons. First, as in other field sciences, the techniques of field data collection greatly influence the final interpretation of phenomena. In our view, some current differences in field techniques used by different research groups have contributed to differences in seismotectonic models that rely heavily on paleoseismic data. For example, the models of characteristic earthquakes and fault segmentation (Wesnousky *et al.*, 1984; Schwartz and Coppersmith, 1984; Schwartz and Sibson, 1989a) currently in vogue in the United States have been partly justified by paleoseismic data collected in trench exposures of normal and strike-slip faults. In Russia, paleoseismic reconstruction relies heavily on slope failure phenomena (see Chapter 8) and the faults themselves are rarely trenched (Solonenko, 1977; Nikonov, 1988a, 1995). Perhaps as a result of this more indirect approach, the temporal and spatial occurrence of large paleoearthquakes in Russia has been interpreted as more random. In a parallel example, the study of paleoliquefaction in unconsolidated deposits in the United States (by geologists and civil engineers) has focused on developing criteria to distinguish coseismic liquefaction features from similar features of nonseismic origin, and on characterizing the responsible paleoearthquake. In European studies of "seismites" in semiconsolidated rocks of Cenozoic and Mesozoic age (by stratigraphers and sedimentologists), sediment deformation is often merely assumed to be seismic in origin, but rarely is this proven or related to any particular fault. These examples suggest that, at this stage in the development of paleoseismology, paleoseismologists would probably benefit from a global-scale discussion and standardization of terminology and field techniques.

The second reason for an emphasis on techniques is that all chapter authors are active field researchers in paleoseismology, and each has helped to develop some of the techniques described. In particular, we emphasize the need to integrate geomorphic and stratigraphic studies of paleoearthquake evidence, by correlating landforms and processes in deformation zones to their corresponding depositional environments and stratigraphy.

The book is aimed primarily at a graduate to professional level audience in geology, geography, or geophysics, although we assume some familiarity with geomorphology (physical geography) and Quaternary geology. Throughout the book, we try to keep in mind the needs of practitioners who collect and interpret paleoseismic data. Other scientists, engineers, and planners who use paleoseismic data in engineering design or land-use planning may find the overview chapters (1 and 2) and the summary of Chapter 9 most useful.

I acknowledge the assistance of many colleagues who shared their knowledge of paleoseismology. In particular, I thank the reviewers of various parts and drafts of the book, many of whom have at least as broad a perspective on paleoseismology as we do. These include T. K. Rockwell, A. J. Crone, S. L. Wesnousky, R. C. Bucknam, S. L. Obermeier, and S. Pezzopane (Chapter 1), A. R. Nelson (Chapter 2), D. A. Ostenaa and M. Hemphill-Haley (Chapter 1), A. R. Nelson (Chapter 2), D. A. Ostenaa and M. Hemphill-Haley (Chapter 3), T. Parsons and J. Zollweg (Chapter 4), J. D. Sims and R. Campbell (Chapter 7), and R. L. Schuster (Chapter 8). Fanchen Kong, V. S. Khromovskikh, and Yoko Ota provided historical perspectives on the development of paleoseismology in China, Russia, and Japan, respectively. In addition A. R. Nelson reviewed much of the book and upgraded its content and exposition to a high standard. Dan and Sue Doylen of Master Graphics (Estes Park, Colorado) provided expert assistance in preparing the figures. Finally, I gratefully acknowledge a decade of support from the U.S. Geological Survey's National Earthquake Hazards Reduction Program, without which my research, and many of the concepts and techniques reported in this book, would never have been developed.

James P. McCalpin
Estes Park, Colorado

Acknowledgments

Thanks are due to the following publishers and professional societies for permission to reproduce copyright material.

A. A. Balkema Publishers: Fig. 2.9
American Association for the Advancement of Science: Figs. 6.21, 6.23
American Association of Petroleum Geologists, Pacific Section: Figs. 5.7, 5.36
American Geophysical Union: Figs. 2.5, 2.16, 3.24, 3.25, 4.5, 5.21, 5.26, 6.10, 6.31, 9.10, 9.18
American Society of Civil Engineers: Fig. 7.28
Annales Tectonicae: Fig. 9.9
Association of Engineering Geologists: Figs. 2.20, 2.23
Blackwell Scientific Publishing Company: Figs. 5.5, 7.3
Brigham Young University: Fig. 2.3
Cambridge University Press: Fig. 9.14
Colorado School of Mines Press: Figs. 3.14, 3.15, 3.28
Earthquake Engineering Research Institute: Fig. 5.28
Elsevier Publishing Company B.V.: Fig. 2.13
Geological Society of America: Figs. 3.11, 3.12, 3.19, 9.10, All © the authors.
Humboldt State University: Fig. 5.27
INQUA Neotectonics Commission: Fig. 2.4
John Wiley & Sons: Fig. 6.4
Journal of Geography (Japan): Fig. 2.11
Macmillan Journals Ltd.: Fig. 5.29
National Academy Press (USA): Figs. 1.1, 5.17, 5.18, 5.20, 6.16, 9.1
New Mexico Geological Society: Fig. 3.18
Oregon Division of Geology and Mineral Resources: Fig. 5.39
Pergamon Press: Fig. 9.15
Royal Society of New Zealand: Fig. 6.7
Seismological Society of America: Figs. 3.7, 3.10, 3.29, 5.12, 9.2, 9.3
Seismological Society of Japan: Fig. 6.15
Society for Sedimentary Geology: Fig. 3.20
Springer-Verlag Publishers: Fig. 5.35

Symposium on Engineering Geology and Geotechnical Engineering:
Fig. 2.6
University of Chicago: Fig. 5.22
University of Washington: Figs. 6.32, 6.33
Utah Geological Survey: Figs. 2.12, 2.14, 2.15, 2.18, 2.22
Yale University: Fig. 5.2

Chapter 1 Introduction to Paleoseismology

James P. McCalpin
Alan R. Nelson

1.1 THE SCOPE OF PALEOSEISMOLOGY

1.1.1 Definitions and Objectives

Paleoseismology is the study of prehistoric earthquakes (Solonenko, 1973; Wallace, 1981), especially their location, timing, and size. Whereas seismologists work with data recorded by instruments during earthquakes, paleoseismologists interpret geologic evidence created during individual *paleoearthquakes.*[1] Paleoseismology differs from more general studies of slow to rapid crustal movements during the late Cenozoic (e.g., neotectonics) in its focus on the almost instantaneous deformation of landforms and sediments during earthquakes (C. R. Allen, 1986). This focus permits study of the distribution of individual paleoearthquakes in space and over time periods of thousands or tens of thousands of years. Such long paleoseismic histories, in turn, help us understand many aspects of neotectonics, such as regional patterns of tectonic deformation and the seismogenic behavior of specific faults or regions.

The driving force behind most paleoseismic studies is society's need to assess the probability and severity of future earthquakes (Wallace, 1986; Reiter, 1995). The past few decades have spared the most highly industrialized countries from the effects of devastating earthquakes, but there is little doubt that earthquakes damaging enough to affect the world economy seriously may occur in cities such as Los Angeles or Tokyo at any time (Wesnousky *et al.*, 1984; Nishenko, 1989; Working Group on California Earthquake Probabilities, 1995). Before 1970, the space and time assessment of earthquake hazard in industrialized countries such as the United States and the USSR was based

---

[1] Throughout this book we affix the prefix "paleo-" to geologic terms associated with earthquakes to indicate that we are referring to prehistoric seismic events. For example, in some areas *paleoliquefaction* features offer widespread evidence of past large earthquakes, and *paleomagnitudes* can be estimated for some well-studied prehistoric earthquakes.

almost solely on the historic earthquake record. Although many geologists (e.g., Allen, 1975; Research Group for Active Faults, 1980) pointed out the danger in this approach, some relatively recent maps of predicted strong ground motion (e.g., Algermissen and Perkins, 1976) were derived solely from historic data. Now most countries with seismically active faults consider paleoseismic data in both regional (e.g., Algermissen *et al.*, 1982, 1990) and site-specific seismic hazard analyses (dePolo and Slemmons, 1990; Research Group for Active Faults, 1991; Vittori *et al.*, 1991; Bonilla, 1991).

Paleoseismology supplements historic and instrumental records of seismicity by characterizing and dating large prehistoric earthquakes (Crone and Omdahl, 1987; Vittori *et al.*, 1991). In most countries, useful seismicity records extend back only a few centuries (Gutenberg and Richter, 1954; Stover and Coffman, 1993) and many active fault zones have no historic record of large earthquakes. For example, studies of prehistoric faulting along the Wasatch fault zone in the western United States (Machette *et al.*, 1992a; Chapters 3 and 9) show that the average recurrence interval between large earthquakes is probably three times longer than the period of historic settlement (145 years). In some other regions, both near to and far from plate boundaries, paleoseismic studies suggest that earthquake hazard estimates based on short historic records may actually overestimate the liklihood of future earthquakes, due to the recent occurrence of large earthquakes on faults with long average recurrence times (Lajoie, 1986; Crone *et al.*, 1992; Adams *et al.*, 1991; Fig. 1.1). Even in China and the Middle East where historic seismicity records span a millennia or more (e.g., Ganse and Nelson, 1982; Ambraseys and Melville, 1982), historic observations are commonly insufficient to identify all seismogenic faults. On a fault that has slipped for millions of years, even a 3000-year record covers only a fraction of a percent of the history of the fault. Much of the seismic history of most faults is accessible only through the techniques of paleoseismology.

For the most part, the paleoseismic record is a record of large (magnitude, $M > 6.5$) or great ($M > 7.8$) earthquakes because geologic evidence of small and moderate-sized earthquakes is rarely created or preserved near the surface. Evidence of past earthquakes can range from local deformation of the ground surface along a crustal fault (fault scarps, sag ponds, laterally offset stream valleys, monoclinally folded terraces), to indicators of the sudden uplift or subsidence of large regions above a plate-boundary fault (warped river terraces, elevated shorelines, drowned tidal marshes), to stratigraphic or geomorphic effects of strong ground shaking or tsunamis far from the seismogenic fault (landslides, rockfalls, liquefaction features, tsunami deposits). A characteristic of most such features is that they formed instantaneously (from a geologic perspective) during or immediately after an earthquake.

Features (deposits or landforms) formed during an earthquake are described as *coseismic* and are commonly contrasted with *nonseismic* features formed by processes of erosion, deposition, and nonseismic deformation. However, during the formation of these nonseismic deposits and landforms, small or moderate earthquakes may have occurred that left no evidence in the geologic record. Seismogenic faults may creep or slip small amounts during small to moderate earthquakes but leave no signs of sudden slip. For this reason, *nontectonic* and *nonseismic* are better adjectives than *aseismic* (no detectable seismicity) for features unrelated to fault slip or strong earthquake shaking. The term *aseismic* should be restricted to seismology.

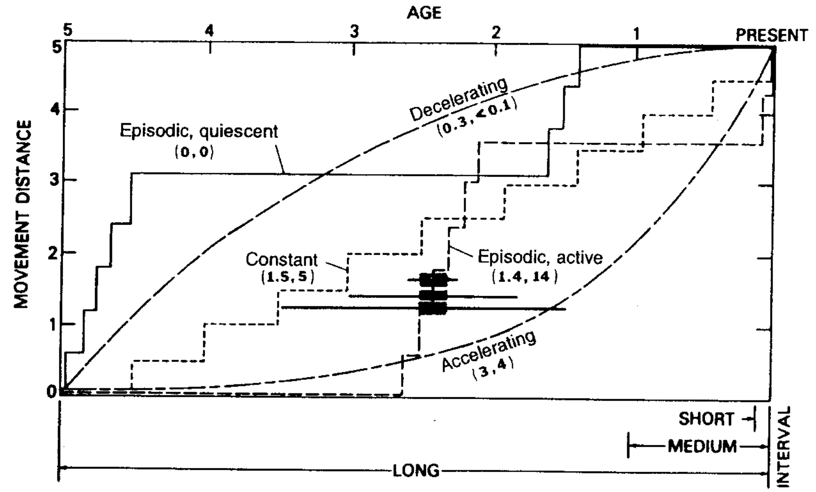

Figure 1.1 Five patterns of fault displacement versus time. Slip rates (shown in arbitrary distance/time units) for all five patterns are the same over the long time interval (bottom), but vary when viewed over medium or short time intervals. Numbers in parentheses under each pattern label are medium-term and short-term rates for that pattern. In the three patterns with a "staircase" shape (episodic and quiescent patterns), vertical steps represent coseismic displacements like those shown in Fig. 1.2. Filled squares with age error bars demonstrate the increasing difficulty of distinguishing among the different patterns of fault slip with increasingly larger errors on ages for fault displacements. [Modified from Pierce (1986).]

Paleoseismologists can only study earthquakes that produce recognizable surface deformation (in the form of landforms or stratigraphic units that reflect changes in surface topography); such earthquakes have been termed *morphogenic earthquakes* (Caputo, 1993). We deal with the topic of the lower limit of detection (threshold) of morphogenic earthquakes in Chapters 3, 7, and 8. Vittori *et al.* (1991) and Serva and Slemmons (1995b) propose wider use of the term *seismites* for all geologic structures genetically related to earthquakes. However, the original definition of seismites referred only to units containing sedimentary structures produced by shaking (Seilacher, 1969), and we see no advantage to a more general use of the term.

Finally, in some publications the term *event* is used too freely as a synonym for *paleoearthquake*. Many erosional, depositional, or even structural "events" are only inferred responses to paleoearthquakes, and commonly it is unclear whether a paleoearthquake or some other type of "event" is being discussed (e.g., Pantosti *et al.,* 1993). For example, fracturing "events" are extensively documented in fault zone trenches near Yucca Mountain, Nevada, but it is unclear whether the fracturing resulted from coseismic slip on the exposed fault, slip triggered by movement on an adjacent coseismic fault (primary evidence), shaking-induced compaction (secondary evidence), or nonseismic compaction (nonseismic evidence).

Paleoearthquakes are *prehistoric* by definition, but does "prehistoric" mean the time before oral records, or the time before contemporaneous written accounts, or the time before written accounts with some quantitative observations of earthquakes? The latter definition is closest to what paleoseismologists commonly consider prehistoric. This broad definition of "prehistoric" somewhat ameliorates the problems caused by poorly defined and varying times of transition from oral to written history around the globe; for example, from about 3000 B.C. for China and parts of the Middle East to later than A.D. 1700 for New Zealand and northwestern North America. Archaeology has contributed much to the understanding of the history of large earthquakes in some regions (Vita-Finzi, 1986); much of what we know of the seismic history of the Middle East and Mediterranean regions before the Christian era has come from *archaeoseismic* investigations (e.g., Ambrasseys and Melville, 1982; Stiros, 1988a; see Chapter 2). The older boundary on the time interval encompassed by paleoseismology studies is commonly the middle (4 to 6 ka, that is, 4000 to 6000 years ago) to early (7 to 10 ka) Holocene, but records of individual earthquakes may extend well back into the late Pleistocene in regions of long recurrence (e.g., Crone *et al.,* 1992; Pezzopane *et al.,* 1994) or unusually well-preserved evidence (e.g., Ota *et al.,* 1993).

Paleoseismic techniques are also used to extend our understanding of large historic earthquakes with limited contemporary descriptions (termed *historical paleoseismology* by Yeats, 1994). Studies of historical earthquakes commonly concentrate on measuring the amount or lateral extent of surface displacement on faults or describing the size and distribution of features (landslides, sand blows) produced by shaking. Earthquakes thus studied range from relatively recent (A.D. 1886, Charleston, South Carolina, USA, Obermeier *et al.,* 1990; A.D. 1857 Ft. Tejon, San Andreas fault, USA: Sieh, 1978a; 1811-1812, New Madrid, Missouri; A.D. 1739, Yinchuan, China, Zhang *et al.,* 1986; A.D. 1703, central Italy earthquakes: Blumetti, 1995) to many centuries old (A.D. 1510, Kondayama, Japan: Sangawa, 1986; 31 B.C., Jericho, Israel: Reches and Hoexter, 1981). In trenches or other types of exposures, most studies also attempt to find evidence of earlier prehistoric earthquakes, whose features can then be compared with the features formed during historic earthquakes.

1.1.2 Organization and Scope of This Book

This book reflects our interest in field-related techniques and our North American perspective. Book chapters are organized by tectonic environment and by whether paleoseismic evidence is primary or secondary (after the distinction of Richter, 1958; the term secondary has also been used to describe subsidiary faulting, e.g., Bonilla, 1982). Primary evidence reflects seismic surface faulting or folding, whereas secondary evidence is a response to strong ground shaking. As explained in the next section, primary and secondary evidence are further grouped into on-fault and off-fault evidence, and as to whether the evidence consists of stratigraphic or geomorphic features. In this introduction (Chapter 1) we explain the scope of paleoseismology and briefly outline its early development. In Chapter 2 we describe and comment on paleoseismic field methods applicable to the study of primary evidence, including various surface mapping, geophysical, and subsurface exploration techniques. Chapters 3 through 6 cover the application of these widely used methods to the development of paleoseismic histories in extensional, volcanic, compressional, and strike-slip tectonic environments, respectively. Techniques for studying secondary features, such as landslides and liquefaction features, are similar in all tectonic environments, including the intraplate interiors of continents, where tectonic processes proceed slowly and easily studied surface fault traces are rare or absent. Because most techniques for studying intraplate paleoseismicity are covered in Chapters 3 through 8, we do not include a separate chapter on intraplate tectonic environments. Chapters 7 and 8 deal primarily with liquefaction and landslide evidence of paleoseismicity, the two most important types of secondary evidence, although other, less common types of evidence are mentioned. In Chapter 9, through a brief discussion of seismogenic models, empirical sets of worldwide data, and case studies, we show how paleoseismic data contribute to the understanding of regional tectonic frameworks. Only when paleoseismic data are viewed within such frameworks can they form the basis for comprehensive seismic hazard assessments.

Some topics in paleoseismology are not covered in this book due to our unfamiliarity with them or to space limitations. The megascale geomorphology of tectonically active regions is mentioned only briefly because the results of regional-scale studies rarely provide information about individual paleoearthquakes. Nor do we thoroughly review dating techniques applicable to Quaternary deposits because several such reviews have recently been published (Rosholt *et al.,* 1991; Rutter and Cato, 1993). A few relatively new areas or techniques of paleoseismic interest are rapidly developing and are not discussed. For example, we say little about faults that displace formerly glaciated bedrock surfaces because of the difficulty of characterizing and dating individual paleoearthquakes in many of these high-latitude regions (Olesen, 1988; Mörner *et al.,* 1989; Ringrose, 1989a,b; Lagerback, 1990; Fenton, 1992, 1994).

1.1.3 The Relation of Paleoseismology to Other Neotectonic Studies

Paleoseismology is an interdisciplinary field of research. It borrows many concepts from seismology, structural geology, and tectonics. However, paleoseismic methodology and techniques are derived primarily from Quaternary geology and related disciplines, such as geomorphology, soil mechanics, sedimentology, archaeology, paleoecology, photogrammetry, radioisotope dating, or pedology (soil science). Most paleoseismic field studies require extensive training or experience in Quaternary geology, itself a highly interdisciplinary field. Thus, it should be no surprise that many significant advances in paleoseismology have been made by geomorphologists and other Quaternary specialists, working at the interface between tectonics and seismology. Paleoseismology is a particularly successful example of applied Quaternary geology (Wallace, 1986).

Paleoseismology is a subdiscipline within the much broader fields of *neotectonics* and *active tectonics*. Neotectonics, or the study of crustal movements during the late Cenozoic (Beloussov, 1980; Vita-Finzi, 1986, p. 14; Mörner and Adams, 1989), encompasses a wide spectrum of topics ranging from satellite and laser-ranging measurements of last year's movements, to isostatic rebound after glacier retreat, to fission-track dating of rates of mountain uplift over millions of years (e.g., Yoshikawa *et al.,* 1981; Reilly and Harford, 1986; Minster and Jordan, 1987; Sabadini *et al.,* 1990; Krinitsky and Slemmons, 1990; Summerfield, 1989, 1991a; Slemmons *et al.,* 1991). Active tectonics includes many of these types of crustal movements, but is limited in its time frame to studies of "tectonic movements that are expected to occur within a future time span of concern to society" (Wallace, 1986; Weldon, 1991). Many neotectonic studies are concerned with long-term structural evolution of large regions and even continents (Gardner, 1989; Summerfield, 1991b; Pavlides and Mountrakis, 1986; Merritts and Ellis, 1994), whereas even the most extensive paleoseismic studies include but part of a plate or plate boundary. Yeats *et al.* (1996) provide the most recent and comprehensive view of the earthquake-related aspects of neotectonics, which they term *earthquake geology*. Neotectonic and active tectonic studies commonly measure the rate and spatial pattern of deformation on faults or folds that result from many paleoearthquakes over tens of thousands or millions of years. In most cases, however, the proportion of coseismic to nonseismic deformation on most such features is unknown. Thus, coseismic earth movements, the major focus of paleoseismic studies, are but a small, albeit dramatic, aspect of neotectonic studies.

Another subfield of neotectonics, closely aligned with paleoseismology, is *tectonic geomorphology*. Tectonic landforms have long interested geomorphologists (Merritts and Ellis, 1994) and by the 1980s tectonic geomorphology (or in European usage, *morphotectonics*) was the subject of several conferences and monographs (Yoshikawa *et al.,* 1981; Ollier, 1981; Morisawa and Hack, 1985; Embleton, 1987). However, the traditional focus of geomorphology on surface form and modern process rather than earth history did not generally yield data on coseismic fold growth, fault displacement, or earthquake recurrence that is the objective of most modern paleoseismic studies. Weathering and erosion prevent many tectonic landforms that are created by multiple surface-faulting events over long periods of time from retaining evidence of individual paleoearthquakes. Nevertheless, geomorphic studies of certain small-scale landforms yield valuable paleoseismic data not obtainable by other means (Chapters 3, 5, and 6). The chief value of large-scale tectonic geomorphology studies lies in the critically important tectonic framework they provide for site-scale paleoseismic studies (Chapter 9). The recent development of tectonic geomorphology, including its integration with paleoseismology, tectonics, and seismology, is discussed by Merritts and Ellis (1994).

Theoretical models that describe the seismogenic behavior of faults, developed from a wide variety of studies in seismology, geodesy, rock mechanics, and structural geology (Bullen and Bolt, 1985; Scholz, 1990; Weldon, 1991), provide another type of framework for interpreting paleoseismic histories for comprehensive seismic hazard analyses. Perhaps the two most important models, covered more fully in Chapter 9, describe the *segmentation* of faults and the *earthquake deformation cycle* (Fig. 1.2). In the segmentation model, large earthquakes, commonly of a *characteristic* size, repeatedly rupture the same part or segment of a fault, less commonly extending into adjacent seg-

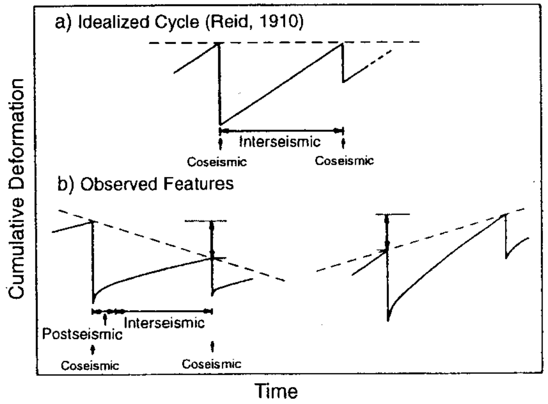

Figure 1.2 Simplified forms of the earthquake deformation cycle. Cumulative deformation (e.g., strain, tilt, displacement) is plotted as a function of time. Step offsets correspond to the occurrence times of major earthquakes. Dashed lines show level at which failure occurs; the level varies with the effects of long-term inelastic deformation. [From Thatcher (1986b). Reprinted with permission from Active Tectonics. Copyright 1986 © by the National Academy of Sciences. Courtesy of the National Academy Press, Washington, D.C.]

ments (Schwartz and Coppersmith, 1984). In many plate-boundary settings, segments of faults have been modeled with a *time-predictable* cycle of tectonic strain accumulation followed by strain release during characteristic earthquakes (Shimizaki and Nakata, 1980; Thatcher, 1986a; Stein *et al.,* 1988). Other studies have emphasized the differing characteristics of successive earthquakes, and long-term patterns of earthquake clustering have been proposed (Sieh *et al.,* 1989; Thatcher, 1990; Chapter 9).

Geodetic and tide gauge measurements, made over periods of many decades before and after some of the largest plate-boundary earthquakes, provide the most detailed data used to develop models of the earthquake deformation cycle (Thatcher, 1986a; Scholz, 1990; Savage and Thatcher, 1992). The cycle begins with *interseismic* strain accumulation, for example in the upper plate above a locked part of a plate-boundary fault as shown by data from the subduction-zone coast of southwest Japan (Chapter 5). The more gradual deformation in the interseismic part of the cycle includes short-term *preseismic* and *postseismic* movements that are generally opposite in direction to coseismic deformation at the same sites. Accumulated strain is released through slip on the locked part of the fault during the coseismic part of the cycle (Fig. 1.2). Near the fault, deformation tends to be large but decays rapidly with time; deformation farther from the fault is of smaller amplitude and decays more slowly. Throughout the earthquake deformation cycle, steady slip on the fault downdip of the locked part may produce long-term interseismic deformation. Most paleoseismic investigations have focused almost exclusively on the strain release (coseismic) part of the earthquake deformation cycle because deformation during large earthquakes commonly produces landforms or deposits that are more distinctive than those produced by slower deformation during the interseismic parts of earthquake deformation cycles. As discussed in later chapters, inferring deformation rates during the interseismic parts of past earthquake deformation cycles requires various types of *paleodatums* to be identified and dated. Paleodatums are landforms or deposits, the initial shape or elevation of which is known precisely enough to allow recognition of small amounts of deformation. Paleodatums are often produced during brief (geologic) time intervals by climate-driven geomorphic processes (e.g., Bull, 1991).

1.2 IDENTIFYING PREHISTORIC EARTHQUAKES FROM PRIMARY AND SECONDARY EVIDENCE

1.2.1 Classification of Paleoseismic Evidence

The only existing classification of paleoseismic evidence comes from Russia, where workers (e.g., Solonenko, 1970, 1973; Nikonov, 1988a, 1995) have subdivided the broad spectrum of "seismodeformations" into seismotectonic (fault-related) features, seismogravitational (shaking-related) features, and gravity-seismotectonic features (a mixed class). We have modified this classification, based on the concepts of Richter (1958, pp. 80-84) and Hagiwara (1982), into three hierarchical levels based on genesis, location, and timing (Table 1-1). At the highest level of classification, evidence is either *primary* or *secondary.* Primary paleoseismic evidence is produced by tectonic deformation resulting from coseismic slip along a fault plane (including growth of fault-related folds) and is equivalent to "seismotectonic deformation" in the Russian system (Nikonov, 1995a). Secondary paleoseismic evidence is produced by earthquake shaking and includes phenonema that the Russians term "seismogravitational." At the second level of classification, paleoseismic features are further distinguished as being on or above a fault trace (*on-fault* or near-field features), or away from or far above a fault trace (*off-fault* or far-field features). A third level of classification, derived from our need to date and correlate paleoearthquakes, distinguishes *instantaneous* features formed at the time of the earthquake (coseismic) from *delayed-response* (postseismic) features formed by various geological processes after coseismic deformation and seismic shaking cease. Finally, paleoseismic evidence is preserved as either landforms (*geomorphic evidence)* or as deposits and structures (*stratigraphic evidence),* and this distinction often determines how paleoseismic field investigations are approached.

This combined genetic and descriptive classification scheme yields 16 categories of paleoseismic evidence (Table 1-1). The geomorphic approach commonly involves inferring the amount of fault displacement and/or the magnitude of paleoearthquakes from measurements of landform deformation. A strength of geomorphic studies is that many measurements can be made over a large area, but geomorphic evidence alone rarely provides precise ages for paleoearthquakes. The stratigraphic approach focuses on inferring magnitude and recurrence by measuring and dating deformed strata in exposures. However, because detailed data are typically obtained from only a few sites, it may be unclear to what extent site data represent deformation throughout the length and width of the fault zone. These two complimentary but different approaches to field investigations form the basis for the internal subdivision of Chapters 3 through 6.

Primary paleoseismic evidence is commonly easy to associate with a particular causative fault—a fault scarp along the base of a mountain front, for example, clearly indicates surface rupture of at least the section of the fault marked by the scarp. Fault scarps, fissures, and folds along the trace of a fault are typical examples of primary, on-fault, instantaneous (geomorphic) evidence (Fig. 1.3). In vertical outcrops or trenches, corresponding stratigraphic evidence consists of displaced or folded strata, zones of sheared sediment, and fissures (Chapters 3, 5, and 6). Primary, off-fault, instantaneous evidence commonly takes the

Table 1-1

Hierarchical Classification of Paleoseismic Features[a]

Level 1: Genesis	**Primary** (Ch. 3–6) (Created by Tectonic Deformation)			
Level 2: Location	On fault		Off fault	
Level 3: Timing	Instantaneous (coseismic)	Delayed-response (postseismic)	Instantaneous (coseismic)	Delayed-response (postseismic)
Geomorphic expression	**1** • Fault scarps • Fissures • Folds • Moletracks • Pressure ridges	**2** • Afterslip contributions to features at left • Colluvial aprons	**3** • Tilted surfaces • Uplifted shorelines • Drowned shorelines	**4** • Tectonic alluvial terraces • Afterslip contributions to features at left
Stratigraphic expression	**5** • Faulted strata • Folded strata	**6** • Colluvial wedges • Fissure fills • Unconformities (faulting-event horizons)	**7** • Tsunami deposits	**8** • Erosional unconformities and deposits induced by uplift, subsidence, and tilting
Abundance of similar nonseismic features	Few	Few	Some	Common

Level 1: Genesis	**Secondary** (Ch. 7-8) (Created by seismic shaking)			
Level 2: Location	On fault		Off fault	
Level 3: Timing	Instantaneous (coseismic)	Delayed-response (postseismic)	Instantaneous (coseismic)	Delayed-response (postseismic)
Geomorphic expression	**9** • Sand blows • Landslides • Disturbed trees	**10** • Retrogressive landslides	**11** • Sand blows • Landslides • Fissures • Subsidence from sediment compaction	**12** • Retrogressive landslides
Stratigraphic expression	**13** • Sand dikes	**14** • Rapidly deposited lake or estuarine sediments	**15** • Sand dikes • Filled craters • Soft-sediment deformation • Turbidites	**16** • Rapidly deposited lake or estuarine sediments
Abundance of similar nonseismic features	Some	Very common	Some	Very common

[a] This classification scheme yields 16 types of paleoseismic features, as numbered consecutively (in bold) in the categories "Geomorphic expression" and "Stratigraphic expression."

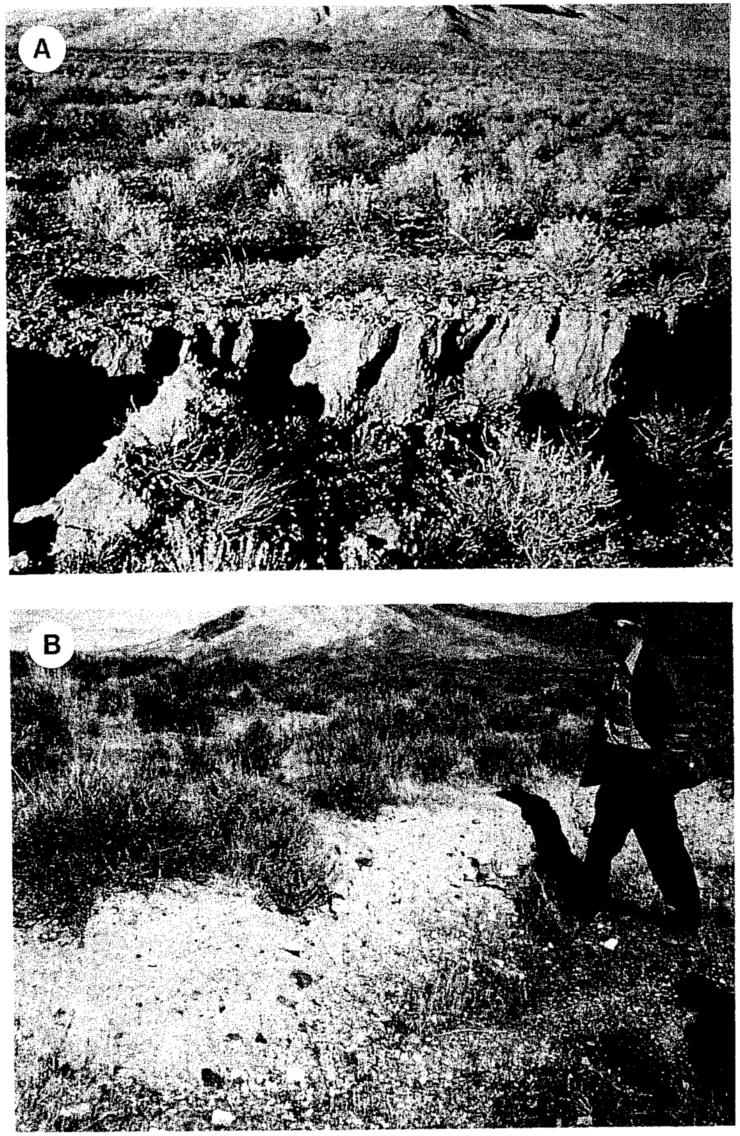

Figure 1.3 Photographs of a fault scarp in Nevada, an example of primary, on-fault, instantaneous evidence. (A) Subsidiary fault scarp of the 16 December 1954 Fairview Peak, Nevada, earthquake. Photo taken approximately 100 m north of U. S. Highway 50, one week after scarp formation. (Courtesy J. S. Williams, Utah State University.) Scarp is 0.5 m high. (B) Same scarp in October 1984, nearly 30 years after formation. Note transformation of the vertical scarp face into a debris-covered slope. At right is Robert E. Wallace, widely regarded in the United States as the "father of paleoseismology."

form of uplifted, subsided, or tilted surfaces some distance from the fault (as long as this deformation is directly produced by seismic slip on a fault at depth). Zones of regional deformation during the largest subduction-zone earthquakes, measuring many tens of kilometers wide and hundreds of kilometers long, are unmistakable primary evidence of slip along this type of plate-boundary fault (Lajoie, 1986; Chapter 5). More localized surface deformation caused by slip on shallower crustal faults that do not break the surface (*blind faults*) may be more difficult to associate with a particular fault (Yeats, 1986b; Chapters 5 and 6). In contrast, primary, delayed-response evidence is usually stratigraphic and results from erosion or deposition induced by uplift, subsidence, lateral displacement, or tilting that occurs hours to hundreds of years after the earthquake. Although tsunami deposits may be found thousands of kilometers from the earthquake source, tsunamis are produced by primary fault displacement of the seafloor, so tsunami deposits are considered primary off-fault evidence (Chapter 5). Whether recorded by geomorphic or stratigraphic evidence, on-fault deformation is commonly larger than off-fault deformation and, therefore, off-fault evidence is more easily confused with features produced by nonseismic processes (Table 1-1; discussed later).

Primary evidence, especially on fault traces, has been the major focus of most paleoseismic investigations. However, this type of evidence has one major weakness for seismic hazard assessments in that it provides no direct evidence of the strength of shaking or the extent of ground failures induced by the paleoearthquake. These critical components of hazard assessment can only be estimated indirectly from primary evidence by applying empirical relations between rupture dimensions, earthquake magnitude, and ground motion and ground failure to off-fault sites (Chapter 9).

Secondary paleoseismic evidence consists of many diverse phenomena caused by earthquake shaking. Geomorphic examples include sand blows, rockfalls, landslides, water level changes, and damaged trees, whereas stratigraphic examples include sand dikes, other liquefaction features, load structures in soft sediment, anomalous beds of silt in lakes, and turbidity current deposits (Vittori *et al.,* 1991; Lucchi, 1995; Chapters 7 and 8). The distinction between instantaneous and delayed-response evidence is more gradational for secondary evidence than for primary evidence because some features (e.g., sand blows, beds of rapidly deposited silt in lakes) may originate during shaking and continue to form for many hours after an earthquake. In other cases, the response of local geomorphic systems does not even begin until earthquake shaking ceases, but the length of the delay varies widely, ranging from minutes (large perennial streams incising into fault scarps) to hours (tsunamis depositing sand in coastal marshes) to years or decades (e.g., development of erosional marine or alluvial terraces, headward erosion above the headscarp of a coseismic landslide, or depositional infilling of subsided terrain). Secondary paleoseismic features are more difficult to distinguish from features produced by nonseismic processes than are primary features (Lucchi, 1995). The greatest amibiguity arises with secondary, off-fault, delayed-response landforms and deposits (Table 1-1). The increased use of secondary, delayed-response features in constructing paleoseismic histories will require a corresponding increased study of similar nonseismic features in differing tectonic, climatic, and geomorphic environments (e.g., Bull, 1991).

The distinction between primary and secondary evidence is not always clear (Richter, 1958, p. 83). For example, slip on shallow faults may be induced by strong ground motions rather than by slip on seismic faults (or faults connected to them), or may be caused by folding above a seismic fault. The surface features thus created look like primary effects of seismic fault rupture, but are actually secondary effects (Yeats, 1986b; Chapter 5).

The strengths and weaknesses of secondary paleoseismic evidence for characterizing paleoearthquakes are nearly the inverse of those of primary evidence. Many types of secondary paleoseismic evidence have a potentially lower *magnitude threshold of formation* than does primary evidence (discussed later). Secondary evidence can also commonly be used more directly than primary evidence to estimate the severity and spatial distribution of prehistoric earthquake ground motions. With some types of secondary evidence, such as sand blows or lateral spread landslides, one can even calculate quantitative measures of ground motion (Chapters 7 and 8). A limitation of secondary evidence (which affects neotectonic synthesis more so than seismic hazard assessment) is that the seismogenic fault responsible for secondary deformation commonly cannot be identified. This ambiguity arises because a given strength of prehistoric ground shaking could have been generated by a nearby, small earthquake or a distant, larger one. However, for many seismic hazard assessments, an inability to determine the source faults responsible for well-characterized prehistoric shaking may not be a critical flaw.

1.2.2 The Use of Modern Analogs and Experiments in Paleoseismology

The study of *modern analogs* of paleoseismic features is a cornerstone of paleoseismology. Almost all geomorphic and stratigraphic indicators that we use to recognize paleoearthquakes in the geologic record were originally identified during large historic earthquakes. Because paleoseismic interpretations are often more rooted in analogy than theory, the more familiar paleoseismologists are with the effects of large, historic earthquakes, the better prepared they will be to recognize and correctly interpret the wide variety of features encountered in paleoseismic studies. Examples of well-studied historic morphogenic earthquakes are cited in Chapters 3 through 8. Paleoseismologists should be familiar with the features produced by large historic earthquakes in their regions of interest or in analogous regions, and they should never pass up the opportunity to visit the epicentral area of a recent morphogenic earthquake, where primary and secondary features can be observed firsthand.

Geology has traditionally supplemented its interpretations (based mainly on analogy) with *experiments* intended to reproduce features in a controlled laboratory setting. With the exception of some studies of fault rupture propagation in sand boxes (e.g., Lade *et al.,* 1984), little experimental work has been performed in paleoseismology. Many of the microscale features of coseismic faulting, such as small fissures and folds, shear fabrics in unconsolidated deposits, clast fabrics in postfaulting colluvium, sand dikes and sand blows, and other soft-sediment deformation structures, might be reproduced in the laboratory. Characterization of such small-scale features could help reduce the present ambiguity regarding the paleoseismic significance of some features, especially in the typically complex exposures that record paleoearthquakes.

1.2.3 The Incompleteness of the Paleoseismic Record

The geologic record of paleoearthquakes is incomplete because (1) many earthquakes are too small to produce observable primary or secondary evidence, (2) special conditions found at few sites are needed to form the most unambiguous types of evidence, and (3) much evidence created by morphogenic earthquakes is quickly eroded, disturbed, or destroyed by common surficial processes.

Primary evidence is not produced by earthquakes that occur on faults at great depth, or those below a certain magnitude threshold of formation, because the resulting surface deformation (or the sedimentary response to it) is too small to be measured (Fig. 1.4). The magnitude threshold of surface faulting varies according to the type of fault, hypocentral depth, material properties of rocks adjacent to the fault, surface site conditions, and the tectonic stress regime. Various compilations of historic data indicate that earthquakes smaller than moment magnitude (M) 5 have not ruptured the surface (summarized in Wells and Coppersmith, 1994; see Appendix 1 of this book for an explanation of magnitude scales). Thus, even for shallow earthquakes, M 5 is probably a lower limit for detecting paleoearthquakes from fault-rupture evidence (Chapter 9). Identifying past earthquakes from folded or tilted surfaces above a fault is dependent on (1) the degree to which identified deformation is coseismic and (2) the precision with which paleodatums, such as shorelines or river terraces, can be measured. In most cases, the precision of such measurements is much lower than the precision of measuring displaced surfaces or strata that extend across faults or folds, and so the lower magnitude limit for detecting paleoearthquakes from evidence of folding or tilting is normally higher than the lower magnitude limit based on evidence of faulting.

Many secondary types of paleoseismic evidence have a potentially lower magnitude threshold of formation than does primary evidence (Fig. 1.4). Even at long durations of shaking, ground accelerations on the order of 0.1 g are necessary for liquefaction (Chapter 7). For a site located directly over the hypocenter of an earthquake, these accelerations can be produced by earthquakes as small as M 5 (Joyner and Boore, 1988), which means that the magnitude threshold for producing liquefaction is (coincidentally) similar to the magnitude threshold for producing significant earthquake damage. Keefer (1984) suggests even lower magnitude thresholds for triggering various types of landslides (Chapter 8).

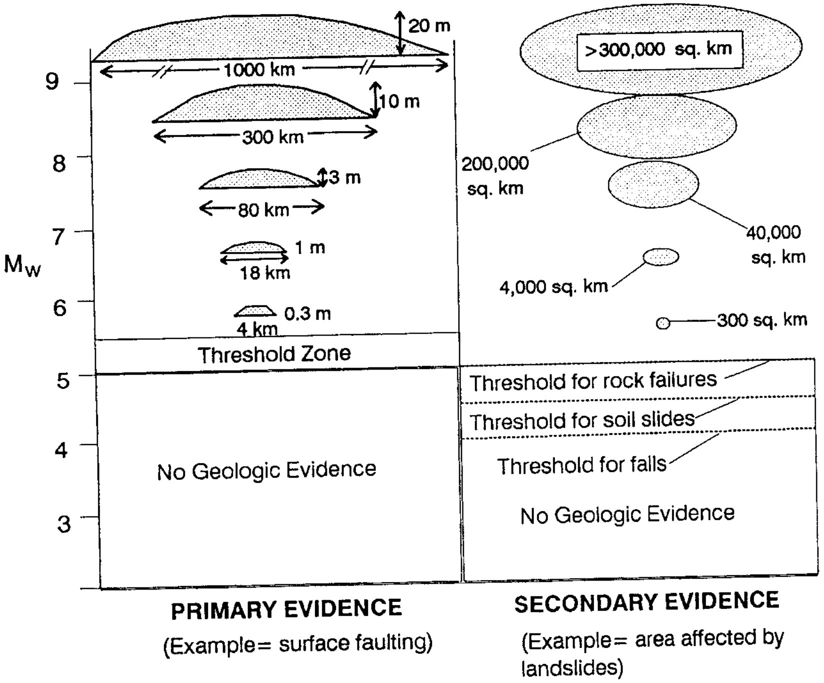

Figure 1.4 Schematic diagram showing the increase in size and extent of two types of paleoseismic evidence with increasing earthquake moment magnitude (M_w), based on measurements following historic earthquakes. The left side of the diagram shows the dimensions of surface faulting (primary evidence) observed in historic earthquakes of various magnitudes. Shaded areas schematically represent the dimensions of surface deformation but are not to scale. Values for lengths (beneath shaded areas) and maximum displacement (to right of shaded areas) are from Wells and Coppersmith (1994). The threshold zone, showing the lower magnitude limit of surface faulting earthquakes, follows Bonilla (1988). The right side of the diagram shows areas affected by coseismic landsliding (secondary evidence) from Keefer (1984); areas are not to scale. The largest area (>300,000 km^2) is for the M_w 9.2 1964 Alaskan earthquake.

Even during earthquakes large enough to produce measurable surface deformation, *special site conditions* are commonly needed to form or preserve recognizable primary or secondary evidence. Relatively flat surfaces in arid areas unobscured by vegetation make even small scarps easily mappable, whereas similar scarps go undetected in rugged, heavily forested terrain (Chapter 3). Sand blows and dikes require a capping layer of low permeability into which they can intrude (Chapter 7). Tsunamis rarely deposit identifiable beds unless abundant sand lies in their paths (Chapter 5). Lateral slip along strike-slip faults may be difficult to recognize unless stream valleys, shorelines, or other linear landforms cross the fault at a high angle. In a similar manner, the absence of secondary ground failures at a site may reflect a lack of material susceptible to failure, rather than an absence of strong ground shaking (Chapter 8). For example, fluctuations in the groundwater table may make sediment susceptible to liquefaction for only part of the year. However, where surface materials can be reasonably inferred to have been susceptible to shaking-induced failure for long periods of time and have not failed, this negative evidence is a powerful indication that ground shaking has not exceeded certain limits (see Chapters 7 and 8).

In those cases where special conditions allow paleoseismic features to form, such features may still require other special conditions to be preserved (Fig. 1.5). Along coasts that suddenly subside during great subduction-zone earthquakes, the preservation of sand sheets spread by coseismic tsunamis is ensured by quick burial with estuarine mud. But on nonsubsiding coasts impacted by tsunamis, such sheets are commonly quickly eroded or made unrecognizable by bioturbation (Chapter 5). Tree throw and other forms of soil bioturbation also commonly destroy evidence of liquefaction in humid climates (Chapter 7). Due to these types of active surface processes, the most recent prehistoric earthquakes are the most easily studied because evidence of them is most abundant and best preserved. To a large degree, the success of paleoseismic studies depends on the ability of investigators to locate sites where surficial processes quickly bury paleoseismic evidence, or where those processes proceed at rates that at least do not significantly erode or disturb the evidence.

In most cases, the *preservation* of primary or secondary evidence of past earthquakes is a matter of the relative rates of erosion and deposition versus deformation (e.g., Wallace, 1986; Schumm, 1986; Bull, 1991). Where deformation rates exceed the rates of geomorphic processes, paleoseismic landforms are created; where the reverse is true, the paleoseismic evidence preserved is likely to be stratigraphic (Fig. 1.5). For example, small fault scarps on steep slopes or in humid climates (where erosion rates are high) may be eroded or buried in a few hundred years, whereas scarps on flat surfaces or in arid climates (where erosion rates are low) may survive for tens of thousands of years. At present, the number of published studies of primary and secondary evidence in arid and semi-arid climates dwarfs the number of studies of evi-

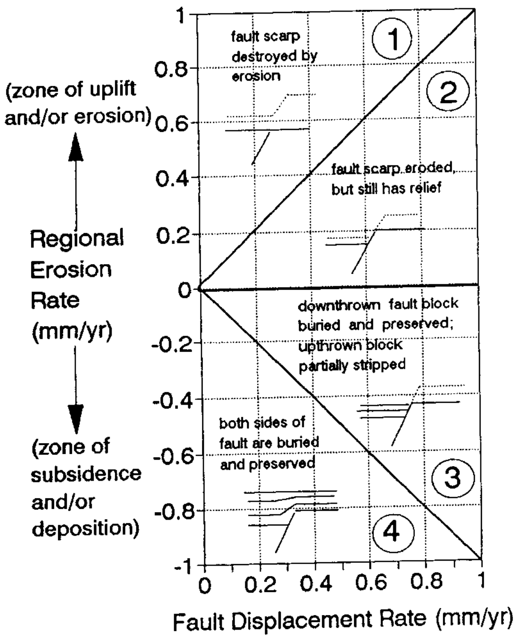

Figure 1.5 Schematic diagram showing the effects of relative rates of deformation versus geomorphic process on the preservation of a fault scarp (an example of primary, on-fault evidence). Many other types of paleoseismic features are subject to the same effects. In quadrant 1 (circled number), the regional erosion rate exceeds the fault displacement rate and the scarp is rapidly destroyed. In quadrant 2, the fault displacement rate is greater than the regional erosion rate, so the scarp is partially eroded yet retains some relief. In quadrant 3, the fault outcrops on a landscape undergoing slow subsidence and deposition, but the scarp is still partially preserved because the fault displacement rate is greater than the regional deposition rate. In quadrant 4, both sides of the fault are buried by sediments deposited at a more rapid rate than the rate of fault displacement. No surface scarp is formed under these conditions, but evidence of paleoseismicity is preserved as onlapping strata in the subsurface.

dence in humid and polar climates. This unbalanced climatic emphasis, a greater reflection of where paleoseismologists have worked than of where morphogenic earthquakes have occurred, results in an unavoidable emphasis in this book on features formed in dry climates where paleoseismic landforms are easily observed.

1.2.4 Underrepresentation versus Overrepresentation of the Paleoseismic Record

A critical issue in many seismic hazard assessments is the extent to which a particular paleoseismic record underrepresents or overrepresents the number

of morphogenic earthquakes during a given period of time. The difficulty of finding well-preserved paleoseismic features has made *underrepresentation* an accepted limitation of paleoseismology since its beginings (Sieh, 1981), whereas the potential for *overrepresentation* is less widely discussed (Nelson and Manley, 1992; Sims and Garvin, 1995). The potential for *both* underrepresentation and overrepresentation should always be addressed in reports of paleoseismology investigations.

As discussed previously, the record of large earthquakes in most climatic and tectonic settings is incomplete due to lack of creation or preservation of evidence. Deformation during large recent earthquakes may obscure evidence of smaller, older earthquakes. Coseismic uplift of several meters can raise a marine abrasion platform well above the zone of wave erosion, but uplift of 0.3 m during a much smaller earthquake may produce only a small marine notch, which will be quickly eroded. In a similar way, a small, steep scarp produced by a recent earthquake may be recognizable on a large, gentle scarp produced by an earlier earthquake; but if a large recent scarp forms on an older small scarp during a large earthquake, the older scarp will almost certainly be obscured by the younger scarp. The initial incompleteness of paleoseismic records and the progressive erosion or disturbance of evidence over time means that the longer the span of time considered, the more incomplete records are likely to be (Ager, 1993).

Paleoseismologists may overestimate the number of past large earthquakes through incorrectly interpreting nonseismic features as evidence of paleoearthquakes. The principle of *geomorphic convergence* or *equifinality* (Chorley *et al.*, 1984; Schumm, 1991) states that similar-appearing landforms can be produced by different, unrelated geomorphic processes. For example, Solonenko (1977a, pp. 41–42) defined seven types of *pseudotectonic* features that mimicked surface fault rupture in central Asia. They include (1) fissures associated with volcanic doming (and collapse) and diapirs from salt tectonics or fractures at fold axes, (2) linear grooves and troughs related to glaciation and ice-marginal drainage, (3) linear canyons excavated along zones of weak rock, (4) gravitational spreading features in high-relief, glaciated areas, (5) selective erosion along fault-line scarps, (6) permafrost features such as frost churning and thermokarst, and (7) man-made features such as old irrigation systems and roads. In the realm of secondary evidence, widespread landslides or rapid sedimentation events in rivers, lakes, and coastal environments caused by infrequent, but severe storms can produce evidence similar to that induced by earthquake shaking (Chapter 5). In addition, a wide variety of nonseismic soft-sediment deformation features mimic similar structures formed by earthquake-induced liquefaction (Chapter 7).

The long-term rate of earthquake activity may also be overestimated if morphogenic earthquakes on a structure are clustered within the time period of preserved geologic evidence. Closely spaced earthquakes recorded by paleoseismic evidence during the short or medium-term window of Fig. 1.1 might lead to a large overestimate of the total number of events that have occurred on a structure over longer periods of time.

Another common way to overinterpret the paleoseismic record is to infer coseismic fault slip from the cumulative tectonic deformation caused partly by gradual interseismic deformation (Fig. 1.2). Laterally offset streams, deformed stream terraces, faceted rangefront spurs, raised marine terraces, and other landforms may have been formed, at least in part, by nonseismic deformation, often termed *creep*. For example, raised shoreline evidence of uplift and tilting of Sado and Ashima Islands on the west coast of central Japan led investigators to conclude that cumulative deformation was the result of earthquakes like those of the past 200 years (Nakamura *et al.*, 1964; Ota *et al.*, 1976). But if some of the slip on the faults beneath such features occurs as creep, then the magnitude and/or number of paleoearthquakes in these areas has been overestimated.

The degree to which coseismic fault slip can be distinguished from interseismic slip (creep) depends not only on the proportion of coseismic (morphogenic) to nonseismic slip but (as with the preservation of all paleoseismic evidence) on the relative rates of local processes (Fig. 1.5). At many sites it is difficult to distinguish the morphologic or stratigraphic responses to rapid preseismic or postseismic deformation from responses to coseismic fault slip. The abrupt change in depositional processes associated with a significant (>1-m) vertical coseismic offset is relatively easy to detect. In most climatic settings a wedge of colluvial debris forms adjacent to near-vertical scarps soon after the surface faulting event (Chapter 3). Coseismic offset on strike-slip faults typically creates little vertical relief, but fault slip can laterally shift zones of erosion and deposition near the fault in ways that are seldom duplicated by nontectonic processes (Chapter 6). Coseismic uplift and subsidence in coastal areas may similarly induce nearly instantaneous lateral shifts in littoral environments that can be recognized as too large to be caused by nontectonic coastal processes (Chapter 5). But when the amount of coseismic displacement is small (typically <0.5 m) and the rates of sedimentation or erosion approach rates of creep, the proportion of coseismic to nonseismic slip and the number of paleoearthquakes may be difficult to determine (Chapter 9). For example, rapid creep may lead to steepened gradients near the fault and to a change in the rate of erosion or deposition (Schumm, 1986).

The issues of the overrepresentation and underrepresentation of the paleoseismic record are frequently complicated by attempts to include qualitative assessments of seismic risk in paleoseismic interpretations. For example, in instances where the origin of some features in an exposure is ambiguous, all features may be assumed to represent past large earthquakes in order to produce a conservative seismic hazard assessment. Such procedures incorrectly mix paleoseismic interpretations with engineering, societal, and political concerns (Reiter, 1990). The most useful assessments are those where all assumptions are clearly stated and the reasoning behind them fully explained.

Problems arising from overrepresentation and underrepresentation can be reduced by applying large doses of caution when interpreting paleoseismic evidence. Tests of hypotheses should employ several different types of data (e.g., trenching, shallow geophysics, paleontology) with constant attention to possible nonseismic causes for field relations. Multiple, independent lines of evidence pointing to the same hypothesis instill confidence in interpretations. We limit our remaining advice on identifying and interpreting paleoseismic features to the following four quotations:

> *The great investigator is primarily and preeminently the man who is rich in hypotheses. In the plentitude of his wealth he can spare the weaklings without regret; and having many from which to select, his mind maintains a judicial attitude. The man who can produce but one, cherishes and champions that one as his own, and is blind to its faults. (Gilbert, 1886, p. 287)*
>
> *I cannot give any scientist of any age better advice than this: the intensity of the conviction that a hypothesis is true has no bearing on whether it is true or not. (Medawar, 1979, p. 39)*
>
> *Perhaps some kinds of field evidence are destined to remain ambiguous. (Vita-Finzi, 1986, p. 23)*
>
> *Progress in paleoseismology has been exciting and gratifying; new advances seem to be just ahead. I fear, however, that at times we have exploited some of our new ideas too enthusiastically. In our enthusiasm, our interpretations can be, and some may have been, carried too far, too soon. I believe that some statements that I, and possibly others, have made in public have been too far-reaching, too positive, and have lacked appropriate caveats of uncertainty. (Wallace, 1987, p. 12)*

1.3 Prehistoric Earthquake Recurrence and Dating

1.3.1 Late Quaternary Dating Methods

Dating methods applicable to the late Quaternary (the past 130,000 years) are a critical aspect of neotectonic studies. Without ages we cannot determine rates of tectonic processes over time spans longer than those of historic records. The central role of dating in paleoseismology, especially as applied in earthquake hazard assessment, is now widely recognized (C. R. Allen, 1986; Crone and Omdahl, 1987). Such recognition has helped stimulate the development of methods with the greatest potential for dating recent earth deformation, such as optical dating (e.g., Forman, 1989; Fain *et al.*, 1992), high-precision conventional and accelerator mass spectrometer (AMS) radiocarbon dating (Linick *et al.*, 1989; Atwater *et al.*, 1991; Sieh *et al.*, 1989; Nelson and Atwater, 1993), surface exposure dating (Dorn and Phillips, 1991), and tree-ring dating (Jacoby, 1989).

A widening array of Quaternary dating methods is potentially applicable to solving problems in paleoseismology. In the past 15 years some completely new methods have been developed and other methods have become far more precise, accurate, and applicable to new types of sample materials. Early overviews of dating methods applicable to neotectonic studies (e.g., Hatheway and McClure, 1979; Mahaney, 1984) have been supplanted by Pierce (1986) and by more general collections of papers that provide detailed discussions of many Quaternary dating methods (Easterbrook, 1988; Rutter *et al.*, 1989; Rosholt *et al.*, 1991; Smart and Frances, 1991; Rutter and Cato, 1993). Pierce's (1986) review is particularly valuable for paleoseismologists because he rates the applicablility of 26 dating methods to studies of active tectonism, explains how they can be used to determine fault histories, and provides a relative assessment of the precision of each method in each age range.

Following Colman *et al.* (1987), Quaternary dating methods can be grouped into numerical age, calibrated age, relative age, and correlated age methods based on the type of result they produce (Table 1-2). *Numerical age* methods yield ages with stated errors derived from analytical standards. *Calibrated ages* are based on systematic changes that depend on environmental variables such as temperature and must be calibrated using numerical ages [this use of the term calibrated differs from that used in radiocarbon dating (Stuiver and Kra, 1986), which is a numerical-age method]. *Relative age* methods provide only a relative ranking of ages on an ordinal scale. *Correlated age* methods are not really dating methods; they rely on a comparison to a standardized series of measurements (Rutter *et al.*, 1989). Although they do not yield ages with easily quantified errors, relative age and correlated age methods are of fundamental importance in providing crosschecks on numerical ages and in allowing numerical ages to be applied to other sites that lack numerical age control.

We make no attempt in this book to further review specific Quaternary dating methods. Table 1-2 provides an initial guide to available methods and examples of particular methods appear in the dating sections of later chapters. Papers about dating methods of potential use to paleoseismologists are published almost every day. We urge, however, all paleoseismologists to keep abreast of recent developments in radiocarbon dating, the most widely applicable dating method in paleoseismology. Few other methods are as accurate as ^{14}C dating in the time span of most interest to paleoseismologists (the Holocene). The past decade has seen a great deal of research devoted to understanding and quantifying the many factors that affect the accuracy and precision

Table 1-2

Classification of Quaternary Dating Methods Applicable to Paleoseismology[a]

Type of result					
Numerical age		Calibrated age	Relative age	Correlated age	
Type of method					
Calendar-year	Isotopic	Radiogenic	Chemical and biological	Geomorphic	Correlation
Historical records	*^{14}C*	*Luminescence*	Amino acid racemization	Soil profile development	*Lithostratigraphy*
Dendrochronology	K-Ar and ^{39}Ar-^{40}Ar	Electron spin resonance	Obsidian and tephra hydration	Rock and mineral weathering	*Tephrochronology*
Varve chronology	*Uranium series*		*Lichenometry*	*Progressive landform modification*	Paleomagnetism
	Cosmogenic isotopes other than ^{14}C (^{210}Pb, ^{36}Cl)		Soil chemistry	Rate of deposition	*Fossils*
			Rock varnish chemistry	*Relative geomorphic position*	*Artifacts*
					Stable isotopes

[a] Modified from Colman *et al.* (1987). Methods in italics are particularly applicable to dating paleoearthquakes in the Holocene. Thick line indicates the type of result most commonly produced by the methods below it; thin line indicates the type of result less commonly produced by the methods below it.

of radiocarbon ages, and work continues to reduce the disturbing degree of interlaboratory analytical variability documented in some recent studies (International Study Group, 1982; Scott *et al.*, 1992). Taylor (1987, p. 15., 106) groups the factors that affect ^{14}C ages into *sample context* (provenance) factors, *sample contamination* factors, *statistical and experimental* factors, and *systemic* factors. Interpretation of ^{14}C ages requires familiarity with the effects of all such factors on ages. Fortunately, the limitations on the accuracy of ages imposed by different types of samples and different methods of pretreatment and analysis (e.g., Waterbolk, 1983; Mook and van de Plassche, 1986; Stafford *et al.*, 1991) are now widely appreciated. Calibration curves (e.g., Klein *et al.*, 1982; Stuiver and Reimer, 1993) that account for the fluctuation of ^{14}C production in the atmosphere are widely used to correct ages to approximate calendar years. Although radiocarbon methods will never be able to distinguish earthquakes that occurred less than a few years apart, recent improvements in the precision of both conventional (Stuiver and Polach, 1977) and AMS radiocarbon methods have provided solutions to earthquake recurrence problems that would not even have been investigated 10 years ago (e.g., Sieh *et al.*, 1989; Atwater *et al.*, 1991). Overviews of these and many other recent ^{14}C developments can be found in Stuiver and Kra (1986), Taylor (1987), Geyh and Schleicher (1990, pp. 162-180), Pilcher (1991), and Taylor *et al.* (1992).

When paleoseismologists suspect that a particular dating method may be useful in solving a problem they should contact a specialist in that dating method. Specialists who have current experience with a particular method can provide advice on optimum sampling strategies, sample requirements, costs, and time required for analysis-factors that frequently differ from year to year and from laboratory to laboratory. Samples collected without the advice of a geochronology specialist may not be worth analyzing. Specialists are also aware of other related dating methods, particularly those still in the developmental stage, and they can suggest other specialists or laboratories who may be able to help with dating problems. Keep in mind, however, that experimental dating methods or those in the early stage of development are unlikely to provide paleoseismologists with useful ages unless a substantial budget for a large number of analyses is available. Paleoseismologists should thoroughly discuss all sampling issues with potential dating laboratories *before* spending valuable field time collecting samples.

Our final comment about dating is that it is difficult to overemphasize the value of obtaining (1) multiple ages on separate samples associated with the same event using the same methods and (2) ages from different types of dating techniques used on different types of sample materials associated with the same event. We know of no field situations where a single analysis on a single sample by any dating method provides a definitive age for a paleoearthquake. One approach is to average multiple ages of the same type on the same type of sample to reduce errors (e.g., Nelson and Atwater, 1993) or to sample above and below the horizon of interest (Biasi and Weldon, 1994a; Chapter 6). All types of dating techniques generate significant analytical and sample-context errors, and for many samples the latter type of errors is commonly a substantial percentage of the age (Pierce, 1986). Many factors that influence ages, particularly in calibrated age and relative age methods, are poorly understood. Through comparisons of ages on the same events determined with different methods, the errors involved in the different methods can be more accurately estimated and ways developed to improve their accuracy and precision (e.g., McCalpin *et al.*, 1994). Different methods also allow dating of different intervals of time, which has an important bearing on understanding the complete recent history of faults (Fig. 1.1).

1.3.2 Patterns in Recurrence

The *recurrence* (timing) of paleoearthquakes is a critical characteristic in assessing the hazard from large earthquakes. In active tectonic regions the recurrence period of moderate to large earthquakes may be so short that they pose a greater hazard than the largest earthquakes, which occur much less frequently (e.g., Nishenko and Bollinger, 1990; Adams, 1992). In contrast, in regions where fault slip rates are low, the recurrence intervals for large (morphogenic) earthquakes may be so long that the earthquakes are not a significant hazard for facilities with design lives of less than 200 years.

The assumption that earthquakes of roughly the same size occur with regular recurrence has been attractive and powerful in the sense that it allows calculation of average recurrence intervals from short- or long-term deformation (slip) rates (e.g., Wallace, 1970; Shimizaki and Nakata, 1980; Sykes and Quittmeyer, 1981; Nishenko and Buland, 1987). But this assumption may not apply to the long-term history of many faults; historic records of large earthquakes show a great deal of variability in their spatial and temporal patterns of recurrence (Allen, 1975). In the plate-boundary regions of the Pacific, such variability appears to be the rule rather than the exception (Thatcher, 1990). Not surprisingly, the results of some of the most detailed paleoseismology studies mirror those of the historic record-as the number and precision of ages for past earthquakes increase recurrence patterns become more complex (e.g., Sieh *et al.*, 1989; Fumal *et al.*, 1993; Machette *et al.*, 1992a, b). The degree of *earthquake clustering* and the extent to which earthquakes on one fault *trigger* earthquakes on adjacent faults (termed *contagion* by Perkins, 1987) are of increasing concern in paleoseismology studies (Chapter 9).

The relations among fault slip rates, recurrence patterns, and the time interval of observations are nicely illustrated by Pierce (1986; Fig. 1.1). Depending on the length and age of the *window of observation,* slip rates (and hence inferred earthquake recurrence and perceived hazard) may vary by an order of magnitude. Figure 1.1 also clearly illustrates the importance of attempting to date individual earthquakes when assessing earthquake hazards. Without multiple ages that span much of the recent history of a fault there is little hope of accurately forecasting its future activity.

Earthquake recurrence may also have a significant impact on the types of evidence that can be used to infer paleoearthquakes. Where large earthquakes occur frequently, episodic shaking is commonly the dominant process in producing some types of slope or ground failures (Chapter 8). In such highly active areas these features can be reasonably inferred to have been caused by earthquakes. For example, recent work in New Zealand shows strong correlations between the times of major historic earthquakes on the Alpine fault and ages for rockfall events derived from lichen diameter measurements (Bull *et al.,* 1994). But where earthquakes are smaller or much less frequent than along major fault zones with high slip rates, nontectonic processes may produce most slope and ground failures. In another example, if great earthquakes occur every few hundred years off the coasts of Washington and Oregon, then most abruptly buried tidal-marsh soils and continental-shelf turbidites in the region were probably produced during earthquakes (Adams, 1990; Atwater *et al.,* 1995). However, if the recurrence of such events is a thousand or more years, many of these features must have formed through nonseismic processes (Nelson *et al.,* 1996; Chapter 5).

1.3.3 Dating Accuracy and Precision and Their Relation to Recurrence

Few studies of past earthquakes have adequately discussed the relations among the accuracy and precision of the methods used to date landforms or sediments associated with paleoearthquakes and the times the earthquakes occurred (Rhoades *et al.,* 1994; some exceptions include Sieh *et al.,* 1989; Nelson, 1992c; McCalpin and Nishenko, 1996). Particularly at plate boundaries where earthquakes occur frequently, determining recurrence patterns is commonly limited less by the applicable types of dating methods than by the accuracy and precision of the methods used. A few ages of high accuracy and precision may provide as much information about the history of a fault as many ages of low precision (Fig. 1.1).

Accuracy is a measure of how close an age is to the time of formation or death of the dated material; *precision* is a measure of the analytical reproducibility of a method, commonly expressed as two standard deviations about a mean. But neither accuracy nor precision measure what is frequently the largest source of error in paleoearthquake dating-sample *context error,* or the error involved in inferring the time of an earthquake from the age of an accurately dated sample (termed *provenance error* by Taylor, 1987, p. 106). In many paleoseismic studies, errors involving the stratigraphic or geomorphic context of samples are frequently inadequately discussed or not even acknowledged because such errors are difficult to estimate. By ignoring context errors and applying ages with only their analytical errors as if they were accurate estimates of the times of past earthquakes, many paleoearthquake histories have been presented with an unjustified degree of accuracy.

1.4 Estimating the Magnitude of Prehistoric Earthquakes

Both primary and secondary evidence are used to estimate the magnitude of paleoearthquakes. Paleomagnitude estimates involve many assumptions, and large errors are often associated with the many parameters that need to be measured in order to estimate magnitudes. The best approach is to use several methods to estimate magnitudes. For a more detailed discussion of this topic see Chapter 9.

Because primary evidence is produced directly by fault rupture, the geographic distribution of primary evidence is related to the area of fault rupture and, hence, earthquake magnitude. The length of fault surface rupture is the parameter most commonly used to estimate magnitude (Fig. 1.4). Estimates of the *surface rupture length* during past earthquakes are compared with compilations of worldwide data on surface rupture lengths during historic earthquakes to estimate ranges of earthquake magnitudes for particular paleoearthquakes (Wells and Coppersmith, 1994). Variations on this procedure involve estimating the area of the fault plane that slipped during past ruptures or the seismic moment, a measure of the total energy released during the earthquake (Kanamori, 1977). In the cases of some of the largest plate-boundary earthquakes along subduction-zone coasts, the lengths or areas of the zones of coseismic uplift or subsidence can be used to estimate earthquake magnitudes (Atwater *et al.,* 1995).

Primary evidence that reflects the relative amount of slip on faults or the warping or folding of surfaces above faults may also be used to estimate magnitude. As with fault length, these methods rely on empirical comparisons with amounts of deformation recorded during historic earthquakes of different magnitudes (Fig. 1.4). Examples include use of the amount of lateral offset of young stream channels, the thickness of colluvial wedges in fault exposures, or the amount of uplift of former shorelines to distinguish magnitude 6 earthquakes from earthquakes of magnitude 7 to 8 (Chapters 3 through 6).

Secondary evidence is less commonly used to infer paleomagnitudes than primary evidence, but in some cases it may provide more accurate estimates of magnitude than primary evidence. More importantly, secondary evidence is the only evidence available for those earthquakes in which the seismogenic fault does not rupture the surface. Mapping the distribution of secondary evidence, such as liquefaction features or earthquake-induced landslides, over a large area may reveal a pattern of variable ground motion intensity. From the areal extent of the features and their relative size, paleoearthquake magnitude may be inferred using empirical methods based on historic observations (Fig. 1.4; Chapters 7 and 8). In addition, engineering-based static and dynamic analyses of the failed material can yield estimates of shaking strength that are independent of historical-empirical correlations.

The accuracy of estimating magnitudes from both primary and secondary features is dependent on the assumption that correlated features are the product of the same paleoearthquake. But several moderate-magnitude paleoearthquakes closely spaced in time may have created features that, after several hundred or thousand years, appear to be the product of one large paleoearthquake. The Dixie Valley-Fairview Peak earthquakes of 1954 (M 7.1 and M 6.8) created two zones of fault scarps 123 km in length in the span of 4 minutes (Doser and Smith, 1989). If the entire zone of scarps were attributed to a single earthquake, empirical relations would suggest a magnitude 7.8 earthquake. Multiple great earthquakes (M > 7.8) have also uplifted or submerged many tens of kilometers of coast as little as a few minutes to a few days apart (e.g., Ando, 1975). Thus, even with significant improvements in dating precision and accuracy, paleoseismological methods will rarely be able to show conclusively whether widespread primary or secondary evidence was produced by one very large earthquake or a series of smaller morphogenic earthquakes occurring less than a few years or decades apart.

1.5 THE EARLY DEVELOPMENT OF PALEOSEISMOLOGY

Not surprisingly, paleoseismology developed first and has grown fastest in countries where rates of tectonic processes are high and where geologic investigations are supported by a sophisticated scientific infrastructure. Our brief outline of some early developments of paleoseismology (partly condensed from Vita-Finzi, 1986; Wallace, 1987; Vittori *et al.,* 1991) focuses on some of the significant advances in the United States, Japan, Russia, and New Zealand.

The notion that the dramatic topography of some regions was created little by little during repeated earthquakes has a long history, extending through most of the current millennium (Vita-Finzi, 1986, p. 9; Bonilla, 1991). The main impetus to understand the history of recent faults arose in the late 1800s and early 1900s from detailed accounts of historic ruptures along active fault zones (Richter, 1958). For example, McKay (1886) recognized that scarps produced by earthquakes in New Zealand in 1848 and 1855 were identical to larger fault-zone features with similar origins, and ruptures produced by the 1891 Nobi earthquake in central Japan led Koto (1893) to similar conclusions. Other earthquakes of this period that stimulated much initial paleoseismic research include the 1906 San Francisco event in the United States (Lawson *et al.,* 1908), the Assam, India, earthquake of 1897 (Oldham, 1899), and the 1923 Kanto earthquake in central Japan (Kaizuka, 1976).

North American investigators frequently look back to the work of Gilbert (1890, pp. 340-362; 1928) who used a number of modern paleoseismic concepts to interpret normal fault scarps along the Wasatch fault in Utah (Wallace, 1980b; Machette and Scott, 1988). To Gilbert, variable fault scarp heights on different alluvial surfaces suggested multiple surface faulting events. By measuring fault scarp heights, he also estimated fault displacement per event and deduced that events were no more frequent during the late Pleistocene high stand of pluvial Lake Bonneville than during its Holocene low stand. His letter to the inhabitants of Salt Lake City, Utah (Gilbert, 1884), on the inevitability of future large earthquakes is one of the first earthquake forecasts based on prehistoric, rather than historic, seismicity. But in most early studies little attempt was made to relate earthquake features which had been carefully described by these early geologists to a specific number or size of paleoearthquakes (Wallace, 1980b). In the early 1900s seismology was still a developing science and could not provide much theoretical support for descriptive fault studies.

In the period during and shortly after the two world wars most paleoseismic studies remained largely descriptive and focused on large landforms, such as fault scarps and raised alluvial and marine terraces. Surface faulting during the 1929 Murchison earthquake (Henderson, 1937) prodded New Zealand geologists into a concerted search for evidence of prehistoric faulting (e.g., Speight, 1938; Cotton, 1950) that culminated in several papers summarizing the geomorphic evidence of paleoseismicity throughout New Zealand (Wellman, 1952, 1953, 1955; Bowen, 1954; Lensen, 1958). In a similar way, Kuno (1936) recognized that the 1-km offset of Pleistocene features on the Tanna fault in Japan was of a similar nature to the 2- to 3-m offset created during the 1930 Idu earthquake. The height and distribution of marine terraces in Japan were used to infer several scales of active folding in Japan during this period (Otuka, 1932), and interseismic crustal movements were distinguished from coseismic movements (Yamasaki and Tada, 1928). Coastal studies of uplift of shorelines and tilting of marine terraces, which began following the 1923 Kanto earthquake (Kaizuka, 1993), progressed rapidly in the decades after the subduction-zone earthquakes of 1946 along the Nankai trough (e.g., Sugimura and Naruse, 1954; Yoshikawa *et al.,* 1964). In Russia, Florensov and Solonenko (1963) used their observations on the rupture trace of the 1957 Gobi-Altai earthquake (M 8.1) with their mapping of late Quaternary fault scarps in Russia and Mongolia to infer that some fault-zone landforms record identifiable paleoearthquakes. In a similar study in Nevada, USA, Slemmons (1957) mapped normal fault scarps along the trace of the Dixie Valley-Fairview Peak earthquakes of 1954. In 1958 Richter briefly summarized much of this early work in his book *Elementary Seismology*.

Paleoseismology emerged as a distinct discipline during the late 1960s and early 1970s. Florensov (1960) and Solonenko (1962, 1970, 1973) were among the first to propose a *paleoseismogeological method*, with an emphasis on the traces of prehistoric surface faulting or "paleoseismodislocations" (палеосейсмодислокаций) and seismo-gravitational failures. The word *paleoseismicity* first appeared in the title of an English-language article about fault plane microgrooves (Engelder, 1974) and the term was being used in Japanese publications (e.g., Huzita and Ota, 1977, p. 135) shortly after. This was the beginning of the "modern" period of paleoseismology in the sense that stratigraphic and/or geomorphic data were used to interpret the characteristics of individual prehistoric earthquakes. For example, slip rates were calculated from the cumulative displacements of landforms of approximately known age, in settings ranging from strike-slip offset of river terraces (Lensen, 1968) to uplift of marine terraces during subduction-zone earthquakes (Yoshikawa *et al.*, 1964). The displacements and rupture lengths observed in historic earthquakes were used to infer the magnitudes of paleoearthquakes, based on the heights and lengths of faults scarps (Slemmons, 1977; Bonilla *et al.*, 1984). Studies of subduction-zone features during this period in Japan (Ota, 1975; Matsuda *et al.*, 1978; Nakata *et al.*, 1979) and documention of the effects of the great earthquakes of 1960 (Plafker and Savage, 1970; Kaizuka *et al.*, 1973) and 1964 (Plafker, 1965, 1969b, 1972) in Alaska and Chile led to advances in the understanding of the earthquake deformation cycle at subducting plate boundaries that have stongly influenced paleoseismic studies since that time. In the continental United States in the 1960s, early work on the San Andreas fault by Wallace (1970) and others, the 1971 San Fernando earthquake (M 6.6) in southern California, and the discovery of young faults in excavations during construction of nuclear power plants and other large facilities in California spurred many investigations into the stratigraphic expression of Quaternary faulting. During the latter part of this period the development of modern paleoseismology in the United States was strongly influenced by Sieh's (1978a, b) detailed geomorphic and stratigraphic work on the San Andreas fault in California. Although Sieh was not the first to use trenches to expose a fault zone (e.g., Converse, Davis and Associates, 1968; Clark *et al.*, 1972), he was the first to demonstrate to a wide audience that earthquake chronologies comparable to some of those based on historic records could be reconstructed through the meticulous mapping and dating of trench-wall sediments. Meehan (1984) and Bonilla (1991) describe these early days of paleoseismology in the United States, particularly the extensive efforts made to derive paleoearthquake magnitude, displacement, and recurrence data from fault-zone exposures.

In the past decade data collected in some detailed paleoseismic studies have been used to develop important new concepts about the earthquake generation process. For example, Schwartz and Coppersmith (1984) proposed that active faults release strain in large *characteristic* earthquakes of a certain size, presumably controlled by fault-plane dimensions and geometry, crustal properties, and strain rates. This concept was accompanied by a complimentary one of *fault segmentation*, which proposed that large earthquakes repeatedly ruptured the same stretch of a fault without breaking through structural barriers to the next segment (Schwartz and Sibson, 1989a, b). Both of these concepts were based on paleoseismic studies of large strike-slip and normal faults in the western United States. Another area where paleoseismic data generated new concepts was in earthquake recurrence. Shimazaki and Nakata (1980), considering the ages of historic and prehistoric subduction-zone earthquakes in Japan, proposed the *time-predictable* recurrence model. This model stated that the displacement in large earthquakes could be predicted based on the time between earthquakes and the assumption of constant long-term slip rate. Other recurrence models and their relations with the characteristic earthquake and segmentation models are discussed in Chapter 9.

Subsequent to its development in tectonically active countries with well-established research traditions, the field of paleoseismology has expanded into areas of lower deformation rates and into countries with rapidly developing scientific infrastructures. Countries where interest in paleoseismic investigations was minimal 10 to 15 years ago, but where active programs are now ongoing, include Argentina, Britain, Canada (Adams, 1994), China, Costa Rica, Ecuador, Greece, Indonesia, Israel, Italy, Mexico, Norway, the Philippines, Sweden, Turkey, Taiwan, and Venezuela. In some areas, including continental interiors and regions where seismogenic faults fail to rupture the surface ("blind faults"; Stein and Yeats, 1989), this geographic expansion has neccesitated a methodological shift in emphasis to secondary paleoseismic evidence such as paleoliquefaction (Obermeier *et al.*, 1990) and earthquake-induced landslides (Jibson and Keefer, 1993). Another new development is that offshore faults are now a more widely recognized coastal hazard (e.g. Wesnousky, 1986; Clarke and Carver, 1992); marine geophysical techniques are increasingly being used to map the deformation created by subaqueous paleoearthquakes (Chapter 2).

For those interested in learning more about the continuing development of paleoseismology we recommend the following: Wallace (1981, 1986, 1987), Sieh (1981), C. R. Allen (1986), Schwartz and Coppersmith (1986), Slemmons and dePolo (1986), Vita-Finzi (1986), Crone and Omdahl (1987), Schwartz (1988a), Weldon (1991), Pantosti and Yeats (1993), and Yeats *et al.* (1996). Up-to-date references and detailed case histories can be found in the following journal volumes: *Journal of Structural Geology* (1991, Vol. 13, No. 2), *Annales Tectonicae* (1992, supplement to Vol. VI), *Quaternary International* (1992, Vols. 15/16), *Zeitschrift fur Geomorphologie* (1993, Supplement Band 94), Prentice *et al.* (1994), Serva and Slemmons (1995a), *Quaternary International* (1995, Vol. 25, No. 1), and *Journal of Geophysical Research-Solid Earth,* special issue on Paleoseismology (1996).

Acknowledgments

Comments by Silvio Pezzopane, Steve Obermeier, and Bob Bucknam improved this chapter.

Chapter 2

Field Techniques in Paleoseismology

James P. McCalpin

2.1 INTRODUCTION

2.1.1 Scope of the Chapter

This chapter describes common techniques used to collect field data in most paleoseismic investigations, regardless of the tectonic setting. The methods fall into two broad categories, depending on whether paleoseismic features are *landforms* (Sec. 2.2) or have *stratigraphic expression* (Sec. 2.3). Basic geomorphic techniques include locating paleoseismic features with remotely sensed imagery and making detailed topographic maps of paleoseismic landforms. Stratigraphic techniques emphasize the mapping of paleoseismic deformation in subsurface exposures and the finding of buried faults with geophysical methods. The section on trenching (Sec. 2.3.2) is particularly detailed in view of the importance of trench studies in identifying and dating paleoearthquakes.

The techniques described in this chapter are mostly basic methods of geologic investigation as typically applied to unconsolidated sediments by Quaternary geologists (cf. Goudie, 1981). We describe those methods that have been most widely used in previous paleoseismic investigations. Therefore, there is an unavoidable emphasis in this chapter on primary paleoseismic evidence, because the majority of published reports have focused on primary evidence, particularly along continental fault traces. Some studies of secondary evidence (e.g., the paleoliquefaction research of Obermeier *et al.,* 1990; Chapter 7) use similar techniques, whereas others (subduction-zone coastal studies of Atwater, 1987; Nelson, 1992a) use the more classical techniques of Quaternary stratigraphy. Other uncommon methods used in some Quaternary studies (e.g., palynology) may be the most useful in some types of paleoseismic studies, especially in those climatic or geomorphic settings where paleoseismologists have performed little work to date.

Many of the generic techniques described in this chapter, such as fault scarp profiling and trench logging, were developed especially for paleoseismic studies. Other techniques, such as geomorphic mapping (Sec. 2.2), shallow coring, and shallow geophysics (Sec. 2.3), were developed for other types of investigations, and have been adapted for use in paleoseismology. In this chapter we describe only the application of these latter techniques to paleoseismic studies; readers should consult the cited literature for further details on theory, methods, and equipment.

2.1.2 Preferred Sequence of Investigations

An ideal sequence of paleoseismic investigations would progress from the *regional scale* (thousands of square kilometers), to the *local scale* (a few square kilometers), to the *site scale* (1 hectare to a few square meters). In many areas some data on the regional neotectonic setting are commonly available, so the emphasis in most paleoseismic studies is usually on the local and especially the site scales. The sequence of topics in this chapter likewise proceeds from the regional scale (e.g., remote sensing), to the local scale (geomorphic mapping), to the site scale (fault-zone trenching, geophysics).

With the success and growing popularity of *fault trenching,* a misconception has arisen that regional- and local-scale Quaternary geologic mapping is no longer necessary in paleoseismic studies, because trenches provide all needed data on paleoearthquake magnitude and recurrence. Nothing could be farther from the truth. Without careful geomorphic mapping along a fault trace, and establishment of a Quaternary stratigraphic framework, trenching is unlikely to be productive. Every time the author has sited trenches without the benefit of local geomorphic maps, the trenches have yielded useless or ambiguous data, and a second round of trenching has been required based on subsequent detailed local geomorphic mapping. The importance of preliminary Quaternary geologic mapping before subsurface investigation cannot be overemphasized.

2.2 MAPPING PALEOSEISMIC LANDFORMS

The first, and often most fruitful, approach to paleoseismic reconstruction should be careful mapping of Quaternary landforms and deposits in the zone of deformation. *Surficial geologic mapping* helps identify deformed geomorphic surfaces and reveals trends in deformation styles and rates across landforms of different ages. Based on the estimated ages of faulted geomorphic surfaces and/or deposits (Sec. 1.3), and their measured displacements, the following variables can be estimated without recourse to stratigraphic investigation: (1) fault slip or surface deformation rates (Fig. 2.1), (2) displacements or tilting per event, and (3) bracketing ages for deformation events. Geomorphic mapping helps indicate where fault traces are the result of single versus multiple events, the approximate size and timing of paleoearthquakes, and whether paleoearthquakes are within the range of certain dating techniques. As stated earlier, we feel that *trenches should never be sited until the geomorphic relations in the area of investigation are thoroughly understood.*

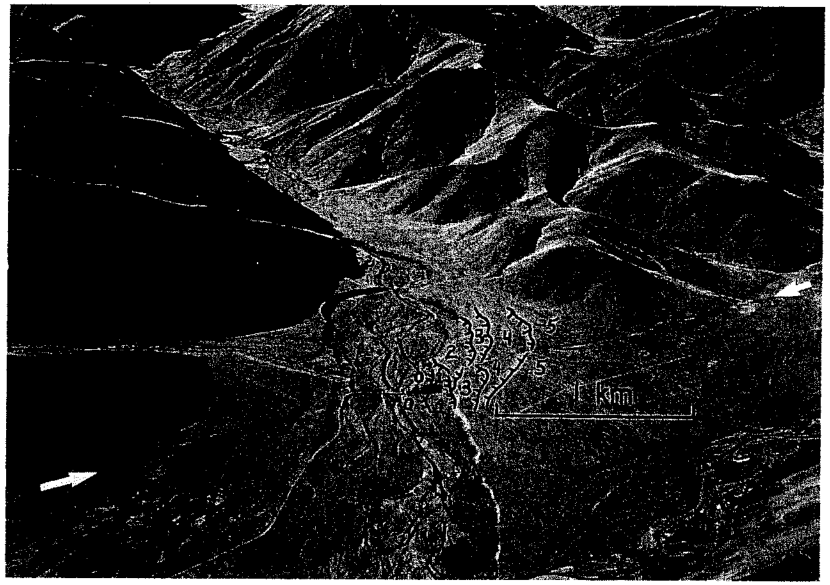

Figure 2.1 Low-oblique aerial photograph taken from a small airplane showing the trace of the dextral Awatere fault (between arrows) at the Saxton River, New Zealand. Six alluvial terraces (0-5), dated by weathering rind thicknesses, are dextrally offset from 8 ± 2 m (terrace 0/1 riser) to 66 ± 5 m (terrace 4/5 riser). Terrace risers are accentuated with black lines, hachures toward lower terrace. Offsets were used by Knuepfer (1992) and McCalpin (1996) to calculate slip rates (3.8 to 7.3 mm/yr) and displacements per event (6 to 8 m).

2.2.1 Locating Surface Deformation

The first step in collecting primary paleoseismic evidence is to identify and map a zone or area of crustal deformation. Active fault traces are the easiest such features to map, and they are expressed at the surface as linear belts of landforms across which vertical relief is evident (i.e., dip-slip faults; see diagrams in Chapters 3 and 5) or where terrain elements are shifted laterally (i.e., strike-slip faults; see diagrams in Chapter 6). Fault traces or narrow folds are usually identified by field inspection, low-altitude aerial reconnaissance, or examination of aerial photographs. (Note, however, that the surface traces of faults created by creep displacement or by *fluid withdrawal* look very similar; cf. Holzer *et al.,* 1979; Jachens and Holzer, 1982; O'Neill and Van Siclen, 1984; Lister and Secrest, 1985).

Almost all commercially available aerial photography is vertical photography, taken with the camera pointing straight down from the aircraft, such that the optic axis is perpendicular to the earth's surface (Fig. 2.2). The geometric properties of such photographs are well known, and *photogrammetric measurements* of true horizontal and vertical distances can be made from stereo pairs. For example, Nelson and Personius (1988) made 298 measurements of vertical surface offset on fault scarps along the Wasatch fault zone, in the United States with 35-year-old black-and-white prints mounted in a photogrammetric plotter (Pillmore, 1989) in a fraction of the time it would have taken to measure scarps in the field.

Cluff and Slemmons (1971) proposed that *low-sun-angle photography* best emphasized the subtle topography along active fault zones (Fig. 2.3). Numerous papers describe the use of various remote sensors for mapping faults and *lineaments,* including satellite scanner images (Glass and Slemmons, 1978; Slemmons, 1981; Wiley *et al.,* 1991; Astaras and Soulakellis, 1991), satellite photography (Muehlberger *et al.,* 1985), side-looking-airborne radar (Wing, 1970), and thermal infrared imagery (Wallace and Moxham, 1967; Sabins, 1967, 1969).

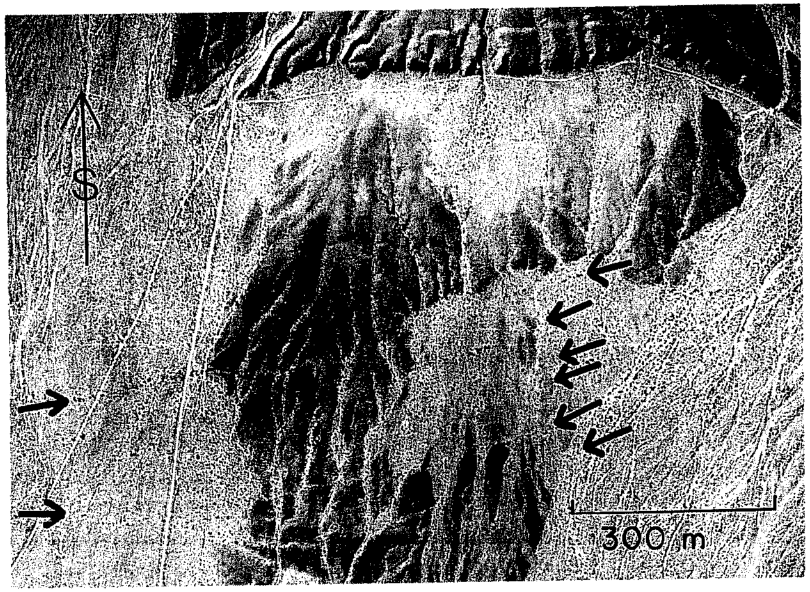

Figure 2.2 Vertical aerial photograph showing east-west-trending normal fault scarps (in shadow at top, and in center) and parallel lineaments (between arrows) that overlie buried faults. Ephemeral streams flow from top to bottom. Note dissection of scarp at top of photo and secondary alluvial deposition on the downthrown fault block at upper center. Lone Mountain fault zone, Nevada. (Photograph courtesy of J. C. Yount.)

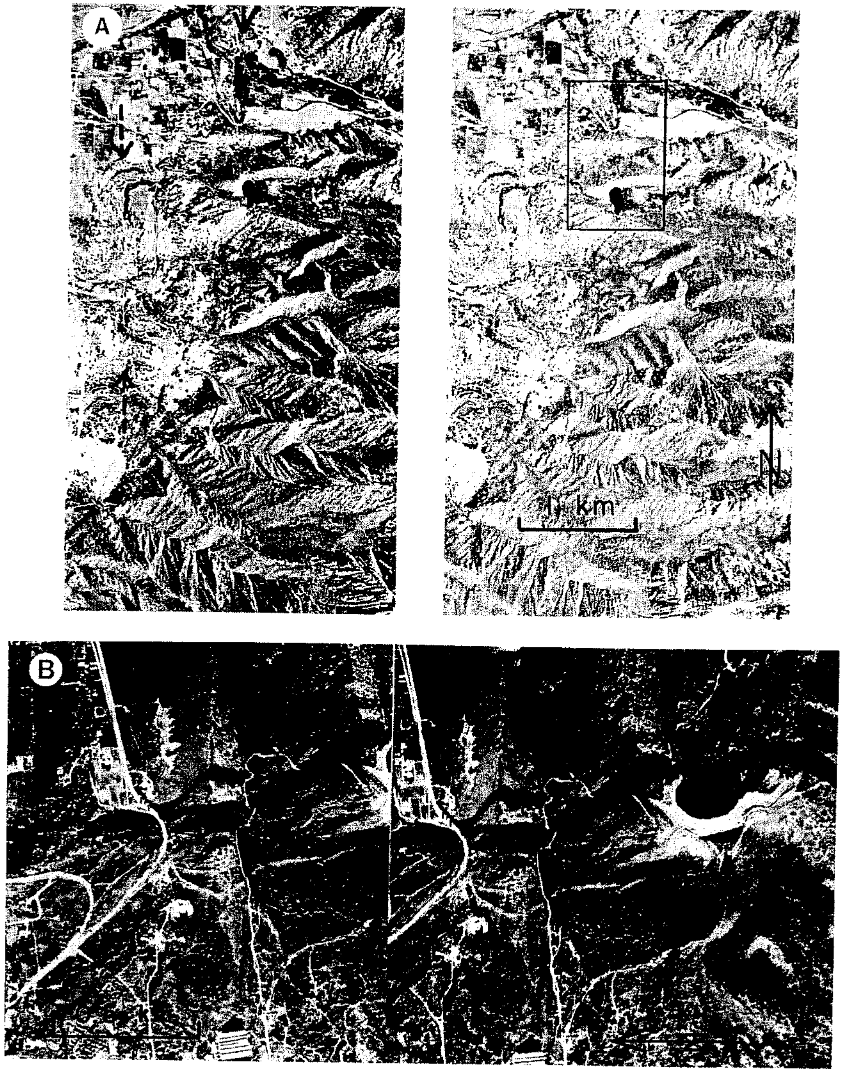

Figure 2.3 Comparison of standard and low-sun-angle stereoscopic aerial photographs. (A) Small-scale (original scale 1 : 50,000) vertical aerial photograph in standard lighting conditions. Fault scarps of the Wasatch fault zone, Utah (between solid arrows) offset Pleistocene lacustrine deposits (lower left and center) and moraines (upper center) at the base of a steep, faceted range front. Box at upper center shows area of Fig. 2.3B. (B) Large-scale (original scale 1 : 6000) low-sun-angle aerial photograph of faulted moraines on the Wasatch fault zone. Multiple synthetic fault scarps (shadowed) and antithetic fault scarps form a graben. Reservoir at far right was placed in a depression behind a terminal moraine, further deepened by graben formation. (Photographs courtesy of Brigham Young University and the Utah Geological Survey.)

Faults are traditionally mapped using solid lines (map unit is displaced, fault can be precisely located), dashed lines (map unit is displaced, fault can only be approximately located), and dotted lines (map unit is not displaced, fault is concealed). Additional line symbols, borrowed from the field of *geomorphological mapping,* may also be useful in emphasizing the style of surface fault expression (Sec. 2.2.2). The suite of map symbols to use will also depend on the scale of the map. On small-scale maps such as the Wasatch fault series, Utah (scale 1:50,000; Machette, 1992), only the three traditional geologic line symbols are used. At larger scales (>1:24,000) more detailed subdivision of tectonic landforms is desirable.

Surface zones of diffuse faulting, folding, and tilting are more difficult to identify on aerial imagery. *Broad zones* of warping, such as that created by blind thrusting or subduction megathrust earthquakes, must be mapped as areas rather than as linear features like faults or narrow folds. These broad zones can often be mapped only after considerable field work has defined the areal limits of deformation, in contrast to well-defined fault zones where photogeologic mapping typically precedes field work. Secondary paleoseismic evidence, such as sand blows or landslides, is often accentuated by variable tones and textures on aerial photographs, rather than by topographic relief (see Fig. 7.13).

2.2.2 Mapping Deposits versus Landforms in Seismic Areas

Paleoseismic features can be mapped either as *structures* deforming geologic deposits (the geologic approach) or as *landforms* (the geomorphic approach). Because Quaternary geologic mapping and geomorphology in North America are grounded in a geologic tradition, we tend to portray paleoseismic features on geologic maps. For example, geologic maps along fault zones (termed *strip maps*) usually include a detailed subdivision of Quaternary deposits, across which fault traces are portrayed by the line symbols previously described. The paleoseismic history of the fault is then interpreted from the interaction of the fault with Quaternary deposits, often aided by displacement measurements plotted on the map at key localities along strike. Examples of such strip maps are a series along the San Andreas fault zone, California (see multiple citations in Wallace, 1990, pp. 19–21), the Wasatch fault zone, Utah (see citations in Machette *et al.,* 1992a), and the Tectonic Map Series of the Geological Survey of Japan (e.g. Tsukuda *et al.,* 1993).

In a *deposit-oriented mapping* system, Quaternary deposits are typically differentiated based on inferred genesis (alluvial, glacial, eolian, lacustrine, mass movement), as interpreted from geomorphology and lithology (Flint, 1971; Catt, 1988). Such broad genetic classes are further subdivided into *second-order map units* based on the particular landform- or process-defined geomorphic environments. For example, within the alluvial class, alluvial fans, stream terraces, and floodplains might be differentiated. Each second-order map unit can be further subdivided by age to form *third-order map units.* In general, a detailed differentiation of Quaternary deposits increases the usefulness of the map for paleoseismic interpretation. The strip maps in the Wasatch fault zone series (scale 1:50,000) with up to 44 Quaternary geologic map units (e.g., Machette, 1992) contain more useful paleoseismic data than, for example, the strip map of the San Andreas fault by Davis and Dubendorfer (1987), which contains only 12 Quaternary map units.

Paleoseismic features can also be portrayed using a landform-oriented mapping system which emphasizes morphology rather than deposits. Geomorphological mapping has a long history in Europe (e.g., Klimaszewski, 1963, 1968; Tricart, 1965; Crofts, 1981), with several sets of mapping symbols proposed (Verstappen and van Zuidam, 1968; Demek, 1972; Demek and Embleton, 1978). Only recently has geomorphological mapping been applied to neotectonics (e.g., Goy *et al.,* 1988; Zuchiewicz, 1989). Most geomorphological maps published to date have scales between 1:25,000 and 1:100,000 and at such scales landforms created by single paleoearthquakes usually cannot be distinguished. Therefore, these maps are best suited for regional neotectonic studies and the reconnaissance phases of paleoseismic investigations, although they may be helpful in locating optimal sites for trenches. We suggest the reader consult Goy *et al.* (1991) for an excellent system of geomorphological map units adapted for neotectonic studies (Fig. 2.4).

2.2.3 Detailed Topographic Mapping

Many landforms produced by paleoseismic deformation are too small (<1 to 5 m high) to be well characterized on existing topographic maps (typical contour interval of 3 to 15 m). Documenting the critical geomorphic details of faulting, from which net displacement or recurrent movement might be deduced, can be done in two ways. Landforms may be mapped directly using commonly used sets of *symbols* for landforms (Fig. 2.4). Although geomorphic maps portray landform shape and spatial relationships well, they are subjective and do not usually contain the actual topographic data by which the landforms were defined. An alternative objective approach is to create *very-large-scale topographic maps* of paleoseismic landforms from which readers may make their own measurement or conclusions. Such detailed maps are very useful for measuring horizontal offsets along strike-slip or oblique-slip faults (e.g., McGill and Sieh, 1991; Grant and Sieh, 1994). A topographic map with landform mapping superposed would combine the subjective and objective approaches described here, but may become too cluttered if too many lines are drawn. We recommend that critical locations along a fault be documented by large-scale geomorphic maps with contour intervals small enough (<0.5 m) to permit precise map measurements of offsets.

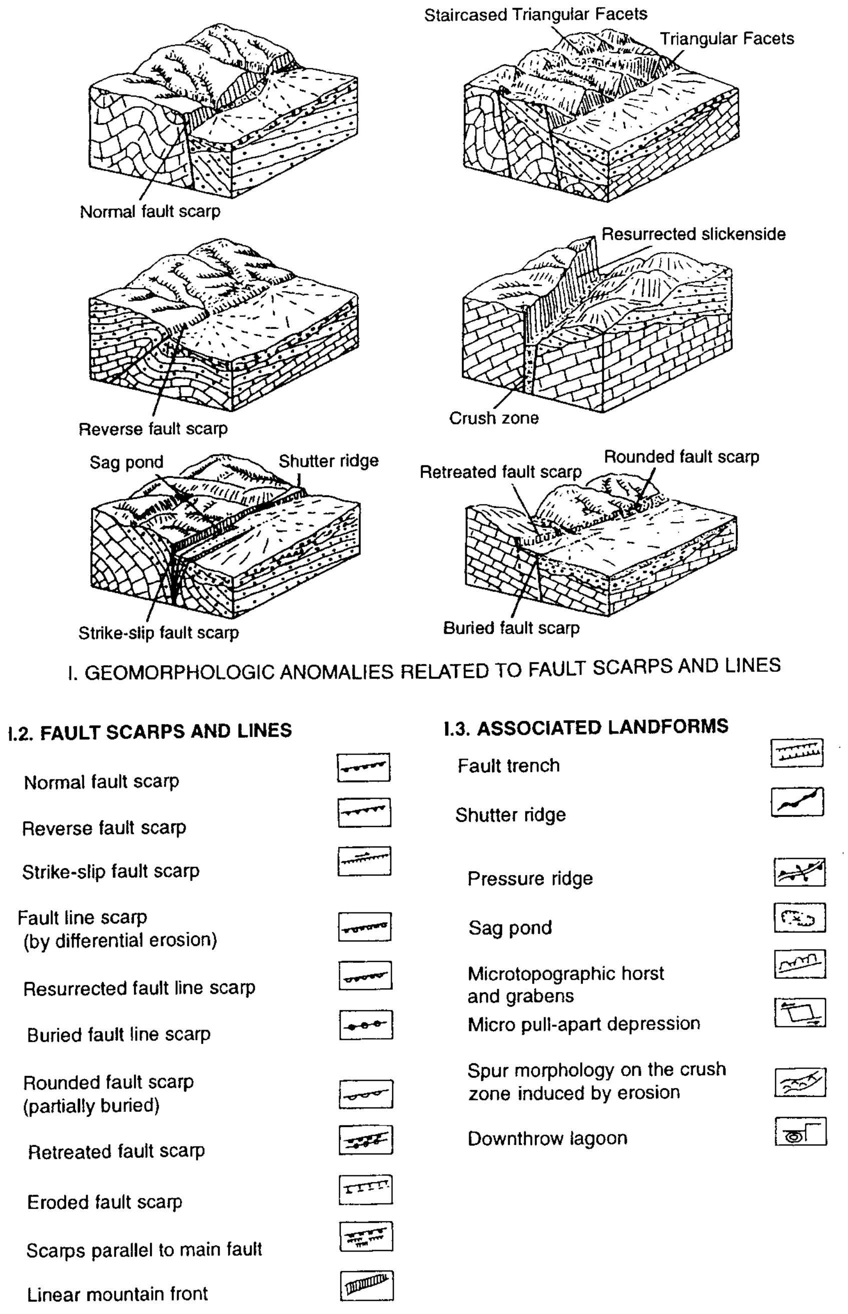

Figure 2.4 Geomorphological mapping symbols and corresponding block diagrams of neotectonic features. *Top:* block diagrams illustrating fault scarps and fault lines. *Bottom:* geomorphic mapping symbols related to fault scarps and fault lines. For the complete set of block diagrams and an additional 62 geomorphic mapping symbols, see Goy *et al.* (1991). (Reprinted with permission from INQUA Neotectonics Commission.)

Topographic maps with scales larger than 1 : 1000 were traditionally constructed by geologists using a plane table, alidade, and stadia rod (e.g., Sieh, 1978b). This time-consuming process has been replaced by surveying ground elevations with a *theodolite* and *electronic distance meter* (EDM). The elevation and horizontal position of the survey points are computed by trigonometry from the vertical and horizontal angles between the base station and the measurement points and the slope distance. Calculations are simplified by use of a *total station,* which consists of an integral theodolite, EDM, and programmable calculator which automatically reduces angle and distance measurements to *x, y,* and *z* coordinates. The *x, y,* and *z* coordinate values stored in the total station can be transferred to a computer and commercial contouring software can then be used to produce a topographic map of any specified contour interval. This method was pioneered by Sieh in California, and excellent examples of maps thus derived are shown in McGill and Sieh (1991) and Grant and Sieh (1994) (Fig. 2.5).

Large-scale base maps may also be produced by *photogrammetric processing* of large-scale aerial photographs (Ghosh, 1988). First, surveyed control points must exist in the map area and be visible in the aerial photographs. Second, the map area must be covered by overlapping, stereoscopic photo coverage. The stereo pair can then be processed in an *analytical stereo plotter* (Chapuis and van den Berg, 1988). One processing option is to create a *digital elevation model* (DEM) from the stereo model. The DEM consists of spot elevation measurements collected on a rectilinear grid of constant horizontal spacing. The grid spacing must be small enough to depict the relief features of interest, but not so small that it approaches the spatial resolution of the aerial photographs. A rule of thumb is that the grid spacing should be roughly half the desired contour interval (J. A. Coe, U. S. Geol. Surv., Denver, CO, personal communication, 1995). Contour maps are then generated from the DEM by computer software.

2.2.4 Topographic Profiling

Topographic profiling is often the easiest method of documenting the vertical component of paleoseismic faulting, folding, or tilt. Profiles measured at right angles to fault scarps provide a measurement of vertical surface offset, which is related to fault displacement by geometric relationships explained in Sec. 3.3.1. Other geomorphic nickpoints, such as shoreline angles or alluvial terrace flat/riser junctions, can be profiled along their strike to detect paleoseismic warping or uplift.

2.2.4.1 Fault Scarp Profiling

Fault scarp profiles are the main source of data on vertical displacement and age of faulting in reconnaissance paleoseismic investigations of dip-slip faults

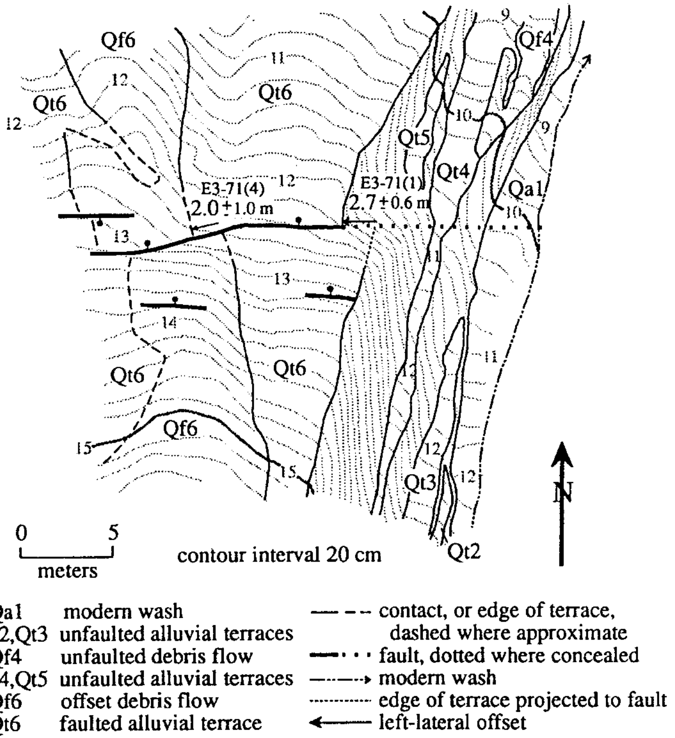

Figure 2.5 Very-large-scale topographic map made by total station measurements, showing fine-scale topography in a zone of 2-m sinistral offsets on the Garlock fault, California. Surficial mapping and surveying of the 620 control points took three days. Critical geological contacts for measuring lateral offsets have been superimposed on the base contours. [From McGill and Sieh (1991); reprinted with permission of the American Geophysical Union.]

(Wallace, 1977; Bucknam and Anderson, 1979; Haller, 1988). The interpretation of normal fault scarp profiles is well advanced (Chapter 3), while reverse fault scarp profiles have received less attention (Chapter 5).

The basic profiling strategy is to measure a number of profiles (preferably 15 to 20) along a fault scarp that is the product of a single faulting event (Machette, 1989). (Based on historic ruptures, scarps higher than 6 m probably result from multiple events; see Tables 3-1 and 5-1.) If profiles are to be dated with the empirical regression technique (Sec. 3.4.1), one should measure profiles with as wide a range in height and maximum slope angle as possible. The *maximum scarp slope angle,* also critical for scarp dating, should be averaged from four to eight measurements made close to each profile site (Machette, 1989), rather than from the single value measured on the scarp profile.

The best sites for profiling, especially if *diffusion dating* is to be performed, are those where creep and rainsplash have been the main scarp-modifying agents, because the strength of these processes is not dependent on slope position. Such sites are often found on the interfluves between gullies that dissect the scarp. Areas affected by sheetwash, rillwash, gullying, slumping, spring sapping, animal tracks, or human disturbances should be avoided. Likewise, areas of eolian or alluvial fan deposition against the scarp should be avoided. If diffusion dating will be performed on profiles, steep faulted surfaces should be avoided (see Sec. 3.4.1).

Most fault scarp profiles are oriented perpendicular to the fault scarp, so that the surface offset measured from the profile can be graphically related to the vertical component of fault displacement (details in Chapter 3). However, if profiles are intended primarily for dating the scarp using erosion-based methods (Chapter 3) rather than for measuring displacement, the profile line should follow the line of steepest slope, so that it parallels the transport vector of material across the scarp. Where fault scarps trend perpendicular to the local slope of terrain (the typical case), a profile perpendicular to fault strike will also parallel the local fall line, and such profiles can be used for both displacement and age estimates. Where fault scarps trend diagonally across local slopes, the fall line runs diagonally across the fault scarp, so scarp profiles laid out to estimate age (as described earlier) will exaggerate displacement. If surface faulting had an oblique component, measurements of vertical surface offset based on fault scarp profiles will underestimate true net slip. This shortcoming cannot be overcome unless well-defined *piercing points* can be identified above and below the fault scarp (see Chapter 6).

The preferred method of fault scarp profiling is somewhat dependent on the degree of surface vegetation cover. On sparsely vegetated fault scarps in the western United States, Wallace (1977) and Bucknam and Anderson (1979) laid a telescoping *stadia rod* directly on the ground surface and measured its inclination with an *Abney level.* The rod is moved sequentially along the profile with the length and inclination of every segment recorded. Profile segments at the scarp base and crest (see definitions in Table 3-3) must be short enough to portray *scarp curvature* accurately, because curvature is a critical factor in diffusion dating (Sec. 3.4.1). If vegetation density precludes laying a rod directly on the surface, scarp profiles can be made by more traditional leveling methods using the rod in a vertical position. Profiles over long distances (across broad scarps or folds) have been made via trigonometric leveling using instruments such as total stations.

Errors in slope angles arise from natural undulations in the ground surface, presence of low vegetation and roots beneath the rod, inaccuracy of the Abney level, and unquantifiable "operator error." Mayer (1984, pp. 305) reports slope angle errors (1 standard deviation) of ±1 to 2° using the Wallace method. Slope segment lengths may contain error from incorrect positioning or misalignment of the rod in each segment, as well as errors in reading the rod length. Scarp heights measured from profiles are affected by uncertainties in both angles and segment lengths. Mayer (1984) reported 1-sigma errors of ±6% to 15% in scarp height when making repeated profiles at the same location with three different individuals and two types of rods. This degree of error has significant implications for direct methods of fault scarp dating (Table 3-8). Error might be diminished by staking or stringing the profile line (to reduce rod misalignments), removing surface vegetation, and using more accurate rods and inclinometers, but no rigorous field tests of these corrective practices have been made.

2.2.4.2 *Terrace Riser Profiling*

Terrace risers are created by fluvial or coastal erosion and define *linear geomorphic datums* that can record paleoseismic deformation. The most commonly used terrace riser in paleoseismology is the wave-cut cliff at the landward edge of a marine terrace. The *nickpoint* at the junction of the wave-cut cliff and marine platform (termed the *shoreline angle*) defines an originally horizontal datum. Similar nickpoints at the base of fluvial terrace risers define a datum that slopes downstream at the stream gradient existing at the time of riser formation. The locus of points defined by these nickpoints forms a *paleodatum* that should record deformation from paleoearthquakes.

In most cases nickpoints have been covered with colluvium, so their elevation must be reconstructed by drilling, geophysics, or profile projection. Bradley and Griggs (1976) describe the use of all three methods to measure the present elevation of shoreline angles on uplifted and tilted marine terraces in California. Most elevations are estimated as the graphical *intersection point* of the projected shoreline platform and the projected wave-cut cliff, using average angles for both projections, and assuming that the original position of the wave-cut cliff was in the center of the present degraded cliff (e.g. McCalpin *et al.*, 1992). LaJoie (1986) provides an extensive summary of measurements made on deformed marine terrace nickpoints.

2.3 MAPPING PALEOSEISMIC STRATIGRAPHY

The stratigraphic expression of paleoearthquakes can range from displaced strata and angular unconformities (primary evidence) to clastic dikes and soft-sediment deformation (secondary evidence; Table 1-1). Such stratigraphic evidence may or may not be accompanied by geomorphic evidence of paleoseismicity. Early paleoseismic investigations concentrated on geomorphic evidence because natural vertical exposures in fault zones are rare. In the absence of such exposures, however, early paleoseismic investigators were faced with the choice of (1) relying only on geomorphic data for the paleoseismic analysis, (2) drilling boreholes or collecting geophysical data, or (3) excavating artificial trench exposures across deformation zones. The development of modern paleoseismology owes much to developments in the latter two of these fields. In the following sections we contrast drilling, trenching, and geophysics as paleoseismic techniques, and describe methods used successfully in previous paleoseismic investigations.

2.3.1 Drilling and Coring

Although it is not generally appreciated, *boreholes* and *shallow cores* have several advantages over trenches for collecting paleoseismic data in certain situations; they can be placed in areas of standing water, shallow groundwater, and intense urbanization with buried pipelines. They are relatively inexpensive, nondisruptive, safe, and can be placed as closely as needed to maintain interhole correlation. Disadvantages are the disruption of delicate structural and stratigraphic features during sampling (depending on the sampling method), and lack of the continuous two- or three-dimensional view that is often essential for interpreting paleoseismic features.

Drilling as described herein includes standard powered well-drilling methods (cabletool, auger, rotary, or percussion) in which the hole is logged either from chips brought up by bailers or in the circulating medium, or by drive samples taken at irregular intervals. Various *thin-wall sampling tubes* are available that will preserve sedimentary structures in all but gravelly materials (Soiltest, 1977). A common approach in urban paleoseismic drilling programs is hollow-stem augering with split-spoon sampling done in conjunction with the Standard Penetration test (cf. Carter, 1982; Hunt, 1984). A truck-mounted auger can drill up to 15 m in most unconsolidated deposits, which is the depth limit in many geotechnical investigations.

The advantages of drilling are its great depth of penetration and the ability to penetrate gravelly, compacted, or cemented Quaternary deposits. Disadvantages of drilling are that it is expensive, obtaining core samples is tedious, and thin stratigraphic units and soils are mixed together by drilling and seldom recognized from chips and cuttings. The main use of drilling in paleoseismology is to *locate correlative strata* across a fault zone so estimates of net displacement can be made. Drilling may also uncover faults that are not expressed at the surface or, conversely, may prove that no fault displacement exists within a certain area. Robison and Burr (1991) drilled 19 borings across a strand of the Wasatch fault zone in an urbanized area in downtown Salt Lake City, Utah, where trenches were impractical (Fig. 2.6). From the drilling data they not only located the fault trace and measured its minimum vertical separation, but the *structure contour map* based on the 19 borings proved that the fault projection on published geologic maps was incorrect. The destructive nature

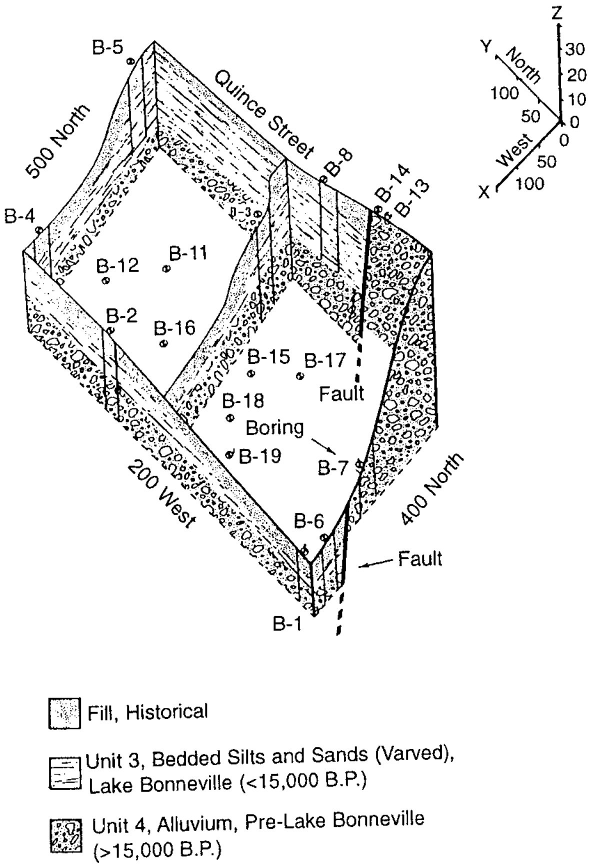

Figure 2.6 Fence diagram showing the generalized subsurface geology in the Wasatch fault zone, downtown Salt Lake City, Utah, based on 19 borings and three shallow trenches. Borings logs within the central portion of the site were omitted for clarity, although boring locations are indicated by numbers. Scale at upper right is in feet. Reprinted with permission of the Symposium on Engineering Geology and Geotechnical Engineering.

and limited spatial data from drilling typically precludes recognition of individual paleoearthquake displacements.

Coring can refer to either shallow hand-coring or continuous coring with powered equipment. Hand-coring has several advantages: It is cheap, portable, and results in continuous core with good preservation of sedimentary structures. Disadvantages are the limited depth penetration (usually <3 m) and inability to penetrate hard sediments. The main use of hand-coring in paleoseismology has been to correlate strata in areas of Holocene tectonically induced sedimentation. For example, Nelson (1992a) used a 1-m-long, 2.5-cm-diameter half-cylinder *gouge corer* to sample and correlate peat and mud marsh sediments in subsided areas of the Oregon coast, USA. Clague and Bobrowsky (1994b) used a *sonic drill* to obtain cores up to 11 m long in marsh sediments. Coring in lakes utilizes *Kuhlenberg piston corers* or the self-contained, gas-operated *Mackereth piston-coring system,* which returns lake-sediment cores up to 10 cm in diameter (Ager and Sims, 1981; Rymer and Sims, 1982; Perkins and Sims, 1983). Cores can then be X-rayed to detect sediment deformation from seismic shaking (see Chapters 7 and 8).

2.3.2 Trenching

Excavation of trenches in deformation zones has become a major element of paleoseismic studies in most countries. Following the early use of trenches in nuclear power plant investigations in the United States (Hatheway and Leighton, 1979; Hatheway, 1982), trenching techniques have expanded to address problems of paleoearthquake faulting, folding, ground failure, and faulting-induced sedimentation. In the following sections we describe in considerable detail the mechanics of excavating and logging trenches. In contrast, siting and interpreting of trenches depend heavily on the types of features being investigated, so those topics are addressed as appropriate in Chapters 3 through 8.

Much delicate paleoseismic evidence may also be destroyed by trenching and backfilling. In this regard paleoseismic trenching is similar to archeologic excavations that so disturb a site that future interpretation must rely on the initial excavation. *Conservation archaeology* (Schiffer and Guterman, 1977) is the concept that some critical sites are better left undisturbed and saved for future excavation using improved techniques, rather than being hastily excavated at present. This concept has not been widely applied to paleoseismology, but it may be appropriate in the future.

2.3.2.1 Location, Orientation, and Pattern of Trenches

The best location, orientation, and pattern for trenches are highly site dependent, so only the most general guidelines are presented here. However, past work has shown that trench placement is such a critical element in paleoseismic investigations that success or failure often depends on it. Stated another way, once a trench is sited the stratigraphy and structure to be exposed is somewhat predetermined. If the investigation is to be successful, the trench must yield the type and quality of data anticipated by the investigator, a result which is not always accomplished.

Trenches across faults are typically sited to optimize data on either *paleoearthquake displacement* or *paleoearthquake recurrence* (Sieh, 1981). The best sites for measuring displacement are where all displacement is concentrated on a single, narrow fault strand, and subsidiary faulting and folding are negligible. The best sites for measuring recurrence (i.e., for dating individual paleoearthquakes) are local fault-zone depressions filled with fine-grained and/or organic interfaulting sediments. Such depressions are often associated with distributed faulting and/or folding, where subsidiary faults created by successive paleoearthquakes are separated vertically and horizontally and can be distinguished. On dip-slip faults, the best trench locations for measuring displacement and recurrence often coincide, such as single-trace, high fault scarps fronted by sediment-filled graben or back-tilted areas (e.g. Swan *et al.*, 1980; McCalpin *et al.*, 1994). On strike-slip faults good sites for measuring displacement are usually poor for measuring recurrence, and vice versa (Chapter 6).

Trench location is also dictated by the number of paleoearthquakes the investigator wishes to observe. Trenches across faults on very young Quaternary surfaces may expose only one or two paleoearthquake displacements, so trench structure and stratigraphy may be relatively simple. Trenches on progressively older surfaces are likely to expose the cumulative deformation from many paleoearthquakes, where the effects of earlier displacements are obscured by those of later displacements. In narrow zones of deformation, multiple displacements often result in complex shearing, cross-cutting, and interfaulting sedimentation and weathering that are difficult to reconstruct; in such situations individual paleoearthquakes, especially older ones, may be overlooked. For example, few investigations have recognized more than four paleoearthquakes in a single trench unless faulting was widely distributed (e.g. Sieh, 1978a; Fumal *et al.*, 1993). Beyond a certain size dip-slip fault scarps may be too large to be completely trenched by available commercial excavating equipment. For example, on the Wasatch fault, Utah, trenches have generally been limited to scarps 10 m high or smaller, and these scarps typically represent only three or four surface-faulting events. Attempts to trench larger scarps (such as the 22-m-high Kaysville scarp, Swan *et al.*, 1980; Fig. 2.7) with standard-size construction backhoes have resulted in incomplete penetration through the colluvial sequence at the scarp base (Chapter 3).

Based on Quaternary geologic and geomorphic mapping and knowledge of local slip rates, the paleoseismologist can usually estimate the number of paleoearthquakes that might be exposed in trenches on various landforms. Trench location is then partly dictated by the goals of the investigation, for example, to characterize only the most recent paleoearthquakes (by trenching young deposits) or to compile a long history of deformation (by trenching older deposits). In addition, trench locations are often restricted by nongeological considerations, such as road access, land ownership, and previous ground surface disturbance. Whenever possible, trenching sites should have undergone minimal prior surface disturbance (grading, filling) which might destroy the critical relationships of faults to shallow deposits, especially the modern soil. However, trenching has been successful where the fault zone was buried beneath artificial fill (Sec. 6.3.3.2).

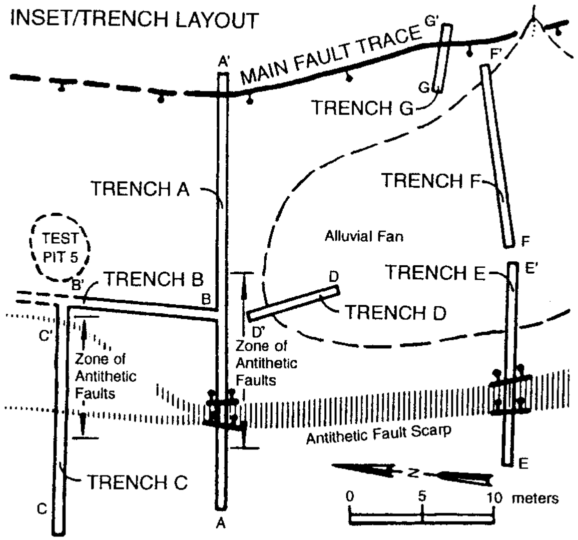

Figure 2.7 Map of multiple trench locations and orientations placed in a graben at the foot of a large normal fault scarp. Fault-perpendicular trenches (A, C, E, G) expose fault planes and colluvium from which the paleoseismic interpretation is made. Trench F was dug to find datable material in the unfaulted alluvial fan. Fault-parallel trenches B and D trace strata deposited in the graben by fault-parallel streams. [From Swan *et al.*, (1981).]

Trench orientation is dictated by the inferred sense of fault displacement, with trenches being aligned roughly parallel to the sense of movement (perpendicular to fault strike for dip-slip faults, Fig. 2.8; parallel to fault strike for strike-slip faults). *Fault-perpendicular trenches* are often used to locate and define the width of strike-slip fault zones, with parallel trenching following to define offsets of piercing points (Chapter 6). Dip-slip paleoearthquakes can often be adequately characterized by a single trench at each site along the fault, especially where displacement is concentrated beneath a single fault scarp. For oblique-slip and strike-slip displacements, multiple trenches are needed to capture the three-dimensional components of slip.

Trenches have also been excavated to study folds (Chapter 5) and various off-fault paleoseismic features such as sand blows (Chapter 7). These trenches are used mainly to expose stratigraphy that was deformed by seismic shaking or deposited in response to earthquake deformation. Trench orientation and placement are not as critical in these cases as long as the trench intersects the features of interest.

Figure 2.8 Photograph showing the orientation and placement of a trench (between arrows) across an 8-m-high normal fault scarp (in shadow). The trench completely traverses the scarp, from well onto the upthrown block, to well onto the downthrown block, thus exposing prefaulting strata on both the footwall and the hanging wall. A zone 10 m wide at the foot of the scarp has been back-tilted toward the scarp; the hinge line of tilting is shown by a dashed line. Grey's River fault, Wyoming (Jones 1995).

A final category of trenches is trenches that are excavated across a construction site to prove or disprove the existence of young faulting not visible at the surface (e.g., Hatheway and Leighton, 1979). The location of such trenches is determined by construction site dimensions rather than by any geological considerations. These types of trenches are hopefully oriented perpendicular to local structural trends, which maximizes their probability of intersecting a fault. It would be coincidental if trenches so sited were optimal for measuring either paleoearthquake displacement or recurrence, so paleoseismic interpretation of the site may often be supplemented by data from better sited trenches beyond the construction site.

2.3.2.2 *Excavation Logistics*

The choices of excavating equipment, trench cross-sectional shape, and shoring strategy are all interrelated and depend on what kind of material is being trenched, the topography at the trench site, how deep the trench is, how stable trench walls are, and whether the wall needs to be photographed. As pointed out by Hatheway and Leighton (1979, p. 178) "the method of excavation that proves to be least disturbing to the host soil and/or rock will also likely prove to be the least expensive." Trenches in unconsolidated deposits are usually excavated by hand if fault scarps are very small (less than 2 m high), although house-sized trenches have been excavated by hand in China (Li and Zheng, 1992). Larger trenches require backhoes or bulldozers.

Early trenches for regional paleoseismic studies in the United States were narrow, deep single slots (*California-style trenches;* Fig. 2.9, B1) across moderate-to-large scarps. This trench shape involves a minimum of material excavated and time consumed, and it can be easily shored. However, due to narrowness only small portions of the trench wall can be seen from any one location, and photographing the wall is difficult (Figs. 2.10A and B). Large numbers of people cannot view the trench at once, as is occasionally required during regulatory review. Shape variations of the California-style trench include *benched trenches* (Fig. 2.9, B3) and *laid-back trenches* (Fig. 2.9, B2). These shapes allow a better view of trench wall stratigraphy and fault relations and can be much more easily photographed. However, because of their large widths they are more difficult to shore. *Bulldozer trenches* (Fig. 2.9, B4) are necessarily much wider than backhoe trenches (Figs. 2.10C and D), and may be used in conjunction with *backhoe slot trenches* to reach maximum depths. Cotton *et al.* (1988) used large *construction scrapers* to excavate a 14-m-deep trench across the San Gabriel fault, California. Mapping vertical walls in a large bulldozer or scraper excavation can be accomplished by bringing loggers up to the face with an *aerial lift,* with control surveyed by electronic survey equipment or photogrammetry.

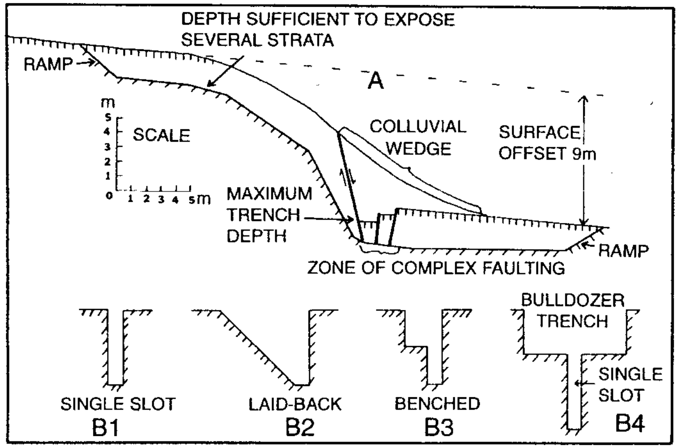

Figure 2.9 (A) Typical longitudinal section of a trench across a fault scarp; compare to Fig. 2.8. (B) Cross sections of various types of trenches. B1, single slot (California-style); B2, laid-back; B3, benched; B4, backhoe trench within a bulldozer trench. [From McCalpin (1989b); reprinted with permission of A. A. Balkema Publishers.]

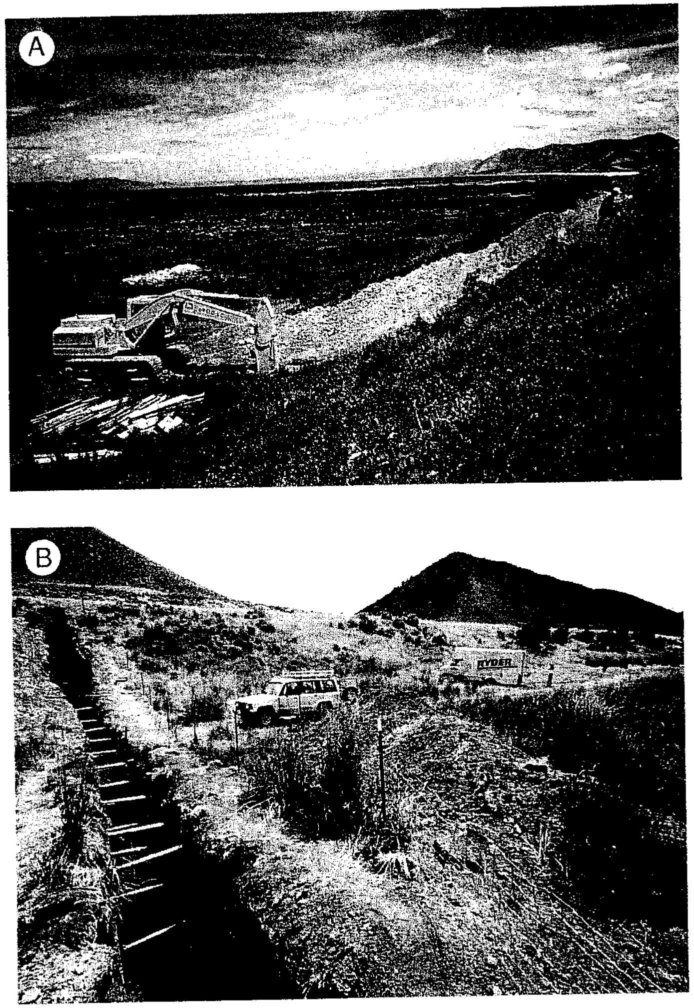

Figure 2.10 Photographs of various types of trenches. (A) Excavating a trench across an 8-m-high normal fault scarp. Eastern Bear lake fault zone, Utah-Idaho (McCalpin, 1993). (B) The finished trench from photograph A, extended well out onto the downthrown block. Supports in trench are hydraulic aluminum shores. (C) Aerial view of stepped bulldozer trench at the Point Conception liquefied natural gas facility. (D) Close-up of benched trench at Point Conception; note persons at far left for scale. (Photographs C and D courtesy of T. K. Rockwell.)

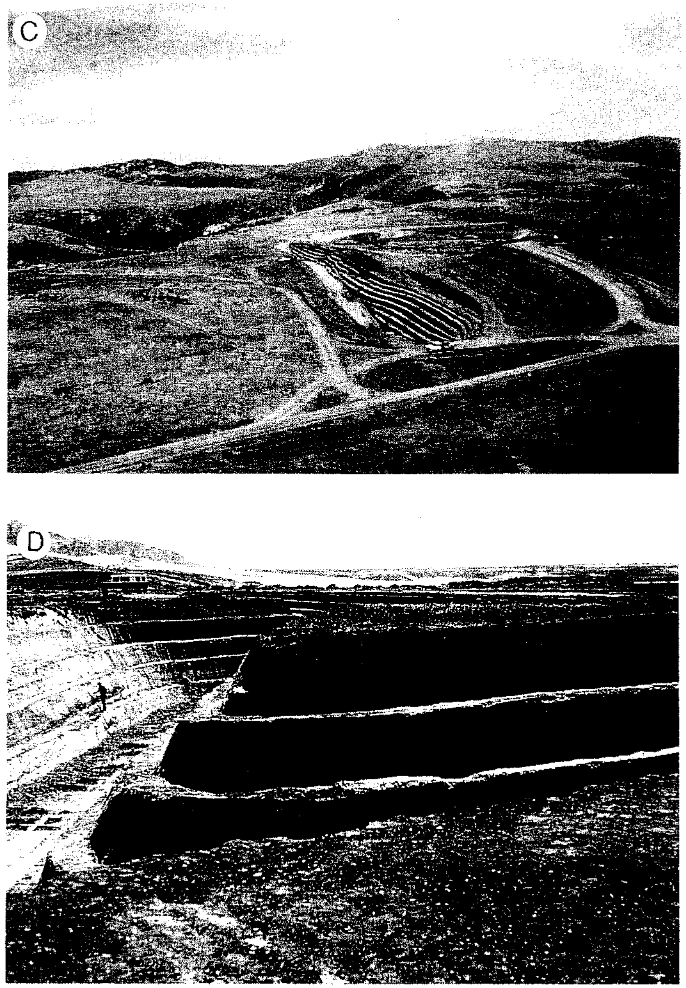

Figure 2.10 *Continued*

An alternative style of trenching is the *Japanese-style open-pit excavation,* in which all trench walls are laid back to a 45° slope (Fig. 2.11). In flat areas such trenches are often nearly square in plan view, becoming more elongated if the trench crosses a scarp with significant vertical relief (e.g., Okumura *et al.,* 1994). Open-pit trenches have several advantages: (1) They can be very deep (note the 13-m depth in Fig. 2.11, cross section), (2) they do not require shoring, (3) the walls can be logged without the need for elaborate scaffolding, (4) the trench walls are easy to view and photograph from outside of the trench, and (5) the excavation is stable enough to form a quasipermanent exposure, such as the Neo-Dani Fault Museum in central Japan (Okada *et al.,* 1992; Sato *et al.,* 1992). The main disadvantage of the open-pit trench style is the size of the excavation and the volume of material that must be removed.

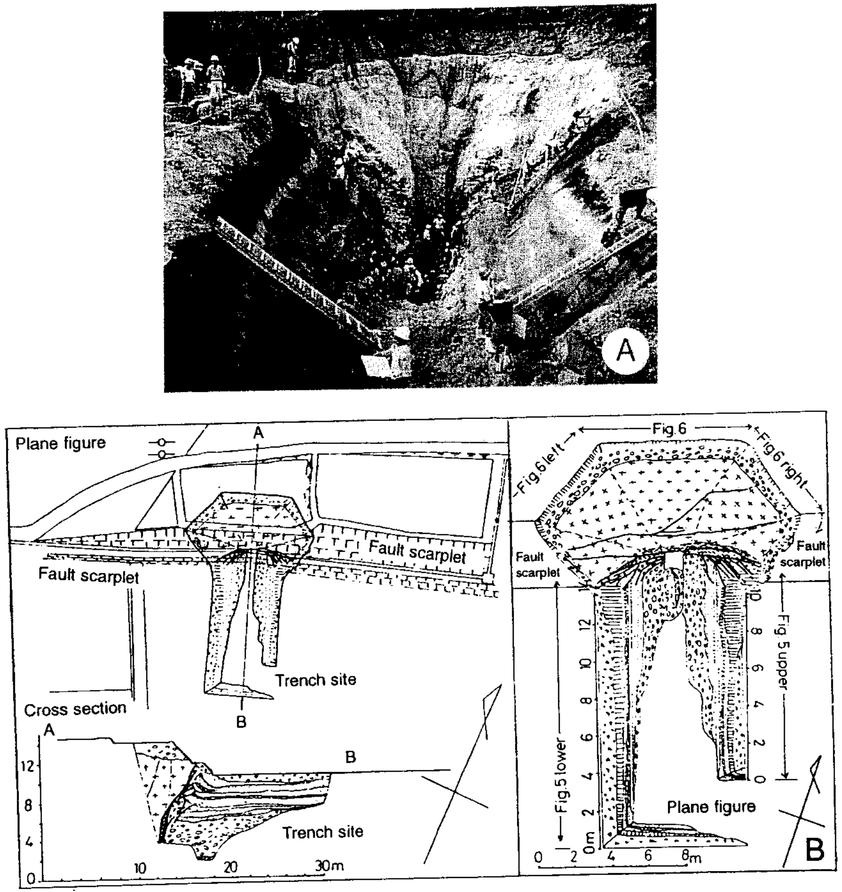

Figure 2.11 (A) Photograph of the 13-m-deep "open-pit" style trench across the Atotsugawa fault at Nokubi, central Japan; (B) Plan views and cross section of the trench shown in part A. The fault scarplet transected by the deepest part of the trench is 5 m high. Patterns shown on the lower trench walls indicate various unconsolidated deposits, primarily terrace gravels (open circles) and sands. The "×" pattern at the upper end of the trench indicates granite that has been thrust over the alluvium. [From Okada *et al.* (1992); reprinted with permission of the *Journal of Geography* (Japan).]

A minor disadvantage is the need to *rectify the trench log* drawn on 45° slopes to a true vertical cross section. However, if the trench is logged by electronic or photogrammetric techniques (Sec. 2.3.2.6) projection of points to a vertical plane is simplified. In view of the many advantages of the open-pit approach, paleoseismologists should consider excavating in the Japanese style if local conditions and project budget permit.

Trenches in consolidated bedrock rarely preserve evidence of individual paleoseismic events, but at critical facility sites where bedrock is at the surface, trenches must be excavated into competent rock merely to prove or disprove the existence of faults. Much of the early trenching done for nuclear power plants in the United States was performed in rock, by drilling and blasting. Hatheway and Leighton (1979) provide a good summary of the excavation and logging techniques utilized in bedrock excavations.

Trenches may be excavated completely before logging begins, or dug incrementally as logging proceeds ahead of backfilling. On dip-slip faults complete excavation is advantageous because the entire trench can be viewed at once and critical areas reexamined. However, due to the instability of trench walls or lack of shores some dip-slip fault trenches may have to be dug and logged in increments. For strike-slip faults incremental excavation and logging of the vertical walls of fault-parallel and fault-perpendicular trenches is often required to measure three-dimensional deformation (e.g., Wesnousky *et al.,* 1991; also see Chapter 6). *Incremental trenching* refers to the progressive excavation of closely spaced, parallel trench walls. After the initial trench is excavated and logged, the logged trench wall is excavated back 20 to 50 cm, and the new exposure is logged. That wall is then cut back 20 to 50 cm parallel to the previous wall, and is again logged. As the trench wall is progressively cut back, many successive wall positions are mapped. The resulting closely spaced, parallel trench logs can then be used to create a three-dimensional diagram of structural and stratigraphic relations in the deformation zone. At present, this technique has mainly been used on strike-slip fault traces, where a 3-D representation is needed to calculate displacement vectors. This method of trenching is totally destructive, however, because excavation consumes the entire feature being mapped. The floors of trenches have also been logged to make *isopach maps* showing horizontal displacement and folding (Sieh, 1978a).

During excavation senior personnel must decide when the trench is deep enough to expose the desired stratigraphy. This decision must often be made while the excavating machinery is still positioned over that portion of the trench in question, since it is usually difficult to get excavating equipment back into position to deepen a narrow trench once it has been completed. It is usually worthwhile to have the backhoe excavate a trench to the full depth reach of the backhoe, if such depth does not initiate caving. This method has the added advantage of often exposing small faults near the bottom of the trench which cannot be seen closer to the surface, either due to masking by surface disturbances or by upward truncations within the stratigraphic package. Because the backhoe bucket or bulldozer blade smears a thin film of cohesive soil onto trench walls, it often is difficult to see stratigraphy in the walls as they are cut. Accordingly, geologists are often tempted to enter the unshored, just-excavated part of the trench to scrape off the walls, inspect the stratigraphy, and determine if key strata have been exposed or whether the trench needs to be deepened.

Numerous fatalities have occurred when vertical walls have collapsed on geologists who were crouched at the base of the trench looking for key contacts. It is probably true that more geologists have been killed in trenches than in earthquakes. Thompson and Tannenbaum (1977) report that about 100 workers are killed each year in construction trench collapses in the United States. Trench walls typically slump in several geologic or topographic situations: (1) at the fault plane, where crushing has reduced material cohesion and possibly created open voids; (2) in the low-density colluvium immediately downslope of the fault; (3) where groundwater outflow is strong, and (4) where cohesionless material (often saturated) ravels out of the freshly cut trench walls and undermines overlying cohesive units—this leads to massive slumping and caving, often along preexisting vertical cracks. Most slumping occurs within minutes after the face has been excavated, due to vibrations from the machinery during continued excavation, but vertical walls may continue to collapse for days after excavation, especially in wet weather. Personnel can be lowered into the trench while standing on the backhoe bucket, but this will not prevent caving.

In the United States, federal regulations require that trenches deeper than 1.5 m be stabilized with shores, or excavated sufficiently wide (or with sloping walls) that personnel can avoid collapsing wall sections [U. S. Occupational Safety and Health Administration (OSHA), 1989]. Single-slot trenches are usually shored with 7-ft-long *hydraulic aluminum shores* which expand from 0.7 to 1.4 m wide (Fig. 2.11B). Cass and Wall (1989) provide an extensive description of shoring options with these units. Trenches too wide for the use of any hydraulic or *screw-type shores* are usually shored with lumber or heavy timbers cut onsite. The trench should be surrounded by a fence immediately after excavation, with "no trespassing" signs prominently displayed. Trench shoring standards used in California are quite comprehensive and may be used as conservative guidelines in the absence of local regulations (California Department of Transportation, 1977; Cass and Wall, 1989).

2.3.2.3 *Preparing for Logging*

Before a trench can be logged the walls must be cleaned and a *reference coordinate system* must be established. In most trench investigations in the United States across dip-slip faults only one wall is cleaned and mapped (logged). This wall is usually chosen to be the shaded one, because it is difficult to trace contacts on a wall which is partly lit by direct sunlight and partly in shadow (e.g, in an east-west-oriented trench, only the southern wall would be logged). If the trench is benched or laid back, the vertical wall chosen for mapping is typically the southern wall. Because of the extra labor involved in cleaning the opposite trench wall, this is usually only done in places to confirm features seen in the logged wall (e.g., the trend of faults and paleochannels). However, we note that the custom in Japan is to log all walls of a trench, and this practice certainly facilitates 3-D reconstructions of slip.

Trench walls are scraped off with various tools to remove soil smeared on walls during excavation; typically 2 to 5 cm will be removed. In very cohesive soils, the wide blade of a mattock or ice axe is necessary to chip loose these surface layers, whereas in less cohesive silts and fine sands, trowels and hoes are effective in scraping thin layers from the trench walls. In granular, coarse cohesionless deposits such as fluvial or deltaic gravels, walls are best cleaned with whisk brooms, paintbrushes, or by blasts of compressed air.

After the walls between the shores are cleaned, a *reference grid* for mapping must be constructed if the trench is to be logged manually (Sec. 2.3.2.6). Typically the grid is composed of horizontal lines of low-stretch nylon string, spaced 1 m apart, attached to the trench wall by large (5-mm × 15-cm) nails. Flagging or tape attached to these lines at 1-m intervals provides the horizontal control (e.g., Figs. 2.16A, 2.18A) or, alternatively, vertical string lines can be placed on 1-m centers. It is often difficult to attach nails to trench walls composed of noncohesive gravelly or friable material. In such cases the level line may be attached directly to a shore or fence post driven into the trench floor. However, it is best to keep the grid lines entirely separate from the shoring system, because a shift in shoring units (due to loss of hydraulic pressure, weight of people climbing on them during logging, etc.) will distort the line grid.

After the first horizontal grid line is set, others are set parallel to it at 1-m vertical intervals. The horizontality of each successive line can be checked by the line (bubble) level, and by measuring the vertical distance between successsive horizontal string lines. If the vertical distance varies by more than 2% (i.e., ±2 cm over 1 m), the line should be releveled. Once all horizontal lines have been strung, flagging or tape is attached to the first level line at 0.5-m intervals. Horizontal distance marks are transferred between the parallel string lines of different vertical heights by means of a plumb line. These plumb line measurements should be checked on each horizontal line by measuring between horizontal tape marks to ensure 2% precision.

If the trench wall is vertical and smooth (a fortunate but rare occurrence), the string line grid will lay tightly against the wall and parallax problems will be minimal during manual logging. However, if the trench wall to be logged is not vertical, or is very irregular with cavities, the vertical string line may diverge significantly from the trench wall. Two approaches to logging are possible in this case. In the first approach, the level lines are kept tightly up against the wall, even though the wall is not a smooth vertical plane; this is the practice in Japanese open-pit trenches. To avoid scale changes on the log, actual measurements in the plane of the (nonvertical) trench wall must be *trigonometrically corrected* later to project onto a vertical plane. Such reduction in the field can be tedious, considering that it may involve hundreds or thousands of measurements. The second approach is to string the grid lines within a vertical plane, using the shoring system as support, with the result that the grid lines may be several decimeters (or even meters) from the logged wall. In this approach contacts on the wall are "sighted" in relation to the grid system, but *parallax problems* may arise if the lines are far from the wall. Such parallax errors may amount to several decimeters and will make construction of the final log difficult.

In most fault-perpendicular trenches on dip-slip faults, the trench reference grid is not tied to any surveyed vertical or horizontal control monuments outside of the trench, because such control is unnecessary for measuring dip-slip displacements or for interpretation. However, fault-parallel and fault-perpendicular trenches across a strike-slip fault, if not contiguous, must be tied together by a *common surveyed datum* if oblique displacements are to be measured accurately (e.g., Grant and Sieh, 1994). This common datum is typically artificial and local and is not tied to any larger geodetic survey or coordinate system. Trenches excavated at construction sites are also tied to the *site survey grid* to ensure that the trench is properly located with respect to planned construction (e.g., Lund and Euge, 1984). The recent commercial development of *global positioning satellites* (GPS) and inexpensive, portable receivers theoretically permits any point on the trench reference grid to be surveyed to centimeter accuracy with respect to latitude, longitude, and elevation, although to date no such use has been described in published papers.

2.3.2.4 Defining Map Units

For a trench log to communicate information to a wide audience, the map units must be defined in a way that emphasizes the sequence of deformation, sedimentation, and weathering exposed at a site. Hatheway and Leighton (1979) differentiate the subjective versus objective approaches to trench logging. In *subjective logging,* the logger first observes the trench wall and makes a geologic interpretation of the structural and stratigraphic relations exposed in the wall. The correctly scaled log is then made to illustrate the primary geologic features. The rock or soil matrix is added in secondary importance; small features that do not bear on the major interpreted structures or strata may not be logged at all. The log is thus schematic (Fig. 2.12) but planimetrically accurate. The subjective approach to trench logging developed during nuclear power plant investigations (Hatheway and Leighton, 1979), where the log was meant to answer specific regulatory questions, such as "Is a fault present?" and, if so, "Is the age of faulting older than some predefined regulatory criterion?" The advantages of a subjective log are that it can be made rapidly and is easy to interpret with respect to regulatory criteria, because all extraneous features that do not bear on the major interpretation have been omitted. The disadvantage of this type of log is that it is difficult to advance alternative interpretations of the log, because the interpretation was integral to drafting the log, and many details have been omitted. The initial enthusiasm for this type of trench log in nuclear safety investigations soon waned when field reviews showed that alternative interpretations of structural relations might be valid, requiring complete re-logging of the trench walls.

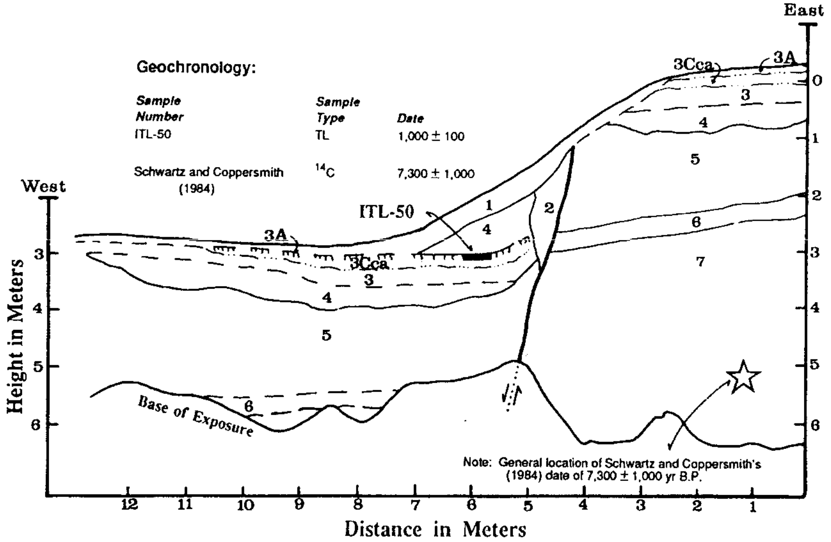

Geochronology:

Sample Number	*Sample Type*	*Date*
ITL-50	TL	1,000 ± 100
Schwartz and Coppersmith (1984)	^{14}C	7,300 ± 1,000

Note: General location of Schwartz and Coppersmith's (1984) date of 7,300 ± 1,000 yr B.P.

Figure 2.12 Example of a subjective trench log. Stratigraphic units and the fault are outlined, but no details of deposit sedimentology or sedimentary structures are portrayed. [From Jackson (1991), Plate 1; reprinted with permission of the Utah Geological Survey.]

In contrast, *objective logging* "attempts to portray equally all physical features of the trench face, larger than a threshold of resolution, in an impartial manner and without regard to relative importance. Both obvious and subtle features are shown with equal resolution, and little subjective interpretation is made during the recording process" (Hatheway and Leighton, 1979, p. 173). This approach seeks only to document what the trench wall looks like (Fig. 2.13). The most extreme example of an objective log would be an unannotated photograph of the trench wall, which showed no interpreted features. The advantage of an objective trench log is that several interpretations can be proposed and tested against the stratigraphic relations portrayed on the log. The log also acts as an archival record of how the trench wall appeared, which may be recognized in the future as containing some newly discovered phenomenon. The disadvantage of this approach is that objective logs may not be readily interpretable as drawn; even an expert may have to study the relations in a log for a time before deducing an interpretation.

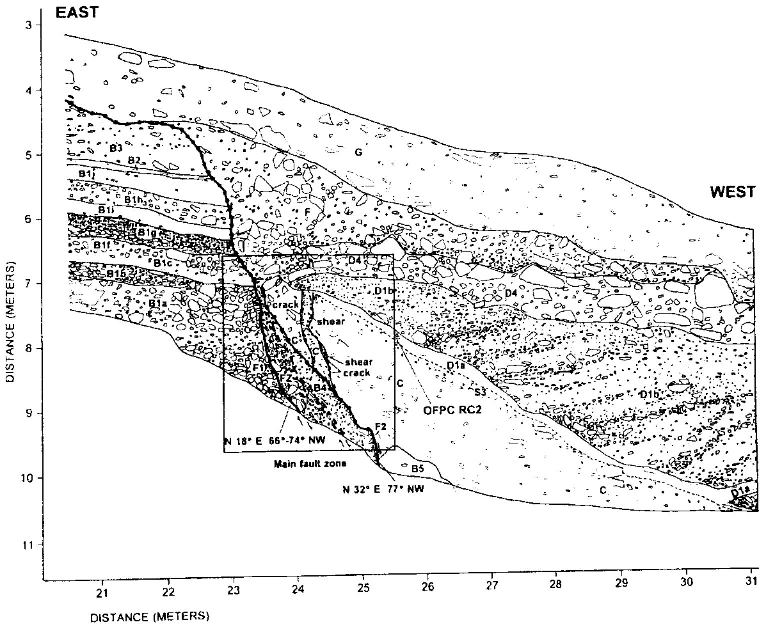

Figure 2.13 Example of an objective trench log, with added linework emphasizing stratigraphic and structural features. Note how the accurate representation of clasts defines sedimentary structures within mappable units, and shear fabric in the main fault zone (in box). [From Olig *et al.*, (1994); reprinted with permission of Elsevier Publishing Company B.V.]

In practice, a judicious combination of the subjective and objective approaches produces trench logs that are sufficiently detailed to act as archival records, yet have sufficient interpretational emphasis that the major elements can be separated at a glance from the minor elements. There must be some interpretational emphasis on a trench log, otherwise it could be replaced by a photograph. As any experienced geologist knows, it is impossible to make a confident geologic interpretation based solely on a photograph of an excavation, without the added information gained by feeling the texture and consistency of deposits exposed in the trench walls.

The *mappable units* defined in a trench exposure are based on the experience of the trench logger. As a general rule, units are distinguished as discrete deposits that are composed of consistent lithology and weathering characteristics (e.g., Miall, 1990). A typical lithologic description of a unit will include the following:

1. Color (Munsell system)
2. Dominant grain size class (gravel, sand, silt, clay), with appropriate modifiers

3. Volume percentage of clasts >2 mm in diameter (gravel)
4. Clast diameter (average and maximum)
5. Clast shape
6. Clast sorting
7. Matrix grain size (often estimated from rheological properties)
8. Matrix compactness (hard versus soft)
9. Bedding thickness
10. Sedimentary structures
11. Weathering or soil formation
12. Fossils
13. Nature of bounding contacts
14. Deformation structures
15. Genetic interpretation

A complementary scheme for defining trench units is *lithofacies codes*, such as that proposed by Nelson (1992b) for deposits found in normal fault zones in semi-arid climates. Lithofacies are differentiated based on the main grain size, modifying grain size, internal structure, an interpretive modifier, and soil horizon development (for examples, see Sec. 3.3).

2.3.2.4.1 Mapping Soils in Trenches

Soils are important markers in trench exposures because they indicate the location of past ground surfaces in the stratigraphic sequence, and their degree of development may indicate the length of time that surface was stabilized. The techniques for recognizing and delineating soil horizon contacts are beyond the scope of this book; see Birkeland (1984) for an excellent summary. Birkeland *et al.* (1991) describe some applications of pedology to neotectonics.

The concept of mapping soil horizons separately from lithologic units often eludes geologists with no training in pedology (e.g., geologists often map soil horizons as lithologic units and become confused when a soil horizon crosses from one lithologic unit into another). However, the interaction of soil profiles with lithologic units is often critical to understanding the sequence of depositional versus tectonic events and their relative timing (Shlemon, 1985). For example, if a soil is developed on tectonically displaced strata and is truncated at the fault scarp along with those strata, the period of soil formation entirely predates faulting. In contrast, if strata are displaced but the soil horizons extend across the fault plane and are developed on other faulted strata, some (perhaps all) of soil formation postdates the faulting.

In most cases soil horizon boundaries will parallel stratigraphic units in the trench, such as buried A (organic) horizons. In this case soils can be mapped as if they were stratigraphic units, differentiated only by a unique symbol or pattern. Where soils are composed of multiple horizons there are two options for trench mapping. The first option is to map the entire soil profile as a single unit, without representing any individual soil horizons. As long as the constituent horizons within the soil profile maintain relatively constant properties and thickness laterally, a single soil description can be used for the entire soil profile. An example is shown in Fig. 2.14, where soils parallel lithologic units, and soil units are portrayed almost as if they were lithologic units (i.e., contact lines are identical to those for lithologic units, and only a light shading distinguishes the soils).

A second option must be used if soil horizons within a soil profile pinch out laterally, change profile properties, or cross from one lithologic unit (parent material) to another. Such complications are common where soils are developed across fault scarps. Because soil contacts and lithologic contacts cross each other, a unique line symbol should be given to soil contacts. Figure 2.15 shows an example of the complex relations created by soil formation that began before the initial faulting and continued during and after faulting, and also fault-induced erosion and colluvial deposition.

The complex interactions between soils and lithologic units are not merely of academic interest. In the absence of material suitable for numerical dating, the degree of soil development can yield an estimate of the relative lengths of time portrayed by soils in the different stratigraphic positions. In Fig. 2.15, the entire 130-ka time span since the formation of the faulted surface is represented by the development of soils 1, 2, 3, 4, and the buried soil. The ratio of development between these soils reflects the amounts of time between successive faulting events. Quantitative estimates of these relative time spans can be made based on the relative amounts of *pedogenic clay* or *calcium carbonate* in each soil; examples are given by Machette (1978), Nelson and Weisser (1985), Birkeland *et al.* (1991), McCalpin (1994), and McCalpin and Berry (1996).

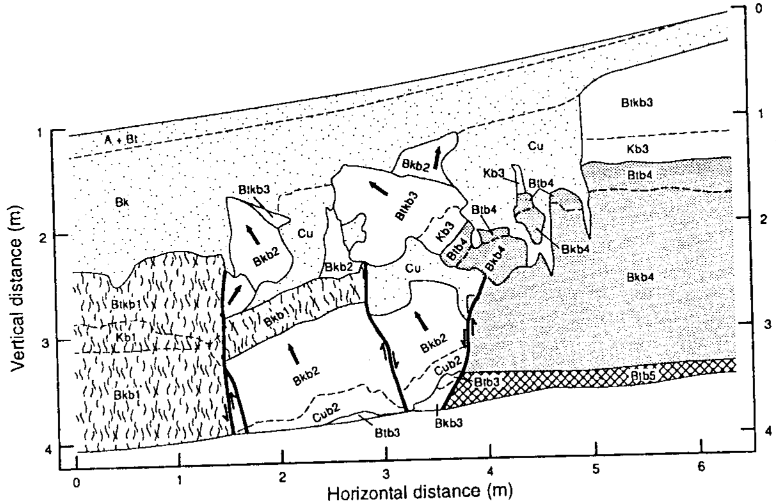

Figure 2.14 Example of soils parallel to lithologic units in a trench wall. Arrows indicate the up direction in each of the rotated soil blocks. Horizon abbreviations A, B, and C denote master horizons; k, calcium carbonate; t, textural B horizon; b, buried horizon; u, material unaffected by pedogenesis. Numbers 2–5 at end of abbreviations indicate horizons belonging to soils of different age. The geometry of the fault scarp before burial by colluvium (small dots) can be evaluated by restoring the rotated blocks to their original positions and restoring the volume of colluvium to the upthrown block. [From Birkeland *et al.*, (1991, p. 48); reprinted with permission of the Utah Geological Survey.]

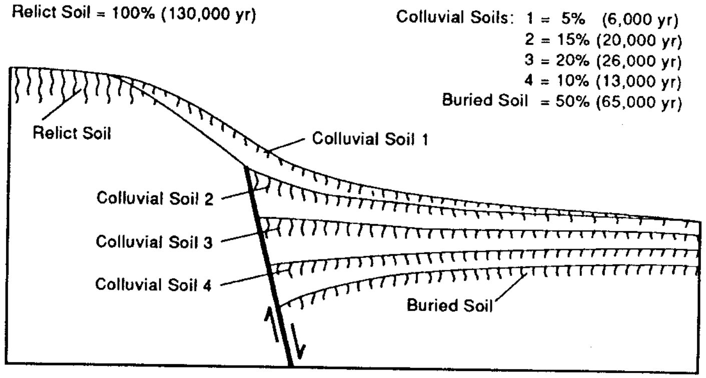

Figure 2.15 Complex soil relations on a fault scarp; note how different soils are superimposed at the scarp crest and toe (far right). In this example, the degree of development of the relict soil (as measured by Profile Development Index, clay or carbonate accumulation) is defined as 100%. The sum of similar soil development indices for the four buried soils and one surface soil on the downthrown block should also equal 100%, neglecting catena variations (see Sec. 3.4.2). The length of time represented by each soil on the downthrown block can be estimated as the product of (1) the ratio of their development to the relict soil (percentage values in upper right), multiplied by (2) the age of the relict soil, resulting in the age spans in parentheses. [From Birkeland *et al.* (1991, p. 45); reprinted with permission of the Utah Geological Survey.]

2.3.2.5 *Identifying and Marking Contacts*

Lithologic units are differentiated as discrete sedimentary deposits characterized by a consistent texture, sorting, bedding, fabric, or color (previous section). Soil units, in contrast, are weathering zones or profiles which may be developed on a single unit, or may be developed across multiple lithologic units. Identifying lithologic and soil units on trench walls is facilitated if lithologic contrasts are emphasized by use of some wall-treatment technique. For example, slight differences in deposit cohesion may be accentuated if the trench wall is left to "weather" for several days or weeks. Wind and rain can then etch out differential relief between different strata and even reveal subtle structures such as cross-bedding in loose sands. Similar relief can sometimes be created by repeated brushing of the face with brooms or paintbrushes.

Coversely, some contacts appear sharper when moist, so walls can be sprayed or misted with a portable water sprayer immediately before logging.

Vague stratigraphic contacts with little textural or color contrasts can often be seen better in diffuse lighting conditions than in direct sunlight. Midday sunlight falls on trench walls at low angles and accentuates (via shadowing) minor irregularities and tool marks at the expense of subtle textural or color variations. Frost *et al.* (1991) suggest that logging at night with artificial illumination, the direction and intensity of which can be controlled, can accentuate subtle stratigraphic and structural features. A corollary use is that of ultraviolet illumination of trench walls at night, which accentuates the fine structure of soils containing calcium carbonate (Kim Thorup, personal communication, 1995). In daylight, vague contacts can often be located by sighting down the length of the trench, nearly parallel to the trench wall. Frost *et al.* (1991) also proposed the use of digital photography and computer image enhancement techniques for identifying structures on trench walls. They suggest that digital techniques such as tone stretching, edge enhancement, band ratioing, and image differencing can be applied to trench wall images to detect features not recognizable with the naked eye. These techniques for "seeing the unseen," while promising, have not yet supplanted our traditional (albeit subjective) visual methods of identifying strata and structures in trenches.

Contacts identified visually are usually accentuated by scribing a line on the trench wall with a knife or edge of a trowel (in cohesive sediments), or placing nails with attached colored flagging along the contact (in cohesionless sediments). In the corresponding trench log, tectonic features (faults, tension cracks, liquefaction features) are rendered with the thickest lines, lithologic contacts with thinner lines, and soil horizon boundaries or facies boundaries within major (genetic) depositional units with very thin or dashed lines.

The critical features in a paleoseismic trench are the deformation features which must be depicted to emphasize their relations with stratigraphic units. The expression of faults and folds in near-surface unconsolidated materials is often more subtle than for faults in bedrock. At times fault traces near the surface are not visible, even though they are known to have ruptured to the surface (Bonilla and Lienkaemper, 1991). Fault traces with a vertical component of displacement are easy to see if multiple stratigraphic units or soils are faulted (Fig. 2.16). This type of stratigraphic offset is primary evidence for dip-slip faulting and also commonly occurs on strike-slip faults. In the absence of stratigraphic offset, faults in unconsolidated deposits are identified from changes in material texture, hardness, or clast fabric along the fault trace.

Fault gouge, created by mechanical crushing of rock and smearing along the fault plane, is rare along faults in unconsolidated deposits because confining pressure near the surface is too low. However, thin (1- to 5-cm), tabular bodies of *translocated sediment* are often found along fault planes. In many cases those bodies are composed of soft sediments (silt, clay, marl) dragged along the fault plane from displaced strata (Fig. 2.16). Such zones of smeared cohesive material often contain granular material or blocks of adjacent strata, often termed "mixture of adjoining materials," "mixed rock," or "tectonic mixing" on trench logs (Bonilla and Lienkaemper, 1991).

Figure 2.16 Photographs contrasting easily visible faults (thick arrows) in well-stratified lacustrine sand and silt with an obscure fault strand (thin arrows) in a massive diamicton (sandy debris–facies colluvium). The main fault (center) places lacustrine sediments in fault contact with scarp-derived colluvium. Horizontal string lines at center and right are 1 m apart. Kaysville trench on the Wasatch fault zone, Utah (Swan *et al.*, 1980; McCalpin *et al.*, 1994).

Fault zones in clast-rich deposits are usually identified by a consistent *clast fabric* different from that observed in adjacent strata. Shear on the fault may rotate clast long axes parallel to the fault plane, resulting in what paleoseismologists often term *shear fabric* (Fig. 2.17). Yount *et al.* (1987) reasoned that on steeply dipping faults, dip-slip fault shear would twirl clasts so their long axes became horizontal (aligned with strike), whereas strike-slip movement would twirl clasts into near-vertical orientations (long axes aligned with dip direction). This speculation is not supported by most exposures along normal faults, in which long axes of fault-zone pebbles typically parallel the dip of the fault (Fig. 2.17). The author is unaware of any laboratory experiments that have reproduced the aligned elongate pebbles seen in many trenches, but such experiments would permit a more confident interpretation of shear fabric.

Faults in unconsolidated deposits are often accompanied by *fissures, open voids,* and *fault-related rubble.* The rubble consists of blocks of adjacent stratig-

Figure 2.17 Close-up photograph of two parallel normal fault strands (between arrows) in gravelly late Pleistocene deltaic deposits, East Bear Lake fault, Utah. Numbers on rod are 10 cm apart. Note anomalous parallel clast fabric and slight discoloration of gravel along the fault strands.

raphy that may have fallen downward into open fissures, been dragged upward along the fault, or both. Fissures and fissure-filling materials (Fig. 2.18) are most common along normal faults (Bonilla and Lienkaemper, 1991).

2.3.2.5.1 *The Problem of Fault Nonvisibility*

In most applications of structural geology, strata that overlie a fault and are not visibly faulted are assumed to postdate faulting. In unconsolidated deposits, however, faults may lose *visibility* even though the host deposits can be proven to have been displaced. Bonilla and Lienkaemper (1991) provide a comprehensive discussion of this problem, which we briefly summarize next. Terms used in the discussion are defined in Fig. 2.19 and Table 2-1.

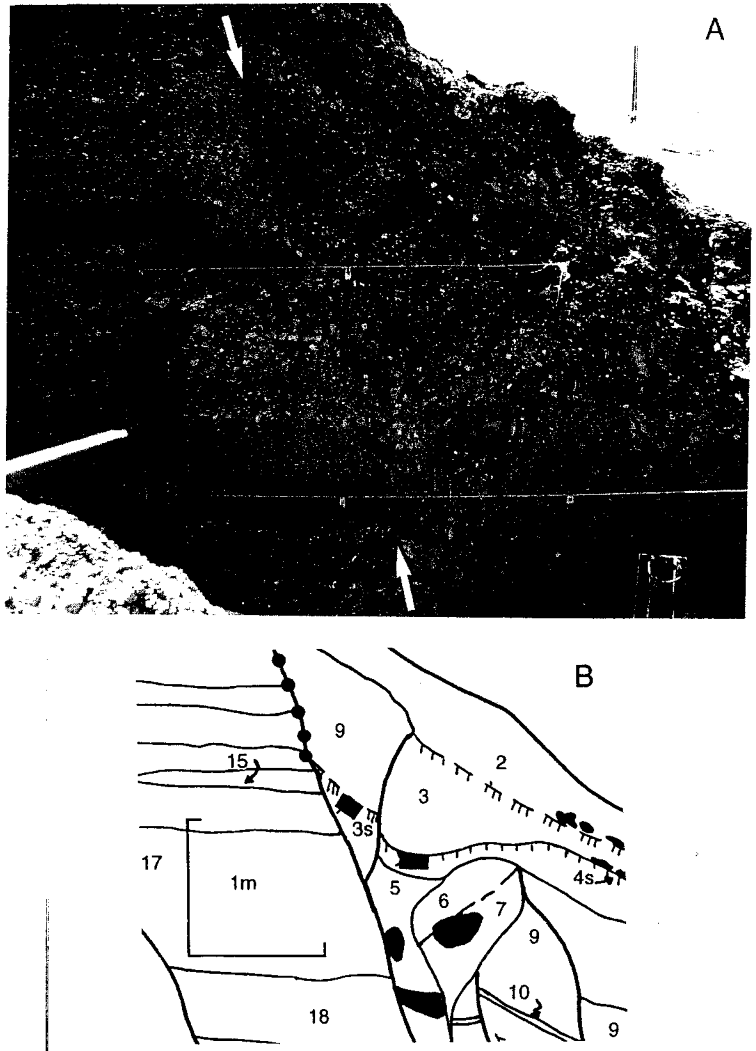

Figure 2.18 Main fault strand of the Wasatch fault zone, Nephi segment, Red Canyon trench (Jackson, 1991). (A) Photograph; string lines, and tags on lines, are 1 m apart. The main fault plane (arrows) cleanly truncates well-stratified alluvial fan gravels (to left). To the right of the fault occurs a 15- to 40-cm-thick zone of mixed sheared gravels and fault-related rubble. Pebble fabric and stratification allow distinction of "shear fabric" from back-tilted blocks farther to right. (B) Subjective log of the photographed portion of trench wall. [From Jackson (1991); reprinted with permission of the Utah Geological Survey.]

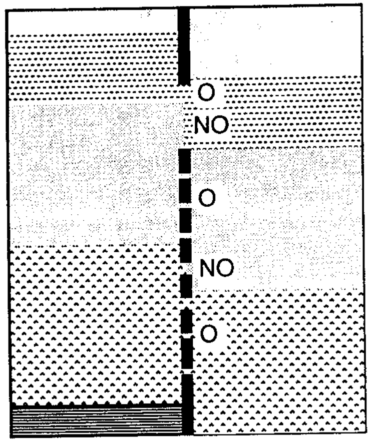

Figure 2.19 Schematic diagram of a simple fault exposed on a trench wall showing designation of obscure segments (O) and not obscure (visible) segments (NO), as defined by Bonilla and Lienkaemper (1991, Fig. 1).

Table 2-1

Definitions of Terms Describing the Visibility of Fault Strands in Vertical Exposures

Term	Definition
Strand	A part of a fault trace exposed in a trench wall; the term is preferable to "segment" as used by Bonilla and Leinkaemper, which has planimetric connotations (Chapter 9)
Principal strand	The fault strand that has the largest real or apparent displacement in a given exposure
Obscure segment	Part of a known fault strand where the fault is not clearly visible in the trench wall, but is visible both higher and lower on the trench wall, or was known to have displaced the ground surface at time of faulting; usually caused by concealment
Dieout up	Where a fault strand ends, or seems to end, upward; caused by concealment or by termination of displacement
Dieout down	Where a fault strand ends, or seems to end, downward; caused by concealment or by termination of displacement
Nonvisibility	A general term that encompasses obscure segments, dieout up, and dieout down
Depth of dieout up	Vertical distance from the ground surface at the time of faulting to the top of the visible part of the fault strand

After Bonilla and Lienkaemper (1991).

Nonvisibility of fault strands can be caused by two general mechanisms, *concealment* or *termination of displacement.* Concealment means that the fault displacement exists, but cannot easily be seen. For example, where a fault is nonvisible under a surface rupture trace, or where it is visible both below and above a stratum but not within the stratum, the cause must be concealment of a true fault trace. Fault strands that are nonvisible immediately after faulting might be concealed due to intergranular movements, bending of the affected stratum, or many small-displacement distributed ruptures. Fault strands that were visible immediately following a paleoearthquake are often progressively obscured through time by soil formation, bioturbation, freeze-thaw, shrink-swell, plastic flow of clay, rearrangement of grains in granular material, or human activities such as plowing. Nonvisible fault segments are far less common in normal faults (5 to 10% of fault strands) than in strike-slip faults (60 to 70% of fault strands) and reverse faults (30 to 60% of fault strands) (Bonilla and Lienkaemper, 1991, p. 18). *Obscure segments* are most common in sand (due to intergranular adjustments) and soil horizons (due to bioturbation and pedoturbation), less common in silt and clay (which are often well stratified), and least common in gravel (where rotated pebbles may show the fault trace).

A second reason for nonvisibility of a fault strand is actual termination of displacement. "Reasoning indicates that all faults must actually end somewhere, and observational evidence supporting this conclusion is provided by experimental fault studies and mine mapping showing fault strands that die out upward, downward, or both" (Bonilla and Lienkaemper, 1991, p. 29). For those faults where the position of the ground surface at time of faulting is known, an astounding 73% of strike-slip fault strands, and 75% of reverse fault strands exposed in trenches, show *dieout up* (Table 2-1), whereas only 15% of normal faults dieout up. At most paleoseimic trench sites it is not possible to distinguish whether dieout up results from concealment, distributed deformation, or termination of displacement, because the position of the ground surface at the time of faulting is not generally known. However, the material properties responsible for concealment of true faults should be similar for strike-slip, reverse, and normal faults, which implies that the minimum of 15% of obscure segments found in normal faults probably represents concealment, while the additional 60% obscure segments in reverse and strike-slip faults may result from termination of displacement.

Repeated faulting alternating with deposition of strata will result in increasing displacement on the fault with depth (Fig. 2.20A). Such *differential displacements* may result from (1) episodic faulting or (2) *attenuation of displacement* in the vertical direction. The proportion of cases caused by these two factors is unknown, but Collins (1990) argues that attenuation is more prevalent. To prove a recurrent faulting origin, the displacements must only abruptly increase with depth at unconformable contacts of each depositional unit; within each unit displacement must be constant. If this condition is *not* met,

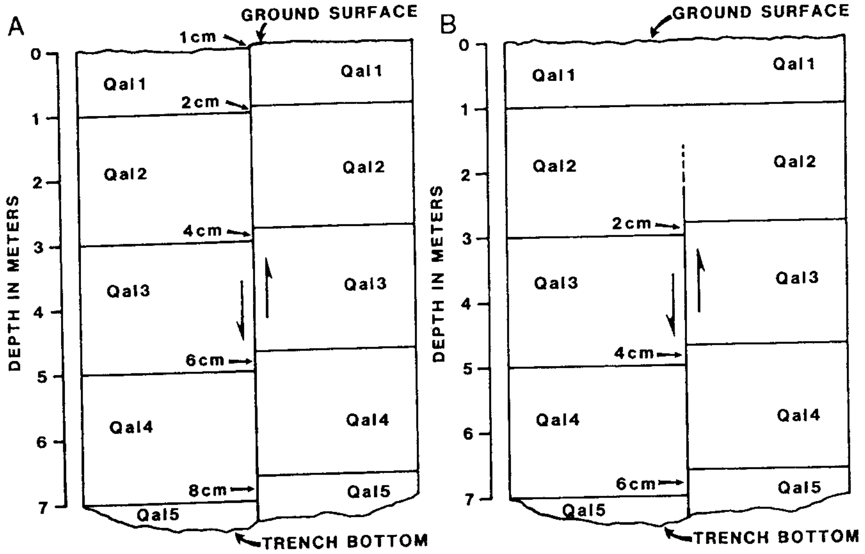

Figure 2.20 Diagrams of decreasing fault displacement upsection. (A) Decreasing displacement of this type may be due to recurrent faulting or to a vertical displacement gradient. (B) Example of a fault trace that dies out before it reaches the surface. This geometry can be caused by (1) latest faulting midway during deposition of Qal2, or dieout up in a faulting event that ruptured the modern ground surface at other locations. [From Collins (1990); reprinted with permission of the Association of Engineering Geologists.]

the increase of displacement with depth may be due to vertical attenuation of displacement in near-surface materials. Such a situation might result from a single faulting event, as shown in Fig. 2.20B. In this example the fault died out upward before it reached the ground surface existing at the time of rupture. This discussion assumes that the faults can be easily observed on the trench wall and are not concealed due to one of the recognition factors discussed earlier.

2.3.2.6 *Logging the Trench*

Once all contacts have been marked on the trench wall, the task of trench logging is mainly mechanical and can be accomplished by a variety of manual or instrumental techniques. In the *manual measurement method*, features on the trench wall are measured in relation to the reference grid with a tape measure. While one person measures the horizontal and vertical distances from trench features to the nearest grid line, a second person plots the position of these *control points* on the trench log. Contacts are then drawn on the log by connecting the control points with lines that mimic the natural, irregular nature of contacts on the trench wall. Some artistry is required. The trench log thus drawn is completed before leaving the trench site, which facilitates

plotting sample locations and making preliminary interpretations. The advantages of the manual logging method are (1) it is inexpensive and requires no equipment more sophisticated than a bubble level and a tape measure, (2) one person can do the logging if necessary although two should be used for safety, and (3) the log is drawn as the trench is traversed and is in nearly final form when the end of the trench is reached. Disadvantages of the method are its lack of planimetric accuracy and the time consumed by measuring thousands of points by hand.

A newer method of *electronic trench logging* involves surveying the positions of control points on the trench wall with electronic surveying instruments, such as the total station (e.g., Lund and Euge, 1984). In this method no string line reference grid need be constructed in the trench. Instead, the total station is mounted at one end of the trench, or outside the trench if the entire wall to be logged is visible from a single point. One person holds the EDM reflector against the trench wall at unit contacts, while the instrument operator surveys the angle and distance to that point. This process is repeated for as many control points as desired. The total station operator can enter codes that distinguish points surveyed on fault contacts, contacts of individual stratigraphic units, and soils.

To create a trench log, the digitized *x, y,* and *z* coordinates of trench contacts must be plotted. Most plotting programs connect control points with straight line segments, so many more control points must be measured on curving or irregular contacts than is necessary in the manual method if lines are to be realistic. Plotting software is available from most manufacturers of total stations, as well as from third-party companies. The advantages of the total station method of logging are increased speed and accuracy, the ability to plot trench logs at any scale, and the ability to project points onto a vertical plane from nonvertical trench walls. The main disadvantages are cost of the equipment, and the need to have a printer or plotter in the field so that a hardcopy log is available for on-site use, and the difficulty of altering contacts during final revision.

Photography can also be used in any trench to document wall relations (Goodman, 1976; see McClay, 1985, for the use of clear overlays, and Frost *et al.*, 1991, for description of video and audio documentation), and in some trenches can actually be used for compiling the log. The method of *photogrammetric logging* developed by Fairer *et al.* (1989) and Coe *et al.* (1991) is described as follows. First, all lithologic, soil, and fault contacts must be marked on the wall clearly enough to be seen on a photograph; this may require colored flagging attached to nails driven into the wall, or spray paint. Second, at least four surveyed control points (with *x, y,* and *z* coordinates) must lie within each stereo pair of photographs that will be taken of the trench wall, and these too must be visible on the photos. Third, geologic notes, Polaroid photographs, and sketches are made relating geologic features to the surveyed

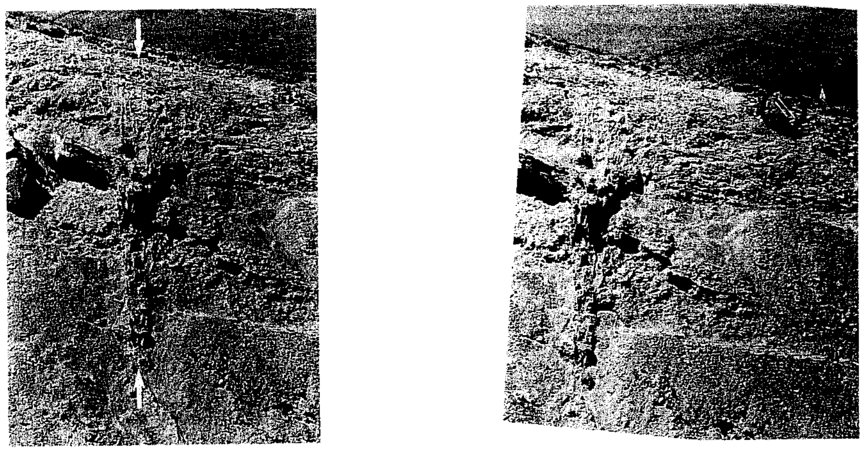

Figure 2.21 Stereo photograph pair used in the photogrammetric technique of trench wall logging. The main fault zone (between arrows) stands out in relief because it has been cemented by calcium carbonate and silica. The irregular, sloping walls of this natural exposure would be difficult to log accurately with the manual measurement technique. Shovels at upper right (circled) are 1.5 m long. Paintbrush Canyon fault at Busted Butte, Nevada Test Site. (Photographs courtesy of J. A. Coe.)

control points, to supply critical data to the plotter operator if uncertainties arise. Fourth, the trench wall is photographed from a constant distance (ca. 2 to 3 m) such that adjacent photographs overlap by 60% (Fig. 2.21). Fairer *et al.* (1989) used a 70-mm-format camera mounted on a dual-tripod system, but any small-format camera will work. Photographs taken at night with strobe lighting are not plagued by daytime shadows.

The overlapping photographs are analyzed in an analytical plotter, which is a computerized stereo plotter commonly used in photogrammetric analyses of vertical aerial photographs. Fairer *et al.* (1989) claim that the photogrammetric method requires only about one-quarter to one-sixth the time of the manual measurement method to produce a final trench log. The main advantage of the photogrammetric method is its accuracy (±6 mm; Coe *et al.*, 1991) and its sophisticated analysis of planimetric measurement errors, which may be required by stringent quality assurance programs. However, millimeter-scale accuracy is rarely necessary for an adequate interpretation of either paleoearthquake displacement or age. The drawbacks to the method are the cost of buying ($100,000 U.S.) or renting an analytical plotter, and widening the trench to 2 to 3 m wide, which is not possible in many instances.

The *scale* of the trench log must allow accurate delineation of features as small as 1 cm, but must not be so large as to make the log unwieldy. A scale of 1:20 is typically used in the United States; at this scale a 5-cm-high feature is 2.5 mm high on the log, about the practical limit of legible drafting. Depending on desired detail, logs can be mapped at scales of 1:10 to 1:50, but should rarely be smaller scale than 1:60, or the log will merely be a "cartoon" of actual wall relations. Some states in the United States have guidelines suggesting appropriate methods and scale used in trench logging (Utah Section, Association of Engineering Geologists, 1987).

2.3.2.7 Retrodeformation of the Log and Final Interpretation

The first version of the trench log forms the basis for the initial interpretation of the style, amount, and age of paleoseismic deformation. Based on the initial log, workers identify the critical structural and stratigraphic contacts (faults and event horizons) that indicate paleoearthquakes, and reexamine them on the trench walls. At this time some attempt is made, in either a rigorous "balanced" sense or less formally, to reconstruct graphically the sequence of deformation by *restoring stratigraphic units* to their predeformation positions (Fig. 2.22). Stratigraphic units are restored to their (inferred) original geometries by graphically reversing the sense of displacement on faults; this procedure is also known as *retrodeformation analysis.*

Retrodeformation analysis is based on several basic stratigraphic assumptions, such as (1) the original physical continuity of faulted beds and (2) the original horizontality of the upper contacts of fine-grained beds. Most examples of retrodeformation analysis are two dimensional; for example, on a vertical trench wall only the vertical components of displacement are restored. Figure 2.23 shows an example of retrodeformation of two faulting events in which beds were both faulted and folded by reverse faulting. This type of analysis requires an understanding of the depositional environments of faulted strata in order to infer their original geometry (see Fig. 2.23 caption). Performing retrodeformation analysis on vertical stratigraphic separations caused by strike-slip displacement is much more problematic, because lateral displacement of nonplanar, nonhorizontal strata produces highly variable and conflicting vertical separations on each fault.

Attempts to make restorations often point out inconsistencies or impossibilities in the initial trench log, such as correlation of units across faults that is opposite to that required by the inferred sense of slip. As much time may be spent in reexamining and relogging critical features in a small part of the trench as was spent in making the entire initial trench log. Although each trench log is different, each must pass the test of being restorable without resorting to unreasonable or physically impossible sequences of events.

To aid the reader in interpreting trenches, Chapters 3 through 7 contain figures of common geometries produced by paleoseismic deformation in various tectonic environments. Some of these geometries are observed so repeatedly in a given tectonic setting that paleoseismologists have defined them as *paradigms* for interpreting faulting history (e.g., the colluvial wedge model of

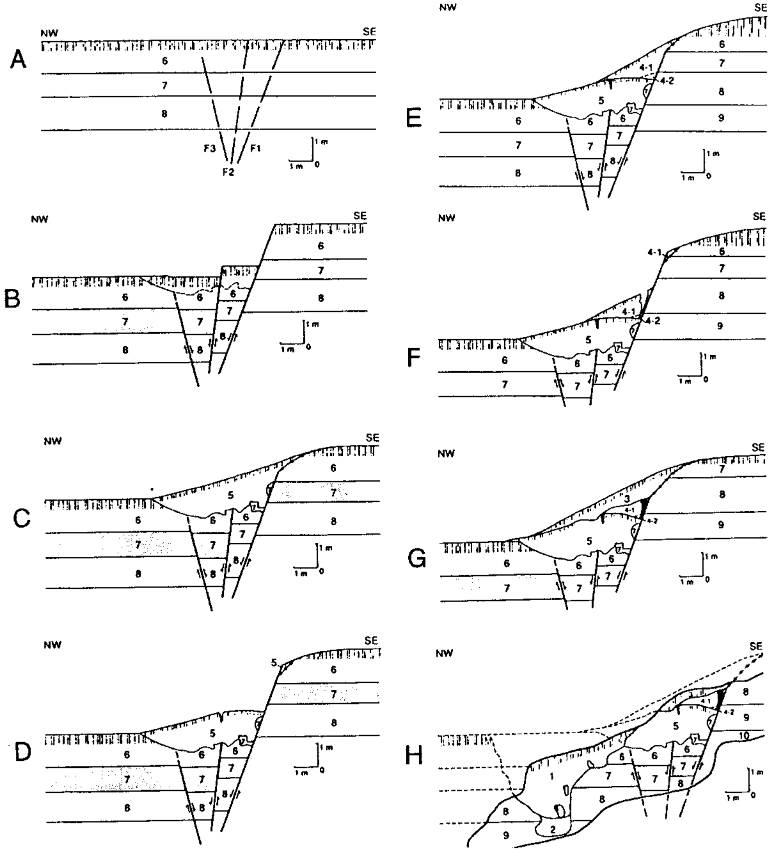

Figure 2.22 Simplified cross sections showing the inferred sequential development of the north wall of the Pole Patch trench, Brigham City segment of the Wasatch fault zone, Utah, USA. (A) Prefaulting stratigraphy. (B) Scarp immediately after the first faulting event; material above dashed line is shattered and eroded. (C) Deposition of first colluvial wedge (unit 5). (D) Second faulting event, displacement on right fault only. (E) Deposition of second colluvial wedge (unit 4). (F) Third faulting event. (G) Deposition of Third colluvial wedge (unit 3). (H) Present configuration of trench (within heavy line). An alluvial channel (units 1 and 2) is cut into the toe of the scarp. This type of retrodeformation analysis does not rely on continuity of strata across the fault, except for the first faulting event. Instead it relies on colluvial wedges as event indicators (see Chapter 3). [From Personius (1991); reprinted with permission of the Utah Geological Survey.]

Schwartz and Coppersmith, 1984). These paradigms form an obvious starting point for interpreting stratigraphic relations in a trench, but blind adherence to them may cause small features incompatible with the paradigm to be overlooked or ignored.

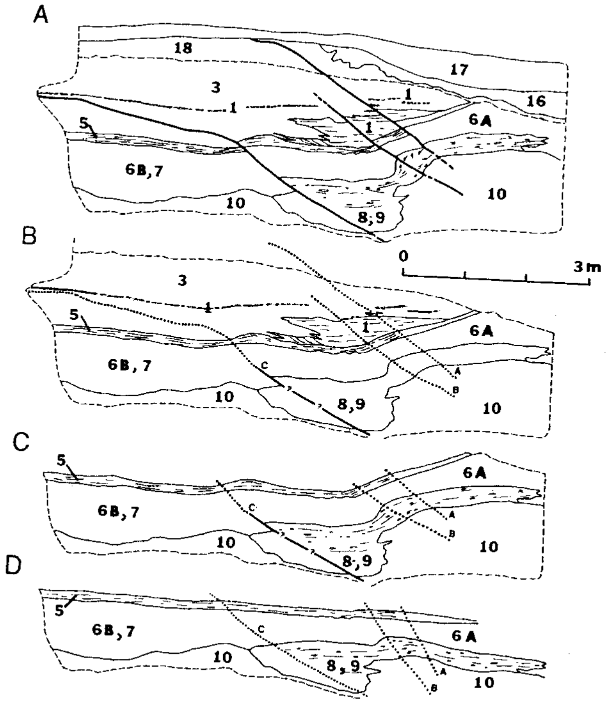

Figure 2.23 Retrodeformation of the log of the Arroyo fault near Point Conception, California. (A) Simplified version of the trench log (detailed log shown in Asquith, 1985, Fig. 6). (B) The exposure after restoring displacement such that units 5 and above are unfaulted. Faults on which all displacement has been reversed are shown as dotted lines. This restoration eliminates all displacement on faults A and B, but leaves a residual displacement on fault C that is attributed to an earlier faulting event. (C) The configuration of units 5 through 10 prior to deposition of units 1 through 3. Note that the right part of unit 5 was not restored to horizontal in views B and C, because unit 1 was clearly deposited as a lens atop a sloping surface. (D) Stratigraphic relations after the remaining displacement on fault C has been "backed out." To restore the right part of unit 5 (a thin clay bed) to horizontal, it and all underlying units must be rotated approximately 15° clockwise. Two faulting events is the smallest number that will explain the observed stratigraphic relations, and thus satisfies Occam's razor as the simplest explanation. There is no direct stratigraphic evidence of individual displacements, such as upward fault terminations at different stratigraphic levels, colluvial wedges, or fissure fills that would indicate more than two faulting events (compare to Fig. 2.22). [From Asquith (1985); reprinted with permission of the Association of Engineering Geologists.]

2.3.3 Geophysical Techniques in Paleoseismology

Geophysical methods can be useful in paleoseismology in three ways (1) for characterizing the subsurface geology in mapped fault zones, (2) for detecting buried faults that have no surface expression, and (3) for characterizing deformation features on the bottoms of lakes and oceans. Paleoseismology requires geophysical systems with high spatial resolution and the ability to distinguish between unconsolidated deposits with very similar material properties. Depth penetration of more than 10 m is usually not required, because the data of interest often lie only a few meters below the surface. The field of engineering geophysics includes shallow site exploration, and texts in that field provide the background for the methods described next. A survey of geophysics applied to fault assessment is given by Krinitsky (1974). A special application of geophysics in volcanic-extensional terranes is locating dike swarms beneath volcanic rift zones (Sec. 4.3.3).

2.3.3.1 Seismic Methods

Seismic reflection and *seismic refraction* methods can contribute to paleoseismology in two ways (1) by detecting faults and (2) by characterizing subsurface strata that have been offset, folded, or tilted by faulting. However, the simple detection of a fault plane may not, in itself, provide any data on the timing and magnitude of individual paleoearthquakes. Because seismic reflection methods image horizontal and dipping reflectors, the method is best suited to detecting vertical separations associated with a dip-slip component of faulting. In contrast, seismic refraction usually does not possess the resolution to detect small paleoseismic features. For example, Pelton *et al.* (1985) could only distinguish the largest faulted units along the 1983 Borah Peak, Idaho, surface rupture trace with seismic refraction.

High-resolution seismic reflection techniques have been successfully used to map subsurface fault structure in zones of Quaternary dip-slip faulting. An early reconnaissance study along the Wasatch fault zone, USA, used the *Mini-Sosie system* (Crone and Harding, 1984a). The system was optimized for detecting normal faults that displace late Quaternary lacustrine and alluvial gravels. In a similar study, Crone and Harding (1984b) used Mini-Sosie to detect buried normal faults between surface fault scarps in a swarm of normal faults. The Mini-Sosie system has also been used to characterize the shallow geometry of the 1983 Borah Peak rupture (Miller and Steeples, 1986; Treadway *et al.*, 1988) and the Quaternary oblique-slip Meers fault, Oklahoma, USA (Myers *et al.*, 1987; Miller *et al.*, 1990). More recent studies of the Wasatch fault zone, USA, have refined the high-resolution method (Benson and Mustoe, 1991; Stephenson *et al.*, 1993). At the Kaysville trench site (Swan *et al.*, 1980; McCalpin *et al.*, 1994), Stephenson *et al.* (1993) were successful in detecting not only fault planes in a complex fault scarp-graben system, but also imaged several subsurface contacts tilted toward the fault. Comparison of detailed seismic reflection records with the trench log (Fig. 2.24) revealed that most details of trench macrostratigraphy could be imaged. However, seismic methods could not differentiate individual colluvial wedges 1 to 2 m thick against the main fault plane, and thus could not independently determine the number of or size of prehistoric displacements.

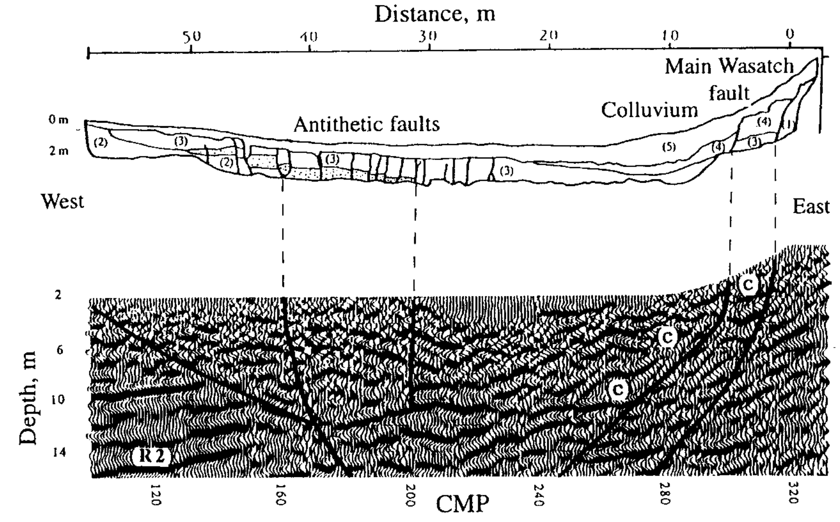

Figure 2.24 Comparison of high-resolution seismic reflection data (lower part) with a trench log (upper part) across a Quaternary normal fault scarp and graben, Wasatch fault zone, Utah. Map units in upper part: 1, late Pleistocene lacustrine sand and silt; 2, Holocene alluvial fan; 3, older colluvium and graben sediments; 4, intermediate-age colluvium; 5, younger colluvium and graben sediments. Figure 2.16 shows the two faults at the right end of the trench log. Seismic data cannot image all the small-displacement faults within the graben (between 25 and 40 m on upper scale), but do indicate a decrease in fault dips that could not be inferred from trench data. [From Stephenson *et al.* (1993); reprinted with permission of the American Geophysical Union.]

Geophysical methods in the *marine environment* have two tasks: (1) to characterize the bathymetry of the water body (geomorphic expressions) and (2) to detect stratification and deformation structures in the sediments underlying the sediment/water interface (stratigraphic expressions). In the following sections we first describe the paleoseismic applications of studies of subsea topography, and then studies of submarine structural geology. The interpretational principles for submarine features are similar to those for terrestrial features, and are summarized by Clarke *et al.* (1985).

Resolution of small-scale (<1-km) seafloor topography requires the use of narrow-beam acoustic imaging systems (Legg *et al.*, 1989). Seafloor mapping over large areas has been performed with long-range sidescan sonars towed at relatively shallow depths. Common systems used to study oceanic fault and fracture zones are *GLORIA* (Searle, 1979) and *SeaMarc I* and *II* (Kastens *et al.*, 1986). The most accurate system is a multiple narrow-beam echo sounder, such as the 12-kHz *SeaBeam* system (Renard and Allenau, 1979; Schlee *et al.*, 1995). SeaBeam has a lateral resolution of 50 to 100 m, with horizontal accuracy dependent on the precision of the ship's position; Legg *et al.* (1989) report accuracies of 500 m in absolute position and 200 m in relative position. Vertical accuracy is as small as 2 to 3 m for the center beam, but may average 10 to 15 m overall in water depths of 1000 to 2000 m. Clarke *et al.* (1985) detected vertical features as small as 1 to 1.5 m high in water depths of 50 m.

Legg *et al.* (1989) used SeaBeam to map the tectonic geomorphology along the dextral San Clemente fault, offshore California, USA. Many of the landforms associated with onshore strike-slip faulting were recognized. In a similar study, Appelgate *et al.* (1992) used SeaMarc I and SeaBeam systems to map a sinistral fault offshore of the Oregon coast, USA. Sinistral displacements of submarine channels amounted to 120 to 2500 m, yielding estimated slip rates of 5 to 12 mm/yr.

The same acoustic reflection profiling techniques just described also return reflections from the interfaces between subbottom stratigraphic units. Clarke *et al.* (1985) distinguish *intermediate-penetration surveys* (depth penetration ≥ 1 km, vertical resolution about 15 m) from *high-resolution surveys* (depth penetration 150 to 400 m, vertical resolution 1 to 1.5 m). Only the latter are capable of imaging stratigraphic evidence from individual paleoearthquakes. Williams and Ingram (1994) suggest that strict criteria must be applied before a fault origin should be assigned to features imaged in subaqueous unconsolidated sediments. Features should be reproducible, have consistent map pattern, show indications of structural growth, be independent from reflection multiples, be independent from current-produced features (ripples, banks), and be consistent with deeper structure. Possible false images that might look like faults are submerged objects (pilings, bulkheads), buried objects (boulders, pipelines), gaseous "bright spots," reflection multiples, and out-of-line features.

In marine paleoseismic studies, geophysical surveys must be integrated with seafloor sampling and geochronology to assess fault slip rate, recurrence, segmentation, and magnitude. The most intensively studied offshore fault in the United States is the Palo Verdes Hills fault (Fig. 2.25) offshore of Los Angeles (Clarke *et al.*, 1985; McNeilan *et al.*, 1996). McNeilan *et al.* (1996) used a multireceiver "boomer" system in Los Angeles Harbor to measure 21 to 24 m of dextral offset, and 3 m of vertical offset, on a 7.8- to 8-ka paleochannel, based on six piercing lines. In the area of the paleochannel they collected 70 km of seismic line within an area of less than 0.33 km^2, with an average trackline spacing of 20 m; horizontal error was estimated as ~1 to 1.5 m. Stratigraphy was assessed through 124 seafloor borings from 10 to 40 m deep, and more than 60 borehole samples (shell, wood, and charcoal) yielded ^{14}C dates between 300 and 14,000 yr B.P. Although this study is the most detailed of its kind to date, individual paleoearthquakes and slip per event could not be determined. Similar (but less detailed) *integrated marine paleoseismic studies* are reported by Pipkin and Ploessel (1985) and Nodder (1993, 1994).

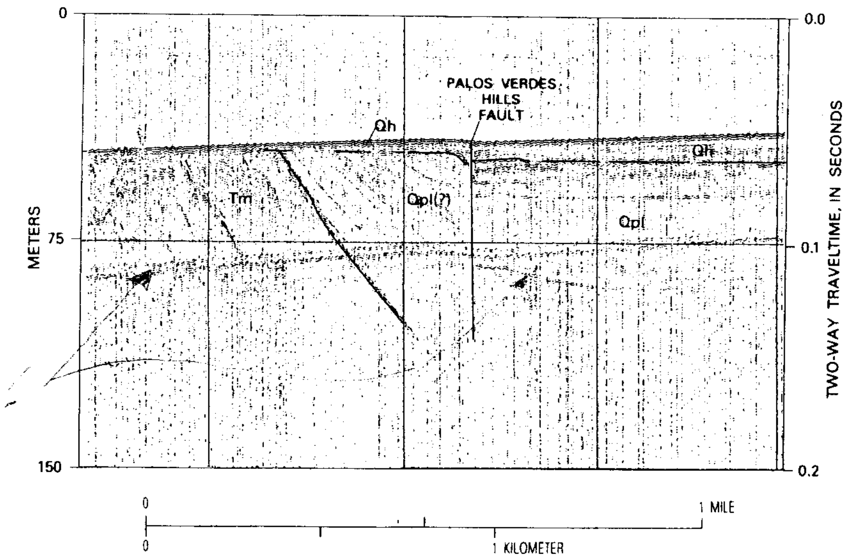

Figure 2.25 Interpreted seismic reflection cross section across the offshore Palos Verdes Hills fault, southern California. Qh, Holocene sediments; Qpl, late Pleistocene sediments. Vertical offset of the seafloor is about 1 m, whereas vertical stratigraphic separation of the Qh/Qpl contact is 3 m, suggestive of multiple faulting events. McNeilan *et al.* (1996) document a strike-slip to dip slip ratio of 5:1 to 6:1 for this fault, so most of the net Holocene slip is not imaged by 2-D geophysical cross-sections. [From Clarke *et al.*, (1985).]

2.3.3.2 Ground-Penetrating Radar

Ground-penetrating radar (GPR) produces subsurface images that superficially resemble seismic reflection results. The similarities arise from the common use of transmitted waves that are reflected and then detected by a receiver on the surface. In contrast to the compressional elastic waves utilized in seismic reflection (frequency = 100 Hz), radar uses transmitted electromagnetic radiation with frequencies from 80 to 300 MHz. Materials with high electrical conductivity such as clay or fluids with high dissolved solids will rapidly decrease the depth of penetration. Subsurface contacts with higher contrasts in dielectric properties return stronger reflections. Studies that have tested GPR for shallow exploration for engineering purposes include Kuo and Stangland (1989) and Hammond *et al.* (1986).

To date, few published studies have applied GPR to zones of active faulting. Bilham (1985) and Bilham and Seeber (1985) used a commercial 80- to 300-MHz impulse radar system with an effective depth penetration of 10 m to examine normal, oblique, and strike-slip faults in the western United States. They found that coarse colluvium and fan alluvium at faulted range fronts did not possess dielectric layering, and so returned few reflections on GPR images. However, prehistoric colluvial wedges were detected at the Borah Peak, Idaho, fault scarp. The colluvial wedges there were imaged by detecting the underlying, clay-bearing buried soils that formed during interseismic periods of landscape stability. In theory, multiple buried soils outlining colluvial wedges could be detected as long as the clay content of each soil was not high enough to absorb too much radiation. Wide zones of faulting were imaged by GPR on the Wasatch fault zone (Smith and Jol, 1995) and the San Andreas fault zone. Well-defined GPR profiles across strike-slip faults were even obtained by Bilham and Seeber (1985) when floating the GPR antenna across freshwater sag ponds and rivers; in contrast, moistened saline soils were opaque to GPR. With a potential resolution of 6 to 30 cm, GPR promises to be a paleoseismic tool superior to seismic reflection in some environments that possess sediments that are neither too clayey nor too saline.

2.3.3.3 Magnetic Methods

Aeromagnetic surveys are a standard exploration tool for detecting large-scale faulting, as shown in the Basin and Range Province, USA (Smith, 1967). Fewer studies have aimed at the characterization of shallow faults in unconsolidated material. Bailey (1974) detected fault gouge with a magnetometer in California. Salyards *et al.* (1992) used the paleomagnetic signature of sediments within 50 m of the San Andreas fault to identify rotations resulting from plastic deformation in a wide dextral shear zone. This plastic deformation accommodated as much displacement as brittle faulting at the main fault, but had not previously been recognized. Recognition of the plastic deformation resulted in doubling the estimate of the Holocene slip rate for this fault location.

2.3.3.4 Gravity Methods

The structural relief resulting from displacement on dip-slip faults can be well expressed as differences in gravitational attraction across the fault. Near-surface faults in unconsolidated material, however, can only be interpreted from gravity data if stations are closely spaced and very accurately surveyed. Benson and Baer (1987) used a Worden gravimeter, with stations on 7.6- to 12.2-m spacings, surveyed to a 3 cm vertical accuracy, to detect buried normal faults in alluvium on the Wasatch fault zone, USA. Residual Bouger gravity anomalies of ±0.2 milligals correlated reasonably well to mapped normal faults, faults discovered in creek banks during their study, and newly inferred faults with no surface expression. However, this application occurred in an optimum setting for gravity contrasts, where low-density alluvium overlying high-density bedrock became abruptly thicker across each fault.

2.4 SPECIALIZED SUBFIELDS OF PALEOSEISMOLOGY

Paleoseismology itself is the parent field of at least two subfields that have been defined previously in published papers, *archaeoseismology* (Karcz and Kafri, 1978) and *dendroseismology* (Jacoby *et al.*, 1988). These two subfields are not based on geological evidence, as is the material covered in this book. Instead, the subfields are defined by a specific type of nongeological evidence, usually secondary evidence, that is used to reconstruct paleoseismic histories. Each of these fields began primarily as dating techniques. Subsequently, the practitioners (archeologists and dendrochronologists, respectively) developed a wider suite of specialized techniques for data collection and interpretation that lies outside the typical scope of their own disciplines, as well as outside of geology or seismology. A detailed treatment of these subfields is beyond the scope this book, but in the following brief sections we offer a summary of principles and key literature.

2.4.1 Archaeoseismology

Archaeoseismology is the study of prehistoric earthquakes based on their effects on man-made objects, usually buildings or other monuments (Karcz and Kafri, 1978). The term "prehistoric" is used rather loosely in this definition, since most cultures sufficiently advanced to build lasting structures also left written records. However, those records are commonly too fragmentary to permit correlation of a recorded earthquake with a particular fault or even with a particular region (see, however, Ben-Menaham, 1981).

Archaeoseismic damage falls into three general categories. First, ancient structures may be deformed and *displaced* by surface faulting. Reches and Hoexter (1981) and Zhang *et al.* (1986) give examples of these two phenomena for Hisham's Palace, Israel, and the Great Wall of China, respectively. Second, walls and towers may *collapse* or *topple* from high ground accelerations during seismic shaking. Rapp (1982) describes this type of evidence at Troy. Third, site-wide, *total destruction* may occur for which earthquakes are the only reasonable explanation. In such destruction floors and roofs have collapsed, precious artifacts (potential loot) have been indiscriminately destroyed, and human bodies remain trapped in debris, in contradiction to local burial customs. Readers interested in case histories are referred to the large compilation in Stiros and Jones (1996).

Since the field was established, there has been heated debate about the criteria for distinguishing coseismic from nonseismic damage in ancient structures. Karcz and Kafri (1978) adopted the conservative view that a paleoseismic origin can only be accepted if all other causes, such as poor construction, soil settlement, or human destruction, could be ruled out. They noted that "the critical examination of field evidence often cited in support of ancient seismicity has shown that the individual features are difficult to distinguish from the features of damage due to poor construction and adverse geotechnical effects." To assess the probability of nonseismic causes, Rapp (1986, p. 56) suggests the following parameters must be analyzed: (1) the mechanical properties of the building materials; (2) the nature and quality of construction; (3) special characteristics of the regolith (overburden), including topography, earth and soil materials, and hydrology; (4) the regional earthquake regime; and (5) archeological evidence for destructive human forces. Similar methodologies for evaluating archeologic damage are given by Karcz and Kafri (1981), Nikonov (1988b), Stiros (1988a, b), and Stiros (1996).

Loose archeologic artifacts in unconsolidated deposits can also be used as stratigraphic markers to correlate strata across faults, and thus to measure and date displacement simultaneously. For example, Noller *et al.* (1994) measured horizontal displacements across the San Andreas fault, California, based on correlation of artifact-bearing colluviums on opposite sides of the fault. In Japan, Sangawa (1992, 1993) described paleoearthquake deformation at archaeologic sites.

2.4.2 Dendroseismology

Dendroseismology is the study and dating of prehistoric earthquakes based on their effects on trees (Jacoby *et al.*, 1988). This subfield may involve merely using dendrochronology as a method to date geomorphic features or deposits deformed by paleoearthquakes. However, the trees themselves may record growth disturbances due to paleoearthquakes, in which case tree rings contain both the evidence for the event and its age.

Tree rings can record evidence of seismic events in three ways (Jacoby, 1987). *Primary dendroseismologic evidence* is created by surface rupture, such as tree roots sheared off by surface faulting, or trees tilted by differential shearing. Trees can also be damaged by coseismic subsidence and drowning, as occurs in subduction-zone megathrust earthquakes (Atwater and Yamaguchi, 1991). *Secondary evidence* is caused by seismic shaking or geomorphic processes induced by the earthquake. Shaking can cause the tree crown or large branches to snap off during high ground accelerations, which decreases the photosynthetic surface and leads to tree death or slower growth. For example, Jacoby *et al.* (1988) report that numerous traumatized trees, some of which had lost their crowns, occur within 10 m of the active (1857) trace of the San Andreas fault; similar trees are not found away from the fault trace. Very narrow or missing growth rings occur beginning in 1813 and 1857, which they interpret to date earthquakes. Trees may also be tilted from coseismic liquefaction or landsliding. Delayed geomorphic responses to earthquakes, such as gully creation, can undermine trees and lead to tilting.

Despite the promise of dendroseismology for very precise dating of paleoearthquakes, the method is limited by the distribution and age of trees, as well as by other factors. Trees can suffer trauma from nonseismic causes such as wind storms, lightning, fire, and being impacted by other falling trees. Less drastic changes in growth rate can be caused by many environmental factors such as moisture availability, disease, and nonseismic geomorphic disturbances such as floods and landslides. To eliminate these nonseismic features as causes of growth changes, dendrochronologists study many undisturbed trees near fault zones. The growth rings of these trees constitute a *control set* that reflects the growth patterns of undisturbed trees of the same species in a similar growth environment. G. C. Jacoby (personal communication) suggests three requirements for a successful application of dendroseismology: (1) The tree damage must be tied to a geologic rupture feature, (2) multiple lines of evidence must exist for the paleoearthquake, and (3) a *master chronology* must be assembled from trees unaffected by the paleoearthquake. For details on methodology, readers are referred to general treatments (Jacoby, 1987, 1989) and the following case histories, arranged by tectonic environment: (1) strike-slip faults, where damage is caused by fault rupture and shaking (Page, 1970; LaMarche and Wallace, 1972; Wallace and LaMarche, 1979; Meisling and Sieh, 1980; Jacoby *et al.*, 1988; Yadav and Kuleshius, 1992); (2) normal faults and rift zones (Ruzhich *et al.*, 1982; Stahle *et al.*, 1992; Sheppard and White, 1995); and (3) subduction zones, where damage is caused by subsidence and drowning (Jacoby and Ulan, 1983; Sheppard and Jacoby, 1989; Atwater and Yamaguchi, 1991; Jacoby *et al.*, 1995).

Chapter 3

Paleoseismology in Extensional Tectonic Environments

James P. McCalpin

3.1 INTRODUCTION

Extensional tectonic forces affect many varied parts of the earth's surface, including oceanic spreading ridges, continental rift zones (East African; Baikal, Russia; Rio Grande, USA), and broad areas of diffuse extension (Basin and Range Province, USA; northern China; Tibet). Recent work has also documented active extension within compressive fold-and-thrust regions (Andes, South America; western Himalayas, Pakistan) as well as extensional reactivation of pre-Cenozoic thrust faults (Overthrust Belt, USA). On a smaller scale, local extension can occur due to transtension along strike-slip faults or stretching over the crests of anticlinal folds.

The paleoseismic studies that form the foundation for this chapter were performed mainly in the semi-arid environment of the western United States. However, modern paleoseismic studies (i.e., studies that utilize both stratigraphic and geomorphic evidence) have been performed on normal faults outside of North America, notably in China (Ding, 1982; Zhang *et al.*, 1982; Deng *et al.*, 1984), Israel (Gerson *et al.*, 1993), Italy (Pantosti *et al.*, 1993; Michetti *et al.*, 1995), New Zealand (Beanland *et al.*, 1990), Peru (Cabrera *et al.*, 1987; Schwartz, 1988b), and Russia (McCalpin and Khromovskikh, 1995). The climate in New Zealand and Russia is considerably wetter, and in Israel considerably drier, than in the western United States, but nonetheless fault scarps and stratigraphic indicators of paleoearthquakes are very similar in all regions. Although the rates of erosion and weathering of paleoseismic landforms and deposits may vary with climate, their overall genesis and geometry as described in this chapter are felt to be largely independent of climate.

This introductory section describes selected historic earthquake ruptures on normal faults that serve as modern analogs for paleoseismic features. In the second section (Sec. 3.2) we discuss geomorphic evidence for paleoearthquakes, proceeding from large-scale to microscale features. The third part of the chapter (Sec. 3.3) describes stratigraphic evidence for paleoearthquakes. At the end of each section we present examples of how field data are used to deduce the number and characteristics of individual paleoearthquakes. The final section (Sec. 3.4) discusses how to date paleoearthquakes using geomorphic and stratigraphic evidence.

3.1.1 General Style of Deformation on Normal Faults

Crustal extension is typically accommodated by *normal faults*, either singly or in sets of parallel synthetic or antithetic faults. Fault dips in the upper crust are consistently 50° to 70°, the result of a horizontal least principal stress combined with Mohr-Coulomb failure of rock with internal friction angles of 20° to 40° (e.g., Davis, 1984, pp. 310–311). At both crustal and smaller scales, normal faulting creates *horsts, grabens*, and *tilted fault blocks*. Progressive rotation of normal fault blocks may tilt older faults into unfavorable geometries for continued extension (Proffett, 1977), and new steeper normal faults develop (Sibson, 1985). A similar evolution for normal faults that reactivate thrust faults is described by West (1992, 1993). Tilting progressively increases the dips of footwall strata, leading to *angular unconformities* in basins ranging from crustal scale (tens of kilometers) to microscale (a few meters). In contrast, synclinal and anticlinal folding is rarely associated with normal faults. Many normal faults are known to decrease in dip with increasing depth (*listric geometry*) based on geophysical and drilling data, but debate is heated on whether listric faults are seismogenic (compare Arabasz *et al.*, 1992, to West, 1993).

3.1.2 Historic Normal Earthquakes as Modern Analogs for Paleoearthquakes

Large earthquakes accompanied by historic normal surface faulting form the modern analogs for paleoearthquake studies of normal faults (Table 3-1). Bonilla (1988) and dePolo (1994) suggest that the threshold of surface rupture is magnitude (M_L or M_s) 5.5 and M 6.3 to 6.5, respectively, based on slightly different data sets and definitions. In the United States our understanding of normal surface faulting is heavily influenced by several M > 7 earthquakes that occurred in the semi-arid Basin and Range Province from 1915 to the present (Fig. 3.1). These earthquakes produced normal fault scarps up to 70 km long and 6 m high in alluvium at the base of mountain fronts, and are responsible for the topical emphasis in this chapter on fault scarp morphology, degradation, and trenching techniques. Similar scarps occur along normal faults in the Baikal Rift, Tibet, China, South America, and elsewhere, so the phenomena and interpretations described in this chapter have application beyond the United States.

Cross sections through historic normal surface ruptures document extensive shattering of surface materials. For example, the main fault rupture of the 1983 M 6.9 Borah Peak, Idaho, earthquake at Doublesprings Pass Road (Fig. 3.2) included 15 faults and 10 tension cracks in a complex horst-and-graben zone up to 85 m wide (Fig. 3.3). All of the complex fault scarp types described in Sec. 3.2.3 (fissures, grabens, back-tilting, step faults) are observed on the Borah Peak rupture (Crone *et al.*, 1987). Both the Borah Peak and the 1959 M 7.3 Hebgen Lake, Montana, ruptures displayed small thrust faults (dip 25° to 30°) on the downthrown block. The steepening of fault dip (*refraction*) near the surface is generally credited with causing complex scarps, as well as other phenomena such as the increase of fault scarp height at the center of alluvial fans (Slemmons, 1957, p. 373) and the downvalley arcuate "bulging" of fault scarps across stream mouths (Wallace, 1984, p. A14).

Table 3-1

Well-Studied Historic Normal Fault Surface Ruptures

Date and magnitude	Area/fault	Maximum displacement[a] (m)	Length of rupture[a] (km)	Reference
a. Ruptures studied immediately after the earthquake				
1954, M_s 6.8	Dixie Valley, Nevada	3.8	45	Slemmons (1957)
1954, M_s 7.2	Fairview Peak, Nevada	4.8	67	Slemmons (1957)
1959, M_s 7.6	Hebgen Lake, Montana	6.1	27	Myers and Hamilton (1964)
1983, M_s 7.3	Borah Peak, Idaho	2.7	34	Crone *et al.* (1987)
1987, M_s 6.6	Edgecumbe, New Zealand	2.9	18	Beanland *et al.* (1989, 1990)
b. Ruptures studied decades after the earthquake				
1857, M_s 7.4	Pitaycachi, Mexico	4.5	75	Bull and Pearthree (1987)
1915, M_s 7.6	Pleasant Valley, Nevada	5.8	59	Wallace (1984)
1980, M_s 6.9	Irpina, Italy	1.2	38	Pantosti and Valensise (1990)

[a] From Wells and Coppersmith (1994).

It appears that the 1983 Borah Peak ruptures preferentially propagated upward through unconsolidated alluvium along preexisting faults, perhaps because these faults possessed lower shear strength than did the adjacent unfaulted alluvium. Several laboratory sand-box faulting experiments (Horse-

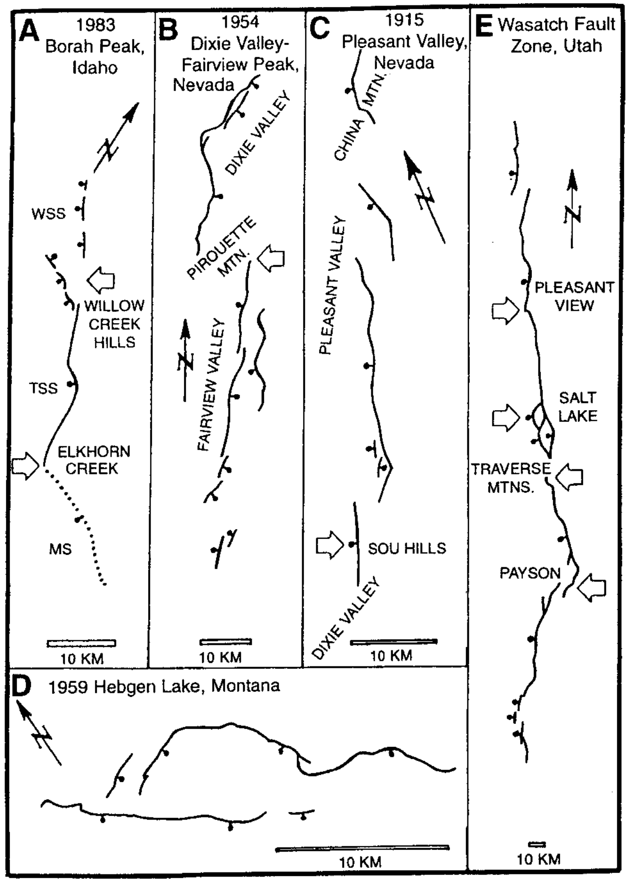

Figure 3.1 Sketch maps of normal fault surface ruptures in the Basin and Range Province, western USA; bar and ball on downthrown sides. Maps A through D show historic ruptures, map E shows the late Quaternary traces of the Wasatch fault zone. Large hollow arrows mark persistent segment boundaries. [From Wheeler, 1989, p. 437.]

field, 1977; Lade *et al.*, 1984) have shown that local *dilatancy* and *strain softening* occur along laboratory-scale normal fault planes, and that "such fault planes represent planes of low resistive shear strength on which motion will preferentially occur during subsequent deformation stages" (Vendeville and Cobbold, 1988). However, new faults also form in most surface-rupturing earthquakes (see next section).

In contrast to the discrete fracturing that occurs when cohesionless gravels are ruptured, cohesive materials (e.g., finer grained or moister sediments, or bedrock) often form *monoclines* when ruptured. The crests of the monoclines are often broken by a *crestal tension fissure* that parallels the strike of the monocline (Fig. 3.4; also Crone *et al.*, 1987). The fault scarp face is typically composed of a planar, forward-tilted slab of the prefaulting ground surface. Because a monoclinal scarp does not expose fresh material on a steep free face, it does not progress through the sequential weathering stages described in Sec. 3.2.4, and thus cannot be dated with diffusion-type techniques (Sec. 3.4), nor will it create colluvial wedges (Sec. 3.3.3). Theoretically a monoclinal scarp could be dated from materials that fell into the crestal tension fissure, but no such application has yet been published.

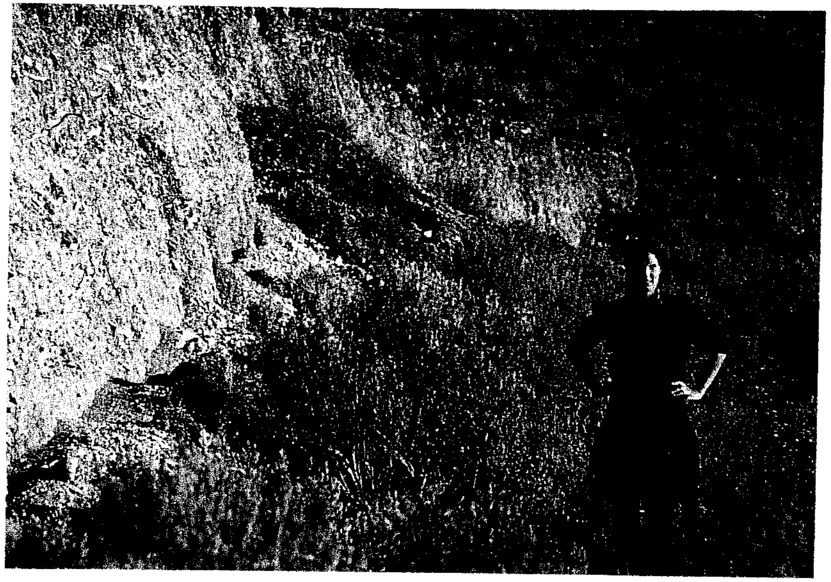

Figure 3.2 The 2-m-high near-vertical fault scarp of the 1983 M_s 7.3 Borah Peak, Idaho, earthquake. The fault here displaces late Pleistocene (age 15–20 ka?) alluvial fan gravels. Photo taken 36 hours after the earthquake, 100 m south of Doublesprings Pass Road. Note the small amount of colluvium at the base of the scarp. Person at right is 1.8 m tall.

3.1.2.1 Variation of Rupture Style in Space and Time

Earthquake surface ruptures typically vary in sense and amount of displacement along strike, and also vary at a given point on the fault between successive paleoearthquakes. In a general sense, vertical displacement on historic normal-fault surface ruptures has been greatest at the center and least near the ends of rupture (Fig. 3.5). The most symmetrical slip pattern is at Pleasant Valley, Nevada (despite the fact that it involved four segments), and the least symmetrical is at Hebgen Lake, Montana (two overlapping ruptures summed together). The lateral variability of vertical surface displacements on a larger scale can be seen at Borah Peak, Idaho (Fig. 3.6).

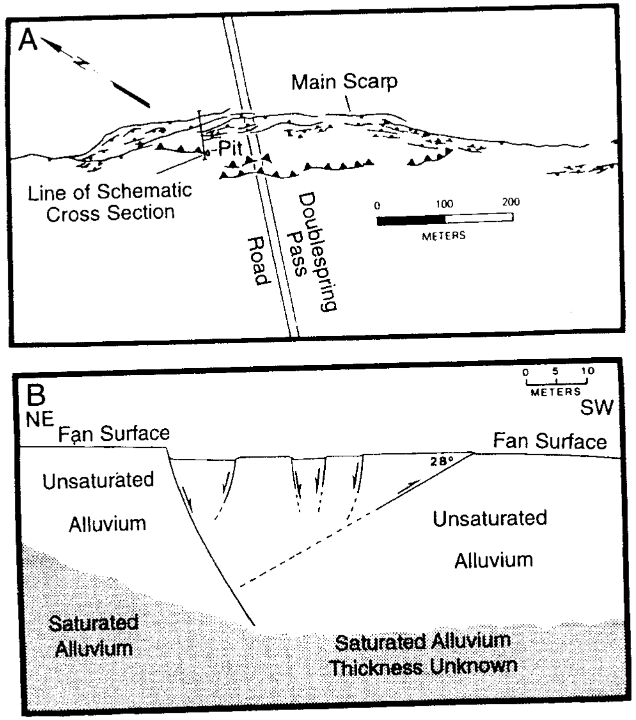

Figure 3.3 (A) Detailed map of fault scarps and (B) schematic cross section near Doublesprings Pass Road, Borah Peak rupture of 1983. (A) Normal faults have ball on downthrown side; thrust faults have barbs on upper plate. Thrust fault exposed in pit dips 28°NE. Note right-stepping en-echelon pattern of antithetic normal faults, suggestive of sinistral slip. (B) Schematic diagram showing inferred fault geometry in the upper 30 m of unsaturated alluvium. Solid lines indicate faults exposed in trenches, dashed lines show inferred projections of faults. [From Crone *et al.* (1987); reprinted with permission of the Seismological Society of America.]

The shorter wavelength variations in surface displacements seen in Fig. 3.6, measured from fault scarp profiles, may represent the complex response of surficial deposits to rupture rather than spatial variations in displacement along the bedrock fault plane. Regardless of the origin of such surface slip variations, however, Salyards (1985, his Fig. 5) demonstrated that the slip pattern from the last paleoearthquake on the Thousand Springs segment of the Lost River fault (Borah Peak earthquake) was almost identical (even in detail) to the pattern of the 1983 rupture. Such consistency of surface slip between ruptures suggests that slip patterns at depth are remarkably similar in each large earthquake (i.e., characteristic behavior).

Few precise data exist on the variation of fault displacement and style between multiple earthquakes at the same point on a fault, because few fault segments have ruptured more than once in historic time. Early workers on the Wasatch fault zone, USA (Swan *et al.*, 1980; Schwartz and Coppersmith, 1984) inferred that, at many trench sites, successive Holocene displacements on the main fault plane had been approximately the same size. This inference was supported mainly by measurements of faulted terrace sequences and colluvial wedge thicknesses exposed in trenches. Later work at some of the same sites revealed variations of about a factor of 2 in inferred net displacement per event (McCalpin *et al.*, 1994). Schwartz and Crone (1985) noted that, in a trench across the 1983 Borah Peak, Idaho, rupture, the 1983 displacements closely mimicked displacement from the prior faulting event in both style and amount (frontispiece, Fig. 3.3). The coincidence of successive displacements is particularly striking because unconsolidated deposits at this location are at least 27 to 35 m thick (Crone *et al.*, 1987). The ratio of 1983 to prior event displacements on 10 fault planes exposed in the trench averages 1.35 but with a large standard deviation (1.23). In other words, on particular fault traces the 1983 displacement ranged from 20 to 350% of the prior event displacement (Schwartz and Crone, 1985, p. 158). Thus, the net displacement across a complex fault zone may be approximately repeatable from earthquake to earthquake, but displacements on individual faults in the zone may vary widely with time.

Other trenches across normal faults (e.g., Machette *et al.,* 1992a, Figs. 10, 16; McCalpin *et al.,* 1992, Fig. 15) reveal fault strands created in earlier events that were *not* reactivated by later events, as well as "new" fault strands that were created only during the latest event (see Sec. 3.3). The creation of new fault strands shows that the location of future ruptures cannot be predicted in detail from the pattern of previous ruptures. The correlation between fault patterns in trenches and those created in laboratory sand boxes is a promising topic for future study, and may offer clues to the mechanics of faulting in natural near-surface deposits.

3.2 GEOMORPHIC EVIDENCE OF PALEOEARTHQUAKES

The primary geomorphic indicator of paleoearthquakes on normal faults is a fault scarp. Normal fault scarps, according to strict definition, vary from mountain fronts thousands of meters high cut on bedrock, to decimeter-scale scarplets that displace Quaternary alluvium and colluvium (Stewart and Hancock, 1990). In this chapter, however, the term *fault scarp* usually refers to a small escarpment in unconsolidated deposits created by direct surface faulting, unless otherwise noted (Fig. 3.7). Historic normal fault ruptures have created parallel fault scarps unconnected to the main scarp (*secondary scarps* as defined by Bonilla, 1982) ranging from 6 to 95% (mean 49%) as long as the main rupture. Normal faulting appears to result in more extensive secondary rupture

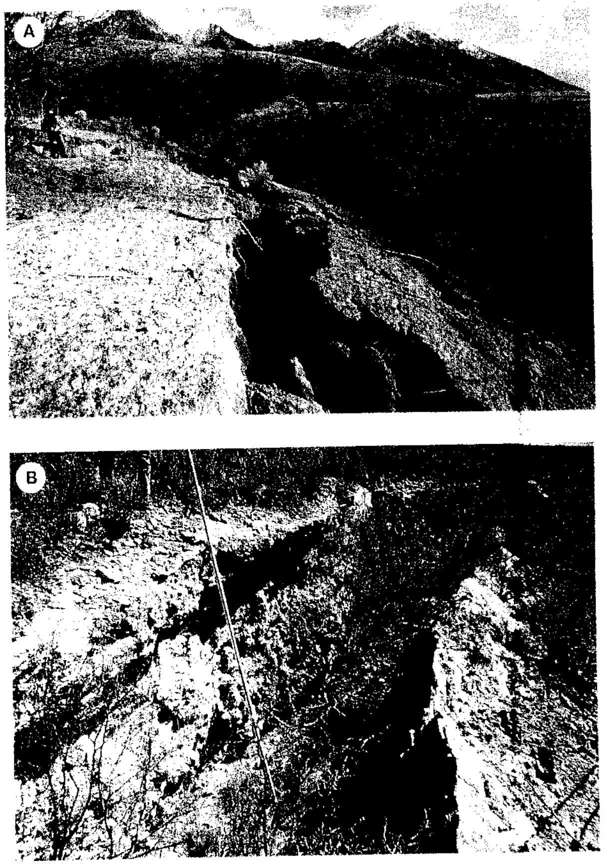

Figure 3.4 Coseismic monoclinal fault scarps developed in different materials, but with a common overall geometry. A prominent crestal tension fissure is developed on each scarp, and a planar, forward-tilted slab makes up most of the scarp face. (A) Scarp in moist, sandy Holocene alluvium, 1983 Borah Peak, Idaho, fault trace, north of Rock Creek. Fissure in center is 0.9 m wide; note person at upper left for scale. Photograph taken 36 hours after the earthquake. (B) Prominent crestal tension fissure (*center*) and forward-tilted slab (*right*) along the 1882 Sonora, Mexico, fault scarp. The faulted Pleistocene alluvial gravels here are cemented to a concrete-like hardness with pedogenic calcium carbonate (caliche) at least 3 m thick, giving the rupture the appearance of a bedrock fault scarp (compare with C). Although the photograph was taken 106 years after the scarp formed, very little material has accumulated in the tension fissure. Rod is 4 m long.

Figure 3.4 (*Continued*) (C) Monoclinal fault scarp in Quaternary basalt, Hawaii Volcanoes National Park, Hawaii. Crestal tension fissure is almost completely filled with basalt blocks; note person at upper center for scale. The date of scarp formation is unknown.

compared to strike-slip and reverse ruptures (Bonilla, 1970). *Overlaps, step-overs*, and *gaps* are common in normal fault surface ruptures. In rare cases a broad *swarm* of normal fault scarps may have nearly equal heights (Crone, 1983, p. 24; Crone and Harding, 1984a,b), in which case it is difficult to label one the "main" and others the "secondary" faults. Scarps in such swarms may have developed in complex space and time patterns (e.g., Fig. 3.27).

3.2.1 Tectonic Geomorphology of Normal Fault Blocks

Studies of large-scale *range-front morphology* are insufficiently precise to identify individual paleoearthquakes, so they fall under the more general heading of neotectonics rather than paleoseismology. However, quantitative geomorphic studies can often suggest a range of vertical slip rates on the normal fault that might be useful in reconnaissance paleoseismic studies. Bull (1984, 1987) used several quantitative measures of range-front tectonic geomorphology (*sinuosity of the range front, valley depth:width ratio*) to define five "classes of relative tectonic activity." Estimated uplift rates for these morphologic classes in arid and semi-arid climates are given in Table 3-2. However, range-front morphology can be controlled by factors other than uplift rate, particularly by climate, lithology, and structure. In humid climates, where erosion rates are greater than in the semi-arid western United States, a more rapid uplift rate may be necessary to maintain youthful-looking range

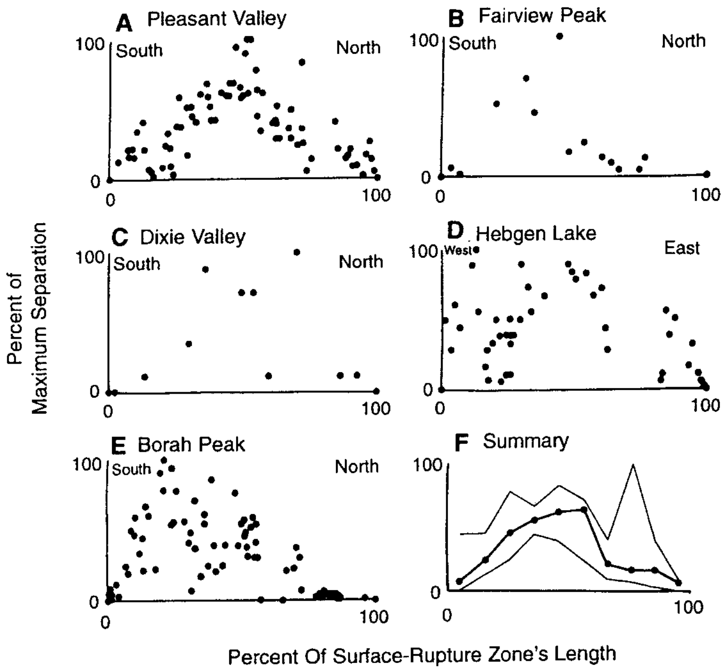

Figure 3.5 Variation in vertical separation along strike for historic normal-fault surface ruptures. All separation data are from fault scarp heights and are expressed as percentages of the maximum separation. Dots connected by a heavy line show median separation, over 10% length increments, from the Pleasant Valley (1915), Fairview Peak (1954), Dixie Valley (1954), Hebgen Lake (1959), and Borah Peak (1983) earthquakes. Light lines show envelope of median separations; anomalously high value at 80% of length is only from Dixie Valley. [From Wheeler (1989, p. 435).]

fronts. Bull (1987) notes that rapidly rising (3 to 8 m/ka) range fronts in humid New Zealand are only in his morphologic activity class 2, whereas in a drier climate like southern California they would probably be in class 1.

Neogene extension in some regions (Italy, Greece) has primarily created Quaternary fault scarps in rolling bedrock hills; such scarps rarely intersect thick surficial deposits (Jackson *et al.,* 1982; Pantosti and Valensise, 1990; Pavlides, 1993). These relatively immature extensional faults in bedrock terrain are more difficult to study, because (1) Quaternary geomorphic surfaces that might be dated are not present, (2) sedimentation in fault zones is minimal, and (3) scarp degradation models cannot be used. The techniques described in this chapter were developed for, and will work best when applied to, fault scarps in unconsolidated (Quaternary) deposits. A few techniques (Sec. 3.2.1) are applicable to surface fault scarps with bedrock exposed on both sides, and

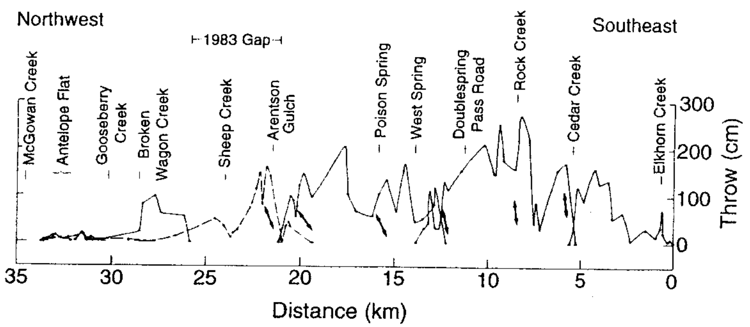

Figure 3.6 1983 M 7.3 Borah Peak, Idaho, USA, earthquake. Solid line is throw along Lost River fault; dashed line is throw along western fault splay; solid dots show measurements. The 1983 gap indicates an absence of faulting on the main range-front fault trace. Arrows show net slip direction from rake of slickensides or displaced cultural features. Vertical exaggeration is 2000×. [From Crone *et al.* (1987, p. 746); reprinted with permission of the Seismological Society of America.]

Figure 3.7 Oblique aerial photograph of the fault scarp of the Star Valley fault (arrows) at Afton, Wyoming. Vertical surface offset is 11 m across the low-gradient alluvial surface at center and left, and 7 m across the small, younger alluvial fan at far right. This scarp was produced by three paleoearthquake displacements of 3 to 4 m each at about 5540, 8090, and 14,000–16,000 yr B.P. [From Warren and McCalpin, (1992); Piety *et al.* (1992); photograph courtesy of L. A. Piety.]

Table 3-2

Classification of Relative Tectonic Activity of Normal Fault-Block Mountain Fronts[a]

Classes of relative activity	Piedmont landforms	Mountain-block landforms	Range-front sinuosity[b]	Valley depth/ valley width ratio[c]	Inferred uplift rate[d] (m/ka)
1—Maximal	Unentrenched alluvial fan	V-shaped valley in bedrock, U-shaped valley in alluvium or soft bedrock			1.0–5.0
2—Rapid	Entrenched alluvial fan	V-shaped valley	1.1–1.3	0.06–0.53 (mean 0.15)	0.5
3—Slow	Entrenched alluvial fan	U-shaped valley	1.6–2.3	0.2–3.5 (mean 1.5)	0.05
4—Minimal	Entrenched alluvial fan	Embayed mountain front	≥2.5	0.4–3.8 (mean 1.7–2.5)	0.005
5—Inactive	Dissected pediment	Pediment embayment	2.6–4.0	0.9–39.4 (mean 7.4)	≤0.005

[a] Adapted from Bull and McFadden (1977); Bull (1984, 1987)

[b] The sinuous length of the mountain-piedmont junction, divided by the straight-line length.

[c] The ratio of valley depth to valley width at a point 0.5 km upvalley from the mountain-piedmont junction.

[d] Uplift rates in semi-arid climates only; in subhumid or humid areas rates may be several times larger for each class.

some others (Sec. 3.3.2) will also work with Quaternary faults that juxtapose bedrock against unconsolidated deposits (such as colluvium).

3.2.2 Features of Bedrock Fault Planes and Other Rock Surfaces

Rejuvenation of a range-front fault scarp by repeated normal faulting can expose new *footwall rock surfaces* to weathering. The boundary between the older, weathered bedrock surface exposed before the latest faulting event, and the newer, unweathered fault-plane surface exposed at the time of the latest event, can be sharp (less than or equal to a few centimeters). Wallace (1984, pp. A22-A25) describes a 7-m-high bedrock fault plane, the "fresh" lower 3 m of which was exposed by the 1915 Pleasant Valley earthquake, and the upper, weathered 4 m of which was presumably exposed by a similar, previous earthquake. The weathered limestone surface contained solution pits and channels up to 1 cm deep and 2 cm wide. In the absence of calibrated measurements on limestone pitting rates, Wallace was unable to determine the age(s) of the earlier 4-m displacement event(s). Similar surfaces exposed

by historic and prehistoric earthquakes are described by Mueller and Rockwell (1995, p. 16) and Pinter (1995, Fig. 6). Newly developed techniques for surface-exposure dating using cosmogenic isotopes (Dorn and Phillips, 1991) may allow dating of such fault planes.

The weathered surfaces of large surface boulders on fault scarps can also display similar discontinuities in weathering. Large clasts exposed on the crest of the (multiple-event) Lone Pine, California, fault scarp have *desert varnish rings* that show the ground level on the pre-1872 fault scarp, before it was lowered by scarp crest erosion following the 1872 earthquake. One very large boulder carries two varnish rings, which Lubetkin and Clark (1988) interpret as evidence for three faulting events, the latest of which was the 1872 event. Cation-ratio dating (e.g. Reneau and Raymond, 1991) could conceivably be used to date the varnish rings directly.

3.2.3 Terminology and Measurements of Normal Fault Scarps

Degraded fault scarps in unconsolidated material are composed of several geomorphic components (Fig. 3.8; Table 3-3). Slemmons (1957), referring to normal fault scarps, defined a *simple fault scarp* as one on which a single fault rupture had displaced the ground surface without measurable rotation of the ground surface. A *complex fault scarp*, in contrast, was defined by either multiple fault traces, or by the ground surface being rotated out of its prefaulting gradient. Complex fault scarps are very common along normal fault ruptures, and are generally ascribed to coseismic failure or slumping of unconsolidated material into an *open void space* caused by fault steepening (refraction) and divergence from the bedrock fault plane at the range front (Fig. 3.9). The failure of unconsolidated deposits into the void space (Fig. 3.9A) then creates either a *back-tilted downthrown block* (B), a *graben* (C), or multiple *step faults* (D). Myers and Hamilton (1964, Fig. 39) propose that a similar fault steepening

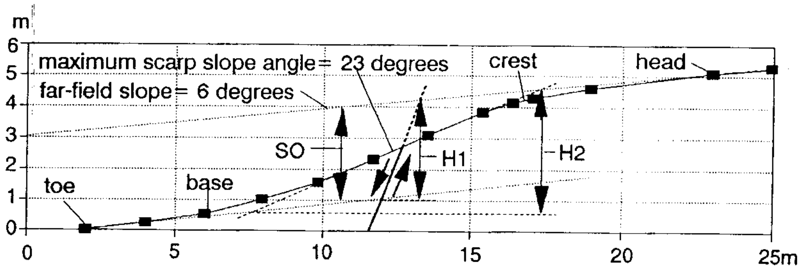

Figure 3.8 Geometry and terminology of a simple fault scarp. Profile constructed by the method of Bucknam and Anderson (1979). Black boxes show ends of measured profile segments; dotted lines show the projections of the upthrown and downthrown surfaces. Terms are defined further in Table 3-3.

Table 3-3

Definitions of Fault Scarp Parameters

		Parts of the profile
Head	H	Edge of the uneroded original upthrown block surface
Crest	C	Point of maximum slope curvature (convex-up) between the scarp head and the steepest part of the scarp face
Face	F	Portion of the scarp profile between the crest and the base
Base	B	Point of maximum slope curvature (concave-up) between the steepest part of the scarp face and the scarp toe
Toe	T	Edge of the uncolluviated original downthrown geomorphic surface
		Angular measurements
Far-field slope	α	Gradient of the faulted geomorphic surface
Maximum scarp slope angle	Θ	Gradient of the steepest part of the scarp face
Fault dip	β	Dip angle of the fault plane underlying the scarp face
		Height measurements
Leveled height	L	Vertical separation between the scarp toe and head, usually obtained by simple leveling. This measurement is typically used in rapid reconnaissance investigations (e.g., Baljinnyam *et al.*, 1993)
Scarp height	H2	As defined by Bucknam and Anderson (1979), the vertical separation between intersections of the plane formed by the steepest part of the scarp face and the planes formed by the displaced original geomorphic surface
Surface offset	SO	Vertical separation between the projections of the original upthrown and downthrown geomorphic surfaces
Vertical fault displacement (throw)	H1	Vertical distance between intersections of the fault plane, and planes formed by the displaced original geomorphic surfaces
Net fault slip	*ns*	Distance, measured on the fault plane, between two points that were originally in contact at the fault plane before faulting. For pure dip-slip motion, equals the distance, measured along the fault plane, between the intersections of the fault plane with the planes formed by the displaced original geomorphic surfaces
Throw on main fault	T_m	Vertical component of fault displacement on the main fault
Throw caused by backtilting	T_t	Vertical component of fault displacement on a main or antithetic fault induced by back-tilting of the downthrown block
Throw on antithetic fault	T_a	Vertical component of fault displacement on an antithetic fault
Net throw	T_{net}	Vertical component of fault displacement across the entire deformation zone, calculated as the difference between synthetic throws (H1, Tm) and antithetic throws (Tt, Ta), or calculated from the surface offset between projected upthrown and downthrown surfaces

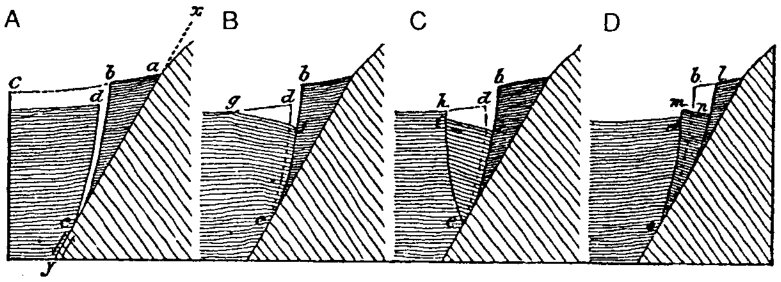

Figure 3.9 Gilbert's theory of formation of complex fault scarps. Close horizontal lines indicate unconsolidated sediments of the hanging wall; wide diagonal lines indicate consolidated bedrock of the footwall. (A) Open tension fissure caused by fault refraction at point *e*. Prefaulting ground surface is defined by *a b c*. The net slip vector is represented by distance *b d*. (B) Back-tilting caused by slumping into the void space. The block of hanging wall alluvium *g d e* slumps to assume the shape *g f e*. The height of the fault scarp *b f* exaggerates the net slip on the fault *b d*. (C) Graben formation. The alluvial prism *h d e* settles and spreads as to occupy the space *i k e*. The difference between the heights of synthetic (*b k*) and antithetic (*h i*) fault scarps is approximately equal to the net throw *b d*. (D) Step-faulting. The alluvial prism *b l e* on the footwall slides down into the tension fissure to assume the position *m n e*. From Gilbert (1890).

occurred in the 1959 M 7.3 Hebgen Lake, Montana, earthquake in an area of level topography not associated with a range front. Refraction is caused by a lack of confining pressure near the surface and the existence of a true tensional stress field (Mercier *et al.*, 1983), resulting in overhanging fault scarps at the surface. On steep colluvium-covered slopes, Witkind (1964, Figs. 21, 24) observed that the surface fault scarp may be upslope or downslope from the bedrock fault due to slope failure in the overlying prism of colluvium.

The geometric relations between fault displacement, original scarp morphology, and present scarp morphology can be complex, but they must be understood to derive fault displacement data from fault scarps. As a general rule, it is preferable to convert *scarp height* values (*L*, H2 in Table 3-3) to *surface offset* values (SO), because the latter does not increase as the scarp broadens with age. A more rigorous approach is to convert SO values to *vertical fault displacement* (H1) values (if possible), because fault displacement (unlike surface offset) is independent of the slope angle of the faulted surface (*far-field slope*). Vertical displacement values calculated from scarp dimensions can be compared along the length of a fault, regardless of changes in far-field slope or scarp age, and can also be compared with long-term vertical displacement rates. However, any conversion to fault displacement values requires an estimate of fault dip (see next section), and fault planes are usually not visible.

The detailed geometric analysis of normal fault scarps that follows assumes that fault motion at the surface was purely dip-slip, with no oblique component.

Detection of an oblique component of slip on fault scarps requires special conditions, either recognizable piercing points on either side of the fault scarp, or planar ridge slopes that have been displaced (Chapter 6). In historic ruptures, piercing points have been roads, fences, canals, and other man-made objects, or linear natural topographic features such as channels, debris-flow levees, or erosional ridges that intersect the scarp. For example, the 1983 M 6.9 Borah Peak, Idaho, rupture displaced an irrigation ditch 2.9 m vertically and 0.43 m left-laterally (Crone *et al.*, 1987, Fig. 6). Measurements of centimeter-level precision are typically not possible for prehistoric earthquakes, because (1) no man-made features are displaced by the rupture and (2) linear topographic or depositional features usually cannot be identified to this precision on either side of the fault scarp. On alluvial surfaces, linear channels or ridges may be present on the upthrown block, but often cannot be found on the downthrown block due to burial by colluvium or alluvium. If linear landforms do intersect the fault scarp, they are often so broadened by weathering that measurement errors are on the same scale as suspected lateral offsets, and relations are thus ambiguous. Special geomorphic situations where oblique slip can be measured more accurately are described in Chapter 6.

3.2.3.1 Simple Scarps

A simple fault scarp is initially formed with a near-vertical *free face* (Fig. 3.2) in most brittle surface materials; in gravels, original dips are typically 78° ± 10° (McCalpin, 1987a). If the fault plane is vertical, surface offset (SO) equals vertical fault displacement (H1). For fault dips (β) less than 90°, surface offset is less than vertical fault displacement, depending on the far-field slope angle (α).

$$\mathrm{SO} = \mathrm{H1}\,(1 - \cot\beta\tan\alpha). \tag{3.1}$$

For a given displacement and fault dip, surface offset is greatest for horizontal far-field slopes ($\alpha = 0$), and decreases to zero as far-field slope approaches fault dip ($\alpha = \beta$). This latter situation is unlikely to occur, except where fault dip (β) is very low and topography (α) is very steep. Fault dips in unconsolidated deposits typically range from 45° to 90°, whereas surface slopes in alluvium and colluvium range from 0° to 35°. The dependence of surface offset on far-field slope should be borne in mind when comparing surface offsets of scarps on steep range front colluvium (α = 25° to 35°) to those of scarps on alluvial terraces or fans (α = 1 to 10°). Where fault dip is steep and faulted surfaces are gentle, there is very little difference between fault throw (H1) and surface offset (SO). With gentler fault dips and steeper faulted surfaces, the difference between H1 and SO increases.

The relation between scarp height (H2) and vertical fault displacement (H1) is more complex, because scarp height increases with time as a scarp degrades and broadens on a surface with some finite far-field slope (α).

$$\mathrm{H2} = \mathrm{H1}\frac{\sin\theta\sin(\beta - \alpha)}{\sin\beta\sin(\theta - \alpha)}. \tag{3.2}$$

For example, one can compare the vertical fault displacement (H1) required to create a 5.6-m-high degraded scarp (H2) on a gentle versus on a steep surface, by solving Eq. (3.2) for H1. A slightly degraded (Θ = 30°) 5.6-m-high scarp on a gentle surface (α = 3°) can be produced by a vertical displacement (H1) of 5.2 m. In contrast, a more degraded scarp (Θ = 22°) of the same height (H2 = 5.6 m) can be produced on a steeper surface (α = 15°) by a vertical displacement (H1) of only 2 m. By the time the scarp has weathered to a 22° maximum angle (only 7° steeper than the faulted surface), there is a considerable elevation difference between the scarp base and crest. In the limit that maximum scarp slope angle (Θ) becomes parallel to far-field slope (α), Eq. 3.2 predicts that scarp height (H2) becomes infinitely large, because $\sin(\Theta - \alpha)$ approaches zero. It may be difficult to recognize a fault scarp once its maximum scarp slope angle (Θ) is within 2 to 3° of the far-field slope angle (α).

3.2.3.2 Scarps with Back-Tilting

Rotation of the downthrown block toward the fault scarp (Fig. 3.9C) causes scarp height to exceed surface offset; the difference increases as the back-tilted area becomes wider and more tilted. Equation (3.3) relates the additional component of vertical fault displacement induced by back-tilting (T_t) to the width of the tilted zone (W_f), the angle of tilt (ϕ), and other previously defined measures of scarp morphology (Table 3-3):

$$T_t = W_f\frac{[\tan\alpha + \tan(\theta - \alpha)]\cos\alpha\sin\beta}{\sin(\beta - \alpha)}. \tag{3.3}$$

Using Eq. (3.3), one can subtract the portion of vertical displacement at the fault scarp due to tilting (T_t) from the apparent vertical displacement at the main fault scarp (T_m in Fig. 3.10) to calculate the true vertical displacement across the fault zone. An example would be a steep scarp (Θ = 25°) with surface offset SO = 25 m, displacing a gentle slope (α = 5°), underlain by a fault dipping at 78° (β), fronted by a zone 100 m wide (W) that is back-tilted toward the fault by 3° (ϕ). Using Eq. (3.1), we calculate T_m (as H1) to be 25.5 m; T_t calculated from Eq. (3.3) equals 5.3 m. Therefore, $T_{\mathrm{net}} = T_m - T_t$ = 25.5 m − 5.3 m = 19.7 m. Note that 19.7 m only amounts to 79% of the apparent vertical displacement (T_m) at the main scarp (25 m). If the back-tilting was not recognized in the field and the height of the main scarp was used to calculate displacement, that value would have overestimated true net vertical displacement by 26%. An alternative procedure for calculating T_{net} would be to measure the net SO between the graphical projections of the

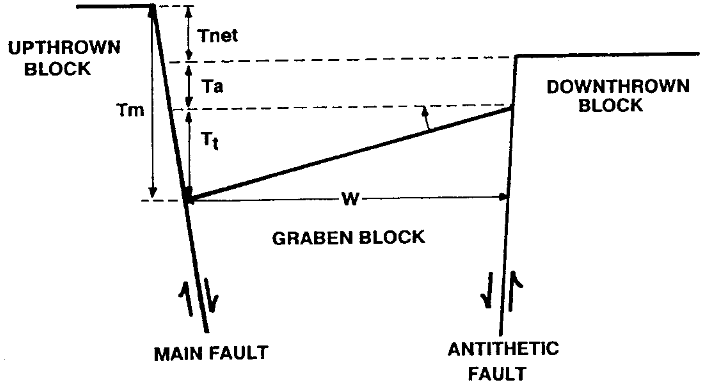

Figure 3.10 Schematic diagram showing the components of displacement in a scarp-graben system, where the graben has been tilted. Terms are defined in the text and in Table 3-3. [From McCalpin *et al.* (1994); reprinted with permission of the American Geophysical Union.]

upthrown and downthrown surfaces, and then calculate H1 from this net SO value using Eq. (3.1).

Back-tilting is usually restricted to within 100 to 200 m from the fault scarp (Vincent, 1985, p. 76), but more subtle tilting has been documented by geodetic surveys at considerably longer distances. Broad *coseismic tilt* of 100 to 500 μrad affected the downthrown block of the Borah Peak, USA, fault scarp over a distance of ca. 20 km from the scarp (Stein and Barrientos, 1985). Elastic dislocation modeling (Savage and Hastie, 1966, 1969; Y. Okada, 1985) implies that downthrown block tilt over 6 to 12 km from the rupture is typical of historic M 6.5 to 7.5 normal surface faulting events. The author is unaware of any study that has used subtle tilting ($\leq 1°$) in the near field to identify or characterize individual paleoearthquakes, independent of other types of evidence. One exception is where tilting is restricted to a graben in the rupture zone itself. In that case, angular unconformities in the graben sediments can be used to reconstruct the sequence of tilting and, thus, faulting (Sec. 3.3.2.3).

3.2.3.3 Scarps with Graben

Graben structures are defined by one or more *synthetic fault scarps* (the largest of which is termed the main fault scarp) and one or more *antithetic fault scarps* (frontispiece, Fig. 3.3). The three geometric components of fault displacement in a scarp-graben system are (1) stratigraphic *throw* at the main fault zone (T_m, approximately equal to initial height of the scarp free face), (2) *tilt* (ϕ) of the graben strata acting over a certain horizontal distance (W) from the main fault, and (3) stratigraphic throw on any antithetic faults (T_a; Fig. 3.10). If all three components are known for an individual faulting event, the net coseismic throw (T_{net}) for that event is measured as the difference between main fault throw and contributions of throw from tilt ($T_t \cong W \tan \phi$) and antithetic faulting, or

$$T_{\text{net}} = T_m - [(W \tan \phi) + T_a] \qquad (3.4)$$

An alternative procedure for calculating net vertical displacement is to measure graphically the surface offset between the displaced far-field slopes, and use Eq. (3.1) to convert surface offset (SO) to net fault displacement (H1). If deposition in the graben has been significant, the components of displacement calculated at the main fault (T_m) and antithetic fault (T_a) will yield minimum values (McCalpin, 1983, pp. 42–43), but the net throw across the zone (T_{net}) will remain the same.

3.2.3.4 Step Faults

Step faults were defined by Slemmons (1957) as parallel fault scarps of similar size and sense of slip created coseismically by collapse of the footwall into a refraction-formed void (Fig. 3.9D). If no rotation occurs in the block(s) between step faults, then the net vertical fault displacement across the fault zone is calculated by summing the vertical displacements (H1) of individual step faults. If block rotation has occurred, the preceding procedure will overestimate net displacement if *backward rotation* has occurred, or underestimate it if *forward rotation* has occurred. To correct for the component of displacement induced by block rotation, one must approximate it as $W \tan \phi$ (as with back-tilted scarps) and either add or subtract that value from the sum of step-fault displacements.

Few ruptures, historic or prehistoric, have been inventoried along their entire length for rupture style and complexity. McCalpin (1983) measured 82 fault scarp profiles at roughly 1.5-km intervals along the 120-km-long Sangre de Cristo fault zone, Rio Grande rift zone. Almost 60% of profiled scarps were simple scarps (as previously defined), whereas graben, step faults, and back-tilted surfaces composed 17, 14, and 10% of profiles, respectively. Crone *et al.* (1987) note that "unusual morphologies" are found along 5 to 10% of the length of the 1983 M 7.3 Borah Peak rupture. Apparently most normal fault surface ruptures produce simple fault scarps; complex fault scarps result from relatively unusual subsurface conditions that lead to fault refraction.

3.2.4 Degradation of a Simple Fault Scarp in Unconsolidated Deposits

Fault scarps formed during paleoearthquakes are soon attacked by weathering and erosional processes. Wallace (1977) presented a conceptual model, based on field observations in the Basin and Range Province, USA, for the degradation of fault scarps in gravelly alluvium and colluvium (Fig. 3.11). The initial fault scarp forms at angles between 60° and 90° (Fig. 3.11A), then begins to ravel by mass movement and erosion to build up a basal colluvial debris and wash slope (Figs. 3.11B and 3.12). As the *free face* retreats, colluvium accumulates, the *debris slope* grows (Fig. 3.11C), and the free face is eventually buried by colluvium (Fig. 3.11D). After this stage, wash processes dominate on the scarp, leading to symmetrical slope degradation on the upper half of the scarp and colluvial aggradation on the lower half (Fig. 3.11E).

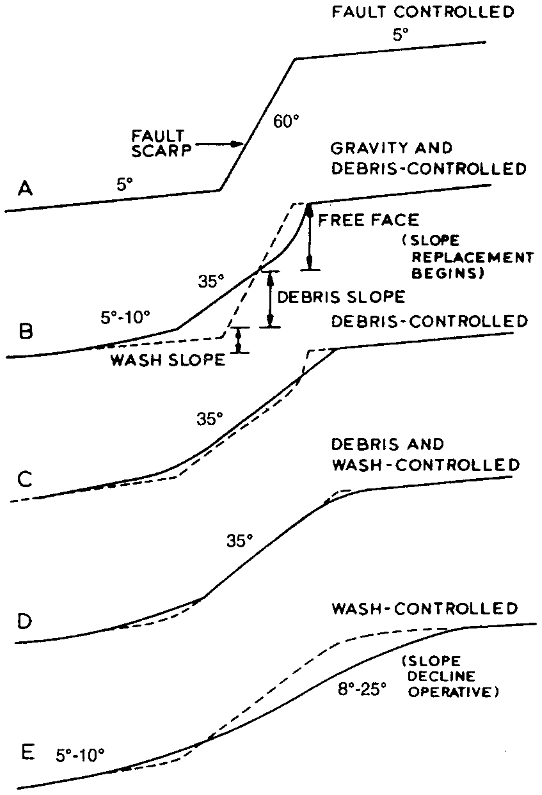

Figure 3.11 Sequence of fault-scarp degradation in unconsolidated materials. To show incremental change, the dashed lines represent the solid lines of the previous profile. (A) Initial scarp; dip is drawn at 60°, although in unconsolidated deposits it is typically steeper. (B-E) Sequential stages of scarp degradation due to gravity processes (B), debris processes (C and D), and wash processes (D and E); see description in text. [From Wallace (1977, p. 1269).] Reprinted with permission of the Geological Society of America.

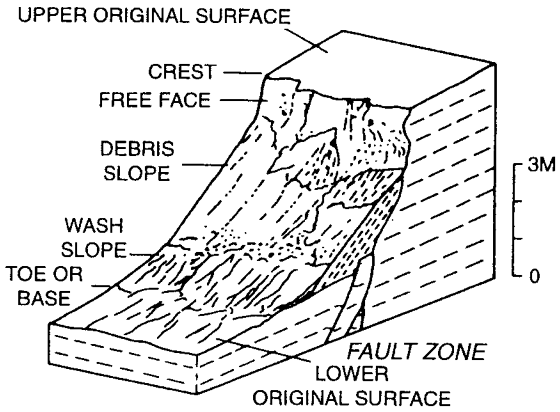

Figure 3.12 Block diagram of a fault scarp in unconsolidated deposits. Terminology is similar to that for degraded fault scarps (Fig. 3.8). [From Wallace (1977, p. 1269).] Reprinted with permission of the Geological Society of America.

This idealized model assumes that (1) the fault scarp in unconsolidated material stands at greater than the angle of repose after faulting, (2) the scarp is buried mainly by colluvium shed from the free face, rather than by widespread deposition (fluvial, lacustrine, eoilian) on the downthrown block, and (3) that erosion and transport of scarp face material are limited only by the strength of geomorphic processes, and not by the availability of loose material (i.e., the scarp face is a *transport-limited slope*; Nash, 1980). Figure 3.13A shows a fault scarp which collapsed into cohesive blocks during coseismic shaking; this scarp bypassed stages A through D in Fig. 3.11, and went directly to the wash stage. At the opposite extreme, the transition from stage A to B (Fig. 3.11) can be retarded by *cementation* of surficial materials exposed in the fault scarp, such as the faulted carbonate-cemented paleosol shown in Fig. 3.13B. Fault scarps in Death Valley, California, are cemented with halite and have retained their free faces for thousands of years (L. W. Anderson, personal communication, 1995).

Wallace (1977, his Fig. 7) suggested age ranges over which *gravity, debris,* and *wash processes* dominated scarp degradation. Based on observations of scarps produced in Nevada in 1915 and 1954, he estimated that 1000 to 2000 years would be required to eliminate the free face completely. Subsequent observations have shown that the rate of free face retreat is a complex function of climate and the mechanical properties of the faulted material. For example, along the subhumid, forested 1959 Hebgen Lake, Montana, rupture, the free face has disappeared in most places in only 30 years (Wallace, 1980a).

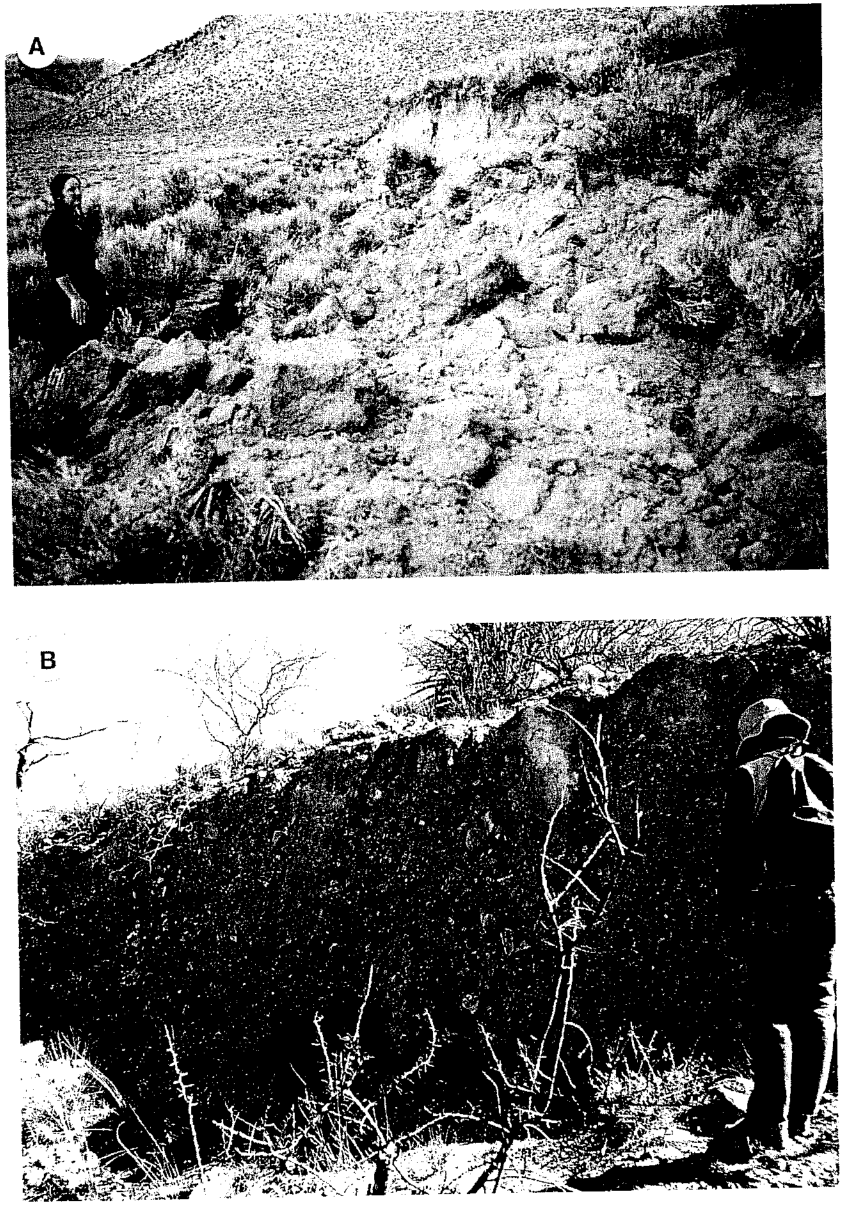

Figure 3.13 Extremes of scarp preservation. (A) Portion of fault scarp in sandy alluvium that collapsed during seismic shaking, 1983 Borah Peak rupture, ca. 150 m north of Doublesprings Pass Road. Uncollapsed near-vertical scarp appears in the distance. Person at left is 1.8 m tall. (B) The 106-year-old fault scarp developed in a cemented carbonate soil horizon (caliche), Pitaycachi fault, Sonora, Mexico, earthquake of 1887 (Bull and Pearthree, 1988). Note the small amount of colluvium that has accumulated at the base of the 2-m-high free face.

Elsewhere free faces still exist, but are preserved mainly by tree-root cohesion. Along the 1983 Borah Peak, Idaho, fault trace, scarps formed in poorly sorted, matrix-rich colluvium maintain nearly vertical free faces. Adjacent scarps that formed in better sorted, matrix-poor stream alluvium had lost most of their free faces and had degraded to colluvial slopes of 30° to 37° within one day after the earthquake. Crone *et al.* (1987) attribute better free face preservation to increased cohesion from silt and clay, and from the apparent cohesion of oriented angular gravel clasts in colluvium. It appears that Wallace's initial 1000- to 2000-yr estimate for free face elimination may be a maximum estimate, applicable only to the slow degradation of cohesive and/or cemented material in the arid climate in which he was working.

The free face/scarp height ratio on historic fault scarps has also been correlated with the mechanical properties of the material exposed in the scarp. Watters and Prokop (1990) show strong positive correlations between free face/scarp height ratios and cohesive strength, peak friction angle, and bulk density of materials composing the 1954 Dixie Valley-Fairview Peak, Nevada, fault scarp. This correlation has been used to date fault scarps (Sec. 3.4).

After the free face is buried, the rate of scarp decline is affected by both lithologic and microclimatic factors. McCalpin (1983, his Figs. 55, 63) showed that scarps composed of finer gravel had declined to lower slope angles than had scarps of the same age composed of coarser gravel, although the relation between slope angle and grain size had significant variation. Pierce and Colman (1986) demonstrated that late-glacial scarps in the western United States that faced south degraded three to five times as fast as identical scarps that faced north.

3.2.5 Geomorphic Features Formed by Recurrent Faulting

3.2.5.1 Interaction of Fault Scarps with Geomorphic Surfaces

Most normal fault scarps in rift zones and regions of diffuse extension displace Quaternary geomorphic surfaces such as alluvial fans, river terraces, or shoreline platforms. When fault scarps cross geomorphic surfaces of different elevation and/or age, changes in scarp height yield important clues as to the history of faulting (see general cases analyzed by Suggate, 1960, and Lensen, 1964a). A common geomorphic setting in extensional regions is fault scarps at a range front displacing the upper parts of alluvial fans. Range-front fault scarps typically intersect fan heads where fanhead incision has created younger-inset-within-older surfaces (Bull, 1991), whereas branch and secondary faults (as defined in Sec. 3.2) can occur near to or downslope from the fan *intersection point* (Hooke, 1967), where younger deposits lie stratigraphically and topographically on older deposits. A single-event fault scarp that postdates all geomorphic surfaces, whether upslope or downslope from the fan intersection point, will maintain a roughly uniform height across geomorphic surfaces regardless of their age. Figure 3.14 shows a single-event scarp that is younger than two erosional surfaces (stage a3); note that scarp height remains constant as the scarp ascends from the younger (Pf) to the older (Bf) surface. Near the intersection point, fan deposits of different ages occur at roughly the same elevation, across which the single-event scarp maintains a constant height (stage b3). Although Fig. 3.14 shows fill terraces, the surface geometry would be the same for strath terraces.

If periods of terrace formation and faulting have alternated, multiple-event fault scarps will be higher where developed across the older geomorphic

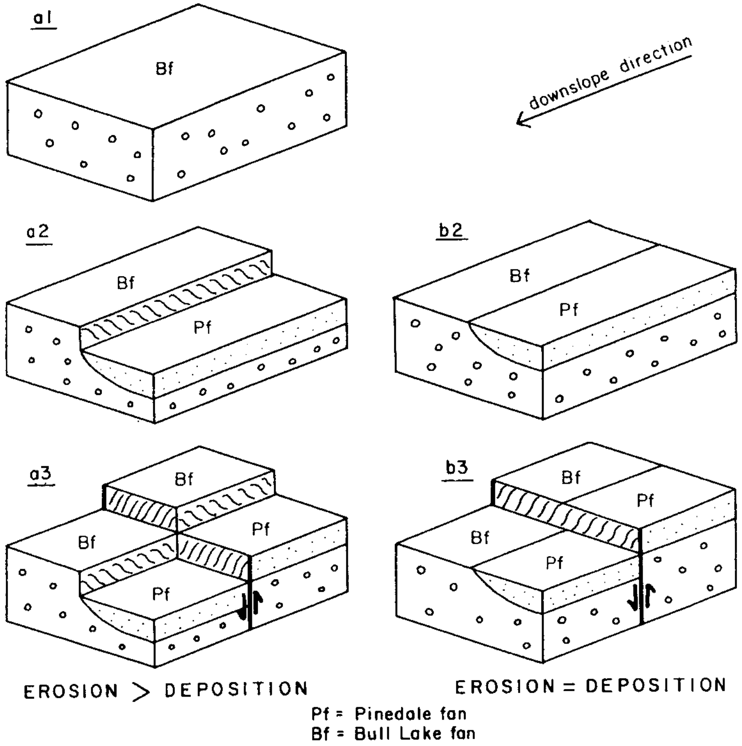

Figure 3.14 Geometry of a hypothetical single-event fault scarp offsetting an alluvial fan terrace sequence. (a1) Deposition of unit Bf. (a2) Channel incision above the intersection point and partial backfilling to create a Pf fill terrace. (a3) Faulting of a height equal to that of the terrace riser. (b2) Channel incision at the intersection point and complete backfilling. (b3) Faulting of equal height to that in stage a3. Note the difference in final geometries (a3 versus b3) depending on whether the faulting occurs above or below the alluvial fan intersection point. [From McCalpin (1983, p. 47); reprinted with permission of the Colorado School of Mines Press.]

surfaces. The increased scarp height on older surfaces merely represents the greater number of cumulative displacements compared to that of younger surfaces. In Fig. 3.15, an older fan (Bf) is deposited (stage a1) and later faulted (stage a2). Erosion then results in formation of a younger channel, which

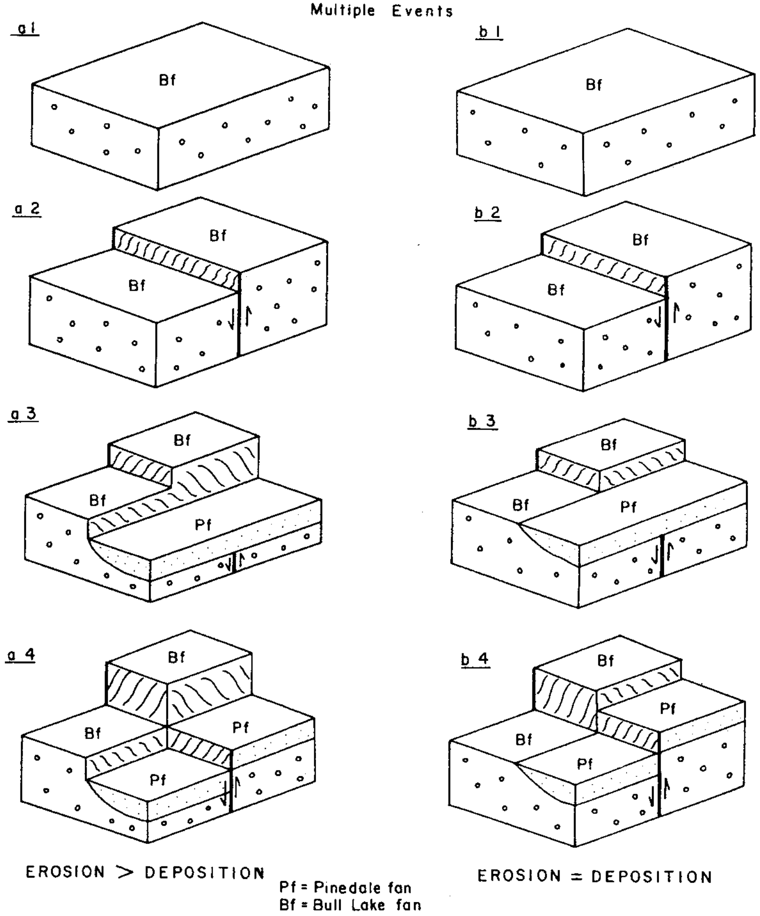

Figure 3.15 Geometry of a hypothetical multiple-event fault scarp offsetting an alluvial fan terrace sequence. (a1) Deposition of unit Bf. (a2) Faulting. (a3) Channel incision into the upthrown and downthrown blocks above the alluvial fan intersection point, and partial backfilling to create a Pf fill terrace. (a4) Renewed faulting of equal height to initial faulting. (b1-b4) Same sequence of deposition, erosion, and faulting at the alluvial fan intersection point, where erosion equals deposition. Note the difference in final geometries (a4 versus b4). The abrupt increase in scarp height between fan surfaces of different age is an indicator of recurrent faulting. [From McCalpin (1983, p. 48); reprinted with permission of the Colorado School of Mines Press.]

erodes through the fault scarp (stage a3). Later faulting not only creates a scarp across the younger channel (Pf), but increases the height of the preexisting fault scarp on the older fan (Bf; stage 4). If recurrent faulting occurs near the alluvial fan intersection point, we see a similar abrupt change in fault scarp height (stage b4), but without the incised younger channel. Downfan from the intersection point, only fault scarps younger than the latest period of deposition are preserved at the surface. Earlier displacements offset the older (buried) deposits in the subsurface; such differential displacements can only be analyzed by indirect subsurface methods (Chapter 2).

In the previous example, the stream had incised into both the upthrown *and* downthrown blocks after faulting. Stream incision into the upthrown block after faulting is expected, because the base level of the stream is suddenly (coseismically) lowered by an amount equal to scarp height. This lowering causes a steep *nickpoint* to develop in the stream bed at the fault trace. The nickpoint then migrates upstream, causing progressive incision into the previous floodplain (e.g., at the 1983 Borah Peak, Idaho, rupture; Vincent, 1985, p. 85). An episodic, fault-induced incision into the upthrown block can create *tectonic terraces* that in profile diverge downstream from the modern channel, and abruptly end at the fault scarp. The vertical separation between the projection of these terraces, measured at the inferred fault plane, provides a first approximation of the vertical fault displacement in individual paleoearthquakes (Fig. 3.16; also Soule, 1978). The approximation will be exact if two conditions are met: (1) The stream incises the scarp after faulting by the full amount of vertical displacement (i.e., full base level recovery), rather than some percentage of vertical displacement, and (2) the terraces are *strath terraces* only, without a significant fill component. Condition 1 will often not be met if an ephemeral stream partly incises the scarp and builds an alluvial fan on the downthrown block. Perennial streams are more likely to incise an amount equal to vertical uplift, because they transport sediment away from the scarp base. Condition 2 will not be met if climatically induced stream degradation and/or aggradation have occurred between faulting events. Nevertheless, tectonic terraces provide geomorphic indicators of individual paleoearthquake displacements that can be measured in reconnaissance, without resort to trenching. If terraces exist in a valley but are not preserved at the fault trace, vertical offsets can sometimes be recognized by projecting terrace profiles to the fault plane. Terrace profiles should be usually be based on elevations of the top of the strath surface, rather than of the terrace surface itself (for reasons explained by Johnson, 1944).

Stream incision into the downthrown block is relatively rare. Where most ephemeral or intermittent streams cross fault scarps, the streams have eroded gullies into the upthrown surface, while simultaneously depositing alluvial fans on the downthrown surface at the mouth of each gully (Chapter 2, Fig. 2.2). The fault scarp thus defines a transition zone between local erosion into the upthrown block, and local deposition on the downthrown block. If a stream incises into both the upthrown *and* downthrown blocks after faulting (such as in Figs. 3.14 and 3.15), it is probable that incision is not due solely to tectonic base level fall, but also results from a nontectonic cause such as *climatic change* in the contributing drainage basin (Bull, 1991).

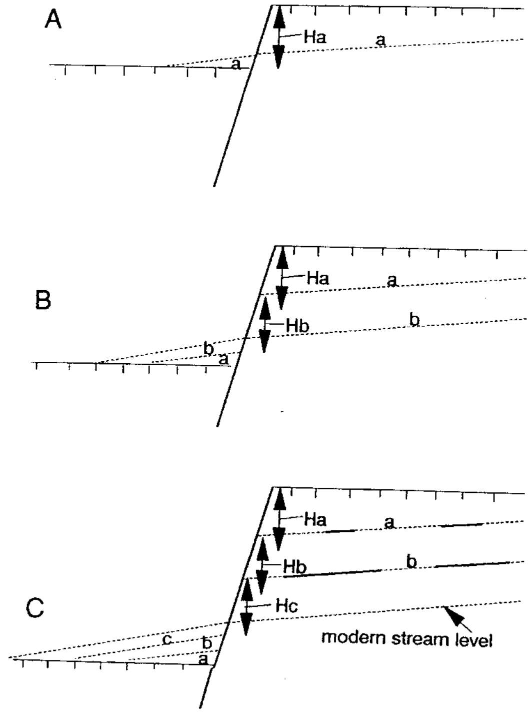

Figure 3.16 Schematic diagram showing tectonic terraces and their projections used to estimate vertical displacement in individual paleoearthquakes. The prefaulting surface is indicated by vertical ticks. (A) The first earthquake faults the prefaulting surface by amount Ha, after which the stream incises 75% through the scarp to the level of tectonic terrace a, where it stabilizes; below the scarp alluvial fan bed a is deposited. (B) A second faulting event displaces the scarp by the same amount (Hb), after which the stream again cuts down 75% through the scarp and creates tectonic terrace b; below the scarp alluvial fan bed b is deposited. (C) A third displacement (Hc) occurs, and the stream cuts 75% of the way through the scarp and down to its modern level and deposits fan bed c. Preserved parts of tectonic terraces a and b are shown as solid lines, eroded parts by dotted lines. The number of paleoearthquakes is thus one more than the number of tectonic terraces. Note that paleoearthquake displacement can only be measured from the heights of tectonic terraces if the degree to which the stream incised the scarp after each earthquake is known. Only in the case of complete (100%) incision does the difference in terrace elevations equal fault displacement per event.

Climatically induced fill or strath terraces formed by perennial streams may sometimes be mistaken for tectonic terraces if formed prior to faulting. After faulting of such a terrace suite, the parts of the terraces downstream from the fault scarp may be buried by widespread fluvial (or marsh) aggradation. The resulting geometry is terraces on the upthrown fault block that apparently have no counterparts on the downthrown block. These upthrown block terraces might thus be mistaken for postfaulting tectonic terraces, when in fact they are prefaulting nontectonic terraces (Jones, 1995).

By successively reversing the latest displacement, it is possible to reconstruct step by step the relative sequence of erosion and faulting for any number of displaced geomorphic surfaces (e.g., Lensen, 1968; see also Sec. 2.3.2.7). In the relatively simple, small-scale field examples described in Figs. 3.14 and 3.15, two assumptions were made that are often not valid for more complex terrace sequences. First, we assumed that the geomorphic surfaces above and below the fault scarp at a given location are the same surface, merely displaced by faulting. If this is true, then the topographic relief between the two surfaces (i.e., the scarp height or surface offset) provides a direct measure of fault displacement. Unfortunately, postfaulting deposition on the downthrown block becomes more common with increasing scarp age, and thus heights of old scarps tend to underestimate cumulative vertical displacement. A second assumption in Figs. 3.14 and 3.15 is that of no lateral offset of terrace risers, indicating that fault movement was purely dip-slip. If a small component of lateral slip *had* occurred, terrace risers would be offset laterally, but riser offset provides only a minimum estimate of true horizontal displacement (Chapter 6). In the extensional terrains of the western United States, where oblique movement on historic ruptures has been on the scale of decimeters, faulted Quaternary terrace risers rarely exhibit evidence of lateral offset (within the precision of field measurements on degraded risers).

A good field example of fault scarp/landform interaction is the five geomorphic surfaces at an incised fanhead offset by a compound range-front fault in the Rio Grande rift, southern Colorado (McCalpin, 1987b). Vertical surface offsets range from 1.4 m on the youngest surface to 23.4 m on the highest surface (Table 3-4). If the youngest, 1.4-m-high scarp was created by a single, characteristic event, then simply dividing 1.4 m into the surface offsets of higher scarps would yield a first approximation of the number of events represented by these scarps. However, the fault scarps have variable maximum angles (Θ) and displace slopes of variable gradient (α), so reduction of surface offset (SO) to vertical fault displacement (H1) is desirable before making any interscarp comparisons (Sec. 3.2.3). Next, if the smallest scarp was created by *two* faulting events, then the larger scarps may have been produced by twice as many, smaller displacements. Clearly, the first task is to confirm by trenching whether the smaller scarps are products of one or two displacements. Trenching the second smallest (3.8-m-high) scarp at this site confirmed that

Table 3-4

Fault Scarp Measurements and Inferred Paleoseismic History, Rio Grande Rift Zone

Type of data	Geomorphic surface	Surface offset (SO) (m)	Vertical fault displacement (H1) (m)	Cumulative number of faulting events		Age of faulted surface (ka)	Slip rate (m/ka)[a]	Average recurrence interval (ka)[b]	
				1.6-m events	2.2-m events			1.6-m events	2.2-m events
Known from trenching	Holocene	1.4	1.6[c]	1[c]		≤10	0.16	≤10	
	Late Pinedale	3.8	3.8[c]		2[c]	15	0.25		7.5
Inferred from scarp profiles	Early Pinedale	8.9	9.1[d]	5.7[e]	4.1[f]	25	0.36	4.4	6.1
	Bull Lake	13.5	14.0[d]	8.8[e]	6.4[f]	140	0.10	15.9	21.9
	Pre-Bull Lake	23.4	24.2[d]	15.1[e]	11[f]	≥250	0.10	16.6	22.7

[a] net vertical displacement divided by the age of the surface.

[b] age of the surface divided by the cumulative number of faulting events.

[c] measured in a trench.

[d] calculated from Eq. (3.1), assuming $\beta = 75°$ (measured in trench), $\alpha = 5°$ for Pinedale and younger surfaces, $\alpha = 7°$ for older surfaces.

[e] net vertical displacement divided by 1.6 m.

[f] net vertical displacement divided by 2.2 m.

the 3.8 m of displacement was produced in two faulting events, an earlier one with vertical displacement of 2.2 m, and a later one of 1.6-m displacement.

The number of faulting events of known displacement (1.6 to 2.2 m) necessary to create the higher, untrenched scarps can be estimated if the surface offsets measured from scarp profiles are converted to vertical displacements using Eq. (3.1). Dividing the measured single-event displacements into the calculated net displacements based on scarp profiles suggests that the early Pinedale, Bull Lake, and pre-Bull Lake scarps were created by 4 to 6, 6 to 9, and 11 to 15 events, respectively (Table 3-4). These estimates can be erroneous if (1) earlier displacements at this site were substantially larger or smaller than the 1.6- to 2.2-m displacements observed in the latest two events or (2) geomorphic surfaces at each profile site have been significantly raised or lowered by deposition or erosion postfaulting. Complication 1 cannot be assessed without trenching older scarps; complication 2 is likely for the two oldest profiles.

3.2.5.2 Profile of a Compound Scarp

A *compound fault scarp* was defined by Slemmons (1957) as a scarp produced by more than one rupture event [also called a *composite fault scarp* (Stewart and Hancock, 1990) or a *multiple-event fault scarp*]. Compound fault scarps often contain multiple breaks in slope, each of which originated in a separate rupture event. The sequential evolution of these nickpoints is described by McCalpin (1983, Fig. 46) and Fig. 3.17 shows a recent example. After the initial scarp formed and degraded to a smooth profile, the scarp in Fig. 3.17 was rejuvenated by the 1983 Borah Peak rupture. If *inflection points* are sharp and the scarp profile is essentially composed of linear segments, it may be possible to distinguish single-event displacements on a compound fault scarp even after considerable weathering (Fig. 3.18). For example, Haller (1988) used histograms of slope angles versus horizontal distance to emphasize subtle scarp inflections. Distinct multiple breaks in slope on the upper part of a degraded fault scarp may indicate inflection points from earlier faulting events, as suggested by Wallace (1980a, Fig. 12; Wallace, 1984, Fig. 24) for the Madison Range, Montana, and Pleasant Valley, Nevada, fault scarps, respectively. However, it is also possible that these subtle inflections in slope were created by (1) small-scale erosional or depositional events on the scarp face or (2) multiple stepfaults created during a single event.

Subsurface exposures would show if the inflections were underlain by small-displacement faults or fissures; if so, they are probably primary tectonic features rather than secondary erosional nickpoints. If inflections do *not* overlie faults, however, it might be difficult to distinguish between various erosional origins for the inflections. If the subsurface exposure reveals only a single colluvial wedge, then scarp profile inflections cannot have resulted from multiple faulting events. Unfortunately, many large fault scarps that are known to be the product of multiple displacements (based on independent geomorphic or stratigraphic relations) do not exhibit multiple breaks in slope. Instead, most of the scarp face is a wide, planar slope at or just below the angle of repose (McCalpin, 1983). On high-slip-rate faults, rejuvenation of the scarp by repeated faulting occurs so often that slope regrading destroys earlier nickpoints (e.g., Wasatch fault zone, Utah; Machette *et al.*, 1992a, b). High, compound scarps that possess large planar faces without nickpoints may indicate short recurrence intervals (a few ka rather than 10s or 100s of ka).

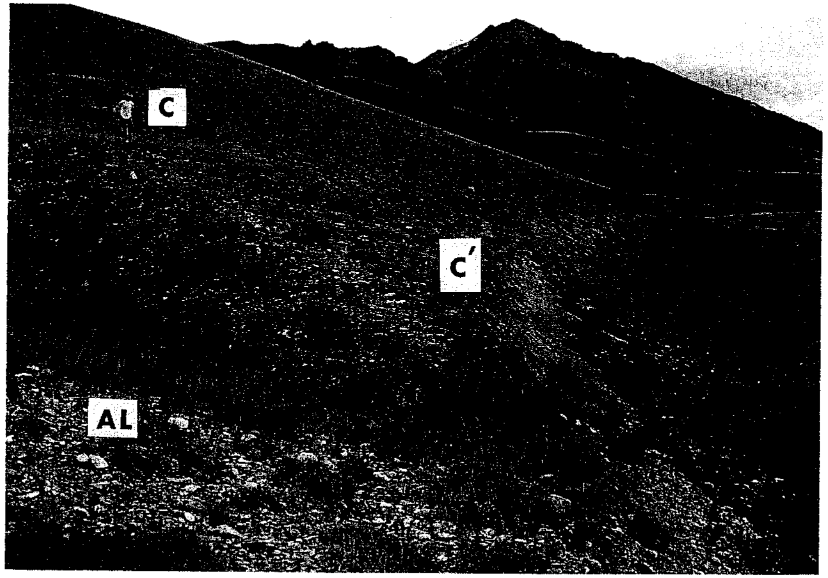

Figure 3.17 Photograph of a compound fault scarp offsetting alluvial terraces on the 1983 Borah Peak rupture. Rock Creek is barely visible as a line of trees at far right. Person (1.9 m tall) is standing to the left of the crest of the prehistoric fault scarp (C), which had been incised 3.5 m by the stream in the left foreground prior to 1983 (AL). The 2-m-high 1983 fault scarp (unvegetated band at right center) has rejuvenated this older fault scarp and created at new inflection point (C') that will retreat upslope, eventually regrading the face of the prehistoric fault scarp (area between C and C'). Post-1983 stream incision into the bed of the stream in left foreground (AL) will create a tectonic terrace that will be 2 m high if the stream incises all the way to the bottom of the 1983 fault scarp.

3.3 STRATIGRAPHIC EVIDENCE OF PALEOEARTHQUAKES

Normal surface faulting results in the instantaneous creation of faults, fissures, and tilted beds, and in the delayed response of fault-induced sedimentation.

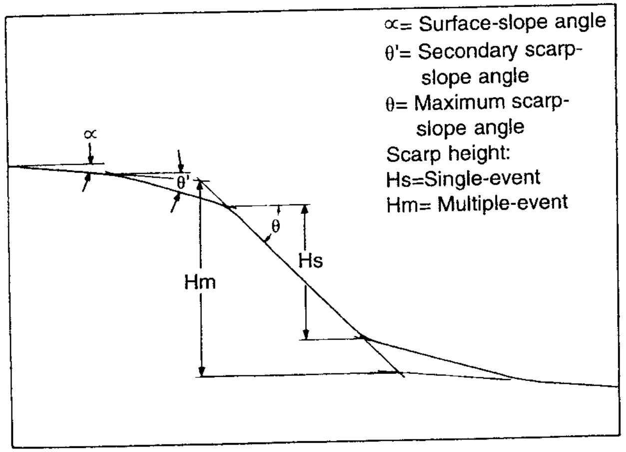

Figure 3.18 Diagrammatic profile of a faceted compound fault scarp, showing how a single-event scarp height (Hs) is graphically determined from the total (multiple-event) scarp height (Hm) and other measures of scarp geometry (see Table 3-3). [From Machette (1982); reprinted with permission of the New Mexico Geological Society.]

The sequence of paleoearthquakes cannot usually be reconstructed from tectonic or depositional features alone, instead, a combined analysis is required. The key to successful interpretation is to distinguish between tectonic versus depositional features, and to distinguish depositional units that predate faulting from those that postdate faulting.

The concepts presented in this section are derived from studies of many trench exposures of normal faults in the western United States, particularly on the eastern margin of the Basin and Range Province. Detailed trench logs illustrating many of the features described herein can be found in the "Paleoseismology of Utah" series of publications (Lund *et al.*, 1991; Personius, 1991; Jackson, 1991; West, 1994; McCalpin, 1994), as well as in Swan *et al.* (1980), Schwartz and Coppersmith (1984), Forman *et al.* (1989, 1991), Machette *et al.* (1992a), McCalpin *et al.* (1994), and Olig *et al.* (1994).

3.3.1 Distinguishing Tectonic from Depositional Features

Most geologists have no difficulty recognizing faults in bedrock, but faults in unconsolidated deposits are often more subtle and can have many modes of expression (Sec. 2.3.2.5). Normal fault scarps form in an extensional stress field, so their characteristics in unconsolidated materials differ from those of reverse and strike-slip ruptures. According to Bonilla and Lienkaemper (1991, Table 17) normal faults are more likely to have *fissures filled with rubble,* and less likely to show *gouge, slickensides, breccia, crushing,* or *polishing* compared to reverse or strike-slip faults. It is difficult to mistake *erosional* or *depositional* contacts in unconsolidated deposits for normal faults because faults almost always have steeper dips (55 to 90°) than erosional contacts. In addition, many clasts along normal fault planes will be rotated such that long axes approximately parallel the fault. Paleoseismologists often refer to this orientation as *shear fabric,* although it has never been reproduced by laboratory shearing experiments. Finally, faults are straighter than most erosional contacts, and often steepen upward.

Despite these criteria, it is often difficult in practice to distinguish sheared *in situ* material from fissure-filling materials or fallen blocks of free face material caught up in a complex normal fault zone. Major construction projects have been delayed and millions of dollars spent to define properly such microstratigraphic relations (e.g., Asquith, 1985). For example, a distinction that must be made at nearly every fault exposure is whether scarp-derived colluvium is in depositional contact or fault contact with upthrown block strata. A depositional contact implies only a single faulting event which is older than the colluvium, whereas a fault contact requires two displacement events- the first to generate the colluvium, and the second to fault it. Due to the tension fissures that are common along normal faults, fault zone stratigraphy is often a confusing assemblage of sheared *in situ* deposits, material that has fallen into fissures in intact blocks, partly disaggregated blocks, and material washed into depressions by running water. Each exposure is different in detail, but Table 3-5 lists some general field criteria for distinguishing between several types of contacts near normal faults.

3.3.2 Sedimentation and Weathering in the Fault Zone

The small-scale patterns of sedimentation and weathering in a normal fault zone are powerful keys to understanding the sequence of paleoearthquakes. This realization, made in the 1970s (e.g., Swan *et al.,* 1980), meant that a separate line of field evidence was available to supplement observations on tectonic landforms, on which fault interpretations had traditionally been based. Because the pioneering work was performed in the semi-arid climates of the western United States, there is an unavoidable emphasis in the following discussion on certain types of sedimentation (loess deposition, debris flows, ephemeral sag ponds) typical of arid and semi-arid, sparsely vegetated terrain (see Nelson, 1992b; Gerson *et al.,* 1993). Although other climatic regimes experience processes that would require modification of the model described herein (e.g., tree throw, cryoturbation), the observations made in the western United States should apply to a wide variety of climates.

3.3.2.1 Scarp-Derived Sedimentation and the Colluvial Wedge Model

The *colluvial wedge model* is a conceptual model that utilizes the stratigraphy of scarp-derived colluvial deposits to interpret faulting history, much as

Table 3-5

Criteria for Distinguishing a Normal Fault Contact from a Depositional Contact in Unconsolidated Sediments

Characteristic	Fault contact	Crack fill	Depositional contact
1. Consistence of material	a. Material in fault zone is sometimes softer than that to either side (strain-softening), unless plastic beds have been smeared along the fault. Rotation of clasts and subsequent dilation due to shearing create voids in the fault zone. Rarely, infiltrating water cements the fault zone, making it harder than adjacent materials; groundwater staining is usually obvious.	b. Crack fill material is softer than adjacent wall material if it fell into the crack during the latest faulting event, and has not subsequently been sheared. Material hardens with successive shearing events, eventually approaching the hardness of hanging-wall material. Animals preferentially burrow into crack fill, creating many krotovinas.	c. Material at the contact is similar in hardness to material on either side.
2. Clast orientation	a. Most clast long axes are oriented parallel to fault dip (50–90°), forming a shear fabric.	b. Crack fill contains many clasts with vertical or near-vertical long axes, which fell "headlong" into the crack. Most clasts have relatively steep orientations, becoming less steep toward the top of the crack fill.	c. Only some clasts are parallel to the contact. Wide variations exist in clast long-axis orientation, with a modal plunge value near the angle of repose for colluvium (ca. 30–40°).
3. Truncation of layers in the abutting colluvium	a. Layers in colluvium maintain constant thickness up to the fault contact; layers are either cleanly truncated by the fault or if plastic, may be drawn out along the fault plane to form a mixed zone.	b. Layers are abruptly truncated at the crack margins; there is no mixed material smeared out along crack sides.	c. Layers in colluvium steepen within 5-10 cm of the depositional contact and begin to thin. Dip of layers approaches, but does not attain, the dip of the contact. No smearing or mixing of plastic beds occurs at the contact.

Wallace's (1977) scarp degradation model did with scarp morphology. Many workers observed that, after formation of historic fault scarps, the loose material exposed on the scarp face (*free face* of Wallace, 1977) falls to the base of the scarp and creates a wedge-shaped deposit of colluvium that overlies the prefaulting surface. Subsequent work on prehistoric scarps (particularly on the Wasatch fault in the late 1970s) showed that the *colluvial wedge* shed from a scarp eventually buried the lower part of the free face, after which the scarp became relatively stable. During stability a soil would form on the colluvium. Subsequent faulting would then lead to deposition of a second colluvial wedge analogous to the first. Multiple faulting should therefore be represented by a succession of vertically stacked colluvial wedges on the downthrown fault block separated by soils, each wedge representing deposition following a surface-rupturing event (Fig. 3.19). Japanese workers (e.g., Okada *et al.*, 1989) term the pattern of colluvial wedge, over- and underlying soils, and the fault plane as the *D-structure* for its resemblance to that letter of the Roman alphabet. However, they emphasize that the wedge-shaped deposit of colluvium is a less important indicator than the absence of the lower soil on the upthrown fault block, because lenses of colluvium can be deposited at the foot of a steep scarp by nontectonic processes. Pantosti *et*

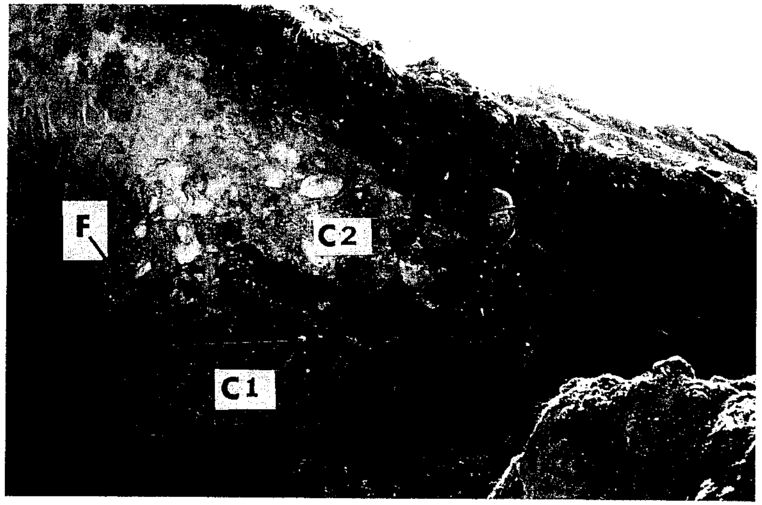

Figure 3.19 Photograph of two superposed colluvial wedges (C1, C2) in a trench across the Bear River fault zone, Wyoming (see West, 1993). The fault is indicated by F. Light-colored, gravelly colluvial wedges taper to the right and are under- and overlain by dark organic soil horizons. Upthrown block to left of fault is composed of Eocene claystone. Radiocarbon ages from soils underlying the two wedges indicate faulting at ca. 2.4 ka and 4.6 ka. Reprinted with permission of the Geological Society of America.

al. (1993) later termed the ground surface at the time of a paleoearthquake as an *event horizon.* An event horizon is stratigraphically defined by either scarp-derived colluvium that buries the prefaulting surface, and/or by unconformities that develop as a result of warping and subsequent deposition. The unconformities typically develop on the downthrown block in fluvial or lacustrine sediments (see Sec. 3.3.2.2). Therefore, the number of event horizons should equal the number of paleoearthquakes.

This simple sedimentologic model has been applied to dozens of faults in the western USA to identify from one to four paleoseismic events (e.g., Forman *et al.,* 1989, 1991; Machette *et al.,* 1992a). Nelson (1992b) proposed a *facies model* for deposition at the base of a single-event normal fault scarp. Two discrete facies of scarp-derived colluvium are defined: *debris facies* and *wash facies* (Fig. 3.20). The debris facies is formed by initial spalling of intact blocks and large rocks from the free face, followed by slumping, sliding, and rolling of loose debris to the foot of the scarp. The basal colluvium in a wedge usually includes the largest clasts and often contains intact blocks of soil horizons or discrete beds from the upthrown block. The toe of many debris wedges is composed of large clasts with little or no matrix, and represents the largest rocks that have rolled to the tip of the wedge. Nelson (1992b) terms this the *sorted debris facies.* The bulk of the debris facies is usually an unsorted, unstratified deposit which, if rich in clasts, shows a downslope fabric. However, many wedges derived from gravel show internal bedding, with clast-supported layers alternating with matrix-supported layers. These layers have been observed within the post-1983 colluvium at the Borah Peak, Idaho, rupture and are thus inferred to result from seasonal geomorphic processes acting on the free face, and do not have tectonic significance (McCalpin and Forman, 1988). Preliminary studies of colluvial clast fabric (McCalpin *et al.,* 1993) show that several orientation subpopulations are present, representing clasts that either slid, rolled, or twirled onto the wedge surface.

After complete disappearance of the free face, slopewash, rainsplash, and creep processes dominate on the scarp slope. Colluvium deposited by these processes (*wash element* in Fig. 3.20) is distinctly finer grained, better sorted, better stratified, and typically more rich in organics than debris facies colluvium (Nelson, 1992b). There is often an abrupt contact between debris- and wash-facies colluvium, which is inferred to represent the abrupt disappearance of the free face. If wash facies deposition rates slow sufficiently, the scarp slope will develop a soil profile.

Not every wedge fits the simple model previously described for two reasons. First, the wedge deposited from a simple fault scarp on a subhorizontal geomorphic surface is thickest at the fault and tapers downslope, forming an obvious wedge shape. Colluvium from successive events, however, is deposited on the sloping surfaces of earlier colluvial wedges, which causes later wedges to extend farther downslope from the fault, and be thinner and less wedge

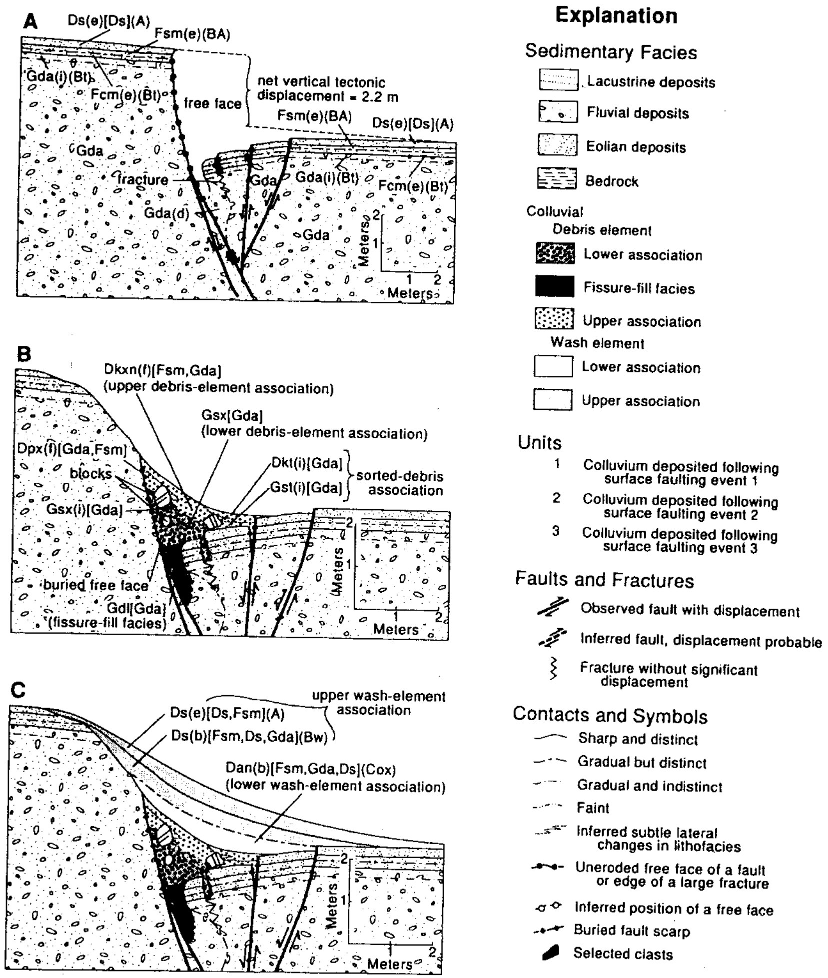

Figure 3.20 Facies model of fault scarp sedimentation from a single-event fault scarp in unconsolidated material. (A) Fault scarp immediately after formation. Diagram shows the basal tension fracture and small-displacement antithetic faults that typically form in unconsolidated sediments. No colluvium has yet been deposited. (B) Scarp after deposition of the fissure-fill facies (solid black) and the upper and lower associations of debris-element colluvium (dotted patterns). The lower association contains more intact blocks of free face materials (including soil blocks and vegetation from the crest of the free face) than does the upper association. At the end of stage B, the near-vertical free face has been destroyed by slope decline. (C) Scarp after deposition of wash-element colluvium. For detailed explanation of facies abbreviations, see Nelson (1992b). [From Nelson (1992b); reprinted with permission of the Society for Sedimentary Geology.]

shaped than earlier wedges (Ostenaa, 1984; Fig. 3.21, this volume). In these elongated colluvial deposits from later faulting events the distinction between debris- and wash-facies colluvium is commonly blurred. This loss of distinction between colluvial facies also occurs below fault scarps on steep far-field slopes (≥25°).

Interpreting the subsurface relations in a trench where colluvium abuts bedrock on a steep slope (e.g., Sullivan and Nelson, 1983, Figs. 4, 5) can be ambiguous. Stewart and Hancock (1988, Fig. 3) claim that the colluvium-bedrock contact will display "tectonic breccias and subordinate slip planes in the Quaternary sediments" if the contact is a fault contact, rather than a depositional contact. Sullivan and Nelson (1983, Fig. 5) argued that because "no evidence exists of shearing along the contacts of the colluvial deposits with the bedrock," and "colluvial units clearly truncate the gouge and breccia of the fault zone," a bedrock fault in Utah had experienced no late Quaternary movement. Criteria for distinguishing fault contacts versus colluvial contacts in trench exposures are described in Table 3-5. Where normal fault scarps are created across very steep (>45°) bedrock slopes, the colluvial products (rockfall) may be transported completely off the slope.

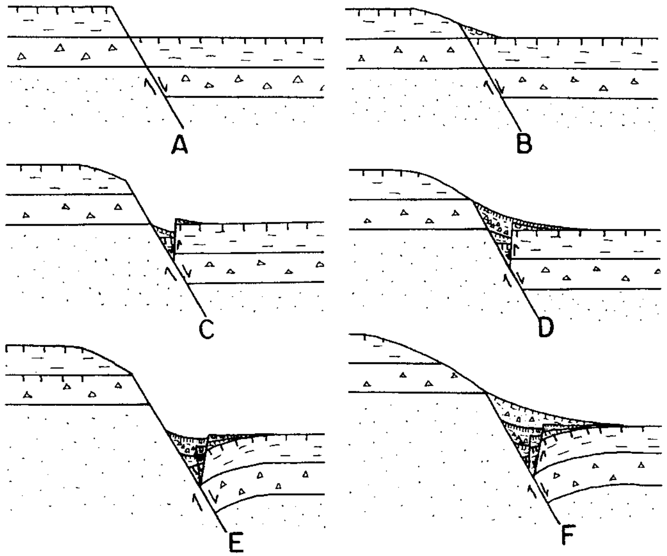

Figure 3.21 Schematic diagrams showing how the provenance of scarp-derived colluvium may vary through successive fault displacements. Vertical ticks indicate soils. (A) First faulting event creates a free face entirely in the unit marked by short dashes. (B) Deposition of the first colluvial wedge, composed exclusively of material derived from the short-dashed unit. (C) Second faulting event creates a basal tension fissure into which the earlier colluvial wedge is dropped. The lower part of the free face at the main scarp is composed mainly of the unit marked by triangles. (D) The second colluvial wedge fills the tension fissure and then progrades out onto the downthrown block. The lower part of the second colluvial wedge is derived mainly from gravity and debris deposition from the lower part of the free face, and is thus composed of material from the triangle unit. As the scarp continues to backwaste and decline, more colluvial material is derived from the upper part of the scarp (upper short-dashed unit). (E) Third faulting event creates a free face in the dotted unit and a new antithetic fault farther to the right of the earlier antithetic fault, which was not rejuvenated in this event. Most of the free face exposes units marked by dots and triangles. (F) The third colluvial wedge buries the earlier two wedges. The sequence of lithologies in the third wedge roughly parallels the stratigraphic sequence exposed in the scarp face; that is, the basal portion is derived from the dotted unit, and the upper (wash facies) portion is mainly derived from the short-dashed unit.

Second, sediment traps formed by complex fault scarps may alter the patterns of deposition at the scarp base. Scarps fronted by large tension fissures commonly have abnormally small colluvial wedges for their scarp heights, because much of early colluvium fell directly into the tension fissure. Likewise, much basal colluvium may be required to fill a graben before a transportational slope away from the scarp is established. To further complicate matters, the style of surface rupture at a given site may change with successive events, such that a simple scarp may form in the first event, a graben may form in the second event, and a somewhat wider graben may form in the third event. Deformation occurring during later events can obscure the original geometry of earlier colluvial wedges. The key to correct interpretation is to reconstruct a sequence of cross sections (see examples in Secs. 2.3.2.7 and 3.3.6) which successively reverse the fault displacements and restore deposits to their prefaulting configurations.

The colluvial wedge model states that each surface rupture is followed by the formation of a discrete colluvial deposit. Therefore, simply counting the number of colluvial wedges should yield the number of paleoseismic events at a site. To do this, one must be able to distinguish between fault-scarp-derived colluvial wedges and other types of deposits that are typically present in fault-zone exposures.

3.3.2.1.1 Identifying a Colluvial Wedge

A colluvial wedge in a fault-zone exposure can be identified from its contact with the fault, the shape of the deposit, and its sedimentology. The part of the wedge closest to the fault can be either in depositional or fault contact with footwall deposits (for criteria, see Table 3-5). For example, colluvium shed from a single-event fault scarp is in depositional contact with the degraded fault free face (Sec. 3.2.4). At the base of the colluvial wedge the buried free face overlies a fault contact between prefaulting deposits. The downward transition from a depositional contact (typical dip 40° to 60°, no shear fabric) and a fault contact (typical of dip 78 ± 10°, with shear fabric) is a key criterion for locating the base of a colluvial wedge (e.g., Fig. 3.25). The lower contact of the wedge is an unconformity over the buried prefaulting ground surface; if back-tilting has occurred it is an angular unconformity. The upper contact of the wedge is either the modern ground surface or an unconformity with the next overlying wedge. Colluvium from a multiple-event fault scarp consists of the unfaulted colluvium from the latest event, which overlies the faulted colluviums from earlier events (Fig. 3.21).

It is often difficult to distinguish the base of scarp-derived colluvium(s) from the top of the prefaulting deposits of the downthrown block, especially if the latter are diamictons. The most direct approach is to examine carefully the uppermost deposit on the upthrown fault block, and try to identify that same deposit underneath scarp-derived colluvium on the downthrown block. A second check is that the volume of scarp-derived colluvium should approximately equal the volume of material eroded from the scarp crest. The area of the eroded material can be estimated by projecting the fault plane upward at a reasonable initial angle (not less than the dip of the fault plane) until it intersects with the projection of the upthrown faulted geomorphic surface. This area should be equal to the area of scarp-derived colluvium on the same trench log. If the eroded area appears significantly larger than the area of colluvium, then the base of the colluvium may still be beneath the trench floor or, alternatively, colluvium could have been removed by lateral stream or shoreline erosion at the base of the scarp. However, the area of colluvium is commonly larger than the inferred area eroded, due to eolian additions to the colluvial wedge (McCalpin, 1983).

3.3.2.1.2 Displacement Estimates from Colluvial Wedges

Scarp degradation models (Sec. 3.4.3) predict that the maximum thickness of scarp-derived colluvium will be limited to half the height of the free face from which it was shed. Thus, a first approximation of initial scarp height is twice the maximum colluvial thickness exposed in a trench or cut. Ostenaa (1984) suggested that this relation only holds true for colluvial wedges that are deposited on nearly horizontal surfaces. For wedges deposited on steeper surfaces, maximum thickness may only range from a small fraction to 100% of the height of the causative free face (Fig. 3.21). Colluvium may also be trapped in rupture complexities such as basal tension fissures, which decreases the volume of the wedge and thus its thickness. In view of the many possible complexities, the rule of thumb "initial scarp height = 2× maximum colluvial thickness" should be used with caution.

In rare cases it may be possible to use *provenance* of colluvial wedges to infer from what part of the upthrown block they were derived and thus estimate displacement. This concept is loosely based on trench observations originally made by Swan *et al.* (1980) on the Wasatch fault zone, Utah. Figure 3.21 shows three distinct stratigraphic units that are faulted in three vertical increments, each of which is roughly equal to unit thickness. Because of this coincidence, the free face in stage A is dominantly composed of the uppermost stratigraphic unit, so colluvial wedge 1 is derived entirely from the upper unit. The second faulting event (C) exposes the middle stratigraphic unit in the free face, so that colluvial wedge 2 is composed of both the middle unit and the upper unit. Likewise, the third faulting event (E) creates a free face composed primarily of the lower two stratigraphic units, which is again reflected in the composition of colluvial wedge 3. The lower part of each colluvial wedge (debris facies) is derived from material exposed in a steep free face, whereas the upper part of the wedge (wash facies) may be derived primarily from stratigraphic units on the crest of the scarp that were eroded during later, wash-dominated stages of scarp degradation (Nelson, 1992a).

All of the preceding estimates are of free face height, and thus cannot detect any component of oblique slip. It is sometimes possible to *detect* oblique slip in trenches excavated perpendicular to normal fault scarps, from slickensides or abrupt stratal thickness changes at the fault, but it is usually impossible to *measure* the amount of oblique slip, without resorting to three-dimensional trenching (Chapter 6).

3.3.2.1.3 Marginal Paleoseismic Evidence: Small-Displacement Faulting at Long Recurrence Intervals

The stratigraphic expression of small displacements on normal faults with long recurrence intervals can be complex and difficult to identify. The following discussion is based on some ongoing paleoseismic investigations of this type at Yucca Mountain in southwestern Nevada (e.g., Menges *et al.*, 1994). Surface displacements commonly are in the range of 5 to 70 cm on faults with recurrence intervals of 10^4 to 10^5 yr. Several types of deposits may develop following surface ruptures depending on the local structural and depositional setting. In many cases deep and relatively wide fissures form over the fault which are subsequently filled with colluvial debris (Fig. 3.22). Small colluvial wedges then cap these filled fissures if a free face exists and sufficient material is still available after filling of the fissure. Small surface displacement (with or without significant fissuring) produces small and thin colluvial wedges with elongate, finely tapered, and flattened triangular shapes (Fig. 3.22) that are difficult to identify uniquely. Wedge recognition is confounded further by the occurrence within thick aggradational sequences of poorly bedded, fine-grained eolian or reworked eolian deposits that are difficult to subdivide into lithologic units. Most of the individual deposits in these sequences have broad sigmoidal (flattened S) to downward-thickening shapes, and are associated with the initial draping and burial of paleoscarps and their scarp-derived colluvium. These units have no tectonic significance and must be carefully distinguished from true scarp-derived colluvial wedges. In addition, gravelly interbeds in aggradational sequences are deposited by channels localized near the fault zone; these interbeds mimic colluvial wedges, but should not be used directly for paleoseismic interpretation. Identification of event horizons and displacement amounts in such settings ideally should incorporate other criteria such as differential displacements of strata or upward termination of fractures.

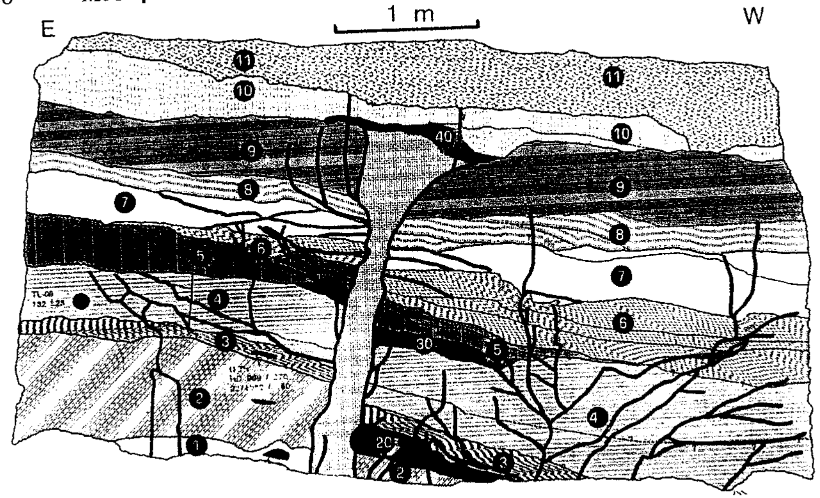

Figure 3.22 Log of Trench 14D on the northern Bow Ridge fault, Yucca Mountain, Nevada. Thick lines show faults and fractures; the upward-flaring patterned area at center is the main fault zone composed of fissure fill. Offset stratigraphic units are differentiated by patterns, with three suspected colluvial wedges marked by the darkest shading. Note how units immediately overlying the suspected colluviums thicken across the main fault, whereas higher units maintain more uniform thickness. [From Menges *et al.* (1994).]

3.3.2.2 Interaction of Colluvium with Other Fault-Zone Facies

Scarp-derived colluvium usually constitutes the largest volume of postfaulting deposits in a normal fault zone, but other facies can be significant. The relative volume of these other facies increases with the size and depth of backtilted areas and graben. Topographic lows created at the base of normal fault scarps are generally filled by a combination of *laterally accreting colluvium* shed from the scarp (described previously) and *vertically accreting graben deposits* of various origins. The type of vertical accretion deposits and their deposition rates are mainly controlled by nontectonic factors, such as the geomorphic regime operating on the faulted surface. In arid and semi-arid areas, direct airfall loess or eolian sand may fill the depression. Semi-arid graben are often filled with sediments derived locally from small gullies that incise the upthrown block. Small alluvial fans form at the mouths of each gully, whereas distal debris-flow sediments spread into the remainder of the graben during severe precipitation events. The intermittent ponds that form during wet seasons may receive vertically accreting sediment from loess or suspended sediment from rare debris flows and stream flows (McCalpin *et al.*, 1994). In more humid climates, perennial ponds in graben (sag ponds) fill with marsh sediments and lacustrine deposits.

Vertically accreting graben deposits interfinger with contemporaneous, laterally accreting colluvium near the base of the fault scarp (Fig. 3.23). The position of the facies interface is determined by the relative rates and loci of deposition of the two facies. Immediately after faulting, colluvium is deposited mainly near the free face. As the scarp broadens with weathering, wash-dominated colluviation (Nelson, 1992a) will push the facies interface away from the scarp. In dry environments wash-facies deposition may prograde completely across the graben between rare periods of fluvial or lacustrine conditions.

Unconformities occur in both the colluvial and graben fill sequences, but their tectonic significance is different. In the colluvial wedge sequence, a soil buried by coarse colluvium usually indicates renewed deposition from a free face after faulting (Swan *et al.*, 1980). In the graben fill sequence, however,

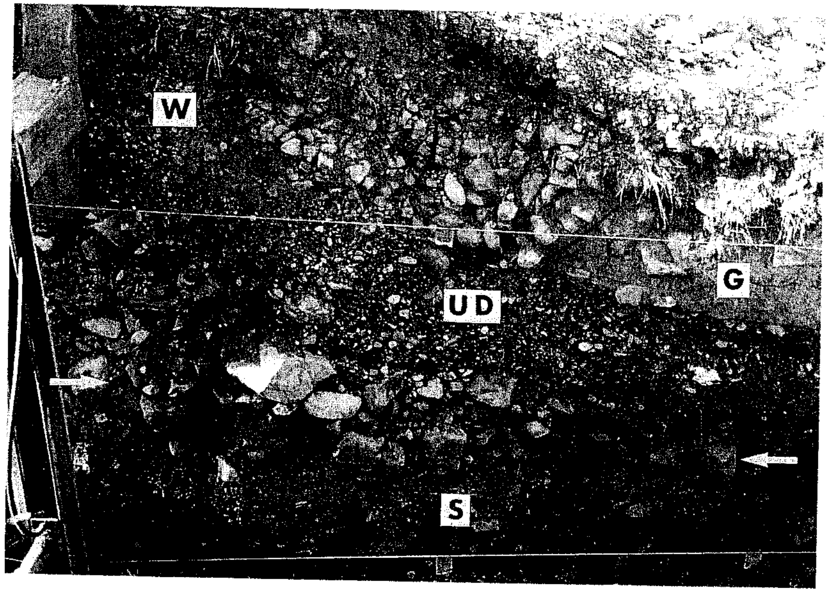

Figure 3.23 Photograph showing the interfingering of scarp-derived colluvium (deposited from left) with graben-fill sediments (at far right). String lines, and tape squares on lines, are 1 m apart. The lower concentration of coarse gravel (between arrows) is the tip of the sorted debris facies of Nelson (1992a). The sorted debris facies is underlain by a matrix-supported soil horizon (S) that predates faulting, and is overlain by finer gravel (UD) of the upper association of the debris element. The upper 0.5 m is generally wash-element colluvium (W), with a concentration of stones at center (a second sorted debris facies) probably induced by human disturbance of the scarp face. On the right margin of the photo fine-grained graben sediments (G) are in contact with the scarp-derived gravels. Photo taken at the middle Sheep Creek trench, Grey's River fault, Wyoming (Jones and McCalpin, 1992; Jones, 1995).

renewed deposition atop a soil only signals a change in eolian, fluvial, or lacustrine depositional processes that may or may not be related to faulting. Renewed faulting may create or increase topographic closure in grabens and back-tilted areas. This faulting then sets the stage for renewed graben deposition, but does not necessarily provide for the necessary sediment transport. However, if streams cross the fault nearby and empty into the graben, local stream incision into the upthrown block after faulting should cause a rapid increase in the rate of fluvial/lacustrine deposition in the graben. *Angular unconformities* are almost certainly caused by tectonic deformation, and are thus event horizons.

Buried soils in the colluvial wedge sequence can often be traced into the graben where they are buried by lacustrine or marsh sediments that indicate temporary ponding, as described previously. Upsection the graben sediments typically change to a more eolian- or fluvial-dominated facies, indicating that the initial closed depression has filled. Thus, unconformities that are continuous throughout both laterally and vertically accreting deposits probably represent individual paleoearthquake ruptures (i.e, are event horizons). Additional unconformities in the graben sequence may merely reflect deflection of streams or debris flow into the graben from geomorphic/climatic events that have no tectonic significance. Correlation of individual graben strata to the colluvial wedge sequence becomes important when datable materials are found in the former but not in the latter (McCalpin *et al.,* 1994).

3.3.2.3 Angular Unconformities in Fault Zones

Angular unconformities in normal fault zones are typically associated with either faulting accompanied by back-tilting or the formation of asymmetric graben, or by monoclinal folding or normal drag along the fault plane. In back-tilted areas, the dip of strata may steepen with increasing age and depth, indicating progressive tilting (usually down toward the main fault) by repeated faulting. The differences between the dip of successive strata provide a basis for reconstructing a chronology of faulting that is independent from colluvial wedge evidence, but which can be physically traced (via facies interfingering) to scarp-derived colluvium. When *restoring* graben strata to their pretilt orientations (i.e., retrodeformation analysis), one must assume that the laminae within fine-grained deposits (silts, clays) in the graben were initially horizontal. A second assumption is that the initial angle of repose of proximal scarp-derived colluvium has not changed significantly through time; the present surface slope on proximal colluvium (typically 35° to 40°) and clast long-axis plunges of 30° to 35° thus indicate initial bedding angles in older colluviums.

An example of this type of analysis comes from the Wasatch fault zone, Utah (McCalpin *et al.,* 1994). Measurements used in this analysis include (1) dips of graben lithofacies contacts (right side of Fig. 3.24) and (2) dips of the upper and lower contacts of colluvial wedges and dips of clast long-axis

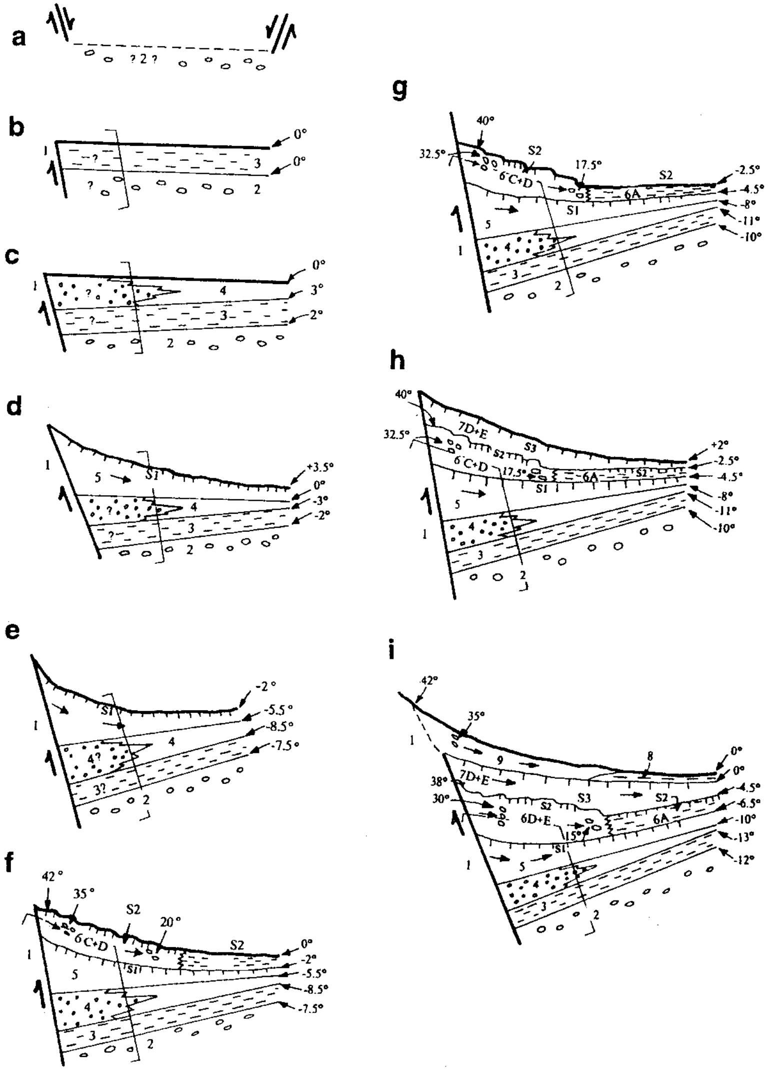

Figure 3.24 Schematic diagrams showing sequence of faulting events (a=oldest) at Kaysville deduced from graben angular unconformities. Stage i reflects the present geometry. Numbers to the right of each diagram show the dip of strata as reconstructed (negative numbers indicate eastward tilt). Unit lithologies: 1, lacustrine sand; 2, alluvial fan gravel; 3, sag pond silt and clay; 4, fluvial gravel deposited in graben; 5,6,7,9, scarp-derived colluvium; 8, sag-pond silt. Colluvial units 6 and 8/9 show interfingering between colluvial and sag-pond facies. [From McCalpin *et al.* (1994); reprinted with permission of the American Geophysical Union.]

fabrics (left side of Fig. 3.24). Five of the contacts between units in the graben are defined by the upper contact of laminated or massive silts and clays (dashed pattern), and are presumed to have been originally horizontal. Three other contacts that define the tops of fluvial sands and gravels (circle pattern) are presumed to have been nearly horizontal when deposited along the graben axis. The paleo ground surfaces of two distal scarp-derived colluvial units (contacts between soil S1/ 6A; soil S3/ 8A) presumably had a slight initial valleyward gradient (2 to 4°?) when they became stabilized. By reversing the effects of the latest event and restoring some graben units to horizontal, the sequence of tilting events that accompanied faulting (Fig. 3.24) is reconstructed.

Downthrown block strata are occasionally tilted forward (away from the main fault) by faulting, due to fault-propagation folding or frictional drag along the fault plane. If deposits are moist and plastic, strata may be folded into a monocline in which the beds approach parallelism with the main fault plane. This geometry is usually associated with cohesive sediments, for example, moist silts and clays of lacustrine origin. Pantosti *et al.* (1993) analyzed a *monoclinal fault trace* in interbedded lake clays and sands that had experienced several Holocene paleoearthquakes. In that study area the monoclinal scarp faced upstream across a perennial stream. Each faulting event created temporary ponding and lacustrine deposition. Sediments in the scarp-base lacustrine basin were folded during each paleoearthquake and then *onlapped* by horizontal strata (Fig. 3.25). The schematic reconstruction of faulting relies heavily on cross-cutting relations between packages of sediment, especially where unconformities are traced into scarp-derived (?) colluvium near the fault plane.

The angular unconformities created by forward-tilting may be useful in paleoseismic interpretation. If downthrown block strata act in a quasiplastic manner (e.g., clayey or silty sands), the monocline may be broken in *domino style* by small thrust faults that dip toward the main fault. In Fig. 3.26, a pronounced angular unconformity exists between the youngest scarp-derived colluvium and folded and thrusted older alluvium and colluvium. (These small thrust faults are secondary to the main normal fault and do not indicate a compressional stress regime). The sequence of events at the trench could be interpreted as follows: 1) initial faulting and scarp formation, (2) deposition of scarp-derived colluvium (heavy dotted lens at lower left) and alluvium (lighter dots and dashes) on the downthrown block ca. 4.5 ka, (3) renewed faulting, which folded and faulted units older units near the fault, and (4) deposition of the youngest scarp-derived colluvium ca. 3.8 ka.

In contrast, the forward tilting in brittle materials (e.g., dry sand and gravels) mainly results in the opening of tension fissures over conjugate normal and thrust faults between tilted blocks. In this geometry the sequence of events could be reconstructed from the superposition of fissure fills and overlying, nontilted, colluvium. Mutiple fissure fills have been instrumental in deciphering

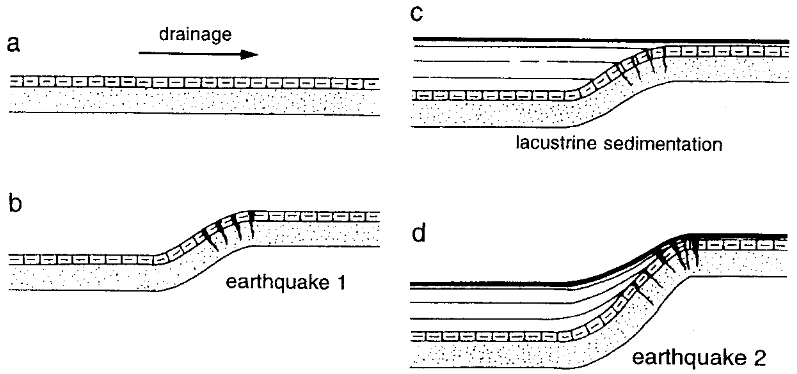

Figure 3.25 Schematic diagrams showing deposition against an upslope-facing scarp in a humid climate. (a) Prefaulting. (b) First earthquake creates an upstream-facing monoclinal scarp split by crestal tension fissures. (c) The stream is dammed to produce a lake, and horizontal lake sediments are deposited over the scarp. The base of the lake sediments is an angular unconformity across the face of the scarp, and a disconformity farther to the left; both are event horizons. (d) The second earthquake rejuvenates the monocline, dragging the lacustrine strata upward and creating new tension fissures at a higher structural level than the first set. Subsequent lacustrine sedimentation upstream of and over the scarp will create a new event horizon like the first. [From Pantosti *et al.* (1993); reprinted with permission of the American Geophysical Union.]

faulting chronologies where displacements in each faulting event are small (5 to 20 cm), for example, at the Nevada Test Site (Menges *et al.*, 1994).

3.3.2.4 Example of Reconstructed Displacements on a Multiple-Event Scarp/Graben System

The fault scarp and tilted graben at Kaysville, Utah (Fig. 3.24), on the Wasatch fault zone were subjected to a simple geometric analysis by McCalpin *et al.* (1994). The vertical displacement in individual paleoseismic events cannot usually be measured directly, because no correlative interfaulting strata are preserved on both sides of the main fault. We can estimate T_m (throw on the main fault plane, as approximated by free face height) for paleoearthquakes by multiplying maximum colluvial thickness by an appropriate factor (Table 3-6, columns 2 and 3). The eastward tilt of the graben during the last four paleoearthquakes is estimated from angular unconformities in the graben fill (Fig. 3.24). These tilts have acted over an estimated horizontal distance of 33 m (W in Fig. 3.10), allowing calculation of T_t via Eq.(3.4). Throw on the main antithetic fault (T_a; beyond the western end of the trench) was measured by Swan and others (1980) at 2.2 m, based on stratigraphic separations of graben-fill units. Using Eq. (3.4) and values for T_m, one can estimate the net throw (T_{net}) for each of the last three surface-rupturing events (Table 3-6). The main sources of uncertainty in this particular analysis are (1) whether all

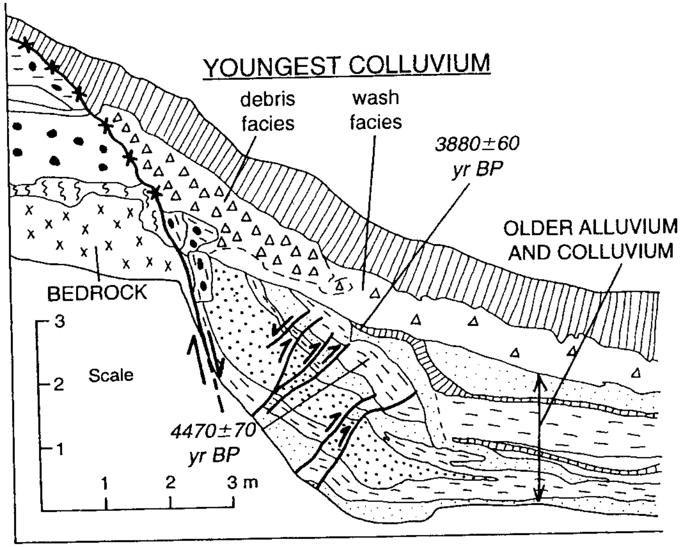

Figure 3.26 Log of trench showing an angular unconformity produced by forward tilt. Vertical line pattern indicates organic soils. Heavy lines show faults, heavy line with ×'s shows the buried scarp free face. At lower center, older scarp-derived colluvium (heavy dots) and interfingering alluvium (fine dots and horizontal dashes) have been tilted up to 55° by drag on the main fault plane accompanying the younger faulting event. Forward-tilting caused by fault drag (?) induced several imbricate reverse faults in the older alluvium and colluvium, but these faults are secondary features to the main normal fault plane (*at left*) and do not indicate a regional compressive stress. Following faulting, the youngest scarp-derived colluvium was deposited atop the tilted beds, creating an angular unconformity. Cook Canyon trench, Rock Creek fault, Wyoming (McCalpin and Warren, 1992).

of T_a (2.2 m) occurred in the latest event, or was partitioned between the two latest events, and (2) what is the appropriate factor (≥ 2) by which to multiply colluvial wedge thickness to estimate T_m.

3.3.2.5 Deposition against Upslope-Facing Scarps

The colluvial wedge model assumes that fault scarps face downslope, and that local geomorphic transport is from the upthrown to downthrown block. A reversal of this process occurs where fault scarps face upslope, especially across drainages [these same comments should apply to *antislope scarps* ("*sackung*") described in Chapter 8]. *Upslope-facing scarps* act as dams to downslope (or downstream) transport, and the deposition of colluvial or alluvial deposits against the scarp may be much more important (volumetrically) than scarp-derived colluvium. Scarps that dam streams may create temporary lacustrine conditions, or at least cause aggradation of floodplain sediments upstream of the fault scarp. Scarp-derived colluvium may not be a volumetrically significant facies in such situations (Pantosti *et al.*, 1993). The aggradation upstream from the scarp often creates a distinctive triangular-shaped alluvial flat.

Table 3-6

Fault Displacement at the Kaysville, Utah, Trench Site[a]

Parameter measured	Faulting event	Maximum colluvial thickness	Vertical displacements (m) Main fault[b] (T_m)	Tilt[c] (T_t)	Antithetic faults	T_{net}[d](m)
Displacement per faulting event	5	1.3	3.5	0 or 1.2	1.7-1.9	
	4	2.4	4.8	1.4	1.1 or 0	2.3-3.4
	3	2.3	4.6	3.2	0	1.4

[a] From McCalpin *et al.* (1994).

[b] Estimated as twice the maximum colluvial thickness for events 3 and 4; as three times the maximum colluvial thickness for event 5.

[c] $T_t = W \sin \phi$.

[d] $T_{\text{net}} = T_m - [T_t + T_a]$

3.4 DATING PALEOEARTHQUAKES

Paleoearthquakes can be dated directly or indirectly. The most *direct techniques* are dating a fault scarp via scarp degradation modeling or by quantitative analysis of scarp soils. Although these techniques directly date the formation of coseismic scarps, age uncertainties are relatively large. *Indirect dating* methods involve bracketing the age of the paleoearthquake by numerical dating of landforms or deposits that predate and postdate faulting. The accuracy and precision of numerical dating may be high, but the ages themselves may not provide close constraints on the age of faulting. Reviews of Quaternary numerical dating methods were cited in Chapter 1 and are not repeated here. This section emphasizes where to collect samples to most tightly constrain the age of faulting, given the occurrence of datable materials. Because radiocarbon dating is by far the most common technique for dating normal fault paleoearthquakes, our examples are generally couched in terms of distribution of organic matter. The reader should consult primary references to see how sampling might differ for other techniques, such as thermoluminescence (Forman *et al.*, 1989, 1991; McCalpin and Forman, 1991; McCalpin *et al.*, 1994) or uranium-series disequilibrium (Peterson *et al.*, 1995).

3.4.1 Direct Dating via Scarp Degradation Modeling

Two kinds of techniques based on degradational processes have been used to date fault scarps. The first is the *diffusion dating technique,* which assumes that the symmetrical erosion and deposition occurring in Wallace's wash-dominated stage (stage E in Fig. 3.11) can be mathematically simulated by a diffusion-type equation wherein

$$\frac{dY}{dt} = K\frac{d^2Y}{dX^2}, \tag{3.5}$$

where:

Y = elevation of points of the surface of the fault scarp
X = horizontal position of points on the fault scarp surface
t = time
K = diffusion constant.

The diffusion approach makes two assumptions about the erosional modification of fault scarps: (1) that the rate of sediment transport is limited only by the strength of the transporting process, and not by the availability of transportable material (i.e., the slope is *transport limited;* Selby, 1993), and (2) that the rate of sediment transport is only a function of scarp slope, and not of position on the scarp. The latter assumption requires that any scarps modeled must have degraded mainly by *creep* and *rainsplash,* rather than by wash processes (*sheetwash, rillwash*) which increase in strength downslope. Scarps that do not meet these criteria (e.g., bedrock scarps that are *supply limited,* scarps eroded by running water) should not be dated via the diffusion equation. (Note that the initial gravity- and debris-controlled stages [Figs. 3.11A-C] cannot be modeled by diffusion, so the time required for them (30 to 200 yr?; Sec. 3.2.4) should be added to the diffusion-based estimate of scarp age). Computer programs (Nash, 1980) and nomographs (Andrews and Bucknam, 1987) based on the diffusion equation yield values of tK for measured fault scarp profiles. Despite early successes in applying this technique to scarps of known age, later work has revealed that the *diffusion constant* (K) is very sensitive to climate, aspect, scarp height (Pierce and Colman, 1986) and grain size (McCalpin, 1983). With the uncertainty in K values induced by the factors listed above, values of tK thus calculated include some uncertainty.

Diffusion analysis of fluvial scarps of known age near fault scarps can yield a local estimate of K, which can then be divided into the product tK to yield fault scarp age (Begin, 1993; *Enzel et al.,* 1994). Optimally, the fluvial scarps from which K is derived should possess the same orientation, height, parent material, and vegetation as the fault scarps to be dated. Fluvial scarps (terrace risers) in New Zealand studied by McCalpin (1989a) were asymmetrical, with the lower half of the scarp yielding a smaller product tK than the upper half. These terrace risers were evidently cut incrementally over hundreds or thousand of years, with the toe of the riser being periodically rejuvenated.

McCalpin (1989c) thus suggested that while K may be constant on the riser, tK of the upper half of the riser approximately dates abandonment of the upper terrace, and tK of the lower half of the riser similarly dates the abandonment of the lower terrace (as suggested by Knuepfer, 1988; see Sec. 6.2.1.1). If the ages of the upper and lower terraces are known, K can be estimated and then applied to dating of nearby fault scarps.

Machette (1989) suggests that, at present, there are two relatively straightforward methods for calculating fault scarp age. The first is a comparison of scarp heights and maximum scarp slope angles to *empirical regressions* of those two variables from dated scarps, using the graph of Bucknam and Anderson (1979). The second is a calculation of scarp age based on the linear-plus-cubic diffusion model of Andrews and Bucknam (1987), wherein:

$$t = t'\ (\mathrm{SO})^2/K_0, \tag{3.6}$$

where:

t = age of scarp (years)
t' = dimensionless scarp age
SO = vertical surface offset across scarp
K_0 = diffusion constant (mass diffusivity) at 0° fan slope.

Values for t' are derived from Table 3-7, which relates maximum scarp slope angle (Θ) to the ambient (far-field) angle of the faulted slope (α). The calibrated interval marked on Table 3-7 indicates the range of data derived from independently dated scarps. Values for K_o have been back-calculated from these dated scarps in the Basin and Range Province, USA, and range from 0.46 to 0.52 m^2/1000 yr.

This linear-plus-cubic diffusion model is extremely sensitive to small changes in α and Θ, and should not be used if $\alpha \geq 10°$, or if $\Theta - \alpha < 10°$ (Hanks and Andrews, 1989). For example, scarps degrade much faster on steeper slopes and the runoff process (not modeled in the diffusion approach) becomes significant. The model should only be applied to single-event fault scarps, because only for those scarps can the prefaulting geometry be estimated with any certainty. (However, Hanks and Schwartz [1987] did use the diffusion technique to date the penultimate faulting event at the 1983 Borah Peak rupture by restoring the scarp to its inferred geometry before the 1983 faulting event.) If a multiple-event fault scarp is profiled, diffusion dating will yield a scarp age older than that of the most recent faulting event (Machette and McGimsey, 1983; Mayer, 1984; Colman, 1986).

Table 3-8 shows an example calculation using Eq. (3.6) and Table 3-7. Almost all of the uncertainty in the age estimate in Table 3-8 (1309 yr) is caused by the inability to measure slope angles in natural terrain closer than ±1°. By comparison, the uncertainties in scarp surface offset and diffusion constant, while seemingly quite large, contribute only a small amount of

Table 3.7

Dimensionless Age Values (t') for Scarp Subject to Linear-Plus-Cubic Diffusion Model and Initial Scarp Slope Angle of 31°

Scarp Angle (θ)	Ambient Angle (α)									
	0°	1°	2°	3°	4°	5°	6°	7°	8°	9°
31°	0	0	0	0	0	0	0	0	0	0
30°	0.017	0.019	0.020	0.021	0.023	0.025	0.027	0.029	0.032	0.034
29°	0.026	0.028	0.030	0.032	0.035	0.037	0.041	0.044	0.049	0.053
28°	0.035	0.038	0.041	0.044	0.048	0.052	0.056	0.062	0.068	0.075
27°	0.046	0.049	0.053	0.057	0.062	0.068	0.074	0.082	0.090	0.100
26°	0.058	0.062	0.067	0.073	0.080	0.087	0.096	0.160	0.118	0.132
25°	0.072	0.078	0.085	0.092	0.101	0.111	0.122	0.136	0.152	0.171
24°	0.089	0.096	0.105	0.115	0.126	0.139	0.155	0.173	0.194	0.220
23°	0.109	0.118	0.130	0.142	0.157	0.175	0.195	0.219	0.248	0.283
22°	0.132	0.145	0.159	0.176	0.196	0.218	0.245	0.277	0.317	0.365
21°	0.161	0.177	0.196	0.218	0.243	0.273	0.309	0.352	0.406	0.474
20°	0.196	0.217	0.241	0.269	0.302	0.342	0.390	0.450	0.525	0.621
19°	0.239	0.265	0.296	0.333	0.377	0.430	0.497	0.580	0.685	0.824
18°	0.291	0.325	0.365	0.414	0.473	0.546	0.637	0.754	0.907	1.11
17°	0.355	0.400	0.453	0.518	0.598	0.699	0.827	0.994	1.22	1.53
16°	0.435	0.494	0.565	0.653	0.764	0.904	1.09	1.33	1.68	2.17
15°	0.537	0.615	0.711	0.832	0.986	1.19	1.45	1.83	2.37	3.21
14°	0.666	0.771	0.902	1.07	1.29	1.58	1.99	2.59	3.50	4.99
13°	0.832	0.976	1.16	1.40	1.72	2.16	2.81	3.80	5.43	8.43
12°	1.05	1.25	1.51	1.85	2.34	3.04	4.12	5.89	9.15	16.2
11°	1.34	1.62	1.99	2.52	3.28	4.45	6.36	9.90	17.5	39.1
10°	1.73	2.14	2.70	3.52	4.79	6.85	10.7	18.9	42.3	
9°	2.27	2.88	3.77	5.12	7.34	11.5	20.3	45.5		
8°	3.06	4.00	5.45	7.83	12.2	21.7	48.7			
7°	4.23	5.77	8.29	13.0	23.1	51.8				
6°	6.06	8.73	13.7	24.4	54.8					
5°	9.12	14.3	25.6	57.6						
4°	14.9	26.6	60.0							
3°	27.4	61.9								
2°	63.4									

Calibrated Interval

Table 3-8

Example Calculation of Fault Scarp Age, Based on Eq. 3.7

Given: scarp surface offset = 3.3 ± 0.2 m; far-field slope = 3 ± 1°; maximum scarp slope angle = 19 ± 1°

From Table 3-7, $t' = 0.357 \pm 0.116$ (see boxed area in Table 3-7).

From Eq. 3.6, $t = 0.357 \pm 0.116\ (3.3 \pm 0.2\ \text{m})^2 / (0.49 \pm 0.03\ \text{m}^2/1000\ \text{yr})$.

Applying the multiplication and division rules for values with unequal standard deviations (Geyh and Schleicher, 1990)

$t^* = (t_1 \times t_2)/\, t_{\pm}\, t^* \sqrt{(\sigma_{t1}{}^2/t_1{}^2) + (\sigma_{t2}{}^2/t_2{}^2) + (\sigma_{t3}{}^2/t_3{}^2)}$

$t = 3.888\ \text{ka}/0.49 \pm 3.888\ \text{ka}\ \sqrt{0.106 + 0.0037 + 0.0037}$

$= 7.935 \pm 1.309$ ka, or 7935 ± 1309 yr

uncertainty in age estimate. To minimize the uncertainty in the final age estimate, efforts should be made to minimize the uncertainties in field slope measurements by making multiple traverses along a given fault scarp, and averaging the results. Due to the variability in natural terrain, however, and errors arising from the scarp profiling techniques (Chapter 2), some uncertainty will always be attached to field slope measurements.

A second technique for directly dating fault scarps uses the decrease in material *cohesion* on the scarp face through time (due to weathering and soil formation) to estimate scarp age (Ingraham *et al.*, 1980; Watters and Prokop, 1990). The cohesion of material exposed in the post-1872 free face of the Lone Pine, California, USA, fault scarp, is greater than the cohesion of material on the bevels of the post-5000-yr and post-10,000-yr scarps. By fitting polynomial equations through cohesion values from different-aged scarps, Watters and Prokop (1990) interpolated the age of an undated scarp from its "parent" and "field" cohesion values. This technique is experimental, and has not been applied over a wide range of faulted parent materials or climate zones.

3.4.2 Age Estimates from Soil Development on Fault Scarps

Soil profiles thin, thicken, change character, and merge across normal fault scarps, and these soil-topographic variations (*catenas*) hold clues to the temporal evolution of the scarp (Berry, 1990; McCalpin and Berry, 1996). Observations in numerous trenches show that four soil variations are common (Fig. 3.27): (1) The relict summit soil is *truncated by erosion* at the scarp crest; (2) the relict toeslope soil *weakens laterally* as it is traced beneath the colluvial wedge sequence, where it forms the prefaulting soil; (3) soil(s) developed on postfaulting colluvium *merge downslope* with the prefaulting soil, to become the toeslope relict soil; and (4) individual horizons *thin* as they pass over the scarp crest *and then thicken* on the colluvial slope, due to increased infiltration,

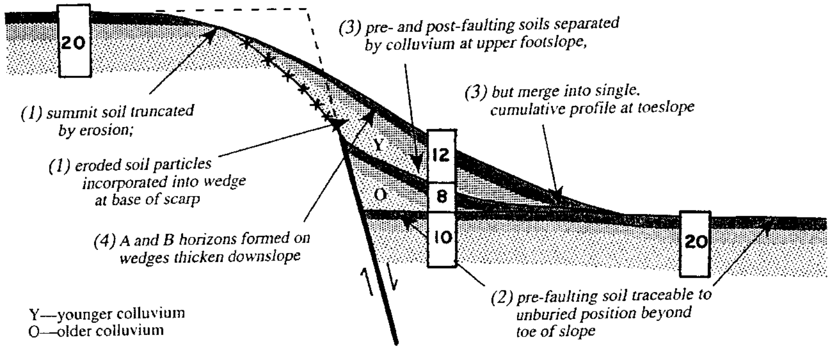

Figure 3.27 Diagram of soil catena relations on a two-event normal fault scarp, showing the four phenomena listed in the text (numbers before phrases). From darkest to lightest, shading represents A, B, and C horizons. Numbers in rectangles are hypothetical profile development index (PDI) values for soils, based on a trench across a faulted 15-ka deposit on the Wasatch fault zone, Utah. The sum of PDI values for the footslope soils (30) is 1.5 times that for the relict summit and toeslope soils (20) due to increased moisture availability and influx of fines on the footslope. Note that the relict soil beyond the toeslope weakens laterally, and is only half as developed beneath the colluvial wedges. If soil formation rates are linear, this implies that initial faulting occurred at about 7.5 ka. Soils on the colluvial wedges suggest that 8/20 of the subsequent geologic time (40% of 7.5 ky = 3 ky) elapsed between the first and second faulting events, and 12/20 of the time (60% of 7.5 ky = 4.5 ky) has elapsed since the second faulting event. [From McCalpin and Berry, (1996); reprinted with permission of Elsevier Publishing Company B.V.]

moisture-holding capacity, and simultaneous deposition and soil formation (*cumulic development*).

The relative soil profile development between the summit and toeslope (relict) soils, the buried prefaulting soil, and the colluvial soils provide a first approximation for faulting history. For example, if faulting occurred soon after stabilization of the displaced landform, then almost all soil formation postdates formation of the fault scarp, so (1) the relict toeslope soil will weaken when traced under the colluvial wedge, until there is no soil at all under the earliest part of the colluvial wedge; (2) soil(s) in colluvium will be very well developed, and will merge gradually with soils above and below the scarp; and (3) the summit soil will show little or no erosional truncation at the scarp crest, since the soil mainly formed *after* the scarp attained its present geometry. Alternatively, if faulting occurred long after stabilization of the landform, then almost all soil formation predates scarp formation, so (1) the buried soil under the colluvial wedge will be nearly as well developed as the full, relict soils above and below the scarp, and "lateral weakening" will be minimal; (2) soil(s) in the colluvium will be weak to very weak; and (3) the summit soil will be strongly truncated at the scarp crest. The two scenarios above represent end-members of faulting chronology, which can be further complicated by recurrent faulting at irregular intervals.

A simple *continuity approach* can yield ratios of soil development times among the various soils, and thus allow estimates of the age(s) of faulting events. This continuity approach requires quantitative measurements for the development of relict and footslope soils, either semiquantitative [such as the *profile development index* (PDI) of Harden, 1982] or quantitative (weight of pedogenic clay or carbonate in the profile, e.g., Machette, 1978). Three assumptions are required for this type of analysis: (1) Soil development rates have been constant over time, (2) soil development rates at all times have been greater on the footslope than above or below the scarp, and (3) the cumulative time for soil formation is the same for the superposed soils under the colluvial footslope as for the stable summit or toeslope soils. If these assumptions are valid, then the development index of the relict soils above and below the scarp should equal the combined development indices of all soils under the colluvial footslope, once those latter indices have been *normalized* to account for their faster development rate due to topographic position. In relation to Fig. 3.27, the continuity equation would read:

$$\mathrm{PDI}_r = \mathrm{PDI}_{pf} + F(\mathrm{PDI}_Y + \mathrm{PDI}_O), \tag{3.7}$$

where

PDI_r = profile development index of *relict* soils above and/or below the scarp, =20 in example

PDI_{pf} = profile development index of the buried *prefaulting* soil under the footslope, =10 in example

PDI_Y, PDI_O = profile development indices of younger (Y) and older (O) footslope soils developed on postfaulting colluvium, = 8, 12 in example.

F = footslope correction factor.

Using the hypothetical values in Fig. 3.27, we may solve Eq. (3.7) for F, resulting in F=0.5. In other words, soils on stable geomorphic surfaces such as the summit soil only develop 50% as fast as do footslope soils. We can normalize footslope PDIs to "summit" development rates by multiplying by 0.5, yielding the following PDI values for Eq. (3.7): 20 = 10 + 4 + 6. Both sides of the equation represent 15 ka, so the time represented by soils Y, O, and pf must be approximately 7.5, 3, and 4.5 ka, respectively.

If the results of the continuity equation are not compatible with independent age evidence for the faulting events, the cause is most likely variable rates of soil development through time (McCalpin and Berry, 1996).

3.4.3 Bracketing the Age of Faulting by Dating Geomorphic Surfaces

In reconnaissance investigations, the age of scarp-producing paleoearthquakes is typically bracketed between the ages of the youngest faulted and oldest unfaulted geomorphic surfaces. Figure 3.28 shows a zone of normal fault scarps which have complex relations with fluvioglacial outwash fans dated at 0 to 10 ka (Hf), 15 to 30 ka (Pf), ca. 150 ka (Bf), and ≥250 ka (pBf). Scarp A displaces Bf but is truncated by Hf and Pf channels, so it must have formed between 150 ka and 15 to 30 ka. Scarp B displaces only Bf, so it can be dated only as younger than 150 ka (i.e., it could be much younger, even younger than scarp A). Most of the scarps between C and D displace Bf but not Pf surfaces, but some scarps (such as D) displace both Bf and Pf surfaces, indicating movement younger than 15 to 30 ka. Scarp E bounds isolated remnants of pBf and displaces Bf and Pf, suggesting a long history of movement continuing to less than 15 to 30 ka. Scarp F offsets pBf but not Bf, indicating latest movement before 150 ka.

The temporal resolution of dating paleoevents with bracketing geomorphic surfaces is controlled by the age span between the surfaces. In the example described above, knowing that a faulting event occurred between 150 and 15 to 30 ka may not be very helpful. Where geomorphic surfaces are created rapidly, resolution is better. In New Zealand, for example, it is common to find 5 to 10 Holocene stream terraces incised at various levels below the latest Pleistocene aggradation surfaces (e.g., Lensen, 1968; Knuepfer, 1988, 1992). These terraces, formed only a few thousand years apart (see Fig. 2.1), can record fault displacements with better resolution than deposits formed by major climatic changes some 10s or 100s of ka apart.

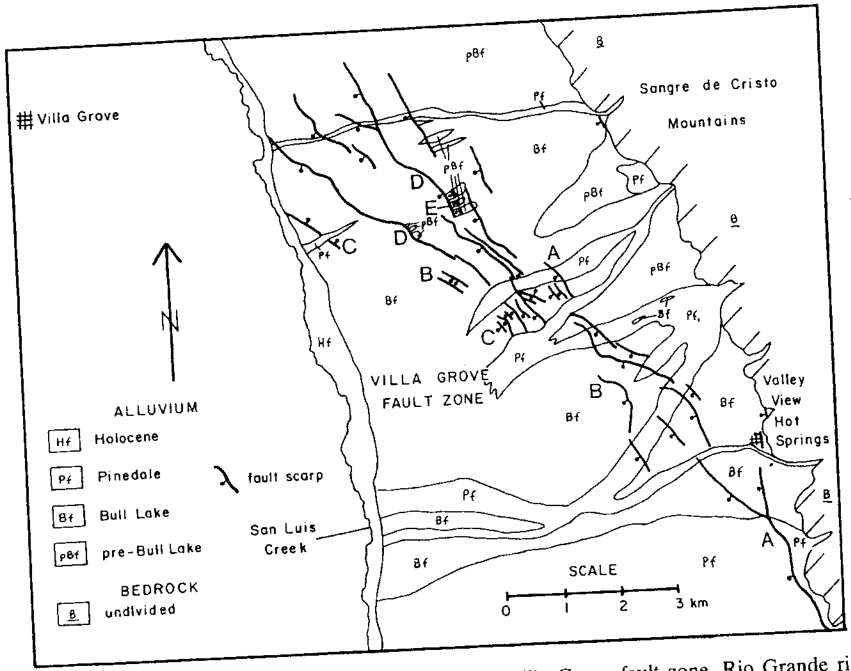

Figure 3.28 Map of fault scarps of various ages, Villa Grove fault zone, Rio Grande rift zone, USA. Based on cross-cutting relationships, the scarps formed over different time intervals; some scarps show a long history of recurrent movement, others appear to be single-event scarps. Ages of scarps: type A, post-Pinedale; B, post-Bull Lake; C, pre-Pinedale, post-Bull Lake; D, post-Pinedale, long history of movement; E, pre-Bull Lake. [From McCalpin (1983); reprinted with permission of the Colorado School of Mines Press.]

3.4.4 Bracketing the Age of Faulting by Dating Displaced Deposits

Similar relative-dating criteria apply for subsurface exposures as for geomorphic surfaces; faulting is younger than the stratigraphically highest faulted bed, and older than the stratigraphically lowest unfaulted bed. Figure 3.29 shows a late Pleistocene deltaic deposit displaced by a series of normal faults that define a 30-m-wide graben. The faults displace units 1, 2, and 3 and are truncated by units 4, 5, and 6. The faulting thus occurred between deposition of units 3 and 4. Further proof of this contention is the different geometry of the faulted versus unfaulted units. Units 1, 2, and 3 are laterally extensive and maintain a constant thickness across the fault zone, suggesting they were deposited before any tectonic relief existed. In contrast, units 4, 5, and 6 are restricted to channels that parallel graben faults, and were probably deposited by streams diverted into the graben axis after faulting. In this example from the Bonneville Basin, the entire delta was deposited (according to the regional ^{14}C chronology; Oviatt *et al.*, 1992) between about 14.5 and 13 ka, with the topset beds (unit 7) being formed about 13.0 to 13.5 ka. Faulting must have occurred slightly before abandonment of the delta, while active channels still

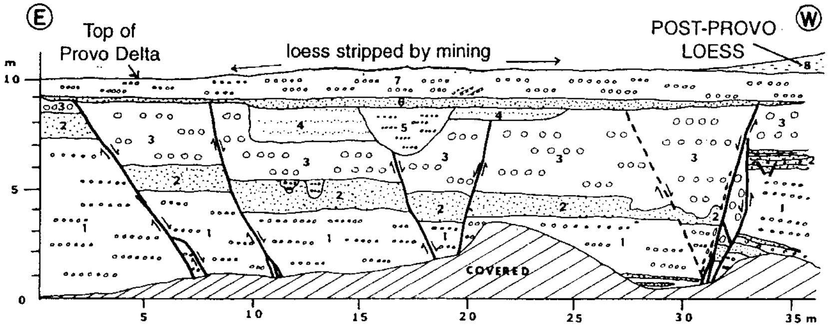

Figure 3.29 Wall of a gravel pit showing truncated normal faults. Because the ages of units 1 and 8 are approximately known from regional 14C chronology, the age of faulting can be roughly bracketed. [From McCalpin and Forman (1991); reprinted with permission of the Seismological Society of America.]

traversed the delta top, but after the bulk of the delta had already formed. Dated strata thus suggest the faulting occurred ca. 13.5 ka.

3.4.5 Bracketing the Age of Faulting by Dating Colluvial Wedges

Many faulting chronologies have been reconstructed from numerical ages on colluvial wedge sediments and on the soil horizons that underlie and overlie the wedge. The choice of dating method and sampling strategy are dictated by the characteristics of sediments and soils in the fault zone. For example, past studies in the eastern Basin and Range Province, USA, have used radiocarbon dating ("conventional" gas-proportional counting and accelerator mass spectrometry, or AMS) and/or luminescence dating [thermoluminescence (TL) and optically stimulated luminescence (OSL)] (Forman *et al.*, 1989, 1991; McCalpin and Forman, 1991; Jackson, 1991; Lund *et al.*, 1991; Personius, 1991; Machette *et al.*, 1992a,b; McCalpin, 1994; McCalpin *et al.*, 1994; West, 1994). In hyper-arid environments where organic carbon is rare, soil precipitates (calcium carbonate, silica) may be dated via uranium-series disequilibrium, TL, and cosmogenic isotopes such as ^{36}Cl. A recent development is AMS ^{14}C dating of microscopic organic material in layers of rock varnish (Paces *et al.*, 1994; Peterson *et al.*, 1995).

Fault-zone exposures in semi-arid regions typically contain *low-organic-content* soils, and bulk samples that span a considerable age range must be collected. In the studies cited earlier, soil A horizons containing ≤5% organic matter required large (1- to 5-kg) samples to yield sufficient carbon for conventional radiocarbon dating. Radiocarbon ages from such bulk samples are termed *apparent mean residence time* (AMRT) ages (see Appendix 2). Machette *et al.* (1992a, his Appendix) discuss application of AMRT ages to faulting chronologies.

Figure 3.30 shows typical age sampling locations in a normal fault exposure and how sample ages constrain the age of the event horizon, that is, the unconformity between scarp-derived colluvium (units 1D, 1W, 2D, 2W) or graben sediments (units 1S, 1.5S, 2S) and the prefaulting soil (sinuous vertical lines). The ages of the two faulting events are most closely bracketed by samples 2 and 3, and 8 and 9, respectively in Fig. 3.30. The age of the event horizon decreases away from the fault due to time-transgressive burial of the soil by laterally accreting scarp-derived colluvium. Thus, samples 4 and 5 provide less close limiting ages on faulting than does sample 3. Scarp-derived colluvium is deposited rapidly (ca. 30 to 200 yr for debris facies, units 1D, 2D), whereas graben sediments may accumulate slowly.

To achieve the closest age constraints, the age of the event horizon (upper soil horizon contact, or UHC) may be extrapolated from the age of several subsamples of the buried soil horizon (Fig. 3.31). The A horizons are buried by proximal, coarse-grained, debris-facies colluvium in the western United States (under semi-arid climates and scrub vegetation) and display mean age trends with depth of 4.6 ± 1.3 yr/mm (McCalpin and Nishenko, 1996), and this age trend can be used to extrapolate the age of the UHC from 5- to 10-cm-thick soil samples, as shown diagrammatically in Fig. 3.31. Age trend with depth is established by dating 1- to 2-cm-thick subsamples (Fig. 3.31C). Each of the subsamples, in turn, yields an AMRT age affected by carbon compounds of various ages and molecular weights. The extrapolated age of the UHC contains uncertainties arising from analytical errors on the soil AMRT age and MRT-correction errors arising from the extrapolation procedure itself (spread between the intercepts from the minimum and maximum age trends with depth, Fig. 3.31D).

Preferred samples for ^{14}C dating have short age spans (charcoal, wood, peat, shells). If low-organic soils are sampled, one should collect material over the smallest vertical stratigraphic thickness practical. This may involve exposing a large (>1 m^2) surface of the sampled stratum and scraping off a

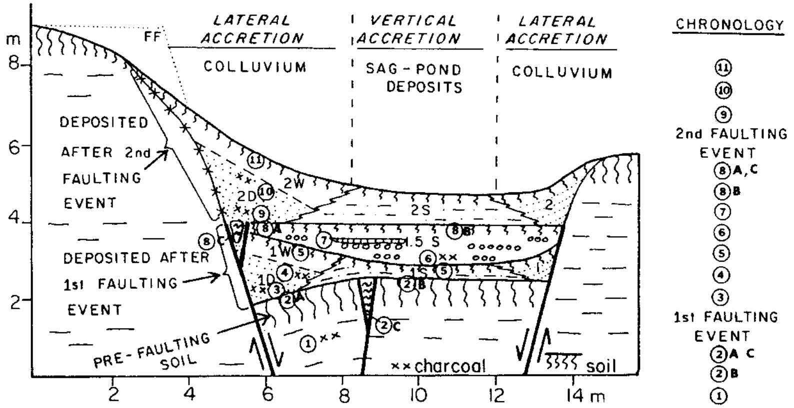

Figure 3.30 Schematic cross section through a normal fault scarp and graben formed by two surface-faulting events; this is a composite section showing features observed in many trenches across the Wasatch fault zone, Utah. Colluvium shed from the main scarp (at left) is divided into debris facies (D) and wash facies (W); both facies grade into coeval sag-pond deposits (1S, 2S). Between faulting events a fluvial deposit (1.5S), containing lenses of gravel (circles), completely filled the graben. Circled numbers indicate potential sites for obtaining radiocarbon samples, and the chronology at right shows which samples most closely constrain the times of the faulting events. Debris facies colluvium is deposited immediately after faulting, whereas sag-pond deposition may be climatically controlled and postdate faulting by decades. Radiocarbon dates from sites 2A and 8A have traditionally been interpreted as the closest maximum limiting ages on faulting, as shown on the chronology at right. However, if radiocarbon ages from soils 2 and 8 are MRT-corrected to reflect the age of soil burial, they become minimum age constraints on faulting, with the closest constraint closest to the fault. Samples from wash facies colluvium (5, 11) and interbedded fluvial deposits (6, 7) do not provide close age constraints on faulting. [From McCalpin and Nishenko (1996); reprinted with permission of the American Geophysical Union.]

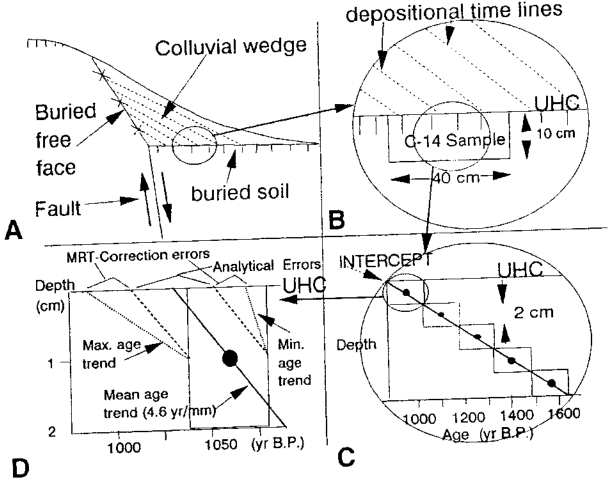

Figure 3.31 Idealized diagrams of a single-event normal fault scarp showing various sources of uncertainty in relating numerical ages to the time of paleoearthquakes. (A) Simplified cross section of the colluvial wedge. Dashed lines show depositional time lines in colluvium. (B) Close-up view of a typical radiocarbon sample, emphasizing the time-transgressive nature of the event horizon [i.e., burial of the upper horizon contact (UHC) of the soil]. (C) Close-up of the 10-cm-thick radiocarbon sample, showing the trend of increasing age with depth and the principle of extrapolating the age of the UHC. (D) Close-up of how age uncertainties are calculated for the event horizon (UHC) immediately above the dated sample. Solid circle shows mean radiocarbon age; surrounding box shows dendro-corrected radiocarbon age, with 2σ limits shown by the horizontal dimension of the box. The vertical dimension of the box indicates sample thickness. The solid line shows a least-squares regression line through the dendro-corrected mean age. The top of the graph represents the UHC of the soil. The total 2σ error range on age of the UHC is composed of an analytical component and a MRT-correction (extrapolation) component. The analytical component is defined by extrapolations of the mean age trend (4.6 yr/mm) from the $\pm 2\sigma$ limits on the age of the uppermost 10-cm-thick sample (dashed lines). The MRT-correction components are defined by extrapolations of the maximum age trend (6.7 yr/mm) from the -2σ age limit and the minimum age trend (3.7 yr/mm) from the $+2\sigma$ age limit (dotted lines).

few millimaters of stratigraphic thickness, usually from the top of the soil horizon if this UHC defines the event horizon. Optimal sample weights and pretreatments are described in Appendix 2.

3.4.5.1 *Example of Detailed Dating*

An exposure of three colluvial wedges and associated soils on the Wasatch fault zone, USA, was closely sampled to examine radiocarbon age variation with depth and organic component, as well as correspondence with TL ages. The radiocarbon ages from an initial set of 10- to 15-cm-thick bulk samples (Fig. 3.32, boxes with crosses), can be compared to a later set of 2- to 3-cm-thick decalcified samples (×'s) dated by AMS. Additional radiocarbon ages on the humic acid and humin fractions of all 12 samples are reported by Stafford and Forman (1993). They found, paradoxically, that the decalcified soil fraction usually dated oldest and the humin fraction youngest for each sample, whereas the reverse is usually true.

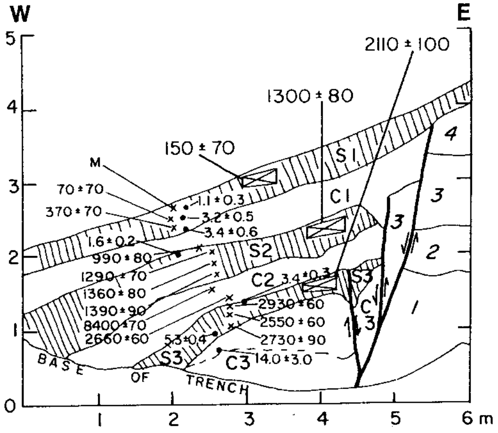

Figure 3.32 Log of trench at Garner Canyon, Wasatch fault zone, USA, showing radiocarbon and TL ages. Large boxes with crosses show correct dimensions of initial bulk radiocarbon samples dated by Machette *et al.* (1992a); ages in large numbers are in ^{14}C yr B.P. Small ×'s show ages in ^{14}C yr B.P. of decalcified soils; M = modern (<200 yr B.P.). Solid circles show TL sample locations and total bleach age estimates (ka). Dimensions of ×'s and solid circles correctly represent sample dimensions. Soil A horizons S1, S2, and S3 are developed on stony colluvial deposits C1, C2, and C3, respectively. Units 1-4 on the upthrown block are gravelly alluvium. The apparent reversal of radiocarbon ages within soil S3 is anomalous and does not occur in the other carbon fractions. [Modified from Stafford and Forman (1993).]

For each organic fraction in the A horizons, the trend of increasing age with depth allows extrapolation of the age of the UHC (as in Fig. 3.31C). Sufficient carbon for AMS dating was even found in the relatively inorganic colluvial deposits themselves (e.g., C2, Fig. 3.32). Age reversals and large disparities occur between the ages of different organic fractions, and indicate that the milligram-size particles of organic matter dated by AMS have complex origins, including reworking of older carbon from sources upslope (e.g., the anomalous 8400 yr B.P. age in deposit C2). However, the basal radiocarbon age from deposit C2 (2660 ± 60 yr B.P.) is similar to the ages from thin samples within underlying soil S3 (2550 to 2930 yr B.P.), which indicates that some small carbon particles in colluvium accurately reflect the age of colluvium. If the age reversal at the top of soil S3 was not present, it might be possible to bracket tightly the age of faulting between the extrapolated age of the event horizon, and the 2660 ± 60 yr B.P. age of the oldest overlying colluvium. Thus, this method of AMS dating of thin samples appears to hold promise for refined dating of paleoearthquakes, compared to the previous method of bulk sampling. Ages might be refined even further with the use of Bayesian statistics, as described in Sec. 6.4.

The correspondence of TL ages with radiocarbon ages is best near the top of each soil and worsens downward. This phenomenon has been observed elsewhere (Forman *et al.,* 1989, 1991) and suggests that the dated silt particles contain a higher amount of inherited TL with depth in soil horizons. Light exposure of silt particles, which erases inherited TL, should increase upward in a soil due to slower deposition rates, bioturbation and pedoturbation. For example, TL total bleach ages are only 600 and 470 years older, respectively, than radiocarbon ages at the tops of soils S2 and S3, but become much older with depth (Fig. 3.32). Similar very old TL ages were observed at the Borah Peak, Idaho fault scarp, where proximal colluvium deposited at the base of the free face in 1983 and sampled in 1985 (true age 2 years) yielded a total bleach TL age of 40 ± 4 ka (McCalpin and Forman, 1988). By comparison, the alluvial fan gravels composing the scarp free face had an estimated age of ca. 15 ka. The 40-ka apparent TL age of colluvium indicates that the dated silt grains not only escaped exposure to light during colluvial redeposition, but they must have already possessed a large (ca. 25 ka) inherited TL component when deposited at 15 ka in the alluvial fan deposits.

Chapter 4

Paleoseismology of Volcanic Environments

William R. Hackett
Suzette M. Jackson
Richard P. Smith

4.1 INTRODUCTION

Faults, tensile cracks, and related extensional features can develop solely as a consequence of magma intrusion, and magma-induced surface faults with co-intrusive displacements of several meters can form aseismically or be accompanied only by shallow, low-magnitude earthquake swarms. *Magma-induced extensional structures* may thus be misinterpreted as coseismic tectonic features (such as those described in Chapter 3), and their seismic potential thereby exaggerated. Special problems exist for paleoseismology in volcano-extensional environments. If traditional methods of assessing slip rates and maximum magnitude are applied without considering the volcanic record or the mechanics of magma intrusion, then the estimated frequencies and magnitudes of paleoseismic events may be erroneous.

Seismicity, surface faulting, magma intrusion and volcanism are expressed within most tectonic settings, and extension of the brittle crust is globally accommodated by a combination of normal faulting and magmatic processes. The relative significance of these processes varies widely from region to region, is dictated by the balance of magma flux relative to regional-extension rates, and has major implications for the pattern and intensity of world seismicity (Parsons and Thompson, 1991). On a worldwide scale, the pattern of earthquakes coincides very closely with that of active volcanoes, and together these reveal the pattern of lithospheric plates. One of the most fundamental of all earth processes, the accretion of new lithosphere along the midocean ridge system, occurs through a complex interplay of tectonic and magmatic extension (Bergman and Solomon, 1990; Kong *et al.,* 1992). In addition to its acknowledged role in the formation of ocean crust, there is growing recognition that synextensional magmatism is an ubiquitous characteristic of highly extended continental terrains (Eaton, 1982; Coney, 1987; Lipman and Glazner, 1991; Parsons and Thompson, 1991; 1993; Harry *et al.,* 1993). For example, in the western Cordillera of the United States, significant flux of mantle-derived magmas into the crust is required in order to explain regional geologic and geophysical observations, and mass-balance calculations indicate that approximately 5 km of the present crustal thickness was added to the crust of the eastern Great Basin during Cenozoic extension and magmatism (Gans, 1987; Glazner and Ussler, 1989).

It has long been known that the intrusion of magma produces earthquakes. *Magma-induced seismicity* commonly exhibits spatial migration, focal mechanisms, and waveform characteristics that differ from those of nonvolcanic sources. The ascent of magma beneath central volcanoes and the lateral injection of dikes beneath volcanic-rift zones are commonly accompanied by fracturing of adjacent rocks, producing co-intrusive seismicity (Brandsdottir and Einarsson, 1979; Klein *et al.*, 1987). *Volcanic earthquakes* (B-type) are typically of low frequency (1 to 5 Hz), commonly occur without a main shock, and sometimes have non-double-couple mechanisms (Minakami, 1974; Foulger and Long, 1984; Shimozuru and Kagiyama, 1989; Foulger and Julian, 1993). These characteristics differ from those of *tectonic earthquakes,* which are commonly of high frequency, include a discrete mainshock-aftershock sequence, and have double-couple mechanisms. A third category of *volcano-tectonic earthquakes* (5 to 15 Hz) incorporates the high-frequency, "tectonic" waveforms that are commonly initiated by magma intrusion (Minakami, 1974; Power *et al.*, 1992). Volcano-tectonic earthquakes are so commonly observed that magmatic intrusion must be viewed as capable of altering stresses within large volumes of the shallow and middle crust.

The purpose of all paleoseismic analysis is to reconstruct the frequency-magnitude history of past earthquakes. Toward this goal, we develop criteria for the recognition of magma-induced, extensional structures, to alleviate their misinterpretation in the paleoseismic record as products of single, large-magnitude earthquakes. In addressing the physical and seismic aspects of magma intrusion, we emphasize *dike intrusion,* which is a widespread process within the upper crust, regardless of magma type or tectonic setting (Emerman and Marrett, 1990; McKenzie *et al.*, 1992). We use this background to describe the growth of discrete volcano-extensional faults and fissures, and the structural development of volcanic-rift zones. Our analysis is based on field observations of magma-induced deformation, the contemporary seismicity of active volcanic zones, and the results of numerical and physical modeling. We assert that volcano-seismic recurrence should be evaluated through careful mapping and geochronometry of the coseismic and postseismic volcanic materials and structures. We suggest modifications or alternatives to traditional paleoseismic methods of field excavation and geochronometry, because the material properties of volcanic rocks and the geometry of volcano-extensional structures commonly differ from those normally selected in paleoseismic investigations. We derive conservative, upper bounds for the maximum magnitudes of volcano-seismic events, using the dimensions and offsets of magma-induced faults. The observational seismicity of active volcanic regions shows that purely magma-induced earthquakes are characteristically of low to moderate magnitude.

Readers may ask why volcano-extensional structures should be included in this book, if they form aseismically or produce only small-to-moderate earthquakes that pose little threat. We can offer several reasons. First, many paleoseismological investigations are done within a regulatory context that dictates *all* seismic sources must be considered within tectonic provinces of interest. Second, magma-induced structures can be mistaken for the products of single, large earthquakes. Although we are not the first to consider volcanic zones or structures as seismic sources, we offer this chapter as an initial step toward full incorporation of magma-induced seismicity into the larger framework of paleoseismology.

4.2 VOLCANO-EXTENSIONAL STRUCTURES

Volcanoes grow as much by intrusion as by eruption (Tilling and Dvorak, 1993). Magma intrusion is accompanied by seismicity and deformation, and much of what is known about the internal workings of volcanoes derives from observational seismology and geodesy. Extensional structures are universally associated with volcanism, and range from small *tensile fissures* to major *normal faults* and *caldera-ring fractures.* Because magma intrusion and volcanism are common in extending regions, purely magma-induced structures are likely to be mingled with regional-tectonic structures. Worldwide examples shown in Fig. 4.1 and discussed in this section are not comprehensive, but are given as indicators of the fact that magmatic processes are important in the tectonics and seismicity of extending regions. The interplay between tectonic and volcano-tectonic sources can be complicated and can vary with time, especially in areas of oblique slip along hotspot tracks, or in transitional regions between strain accommodation by magmatism and normal faulting. Regional-tectonic and magma-induced structures are not always easily distinguished; in Section 4.3 we offer criteria for recognition. Bearing this caveat in mind, we schematically show in Fig. 4.2 the great variety of volcano-extensional structures that develop as a consequence of magma withdrawal, intrusion, and eruption.

4.2.1 Worldwide Examples of Volcano-Extensional Structures

An assortment of diverse tectonic settings is shown in Fig. 4.1, for which magma intrusion is known or assumed to participate in crustal extension. The eastern Snake River Plain of Idaho (Fig. 4.1A) occupies the bimodal-volcanic track of the Yellowstone hotspot (Pierce and Morgan, 1992). The region

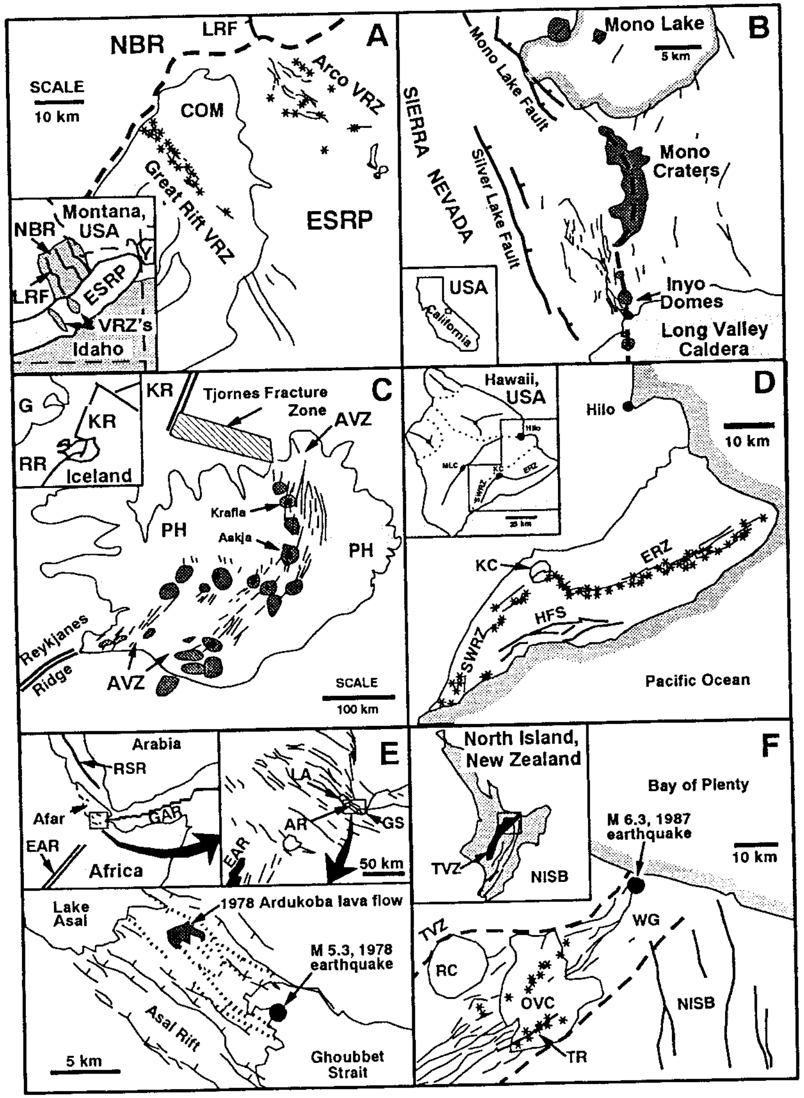

Figure 4.1 World examples of volcano-extensional regions. Symbols apply to all maps: solid lines, fissures and faults related to dike intrusion; heavy solid lines, tectonic faults; asterisk, volcanic vent; areas with stippled margin, lakes or water bodies. (A) Eastern Snake River Plain (ESRP), Idaho, USA. Adapted from Kuntz *et al.* (1988, 1990). Y, Yellowstone; COM, Craters of the Moon; NBR, northern Basin and Range; LRF, Lost River fault; VRZ, volcanic-rift zone. (B) Faults and volcanic features of the Long Valley–Mono Craters area, eastern California. Adapted from Bursik and Sieh (1989). (C) Iceland and adjacent-seafloor tectonic elements. Adapted from Rubin (1990) and Palmason (1981). RR, Reykjanes Ridge; KR, Kolbeinsey Ridge;

surrounding the eastern Snake River Plain extends by recurrent movement of seismogenic normal faults in the northern Basin and Range province. In contrast, the eastern Snake River Plain volcanic province is relatively aseismic above (local magnitude) M_L 2.0 (Jackson *et al.,* 1993) and its extension may be accommodated by dike intrusion along volcanic-rift zones (Smith *et al.,* 1989; Rodgers *et al.,* 1990; Parsons and Thompson, 1991; Smith *et al.,* 1996). The low relief and low elevation of the eastern Snake River Plain reflect the absence of major normal faulting as a mechanism of extension. This may be explained by low deviatoric stresses, as a result of magma overpressure exerted during emplacement of dikes along the volcanic-rift zones. The major products of eastern Snake River Plain magmatism are isolated rhyolite domes, subsurface basalt-dike swarms, eruptive fissures, basaltic shield volcanoes, tephra cones, lava fields, *tensile fissures, normal faults,* and *monoclines,* the latter three of which mimic tectonic structures (Kuntz *et al.,* 1992; Hackett and Smith, 1992). Although the spacing and orientation of volcanic-rift zones on the eastern Snake River Plain is similar to that of the normal faults in the northern Basin and Range, reflecting upper-crustal structure and northeast-southwest extension, the rift zones do not correlate directly with major normal faults in the surrounding Basin and Range Province. The eastern Snake River Plain is unique because it is a region where extensional magmatism has been proposed to explain the low deviatoric stresses, the relative aseismicity in comparison to the surrounding Basin and Range Province, the presence of small normal faults within the volcanic-rift zones, and the absence of large tectonic faults across the volcanic province.

In the Mono–Inyo region of eastern California (Fig. 4.1B), the movement of range-front faults of the Sierra Nevada has apparently been affected by silicic-dike injection beneath the Long Valley caldera and the Mono Craters-Inyo Domes. Bursik and Sieh (1989) suggest that Mono–Inyo dike intrusion during the past 40,000 yr has accommodated crustal extension in the region, causing cessation of movement along the adjacent Silver Lake fault. Magmatic

G, Greenland; AVZ, active volcanic zone (neovolcanic zone); PH, pre-Holocene volcanic rocks (light stipple). Central volcanoes (Krafla, Askja, and others unlabeled) indicated by dark stipple. Tjornes fracture zone is a region of transcurrent faulting. (D) Island of Hawaii, USA, and Kilauea volcano. Adapted from Peterson and Moore (1987) and Holcomb (1987). MLC, Mauna Loa caldera; KC, Kilauea caldera; ERZ, east rift zone; SWRZ, southwest rift zone; HFS, Hilina fracture system. (E) Asal rift area, Republic of Djibouti, East Africa (adapted from Stein *et al.,* 1991). EAR, East-African rift; GAR, Gulf of Aden rift; RSR, Red Sea rift; AR, Asal rift. Heavy dotted lines show fault traces activated during the 1978 episode of dike intrusion, seismicity, and volcanism. (F) North Island, New Zealand, and the Taupo volcanic zone. Adapted from Nairn and Beanland (1989) and Cole (1990). TVZ, Taupo volcanic zone; RC, Rotorua caldera; OVC, Okataina volcanic center; NISB, North Island shear belt; TR, Tarawera rift; WG, Whakatane graben.

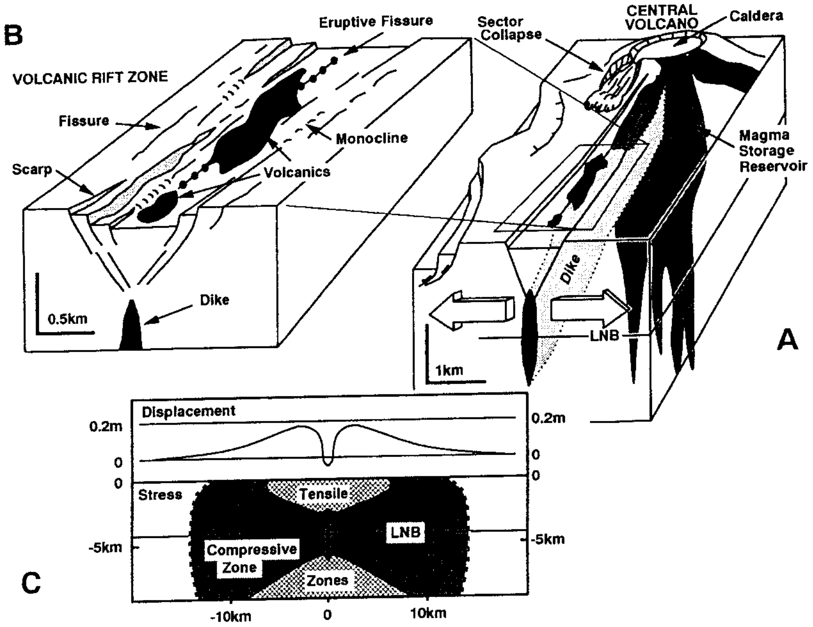

Figure 4.2 Schematic diagram, summarizing the configurations of volcano-extensional structures and their relationship to magmatic processes. LNB, level of neutral buoyancy (Ryan, 1987). (A) Brittle deformation associated with upper-crustal magmatism. (B) Dike-induced structures along a volcanic-rift zone. (C) Results of numerical elastic-deformation model of dike intrusion (modified from Rubin, 1992) are comparable to observed brittle-deformation features of B. Upper part of diagram shows a vertical-displacement profile above a dike of 1-m thickness, extending from 1 to 6 km deep. Lower part of the diagram shows the compressive and extensional zones that develop around a dike as a result of magma pressure. [Parts B and C from Smith *et al.* (1996); reprinted with permission of the American Geophysical Union.]

products consist of subsurface rhyolitic dikes, tensile fissures, normal faults, monoclines, rhyolite domes and tuff rings, and isolated basaltic vents. Since 1980, Long Valley caldera has experienced seismic unrest and resurgent uplift of the caldera floor. The patterns of uplift and seismicity, particularly the possible occurrence of non-double-couple events (Julian and Sipkin, 1985), suggest ascending magma, but explanations for the caldera unrest at Long Valley are equivocal because the caldera is intersected by tectonic-normal faults of the Sierran range front, and most earthquakes have double-couple mechanisms. We include the Long Valley region because it is an area where magmatic processes are thought to influence local tectonics and seismicity.

Iceland is an emergent portion of the mid-Atlantic Ridge, where voluminous basaltic-magma production related to a mantle plume has produced several, historically active magmatic belts (Gudmundsson, 1986; Rubin, 1990; Ryan, 1990; Fig. 4.1C). Magmatic features include large central volcanoes with summit calderas, tephra cones, isolated silicic-to-intermediate centers, and extensional structures related to dike emplacement along volcanic-rift zones. In the axial region, crustal extension is accommodated largely by dike intrusion into volcanic-rift zones that emanate from central volcanoes. Historical seismicity and geodetic monitoring along the volcanic-rift zones (Bjornsson *et al.*, 1979) has contributed greatly to understanding the dynamics of dike intrusion, the formation of co-intrusive extensional structures, and the evolution of volcanic-rift zones. During seafloor-spreading, older crust is displaced outboard of the active volcanic zones. In these outlying areas, magma supply is small and the volcanic pile is tectonically tilted on regional normal faults, exposing Tertiary dikes and their related extensional structures (Palmason, 1981).

The Hawaiian islands occur along the track of a north Pacific, oceanic-intraplate mantle plume. Although the tectonic setting differs from that of Iceland, Hawaiian volcanic-rift zones have much in common with their Icelandic counterparts, including the growth of large basaltic-shield volcanoes with summit calderas and volcanic-rift zones. These features are well displayed on the island of Hawaii (Fig. 4.1D), which consists of five coalesced Quaternary shield volcanoes, two of which (Mauna Loa and Kilauea) have frequently erupted in historic times. Many cycles of volcanism, intrusion, ground deformation, and seismicity have led to an unrivaled knowledge of the magma dynamics (Decker *et al.*, 1987; Tilling and Dvorak, 1993). Magma ascends along a central conduit beneath Kilauea caldera, where it is stored in a shallow (2- to 5-km deep) chamber, from which dikes intrude radially into several volcanic-rift zones. As a result, the southern part of the island between Kilauea's east and southwest volcanic-rift zones is being pushed seaward. Normal faults of the Hilina fracture system represent the headwall of a large slump block that is undergoing seaward gravitative failure. Deep (ca. 15 km; $M > 6$) earthquakes, spatially unrelated to the magma-storage system, have focal mechanisms indicating that the entire southern sector of the island is moving seaward, along a decollement of pelagic sediment on which the island grew (Decker, 1987; Wyss, 1988; Gillard *et al.*, 1992). Strain release in the form of moderate-sized tectonic earthquakes have occurred between the active Mauna Loa and Kilauea volcano centers (Endo, 1985; Jackson *et al.*, 1992).

Plate divergence encroaches onto continental east Africa, near the Afar triple junction (Fig. 4.1E). Geologic mapping and radiometric-age determinations in the Asal rift area, Republic of Djibouti, suggest that magmatic activity waxes and wanes because extension continuously affects the rift (Stein *et al.*, 1991). During times of low magma input, significant structural relief accumulates via displacements on tectonic-normal faults. During times of accelerated magmatism, lasting on the order of 10^5 yr, volcanic materials fill the structural basins, and dike injection accommodates much of the extension. A dike-injection event in 1978 resulted in about 2 m of extension, and was accompanied by eruption of the Ardukoba lava flow and a (body-wave magnitude) M_b 5.3 earthquake (Ruegg *et al.,* 1984; Stein *et al.,* 1991). Geodetic and seismic monitoring constrains the dike dimensions and geometry (Table 4-1), and shows that preexisting dike-induced graben faults are reactivated by recurrent dike intrusion, in places with up to 0.8 m of vertical slip.

The Taupo volcanic zone, North Island, New Zealand is an ensialic, backarc basin that is developed landward of the Taupo-Hikurangi subduction system, a zone of regional compression (Fig. 4.1F). Oblique slip along the plate boundary is accommodated by extensional tectonics, caldera-related silicic volcanism, and inferred magma intrusion in the Taupo volcanic zone (Cole, 1990). The right-lateral component of slippage occurs within the adjacent North Island shear belt. Aligned silicic domes of the Okataina and other volcanic centers indicate the presence of subsurface rhyolite dikes. In 1886, a basaltic dike produced several meters of dilation and was accompanied by fissure-fed, explosive volcanism along the Tarawera rift (Nairn and Cole, 1981). These observations suggest that extension is partly accommodated by magma intrusion, although the record of observational seismicity is ambivalent in this regard (Sherburn, 1992a). Based on field observations during the 1922 earthquake swarm (estimated maximum-magnitude range of 6.0 to 7.5), Grindley and Hull (1986) tentatively suggest that ground fissuring and earthquake swarms may occur unpredictably throughout the Taupo volcanic zone as a result of basaltic-dike intrusion. The absolute uplift of the western Whakatane graben during the 1987 M_L 6.3 Edgecumbe earthquake (Smith and Oppenheimer, 1989) is attributed by Nairn and Beanland (1989) to protracted, late-Quaternary magma intrusion and heating beneath the area.

4.2.2 Central Volcanoes and Calderas

Contemporary seismicity and magma dynamics have been thoroughly investigated at the intraplate volcanoes of Hawaii (Decker *et al.,* 1987) and Iceland (Ryan, 1990; Rubin, 1990), as well as at composite volcanoes situated along convergent margins (Latter, 1989; McGuire *et al.,* 1991). Beneath *central volcanoes,* magma ascends from sources in the lower crust and upper mantle, and is commonly heralded by earthquakes as deep as 35 km. The magma-conduit systems beneath many volcanoes are seismically well defined and culminate in shallow reservoirs. Other central volcanoes, such as Nevado del Ruiz, Colombia, are spatially associated with local seismicity but do not have single, well-integrated conduit systems or vent complexes near the surface (Zollweg, 1990). Magmatic storage generally occurs worldwide at depths of 2 to 4 km, probably due to the combined effects of neutral buoyancy (the level where magma and crustal densities are equivalent; Ryan, 1987) and decreased tensile strength of rocks in the shallow crust (Gudmundsson, 1984a).

Calderas are broad collapse depressions, marked by ring faults or broad flexural zones, and are generally 2 to 60 km across. Caldera structures occur in virtually all tectonic and volcanic settings, and withdrawal of magma from shallow reservoirs is their fundamental mechanism of formation, regardless of magma type or eruption style. In basaltic systems, withdrawal of magma from subcaldera chambers commonly occurs by the lateral injection of dikes into volcanic-rift zones, at shallow depths (<4 km) and may or may not be accompanied by volcanism. In silicic systems, withdrawal occurs by explosive evacuation of the chamber, with eruption and wide dispersal of pumiceous pyroclastic-flow and tephra-fall deposits.

Several calderas have been sites of earthquakes and other signs of historical unrest, including uplift or deflation of their floors due to subterranean flux of magma or hydrothermal fluid (Dzurisin and Newhall, 1984; De Natale and Pingue, 1993). Contemporary seismicity and geodesy are closely monitored at the Quaternary silicic calderas of Yellowstone, Long Valley, and Taupo, in light of their past eruptive histories (Pitt *et al.,* 1979; Pelton and Smith, 1982; Julian and Sipkin, 1985; Dzurisin *et al.,* 1986; Langbein *et al.,* 1993; Sherburn, 1992b) (Figs. 4.1A, B, and F). All three calderas have well-defined ring-fracture systems and are intersected by regional tectonic faults. Their structural complexity therefore confounds seismic interpretations as to tectonic versus magmatic mechanisms. Geodetic and seismic patterns nonetheless indicate a strong interaction between magmatic and regional-tectonic processes (Bursik, 1992; Smith and Braile, 1994).

Large-scale caldera collapse and its affiliated seismicity have been observed only twice during the past century. Earthquakes were associated with the 1968 collapse of the summit caldera of Fernandina, a large basaltic-shield volcano of the Galapagos Islands (Filson *et al.,* 1973). Abe (1992) describes the seismicity associated with one of the century's largest eruptions, involving the formation of a caldera near Mount Katmai, Alaska, in 1912. In both cases the seismicity was coincident with caldera collapse and at Katmai, with the explosive eruption of silicic pumice.

4.2.3 Volcanic-Rift Zones

When magma pressure in the upper part of a conduit or reservoir exceeds the strength of the surrounding rocks, bladelike *dikes* propagate outward from the reservoir along self-generated fractures at depths of 2 to 4 km. These dikes have heights (vertical dimensions) of several kilometers, and lengths that may extend tens of kilometers from the central magma conduit. The dikes intrude perpendicular to the direction of least compressive stress, which is influenced by the combined effects of mass loading by the volcanic edifice, and the regional stress field (Ryan, 1990; McGuire and Pullen, 1989).

Table 4-1

Dimensions of Dikes, Faults, and Graben Produced by Dike Injection in Volcanic-Rift Zones

Location[a]	Volcanic rift zone[b]		Dikes[c]				Faults[d]					Graben[e]		Observations[f]	References
	Length (km)	Width (km)	Length (km)	Thickness (m)	Height (km)	Basal depth (km)	Length (km)	Basal depth (km)	Dip (°)	Offset (m)	Total offset (m)	Length (km)	Width (km)		
Iceland															
Krafla, 1975	80	4–10					0.35–3.5				42 M		2–3	Outcrops	1,2
Krafla, 1975										0.05–0.7		10	5	Outcrops	3,4
Krafla, 1975						4–6				1.0 m				Seismicity	5
Krafla, 1977				2.6	7.2	8.5		2,1	70	1.6,1.3				Geodetic/modeling	6
Krafla, 1978				1.5	4.5	6	6,5		55,50	1.7,1.3				Geodetic/modeling	6,7
Eastern			22 m	0–26					42–90		0.5–8			Outcrops	8,9
Tertiary dikes				4.1 A					69 A		2.7 A			Outcrops	8,9
Northwestern			9.6 m	0–23					69 A		0.5–25			Outcrops	9,10
Tertiary dikes				4.3 A							5.3 A			Outcrops	9,10
Thingvellir	12	7.5					8 M				40 M			Outcrops	9,11
Swim							11 M				14 M			Outcrops	9,11
Eyrarfjall-			1.5 A	0.02–25					53–89		0.5–150			Outcrops	12
Karastadir				1.3 A					75 A		10 A			Outcrops	12
Hawaii, USA															
Kilauea rift zones															
East, 1968					0.5–1									Geodetic	13
East, 1980	60 S	4–6	3		2.5	3								Seismicity	14,15
East, 1981					3									Geodetic	16
East, 1982			2.5		2.5	3								Seismicity	14
Southwest, 1971	30	1–3			3.8									Geodetic	15,16,17
Southwest, 1981			2		1	2								Seismicity	14
Southwest, 1982					3	7								Geodetic	18
Oahu				0.05–6.7										Outcrops	19
Koolau Volcano				0.73 A										Outcrops	19
New Zealand															
Tarawera, 1988	17	5		1–2,12 M										Outcrops	20
Afar, Africa															
Afar	15 S	11.5 RV									150 RW		7.5 RIR	Outcrops	21
Asal, 1978	10	3–4	20	1.5–3			4–12			0.15–0.5				Geodetic/Outcrops	22,23,24
Asal, 1978			4.9		3.5	4.5	4–14	1–3.2	60–80	0.1–0.45				Geodetic/Modeling	21
Snake River Plain, Idaho, USA															
Arco rift	20	6					3–5				12.5 M	3.3	0.7 M	Outcrops	25,26,27
Great rift	85	2–8	6.2	0.5–1								6.2	1.2–2.2	Outcrops	27
California, USA															
Medicine Lake	10	2	4 M											Outcrops	28
Long Valley			8.5		6	8								Seismicity	29
Inyo Domes															
Mono Craters	25	10	25 M	8			13 M		60–80		100 m	0.7	0.6	Outcrop/Drilling	30,31,32,33

[a] Location of the volcanic-rift zone and the year of the dike-injection event, if observed.

[b] Dimensions of lengths and widths of volcanic-rift zones containing surficial features resulting from dike injection.

[c] Dimensions of lengths, thicknesses, heights, and basal depths of dikes within volcanic-rift zones.

[d] Dimensions of surficial lengths, basal depths, dips, offsets (observed during dike injection), and total vertical offsets of normal faults within volcanic-rift zones produced by dike injection.

[e] Dimensions of length and width of graben produced by dike injection.

[f] Types of observations used to assess dimensions of extensional-volcanic features: "Outcrops" indicate field observations; "seismicity" and "geodetic" measurements observed during dike injection event; "modeling" indicates results of geodetic modeling; and "drilling" indicates observations obtained from boreholes.

Key: M, maximum value; A, average value; m, minimum value; S, subaerial exposure; RV, rift valley; RW, rift wall; RIR, rift-in-rift.

References (1) Opheim and Gudmundsson, 1989; (2) Tryggvason, 1983; (3) Sigurdsson, 1980; (4) Bjornsson *et al.*, 1977; (5) Brandsdottir and Einarsson, 1979; (6) Rubin, 1992; (7) Rubin and Pollard, 1988; (8) Gudmundsson, 1983; (9) Gudmundsson, 1984a; (10) Gudmundsson, 1984b; (11) Gudmundsson, 1987; (12) Forslund and Gudmundsson, 1991; (13) Jackson *et al.*, 1975; (14) Karpin and Thurber, 1987; (15) Holcomb, 1987; (16) Pollard *et al.*, 1983; (17) Rubin, 1990; (18) Dvorak and Okamura, 1987; (19) Walker, 1987; (20) Nairn and Cole, 1981; (21) Stein *et al.*, 1991; (22) Le Dain *et al.*, 1979; (23) Tarantola *et al.*, 1979, 1980; (24) Abdallah *et al.*, 1979; (25) Hackett and Smith, 1992; (26) Smith *et al.*, 1989; (27) Kuntz *et al.*, 1988, 1992; (28) Fink and Pollard, 1983; (29) Savage and Cockerham, 1984; (30) Heiken *et al.*, 1988; (31) Mastin and Pollard, 1988; (32) Sieh and Bursik, 1986; (33) Bursik and Sieh, 1989.

Volcanic-rift zones are belts of aligned volcanic vents and associated magma-induced extensional structures such as subparallel normal faults, anastomosing tensile cracks, monoclines, and eruptive fissures (Figs. 4.3, and 4.4). Volcanic-rift zones are always underlain by dike complexes and the largest volcanic-rift systems are thousands of kilometers long by a few tens of kilometers wide at the midocean ridges. The smallest systems are a few kilometers by several hundred meters in the case of isolated, monogenetic volcanoes fed by single dikes. In Table 4-1 we compile dimensional information on dikes and *dike-induced extensional structures,* with the intent of portraying their overall dimensions in comparison to tectonic features. The dimensions are derived from outcrop measurements, inversion of geodetic data to derive subsurface-dike parameters, co-intrusive seismicity, and research drilling. The overall lengths of subaerial volcanic-rift zones vary from 10 to 85 km, and all are less than 10 km wide. Dike thicknesses range from <1 m (mafic) to 25 m (silicic); most are basaltic in composition and 2 to 4 m thick. Dike lengths are several kilometers to several tens of kilometers; Icelandic dikes are known to have lengths of the order 60 km. Heights (<1 to 7.5 km) and basal depths (2 to 8.5 km) of dikes are consistent with the 2- to 4-km depth along which dikes propagate (Gudmundsson, 1984a; Ryan, 1987). In Table 4-1, depths to dike tops do not exceed 4 km. *Dike-induced normal fault* lengths are short (<14 km), dips are steep (mostly 70 to 80°), and co-intrusive offset is usually <2 m.

Geodetic measurements, co-intrusive seismicity, and field observations during intrusive episodes conclusively support the idea that magma intrusion causes surface faulting along volcanic-rift zones. Migrating outward at rates of 0.1 to 6 km/h (Klein *et al.*, 1987; Einarsson, 1991), the propagating dikes incrementally form normal faults and fissures, resulting in swarms of small, shallow earthquakes (Table 4-2). Elastic and inelastic tumescence of the ground surface occurs over a broad area up to 10 km wide, centered on the dike top (Fig. 4.2C). Extensional structures such as normal faults, fissures, and monoclinal flexures occur within a narrow, several-kilometer-wide belt centered above the propagating dike, as in the so-called Icelandic *fissure swarms.* Repetition of the process forms subsurface dike swarms and complex, overlapping surface-deformation features. Most dike-induced *fault scarps* are <1 m high, but emplacement of thick dikes or reactivation of preexisting structures by multiple dike intrusions may produce fault scarps >10 m in height (Table 4-1; Thingvellir and Krafla).

4.2.4 Magma-Induced Slope Instability

Steep-sided volcanoes are inherently unstable, and collapse of their flanks is marked by horseshoe-shaped craters, similar in form to nonvolcanic landslide scarps. *Failure and mass movement* are commonly limited to unstable volcanic

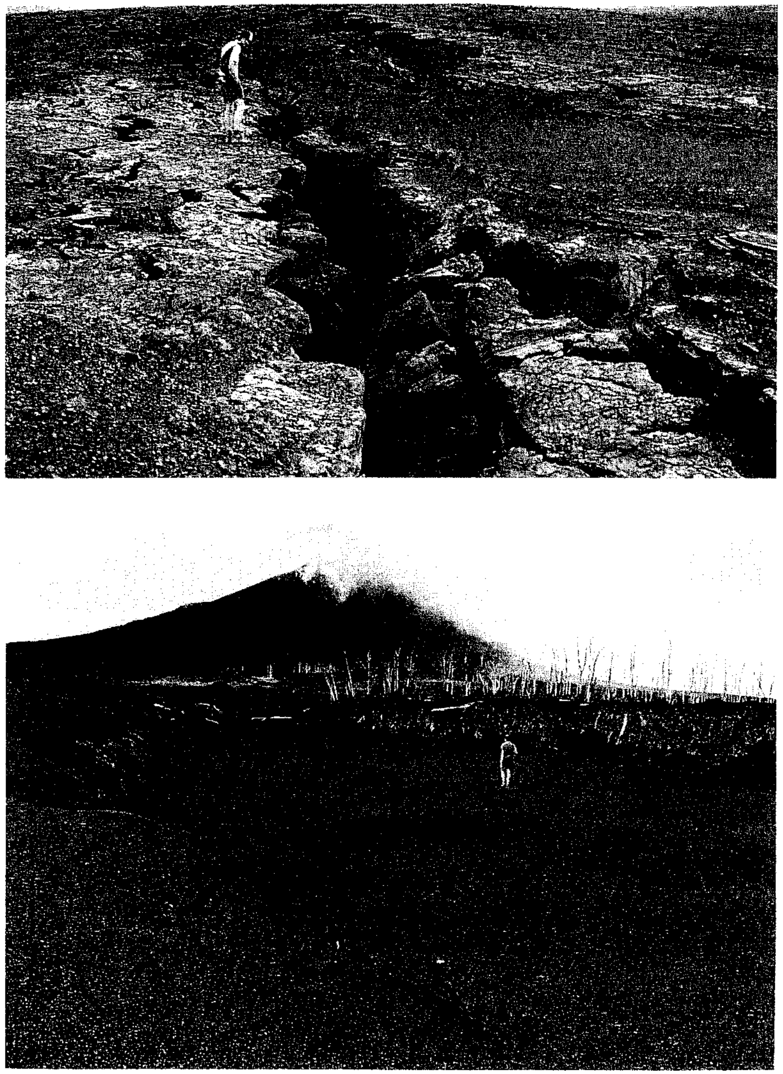

Figure 4.3 (A) Fissures induced by basaltic-dike intrusion along the southwest rift zone of Kilauea volcano, Hawaii. (B) Small graben with 3-m scarp, formed by dike intrusion associated with the 1983–1990 eruptive episodes of Puu Oo (active vent in background), east rift zone of Kilauea volcano, Hawaii. [From Smith *et al.* (1996); reprinted with permission of the American Geophysical Union.]

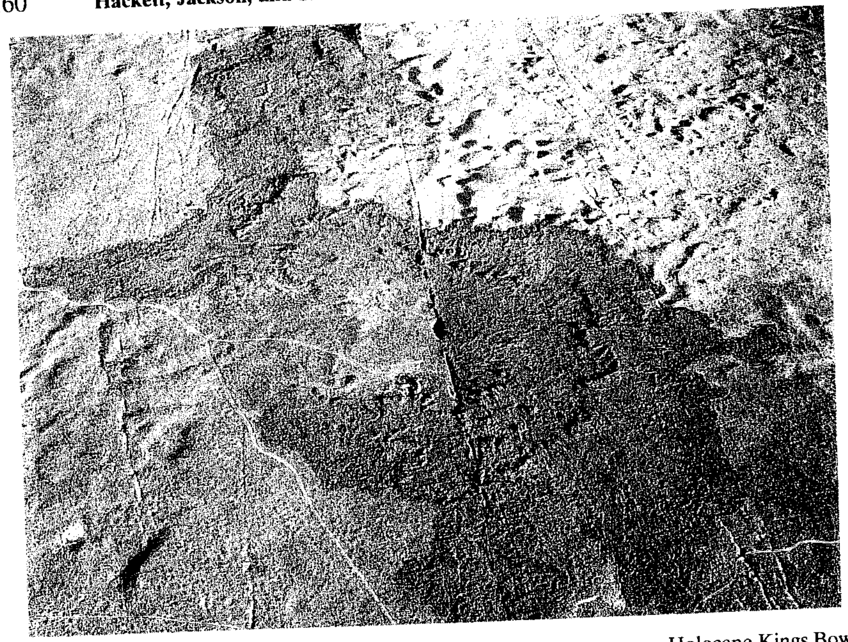

Figure 4.4 Aerial photograph of basaltic dike-induced fissure swarms, Holocene Kings Bowl lava field, eastern Snake River Plain, Idaho. [From Greeley and King (1977); photograph courtesy of Ronald Greeley.]

slopes as a result of loading by eruptive materials or from oversteepening due to shallow magma emplacement (Moore *et al.*, 1989; Borgia *et al.*, 1992). However, failure and mass movement can also involve entire volcanic piles (as shown on Fig. 4.1D) and generate large-magnitude earthquakes. Along the East Rift Zone of Kilauea volcano, the wedging action of dikes appears to be widening the volcanic-rift zone down to a depth of about 8 km. The widening is accommodated by intermittent, seaward movement of the south-eastern slopes of the island of Hawaii, along a subhorizontal decollement of seafloor sediment on which the volcano grew (Decker, 1987). Swanson *et al.* (1976b) used geodetic data to document the accumulation of compressive strain seaward of the volcanic-rift zone (schematically depicted by the arrow in Fig. 4.2A). In 1975, strain was released in the (surface-wave magnitude) M_s 7.2 Kalapana earthquake on the south flank of Kilauea volcano (Fig. 4.1D).

Deformation due to intruding magma (*tumescence*) and a probable magma-induced M_L 5.1 earthquake were both important contributors to the May 18, 1980, catastrophic slope failure and lateral blast of Mount St. Helens, USA (Lipman and Mullineaux, 1982). At another composite volcano, McGuire *et al.* (1991) report 3.6 m of horizontal displacement and instability on the upper flanks of Mt. Etna, and associate the deformation with dike emplacement over a 7-yr period. Moriya (1980) identifies several Japanese volcanoes with large avalanche scars, and notes that the long axes of the scars are oriented normal to aligned fissure vents and cones. Siebert (1984) suggests an apparent tendency for composite volcanoes with subparallel dike swarms to undergo large-scale sector collapse and generation of debris avalanches.

4.3 CRITERIA FOR FIELD RECOGNITION OF VOLCANO-EXTENSIONAL FEATURES

Many of the volcano-extensional structures that we have described, those with clear relationships to central volcanoes and circular structures related to caldera collapse, are recognized using the conventional field techniques of volcanic and structural geology. We do not discuss them further. For landslides, we refer the reader to Chapter 8 of this book. We find it more beneficial to discuss the linear-extensional structures and zones that are related to dike intrusion. These features occur within large extensional regions, such as the Basin and Range Province of the western United States and the Afar region of eastern Africa, where they may be juxtaposed with regional-tectonic structures such as range-bounding normal faults. Within this context, dike-induced extensional structures could be interpreted as being of tectonic origin. As we show in Sec. 4.3.4, a mechanistic distinction between magmatic and tectonic structures can be problematic, because major tectonic structures may be capable of supporting large-magnitude earthquakes, but purely magma-induced structures generally cannot. The diagnostic criteria we discuss for recognizing dike-induced extensional features include results of dike-emplacement modeling, the tectonic geomorphology of volcanic-rift zones, and geophysical methods for identifying magmatic intrusions beneath extensional structures.

4.3.1 Results of Empirical and Numerical Modeling

Numerical and scaled-empirical experiments on dike intrusion provide a foundation for understanding the origins of dike-induced deformational structures. Numerical modeling of elastic media gives information on the relationships between dike geometry, stress and strain distributions, and surface deformation (Pollard *et al.*, 1983; Marquart and Jacoby, 1985; Rubin and Pollard, 1988; Mastin and Pollard, 1988; Rubin, 1992; 1993; Roth, 1993). In *numerical-elastic experiments,* dike intrusion produces broad uplift, with narrow subsidence centered above the propagating dike (Fig. 4.2C). The locations of displacement (or strain) maxima are a function of the ratio of dike height (vertical dimension of the dike) to dike depth (distance of dike top below surface). Displacement or strain maxima are symmetrical for a vertical dike, but asymmetrical for

Table 4-2

Maximum Magnitudes and Focal Depths of Earthquakes Associated with Dike Injection

Location[a]	Rifting event[b] (Year)	Maximum magnitude[c]	Focal depth(s)[d] (km)	References
Iceland				1,2
Krafla	1975–76	5.0[e]	0–4	3
Krafla	1977	3.8[e]	0–6	4
Krafla	1978	4.1[e]	1–4	
Hawaii, USA				
Kilauea rift zones				
East	1965	4.4 (M_L)	0–8	5
East	1968, Aug.	3.3	<5	6
East	1968, Oct.	3.1	<6	6
East	1969	4.7	<7	7
Soutwest	1975	3.0	nd	8
East	1976–77	4.0	<10	8
East	1980, Aug.	3.0 (M_c)[f]	0.5–3	9
East	1980, Nov.	3.1 (M_c)[f]	0.7–4	9
Southwest	1981	3.4 (M_c)[f]	1–2	9
East	1982	3.0 (M_c)[f]	0.5–3	9
Japan				
Izu Peninsula[g]	1989	5.5 (M_{JMA})	<8	10,11,12
Africa				
Asal, Afar	1978	5.3 (M_b)	0–6	13,14
New Zealand				
Taupo volcanic zone[h]	1964–65	4.6	4–8	15
Taupo volcanic zone[h]	1983	4.3	6–10	15
California, USA				
Mono Craters[i]	1325 ± 20	>6.5 (M_s)	nd	16
Italy				17,18
Mt. Etna	1989	3.3 (M_L)	<4	19
Mt. Etna	1991	3.3 (M_L)	<6	
Mean $\pm 1\sigma$; $n = 19$[j].		3.9 ± 0.8		This Chapter

[a] Worldwide dike-injection events associated with mafic magma except for Mono Craters, which is associated with silicic magma and Mt. Etna, which is associated with intermediate magma. Composition of magma for New Zealand episodes is unknown.

[b] An episode of dike injection and associated seismicity having a known beginning and end.

[c] Maximum magnitude reported for the dike-injection event. Magnitudes: M_L, Local or Richter; M_c, Coda; M_{JMA}, Japan Meterological Agency; M_b, Body-wave; M_s, Surface-wave. No definition of magnitude scale was reported for values without magnitude designation.

[d] Depth range of volcanic seismicity and maximum magnitude earthquake associated with the dike-injection event.

[e] Einarsson (1991) reports earthquakes of magnitude ≥5.0 are usually associated with caldera deflation events and magnitude <4.0 with dike injection at Krafla.

[f] Coda magnitudes greater than amplitude magnitudes for these events (Nakata *et al.*, 1982; Tanigawa *et al.*, 1981, 1983).

nonvertical dikes (Pollard *et al.*, 1983). These findings reflect the calculated stress field around the dike (Pollard *et al.*, 1983; Fig. 4.2C), and are generally consistent with field and geodetic observations along active volcanic-rift zones undergoing dike intrusion, such as those of Iceland and Afar (Rubin, 1992).

Because real-earth deformation is inelastic, normal faults and fissures develop where the tensile zone above the dike top interacts with the earth's surface (Rubin, 1992). Although the regions alongside the propagating dike are under compression (Fig. 4.2C), compressional structures are rarely observed in nature (Pollard *et al.*, 1983) because the magnitude of the compressive-stress change is small in relation to the compressive strength of the rocks. In contrast, the tensile stress often exceeds their tensile strength, because rocks are inherently weaker in tension than in compression.

Surface faulting and the formation of other inelastic structures have been investigated using *physical-analog models* of dike injection (Mastin and Pollard, 1988). Vertical dikes simulated with cardboard sleeves are inserted into boxes filled with flour-sugar mixtures representing the brittle crust. Strain measurements are made during successive stages of dike dilation, including fissure-and-fault development (Fig. 4.5). Fissures appear in two symmetrical zones when dilation of the sleeve is about 10% of the sleeve depth, and continue to form progressively inward with additional dilation. Most fissures are oriented parallel to the sleeve plane. A shallow *topographic trough* forms above the sleeve top and is flanked by two broad topographic highs, outboard of the fissure zones. When sleeve dilation approaches about 20% of the sleeve depth, dip-slip movement produces *monoclines* and a central *graben.* Subsurface extensional fractures develop, accommodate dip-slip movement, and propagate by connecting with extensional features in adjacent layers and with surface fissures, forming nearly vertical normal faults at the surface but decreasing to 70° dips at depth. Fault depths are shallow; they extend only

---

[g] This earthquake is interpreted to have triggered magma movement, but was part of an earthquake swarm that began 10 days prior to a dike-fed submarine eruption (10, 11, 12).

[h] Possibly associated with tectonic subsidence of the basin or triggered by dike injection (15).

[i] Minimum estimate of the largest of five historic earthquakes based on liquefaction deposits as per (16). These earthquakes may be associated with movements along tectonic faults.

[j] Mean and one standard deviation computed based on magnitudes as presented. Mono Craters not used because it was a minimum estimate.

nd: No data obtained.

References: (1) Einarsson and Bjornsson, 1979; (2) Bjornsson *et al.*, 1977; (3) Brandsdottir and Einarsson, 1979; (4) Einarsson and Brandsdottir, 1980; (5) Bosher and Duennebier, 1985; (6) Jackson *et al.*, 1975; (7) Swanson *et al.*, 1976a; (8) Dzurisin *et al.*, 1980; (9) Karpin and Thurber, 1987; (10) Okada and Yamamato, 1991; (11) Takeo, 1992; (12) Oura *et al.*, 1992; (13) Abdallah *et al.*, 1979; (14) Lepine and Hirn, 1992; (15) Grindley and Hull, 1986; (16) Sieh and Bursik, 1986; (17) Bonaccorso and Davis, 1993; (18) Barberi *et al.*, 1990; (19) Ferrucci and Patane, 1993.

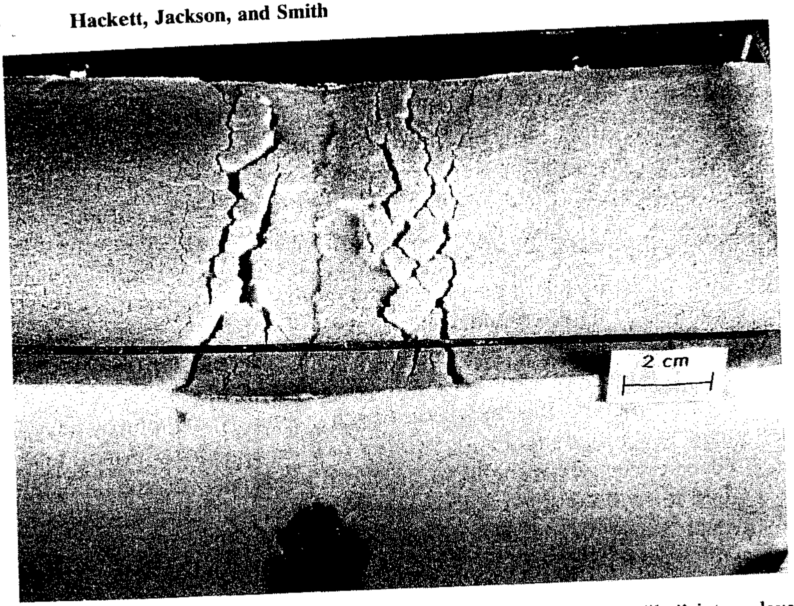

Figure 4.5 Fissures and graben formed by intruding a cardboard "dike" into a layered, sugar-flour mixture. Photograph taken at maximum dilation when the linoleum sleeve approached 0.2 times the depth to the top of the sleeve. [Mastin and Pollard, 1988, p. 13,229; copyright by the American Geophysical Union; courtesy of Larry Mastin.]

slightly deeper than the dike top. The total horizontal component of strain (i.e., extension) is about 60 to 75% of the dike thickness. Thus, inelastic structures of the physical models are generally consistent with (1) the elastic-strain profiles of numerical experiments; (2) geodetic-inversion models showing that faults extend only above and ahead of propagating dikes (Du and Aydin, 1992); and (3) field, geodetic, and seismic observations on active volcanic-rift zones (Rubin, 1992).

With reference to Table 4-1, implications of the physical models for geologic field investigations include the following:

1. The magnitude of cumulative fault throw at the surface above the intruding dike, and the horizontal extension, are proportional to the dike thickness, with thicker dikes producing more pronounced graben, normal faults, and fissures. Basaltic dikes are generally 1 to 6 m thick. Hence, the dike-induced vertical and horizontal strain measured in the field for single basaltic dikes should be on the order of several meters. Thicker dikes (rhyolitic dikes can be tens of meters thick) should produce proportionately greater strain, and this is consistent with the more pronounced structures observed above silicic dikes (with throws of 10 m or more) relative to basaltic dikes (Mastin and Pollard, 1988).

2. Graben width is related to dike depth, such that deeper dikes produce wider zones of extension than shallower dikes. Few dike-induced graben in volcanic-rift zones are greater than 2 km wide, suggesting that dikes generally do not induce surface faulting until they are within a few kilometers of the surface. The small offsets and rupture areas of dike-induced faults suggest that the magnitudes of associated seismicity will be small, as discussed in Sec. 4.4.3.1.

4.3.2 Volcano-Tectonic Geomorphology

Although discrete, dike-induced structures are morphologically similar to non-magmatic-extensional structures, the bilateral symmetry, lack of net vertical displacement across graben, small-scale offsets of individual structures, and association with eruptive fissures along volcanic-rift zones are *diagnostic indicators* of magmatic origin. Perhaps the best criterion for identifying volcano-extensional features is their inferred or demonstrated relationship to cogenetic volcanic materials (Fig. 4.2B). Within volcanic-rift zones, extensional structures commonly occur as a diffuse belt several kilometers wide, and commonly with a central graben that is symmetrically disposed around a central eruptive fissure. Tensional fissures are most abundant (Fig. 4.3), indicating that most of the deformation is purely dilatational. Magmatically induced normal faults involve no major displacement or rotation of crustal blocks. Most offsets are less than 1 m, but may reach several tens of meters where thick (silicic) or numerous dikes are involved. Vertical displacements typically vary greatly along strike, and individual faults are short (hundreds of meters to about 10 km; Table 4-1), commonly grading into monoclines or purely tensional fissures.

On the regional scale, extensional magmatism produces diffuse belts of volcanism, fissuring, and subdued normal fault scarps. Even after millions of years of basaltic volcanism and dike intrusion as in Iceland and the eastern Snake River Plain (Figs. 4.1A and C), the terrain is topographically subdued. This is in contrast to extensional provinces that lack substantial magma flux into the upper crust (Parsons and Thompson, 1991), where recurrent faulting is a primary mountain-building process that produces several kilometers of vertical offset and substantial topographic relief.

4.3.3 Geophysical Evidence of Intrusive Bodies and Structures

Because the surficial features of volcanic-rift zones result from dike intrusion, geophysical evidence of subsurface dikes will lend confidence to interpretations of magmatic versus tectonic origin. The geophysical signatures of dikes result from physical contrasts between dikes and surrounding rocks, or from changes in properties related to structural offset, and are observable with potential-field and electrical methods.

The densities and magnetic susceptibilities of shallow igneous intrusions commonly differ from those of the surrounding country rocks, and the resulting potential-field geophysical anomalies can be used to make inferences on the depth and shape of the intrusions (Telford *et al.*, 1990). Electric-field anomalies and their associated magnetic anomalies are also used in mapping the configuration of subsurface fluids, which is influenced by volcanic materials and structures (Keller and Rapolla, 1974). Geomagnetic and gravimetric methods have proven particularly useful for understanding the subsurface structure of volcanoes and their intrusive roots (Yokoyama, 1974).

The densities and magnetic susceptibilities of solidified *mafic* intrusions are generally greater than those of country rocks, and this includes basaltic dikes intruded into compositionally similar lava flows (Schoenharting and Palmason, 1982; Flanigan and Long, 1987). The growth of secondary magnetite in deuteric envelopes around the intrusions commonly enhances the magnetic contrast with country rocks (Bleil *et al.*, 1982). The volcanic-rift zones of Hawaii possess characteristic magnetic patterns, primarily long-wavelength, linear, magnetic-low zones, probably depicting rocks that have been chemically and mineralogically altered by hydrothermal fluids at depths greater than 1 km (Hildenbrand *et al.*, 1993). Shorter wavelength, positive anomalies probably reflect slowly cooled, unaltered intrusions. As a result of these factors, linear, symmetrical, magnetic anomalies, together with geologic information, have been used worldwide for the mapping of mafic dikes and dike swarms within several igneous provinces: the Columbia Plateau (Swanson *et al.*, 1979); East African Rift System (Halls *et al.*, 1987); Auckland volcanic field (Rout *et al.*, 1993); Canadian Shield (Schwarz *et al.*, 1987); and Basin and Range Province, USA (Zoback and Thompson, 1978; Blakely and Jachens, 1991).

Electrical and potential-field anomalies, in combination with volcanic- and structural-geologic information, can be used to identify the shallow intrusive masses that commonly underlie volcanic zones. The high-level impoundment of groundwater by dikes (Stearns, 1985) or steep local water-table gradients due to abrupt changes in hydraulic conductivity (Mundorff, *et al.*, 1964) are widespread in known areas of intrusion and eruption. Broad (>3-km) self-potential anomalies occur along the volcanic-rift zones and beneath the summit caldera of Kilauea volcano (Jackson and Kauahikaua, 1987). Hermance *et al.* (1984) show that magnetotelluric observations can indicate important physical features associated with caldera structures, including the location and offset of major boundary faults because of the high resistivity contrast between caldera fill and crystalline basement, and the structural control of saline hydrothermal-fluid flow.

4.4 PALEOSEISMOLOGICAL IMPLICATIONS AND METHODS

4.4.1 Excavation and Geochronometry

In this section, we discuss selected approaches to the geochronometry and excavation of magma-induced structures. In contrast to the poorly consolidated sedimentary materials that are shed from rising normal faults and that are typically sought for paleoseismic excavation (Chapter 3), volcanogenic structures and materials are commonly developed in volcanic bedrock, which is composed of strongly lithified materials that do not produce well-developed *colluvial wedges*. In addition, many volcanogenic structures are monogenetic (*nonrecurrent*) and have small displacements; these factors further diminish the potential for colluvial wedge development. Therefore, magma-induced structures should be carefully chosen for excavation and geochronometry. As discussed later, it may be more productive to demonstrate cogenetic or relative relationships with volcanic deposits, rather than to attempt excavation and dating of the deformational features themselves.

Some of the possibilities and problems for dating volcano-extensional structures are shown in Fig. 4.6. Tensile fissures can be viable sites for excavation and dating because they are a common type of magma-induced structure and because they are sediment traps. However, their irregular vertical geometry and the potential complexity of their sediment fill preclude traditional backhoe-trenching operations (Figs. 4.6A and B). Hand excavation is required in many cases, proceeding more along the lines of archaeological excavation than paleoseismic trenching. Magma-induced faulting and fissuring are commonly expressed in resistant lithologies such as lava flows. As a result, scarps degrade slowly and contribute blocky debris to noncolluvial-sediment wedges (Fig. 4.6D).

Here we cite some successful applications of geochronology from the current literature to illustrate the emerging methods that can be used to date volcanic materials, structures, and surfaces. Bursik and Sieh (1989) use radiocarbon dating to constrain the timing of dike intrusion in the Mono–Inyo area of California (Fig. 4.1B), and Kuntz *et al.* (1986) develop meticulous pretreatment procedures for dating Holocene basaltic-lava fields on the eastern Snake River Plain, Idaho. Forman *et al.* (1993, 1996) show that heating of fine-grained sediment beneath basaltic lava flows effectively resets the thermoluminescence ages of the sediment, and "baked" sediment is therefore useful for dating young lava flows. Sediment in fissures or on scarps can potentially be dated by radiocarbon or thermoluminescence, assuming that the materials are carefully excavated and their genetic relationships are well understood (Fig. 4.6). Problems include (1) uncertainty surrounding whether the sample represents early accumulation; (2) inadvertent sampling of col-

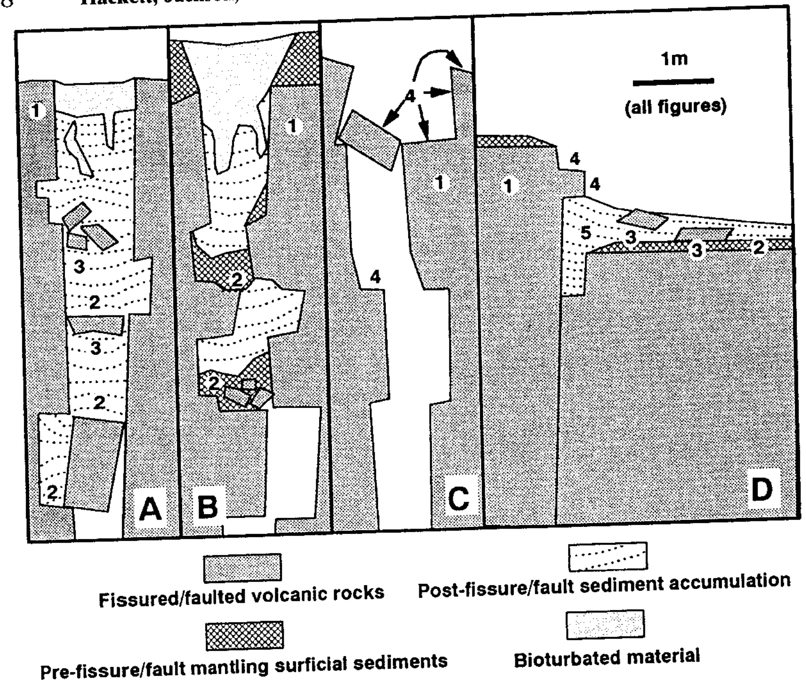

Figure 4.6 Schematic, near-surface cross sections of volcano-extensional structures. Single-deformation events are depicted; recurrent slip or fissuring would produce more complicated schemes. Panels A through D indicate geometric and lithologic configurations to which geochronometry could be applied: (A) Magma-induced fissure in resistant volcanic rock; fissure fill consists of blocks of volcanic-wall rock and postfissure sediment. (B) Fissure as in A, but developed within volcanic rock having a mantle of surficial sediment; infilling consists of three components: volcanic blocks, clasts of mantling sediment, and a matrix of postfissure sediment derived from deflation of the surrounding surficial-sediment cover, as well as from distant sources. (C) Magma-induced fissure with no sediment fill. (D) Scarp developed in lithified volcanic rock. Volcanic blocks are of colluvial origin, but the sedimentary wedge is transported material, not derived from scarp degradation. Numbers 1 through 5 refer to potential geochronometric methods: (1) Conventional dating of deformed volcanic rocks, to constrain maximum age of deformation (e.g., argon-isotopic dating of lava, or radiocarbon dating of charred vegetation beneath the lava). (2) Dating deep portions of postdeformational sediment fill by radiocarbon or thermoluminescence, to constrain the minimum age of deformation. (3) Dating the time that blocks have fallen from the fissure or scarp, using thermoluminescence or radiocarbon on sedimentary or organic material beneath the blocks. This gives a conservative minimum age because blocks can fall long after deformation. (4) Use of *in situ* cosmogenic radionuclides to date pre-, syn-, and postdeformational geomorphic surfaces. (5) Conventional trenching investigation of surficial sediment accumulated at the base of a scarp. [From Smith *et al.* (1996); reprinted with permission of the American Geophysical Union.]

lapsed clasts of mantling-surficial sediment that may be substantially older than the deformation; (3) the possibility that deformation occurred in a series of small steps, each of which disrupted the accumulating sediment; and (4) bioturbation by burrowing rodents and insects. On the other hand, rodents leave middens that can be dated by radiocarbon dating (Betancourt *et al.*, 1991).

Cation-ratio dating of rock varnish is an empirical surface-exposure dating method that can be applied to volcanic rocks (Reneau and Raymond, 1991), and *in situ* produced, cosmogenic radionuclides are increasingly being used for dating geomorphic surfaces. Volcanic olivine (Cerling, 1990; Kurz *et al.*, 1990) and plagioclase (Poreda and Cerling, 1992) are suitable minerals for cosmogenic helium and neon dating of lava surfaces. Cosmogenic ^{36}Cl is used by Zreda *et al.* (1993) to date a young basaltic-eruption complex, and Jannik *et al.* (1991) use it to establish a chronology of lacustrine sedimentation. We mention these examples because they can potentially be applied to date lava-flow surfaces that have been cut by fissures, lava-flow surfaces on blocks that have been rotated to expose new surfaces during or after deformation, and certain sediment-infilling or -mantling materials.

4.4.2 Recurrence Intervals

Magma-induced faults may lack sufficient displacement or suitable materials for the development of colluvial wedges, and many are monogenetic features, unlikely to have undergone recurrent movement. An alternative to the excavation and direct dating of magmatic faults and fissures is to focus on mapping and dating of the associated volcanic materials. Because earthquakes in volcanic-rift zones occur as a consequence of dike injection during magmatic cycles, earthquake recurrence on volcanic-rift-zone faults can be estimated by establishing the recurrence interval of volcanic cycles. Establishing volcanic-recurrence intervals requires thorough knowledge of volcanic processes and the regional patterns of volcanism, and takes into account the nature of vent clusters (single dikes can produce many aligned vents). A means of estimating the general proportion of eruptive to noneruptive cycles should also be sought, because not all dikes erupt.

Even when precise and sufficient age determinations are available from volcanic rocks to establish confidently volcanic-recurrence intervals, the information is not analogous to that established by paleoseismic studies of individual normal faults. Rather than being a "one scarp per earthquake" situation, each cycle of recurrent volcanism may involve several dike-injection events, and each dike in turn may or may not generate earthquake swarms. Volcanism, like recurrent faulting, is episodic and not continuous, and therefore a viable approach is to estimate volcanic recurrence using relative and absolute chronology, and to use that interval in estimation of magma-induced seismic recurrence. Conservatism is introduced by decreasing the ratio of volcanic vents per dike intrusion (i.e., assuming one vent per dike-injection episode), and by adopting a maximum magnitude that is consistent with the largest measured fault dimensions. Added conservatism is achieved by assuming that each dike-intrusion episode produces a maximum-magnitude earthquake, even though the observed seismicity during numerous dike-intrusion episodes indicates substantial variation in maximum magnitude (e.g., Table 4-2, Kilauea and Krafla rift zones).

4.4.3 Maximum Magnitude

We discuss worldwide observational seismology in terms of three geologic settings, and then we compare these data to calculated moment magnitudes based on fault dimensions. Table 4-2 is a compilation of *maximum magnitudes* of earthquakes associated with dike intrusion, mainly along volcanic-rift zones. Table 4-3 gives maximum magnitudes of earthquakes at some calderas and central volcanoes, which owing to their greater depth range and structural complexity than purely dike-induced settings, generate larger magnitude earthquakes. Table 4-4 lists some maximum magnitudes of "tectonic" earthquakes that may have been triggered by adjacent magma intrusion. In contrast to the seismicity associated with shallow magma intrusion, the large magnitudes of these earthquakes are due to the larger rupture areas of their source faults. In Table 4-5, we calculate moment magnitudes from known or reasonably assumed fault dimensions for dike-induced normal faults. In the accompanying discussion, we identify these calculated values as an upper limit of maximum magnitude, and compare them to the observational data of Table 4-2.

4.4.3.1 Earthquakes Associated with Dike Injection

Maximum magnitudes of observed earthquakes during dike-injection events are given in Table 4-2, ranging from M 3.0 to 5.5 and largely from the Icelandic and Hawaiian basaltic-rift zones. Dike-induced earthquakes in Iceland and Hawaii rarely exceed (magnitude) M 5, and maxima are more commonly near M 4. Other areas such as Africa, Japan, New Zealand, and Mono Craters have greater maxima, ranging from M 4.6 to 5.5. These larger earthquakes may occur where dike injection is relatively infrequent, where the seismogenic crust is thicker, or where dikes have greater thicknesses (also see discussion of Table 4-4).

The mean of 20 maxima cited in Table 4-2 is M 3.9 ± 0.8. Dike-induced earthquakes have such low magnitudes for several reasons. Local fracturing of small volumes of adjacent country rocks by the intruding magma should not produce large earthquakes because fault area and fault slip are small, as indicated in Table 4-1. With the exception of deep conduits arising from

Table 4-3

Maximum Magnitudes and Focal Depths of Earthquakes Associated with Calderas and Central Volcanoes

Location[a]	Rifting event[b] (Year)	Maximum magnitude[c]	Focal depth(s)[d] (km)	References
Iceland				
Heimaey Volcano	1973	4.0	15–25	1
Bardarbunga Caldera[e]	1974	5.0 (M_b)	nd	2
Krafla Caldera	1975–76	5.0[f]	0–4	1,3
Krafla Caldera	1977	3.8[f]	0–6	4
Krafla Caldera	1978	4.1[f]	1–4	5
Grimsvotn Caldera	1983	4.0	nd	6
Hekla Volcano	1991	3.0	nd	7
Hawaii, USA				
Kilauea Caldera	1968, Oct.	<3.3	<6	8
Kilauea Caldera	1969	2.0	<5, 15–35	9
Kilauea Caldera	1976–77	4.0	<10	10
Galapagos Islands				
Fernandina Caldera[g]	1968	5.4 (M_b)	nd	11
Alaska, USA				
Katmai Caldera	1912	7.0 (M_s)	nd	12
Redoubt Volcano	1989	2.2	8	13
Kamchatka, USSR				
Shiveluch Volcano	1964	5.3[h]	nd	14
Plosky Tolbachik Volcano	1975–76	5.0[h]	10–20	14,15
Kliuchevskoi Volcano	1983	3.5[h]	10–15	16
Gorely Volcano	1985	6.0	nd	17
Washington, USA				
Mount St. Helens Volcano	1980	5.1 (M_L)	0–7	18
Italy				
Mt. Etna Volcano	1974	4.5	nd	19
Mt. Etna Volcano	1983	3.2	<3	20
Phlegraean Fields Caldera	1982–84	4.0 (M_L)	2.5	21
Luzon, Phillippines				
Mt. Pinatubo Volcano	1991	5.7 (M_b)	nd	22
Mexico				
El Chichon Volcano	1974	4.5 (M_c)	<20	23
Chile, South America				
Lonquimay Volcano	1988–89	5.3 (M_w)	<10	24
Columbia, South America				
Nevado del Ruiz Volcano	1985–86	3.5 (M_c)[i]	<7	25
Papua, New Guinea				
Rabaul Caldera[j]	1983–85	5.1 (M_L)	0–4	26

continues

Table 4-3

Continued

Location[a]	Rifting event[b] (Year)	Maximum magnitude[c]	Focal depth(s)[d] (km)	References
Indonesia				
Galunggung	1982	3.8	nd	27,28
Merapi	1984	2.5	nd	27,28
Anak Ranakah	1987	4.0	nd	27
Banda Api	1988	4.0	nd	27
California, USA				
Long Valley Caldera	1978	5.3 (M_s)[k]	7	29
Long Valley Caldera	1980	6.1 (M_s)[k]	8–10	30
Long Valley Caldera	1982–83	5.2 (M_L)	<8	30
Wyoming, USA				
Yellowstone Caldera[l]	1975	6.1 (M_L)	<6	31,32
Japan				
Izu Islands	1982	6.4 (M_{JMA})	20	33
Izu Islands	1983	6.2 (M_{JMA})	1–13	33,34
Mean ± 1σ; $n = 36$[m]		4.5 ± 1.2		This Chapter

[a] Worldwide calderas and central volcanoes selected. Krafla, Bardarbunga, Kilauea, Fernandina, Kamchatka, and Izu Islands are associated with mafic magma; Heimaey, Grimsvotn, Hekla, Mount Redoubt, Mount St. Helens, Mount Etna, Phlegraean Fields, Mount Pinatubo, El Chicon, Lonquimay, Nevado del Ruiz, Galunggung, Merapi, Anak Ranakah, and Banda Api are associated with magmas of intermediate compositions; Katmai, Rabual, Mono Craters, Long Valley, and Yellowstone calderas are associated with silicic magma.

[b] An episode of volcanism and seismicity having a known beginning and end associated with magma movement unless indicated.

[c] Maximum magnitude reported for volcanic event. Magnitudes: M_b, body wave; M_L, local or Richter; M_w, moment; M_s, surface wave. No definition of magnitude scale was reported for values without magnitude designation.

[d] Depth range of volcanic seismicity and maximum-magnitude earthquake associated with the volcanic event.

[e] Brittle failure of the shallow crust in response to stress changes caused by pressure fluctuations in the magma chamber (2).

[f] Earthquakes of magnitude ≥5.0 are usually associated with caldera deflation events and magnitude <4.0 with dike injection at Krafla (2).

[g] Seismicity associated with collapse of caldera (11).

[h] Conversion to magnitude using $M = (K_s - 4.6)/1.5$; where M is the magnitude determined from surface waves; K_s is the mean energy class determined as the arithmetical mean from short-period S-waves of several stations (15).

[i] Maximum magnitude may be 4.0, but was not well-recorded (J. Zollweg, personal communication, 1993).

[j] Seismicity associated with movement along ring faults of the caldera (26).

[k] Earthquakes have non-double-couple mechanisms indicating tensile failure under high fluid pressure or simultaneous strike-slip and normal motion on separate faults (29, 30).

magma-source regions, dikes tend to propagate at shallow levels (<4 km), and the associated extensional structures have correspondingly small depths because rock fracturing occurs above and ahead of the propagating dikes (Du and Aydin, 1992). Typically, the slope of the earthquake frequency-magnitude recurrence curves are greater than or equal to 1, indicating low effective stress in regions of active dike injection (Bjornsson *et al.*, 1977). Earthquakes nucleated within the shallow regions of the brittle crust are inhibited from becoming large, because ruptures do not propagate into deeper, higher strength regions (frictional strength, stress drop, and ambient stress all increase with depth; Das and Scholz, 1983). This contrasts with extensional-tectonic ruptures, which commonly nucleate in the midcrust, near the brittle-ductile transition (Sibson, 1982; Smith and Bruhn, 1984; Scholz, 1988). At these depths (>10 km), rigidity is higher than for near-surface rocks, and ruptures must have relatively large areas and moments in order to break the surface. Faults with several meter displacements and several kilometer lengths form incrementally during dike propagation at rates of several kilometers per hour, and in some instances aseismically rather than in a catastrophic episode of strain release. Thus, Brandsdottir and Einarsson (1979) observed fault displacements of 1 m and extensive fissuring along the Krafla rift zone of Iceland, but the associated earthquakes did not exceed M 4.0.

4.4.3.2 Earthquakes at Calderas and Central Volcanoes

Ito's (1993) analysis of large earthquakes near active volcanoes in Japan shows that all large earthquakes (M > 6) occurred at distances greater than 10 km from active centers, and at shallower depths beneath active centers than elsewhere in the region. These observations are closely correlated with subsurface alteration and surface heat-flow values, suggesting that the seismogenic layer near the centers of active volcanoes is thin. Table 4-3 lists

---

[l] Normal faulting equivocally associated with magma movement or regional tectonic strain release (31).

[m] Mean and one standard deviation computed based on magnitudes as presented.

nd: No data obtained.

References: (1) Einarsson and Bjornsson, 1979; (2) Einarsson, 1991 (3) Bjornsson *et al.*, 1977; (4) Brandsdottir and Einarsson, 1979; (5) Einarsson and Brandsdottir, 1980; (6) Einarsson and Brandsdottir, 1984; (7) Gudmundsson *et al.*, 1992; (8) Jackson *et al.*, 1975; (9) Swanson *et al.*, 1976a; (10) Dzurisin *et al.*, 1980; (11) Filson *et al.*, 1973; (12) Abe, 1992; (13) Power *et al.*, 1992; (14) Fedotov *et al.*, 1983; (15) Zobin, 1990; (16) Gorel'chik, 1989; (17) Bulletin of Volcanic Eruptions, 1987; (18) Endo *et al.*, 1981; (19) Guerra *et al.*, 1976; (20) Patane' *et al.*, 1984; (21) Branno *et al.*, 1984; (22) National Earthquake Information Center, 1991; (23) Medina *et al.*, 1992; (24) Barrientos and Acevedo-Aranguiz, 1992; (25) Nieto *et al.*, 1990; (26) Mori *et al.*, 1989; (27) W. Tjetjep, personal communication, 1993; (28) McClelland *et al.*, 1989; (29) Julian and Sipkin, 1985; (30) Savage and Cockerham, 1984; (31) Pitt *et al.*, 1979; (32) Eaton *et al.*, 1975; (33) Bulletin of Volcanic Eruptions, 1986; (34) McClelland *et al.*, 1989.

Table 4-4

Maximum Magnitudes and Focal Depths of Tectonic Earthquakes Possibly Triggered by Magma Intrusion

Location[a]	Earthquake date/ volcanic event[b] (Year)	Maximum magnitude[c]	Focal depth(s)[d] (km)	References
Iceland				
Tjornes/Krafla	1975–76	6.3	nd	1
Hawaii, USA				
Kau/Kilauea	1968	8[e]	9[e]	2
Kaoiki/Mauna Loa	1962	6.1 (M_L)	nd	3
Kaoik/Mauna Loa	1874	5.5 (M_L)	5	3
Hilina/Kilauea	1975	7.2 (M_s)	5–6	2,4
Mauna Loa	1982	5.6	10–14	5
Kaoiki/Mauna Loa	1983	6.6 (M_L)	11	3,6
Kilauea	1989	6.1 (M_s)	9	7
Kiluaea	1989	5.0 (M_L)	9	7
Japan				
Izu Peninsula	1930	7.0 (M_{JMA})	nd	8,9
On-Take, Honshu	1984	6.8 (M_{JMA})	2	5
Unzen, Kyushu	1984	5.7 (M_{JMA})	nd	5
New Zealand				
Taupo volcanic zone	1922	6–7.5[f]	nd	10
Taupo volcanic zone[g]	1964–65	4.6	8	10
Taupo volcanic zone[g]	1983	4.3	6–10	10
Edgecumbe/Taupo volcanic zone	1987	6.3 (M_L)	8	11
California, USA				
Mono Craters[h]	1325 ± 20	>6.5 (M_s)	nd	12
Wyoming, USA				
Yellowstone Caldera[i]	1975	6.1 (M_L)	<6	13,14
Italy				
Mt. Etna	1991	5.4 (M_L)	<6	15
Mean ± 1σ; $n = 18$[j]		6.1 ± 1.0		This Chapter

[a] Worldwide volcanic rift zones, calderas and central volcanoes selected. Where provided, name of the fault system or earthquake/name of the caldera or volcano.

[b] Date of tectonic earthquake or episode of volcanism (magma movement) which may have triggered the earthquake.

[c] Maximum magnitude reported for triggered earthquakes. Magnitudes: M_L, local or Richter; M_s, surface-wave; M_{JMA}, Japan Meteorological Agency. No definition of magnitude scale was reported for values without magnitude designation.

[d] Depth of maximum magnitude earthquake.

[e] Estimated based on intensity distributions (2).

[f] Magnitude range based on Modified Mercalli intensity 7 (14). The maximum magnitude of 7.5 was used to determine the mean and standard deviation.

[g] Possibly associated with tectonic subsidence of the basin or triggered by dike injection (8).

maximum-magnitude earthquakes associated with magma movement at calderas and central volcanoes, where factors other than pure dike injection may influence the size of earthquakes. Maximum magnitudes range from M 2 (Kilauea) to M 7 (Katmai) and the mean of 36 values is M 4.5 ± 1.2. This compilation suggests that magma propagation beneath central volcanoes and calderas may generate somewhat larger earthquakes than simple dike intrusion (Table 4-2).

The 1968 Fernandina and 1912 Katmai earthquake sequences are of particular interest because they were coincident with catastrophic caldera collapse (Table 4-3). In both cases, the calculated kinetic energy releases, based on the volume change due to the gravitative failure of the caldera blocks, generally agreed with seismic-moment calculations (cumulative energy release based on instrumental recordings) (Filson *et al.*, 1973; Abe, 1992). The "tectonic" characteristics and overall conformation of the energy calculations indicate that the release of seismic energy is consistent with downfaulting of the observed caldera volumes.

4.4.3.3 Tectonic Earthquakes Induced by Magmatic Processes

Table 4-4 lists the maximum magnitudes of tectonic earthquakes that were triggered directly or indirectly by magmatic processes. The values range from M 4.3 (Taupo volcanic zone) to M ~ 8 (Hawaii), and the mean of 14 values is 6.2 ± 1.1. These earthquake sequences have characteristics that are typical of tectonic earthquake sequences in nonvolcanic areas, including main shock-aftershock groups, and b-values similar to tectonic swarms. The coincidence of an M 6.3 earthquake in the Tjornes fracture zone (Fig. 4.1C) with dike injection along the Krafla rift zone suggests a direct, mechanistic relationship. A typical mainshock-aftershock sequence (maximum magnitude M_L 4.5; Table 4-4) was observed in 1991 on Mt. Etna, one day after a dike-induced earthquake swarm (maximum magnitude M_L 3.3; Table 4-2) (Ferrucci and Patané, 1993). The earthquakes associated with the M_L 4.5 event have epicentral

---

[h] Minimum estimate of the largest of five historic earthquakes based on liquefaction deposits as per (12). These earthquakes may be associated with movements along tectonic faults.

[i] Normal faulting equivocally associated with magma movement or regional tectonic strain release (13).

[j] Mean and one standard deviation computed based on magnitudes as presented. Mono Craters not used because it is a minimum value.

nd: No data obtained.

References: (1) Bjornsson *et al.*, 1977; (2) Wyss, 1988; (3) Jackson *et al.*, 1992; (4) Lipman *et al.*, 1985; (5) Bulletin of Volcanic Eruptions, 1987; (6) Buchanan-Banks, 1987; (7) Bulletin of Volcanic Eruptions, 1992; (8) Nasu, 1935; (9) Kuno, 1954; (10) Grindley and Hull, 1986; (11) Cole, 1990; (12) Sieh and Bursik, 1986; (13) Pitt *et al.*, 1979; (14) Eaton *et al.*, 1975; (15) Ferrucci and Patane, 1993; (16) Eiby, 1968.

Table 4-5

Calculated Moment Magnitudes from Fault Dimensions for Normal Faults in Volcanic-Rift Zones

Location	Volcanic rift zone or episode	Surface rupture length[a] (km)	Rupture width[b] (km)	Rupture area[c] (km^2)	Calculated moment magnitudes[d] for: Surface length	Rupture width	Rupture area	Observed maximum magnitude[e]
Observed geometries[b]:								
Iceland	Krafla, 1978[f]	6	1.3	7.8	6.0	4.3	4.9	4.1
Africa	Asal, 1978[g]	12	3.5	42	6.3	5.3	5.6	5.3
Estimated Geometries[b]:								
Iceland	Krafla, 1975[f]	3.5	3.5	12.3	5.7	5.3	5.1	5.0
	Krafla, 1978[f]	6	4	24	6.0	5.4	5.4	4.1
	Thingvellir[h]	11	4	44	6.3	5.4	5.7	NA
Africa	Asal, 1978[g]	12	4	48	6.3	5.4	5.7	5.3
USA, California	Inyo Domes[i]	13	4	52	6.4	5.4	5.7	NA
USA, Idaho	Snake River Plain, Arco Rift Zone[j]	5	4	20	5.9	5.4	5.3	NA
		Mean ± 1σ, $n = 8$[k]			6.1 ± 0.2	5.2 ± 0.4	5.4 ± 0.3	
		Mean ± 1σ, $n = 24$[k]				5.6 ± 0.5		

[a] Maximum normal fault length observed at the surface in the volcanic-rift zone or from a volcanic episode produced by dike injection.

[b] For "Observed geometries", rupture width is the maximum-downdip width of the normal fault or depth to the dike top, based on modeling of geodetic data and seismological observations. For "Estimated geometries," rupture width is based on maximum depth for dike propagation, 2-4 km (Gudmundsson, 1984a; Ryan, 1987). In cases where lengths are less than 4 km, the downdip width is assumed to be equivalent to its length. The intent is to estimate the maximum area possible.

[c] Rupture area = surface-rupture length × rupture width.

[d] Calculated using the following relationships (Wells and Coppersmith, 1994): $M_w = 5.03 + 1.19 \times \log_{10}(SRL)$; $M_w = 4.01 + 2.29 \times \log_{10}(RW)$; $M_w = 4.01 + 1.0 \times \log_{10}(RA)$; where M_w = moment magnitude, SRL = surface rupture length, RW = rupture width, and RA = rupture area.

[e] Observed maximum magnitudes obtained from Table 4-2. NA indicates magnitudes not available beacause on no instrumental recordings.

[f] Rubin and Pollard, 1988; Opheim and Gudmundsson, 1989; Rubin, 1992.

[g] Le Dain *et al.*, 1979; Tarantola *et al.*, 1979, 1980; Abdallah *et al.*, 1979; Stein *et al.*, 1991.

[h] Gudmundsson, 1987.

[i] Mastin and Pollard, 1988.

[j] Smith *et al.*, 1989; Kuntz *et al.*, 1990.

[k] Mean and one standard deviation computed using both observed and estimated geometries for surface length, rupture width, and rupture area, and all calculated moment magnitudes combined.

distributions and focal mechanisms indicating transcurrent displacement, as a tectonic response of the volcanic pile and underlying basement to stresses associated with dike intrusion. Other relationships are more ambiguous, such as the M 7.0 Izu, Japan earthquake and the M 4.3 to 7.5 Taupo volcanic zone earthquakes, New Zealand (Table 4-4).

Seismicity associated with magmatic processes is not always directly coincident with magma intrusion. In some cases, differential stress associated with prolonged magma intrusion is accumulated on nearby structures that sometimes lack surface expression until some stress threshold is exceeded and a large-magnitude, "tectonic" mainshock-aftershock sequence occurs. Examples of such phenomena include the 1983 M_L 6.6 Kaoiki, Hawaii, earthquake (Buchanan-Banks, 1987), which involved strike-slip displacement midway between the active volcanoes Mauna Loa and Kilauea, and was probably generated by differential compressional stresses associated with inflation of the magma reservoirs beneath both volcanoes. Bryan (1992) cites structural complexities observed from focal mechanisms as evidence for small-earthquake triggering of large-scale energy release at the bases of volcanic edifices. Swanson *et al.* (1976b) use geodetic data to show that intrusions within Kilauea's east rift zone during the 1960s and early 1970s were wedging the rift apart, and that much of the widening was being accommodated by compression and uplift on the south flank of the rift zone. The eventual failure of the adjacent Hilina fault system (Fig. 4.1D) produced the M_s 7.2 Kalapana earthquake in 1975.

Instead of inducing earthquakes on adjacent structures, the stresses imposed by intruding magma also seem capable of operating in the converse sense: Magma intrusion in extensional terrains is believed to inhibit seismicity by supplanting tectonic normal faulting (Parsons and Thompson, 1991). Thus, Bursik and Sieh (1989) attribute the absence of Holocene oblique-slip faulting along a portion of the Sierran range front to extensional magmatism of the adjacent Mono Craters (Fig. 4.1B). The relative aseismicity and low relief of the eastern Snake River Plain volcanic province, in contrast to the surrounding seismically active, topographically rugged Basin and Range (Fig. 4.1A), is attributed to the substitution of basaltic-dike intrusion for normal faulting in the eastern Snake River Plain (Smith *et al.*, 1989; Rodgers *et al.*, 1990; Parsons and Thompson, 1991; Hackett and Smith, 1992; Jackson *et al.*, 1993).

4.4.3.4 Comparison of Moment-Magnitude Calculations to Observational Seismicity

Table 4-5 gives the results of moment-magnitude calculations for normal faults within volcanic-rift zones based on surface-rupture lengths, rupture (down-dip) widths and rupture areas, using the empirical relationships between these fault-rupture dimensions and moment magnitudes (Wells and Coppersmith, 1994). The unweighted mean of 24 moment-magnitude calculations is 5.6 ± 0.5, and expectedly this result is greater than the observed earthquake maxima during dike-injection episodes (See Table 4-2). In the moment-magnitude calculations of Table 4-5, field observations of surface-rupture lengths are used to assess moment magnitude from the empirical relationships of Wells and Coppersmith (1994). Subsurface-rupture lengths are not used, since it is difficult to determine subsurface-rupture dimensions of dike-induced normal faults, based on the typically diffuse seismic swarms associated with incremental fault ruptures (as opposed to tectonic mainshock-aftershock seismicity patterns). Rupture widths are determined from the estimates of down-dip fault widths based on the shallow crustal depths (2 to 4 km) along which dikes propagate. We assume that normal faults terminate near the tops of the dikes, and possibly extend as deep as 4 km. The surface-fault lengths and down-dip widths are then used to estimate the rupture areas.

The moment-magnitude calculations based on these fault-rupture dimensions assume single-rupture events, therefore the results give an upper bound for the moment magnitudes of purely magma-induced earthquakes. This is because the dike-induced faults in fact ruptured incrementally, produced many earthquakes, and were formed in the shallow crust, where deviatoric stress and rigidity are lower than at depth. Typical values for midcrustal rigidity are about 3 × 10^{11} dyne/cm^2 (Hanks and Kanamori, 1979), but shear modulus decreases rapidly within a few kilometers of the surface, and crustal rigidity in the shallow crust where dikes are intruded is therefore likely to be lower. Thus, crustal rigidity values ranging from 0.5 to 1.8 × 10^{11} dyne/cm^2 are required in order to account correctly for observed deformation volumes (Filson *et al.*, 1973; Mori *et al.*, 1989; Stein *et al.*, 1991).

Wells and Coppersmith (1994) also develop relationships between moment magnitude and maximum displacement, average displacement, and subsurface rupture length. The displacement–magnitude relationships are not used because deformation associated with earthquakes having moment magnitudes of less than approximately 5.7 may be a secondary effect from ground shaking and not due to primary rupture of the fault (Wells and Coppersmith, 1994). Furthermore, displacements along dike-induced normal faults may not form during single-event ruptures, but are commonly the result of many incremental displacements during dike intrusion, or of multiple dike-intrusion events.

A sound approach to estimating the maximum magnitude from the empirical relationships of moment magnitude and the fault-rupture dimensions shown in Table 4-5 is to apply weighting factors to the rupture dimensions. Rupture dimensions which are best constrained are given higher weights. A weighted average can then be calculated to derive a maximum moment magnitude.

4.5 CONCLUSIONS

From the standpoint of natural hazards, magma-induced earthquakes are important because they can cause significant damage and injury in the epicentral region, and they frequently occur prior to eruptive activity. Many earthquakes in volcano-extensional regions are directly related to magma intrusions, particularly dikes, which propagate along self-induced fractures and cause deformation on extensional faults and fissures. Other earthquakes result from redistribution of the load of the volcano or from caldera collapse. Still others, tectonic earthquakes in the vicinity of volcanoes, are indirectly induced by magma.

Volcanic-rift zones are diffuse belts of extensional ground deformation, dominated by tensional fissures and small-offset normal faults, and underlain by dike swarms. Eruptive fissures commonly bisect a central graben, or lie between two sets of anastomosing fissures. Normal faults, monoclines, and fissures developed along volcanic-rift zones are individually similar to those formed by nonmagmatic tectonic mechanisms. The aggregate geometry of the surface-deformation features, their spatial and temporal association with cogenetic volcanic materials, and geophysical evidence for shallow magma intrusions are among the criteria for distinguishing magma-induced extensional structures from nonmagmatic ones.

Recurrence estimates of magma-induced faulting and seismicity should be based largely on geochronology and mapping of the coseismic volcanic materials, rather than on trenching of surface faults or fissures. Postseismic colluvial wedges are usually not observed in volcano-extensional terrains, due to the small throws of magma-induced faults and the erosional resistance of lithified volcanic materials. Fissures and scarps in these environments can sometimes be dated by the innovative use of conventional geochronologic methods, such as thermoluminescence dating of baked sediments beneath cogenetic volcanic materials, or the use of *in situ* cosmogenic radionuclides to date geomorphic surfaces exposed during deformation. An integrated approach should be adopted, incorporating multiple geochronometric methods.

Coseismic field investigations of the Icelandic and Hawaiian volcanic-rift zones clearly demonstrate that meter-scale displacement of dike-induced normal faults occurs without large-magnitude seismicity. During the last century, worldwide observations of dike-induced seismicity indicate that such earthquakes rarely exceed M 5.5 and most have M < 4.5. Earthquakes at calderas and central volcanoes have somewhat higher maxima (M 6.5 to 7.0), owing to greater depths of origin or to the energy released by fracturing of large volumes of roof rocks atop shallow magma chambers. The maximum magnitudes of earthquakes associated with two caldera-collapse events (Galapagos and Katmai) generally conform with the calculated energy released by down-drop of the observed caldera volumes.

Indirectly related to volcanism but nonetheless important are the large-magnitude (M 7+) tectonic earthquakes that can occur on adjacent structures as a result of protracted magma intrusion or direct triggering. Such earthquakes are most likely to occur in non- extensional settings where compressional stress can accumulate near intrusions. Knowledge of magmatic processes and volcanic recurrence should influence the assessment of seismic recurrence along adjacent tectonic structures, but traditional paleoseismic techniques and empirical moment magnitude–fault rupture dimension relationships can be applied to these structures.

Assumptions that might lead to overestimation of earthquake frequency and magnitude in volcanic-rift zones include (1) association of a dike-intrusion event with each volcanic vent; (2) association of a maximum-magnitude earthquake with each dike-intrusion event; (3) treating the rupture mechanics of normal faulting during dike injection as if it were analogous to fault rupture during large-magnitude, tectonic earthquakes; and (4) using midcrustal rigidity values in moment-magnitude calculations for shallow, dike-induced events. These overestimates can be rectified by incorporating dike-intrusion and volcanic-rift zone concepts into the assessment: (1) use of geologic information to group volcanic vents into eruptive episodes confidently, based on physical and chronologic relationships; (2) use of statistical compilations of worldwide, co-intrusive seismic sequences to quantify the probability of a maximum-magnitude event; (3) application of the mechanics of dike intrusion, which shows that most dikes propagate laterally in the shallow crust at rates of several kilometers per hour; dike-induced faults therefore develop incrementally, in tandem with dike propagation, rather than catastrophically; and (4) use of more reasonable values for crustal rigidity in shallow-crustal environments, based on observed lithologies and seismic velocities in the region of interest.

The influence of local magma intrusion on the seismicity of adjacent tectonic structures is in some places unequivocal, in other places debatable, and in still others yields diametrical consequences: magma intrusion seems capable of inducing, inhibiting, and changing the style of tectonic extension. Magma intrusion, volcanism, and tectonism are concurrent processes of crustal extension. The nature of their interaction is an emerging area of inquiry that will occupy geologists and seismologists into the foreseeable future. We offer this contribution as a first step toward the incorporation of volcanic seismicity into the field of paleoseismology. We will have achieved our purpose if this discussion helps paleoseismologists to recognize volcano-extensional structures, to interpret them within the context of magmatic processes, and to advance the field by developing and applying some of the methods we have suggested.

Acknowledgments

Our current thinking has evolved as a result of many discussions over several years of collaboration with private and government researchers at the Idaho National Engineering Laboratory, where we have attempted to assess seismic hazards within the aseismic, volcano-extensional environment of the eastern Snake River Plain. We are grateful to Kevin Coppersmith, Steve Forman, Mark Hemphill-Haley, Nick Josten, Larry Mastin, Jim McCalpin, Tom Parsons, Dave Pollard, Dave Rodgers, Walt Silva, George Thompson, Peter Wallmann, Don Wells, Ivan Wong, and Jim Zollweg for helping us to formulate and focus our ideas. The manuscript was improved through constructive reviews by Jim McCalpin, Tom Parsons, Jim Zollweg, and Bob Creed. This work was supported by the U.S. Department of Energy, Office of New Production Reactors, and Office of Environmental Restoration and Waste Management, under DOE Idaho Field Office contract DE-AC07-76ID01570.

Chapter 5

Paleoseismology of Compressional Tectonic Environments

Gary A. Carver
James P. McCalpin

5.1 INTRODUCTION

Large compressional earthquakes in the upper crust, and even larger plate-boundary earthquakes in subduction zones, produce surface deformation recorded by displacements on reverse or thrust faults, by growth of surface folds, and by changes in the elevation of the land surface. Study of such stratigraphic and geomorphic features yields information about the size and recurrence of large earthquakes that is not available from historic sources in many regions. Coupled with regional-scale knowledge about structure, geophysics, and landscape development, such data allow characterization of seismic fault source zones in regions dominated by compressional tectonics (Chapter 9). We begin this chapter with a brief overview of compressive structures on regional scales and then focus on paleoseismic evidence for coseismic compressive deformation on local and site scales. Most examples are drawn from our experience in western North America.

Convergent plate margins—the great belts of active tectonism, seismicity, and volcanism that release most global seismic energy (Minster and Jordan, 1987)—are the largest and most widespread compressional tectonic environments. The majority of the earth's major earthquakes have occurred on the largest of these belts, the circum-Pacific "Ring of Fire" (Zhang and Schwartz, 1992) (Fig. 5.1). Another great belt of plate convergence and continental collision extends through central Asia and the Mediterranean. Plates are also converging along the Antillies and the Windward Islands in the eastern Caribbean, and in the Scotia arc of the south Atlantic Ocean. Other regions dominated by compressional tectonics include the great zone of continental collision between India and Asia (Molnar and Qidong, 1984) and the subduction and collision zones in northern Africa, southern Europe, and the Middle East (Meghraoui *et al.*, 1986; Vita Finzi, 1986) . Local compressional tectonic environments are found at restraining bends or stepovers along transform and strike-slip faults, along transpressive strike-slip faults, in fold and thrust belts in some backarc regions, and in some continental interiors.

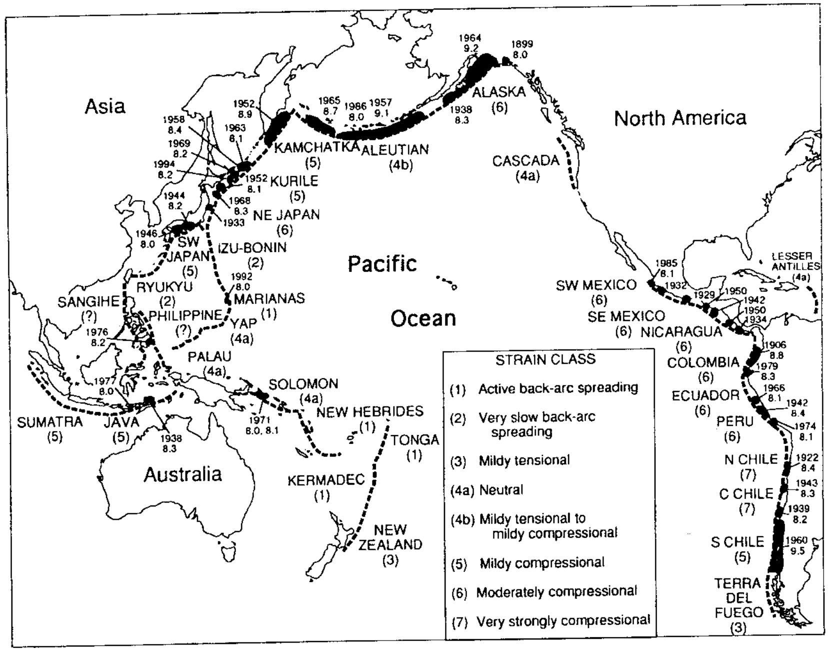

Figure 5.1 Principal Pacific rim subduction zones and some modern great subduction earthquakes ($M_w > 8$). Classification of the subduction zones is based on Jarrard's (1986) comparison of large-scale structure and kinematic characteristics and reflects a range from strongly extensional (Class 1, back-arc spreading) to strongly compressive (Class 7, active folding and thrusting). Most of the modern great subduction earthquakes have occurred along the eastern and northern Pacific where (in general) younger oceanic plates are subducting beneath continental margins. Earthquakes of $M_w < 8$ are common along subduction zones in the southwestern Pacific, where generally older oceanic plates are subducting beneath other oceanic crust, but few great earthquakes have been recorded.

Stratigraphic and geomorphic features formed by compressive faulting and folding are commonly more diverse, and occasionally more subtle, than those formed by extensional or strike-slip faulting. Most field evidence for compressive paleoearthquakes reflects sudden changes in local rates of deposition or erosion that indirectly result from earthquake-induced surface deformation. In some instances certain types of field relations, such as stratigraphically bracketed fault slip (Sec. 5.3.4), record the size of individual earthquakes. More commonly, evidence from a single site cannot be assigned an unambiguous paleoseismic origin until similar evidence, from multiple sites, is shown to be of similar origin and age. Paleoearthquake characteristics such as magnitude, location, and the source fault often become apparent only after observations at many sites are integrated into a composite view of coseismic deformation across a large region. In such situations, accurate interpretation of paleoearthquakes depends on understanding both the regional tectonic setting and the regional and local patterns of coseismic deformation.

5.1.1 Organization of This Chapter

Due to the wide variety of compressional tectonic environments, this chapter is subdivided somewhat differently than the chapters on extensional (Chapter 3) and strike-slip (Chapter 6) environments. Paleoseismic features formed by reverse or thrust faults on land are described in a manner similar to that used in Chapters 3 and 6; that is, geomorphic evidence first (Sec. 5.2) and stratigraphic evidence second (Sec. 5.3). Evidence for prehistoric secondary fault displacement (Sec. 5.4) and coseismic folding (Sec. 5.5) is described separately. Dating methods are not discussed in a separate section, but are integrated into Secs. 5.2 through 5.5.

The coseismic deformation associated with subduction zone earthquakes is sufficiently unique that it demands a separate treatment in Secs. 5.6 through 5.10. There are several reasons for this organizational distinction. First, the seismogenic megathrust crops out on the seafloor under great water depths, so on-fault paleoseismic evidence (the focus of most on-land fault studies) cannot be directly observed. Second, the main paleoseismic indicator on land masses near subduction zones is regional vertical deformation, usually as evidenced by relative sea-level changes. Third, the presence of paleo sea-level datums often allows reconstruction of the interseismic as well as the coseismic parts of prehistoric earthquake deformation cycles, something that is generally not possible on continental faults. The best preserved paleoseismic indicators, and the means of interpreting them thus fall more under the classical fields of Quaternary stratigraphy and geomorphology, rather than utilizing the more specialized fault profiling and trenching techniques developed for study of most on-land faults.

5.1.2 General Style of Deformation in Compressional Zones

The most common seismogenic structure in compressional tectonic environments is the *thrust fault* (a low-angle reverse fault). Movement on thrusts results in thickening of the vertical section of crust cut by the fault and shortening of the horizontal distance across the fault. In many geologic environments, thrust faults bifurcate as they project toward the surface, producing complex fault systems at the surface. Individual fault splays at all scales separate *thrust-bounded slices* of rock, and these slices are often stacked by repeated fault offset. At depth the splays merge and the dips of the faults decrease until they merge into near horizontal *detachments* below which shortening does not occur through brittle deformation.

or at the ends of overlapping imbricate faults. Other structural indications of possible segment boundaries are sharp changes in orientation of the fault, intersections with branch faults, abrupt changes in dip, and changes in net slip (Knuepfer, 1989). Geomorphic expressions of segmentation may be seen as differences in height of uplifted topography on the hanging wall, or abrupt changes in strike and limits of surface folding. However, few detailed studies have been conducted on the segmentation of shallow intraplate thrust faults.

5.1.3 Historic Thrust Earthquakes as Modern Analogs for Paleoearthquakes

Well-studied historic thrust-fault ruptures form modern analogs for interpreting the paleoseismic record (Table 5-1), and include earthquakes in fold and thrust belts (Algeria, 1980), convergent continental plate boundaries (*collision zones;* Iran, 1978; Armenia, 1988), regions near transpressive bends in plate-boundary transform faults (California, 1952, 1971, 1983; New Zealand, 1971), and stable continental interiors (Australia, 1968, 1979, 1986, 1988). These historic thrust earthquakes have produced a wide spectrum of shallow structures and scarp morphologies, resulting from both slip on multiple fault planes and folding. For example, fault-propagation folds and fault-bend folds typically formed in the hanging wall in unconsolidated or semiconsolidated deposits (e.g., Berberian and Qorashi, 1994). These folds occur at all scales and commonly reflect changes in dip of the underlying thrust where it intersects stratigraphic sequences of differing character.

Table 5-1

Well-Studied Historic Reverse and Thrust Fault Surface Ruptures

Date and magnitude[a]	Fault/area	Maximum displacement[a] (m)	Rupture length[a] (km)	Reference
1952, M_s7.7	Kern County, California	3.0	57	Buwalda and St. Amand (1955)
1968, M_s6.9	Meckering, Australia	3.5	37	Gordon (1971); Gordon and Lewis (1980)
1968, M_s7.1	Inangahua, New Zealand	1.8	5	Lensen and Otway (1971)
1971, M_s6.5	San Fernando, California	2.5	16	USGS (1971); Bonilla, (1973); Kahle (1975)
1978, M_s7.5	Tabas-e-Goldshan, Iran	3.0	85	Berberian (1979); Haghipour *et al.* (1979)
1979, M_s6.1	Cadoux, Australia	1.5	15	Lewis *et al.* (1981)
1980, M_s7.3	El Asnam, Algeria	6.5	31	Yielding *et al.* (1981); Philip and Meghraoui (1983)
1986, M_s5.8	Marryat Creek, Australia	0.9	13	Machette *et al.*, 1993
1988, M_s6.3–6.7	Tennant Creek, Australia	1.1	32	Crone *et al.*, 1992
1988, M_s6.8	Spitak, Armenia	2.0	25	Philip *et al.* (1992)

[a] From Wells and Coppersmith (1994).

Perhaps due to the complex interaction of faulting and folding, surface displacement on thrust faults tends to be irregular along strike, even more so than for other fault types (Fig. 5.3). [See Baljinnyam *et al.* (1993, their Fig. 44) for a geometric reconstruction of displacement from fault scarp dimensions.] Measurements of fault separation between piercing point landforms neglect the off-fault deformation and provide only a minimum measure of the actual (geodetic) displacement in the shallow subsurface. As in normal surface faulting, the maximum displacement often occurs in one or more isolated peaks and it far exceeds the median or mean displacement. Unlike the normal and strike-slip ruptures described in Chapters 3 and 6, the thrust ruptures shown

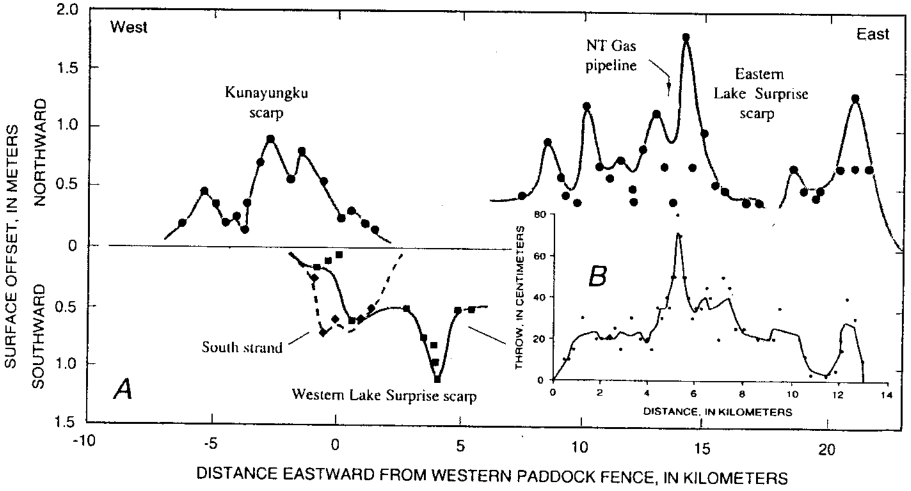

Figure 5.3 Vertical surface offset (or fault throw) along strike in two historic thrust faulting earthquakes. (A) Vertical surface offset associated with the 1988 M_s 6.3–6.7 Tennant Creek, Australia, earthquakes. Field measurements shown by solid symbols, curve represents smoothed data. From Crone *et al.* (1992). (B) Fault throw associated with the 1986 M_s 5.8 Marryat Creek, Australia, earthquake. Small circles show field data, line represents smoothed data. From Machette *et al.* (1993). Note how maximum offset occurs in a narrow spike and is roughly twice as large as average offset.

in Fig. 5.3 do not have long tails of low slip; instead, slip decreases abruptly at the ends of the rupture. There are insufficient data on thrust ruptures to determine if such a pattern is typical. Wells and Coppersmith (1994, Table 3) note that empirical regressions of reverse fault displacement (average and maximum) on historic earthquake magnitude shows 50% more variance than for other fault types.

One of the best documented examples of combined coseismic folding, thrust faulting, and secondary faulting occurred in northern Algeria during the 10 October 1980 El Asnam earthquake ($M_s = 7.3$). Focal mechanism studies indicate that rupture initiated at a depth of about 12 km and extended along a 30-km-long northeast trending northwest dipping thrust fault (Ouyed *et al.,* 1981). The rupture propagated to the surface along the base of low anticlinal hills on the margin of the Chelif Valley (Fig. 5.4). Concrete irrigation ditches were offset and shortened, and moletrack scarps formed in cultivated fields and orchards and across the valley floor where the scarp was 3.2 m high (King and Vita-Finzi, 1981). Net slip at depth was estimated to be as much as 6 m based on seismic moment, but thrust offset at the surface was considerably less. The slip deficit appears to have been taken up by the growth of the anticlines in the hills above the rupture surface.

King and Vita-Finzi (1981) observed several types of geologic evidence produced by the coseismic folding. Numerous secondary normal fault scarps up to several meters high formed along the crests of a large asymmetrical anticline in the upper thrust sheet. The normal faults faced both northwest and southeast and bounded long shallow compound grabens aligned in a 1- to 2-km-wide zone, subparallel to the thrust, along the fold hinge line. The normal faults were interpreted to be the result of tension (i.e., bending-moment faults) produced in the upper part of the anticline as it flexed during the earthquake. Long-term growth of the anticline is reflected by increasing bedding dips of successively older Quaternary and late Tertiary sediments. Paleoslip on some of the bending-moment normal faults was indicated by degraded pre-1980 scarps that were reactivated during the earthquake.

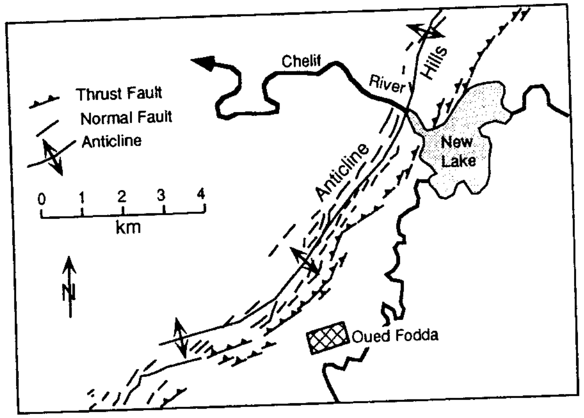

Figure 5.4 Map showing deformation during the 1980 El Asnam, Algeria, earthquake (modified from King and Vita-Finzi, 1981). Surface rupture on the seismogenic thrust produced small discontinuous scarps along the base of the anticlinal hills. More obvious in the field shortly after the earthquake were many normal fault scarps and grabens along the crest of the hills. These normal faults reflect coseismic growth of the anticline above the thrust. Additional evidence of growth of the fold during the earthquake was damming of the Chelif River near the axis of the fold almost 2 km downstream of the surface rupture on the thrust.

A second geologic response to coseismic fold growth was disruption of the Chelif River where it crossed the anticline. Immediately following the earthquake, a lake 5 to 6 m deep formed upstream of where the river crossed the deformed zone. King and Vita-Finzi (1981) report "the lake was dammed not by the thrust fault scarp, but by a gentle upwarp 1 km further down the valley." The upwarp corresponds with the crest of the anticlines cut by the normal faults. Investigation of stratigraphy near the lake revealed evidence for previous ephemeral lakes presumably formed by similar paleoseismic displacements on the El Asnam thrust. Late Holocene fluvial terraces that cross the fold downstream from the lake are also progressively deformed. Archaeological materials in the folded alluvial and lake deposits allowed estimates of the age of the pre-1980 event at about 500 yr B.P.

5.2 GEOMORPHIC EVIDENCE OF THRUST PALEOEARTHQUAKES

The most direct geomorphic evidence of a paleoearthquake in a continental compressional environment is a thrust fault scarp. However, many, large shallow thrust earthquakes are generated by fault rupture that is confined to the subsurface, and no fault-zone landforms may be created. Thus, in compressional tectonic environments many M < 7 paleoearthquakes may not be accompanied by any recognizable geomorphic expression of faulting. If thrust fault scarps are created, they are typically more sinuous and irregular than for other fault types, being composed of either short, disconnected sections (Gordon and Lewis, 1980; Crone *et al.,* 1992) or producing a continuous but "serrated" rupture trace with zigzags on the scale of meters (photographs in Haghipour *et al.,* 1979). Where thick sequences of late Cenozoic sediments are faulted, the thrusts commonly reach the surface as imbricate faults, with many discrete slip planes.

Over geologic timescales, repeated thrusting typically juxtaposes hard bedrock in the hanging wall against youthful poorly consolidated footwall sediments. This contrast in material properties tends to concentrate slip in a narrow zone at the base of a geomorphically distinct, uplifted, and (commonly) folded range front. Here active slope processes, stream erosion, and alluvial fan deposition may act together to obscure the fault trace (Beanland *et al.*, 1986). Newer thrusts may cut rolling terrain on the hanging wall or gentle depositional slopes on the buried footwall, having propagated through some thickness of unconsolidated sediments.

Paramount in the recognition of past slip events on thrust faults is information on the near-surface structure and kinematics of the fault at the place where the paleoseismic evidence is found. Considerable along-strike variability in structural style and scarp type is common on many thrusts, and complex structure is more common than a single simple fault, especially in those depositional environments most likely to record surface faulting events. Because thrusting characteristically distributes slip on multiple imbricate faults and as off-fault folding, the paleoseismic study of thrusts requires measurements across the entire zone of surface deformation.

5.2.1 Initial Morphology of Simple Thrust Fault Scarps

The initial form of a thrust fault scarp can be more varied than for other fault types, due to the complex nature of mixed low-angle faulting and folding, and to the complex response of surficial materials. Gordon (1971) and Philip *et al.* (1992) described eight and seven types of thrust fault scarp morphologies, respectively, based on historic surface ruptures in Australia (1968) and Armenia (1988) (Fig. 5.5). The controls on scarp morphology include amount of slip, sense of slip, geometry of the fault(s), properties of surficial materials, and topography (Weber and Cotton, 1980, p. 20; Philip *et al.*, 1992, p. 144).

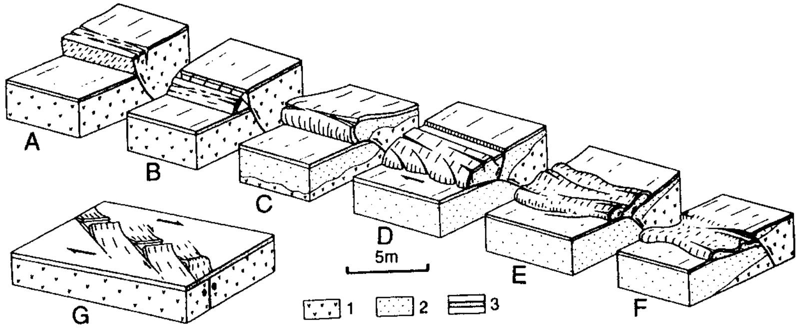

Figure 5.5 Types of thrust fault scarps produced along the Spitak fault during the 1988 M_s 6.9 Spitak, Armenia, earthquake. (A) Simple thrust (or reverse) scarp. (B) Hanging wall collapse scarp. (C) Simple pressure ridge. (D) Dextral pressure ridge. (E) Back- thrust pressure ridge. (F) Low-angle pressure ridge. (G) En-echelon pressure ridges. 1, bedrock; 2, soft Quaternary sediments; 3, turf. [From Philip *et al.* (1992); reprinted with permission of Blackwell Scientific Publishing Company.]

Steeply dipping (>45°) reverse faults in bedrock produce *simple thrust scarps,* such as those shown in Fig. 5.5A and Fig. 5.6. Steep faults in brittle unconsolidated materials result in *hanging wall collapse scarps* (Fig. 5.5B), which result when the overhanging scarp collapses, usually during seismic shaking. At lower dip angles, thrust faulting produces *pressure ridges* (Figs. 5.5C–F). The type of pressure ridge is dependent on surface material rheology and the magnitude of slip. More brittle materials produce more fissuring of the leading edge of the thrust (Figs. 5.5C and D), whereas more displacement increases the chance of developing a secondary normal fault in the hanging wall (Fig. 5.5D). In plastic surface materials (moist silt and clay, turf), pressure ridges have smoother fronts and may display *backthrusts* (Fig. 5.5E) or low-angle pressure ridges (Fig. 5.5F), but as thrust displacement decreases below ca. 1 m all pressure ridge types merge into a single type of small *moletrack.*

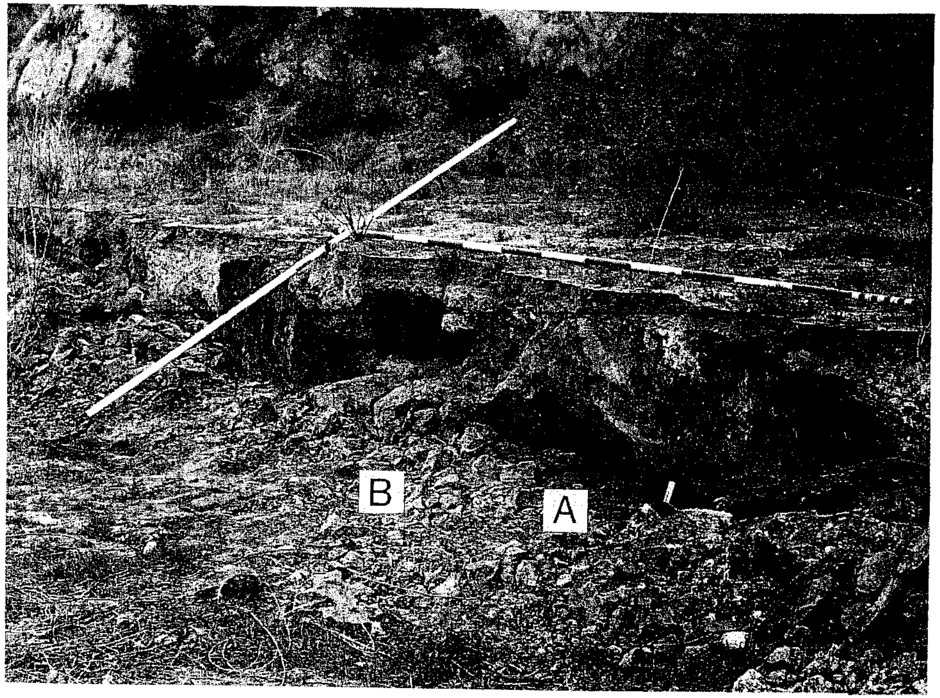

Figure 5.6 Photograph of the fresh overhanging reverse fault scarp created by the 1971 M_L 6.6 San Fernando, California, earthquake. Faulted material is a weakly consolidated Tertiary sandstone. Large divisions on the horizontal rod are 0.3 m, scarp is ca. 1 m high. Above A, an overhanging scarp is defined by the fault plane that dips at 65° (compare to Fig. 5.11A). Above B, the overhang has collapsed, resulting in a hanging wall collapse scarp (Figs. 5.5B, 5.11B). [Photograph courtesy of Virgil Frizzell and the U. S. Geological Survey. From USGS (1971).]

An increasing oblique component of slip results in en- echelon pressure ridges (Fig. 5.5G) or oblique tension fissures in pressure ridge fronts (Fig. 5.5D).

Hanging wall ramp folds generated by changes in fault dip at shallow depths (meters to tens of meters) can generate distinct geomorphic *facets* at the top of scarps. These facets resemble the planar bevels in the upper parts of large compound normal fault scarps that sometimes reflect multiple paleoearthquakes. On thrusts, however, the facets may be part of the initial scarp form and independent of the paleoseismic history of the fault and degradational processes acting on the scarp. Some thrust tips form propagation folds at the surface with decreased slip on the fault tip. These folds can also produce multifaceted scarp profiles (Suppe, 1983).

Widely distributed slip generally does not result in the formation of steep scarps, but rather pervasive ground cracking and gentle flexure of the ground surface across a wide fault zone. Microfaulting may occur locally, and mesoscale thrusts may also be present in zones of distributed slip. Where this style of surface thrusting deforms low-gradient terraces the fault trace is expressed as a wide gentle warp of the terrace surface.

5.2.2 Degradation of Thrust Fault Scarps

Surface displacement on a single thrust fault plane initially results in an overhanging scarp, but in unconsolidated deposits such overhangs collapse during or soon after creation. For example, even in weakly consolidated Tertiary sandstone and conglomerate faulted by the 1971 San Fernando, California, earthquake, >50% of the ca. 0.3- to 1-m-high overhanging free face (Fig. 5.6) had collapsed after three months (Kahle, 1975, p. 133). The *collapsed tip* of the hanging wall thus creates a free face and a steep debris slope that buries the fault tip. If the free face exceeds the angle of repose in unconsolidated materials, the scarp will progress through successive gravity-, debris-, and wash-dominated degradation stages similar to those described earlier for normal faults (Chapter 3). Many degraded reverse fault scarps are asymmetric in cross-profile, with the steepest part of the scarp lying downslope of the scarp midpoint. This asymmetry, caused by repeated overriding of the scarp-derived colluvial wedge (Sec. 5.3.2), contrasts with the general symmetry of normal fault scarps (Chapter 3). Where repeated movement has generated a high escarpment, reverse faulting may be expressed as a long chain of landslides which obscures the fault trace itself. Such landslides formed along much of the length of the Patton Bay fault scarp on Montague Island during the 1964 Alaskan subduction earthquake (Plafker, 1969a).

5.2.3 Interaction of Thrust Fault Scarps with Geomorphic Surfaces

Youthful surface thrusting is most easily recognized if planar landscape features such as fluvial or marine terraces, alluvial plains, fans, and other constructional geomorphic surfaces are cut by the fault. Thrust faults are often difficult to recognize where the fault crops out in areas of steep or irregular topography. In such settings fault scarps become difficult to distinguish from landslide and sackung scarps (see Chapter 8), and are quickly removed by rapid erosion. Thus, one strategy useful in identifying active thrusts is to examine terraces and other planar geomorphic surfaces for evidence of offset or warping. Because many thrusts reach the surface as broad zones of distributed displacement or folding, the offset may not be concentrated on a distinct scarp and may become apparent only after careful examination of the terrace, or after measuring and plotting long topographic profiles that cross the fault.

5.2.3.1 Fluvial Terraces

The interaction of cyclic fluvial terrace cutting, such as that associated with glacial-interglacial climate changes, and recurrent surface faulting can result in terrace sequences that record the faulting history. If terraces are the result of processes independent of movement on the fault, offset produces vertical displacement of the terrace profile. Paleoseismic events or groups of events are thus recorded by sequentially larger vertical separations on higher regional terraces, in a manner similar to that for normal faults (Chapter 3) (see also Beanland and Barrow-Hurlbert, 1988, Fig. 10). Additionally, paleoseismic records are formed when faulting crosses actively aggrading floodplains. Surface offset of vertically accreting overbank sediments produces scarps, moletracks, secondary faults and fractures, and other fault line disturbance of the bedded floodplain sediments that become unconformably overlain by subsequent overbank flood sequences. Such paleoseismic events show up as unconformities bounding progressively more deformed flood plain sediments (Sec. 5.3.5).

Broadly distributed thrusting, surface warping, and folding cannot generally be detected except where planar geomorphic surfaces are deformed. Wide zones of folding, warping, or distributed microfaulting result in obvious disturbance of terraces and in different terrace elevations across the fault. Careful surveys of the terrace and plotting of profiles are often necessary to detect the fault and measure the vertical separation. The elevation differences between the correlative terrace segments on either side of the zone of deformation represent the vertical separation across the fault and provide the best datum for measurement of fault slip, even if a single narrow fault zone cannot be pinpointed in the field.

5.2.3.2 Marine Terraces

Along uplifted coasts raised marine terraces are excellent geomorphic reference surfaces that record thrust faulting and folding. Paleoearthquakes can be interpreted from differences in the elevation along the shore-parallel profile of faulted late Holocene terraces on rapidly emerging coastlines. Sudden elevation differences in the profile are interpreted to reflect the vertical component of displacement on the fault. Where late Holocene terraces are faulted, reverse or thrust displacement lifts the shoreline and raises the terrace on the upthrown side of the fault. If vertical displacement is great enough a new shoreline is established seaward of the newly raised terrace. Simultaneously the shoreline on the downfaulted side of the fault may be submerged and a new shoreline established landward of its pre-earthquake position.

Using such evidence, paleoearthquakes have been interpreted on the Seattle fault in Puget Sound, Washington (Bucknam *et al.*, 1992). The Seattle fault is not exposed at the surface, but its location is indicated by a large gravity anomaly that strikes east-west across the southern part of Puget Sound. On the eastern side of Whidbey Island a broad late Holocene terrace is elevated about 7 meters above sea level south of the fault. North of the fault this terrace is absent, and late Holocene subsidence has been dominant, as indicated by salt marsh peats and archeological sites buried by tsunami sand deposits. The subsidence has been dated to about 1100 yr B.P. (Atwater and Moore, 1992).

Where thrusts intersect emerging coastlines, long-term (late Pleistocene) slip rates can sometimes be determined from raised and faulted glacioeustatic marine terraces (Fig 5.7). If the fault cuts flights of terraces (Fig. 5.7A), cumulative displacement can be measured across the fault for each high sea-level stand represented in the terrace sequence (Fig. 5.7D). The vertical component of displacement is reflected by the scarp height, that is, the elevation difference across the fault for each of the terraces. A check on the long term slip rate is possible by comparing the uplift rate determined from the terrace elevation and the age of terraces on either side of the fault (Figs. 5.7B and C; see also Lajoie, 1986). The difference in uplift rates (0.77 to 0.33 mm/yr in Fig. 5.7) should match the vertical rate for separation on the fault (in Fig. 5.7D, 0.42 mm/yr). Although these slip rates do not define parameters of any individual paleoearthquakes, they do provide a starting point from which to estimate possible combinations of displacement per earthquake, number of earthquakes, and recurrence (see Chapter 9).

5.2.3.3 *Coseismic Terraces*

Paleosurface rupture can sometimes be represented by anomalous fluvial and marine terraces where a stream traverses the hanging wall of a thrust fault. The formation of nickpoints in rivers or streams on the hanging wall of the Patton Bay fault during the 1964 Alaskan earthquake illustrates the process for forming coseismic terraces (similar to the tectonic terraces described on normal faults, Sec. 3.2.5.1). If the stream gradient is low, faulting sometimes raises the hanging wall sufficiently to initiate downcutting into the floodplain. The portion of the stream on the footwall may also be lowered enough to cause deposition. Under extreme cases fluvial systems that cross thrusts and are antecedent to the associated fold and thrust mountains have been dammed

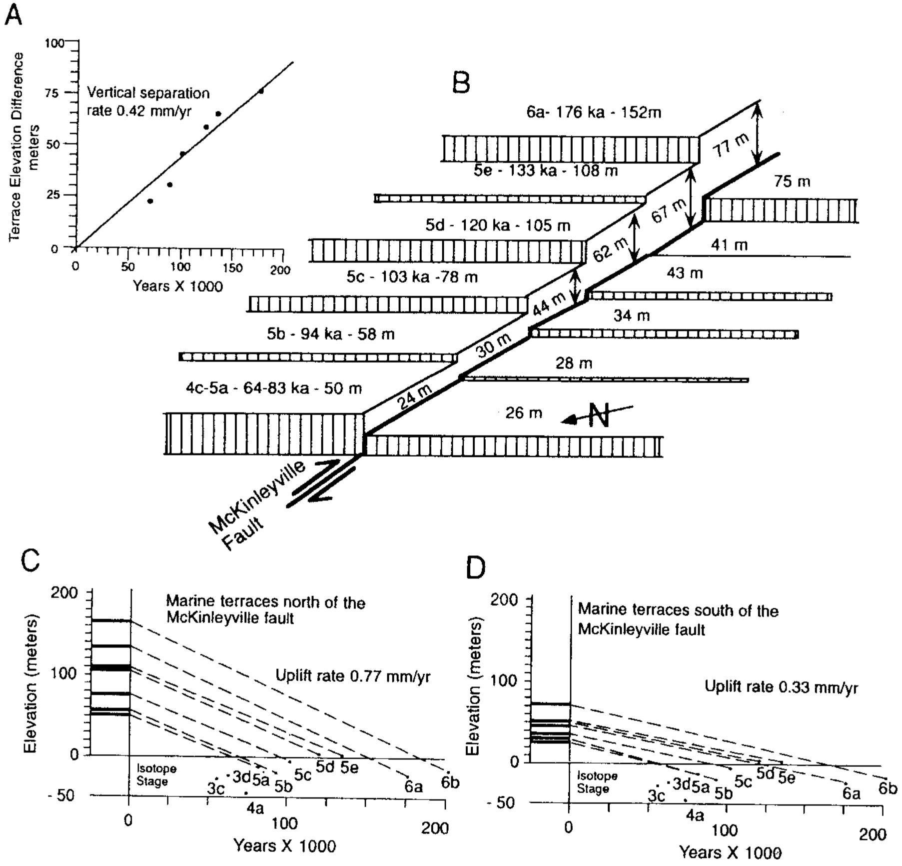

Figure 5.7 Diagram of faulted marine terraces at McKinleyville, northern California. (A) Located in the Mad River fault zone, an upper plate thrust system at the southern end of the Cascadia subduction zone, flights of raised glacioeustatic marine terraces record uplift on either side of the McKinleyville fault. Differences in uplift rates across the fault produce different elevation spacing of terrace treads. The terraces can be distinguished by the soil profiles that reflect a late Pleistocene chronosequence. (B) The vertical separation for each terrace age provides a basis estimate of the fault's late Pleistocene slip rate. (C) and (D) Uplift diagrams showing uplift tie-lines between late Pleistocene highstands (horizontal axis) and present terrace elevation (vertical axis) for the terrace flights on the hanging wall and footwall blocks. The diagrams show relatively constant uplift rates and serve as a check on the age assignments for the terraces (Bull, 1985). [From Carver and Aalto (1992); reprinted with permission of the American Association of Petroleum Geologists.]

by fault displacement. Where such processes occur they are usually cyclic and produce a record of past fault displacements as raised terraces on the upthrust block and buried sediment layers deposited in response to defeat of the stream. (For the response of streams to coseismic folding, see Sec. 5.5.3).

5.3 STRATIGRAPHIC EVIDENCE OF THRUST PALEOEARTHQUAKES

The simplest stratigraphic expression of a surface thrust fault is a single discrete slip plane between the hanging wall and footwall. If slip is repeatedly concentrated in the same narrow zone, large contrasts in materials are common where older more consolidated rocks are thrust over younger less consolidated surficial sediments. Deformation tends to be concentrated at the lithologic boundary where *gouge* or *cataclastic rock* is produced. *Breccia* and *slickensides* are more common, and *fissures* and *rubble* less common, on reverse faults than on other fault types (Bonilla and Lienkaemper, 1991); evidently near-surface compression across the fault zone promotes grinding and prevents the formation of voids. Where poorly consolidated sediments are in fault contact, usually in the footwall, distributed intergranular shear may accommodate some of the total slip. This distributed slip results in clast rotation and the development of an *imbricate fabric* subparallel to the fault plane.

Thrust fault traces are relatively easy to recognize in exposures unless they flatten to subhorizontal or become parallel to bedding in the footwall, as occurred in well-sorted sand and silt beds along the Dunstan fault in New Zealand (Beanland *et al.*, 1986). In poorly stratified gravel, the fault zone can be up to 1 m wide and defined primarily by *oriented clasts* (Fig. 5.8). In eolian sand, the Tennant Creek, Australia, thrust fault was expressed as a 3-m-wide zone of eight parallel thrust faults that had an aggregate net slip of 2.4 m (Crone *et al.*, 1992, pp. A18–A19). The association of multiple, parallel, small-displacement strands with faulted sand was previously noted for normal faults (Chapter 3). If the near-surface deposits are clay rich and saturated, ductile deformation can accommodate much or all of the fault slip and fault propagation folds may form at the thrust tip.

Several trenches have shown that displacement on reverse fault strands may tend to migrate toward the hanging wall over time (Weber and Cotton, 1980; McCalpin, 1989b; Tsukuda *et al.*, 1993, their Fig. 9). This geometry results from successive truncation of earlier refracted thrust traces by later fault traces that refract at higher stratigraphic levels (Fig. 5.9). The implication is that thrust fault *refraction* occurs at a roughly constant depth below the ground surface at a given site, and due to fault-zone deposition, that depth rises stratigraphically with every earthquake. In the idealized geometry of Fig. 5.9, each *colluvial wedge* overlies the fault that immediately predates it, and each wedge is truncated at its upslope end by the next younger fault. This simple pattern can be complicated by continued minor displacements on the earlier, *tectonically beheaded faults*, which leads to *injection* of fault zone breccia into the proximal part of the colluvial wedge. Figure 5.10 shows a field example analogous to Fig. 5.9, where much of the fault zone material is liquefied sand injected between bodies of fault breccia.

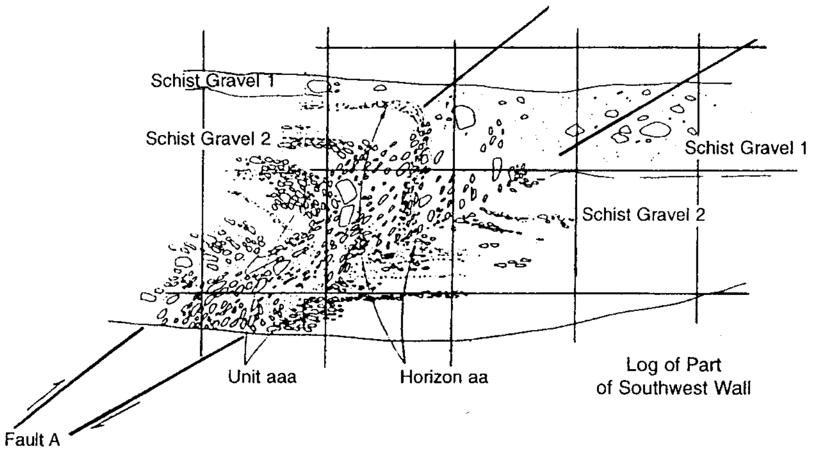

Figure 5.8 Trench log through a reverse fault zone showing definition of the fault by imbricate clast fabric. Grid spacing is 2 m; clasts are drawn to scale. The zone of reoriented clasts is up to 1 m wide. Note the difference in vertical offsets between the schist gravel 1/schist gravel 2 contact across the fault zone (1.1 m) and between horizons aa and aaa in schist gravel 2 across the fault zone (2.3 m). These differences are indicative of multiple faulting events. Trench log DC 316 on the Pisa Fault, South Island, New Zealand. [From Beanland *et al.* (1986); reprinted with permission of the Royal Society of New Zealand.]

5.3.1 Structure and Evolution of Reverse Fault Scarps

Reverse faults (dip > 45°) typically form scarps steeper than the angle of repose of faulted materials (e.g., simple thrust scarps and hanging wall collapse scarps, Figs. 5.5A and B). Tight fault-propagation folds can also produce steep scarps (Carver, 1987b). Both types of scarps may generate scarp-derived colluvium. This colluvium is deposited by gravity, debris, and wash processes as the scarp degrades by parallel retreat and slope decline, in a manner similar to that described for normal faults (Sec. 3.2.4). Scarp-derived colluvium exposed in trenches across reverse faults generally fines upward, but colluvial facies have not been characterized in as much detail as for normal faults (e.g., Nelson, 1992b). Nevertheless, some generalizations can be made based on published trench logs.

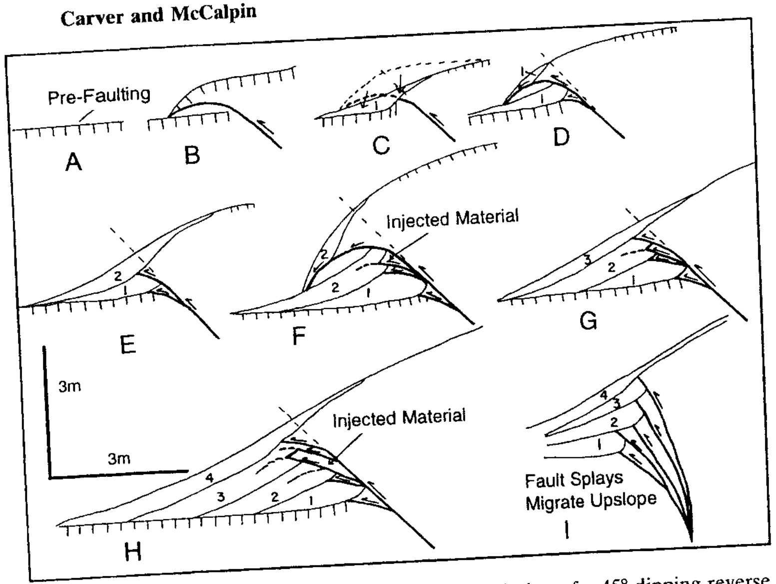

Figure 5.9 An idealized sequence of stages in the evolution of a 45°-dipping reverse fault. Scale at left is approximate. (A) Prefaulting geomorphic surface. (B) First faulting event; fault propagates upwards on a 45° plane, and then refracts to a lower angle near the surface and the overhanging fault tip sags and deforms. "Bulldozing" of the tip may occur, but is not shown. (C) Overhanging fault tip collapses onto prefaulting ground surface, creating colluvial deposit 1. (D) Second faulting event. Fault slip propagates upwards on a 45° plane (dashed line), beheads the refracted part of the first-event fault plane, and then refracts to a lower angle at a higher stratigraphic level, forming an overhanging fault tip. Colluvial deposit 1 is truncated and its proximal part is carried up on the hanging wall. (E) The overhanging tip collapses, and colluvial deposit 2 is formed. (F) Third faulting event. The reverse fault again propagates to a higher stratigraphic level on a 45° plane, beheading the refracted fault plane from the second faulting event. In addition, minor movement on the beheaded fault section(s) results in injection of fault breccia into the lower part of colluvial deposit 2. The reactivated part of the refracted fault (dashed line) flattens and loses definition in the colluvium. The proximal part of colluvial deposit 2 is truncated and carried onto the hanging wall. (G) Collapse of fault tip and eventual deposition of colluvial deposit 3. (H) Geometry after a fourth faulting event, tip collapse, and deposition of colluvial deposit 4. More fault breccia has been injected into the base of colluvial deposit 3. All earlier colluvial wedges (1, 2, 3) are truncated by faulting, only the latest wedge (4) overlies the fault. (I) Alternative geometry where fault refraction occurs at a greater depth, and no injection of breccia occurs.

The basal component of colluvium (lower association of the debris element) is composed of rubble from the collapsed tip of the overhanging fault scarp (Figs. 5.6, 5.11A and B). The rubble may include blocks of the prefaulting surface soil horizons as well as pieces of the hanging wall. Blocks of soils and hanging-wall strata typically possess steep or overturned bedding orientations. The fragile nature of many unconsolidated blocks suggest that they were rapidly shed from the overthrust fault tip and were never exposed to significant moisture or weathering. Such rapid burial of soil blocks, engulfment by a matrix, and subsequent preservation can be accomplished by wind and gravity transport of loose material exposed in the scarp face. Prehistoric collapsed-tip rubble was recognized by Bonilla (1973) in trenches across the 1971 San Fernando, California, rupture, and was used to date the penultimate faulting event.

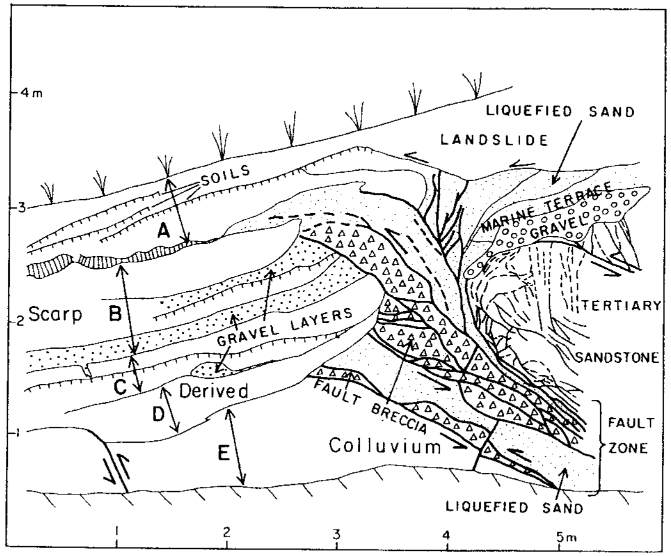

Figure 5.10 Simplified trench log of a natural seacliff exposure of the Frijoles fault, coastal California. Five units of scarp-derived colluvium (A-E) are in contact with a complex reverse fault zone. The fault zone is composed of fault-bounded slices of coarse-grained fault "breccia" (derived from Tertiary sandstone and marine terrace gravels) and sand injected while liquefied. Note how the lowest faults and breccia zones truncate colluvium E but are truncated by colluvium D. Higher faults truncate colluviums B and C but are overlain by colluvium A. Compare to Fig. 5.9. [Adapted from Weber and Cotton, 1980 (Plate XIV).]

As a scarp face continues to degrade, smaller clasts and blocks and loose grains are deposited by gravity and debris processes (upper association of the debris element; Fig. 5.11 C). After burial of the free face, wash processes should dominate scarp decline and result in deposition of the finer wash element colluvium (Fig. 5.11D).

Subsequent fault displacement thrusts the hanging wall over the colluvium on the lower part of the scarp and triggers a new episode of colluvial transport and deposition. Repeated cycles of fault slip and scarp degradation should produce *stacked colluvial wedges* on the footwall, each wedge composed of recognizable facies, that record a complete history of the faulting history over the age of the scarp (Figs. 5.11E-H). [*Note:* In Japanese literature the couplet of a colluvial wedge and buried soil is termed the "D structure"; see Chapter 3 and Okada *et al.* (1989), for an excellent chronological interpretation of

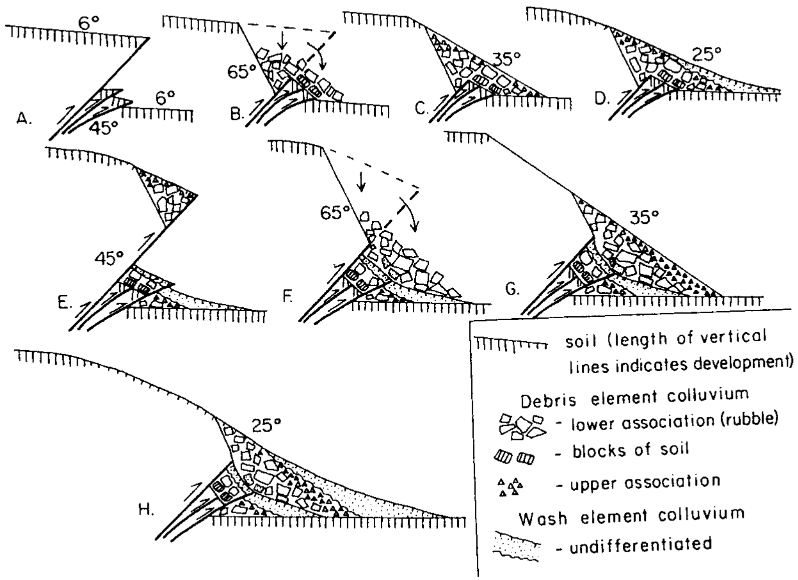

Figure 5.11 Schematic diagrams showing the deposition of colluvium from a two-event reverse fault scarp. Vertical offset in each event is envisioned to be on the order of 0.5 to 3 m. (A) Initial faulting (45° dip) of a sloping (6° slope) geomorphic surface with a well-developed soil. Faulting creates an overhanging scarp; note two subsidiary thrusts at scarp base. (B) Overhanging part of scarp collapses, forming an apron of rubble (compare to Fig. 5.6, location B). The lower association of debris element colluvium is composed of blocks of soil and hanging wall material. (C) Free face retreats and the finer, upper association of debris element colluvium is deposited. The colluvial apron stabilizes at the angle of repose (35°) once the free face is buried. (D) Wash element colluvium is deposited as the scarp declines (shown here at a maximum angle of 25°); a weak soil forms. (E) A second faulting event doubles the height of the scarp. The lower subsidiary fault is slightly reactivated, but the higher one is not. The proximal part of the colluvial wedge is translocated to the hanging wall of the rejuvenated scarp. (F) The overhanging part of scarp collapses. The debris element colluvium deposited after the second event thus includes material recycled from the proximal colluvial wedge from the first event. (G) The free face retreats and upper association debris element colluvium is deposited. (H) Wash element colluvium is deposited. The two faulting events can be deduced from (1) the existence of two colluvial wedges, (2) the fact that the lower wedge is in fault contact, but the upper wedge is in depositional contact, with the hanging wall, and (3) the subsidiary faults terminate upward at different stratigraphic levels.

multiple D structures.] Published examples of multiple colluvial wedges in reverse-fault exposures include Weber and Cotton (1980), Sarna-Wojcicki et al (1987), Swan (1988), Meghraoui *et al.* (1988), and Okada *et al.* (1989).

Lagerback (1990, 1992) describes how postglacial (ca. 9 ka) subaqueous reverse faulting in Sweden created a "colluvial wedge" by slumpage and flowage of till, which was later overlain with littoral deposits before Holocene emergence. The wedges are longer, thinner, and more undulatory (Lagerback, 1992, his Fig. 7) than the subaerial wedges described in this chapter. He also suggests that subaqueous faulting liquefied and partially resuspended clasts in the glacial till, thus forming a distinctive "seismically graded till" that can be used as a paleoearthquake indicator. However, neither subaqueous wedges nor graded tills have been described following historic earthquakes, so the mechanics of their origin can only be inferred at this time.

5.3.2 Structure and Evolution of Thrust Fault Scarps

Thrust faults (dip <45°; often 30° or less) typically refract to low angles near the surface and form scarps or pressure ridges, the slopes of which are below the angle of repose (Fig. 5.5). In many cases the surface cover of grass, turf, or peat is not broken except for minor tension cracks, even though the scarp may be up to several meters high (e.g., the 3.2-m-high scarp at El Asnam). These thrust scarps do form steep free faces and thus can generate colluvial wedges, but wedges are usually composed of wash-element colluvium. However, trenches through thrust faults have occasionally exposed coarse, chaotically bedded debris beneath the overriding fault that superficially resembles scarp-derived colluvium. Much of this material is probably derived from fault brecciation in the subsurface and from the advance of the thrust tip over the prefaulting ground surface.

Weber and Cotton (1980, pp. 28–29) describe a generic scenario that is useful for visualizing the complex process of thrust faulting in near-surface unconsolidated deposits:

> *The hanging wall block is thrust up and over the footwall to form a hump (pressure ridge) or moletrack scarp. The hanging wall block slides out on the former ground surface so that soft sediments and soils are "bulldozed" up in front of the lip of the overthrust block. The leading edge of the overthrust block is a relatively thin wedge of soft sediments that is pushed along the ground surface. Eventually, the frictional resistance to movement along the base of the overthrust plate exceeds the strength of the sediments in the overthrust plate, and the movement is transferred from the original shear surface to a second or possibly more shear surfaces that splay off of the main fault break. During one faulting event, it is probable that several fault breaks will splay out from the same main fault. Many of these faults will flatten near the surface and become parallel to bedding on the footwall block. . . . The soft sediments of the footwall . . . are also deformed by drag underneath the (overriding) plate. Some of the sediments on the footwall block that are initially shoved ahead of the "bulldozing" upper plate do not maintain that position because the fault overrides the brecciated rock as the hanging wall block is pushed*

> *farther and farther out over the footwall block. . . . Much of the deformation of sediments on the footwall block is the result of . . . a "rolling and mixing" action that apparently produces extensive sub-fault conglomerate masses and breccias. . . . There are few shear planes in these sub-fault conglomerates, which appear to have been produced by grain and clast rotation, lateral and vertical transportation, and a rolling or dragging action beneath the fault plane. . . . Much of the material in these brecccias and conglomerates is thought to have originated as fault breccia, fault gouge, and colluvium and slopewash eroded off the fault scarp. These materials, deposited between fault movements and also created during previous episodes of fault movement, eventually were overridden by subsequent fault movements, and the broken rock masses were incorporated into the "sub-fault" conglomerates.*
>
> *Some of the fault breccias do not originate as masses of rock crushed, rolled, and dragged along under the overthrust plate. The lip of the overthrust plate itself brecciates and breaks up into masses of mixed rock with a clayey matrix. Consequently, the near-surface portion of the fault zone consists of a wide zone of broken and mixed rock. . . . Another feature present in sub-fault masses of mixed and deformed rock is evidence of local "underthrusting" associated with the "bulldozing." Where jumbled masses of rock material on the footwall block seem to have been pushed ahead of the lip of the thrust, they are sometimes underlain by what appears to be the lip of the over thrust block that has acted in a manner similar to that of a bulldozer blade.*

Based in part on these observations, Weber and Cotton (1980, pp. 30–37) proposed a model for recognition of multiple faulting events on thrust (and reverse) faults. The model assumes that the initial scarp form is a pressure ridge made of crushed material, subject to subaerial erosion and weathering. The major processes acting on the pressure ridge are assumed to be sheetwash and rillwash. The following stratigraphic relations should be observed after a single faulting event: (1) a wedge of scarp-derived (wash element) colluvium that thins away from the fault, derived from the upthrown block, (2) this colluvium buries the prefaulting soil, (3) the buried soil is offset by the fault plane, and (4) the soil horizon on the hanging wall block is thin or absent near the fault and thickens away from the fault. All four of these phenomena are shown in Fig. 5.11D.

Weber and Cotton (1980) further propose four main criteria to recognize repeated fault movements (see Figs. 5.11E–H). First, each earthquake is represented by a colluvial wedge and buried soil. If displacement per event is <0.3 to 0.5 m, however, colluvium may not be recognizable and the only evidence of faulting is thickening of soil horizons on the footwall (Weber and Cotton, 1980, p. 33). The second criterion is cross-cutting relations. Colluvial units overlie older faults, but are truncated at their upslope limits by younger faults (Fig. 5.9A). Within the main fault zone, younger, steeper faults truncate older, flatter faults. Fault geometry often suggests an apparent upward and upslope migration of faulting in sediments of the footwall. Third, wedges of fault breccia are injected into overlying sedimentary layers (colluvium and alluvium) on the footwall (Fig. 5.9A, stages F, H). Fourth, fault breccia created by thrust-tip "bulldozing" can be interbedded with fluvial, eolian, or lacustrine deposits. The coarse rubbly deposits formed by breccia injection and by bulldozing of the fault tip may superficially resemble colluvial wedges, but they did not necessarily accumulate on a prefaulting ground surface, and thus their lower contacts are not necessarily event horizons. The possible confusion in differentiating colluvial, injection, and bulldozed debris beneath reverse faults points out the need for a future systematic study of reverse- and thrust-fault zone sedimentology, similar to that performed by Nelson (1992b) on normal faults. However, even in the absence of coarse debris on the footwall, paleoseismic reconstruction can be based on identifying lenses of finer wash element colluvium and cross-cutting relationships (Fig. 5.12).

The displacement attributable to individual paleoearthquakes is typically estimated from a retrodeformation analysis of the trench log (Sec. 2.3.2.7). As with historical ruptures, the reconstructed paleoseismic displacements may vary markedly along strike. For example, Hull (1987) cites a 20% difference in net slip determined in two paleoseismic trenches only 20 m apart. Some of this variance is contributed by large-scale folds with amplitudes that can exceed half of the total vertical separation across the fault zone. To expose such folding completely, Beanland *et al.* (1986) suggest that trenches must be extended tens of meters away from the fault scarp itself. Even if folds are measured, however, the intrinsic along-strike slip variance will likely remain high.

5.3.3 Soils on Thrust Fault Scarps

Surface weathering profiles (soils) are commonly developed in the upper parts of the colluvial sheets shed from fault scarps. These soils become buried when additional faulting results in the formation of new colluvial sheets. Soil formation on growing thrust scarps is complex and not thoroughly investigated. We do know that different soil properties characterize different slope positions on the scarp (Burke and Carver, 1989). The upper parts of scarps are areas of erosion of the uplifted fault tip. Where thrust faults cut upland terrain and are not influenced by off-fault deposition, erosion of the scarp crest is cyclic and driven by coseismic displacement of the fault. Each erosion cycle is initiated by a faulting event and proceeds from rapid gravity-dominated transport of debris off the new fault tip in the immediate postseismic interval, to slow creep of weathered material from the degraded fault tip prior to the next event. Over many seismic cycles, weathering products generated in scarp crest area are

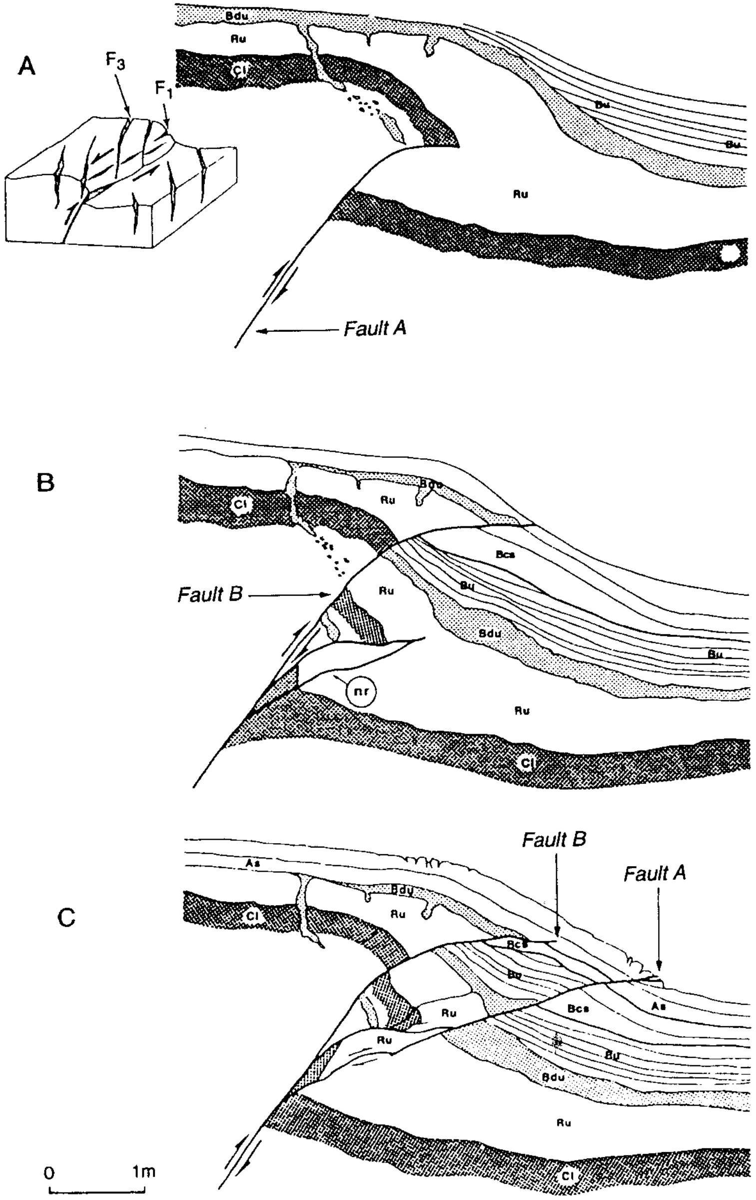

Figure 5.12 Reconstruction of faulting and deposition on the El Asnam thrust fault. (A) Thrust movement on fault A displaces beds Cl and Ru and creates a fault-propagation fold at the surface, defined by soil Bdu (light shading). Postfaulting sediments (Bu) onlap the scarp. (B) Renewed faulting propagates upward past the refraction point of fault A and creates fault B, which also refracts to a lower angle but at a higher level. Fault B, truncates onlapping units Bu and Bcs. A new subsidiary fault (nr) forms near the beheaded part of fault A. (C) During the 1980 earthquake, fault A is reactivated and reaches the ground surface, displacing soil As that covers the entire scarp. Fault B is not reactivated. Due to the small displacements and the tendency to form fault-propagation folds at this site, scarp-derived colluvium is mainly composed of the wash element. [From Meghraoui *et al.* (1988); reprinted with permission of the Seismological Society of America.]

removed during downslope transport of the colluvium and the profile development at the crest is minimal.

Below the thrust the colluvial sheets and their weathering profiles are preserved by overthrusting and resulting burial by the new colluvium. The result over multiple seismic cycles is the accumulation of stacked buried colluvium with buried soils reflecting the weathering that accrued on the lower part of the scarp during each interseismic interval (Fig. 5.11H). Where these weathered materials accumulate at the toe of the scarp the profiles are thickest and most strongly developed. Below the toe the soil profiles on stacked colluvium may merge into a single soil, as occurs in normal fault scarps (Fig. 3.27). Within a sequence of stacked soils the profile development generally increases with lower slope position (a similar phenomenon was described for normal faults in somewhat more detail; see Sec. 3.4.2). Some soil parameters such as clay content and rubification increase in each successive soil in the stack, reflecting a general increase in weathering of the upper part of the scarp (Fig. 5.13).

5.3.4 Stratigraphic Bracketed Offset

Where surface faulting occurs in active depositional settings, individual slip events are often recorded by bracketing strata. Such environments as river floodplains, shallow lakes and ponds, tidal marshland, or aggrading coastlines and dunes are likely environments for preservation of slip events and scarp growth by quick burial. Slip on the main fault (as well as on secondary faults, including normal faults in the hanging wall) produces offsets of preexisting bedding, surface colluvium, and soil. In many places postseismic grading of the scarp removes the constructional microtopography generated by the fault slip before subsequent sediments cover the site. However, occasionally a scarp is buried and details of its morphology are preserved in the stratigraphy.

The unconformity above the faulted sequence records the paleoearthquake and any postseismic modification of the surface trace prior to burial. Unfaulted sediments above the unconformity postdate the fossil earthquake. Where rapid sedimentation has persisted during multiple seismic cycles, a sequence of stacked *unconformity-bounded interseismic sediment packages* may result

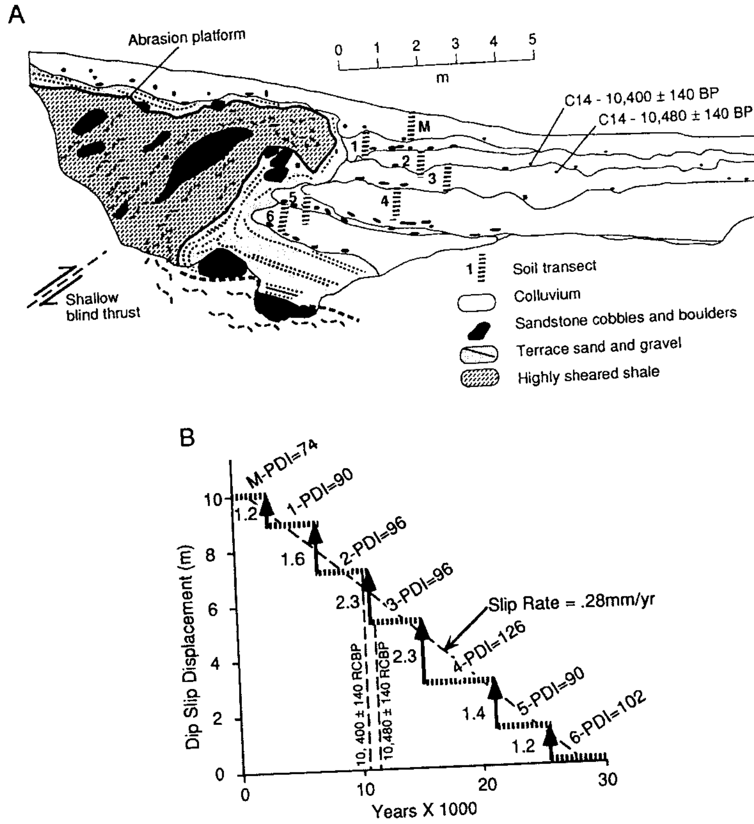

Figure 5.13 (A) Log of a trench across one of the traces of the Mad River fault where it displaces a late Pleistocene terrace near Humboldt Bay, California. At this site, underlain by very ductile highly sheared shaley melange, the thrust is blind and displacement reaches the surface as a sharp overturned fault-propagation fold. The marine terrace platform (heavy line) and overlying terrace sand and gravel are overturned in the forelimb of the fold. Six stacked colluvial sheets, each with a stone line at the base and containing a buried soil (soil profiles 1–6), extend downslope from the overturned fold limb. A modern active colluvial sheet mantles the scarp at the surface. The colluvium is interpreted to have formed by slope processes on the scarp face between slip events. Coseismic growth of the fold preserved the colluvial layers below the overturned limb and generated new colluvial sheets that buried the downfaulted lower part of the scarp. (B) Diagram of the slip history deduced from the buried soils and two AMS ^{14}C ages on small pieces of detrital charcoal. Soil parameters measured in the field and lab were used to calculate a profile development index (PDI) for each colluvial layer using the methods described by Harden (1982). We assume that the initial (parent material) PDI of each scarp-derived colluvial deposit was equal to the PDI of the underlying soil, because that soil should have been exposed on the scarp crest after faulting and rapidly reworked into the next higher colluvial wedge. The ^{14}C ages are plotted relative to their stratigraphic position and provide rough calibration for the PDI-based slip history.

(Fig. 5.14). Faults produced by each earthquake are truncated by the unconformity corresponding to the earthquake that produced them. Faults generated by previous earthquakes are truncated by unconformities and covered by sediments lower in the sequence. Faults that have recurrent movement exhibit greater displacement of lower unconformity-bounded sediment sequences. In settings where such sediment sequences and fault relationships are preserved, the deposits laid down across the fault must be thick enough to bury completely the scarp and lap across both the footwall and hanging-wall blocks. Where sedimentation rates cannot keep up with scarp growth, the stacked interseismic sediment packages are preserved only on the downdropped side of the fault, the elevated block is subject to weathering and erosion, and the surface trace is commonly covered by sheets of scarp-derived colluvium.

Surface fault displacement and resulting disturbance of the ground along the fault trace, often coupled with a marked localized increase in surface erosion rate immediately following the earthquake, can produce postseismic pulses of deposition followed by reduced intersesimic sedimentation and soil development. Thus, under ideal conditions unconformity-bounded sediment sequences may reflect these depositional rate changes. For example, coarse

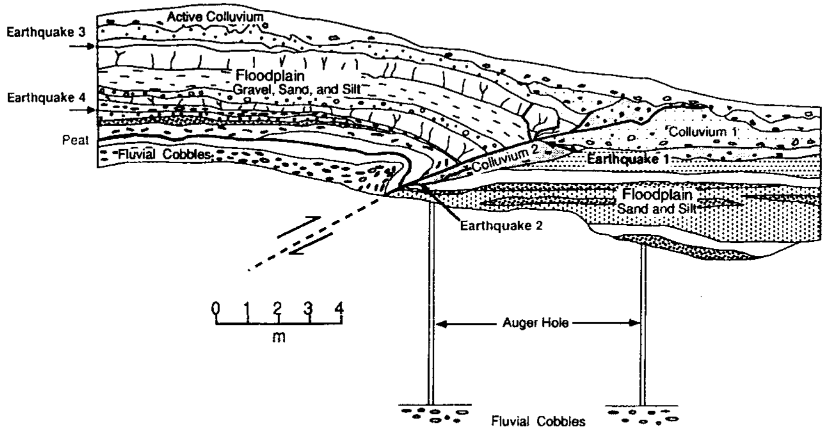

Figure 5.14 Trench log at the Blue Lake site across the McKinleyville fault, showing the effects of repeated thrust faulting in a depositional environment dominated by vertical fluvial accretion. Four paleoearthquakes are inferred. Earthquake 1 (most recent) and earthquake 2 (penultimate) are indicated by overthrust scarp-derived colluvial wedges (colluvium 1 and colluvium 2, respectively). These two events postdate the development of the scarp and the cessation of floodplain sedimentation. Prior paleoearthquakes (earthquake 3 and earthquake 4) occurred during vertical accretion of floodplain overbank sediments. Earthquake 3 is represented by fault splays that displace floodplain sediments below the event horizon and are overlapped by younger sediments. Earthquake 4 (the oldest) is expressed as an angular unconformity that truncates beds that are overturned adjacent to the fault below the unconformity.

high-energy deposits, cut and fill structures, and other indicators of high-energy deposition in the base of a sediment package may grade upward into finer grained parallel stratified material containing a soil at the top.

5.3.5 Fault-Onlap Sedimentary Sequences

The surface expression of many thrust faults in thick unconsolidated sediments is not restricted to a narrow zone of faulting, but rather is commonly distributed across a broad zone on many small displacement faults and accommodated by broad warping and surface folding. Coseismic growth of broad warps in floodplains, marshes, and other *vertically accreting* depositional environments lowers the footwall block relative to the hanging wall and increases the prism available for sediment accumulation. At sites where the vertical displacement elevates the upthrown side of the fault above the limits of deposition (e.g., above the reach of overbank flood flow on a river floodplain or high tide in a tidal marsh), postseismic sedimentation produces layers of sediment that *onlap* the scarp (Carver and Burke, 1989). In many cases these sediments will not overlie any (truncated) surface faults that can be used to bracket faulting events. Restabilization of the landscape following deposition on the downdropped side of the fault is commonly followed by soil formation or peat accumulation (Fig 5.15). Repeated faulting produces *stacked onlap sequences* on the downfaulted side of the fault, each capped by a buried soil or peat layer. The sediments thin as they onlap the warped area along the fault and the soils merge into a single profile on the upthrown side. Abundant plant fossils and charcoal are sometimes present in such deposits and can provide ^{14}C samples useful in limiting the age of faulting events.

5.3.6 Summary of Stratigraphic Evidence for Thrust Paleoeathquakes

The type of stratigraphic evidence created during and after paleoearthquakes on thrust faults is determined by the geometry of near-surface faults and folds and the local depositional environment. Figure 5.15 shows one conceptual view of the continuum of fault-zone stratigraphic geometries. If surface materials are noncohesive and dry, discrete faults form. High-strength materials are typified by single fault strands, narrow scarps, and collapsed fault tips buried by scarp-derived material (lower left). In low-strength materials (e.g., loose sand) wide scarps are formed by distributed conjugate faults (upper left), and no single fault has enough relief to shed a preservable colluvial wedge. In moister or more cohesive surface materials, ductile deformation and folding increase. Sharp fault-propagation folds give rise to colluvial wedges (lower right), whereas open fault-bend folds are often onlapped by vertical accretion deposits (upper right). However, if a broad gentle scarp is formed in a dominantly erosional environment, no paleoseismic indicator strata may be depos-

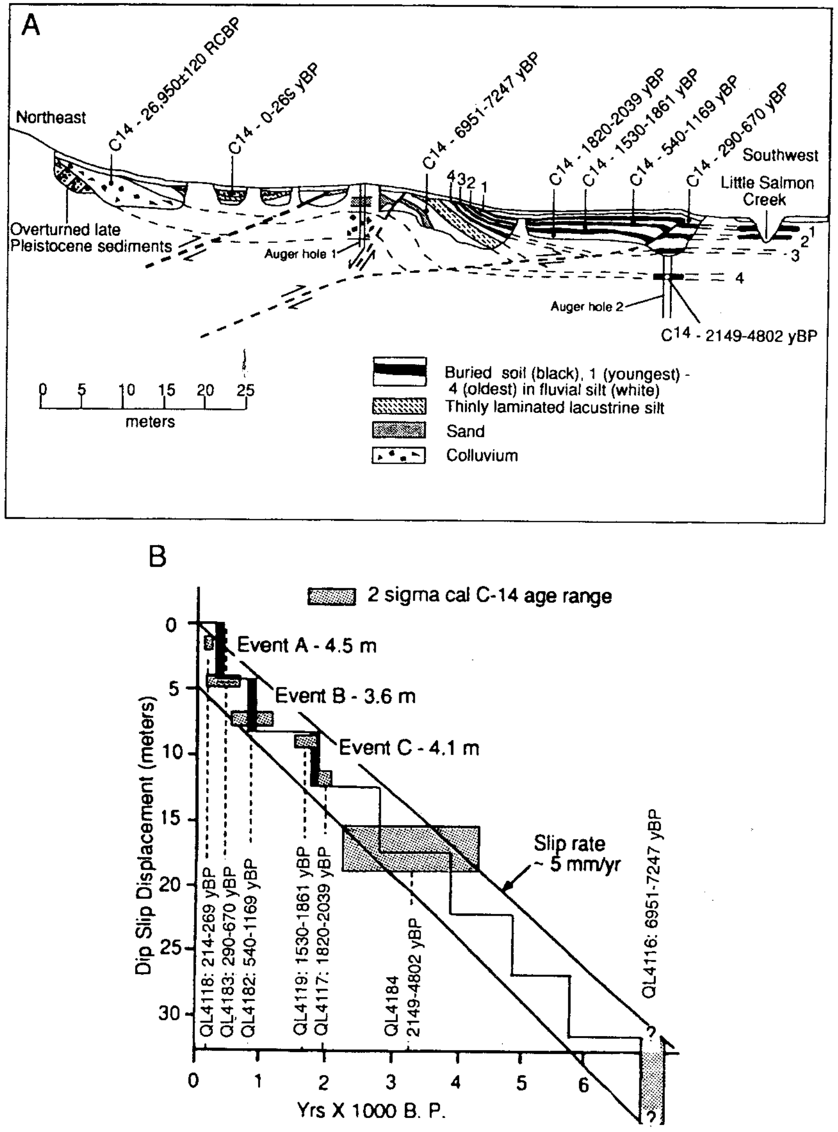

Figure 5.15 (A) Generalized trench log across the west trace of the Little Salmon fault in northern California. The fault reaches the surface in large part as a growth fold above the fault tip. Progressively deformed sediments capped by soils [(1 youngest), to (4 oldest)] onlap the fold and fault tip. These soils are interpreted to record the coseismic growth of the fold and propagation of the fault tip with each slip event. (B) The slip history diagram shows the late Holocene slip rate and paleoseismic history for the last three events represented by the stratigraphy exposed in the trench.

ited. Although Fig. 5.15 is based only on examples from northern California, the general relations shown should apply to any area with similar surface materials and depositional environments.

5.4 PALEOSEISMIC EVIDENCE OF SECONDARY FAULTING

Paleoseismic histories derived from secondary faults are good proxies for events on the underlying thrusts, especially where the underlying seismogenic thrust does not extend to the surface. The paleoseismic indicators for these faults are similar to those for active normal faults, and may include the development of colluvial wedges and faceted compound scarps. However, the geometry and amount of secondary fault displacement may be difficult to relate to slip on the underlying seismogenic reverse fault, as described later.

5.4.1 Flexural Slip Faults

Coseismic flexural-slip faulting was observed during the 1980 El Asnam, Algeria, earthquake (Philip and Meghraoui, 1983), and the 1968 Inangahua, New Zealand, earthquake (Lensen and Otway, 1971). Flexural-slip faults may show geomorphic and stratigraphic evidence of multiple coseismic displacements, and these can be used as indicators of the paleoseismic history of the underlying thrust fault. As shown in Fig. 5.16, the flexural-slip faults, which have a vertical or normal fault geometry at the surface, are upthrown toward the synclinal axis. Because modern streams typically flow toward synclinal axes (e.g. Ota and Suzuki, 1979; Rockwell *et al.*, 1984), flexural-slip fault scarps often face upstream and pond local drainage.

A classic area for Quaternary flexural-slip faults is the Grey-Inangahua depression in New Zealand, where a swarm of eight parallel flexural-slip fault scarps displaces two fluvial terraces of different ages; scarps are 1.5 m higher on the older terrace (Fig. 5.17). The height difference was inferred to reflect the displacement during a single faulting event (Yeats, 1986a). Even larger, multiple-event (?) scarps (up to 12 m high) are found nearby at Blackball, New Zealand. Yeats (1986a, b) noted that the local drainage had ponded against the base of the flexural-slip scarps (Fig. 5.18) and argued that such ponding could only be produced by sudden, coseismic rise of the scarp (as opposed to more gradual creep, which would have been unable to defeat the streams). Similar flexural-slip scarps in the Ventura Basin, California (Fig. 5.17), displace multiple alluvial fan surfaces dated between 4 to 5 ka and 200 ka. Rockwell *et al.* (1984) and Rockwell (1988) used the increasing fault scarp heights and tilting in successively older deposits to reconstruct the chronology of Quaternary folding.

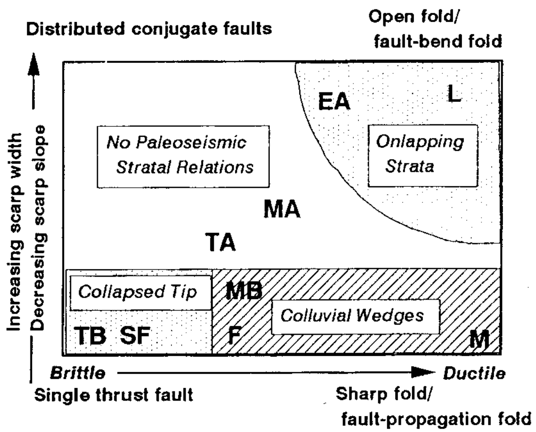

Figure 5.16 Types of stratigraphic evidence of paleoearthquakes associated with various combinations of surface deformation style and scarp morphology along thrust faults. Large bold letters indicate trench logs that show indicated features. Logs in this chapter include: M, Mad River fault, School Road trench (Fig. 5.13); L, Little Salmon fault, Little Salmon Creek trench (Fig. 5.15); MB, McKinleyville fault, Blue Lake trench (Fig. 5.14); EA, El Asnam trench, Algeria (Fig. 5.12); SF, San Fernando, California, fault scarp (Fig. 5.6); F, Frijoles fault exposure, California (Fig. 5.10). Other trench logs (MA, McKinleyville fault, Airport trench; TA, Trinidad fault, Anderson Ranch; TB, Trinidad fault, Jager property) are shown in Woodward-Clyde (1980). [Modified from Carver (1987b).]

Yeats (1986b) also points out that flexural-slip faults, because they are restricted to folds and their displacement decreases to zero at the fold axis, are probably not seismogenic structures themselves. Rather, flexural-slip faulting results from coseismic (usually synclinal) folding, which itself is caused by coseismic fault displacement on a reverse fault that lies beneath, or adjacent to, the fold. Based on similar reasoning, Lensen (1976) distinguished between the *earthquake-generating reverse fault* and the resulting *earthquake-generated flexural-slip faults.* To date, few detailed paleoseismic investigations (e.g. trenching) have been performed on flexural-slip faults, although this is a promising field for future research in areas where most seismogenic thrusts are buried (e.g., Stein and Yeats, 1989).

5.4.2 Bending-Moment Faults

Bending-moment faults have also been observed to form in large historic thrust-fault earthquakes, most notably in the 1980 El Asnam, Algeria, earthquake (King and Vita-Finzi, 1981; also Sec. 5.1.3). In some places the normal fault scarps ("extrados fractures" of Philip and Meghraoui, 1983) that formed on the anticlinal crest in 1980 were clearly rejuvenations of earlier, degraded

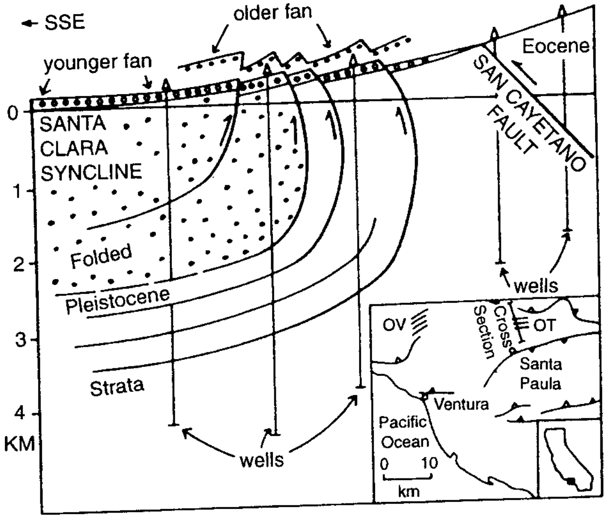

Figure 5.17 Diagrammatic cross section of flexural-slip faults in the Ventura Basin, California. Southward-directed thrusting by the San Cayetano fault (at right) produces tightening of the overturned limb of the Santa Clara syncline (center). Tightening of the fold then produces differential slip between the near-vertical bedding planes on the fold limb, which creates fault scarps at the surface. Note how the older fan has been deformed more than the younger fan. [From Yeats (1986b); reprinted from Active Tectonics. Copyright© 1986 by the National Academy of Sciences. Courtesy of the National Academy Press, Washington, D.C.]

normal fault scarps that had formed in paleoearthquakes (see also Fig. 5.19). Such well-formed normal fault scarps could be studied via the techniques of Chapter 3, and the resulting paleoseismic history could then be used as a surrogate (albeit possibly incomplete) history for the underlying, more poorly expressed thrust fault.

The most detailed paleoseismic investigations of bending-moment faults to date have been made across fault-propagation monoclines in the Transverse Ranges of southern California (Yeats, 1986b). Scarps overlying the traces of the Ventura and Camarillo reverse faults were trenched in the 1970s and 1980s. On the former fault, the broad scarp was underlain at two locations by monoclinally folded beds, displaced near the surface by numerous small-displacement normal faults (Fig. 5.20). Sarna-Wojcicki *et al.* (1976) and Gardner and Stahl (1977) interpreted the normal faults as bending-moment faults on the upper part of a monoclinal flexure. On the Camarillo fault, trenches across the lower part of the fault scarp revealed a set of conjugate, high- and low-angle reverse faults which were interpreted to result from bending-moment compression at the base of a monocline. In both trenches the chronology of faulting was reconstructed mainly from stratigraphic truncation of fault strands (*upward terminations*; see Sec. 6.3.3), because the lack of large displacements on individual faults meant that no colluvial wedges were formed. Although the ages of displaced sediments can be used to date periods of fault movement, the amount and sense of displacement on the bending-moment faults cannot at present be extrapolated to infer the amount and sense of displacement on the underlying, seismogenic reverse faults (Yeats, 1986b, p. 69). Future work on this topic should concentrate on documenting the relationship between displacement on these secondary bending-moment faults, and the amount of coseismic folding and/or reverse fault displacement.

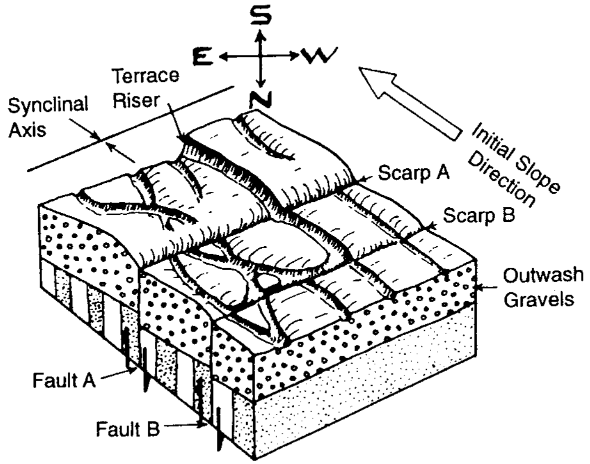

Figure 5.18 Block diagram of flexural-slip fault scarps displacing late Pleistocene outwash terraces at Giles Creek, New Zealand. This diagram shows a surface geometry similar to that of the faulted fans at the top of Fig. 5.17. [From Yeats (1986b); reprinted from Active Tectonics. Copyright© 1986 by the National Academy of Sciences. Courtesy of the National Academy Press, Washington, D.C.]

5.5 PALEOSEISMIC EVIDENCE OF COSEISMIC FOLDING

Coseismic surface fold growth has been observed during many large compressional earthquakes, and is often the only surface expression of thrust displacement on underlying blind faults (Stein and King, 1984). Coseismic folding includes both horizontal and vertical movements of the ground surface that reflect the geometry of the underlying fault, but generally only the vertical movement is preserved as geologic evidence.

The theoretical understanding of fault-propagation folds is relatively well established (Suppe, 1983). Dislocation models for rupture on buried thrusts predict general uplift of the area above the rupture surface resulting from thrust transport and internal flexing of the hanging-wall block. The models

Figure 5.19 Shadows highlight four large, and many small, upslope-facing bending-moment fault scarps on the crest of an anticlinal ridge in the Don Miller Hills near Katalla, Alaska. The anticline is part of an extensive fold and thrust belt in the subduction margin at the eastern end of the Alaskan subduction zone. The smooth glacially abraded surface offset by the faults dates from the latest Pleistocene deglaciation of the region (ca. 13 ka). Sediments ponded on the upslope side of the scarps are likely sites for paleoseismic studies and may contain indirect evidence for the timing of coseismic slip on the underlying thrust faults.

also predict elastic thinning and subsidence of a broad backstop region behind the downdip limit of fault rupture (Suppe, 1985; Marshall *et al.*, 1991). During large blind thrust earthquakes these areas undergo vertical displacement of up to several meters for very large earthquakes. The size of these areas of uplift and subsidence varies with the size of the rupture surface, dip of the fault, and depth and amount of slip. Geometric complexity of the thrust complicates the pattern of surface deformation. Abrupt changes in dip of the thrust or reversals of dip direction (fault wedges) produce upward-propagating axial surfaces in overlying anticlines that grow during fault slip.

In contrast to this theoretical understanding, the paleoseismic study of active surface folds has lagged behind that of surface faults. To date, long-term slip rates on folds have been measured from folded datums of known age such as late Pleistocene fluvial and marine terraces, and folded late Quaternary sediment sequences (e.g., Rockwell *et al.*, 1988). Long-term slip rates and average folding recurrence estimates can also be made from simple interpretations of underlying thrust depth and dip, but such estimates are generally not precise enough to characterize individual paleoearthquakes reliably. In his review of modern paleoseismic techniques, Schwartz (1988a, p. 31) remarks “It is unclear, at least at present, how earthquake recurrence intervals can be well constrained in folded deposits or how we can distinguish folds that are surface expressions of seismogenic faults and those that are not. This is certainly an area for future research.”

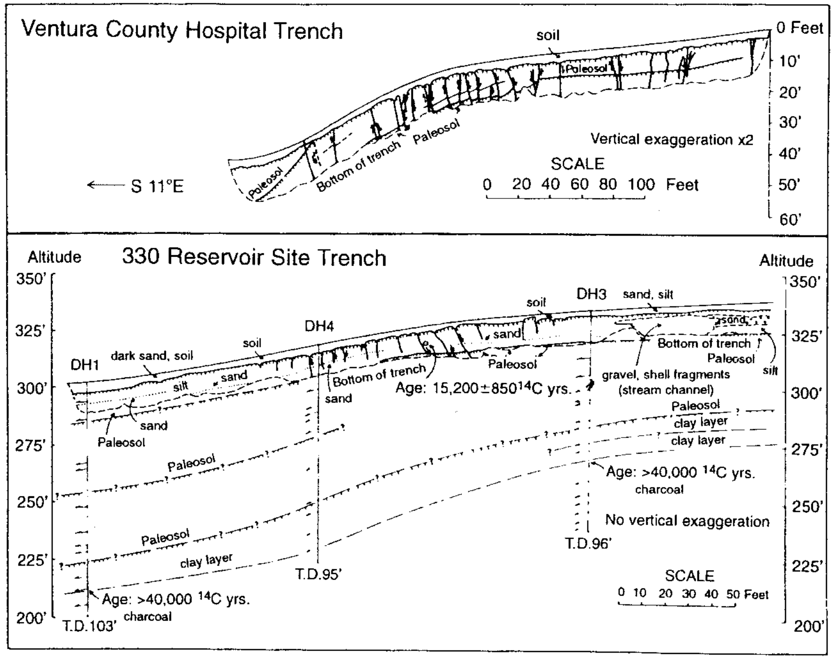

Figure 5.20 Sketches of two trenches across the scarp of the Ventura fault, California, showing the style of small extensional bending-moment faults developed in a monoclinal flexure over the buried thrust trace. [From Yeats (1986b); reprinted from Active Tectonics. Copyright 1986 by the National Academy of Sciences. Courtesy of the National Academy Press, Washington, D.C.]

Some breakthroughs in the study of paleoseismic folds seem imminent. For example, techniques for balancing cross sections, using detailed surface and subsurface structural and stratigraphic data to account for geometric and temporal characteristic of the folding, can improve slip rate and recurrence estimates (Suppe, 1985). In addition, detailed geodetic measurements of coseismic fold growth have recently been made where geodetic nets were established in urban areas before the earthquake [e.g., the 1994 Northridge, California, earthquake; U.S. Geological Survey Staff (USGS), 1994].

5.5.1 Geomorphic Evidence of Active Surface Folding

The geomorphic expression of surface folds depends on the subsurface geometry of the blind thrust fault, the depth to the buried thrust fault tip, and the response of surficial materials to propagation of the buried fault tip. The geometry of most surface folds is distinctive and includes planar limbs and sharp hinge lines characteristic of fault-bend and propagation anticlines (Suppe, 1983, 1985). The folds are typically asymmetrical with steep forelimbs and gentle back limbs. Multiple hinge lines cut the limbs. Many folds have broad planar crests. Observations from historic earthquakes indicate that growth of these folds occurs suddenly during rupture of underlying thrust as the upper thrust sheet moves across bends in the fault and through the axial planes that propagate toward the surface. In some places these axial planes intersect the surface at distinct hinge lines where the attitude of beds and folded geomorphic surfaces abruptly changes. The mechanics of the migration of axial planes through the near-surface sediments are not well understood, but probably include pervasive intergranular shear, flexure slip, and plastic flow, depending on the texture and rigidity of the rock or sediment.

In contrast to primary surface faulting, where evidence of slip on the seismogenic fault is directly observed, coseismic folding often results in deformation that often is not concentrated along an identifiable fault zone, but instead includes a large area above the fault rupture. The width of the fold is influenced by the depth at which the blind thrust transitions into the fault-propagation fold. At very shallow depths folds are sufficiently narrow that they create scarps similar to those created by distributed surface faulting (see Fig. 5.13). At sites where the surface processes are sensitive to such elevation changes, paleoseismic evidence of coseismic folding is preserved as local deposition or erosion caused by vertical displacement or tilting, usually associated with the regrading of rivers and streams or shorelines crossing the deformed area.

To date little attention has been paid to the possible effects of propagation of a fold axial surface through a structure (for example a large dam), but such an occurrence may constitute an unrecognized type of seismic hazard associated with large compressional earthquakes.

5.5.1.1 Fluvial Datums for Detecting Coseismic Fold Growth

The most common geomorphic datums on which historic or prehistoric folding have been measured are fluvial channels and terraces. In the classic study of the Ventura Avenue anticline, Rockwell *et al.* (1988) reconstructed the fold shape from isolated, uplifted fluvial terrace remnants, and deduced vertical folding rates (from 4 to 20 mm/yr) for several discrete time periods in the late Quaternary. In the Los Angeles Basin, Bullard and Lettis (1993, p. 8368) used "detailed Quaternary mapping of terraces and surfaces, longitudinal stream and terrace profiles, and construction of a topographic residual map" to measure deformation above the Elysian Park thrust fault. From surface mapping they estimated uplift rates of 0.1 to 0.2 mm/yr and tilting of 0.2 to 0.5 rad/yr over the past 750 ka, and inferred that the underlying blind thrust was composed of two distinct 6- to 8-km-long segments with independent deformation histories. Most geomorphic investigations of Quaternary folds have failed to deduce parameters for individual paleoearthquakes, however, because multiple deformation events occurred between the formation of each successive geomorphic datum (the same limitation often affects the interpretation of faulted terrace sequences, e.g., Sec. 6.2.1.1). Instead, only the more general patterns of folding, fold segment boundaries, and average slip rates can typically be estimated from landforms.

Studies following the 2 May 1983 Coalinga, California, earthquake (M_s = 6.5), summarized next, provide an example of how one might infer paleoearthquake parameters from warped terraces and alluvial plains (King and Stein, 1983; Stein and King, 1984). [Similar studies that analyze progressively deformed terraces are Vita-Finzi (1986) and Molnar *et al.* (1994).]

The 1983 earthquake occurred on a buried reverse fault in central California under the aptly named Anticline Ridge. Seismological data constrained the rupture to a northwest striking fault dipping about 65° to the northeast (Kanamori, 1983). The fault rupture initiated at a depth of about 10.5 km and did not break to the surface. Level lines had been established across Anticline Ridge prior to the earthquake to monitor subsidence due to oil withdrawal. Resurveys of the leveling lines after the earthquake show that the anticline grew coseismically by about 0.5 m (Stein, 1983). Channel profiles along Los Gatos and Zapato Creeks (antecedent streams crossing Anticline Ridge near the southeast end of the 1983 rupture) were also surveyed shortly after the earthquake and showed a gentle arch where they crossed the anticline axis (Stein and King, 1984). Where streams cross the anticline they are incised about 10 m, compared to an incision of only ≤ 5 m on either side of the fold.

Stein and King (1984) identified four lines of evidence (mostly geomorphic) for paleoseismic fold growth here: (1) warped stream terraces across the fold, (2) a topographic "hump" where the fold projects across an alluvial plain, (3) increased stream sinuosity upstream of, and decreased sinuosity downstream of, the fold, and (4) clayey sediments upstream of the anticline, suggesting a paleo-lake or -marsh (similar to that formed in the the 1980 El Asnam earthquake; see Fig. 5.4). King and Stein (1983) proposed that the mean repeat time between earthquakes could be calculated from the vertical dimensions of the fold crest as

$$T = AU/H, \qquad (5.1)$$

where:

T = repeat time between uplift events
A = age of youngest stratum uplifted a distance H at the fold crest
U = amount of coseismic uplift of the fold crest during a major ($M = 6$ to 7) earthquake
H = structural component of the height of the fold crest.

At Coalinga, they assumed $H = 0$ to 10 m, $A = 2500$ to 10,000 yr, and $U = 0.6$ m, yielding a mean repeat time (T) = 200 to 600 yr for morphogenic, blind thrust earthquakes. They also assumed that the entire height of the "hump" in the alluvial plain was attributable to coseismic deformation.

Subsequent to 1984, Atwater *et al.* (1990) performed a more detailed stratigraphic study of the epicentral area and concluded that much of Stein and King's (1984) geomorphic evidence for paleofolding events was nontectonic in origin. In particular, (1) the alluvial plain hump was formed mainly by stream deposition, (2) the changes in stream sinuosity were opposite to that of lab-scale streams across growing anticlines (Schumm, 1977; Ouchi, 1985), and (3) the "clayey sediments" were mostly fluvial silt and fine sand, and in four core holes and several kilometers of streamcuts no evidence of Holocene lakes or marshes was observed. Holocene alluvium is well exposed in 3- to 10-m-high steambanks along Los Gatos Creek, and buried fluvial paleosurfaces dated at 2, 2.5, and 5 ka showed only slight (1 to 2 m) warping across the anticline. Based on this stratigraphic data, Atwater *et al.* (1990) concluded that vertical uplift rate of the anticlinal crest over the past 7 ka had been ≤0.2 to 0.4 m/ka, and that the return period between morphogenic earthquakes (of similar size to the 1983 event) was >200 to ca. 1000 yr. This pair of studies suggests that geomorphic evidence alone will not be sufficient for accurately characterizing individual paleofolding events.

Future refinement of techniques will evidently be necessary before individual paleofolding events can be characterized to the same level of detail now attained for paleofaulting events. Several approaches seem to hold promise: (1) detailed field studies of geomorphic responses to future coseismic folding events, (2) lab-scale streamtable simulations of streams crossing folds, and (3) conceptual modeling (e.g., Molnar *et al.*, 1994) of the relation between uplift, stream processes, and the resulting alluvial stratigraphy.

5.5.2 Stratigraphic Evidence of Active Surface Folding

To date few studies (aside from Atwater *et al.*, 1990) have used stratigraphic evidence to identify and characterize coseismic folding events. Where blind thrusts approach very near to the surface and folds are tight, the fault-propagation scarp created may be steep enough to generate colluvial deposition and onlapping deposits similar to that of a fault scarp (Fig. 5.15). In most cases, however, the folds are too broad to form well-defined scarps and instead create anticlines of considerable width.

Conceptual models predict the geometries of onlapping and offlapping strata as a function of relative rates of sediment accumulation and uplift of the fold crest. When rates of deposition are consistently greater than rates of crestal uplift, the fold is overlapped (Fig. 5.21B). If deposition rates are less than uplift rates, offlap results (Fig. 5.21C). Reversals in the relative magnitude of these rates causes a switch in the bedding geometry, as shown in Figs. 5.21D and E. In a paleoseismic framework, coseismic deformation is instantaneous and thus uplift rate far exceeds deposition rates over short time periods. Following the earthquake, the uplift rate falls to zero and deposition rates (regardless of their magnitude) exceed uplift rates. In geomorphic settings with high deposition rates, such an alternation of instantaneous uplift followed by quiescence would theoretically create a depositional sequence of offlap, onlap, and overlap as shown in Fig. 5.21E. To date, studies of Quaternary stratigraphy near active folds have not documented relations such as those

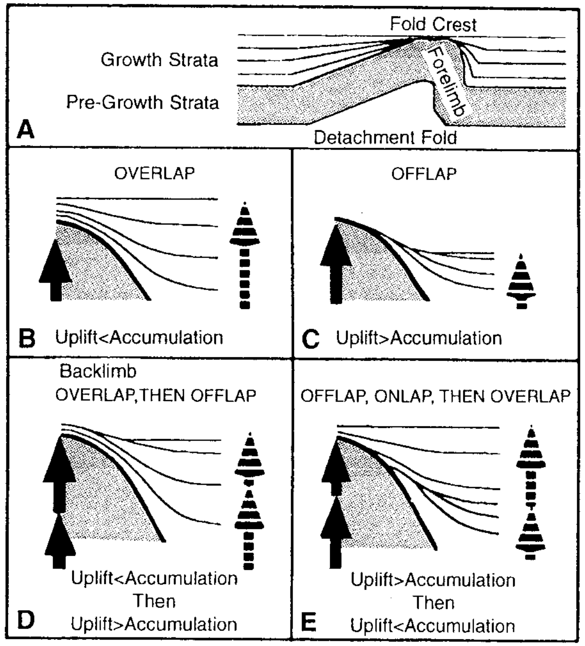

Figure 5.21 Conceptual diagrams of geometric relations between a growing fold and deposition on the flanks of the fold. (A) Nomenclature. (B) Overlap created when uplift rates are less than deposition (accumulation) rates. (C) Offlap created when uplift rates are greater than deposition rates. (D) Overlap then offlap created by initially low uplift rates which then become greater than deposition rates. (E) Offlap, onlap, then overlap created by initially high uplift rates which then decrease to less than the deposition rate. [From Burbank and Verges (1994); reprinted with permission of the American Geophysical Union.]

described here. At Coalinga, for example, Holocene alluvial units exposed in streamcuts in the anticline are folded nearly concordantly and no onlapping or offlapping was observed (Atwater *et al.*, 1990).

Another possible application of stratigraphy to coseismic folding relates to upwarped river terraces above anticlines. Molnar *et al.* (1994) showed that upwarped strath terraces over the anticline may be traced to buried fill terraces upstream and downstream of the anticline (Fig. 5.22). It is often difficult to find datable material on upwarped strath terraces that would help to constrain the timing of uplift. However, if those same surfaces are buried by partial damming and slackwater deposition upstream from the anticline, there may be an increased potential for finding datable organic material in the slackwater sequences. Again, this concept has yet to be field tested.

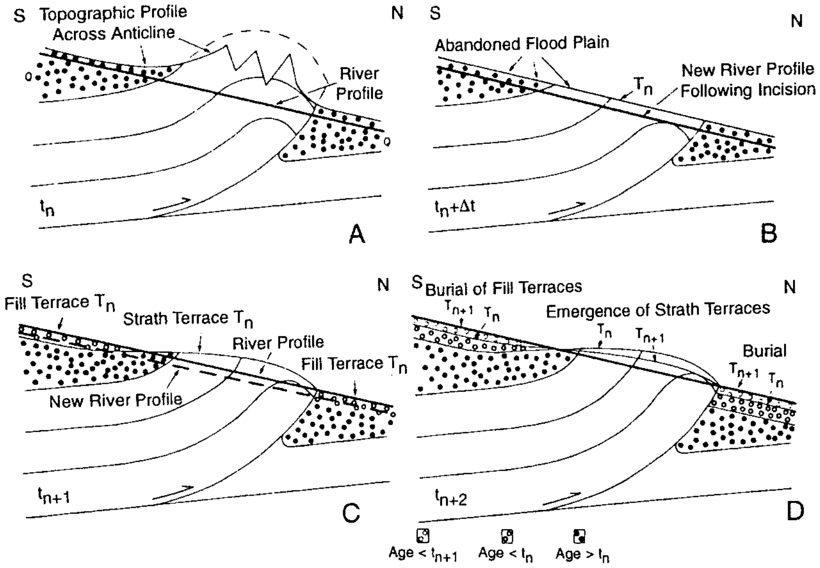

Figure 5.22 Diagrammatic cross sections showing the sequential development and deformation of fluvial terraces over an active anticline. (A) Time t_n; initial river profile through the anticline is shown as a heavy line. (B) Time $t_n + \Delta t$; river incises and leaves the t_n-stage floodplain abandoned as a terrace (terrace T_n). (C) Time t_{n+1}; folding upwarps terrace T_n over the anticline. The river then incises to a new level in the anticline (heavy line, River Profile) while simultaneously aggrading upstream and downstream of the anticline. This aggradation (open circles) buries the parts of the T_n terrace flanking the anticline. At the end of this time period, further incision occurs to the level of the dashed heavy line (New River Profile) and creates fill terraces on the flanks of the anticline (Fill Terrace T_n). Note that Terrace T_n, as it exists at the end of this time period, is a diachronous surface, with Fill Terrace T_n being younger than Strath Terrace Tn. (D) Time t_{n+2}; the New River Profile from the previous step (C) is upwarped over the fold, and the river incises the fold to form a new floodplain level (heavy line). This incision creates warped terrace T_{n+1} over the anticline. Terrace T_{n+1} has been upwarped once, and terrace T_n has been upwarped twice. On the flanks of the anticline, aggradation buries the T_n fill terrace and forms the fill part of terrace T_{n+1} (open circles), which is again younger than the strath part of the same terrace. Thus, alluvium on the flanks of the anticline is in younger-over-older stratigraphic superposition, whereas strath terraces over the anticline are nested in an oldest-equals-highest geometry. [From Molnar *et al.* (1994); reprinted with permission of the University of Chicago.]

5.6 PALEOSEISMOLOGY OF SUBDUCTION ZONES

5.6.1 Introduction

The majority of large compressional earthquakes result from plate convergence at subduction zones. The largest shocks are produced by slip on plate-bounding thrust faults, sometimes called *megathrusts,* and rupture of the entire thickness of the brittle lithosphere. Forearc and backarc thrust belts in the upper plate, and normal and strike-slip faults in the subducting plates also contribute to the seismicity of many subduction zones.

The three fundamentally different configurations of converging plates are: (1) convergence between two oceanic plates with subduction of the younger plate beneath the older plate, (2) subduction of an oceanic plate beneath the margin of a continental plate, and (3) collisions between two continental plates. Except for continental collisions, plate convergence results in the formation of *subduction zones* where one plate descends beneath the other and extends deep into the earth's interior. Along most subduction zones the *forearc,* the upper plate between the trench and the volcanic arc, is composed predominantly of accreted marine rocks that are typically strongly tectonized. The trenchward part of most forearcs are active *accretionary complexes,* in which large systems of thrust faults and fault-generated folds accommodate some of the plate convergence.

The principal fault in a subduction zone is the megathrust, the plate-bounding thrust fault that accommodates the relative movement between the plates. At plate scales these huge thrusts are linear or broadly curved to form smooth arcs hundreds or thousands of kilometers long. However, the regional structures and kinematics of megathrusts are complex and vary greatly (Plafker and Savage, 1970). At shallow depths the megathrust separates overlying highly deformed accreted sediments in the tip of the accretionary wedge from underlying subducted marine sediments and oceanic crust. The subducting sediments are poorly consolidated and contain large quantities of water, factors that tend to reduce coupling between the plates and promote *aseismic slip* (Pacheco *et al.,* 1993). As subduction proceeds some of the sediments are scraped off the descending plate and accreted to the tip of the growing accretionary wedge. The sediments that are not accreted move deeper, and dewatering takes place. The water is forced upward along the megathrust and along faults in the overlying accretionary wedge. Dewatering increases the coupling forces and promotes locking that results in *stick-slip motion* between the plates. Roughness of the descending plate, especially large-scale irregularities in the upper surface such as large seamounts or groups of seamounts, submarine plateaus, or fracture zones, creates *asperities* and increases the locking between the plates, promoting seismic subduction. As the oceanic plate descends it transports cold surface sediments down the subduction zone and depresses the temperature along the megathrust. Slick-slip behavior is possible as long as temperatures remain relatively low, less than 300° to 350°C (Hyndman and Wang, 1993). Above these temperatures stable sliding prevents the accrual of elastic strain and promotes aseismic subduction. Heat flow measurements above downgoing oceanic slabs and thermodynamic modeling of subduction zones indicate that the 350°C isotherm generally lies at a depth of 25 to 40 km.

The seismogenic processes from one subduction zone to another, or from one segment of a long subduction zone to another, vary considerably. Where older oceanic crust is being subducted, plate convergence proceeds by largely aseismic processes, although some of these subduction zones have high levels of seismicity that include abundant small and moderate size earthquakes. In such zones the subducting plate dips steeply and is weakly coupled to the overlying plate. Plafker (1972) classified these as the *Marianas type* of subduction zones. In contrast, subduction zones of the *Chilean type* (Plafker, 1972) are strongly coupled and characterized by seismicity dominated by infrequent very large earthquakes. Chilean-type zones include those that are subducting relatively young oceanic crust at a low dip angle. Subduction zones of the Chilean type that have produced great interplate earthquakes during the last half century include S. Chile ($M_w = 9.6$, 1960), Alaskan ($M_w = 9.2$, 1964), Central Aleutians ($M_w = 9.1$, 1957; $M_w = 8.7$, 1965), and Colombia ($M_w = 8.3$, 1979).

Jarrard (1986) compared 26 parameters for 39 subduction zones and concluded they could be grouped into seven classes (Fig. 5.1). Parameters included dimensions, age, and structural characteristics of both the descending slab and the upper plate, as well as the geometry and rate of relative motion between the converging plates. The age of the subducting plate and secondarily the rate of convergence appear to be among the most important parameters in determining the nature of subduction zone seismicity. The largest earthquakes ($M > 8.5$) are produced where young plates are subducting at the highest rates (Jarrard's classes 5–7), whereas slower convergence of older oceanic crust (Jarrard's classes 1–4) yields maximum earthquakes in the $M = 7$ to 8 range (Heaton and Kanamori, 1984).

The upper plate accretionary margins of subduction zones are commonly cut by large active faults. Trenchward vergent thrust systems are the most common fault type in upper plate margins, although arc vergent thrusts are also common. These faults reflect permanent strain resulting directly from convergence and demonstrate that plate-bounding thrusts have sufficient strength to transmit motion into the upper plate. Thrust mechanisms for shallow small and moderate magnitude earthquakes in the forearc of some subduction zones indicate that some of these faults are seismogenic, but large historic earthquakes clearly resulting from displacement on upper plate thrusts have been rare, and some subduction zones where large youthful thrusts are present exhibit little or no shallow compressional seismicity. One possible explanation of the apparent lack of large-magnitude earthquakes on forearc thrusts is that these faults represent upward branching imbricate splays from the megathrust and experience displacement only during subduction earthquakes involving slip on the megathrust. Such displacement occurred during the 1964 Alaskan earthquake when large surface displacements developed on the Patton Bay and Hanning Bay faults on Montague Island in Prince William Sound.

High-angle strike-slip faults are also common in some forearc settings, especially where convergence is strongly oblique. In Japan, the Median Tectonic Line, a large strike-slip fault system in the forearc of the Nankai subduction zone, is interpreted to accommodate the oblique component of convergent motion between the Philippine plate and the Asian plate. Although the principal faults composing the Median Tectonic Line have not produced a large earthquake in the past thousand years, a secondary conjugate fault to the Median Tectonic Line produced a M_W 7.0 earthquake near the city of Kobe in January 1995 that resulted in severe damage and more than 5000 fatalities (Comartin *et al.,* 1995).

5.6.2 Segmentation of Subduction Zones

Segmentation of plate-boundary megathrusts in subduction zones is apparent from historic subduction earthquakes. Although the largest of these earthquakes has produced ruptures more than 1100 km long, few have ruptured the entire length of the subduction zone. Thus, great historic subduction earthquakes have usually been restricted to a segment of the convergent margin. In the few localities where multiple seismic cycles have been recorded, the segmentation has differed from one cycle to the next. The long written history of subduction earthquakes on the Nankai trough in southwest Japan includes as many as eight earthquake cycles since A. D. 684 (Fig. 5.23) (Ando, 1975; Yonekura, 1975). The great earthquake of 1707 ruptured the entire length of the subduction zone. However, in 1854 the entire zone broke in two separate earthquakes, and in 1944 and 1946 two ruptures covered much of the zone. Based on these and earlier earthquakes, up to four segments can be identified. In most seismic cycles the entire zone ruptured within a time period of less than three years. Similar earthquake sequences have occurred

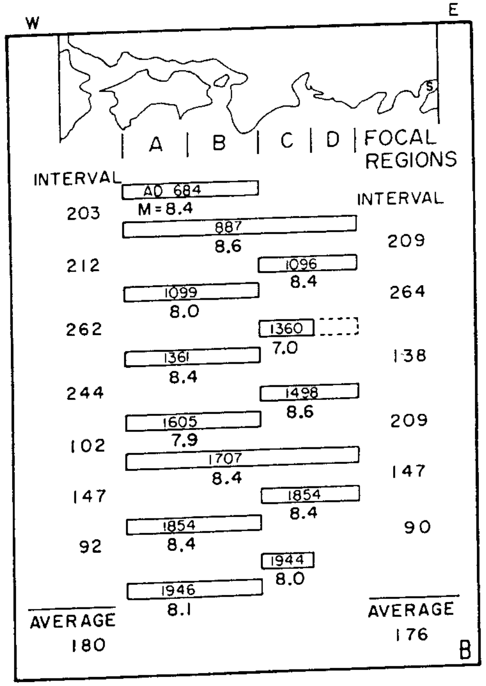

Figure 5.23 Historic records of subduction earthquakes on the Nankai subduction zone along southwest Japan show that five of the seven observed seismic cycles ended with a pair of earthquakes, each extending over about half of the length of the subduction zone. Two cycles ended with single long ruptures that broke most of the zone. Four of the multiple segment cycles produced a pair of earthquakes separated by a few years or less, illustrating temporal clustering of subduction earthquakes also seen on the Aleutian–Alaskan subduction zone during the 1957–1965 period (see Fig 5.1). Modified from Yonekura (1975).

along the Mexico and Colombia subduction zones (Thatcher, 1990). The great 1960 Chile earthquake broke across two separate rupture segments that had ruptured separately in 1835 and 1837. This behavior of different segmentation in successive seismic cycles may be typical of many subduction zones.

Analysis of *aspect ratios* of rupture length to width for subduction zones earthquakes worldwide shows that most range between 2 and 4, but a few have been as large as 9.7 (1965 Rat Island earthquake, Aleutian subduction zone) (Geomatrix, 1995). Unusually long ruptures associated with giant subduction earthquakes probably reflect domino-like triggering of slip on a series of potential rupture segments anchored on asperities. The length of each segment is probably close to the seismogenic width of the zone. Some convergent margins, notably the south Chile, the Aleutian, and possibly the Cascadia subduction zones, may be characterized by long ruptures that span multiple

potential segments. The 1957, 1964, and 1965 subduction earthquakes broke more than 3000 km of the Aleutian subduction zone. In the paleoseismic record the three separate events would not easily be distinguished, and such a series of earthquakes might be misinterpreted as a single giant rupture event.

The ends of rupture segments of some historic subduction earthquakes coincide with prominent structures in lower plates. The 1960 Chile earthquake initiated in the vicinity of the subducted Mocha fracture zone where juxtaposed oceanic lithosphere of different ages is being subducted. The rupture propagated south to the Chile triple junction where the Chile rise intersects the Peru–Chile trench. Fracture zones, groups of seamounts and oceanic plateaus, and subducting plate boundaries between oceanic plate systems are good candidates for termination points of subduction earthquake rupture. Offsets, gaps, or abrupt changes in strike or dip of the Wadati–Benioff zone may also delineate possible segment boundaries (Burbach and Frolich, 1986). Changes in the geometry of the downgoing plate as reflected in the location and offset of aligned arc volcanoes have also been identified as possible segmentation indicators (Guffanti and Weaver, 1988).

Upper plate structures have also been related to seismic segmentation of long subduction zones. The 1957 Aleutian earthquake (M 8.6) ruptured 1200 km of the central Aleutian subduction zone, where the architecture of the upper plate includes large strike-slip faults bounding rotating blocks that accommodate the arc parallel component of oblique convergence. The megathrust rupture propagated across several of these strike-slip faults (Ryan and Scholl, 1989; Ekstrom and Engdahl, 1989). In 1986 a M 8.0 earthquake reruptured a part of the 1957 rupture zone. This rupture may have terminated at one of the strike-slip faults in the upper plate. These earthquakes show that ". . . regions of high moment release, asperities, vary from earthquake to earthquake . . ."(Boyd *et al.,* 1992).

5.6.3 Surface Faulting: Upper Plate versus Plate-Boundary Structures

During the 1964 Alaskan earthquake slip appears to have been distributed on several imbricate thrust faults in the accretionary wedge as well as the megathrust. Up to 7.8 m of dip-slip displacement at the surface was measured on the Patton Bay fault on the southeast side of Montague Island, and up to 6 m of dip-slip displacement occurred on the Hanning Bay fault on the opposite side of the island (Plafker, 1969a). The marked decrease in uplift trenchward of these faults, which dip landward at 50° to 75° at the surface, suggests they probably merge with the megathrust at depth and during the 1964 event they accommodated a significant part of the total interplate slip. Sea-floor scarps and analysis of arrival characteristics of the tsunamis generated by the earthquake suggest the large surface displacements extended southwest of Montague Island to at least the latitude of Kodiak Island. No other surface faulting was found.

Late Cenozoic reverse and thrust faults and folds have been mapped on the sea-floor in the outer part of the accretionary margin of the Aleutian–Alaskan subduction zone, and some of these faults have been identified on land on Hinchinbrook, Hawks, and Montague Islands and on the mainland near Cordova and the Rude River Valley (see Fig. 5.32). These faults deform late Pleistocene glacial deposits and landforms, and displace latest Pleistocene marine limit shorelines and Holocene sediments. Most of the known on-land thrusts in the accretionary fold and thrust belt were not active in 1964, but have experienced displacement in the latest Quaternary. Additionally, none of these faults has generated surface displacement of a large earthquake independent of the 1964 earthquake. The likely interpretation is that the fold and thrust belt faults act in concert with the megathrust by partitioning slip from the plate boundary. Probably these faults do not produce large earthquakes and accrue slip independent of the megathrust. The faults in the Rude River–Hinchinbrook Island region that possess latest Pleistocene and Holocene scarps probably reflect previous great subduction earthquakes with slip occurring on different accretionary wedge thrusts than those activated in 1964.

Several of the Cascadia fold and thrust belt faults that come onshore in northern California have experienced late Holocene displacements. The question of whether these faults slipped independent of the megathrust, or accompanied interplate subduction earthquakes, is important to the assessment of the seismic hazard posed by the subduction zone. Seismic refraction and reflection profiling of the seafloor offshore of the Pacific Northwest shows many such faults are present in the outer part of the upper plate, but no seismicity has been associated with these faults. Similar fold and thrust belts are known along other convergent plate boundaries where a young oceanic plate is being subducted; the faults also are characterized by little or no seismicity. The Patton Bay and Hanning Bay faults described earlier are the only well-documented examples of fault rupture of thrusts in the accretionary fold and thrust belts along subduction zones that are similar to Cascadia.

Trenches across the Mad River and McKinleyville faults, two of the principal on-land thrusts in northern California, indicate these faults have experienced several displacement episodes during the Holocene (Figs. 5.13 and 5.14). The trench exposures show these faults have long recurrence intervals (several thousand years) relative to the several-hundred-year repeat time of subduction earthquakes suggested for Cascadia from most paleoseismic evidence. If these fault rupture episodes were coeval with slip on the underlying megathrust, only a few of the megathrust earthquakes are represented in the paleoseismic record of these faults. The Little Salmon fault, another of the large fold and thrust belt structures near the south end of the subduction zone, has experienced displacements as large as 7 meters repeatedly during the late Holocene. Trenches excavated across the fault where it crosses Little Salmon Creek valley exposed faulted and folded overbank silts and organic soils that record at least three individual displacement events (Fig. 5.15). Carbon-14 age estimates for the three paleoearthquakes suggest they occurred about 300, 700, and 1600 years ago (Clarke and Carver, 1992). These age estimates are permissively correlative with three of the four most recent subduction zone paleoearthquakes interpreted from coastal uplift and subsidence evidence, and allow the interpretation that the paleoslip recognized on the Little Salmon fault was generated during great megathrust earthquakes similar to the faulting in Prince William Sound during the 1964 Alaskan earthquake. However, the paleoearthquake chronology of any one accretionary wedge thrust is likely to reflect only some of the large or great earthquakes on the megathrust.

5.6.4 Historic Subduction Earthquakes as Modern Analogs for Paleoearthquakes

Large subduction earthquakes differ in scale and process in some important ways from most shallow crustal earthquakes. During subduction earthquakes fault rupture propagates entirely through the brittle lithosphere and produces elastic response of the crust. At the earth's surface above and adjacent to the rupture, large horizontal and vertical displacements accompany the earthquake. The wide rupture resulting from the shallow dip of many megathrusts, the long rupture length (>100 km), and the long recurrence intervals (10^2 to 10^3 yr) for megathrust earthquakes result in much larger rupture areas (10^3 to 10^5 km^2), displacements (5 to >20 m) and magnitude ($M_w = 7.5$ to 9.5) than most crustal earthquakes.

The most important feature of large subduction earthquakes is the regional coseismic deformation above the plate-boundary megathrust and the elastic relaxation of the forearc. These regional strains are expressed as vertical changes in land level, with the area above the rupture surface uplifted, and the area between the volcanic arc and the downdip edge of the rupture subsided (Fig. 5.24). Since most subduction zones are located along coastlines, these vertical motions are often recorded in the shoreline deposits and landscapes.

Observations of coseismic land-level changes associated with modern subduction zone earthquakes provide the main analog used to identify interplate paleoearthquakes along subduction zones. Affected coasts may rise or fall instantaneously during earthquakes (coseismic uplift or subsidence) and/or change elevation more slowly during *postseismic* and *interseismic* periods (aseismic uplift or subsidence). When great earthquakes ($M > 8$) occur at the boundary between the subducting and overriding plates, the region nearest

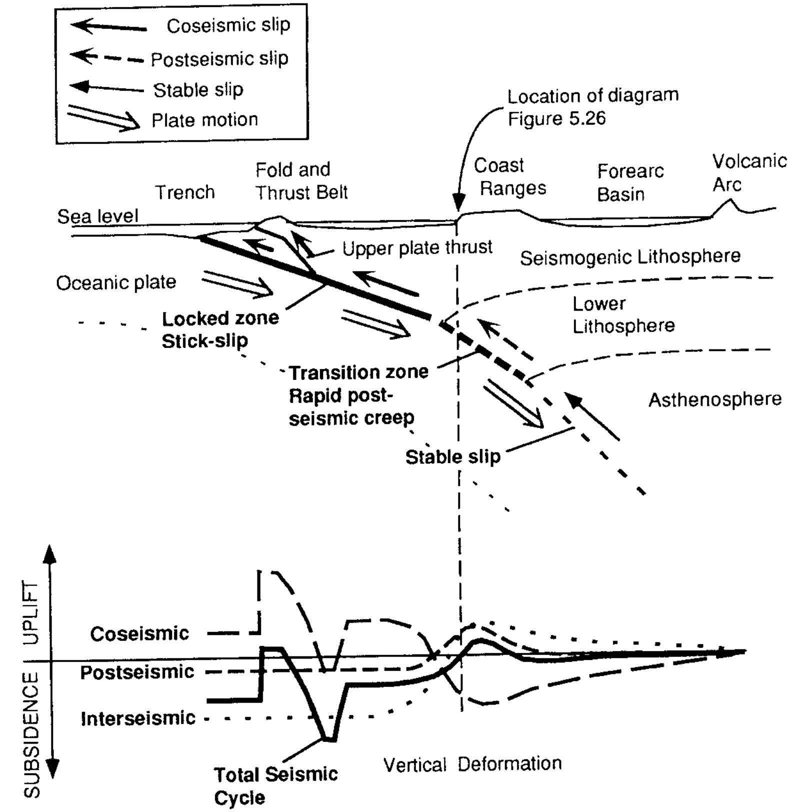

Figure 5.24 Pattern of deformation across a Chilean-type subduction zone (Plafker, 1972) for interseismic, coseismic, and postseismic parts of the seismic cycle. During the long duration interseismic part of the cycle, the locked zones of the megathrust are coupled and the upper plate is carried toward the arc and down with the descending oceanic plate. Compression of the backstop region above the transition zone and the deep stable sliding part of the megathrust generates uplift near the arc. During megathrust earthquakes, coseismic slip on the locked zone produces uplift above the megathrust rupture and elastic relaxation and subsidence between the downdip end of rupture and the arc. Slip on upper plate thrusts can generate localized and permanent uplift and subsidence in the fold and thrust belt. Rapid creep accommodates the slip deficit on the megathrust in the transition zone during the relatively short postseismic interval following the earthquake. This rapid creep produces rapid rebound in the area of coseismic subsidence.

the subduction trench (60 to 160 km wide) is commonly uplifted; at the same time a parallel zone arcward of the zone of uplift may subside (Fig. 5.24) (Plafker, 1972; Ando, 1975; Thatcher, 1984). Local areas in the zone of coseismic uplift can also be thrust upward during slip on imbricate thrust faults or growth of folds within the upper plate (Plafker, 1969a; Plafker and Rubin, 1978; Page *et al.*, 1989; Yonekura and Shimazaki, 1980; Berryman *et al.*, 1989; Ota *et al.*, 1991). Because only large plate-boundary earthquakes produce enduring land-level changes large enough to be recorded in most environments, the precision of these methods limits the threshold of detection of earthquakes along subduction zones to earthquakes of high magnitude. In this sense, the smallest morphogenic earthquakes of some subduction zones may be larger than the largest earthquakes produced by fault zones in some other tectonic settings.

Many of our inferences about past land-level changes during subduction zone earthquakes are based on observations following two of the largest earthquakes of this century, the 1964 M_w 9.2 earthquake in southern Alaska and the 1960 M_w 9.5 earthquake in south-central Chile. Much recent North American research has centered on identifying and dating evidence of prehistoric coseismic land-level change along the coast of western central North America in an attempt to assess the potential for subduction-zone earthquakes on the Cascadia subduction zone (Rogers *et al.*, 1995). Both the 1960 and 1964 earthquakes occurred on tectonically similar subduction zones (Heaton and Kanamori, 1984) situated along midlatitude coasts with landforms, sediments, and climates generally similar to those at Cascadia, so those earthquakes in particular have been studied as modern analogs.

The March 26, 1964, Alaska earthquake ($M_w = 9.2$) resulted from slip on an 850-km-long portion of the Alaskan–Aleutian subduction zone that released stresses accumulated from about 6 cm/yr of convergence between the Pacific and North American plates (Demets *et al.*, 1990). The earthquake was felt over more than a million square kilometers, and caused widespread damage across more than 100,000 km^2. The fault displacement propagated along the megathrust underlying Prince William Sound, southeast Kenai Peninsula, and the Gulf of Alaska offshore of Kodiak Island in south-central Alaska (Fig. 5.25), raising a 150- to 200-km-wide and 800- to 900-km-long part of the floor of the Gulf of Alaska between the trench and the eastern side of Kenai Peninsula and Kodiak Island. An equally large region between the uplifted area and the volcanic arc subsided as much as 3 m. Because the rupture was in part located beneath hundreds of miles of coastline the patterns, styles, and magnitude of coseismic vertical deformation were extensively recorded (Plafker, 1969b). Especially useful in mapping and measuring the uplift was the elevation of sessile intertidal plants and animals (barnacle and alga lines) above their life zones. Regional changes in the land level of 1 to 3 m extended over an area of about 150,000 km^2, with as much as 9 m of localized uplift on Montague Island along thrust faults activated during the earthquake. Thrust displacement and uplift of the seafloor generated large trans-Pacific tsunamis. Alternating mud–peat and peat–mud couplets, reflecting interseismic sedi-

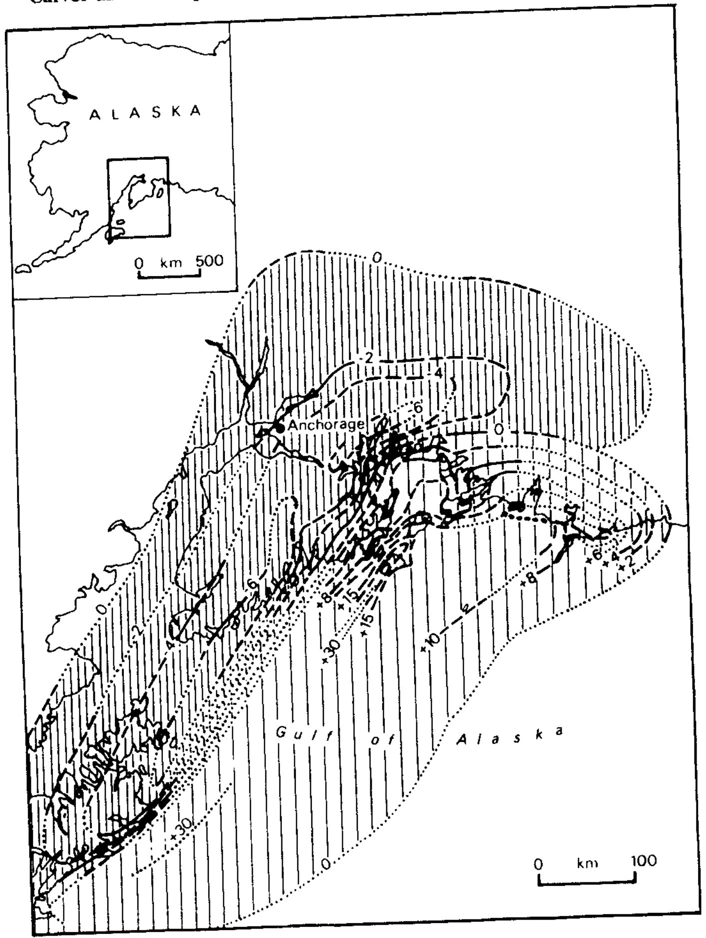

Figure 5.25 Coseismic deformation produced by the 1964 Alaskan earthquake. Regional subsidence (closely spaced lines) and uplift (widely spaced lines) encompassed most of the forearc along the length of the rupture. The axis of maxium regional subsidence and maxium regional uplift were located near the zero isobase (no land-level change). Measurements are in feet. From Vita-Finzi (1986), after data in Plafker (1969a).

mentation punctuated by sudden emergence or submergence, were also observed to form (Bartsch-Winkler and Schmoll, 1987).

Subduction earthquakes produce strong shaking over large regions that is commonly of unusually long duration and rich in relatively long periods, factors that favor generation of liquefaction and trigger slope failures. In Alaska ground motion lasted as long as 5 min at some locations and triggered

thousands of landslides in the mountains and along the coast. Many large landslides were triggered over more that 150,000 km^2. Some of these involved the collapse of entire mountainsides and minor peaks in the Chugach and Kenai mountains (Plafker 1969b). Strong shaking caused widespread liquefaction and other forms of seismically induced ground failure in coastal lowlands, river deltas, and along lake margins. Shaking induced submarine landslides that produced >20-m waves in Valdez Arm, Resurrection Bay, and other deep fjords near the epicenter.

The earthquakes of 20–21 May 1960 (M_w 9.5) in south-central Chile produced a pattern of land-level changes generally similar to those in Alaska (Plafker and Savage, 1970; Plafker, 1972). A trenchward belt of coseismic uplift about 100 km wide and nearly 1000 km long raised the sea-floor and several offshore islands as much as 4 to 6 m, and an adjacent belt of forearc subsidence drowned much of the south-central Chile coast. Strong shaking accompanied the main shock and lasted several minutes, triggering widespread liquefaction, ground failure, and landslides. The main shock was preceded by 12 hours by a M 8 foreshock and was followed by many large aftershocks that generated additional local strong shaking. Seafloor uplift caused a large trans-Pacific tsunami with 5- to 15-m run-up heights common along the Chilean coast.

Regional coseismic land-level changes reflecting similar patterns of deformation were observed during smaller subduction earthquakes in southwest Japan (1944, M_w 8.0; 1946, M_w 8.1: Ando, 1975), Mexico (1985, M_w 8.1: Bodin and Klinger, 1986), Chile (1985, M_w 7.9: Castilla, 1988), Costa Rica (1991, M_w 7.4: Plafker and Ward, 1992), and northern California (1992, M_w 7.1: Carver *et al.,* 1994b). The principal field evidence of the land-level change associated with these earthquakes was the mortality of intertidal organisms, although small raised terraces were generated in Mexico by the 1985 Michoacan earthquake. These earthquakes were in the magnitude range of 7 to 8 and resulted in maximum vertical land-level changes in coastal regions of about 1 m, insufficient to produce widespread geomorphic or stratigraphic evidence. In contrast, the 1964 Alaska and 1960 Chile earthquakes produced widespread geomorphic and stratigraphic records where coseismic uplift exceeded 1 m.

The processes of regional coseismic uplift and subsidence, widespread long duration shaking with attendant large landslides, liquefaction, and tsunami, when located along a coast above a subduction zone, produce the unique geologic signature of large megathrust earthquakes. The earthquake causes sudden changes in geologic process, which are typically reflected by an unconformity or sharp contact between pre- and postearthquake sediments, or by landforms formed by contrasting processes and environments. Certain coastline environments, such as salt marshes, river and stream deltas, intertidal wave-cut benches, and reefs are excellent recorders of the sudden vertical changes in elevation along the rupture segment, and act as geological "archives" of subduction earthquakes.

5.6.5 The Earthquake Deformation Cycle in Subduction Zones

Geologic and geodetic observations of vertical movements of the earth's surface along subduction zones show that significant changes in land level take place *between,* as well as during, subduction earthquakes. Vertical movement rates may be especially high during a relatively short (decades-long) postseismic period following great subduction earthquakes as displacement propagates downward along the deeper part of the plate interface, and the deeper lithosphere and possibly the upper asthenosphere, compensate for the slip deficit. Tide records for the 25 years following the 1964 Alaska earthquake show uplift of more than 20 mm/yr in the region of principal coseismic subsidence (Savage and Plafker, 1991). Over the same interval, tide stations in the region of coseismic uplift have subsided at rates up to 10 mm/yr. Geodetic observations across the Kenai Peninsula (Cohen *et al.,* 1995) and resurveys of tidal benchmarks across the Kodiak Archipelago (Gilpin *et al.,* 1994b) also show uplift rates considerably larger than those expected from plate convergence. These high movement rates, if they continue, will compensate for the 1964 coseismic displacements in a century or two, or a much shorter time than the 700-year recurrence interval indicated from paleoseismic studies.

Barrientos *et al.* (1992) likewise show that rapid uplift has occurred over the region of the Chile coast that subsided during the 1960 earthquake, with initial high uplift rates decreasing after about 16 years. They interpret the pattern of vertical deformation as relaxation of the upper lithosphere in response to propagating creep on the downdip extent of the coseismic rupture surface. Aseismic land-level changes over the region of coseismic subsidence in southwest Japan have been deduced from an array of 15 tide gauges for the 50 years ($\sim$30 % of the historic recurrence interval of 176 yr) following the 1944 and 1946 subduction earthquakes (Savage, 1995). Initially high uplift rates that lasted about a decade were followed by relatively linear uplift at a rate about twice that predicted from modeling plate convergence. Most models of the earthquake deformation cycle generalized from data from Japan and Alaska (Chapter 1) show that rates of aseismic movement generally decrease with distance from a fault and with time following an earthquake (Thatcher, 1986a; Savage and Plafker, 1991).

Dislocation models predict interseismic subsidence of the trenchward part of the upper plate above the locked segment of the megathrust (Fig 5.25). The arc-ward part of the upper plate undergoes coseismic subsidence during megathrust earthquakes as the result of elastic thinning behind the megathrust rupture, but then undergoes gradual uplift between earthquakes. This oscillation in land level over repeated seismic cycles helps explain why most of the regions that undergo coseismic uplift lie below sea level, while regions characterized by coseismic subsidence are mostly above sea level and include coastal mountains and upland areas. Therefore, large-scale landscape characteristics typically reflect the long-term deformation of coastal regions along subduction zones as dominated by interseismic deformation, which is often opposite to the sense of coseismic deformation and the appearance of the postseismic coastline morphology. For example, the prominent shoreline terrace produced by uplift of the Prince William Sound region during the 1964 Alaskan earthquake is the only emergent aspect of that coast's geomorphology; no raised Holocene terraces are found landward of the 1964 terrace. The geomorphic evidence for emergence is present only during the early part of the interseismic cycle (postseismic part). Prior to the 1964 earthquake in Prince William Sound, shorelines were drowned (submergent morphology) and showed little evidence of Holocene uplift.

Stratigraphic and geomorphic features of some coastal environments, such as salt marsh and shallow tidal bays, river and stream deltas, wave-cut platforms, and coral reefs may record both coseismic and interseismic elevation changes and in this way archive evidence of subduction earthquakes. Geodetic measurements of interseismic subsidence and uplift for some subduction zones indicate that rates are great enough to compensate for much or all of the coseismic elevation changes between slip events, so that little long-term elevation change is produced. Permanent coseismic uplift, as indicated by some raised glacioeustatic marine terraces and other emergent features, often represents localized upper plate deformation, usually generated by slip on thrust faults or folds in the accretionary wedge (e.g., Middleton Island; Plafker, 1969b; California coast, see Secs. 5.9 and 5.10).

5.7 LATE QUATERNARY SEA LEVEL

Sea level serves as the physical control on most geological and biological processes in coastal areas, and these processes in turn produce the specific datums used in geomorphic and stratigraphic field studies of subduction zone paleoseismology. Subduction earthquakes are generally recorded by geologic evidence (such as sharp unconformities) that indicate sudden changes in relative sea level. In contrast, interseismic deformation usually appears in the geologic record as gradual changes in shoreline facies and microenvironments. Reconstruction of the relative sea-level changes that result from repeated deformation cycles thus requires detailed information about any late Holocene changes in relative sea level that are independent of local vertical land-level motions (Fig. 5.26).

The level of the ocean surface along a shoreline is not static, but is constantly undergoing both short- and long-term changes. Some of these changes repre-

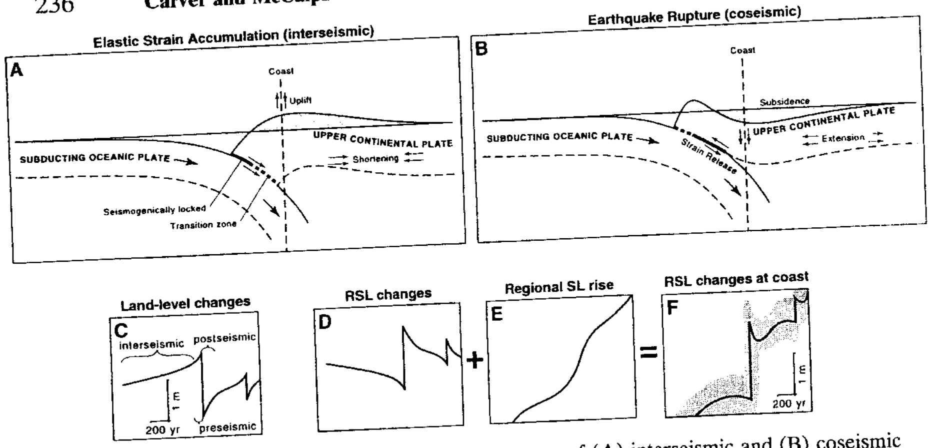

Figure 5.26 Schematic diagrams showing the pattern of (A) interseismic and (B) coseismic deformation associated with a subduction zone megathrust during an earthquake deformation cycle. (C) Land-level changes at the coast during two earthquake deformation cycles of different amplitude (scale approximate). (D) Relative sea-level (RSL) changes produced by the two cycles during a period of no change in regional (eustatic) sea level. (E) A gradual rise in RSL during the cycles that does not include short-term or small-scale changes in local and regional sea level. (F) RSL changes at a coast resulting from the sum of parts (D) and (E). In parts (A) and (B), the solid and thin dashed lines mark the megathrust; the thick dashed line is a transition zone between the locked and plastically deforming parts of the plate boundary. Shading shows the relative amount of uplift and subsidence of the upper plate during the (A) interseismic and (B) coseismic parts of the deformation cycle. The shaded band in part (F) shows ±0.5 m of uncertainty in estimates of former RSLs determined from geomorphic or stratigraphic data. [From Nelson *et al.* (1996); reprinted with permission of the American Geophysical Union.]

sent absolute differences in the level of the water surface relative to the geoid. They include short-term fluctuations such as diurnal tides, periodic storm surges, short-term excursions caused by variations in sea surface temperatures and wind patterns, and other meteorological conditions. These changes in sea level may be local or regional. Longer term rise or fall of eustatic sea level affects all of the world's open oceans and is caused by changes in global ice volumes, glacioisostatic- and hydroisostatic-induced variation in the shape of the geoid and tectonic modification of the shape and size of the ocean basins (Morner, 1976; Clarke *et al.,* 1978). Absolute sea level also varies from place to place due to a variety of local conditions including the latitude, the shape of the coast, and regional or local ocean currents.

Tectonic uplift or subsidence produces apparent changes in sea level along the deformed portion of the coast. These apparent sea-level changes are the inverse of the vertical movements of the land, and can cause responses in shoreline processes that are indistinguishable from those produced by changes in absolute sea level. At any point along a coast the sum of the *absolute sea level* and the *apparent sea level* determines the position of the water surface, or the *relative sea level* (Lajoie, 1986). Paleoseismic methods for identifying subduction earthquakes rely on recognizing apparent sea level changes by comparing the elevation of past relative sea levels with those expected from the history of absolute sea level.

During the Quaternary period sea levels fluctuated by 100 to 150 m over intervals of thousands to tens of thousands of years in response to large-scale, long-term climatic changes (Bloom, 1977). Low sea-level stands were produced by withdrawal of water from the global oceans to nourish continental ice sheets and greatly expanded alpine glaciers during each of the Pleistocene glaciations. Glacial minimum sea levels were at least 140 m lower than present. Interglacial sea levels ranged within a few tens of meters of present sea level, with the highest late Pleistocene (stage 5) interglacial sea stands a few meters higher than present sea level. During still stands, coastal processes formed enduring shoreline features, particularly wave-cut terraces, beach berms, and coral reefs that preserved a record of the sea level. Where long-term uplift was sufficient to raise these strand lines above the present sea level, the emergent shoreline markers provide a measure of the net tectonic uplift.

Following the last sea-level minimum about 20,000 to 15,000 years ago, sea level rose rapidly as the continental ice sheets retreated. Detailed studies of late Holocene sea levels on tectonically stable coasts indicate that *eustatic sea level* has been nearly stable or oscillating within a few meters of present levels during the last 6,000 years (Bloom, 1970; Schofield, 1973). Most studies suggest the recent rise has not been constant, but the shape of the eustatic sea-level curve for the late Holocene is not well established and probably has been slightly different at different latitudes and along different coasts. Some studies of tectonically stable sites suggest a high stand near or slightly above present eustatic levels was reached about 5 to 6 ka following very rapid early and mid-Holocene rises. A slight decrease in eustatic sea level may have occurred along some coasts in the northern Pacific between 4 to 5 ka (Calhoun and Fletcher, 1994; Grossman *et al.,* 1994; Mason and Jordan, 1994). Minor fluctuations occurred as glacioisostatic adjustments reequilibrated land levels to the interglacial distribution of glacial ice and flooding of continental shelf and coastal margins (Clarke *et al.,* 1978). Estimates of eustatic sea level for the last several thousand years suggest a generally slow rise with the rate accelerating in the past century to 1.5 to 2 mm/yr (Douglas, 1991).

Landforms and deposits with a known relation to sea level can serve as geologic index points to paleo sea levels. To be useful in reconstructing the elevation of past sea levels, an index point must have known age, elevation, indicative meaning, indicative range, and tendency (Nelson *et al.,* 1996). "Indicative meaning" is the vertical relation between the index point and the former reference water level (usually mean high tide or mean high water level). "Indicative range" is the vertical range of uncertainty in the index point's relation to the reference water level. Indicative meaning and range differ widely according to the type of index point and the form of the tidal curve (van de Plassche, 1986). "Tendency" reflects whether the index point records an increase or decrease in water level or salinity; movement of marine water toward a site defines a positive tendency.

5.7.1 Sea-Level Index Points along Erosional Shorelines

Along exposed, erosional coasts, emergent shoreline landforms known as *strand lines* provide a record of past sea levels (Lajoie, 1986). For erosional shorelines the principal datum is a *wave-cut shore platform* that commonly forms near the lower intertidal elevation (Bradley and Griggs, 1976; Merritts, 1996). Commonly shore platforms form at or near the level reached by low tides, and platforms grow in width landward as the coastal slope retreats. Shore platforms commonly have microrelief of several meters, particularly where they are cut into heterogeneous rock assemblages, and an initial seaward slope of several degrees (Bradley and Griggs, 1976). Both of these facets introduce uncertainties in relating the elevation of the platform to a past reference water level (Lajoie, 1986).

A variety of high-energy shoreline sediments cover parts of many wave-cut platforms. These deposits include coarse littoral and beach sands and gravels, and boulder and cobble lag deposits in the surf zone and active beach. Soils, terrestrial peats, freshwater marsh and lacustrine sediments, and dunes commonly form on terraces following emergence. The cover sediments overlying wave-cut platforms commonly contain datable material and also stratigraphic records related to local relative sea level (Clarke and Carver, 1992; Merritts, 1996). Terrace cover sediments can vary in thickness and add further uncertainty in assessing the elevation of the terrace surface relative to sea level at the time the terrace was cut.

The shoreward edge of wave-cut platforms, or *shoreline angle* (Lajoie, 1986), provides the best sea-level index point. According to Rose (1981), active shoreline angles around the North Sea have an indicative meaning of +1.5 to 2.0 m above mean sea level, with an indicative range (1σ) of ±0.4 to 0.6 m. By comparison, constructional beach ridges are more affected by large storms and have indicative meanings and ranges of 1.8 ± 0.8 m to 3.9 ± 1.4 m (relative to mean sea level). Shoreline angles are often buried by post-emergence colluvium shed from the adjacent wave-cut cliff. Detecting the shoreline angle beneath these cover sediments requires drilling or geophysics (Bradley and Griggs, 1976), which induces further components of uncertainty in the elevation of the sea level index point.

Because elevation changes from deformation during a single subduction earthquake are <2 to 3 m (often <1 m), the rather large indicative ranges of shoreline angles (plus the added elevation uncertainty associated with buried shoreline angles) combine to make shoreline angles only marginally useful in assessment of coseismic vertical movement, except after the largest ($M > 8.5$) subduction earthquakes. Often biological features, such as the borings made by sessile intertidal molluscs, have smaller indicative ranges in the decimeter range, and if preserved are better index points than the more ubiquitous but less precise shoreline angles.

On tectonically active coasts, platforms are cut during the interseismic intervals when relative sea level is static or slowly rising. Coseismic uplift raises these platforms, creating emergent terraces if the amount of uplift is large enough to elevate the platform above the high tide level. Along coastlines where coseismic uplift is exceeded by local sea-level rise, shore platforms may be reoccupied repeatedly during successive deformation cycles (e.g., Leonard and Wehmiller, 1992); such reoccupation further complicates using platforms as index points.

5.7.2 Sea-Level Index Points along Depositional Shorelines

Depositional intertidal environments are usually found in bays and estuaries and along sheltered coastlines, or where active tectonic subsidence has drowned the topography. Where sediments are abundant, such as near large river mouths, sea level is commonly approximated by extensive tidal mud flats, salt marshes, barrier bars, storm berms, beach and dune complexes, and intertidal delta fronts. Such environments provide the most complete record of local sea level and are the most sensitive to small sea-level changes. Because deposition at such sites often continues throughout the seismic cycle, stratigraphic records of both the interseismic and coseismic land-level changes may be preserved. Abundant datable material is commonly preserved in such settings.

Because many depositional processes, as well as the life zones of certain sessile intertidal plants and animals in sheltered shoreline environments, are restricted to narrow vertical ranges, detailed sedimentologic and biostratigraphic analysis can sometimes resolve the magnitude of land-level change with sufficient precision (≤ 0.5 m) to identify subduction paleoearthquakes. Most sensitive are *salt marshes,* which contain distinctive plant communities that colonize tidal flats at or just below the highest tide level (highest high water level, or HHWL). These salt-tolerant herbaceous plants occupy overlapping zones commonly less than 1 m in vertical extent (Fig. 5.27). Salt marshes are initiated by pioneering plants that colonize the highest part of the *intertidal mud flats.* The mud flats emerge due to sedimentation or lowering of local sea level. Different flora characterize low and high marsh zones. Along the north Pacific coast native low marsh species include *Carix lyngbyei, Distichlis spicata, Triglochin maritimum, Salicorni virginica,* and *Deschampsia caespitosa.* High marsh floral zones also locally contain these low marsh species,

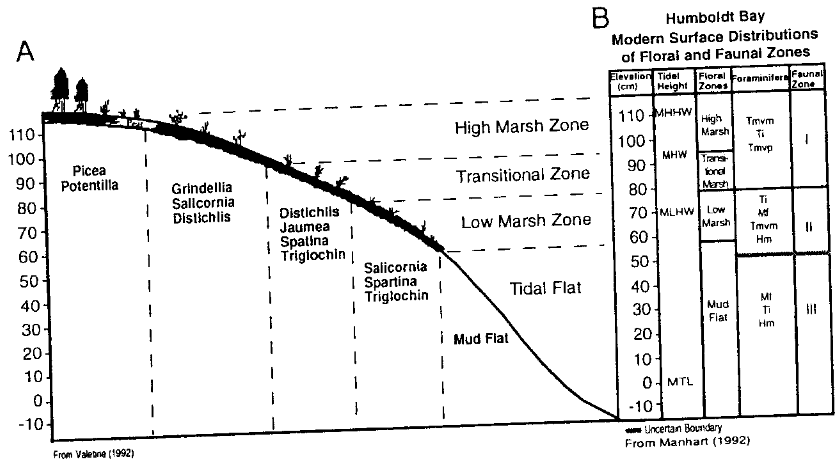

Figure 5.27 Diagram of salt marsh zonation showing the vertical ranges of diagnostic salt marsh plants and foraminifera in Humboldt Bay, northern California. Tmvm, *Trochammina macrescens v. macrescens;* Tmvp, *Trochammina macrescens v. polystoma;* Ti, *Trochammina inflata;* Mf, *Milliammina fusca;* Hm, *Haplophragmoides manilaensis.* [From Li (1992); reprinted with permission of Humboldt State University, California].

and also commonly include *Potentilla pacifica, Grindelia stricta, Triglochin concinnum, Jaumea carnosa, Plantage maritime,* and *Orthocarpus castillejoides.* The specific assemblage and vertical range of salt marsh herbs varies regionally and locally, but in general does not exceed about 2 m. Within the salt marsh environment, low, middle, and high marsh subzones can often be recognized by indicative assemblages and index species (Fig. 5.27). At sheltered sites the upper limit of these salt-tolerant assemblages is often sharp, with Sphagnum moss, terrestrial herbs and grasses, and vascular trees dominating the flora a few decimeters above the high tide line.

At and just below the highest tide level are narrow zones containing distinct assemblages of sessile intertidal foraminiferids and marine and brackish water diatoms (Hemphill-Haley, 1992; Jennings and Nelson, 1992). Microfossil assemblages of these organisms incorporated in the stratigraphy can be used to estimate the elevation of the horizon at the time of deposition relative to the local sea level. Foraminifera indicative of high marsh environments in the north Pacific are typically dominated by *Trochammina macrescens* v. *macrescens, T. macrescens* v. *polystoma,* and *Trochammina inflata.* Low marsh assemblages are locally variable but consistently include *Miliamma fusca.* Diatoms (microscopic unicellular plants) proliferate in marine, brackish, and freshwater aquatic environments, and their siliceous shells, ranging from 10 to 50 μm in size, are commonly abundant in marsh sediments. As with intertidal Foraminiferid, different species of diatoms flourish in microenvironments with restricted salinity and reflect narrow vertical zonation in the upper intertidal level. Quantitative microstratigraphic analysis of sediment samples spaced millimeters apart across mud–peat and peat–mud boundaries is necessary to detect relative sea-level changes (Mathewes and Clague, 1994). Although the indicative range of individual species is often in the decimeter range, overlapping of species assembleges may define an indicative range in the centimeter range (e.g., Hemphill-Haley, 1992; Nelson and Kashima, 1993).

Coseismic land-level changes are reflected by abrupt replacement of indicative assemblages, while gradual changes expected from longer term interseismic motions involve a transition in species composition over centimeters or decimeters of stratigraphic section (showing positive or negative tendency). Biostratigraphic changes in tendency may be identified within lithologically homogenous units, for example, a change from freshwater to brackish diatoms found several centimeters below a sharp peat-mud contact. Such biostratigraphic evidence shows that the rise in relative sea level preceded the sharp lithologic contact, implying a gradual rather than an abrupt sea-level change (Nelson *et al.,* 1996).

5.8 THE COSEISMIC EVENT HORIZON

Most paleoseismic evidence of subduction earthquakes is the direct result of either a sudden land-level change, shaking-induced liquefaction and mass movement, or tsunami run-up along the coastline adjacent to the rupture segment. Each of these coseismic processes results in a wide range of stratigraphic and geomorphic features. Recognition of landforms and stratigraphic horizons representing paleoearthquakes requires detailed microstratigraphic and geomorphic methods to demonstrate the sudden nature of the coseismic processes, and to distinguish evidence of paleoearthquakes from that of non-earthquake events such as storm surges, unusual tides, and other transient marine processes (Shennan, 1989; Nelson, 1992a; Nelson *et al.,* 1996).

Coseismic uplift creates a temporarily emergent shoreline. Emergence is then followed by colonization of the emergent surface by terrestrial plants, accumulation of terrestrial peat and locally derived sediments, and soil development. Geologic evidence of the suddenness of uplift may be preserved by a sharp contact between the active preseismic intertidal surface (either a wave-cut platform along erosional coastlines or beach berms, tide flats, or salt marshes in depositional settings) and the overlying subaerial sediments such as dune sand or freshwater peat. Supporting evidence of sudden uplift includes preservation of assemblages of intertidal mollusks in living position in raised beach and bay sediments (Lajoie, 1986), and borings in raised wave-cut platforms and shoreline boulders containing fossil borrowing clams (*Pholadidae* *penitella*) (Merritts, 1996). In such cases the fossil shell provides datable material suitable for estimating the age of the uplift event. Along sandy coasts with prevailing onshore wind, sudden uplift can trigger dune building by raising intertidal sandflats above the high water level and promoting dune building that buries the raised shoreline (Carver and Aalto, 1992), preserving datable plants and trees in the dunes. If emergence raises the upper intertidal zone into a subaerial environment that is not conducive to accumulation and preservation of sediment, weathering, soil development, and erosion modify the preuplift surface.

5.8.1 Characteristics of Coseismic Event Horizons

Where coseismic subsidence submerges the coast, the *event horizon* is commonly preserved as a contact between underlying terrestrial or upper intertidal wetland peats and soils, and the overlying lower intertidal mud or sand (Atwater *et al.*, 1995). Unfortunately, alternating mud–peat couplets can form in a variety of ways in addition to cycles of land-level change resulting from subduction earthquakes. Nontectonic variations in local sea level that produce peat–mud sequences include (1) short-term changes in ocean currents and sea surface temperatures, (2) changes in coastline morphology including breaching or growth of barrier spits, (3) migration of tidal channels and delta distributary systems, and (4) gradual local subsidence associated with compaction of thick sediment fills (Shennan, 1989; Nelson, 1992a; Nelson *et al.*, 1996). A critical need in paleoseismology is distinguishing mud-peat and peat-mud contacts that represent coseismic and interseismic land level changes from similiar stratigraphic features produced by nontectonic sea-level changes. Nelson *et al.* (1996) propose five general *field criteria* for recognizing abrupt coseismic subsidence of coasts: (1) suddenness of submergence, (2) amount and permanence of submergence, (3) spatial extent of submergence, (4) coincidence of tsunami or liquefaction sands at the event horizon, and (5) synchroneity of submergence.

The *suddenness of submergence* is reflected by the abruptness of the contact between sediments containing evidence of distinctly different elevations relative to sea level. In many bays and estuaries, sudden submergence places vegetated coastal wetlands into newly formed, highly active subaqueous depositional environments where quick burial by intertidal mud and sand is possible. In such settings the above ground stems and leaves of herbs and sedges are entombed in the mud and preserved in upright growth position (Fig. 5.28) (Atwater, 1987; Jacoby *et al.*, 1995). The stumps of trees growing along the pre-earthquake shoreline and in brackish coastal wetlands may also be buried and preserved in intertidal mud following large subsidence events. Fossil plants entombed in growth position, especially trees, provide high-quality material for high-precision radiocarbon dating. Other indicators of sudden submer-

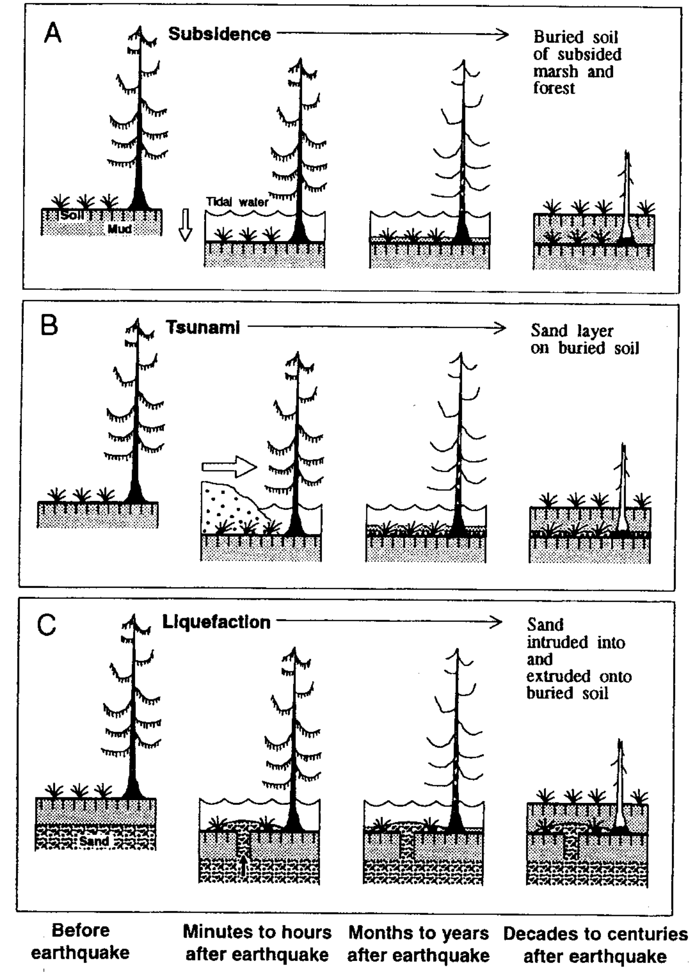

Figure 5.28 Diagram showing three of the principal processes that produce the most diagnostic paleoseismic evidence of subduction earthquakes in coastal environments. (A) Soils or vegetated upper intertidal tidal wetlands that are coseismically subsided into a lower intertidal zone and covered by marine or estuarine sediments. Evidence of coseismic suddenness of the event includes (1) fragile aboveground stems and leaf bases of herbaceous plants entombed in growth position in the marine sediments, (2) tree ring cross-matches that show synchroneity of death for the buried trees, and (3) normal tree ring growth suddenly terminated at tree death. (B) Tsunami sediments deposited directly on a subsided surface. (C) Liquefaction sediments vented directly on a subsided surface. [From Atwater *et al.* (1995); reprinted with permission of the Earthquake Engineering Research Institute.]

gence are an abrupt change from subaerial to intertidal pollen, diatoms, or foraminifera at the peat–mud contact. Finally, in coseismic peat–mud sequences, peats do not coalesce when traced to the upper edges of tidal wetlands, but remain separated by mud units.

Few nontectonic mechanisms can quickly cause a permanent relative sea-level change of >0.5 m, so the *amount and permanence* of sea-level change is a critical criterion. Field evidence for >0.5-m change in relative sea level includes lithologic (peat–mud) or biostratigraphic successions that bypass one or more intermediate facies or faunal zones, which would have been present if subsidence was gradual (Hemphill-Haley, 1995). If the peat–mud environments brought into contact differ in indicative meaning by >0.5 m, and the change in relative sea level is permanent, a coseismic origin is indicated. Permanence of change is harder to prove, since areas subsided for short terms (hours, days) in regions of high deposition rate can accumulate enough sediment that subsidence may appear "permanent."

Changes in relative sea level due to earthquakes should have a much wider *spatial extent* than vertical changes of similar magnitude that may result from nontectonic mechanisms such as channel or bar migration or river flooding, which should be restricted to individual estuaries. In the Pacific Northwest, event horizons that can be correlated between core holes over an entire estuary (hundreds of meters to a few kilometers laterally) or between estuaries are often considered to be coseismic, whereas thinner peat–mud couplets that pinch out over distances of a few tens to hundreds of meters may reflect nontectonic sea-level changes affecting only part of the marsh (Peterson and Darienzo, 1991).

The *coincidence of tsunami sands or liquefaction features* with peat–mud contacts is a strong independent indicator that the contact is coseismic. However, storm waves can also deposit sand in tidal marshes, so the sedimentology and geometry of sands should be assessed to distinguish storm-related sand from tsunami sand (see Sec. 5.8.3). Coseismic liquefaction features include clastic dikes, sills and sand blow deposits extruded during liquefaction, and ground failure structures including lateral spreads, slumps, and landslides (Chapter 7). Where such features can be stratigraphically traced to buried peat–mud contacts, evidence for coseismic origin is strengthened. Although liquefaction produces enduring deposits in stable geomorphic settings, many liquefaction features (particularly delicate sand blow deposits) are not easily preserved in highly active intertidal or fluvial environments.

Finally, earthquakes are much more likely to create *synchronous submergence* over broad reaches of a coast than are nontectonic mechanisms like bar formation or river flooding, which would occur at different times in every estuary. Eustatic changes in sea level would likely induce gradual changes in relative sea level, of slightly different age and stratigraphic expression, in estuaries with different shapes, tidal ranges, and sediment inputs. Wide synchroneity of submergence, when combined with suddenness of submergence, is thus good evidence for a coseismic origin. Demonstrating the synchroneity of submergence between noncontiguous sites is limited by the precision of dating methods. Radiocarbon ages of buried peats in Cascadia typically possess 2σ uncertainties of 200 to 500 calendar years (Nelson, 1992c; Nelson *et al.*, 1996), a range too broad to demonstrate synchroneity. At present, only tree ring dating (Sec. 5.8.2) has sufficient precision to show convincingly synchronous subsidence over broad areas.

The more of the five listed criteria that a contact satisfies, the more likely it is to have a coseismic origin. Nonseismic mechanisms can form peat–mud contacts that might satisfy one, or perhaps two, of the above criteria, but it is unlikely that any nonseismic contact could satisfy more than two of the coseismic criteria.

5.8.2 Earthquake-Killed Trees

Earthquake-killed fossil trees provide unique material for high-precision radiocarbon dating of paleoearthquakes. The dating technique requires samples of wood from earthquake-killed trees that include small numbers of annual rings of known ring position relative to the outermost ring (Atwater *et al.*, 1991; Nelson *et al.*, 1995). Two or more samples separated by at least a few decades (based on the count of annual rings in the section) are carefully cut from the same root or trunk section. The differential age of the samples obtained from the radiocarbon analysis can be compared with the dendrochronological age difference to verify the precision of the analysis. The technique is especially useful for young samples that yield multiple calibration ages (Fig. 5.29). In such cases samples can be collected from trees with many annual rings that produce single calibrated ages, and the sample age can be adjusted by adding the annual ring count from the sample to the outermost ring. For some of the intervals that yield multiple calibrated ages the relative age of samples determined from annual rings (i.e., older versus younger) and the relative ages determined from high-precision radiocarbon analysis can be compared to assess which of the multiple calibration ages is correct. The similarity of difference in the relative ages allows discrimination of which of the several calibrated ages is valid.

The death process and characteristics of earthquake-drowned forests are particularly important to the paleoseismology of subduction zones because tree rings provide the most sensitive time records of subsidence (Atwater *et al.*, 1991). At many places along the Alaskan coast in 1964, the seaward margin of the spruce forest was drowned. Reconnaissance of earthquake-killed trees at Turnagain Arm, Alaska, shows that trees completely submerged below the high water level died during the first growing season following the 1964 earthquake. Trees that were only partially submerged often survived for one

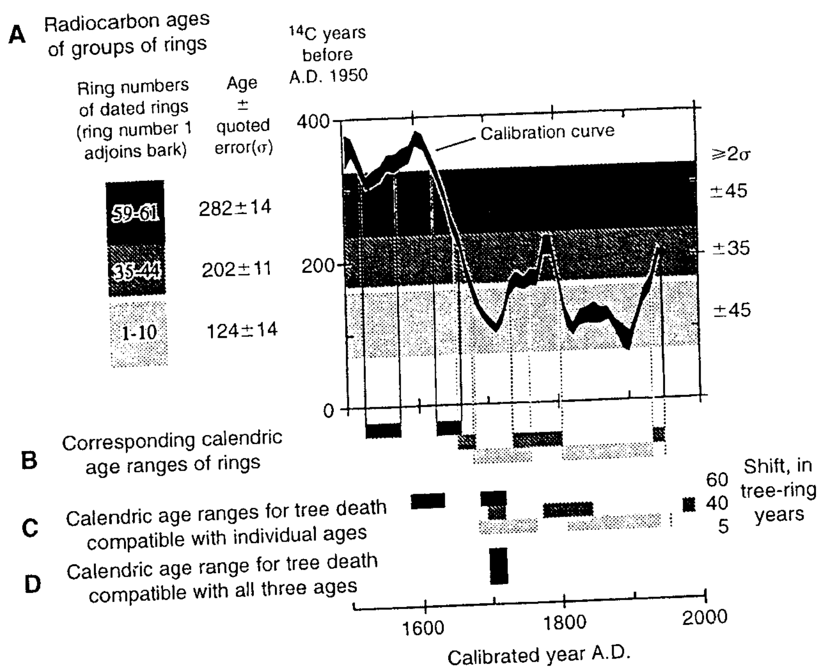

Figure 5.29 High-precision age estimates for paleosubduction earthquakes can be obtained by dating multiple samples of selected ring sequences from an earthquake-killed tree. The radiocarbon ages are matched to the calibration curve and the resulting calenderic ages are corrected for tree death date by ring counts. If the age is correct, the multiple calibrated and ring-count corrected ages for tree death should the same. [From Nelson *et al.* (1995); reprinted with permission of Macmillan Journals Ltd.]

or more growing seasons, although their growth was usually retarded. Where only part of the root systems of trees was submerged, only those roots and the branches sustained by those roots were killed immediately, the remainder of the trees continued to grow. Such trees exhibit roots that have different death ages (Jacoby *et al.*, 1995). Fossil forests thus offer one of the best opportunities to test the key criteria of suddenness and synchroneity of submergence.

5.8.3 Tsunami Deposits

Subduction earthquakes generate seismic sea waves (tsunamis) by several processes, including (1) deforming the seafloor and elevating or depressing the overlaying water column, (2) shaking and excitating the water column by

long-period seismic waves, and (3) triggering submarine or coastline landslides that displace large volumes of water. Tsunamis generated by submarine landslides can locally reach exceptional run-up heights of many tens to hundreds of meters, as occurred in Lituya Bay, Alaska, in 1958 and Valdez, Alaska, in 1964. However, these extreme run-up heights from landslide-generated tsunamis are typically limited to a small part of a coastline, often a single bay, and attenuate rapidly away from the point of origin.

Tsunamis produced from coseismic uplift and subsidence of the seafloor during large subduction earthquakes are commonly regional or transoceanic in extent. Run-up is greatest along the coast adjacent to the rupture and attenuates slowly with distance from the source. The run-up height of waves along open coastlines above the rupture in Alaska (1964) and Chile (1960) generally ranged between 5 and 10 m above normal tide level, with maximum local run-up reaching as much as 30 m in Chile (Plafker, 1972; Plafker and Savage, 1970). The 1960 Chile earthquake caused considerable damage to coastal property in Hawaii and Japan from 4- to 6-m-high waves. The 1964 Alaska tsunami produced run-up heights of 2 to 4 m at many points along the coast of Washington and Oregon, and waves of almost 5 m at Crescent City in northern California.

Tsunamis produced by regional seafloor deformation during subduction earthquakes typically include trains of waves with periods of several tens of minutes. Successive wave crests arrive along the coast for several hours and create repeated landward surges, followed by seaward return flows of the marine water. The rise and fall of sea level associated with the arrival of each wave at the coast is typically rapid; water levels can change several meters or more in a few minutes. Some combinations of wave height and coastal morphology produce tsunami bores, breaking walls of water that rush ashore with great force. More commonly run-up takes the form of a turbulent surge of water that flows rapidly landward as the level rises. The incoming surge may last for many minutes. If the wave length is long and the coastal morphology allows water levels on land to equilibrate with the tsunami wave height rapidly, the flow may become static for several minutes during the arrival of the crest, before the flow reverses and flood waters drain. Return flow is also commonly rapid and turbulent, but flow directions are strongly controlled by topography and follow preexisting drainage channels, as opposed to the more landward overland flow associated with the arrival of the wave crest. Debris berms composed of driftwood, broken or uprooted trees, and boats, pieces of buildings, and automobiles are commonly piled along the inland limit of significant flooding. Locally, large dense objects including boulders or blocks of concrete and masonry have been transported by the landward surge of large waves.

From a paleoseismiological standpoint, the tendency for tsunamis to transport and deposit sand and silt in the coastal zone is most important. Thin, often discontinuous, sand sheets have been observed in areas inundated by several modern tsunamis (Chile, 1960: Bourgeois and Reinhart, 1989; Alaska, 1964: Plafker and Kachadoorian, 1966; Clague *et al.* 1994; Nicaragua, 1992: Bourgeois and Reinhart, 1993; Satake *et al.,* 1993; Japan, 1993: Hokkaido Tsunami Survey Team, 1993; Indonesia, 1992: Yeh *et al.,* 1993). The 1964 Alaska case may be typical. Reconnaissance of tidewater sites on the eastern side of Kodiak Island 30 years after the earthquake shows the waves did not generate preserved geologic deposits along the majority of the coastline (Carver *et al.,* 1994a). However, where environments were favorable for deposition and preservation, the waves are mainly recorded as thin discontinuous sand sheets. These sites are located where abundant sand is present seaward of a coastal lagoon, marsh, or other low-lying deposition site. At most sites the 1964 tsunami is represented by a thin (<10 cm), well-sorted, massive sand lying sharply on the pre-earthquake surface. At some locations the sand is normally graded and locally contains rip-up peat clasts, scattered pebbles and cobbles, and woody debris. Sand sheets deposited on tidal delta fronts at Kalsin and Middle Bay on Kodiak Island show as many as four upward-fining sequences of well-sorted sand (Fig. 5.30). Records of the height and timing of seven waves were obtained from a stream gauge near the mouth of Myrtle Creek at Kalsin Bay (Plafker and Kachadorian, 1966) and show these deposits were left by waves with 4- to 6-m run-up heights and periods of 35 to 55 min.

Paleo tsunamis have been inferred from sand layers in coastal stratigraphy at many localities along the Cascadia subduction zone (Atwater, 1987; Reinhart and Bourgeois, 1987, 1989; Darienzo and Peterson, 1990; Reinhart, 1992; Clague and Bobrowsky, 1994a, b; Kelsey *et al.,* 1994; Hemphill-Haley, 1995) and locations as far apart as Scotland (Long *et al.,* 1989) and Japan (Minoura and Nakaya, 1991; Minoura *et al.,* 1994). The deposits have been found in marsh stratigraphy and in cores from coastal lakes and ponds and generally consist of one layer of well-sorted medium and fine sand. Some layers are composed of several upward-fining sequences interpreted to represent successive wave pulses, whereas other deposits are massive.

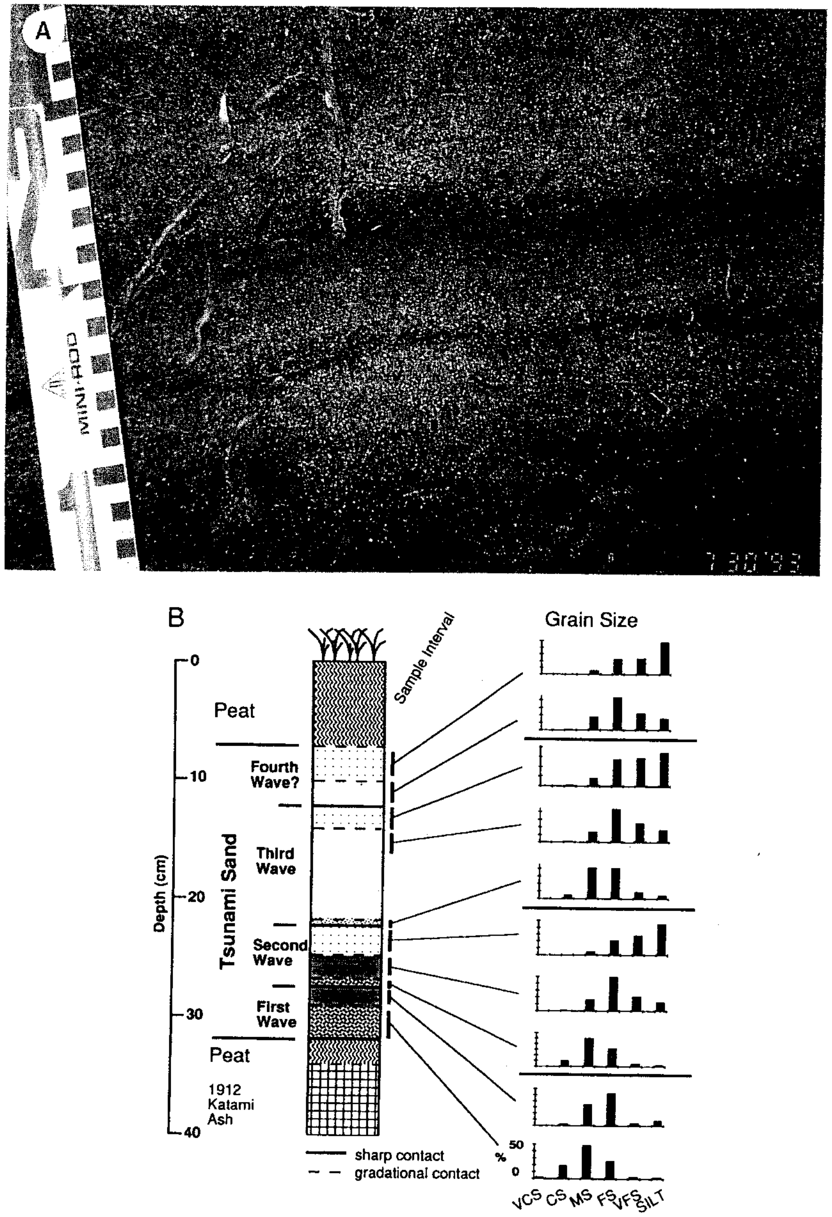

Figure 5.30 (A) Photograph and (B) stratigraphy and grain size distribution of the sand sheet deposited at Middle Bay on Kodiak Island by the tsunami from the 1964 Alaska earthquake. The tsunami at this location included at least six waves with run-up heights of up to about 4 to 6 m. The deposit is a 25-cm-thick sand sheet composed of up to four upward-fining sequences that are interpreted to have been deposited by successive wave pulses. The mean grain size of each of the four upward-fining sequences also decreases upward, perhaps reflecting winnowing of the available sand by each wave pulse. Tsunami sands at some nearby sites do not show upward fining, but instead are massive.

Sand beds are also deposited in intertidal and marsh environments by channel migration, river floods, and storms, so some criteria are needed to distinguish tsunami sand from nontsunami sand (Dawson *et al.,* 1991). Field criteria for a tsunami origin would suggest strong landward currents of unusual strength, and an offshore or bayward sand source, and include (1) landward thinning of the sand sheet (Reinhart, 1992), (2) landward fining of the sand, (3) a marine source for the sand, as indicated by marine diatoms (Kelsey *et al.,* 1994), and (4) landward rise of the sand sheet and onlapping of sand onto subaerial deposits or soils (Atwater and Moore, 1992; Clague and Bobrowsky, 1994b).

5.8.4 Summary of Stratigraphic Evidence for Paleoseismicity

The postseismic and interseismic stratigraphy of coasts above active subduction zones results from a complex interplay between coseismic movement (uplift and subsidence), interseismic movement (uplift and subsidence), the ratio of net coseismic to interseismic movement, and nontectonic factors such as coastal geomorphic processes and deposition rates. Figure 5.31 represents a preliminary attempt to show how these factors combine to produce certain types of stratigraphy, as described in Secs. 5.9 and 5.10. The representation neglects factors such as eustatic sea-level changes, so it must be viewed more as an aid to visualization than as a rigorous predictive model. Nevertheless, the diagram does accurately portray the type of stratigraphy encountered at various locations on coasts of the Pacific Northwest.

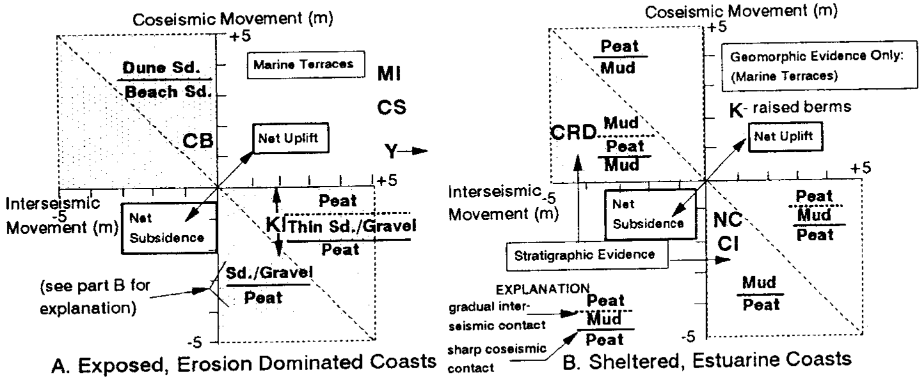

A. Exposed, Erosion Dominated Coasts

B. Sheltered, Estuarine Coasts

Figure 5.31 Schematic diagrams showing how permutations of coseismic movement (vertical axis), interseismic movement (horizontal axis), and coastal deposition rates (parts A, B) affect coastal morphology and stratigraphy (diagrammatic sections in various quadrants; see explanation). Shaded areas show the usual fields of coseismic uplift followed by interseismic subsidence (upper left) and coseismic subsidence followed by interseismic uplift (lower right). Dashed diagonal line separates regions of net uplift and net subsidence. Field examples described in the text from Alaska and Cascadia are shown by bold letters. (A) Exposed coasts of low deposition rate. MI, Middleton Island; CS, Cape Suckling; Y, Yakataga–Icy Bay; CB, Clam Beach; KI, Kodiak Island. The first three listed sites have undergone both coseismic and interseismic uplift, hence their marine terrace geometries. (B) Sheltered coasts with high deposition rates. K, Katalla; NC, northern Cascadia; CRD, Copper River delta; CI, Cook Inlet.

On exposed, erosion-dominated coasts, net subsidence results in drowning of the coast and submergence of any paleoseismic stratigraphy. Net uplift results in flights of marine terraces veneered with thin littoral sediments. Where coseismic movement is almost exactly matched by equal but opposite interseismic movement, and deposition rates are low, the rocky coasts eventually return to their former positions with respect to sea level, and little geologic evidence may be created from even great paleoearthquakes (e.g., much of the Prince William Sound coast).

On sheltered coasts and embayments with higher deposition rates, various combinations of coseismic and interseismic movement produce peat–mud sequences. Where net subsidence is greater than deposition, the coast will be drowned and paleoseismic stratigraphy submerged. Marine terraces and raised berms form in areas of net uplift, usually areas affected by local upper plate faults and anticlines. Only where coseismic and interseismic movements are opposite in sign and tend to cancel, and deposition rates are moderate to high, will peat–mud sequences form and be accessible for paleoseismic study.

5.9 PALEOSEISMIC EVIDENCE OF COSEISMIC UPLIFT

At present, the level of paleoseismic investigations for most subduction zones is reconnaissance level at best, and detailed studies have been conducted at only a few localities on those subduction zones that have received the most attention. No subduction zones have been studied in sufficient detail to allow more than a general characterization of the late Holocene paleoeoseismicity, and for those the record extends back only a few cycles. Much of the field evidence interpreted to reflect subduction earthquakes is the result of studies in Alaska and along the Cascadia subduction zone. Although we discuss only North American case histories here, due to our familiarity with the field evidence, similar studies in Japan (e.g., Ota, 1975; Ota and Yoshikawa, 1978; Yonekura, 1975; Matsuda *et al.,* 1978; Maemoku, 1988, 1990) and Chile (Plafker, 1972; Atwater *et al.,* 1992; Nelson and Manley, 1992; Bartsch-Winkler and Schmoll, 1993) describe many of these same phenomena.

5.9.1 Alaska

Paleoseismic evidence of coseismic uplift on the eastern part of the Aleutian–Alaskan subduction zone has been described for the Yakataga coast near Icy

Bay (Jacoby and Ulan 1983), at Cape Suckling (Plafker, 1969b) and Middleton Island (Plafker and Rubin, 1978; Plafker *et al.*, 1992). The principal evidence is flights of raised late Holocene terraces that are interpreted to have been elevated suddenly during rupture of the eastern end the subduction zone.

Yakataga–Icy Bay: The Yakataga coast is situated along the Yakataga segment of the subduction zone which did not break in 1964 (Fig. 5.32). Coastal processes along the Yakataga segment are dominantly erosional. Between Cape Yakataga and Icy Bay much of the present shoreline is bordered by wide intertidal wave-cut shore platforms and actively retreating sea cliffs. The lowest emergent terrace is about 8 to 10 meters above the active shore platform, and each of the older late Holocene terraces is elevated 8 to 10 m above the next (Jacoby and Ulan, 1983; Plafker *et al.*, 1992). Radiocarbon age estimates for the terraces range from about 1000 years for the lowest to about 5000 years for the highest. The terraces are continuous along most of the coast between Icy Bay and Cape Yakataga, a distance of about 60 km.

The flights of raised terraces along the Yakataga coast indicate rapid uplift, probably largely coseismic and associated with rupture of the eastern end of the Aleutian-Alaskan subduction zone. The presence of these bold late Holocene terraces and the lack of historic rupture along the Yakataga of the coast has led some paleoseismologists to identify this segment as the likely site for a future great subduction earthquake (Nishenko and McCann, 1981).

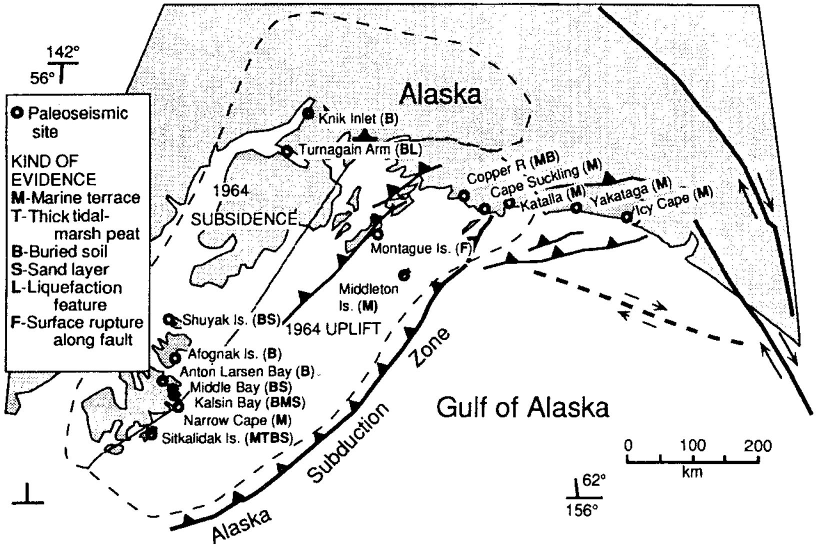

Figure 5.32 Map of the eastern end of the Alaska–Aleutian subduction zone, showing locations of principal sites of paleoseismic evidence mentioned in the text. Dashed lines outline areas of coseismic subsidence (to the northwest) and uplift (to the southeast) in 1964.

Cape Suckling: Cape Suckling, located at the eastern end of the 1964 rupture, was uplifted about 1.5 m in 1964. Evidence of three previous episodes of uplift are present in the form of three raised late Holocene marine terraces at Cape Suckling and on Kayak Island. There terraces are presently at elevations of 6 to 25 m. Conventional radiocarbon age estimates for the four uplift events along the Yakataga coast indicates that the most recent dates to about 700 to 900 years ago, with the others occurring within the past 4000 yr (Plafker, 1969b).

Middleton Island: At Middleton island about 3.3 m of uplift in 1964 produced a new terrace (Plafker, 1969b; Plafker and Rubin, 1978; Plafker *et al.*, 1992). The uplift of Middleton Island in 1964 produced terraces that are about half as high as those produced by the last three strain cycles recorded by elevated terraces on the island. Several alternatives have been suggested for this difference between the 1964 event and the paleoseismic record of past events to affect the island. One hypothesis is that much of the slip was partitioned onto the Montague Island thrust system in 1964, but not in previous earthquakes. This explanation is consistent with the lack of obvious evidence for anomalously large amounts of uplift resulting from upper plate thrusting on Montague Island and evidence for repeated late Holocene growth of the Patton Bay, Hanning Bay, or other thrust faults on the islands of northern Prince William Sound. An alternative hypothesis explains the uplift deficit by assuming that future contributions will be made from the Yakataga segment of the subduction zone, and that uplift will increase to the full amount recorded by the pre-1964 terraces when the Yakataga segment ruptures. This hypothesis requires that the rupture surface in 1964 will be reactivated at its eastern end along with the section of the fault that remained locked in 1964.

Katalla: In addition to raised terraces, several of the late Holocene uplift events that affected the eastern end of the Aleutian–Alaskan subduction zone are represented by elevated lagoons, storm berms, and delta tidal flats in the lower Katalla River valley (Fig. 5.33). During the late Holocene the Katalla River valley has been the location of rapid coastal progradation. Large storm berms have repeatedly formed across the mouth of the Katalla valley, each seaward of the previous one by hundreds of meters. Small lagoons, tidal flats, and salt marshes developed behind the berms. More than 20 prominent storm berms are preserved in the lower 5 to 7 km of the valley. The present active beach berm and lagoon has formed since the 1964 earthquake, which caused about 1 m of uplift. The pre-1964 tidal lagoon and salt marsh were elevated above the highest tides and the marsh is being replaced a juvenile spruce forest. Former tidal flats and marsh surfaces behind relic storm berms further inland are separated by elevation differences comparable to the riser heights of the prominent terraces along the Yakataga coast. Stratigraphy of the raised tidal lagoons shows marine mud and salt marsh peat containing fossil salt

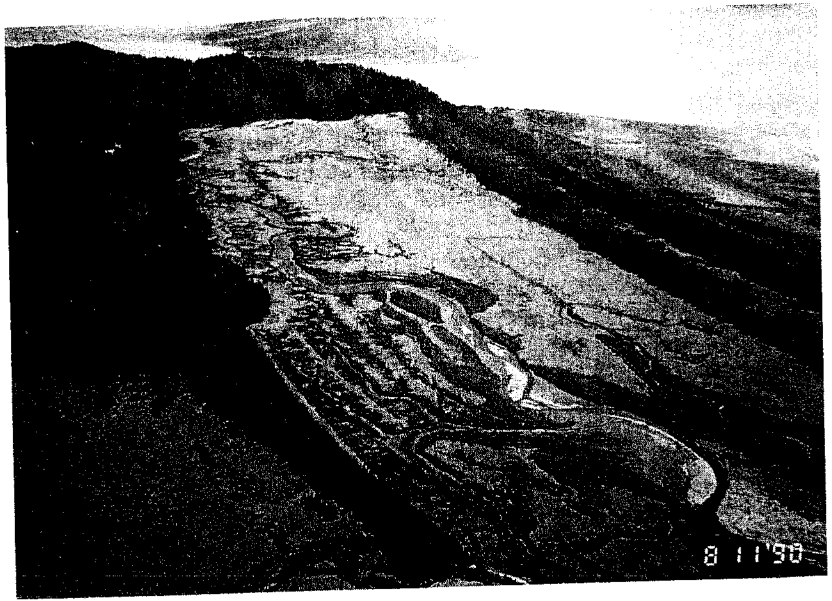

Figure 5.33 The lower Katalla River valley, located on a rapidly emerging coast supplied with large volumes of sediment from glacial meltwater rivers, is rapidly prograding and leaving a record of former shorelines as large forested storm berms. Marshes between the berms contain peat with salt marsh plant fossils, capping intertidal mud containing marine shells. The elevation of the berm–marsh sequences increases inland, reflecting repeated episodes of uplift. During the 1964 earthquake the region was elevated about 1 m. Subsequent to uplift, a new storm berm and lagoon have formed seaward of the 1964 beach, and spruce trees have become established on parts of the pre-earthquake salt marsh.

marsh plants, which are sharply overlain by subaerial sphagnum peat and subaerial plants and trees.

Copper River Delta: The most detailed and best documented paleoseismic record for the eastern end of the Aleutian–Alaskan subduction zone is based on interpretation of sediments accumulated in the extensive delta of the Copper River (Plafker *et al.*, 1992). The delta is located near the eastern end of the coast uplifted in 1964. During the earthquake the delta was raised about 2 m. Prior to the 1964 uplift the delta front included an area of several hundred square kilometers of unvegetated muddy tidal flats and intertidal marsh between distributaries of the Copper River, a large, highly seasonal and very sediment-laden river. The earthquake elevated this region sufficiently to force the coastline seaward by several kilometers and to raise large tracts of the delta front above the reach of the highest tides. These former mud flats and marshes have quickly been colonized by dense vegetation. Preuplift sites

of marine mud and sand deposition are now forming postuplift peats and organic soils.

The stratigraphy along the front of the delta consists of 2- to 3-m-thick layers of marine silt interbedded with 10- to 20-cm-thick sequences of peat and organic soil (Fig. 5.34). Some of the soils contain roots and stumps of trees that grew while the delta front was emergent. The silt is laminated, with the laminations (each 5 to 15 mm thick) probably reflecting seasonal deposition of glaciofluvial sediment from the river. These silt layers were deposited on the submerged delta front when the delta was in the "down" position during the latter part of the interseismic interval. The alternation of marine and subaerial sediments shows the surface has oscillated above and below sea level repeatedly during the late Holocene. The peats were formed after uplift events raised the mud flats, as in 1964, and marshes and forests replaced the intertidal environments of the preseismic intervals. A gradual postseismic and eustatic sea-level rise submerged the delta surface, drowned the marshes and forests, and initiated silt deposition. Continued subsidence and deposition formed the thicker silt layers between uplift events. Tide gage records at Cordova, located at the western edge of the delta, show a relative sea-level rise of 9.7 ± 0.5 mm/yr since 1964, a rate that will resubmerge the delta front within about two centuries (Savage and Plafker, 1991).

5.9.2 Cascadia Subduction Zone

Along most of the southern Oregon and northern California coast, raised late Pleistocene glacioeustatic marine terraces record long-term net uplift (Carver, 1987a; Kelsey and Carver, 1988; Merritts and Bull, 1989; Kelsey, 1990; McInelly and Kelsey, 1990). The raised terraces are located along parts of the coast that are closest to the subduction zone deformation front (Fig. 5.35), presumably seaward of the zero isobase which probably intersects the shoreline in central Oregon (Peterson *et al.*, 1993). Seismic reflection and refraction surveys of the continental shelf and slope along the Cascadia subduction zone reveal that a 70- to 100-km-wide belt of young thrusts and folds deform the seaward tip of the upper plate (Clarke, 1992; Goldfinger *et al.*, in press). The southern part of the fold and thrust belt intersects the coast and extends onshore in southern Oregon and northern California. Late Quaternary growth of the fold and thrust belt has thus strongly influenced the vertical movements of this part of the coastline, and has produced net uplift at some places and subsidence along other parts of the coast. The large differential vertical tectonic motions of the southern Oregon and northern California coasts are in striking contrast to the relatively uniform and small vertical movements during the late Quaternary along the northern Oregon and Washington coasts.

Raised late Holocene marine terraces are present along some parts of the coast in northern California at the south end of the Cascadia subduction zone

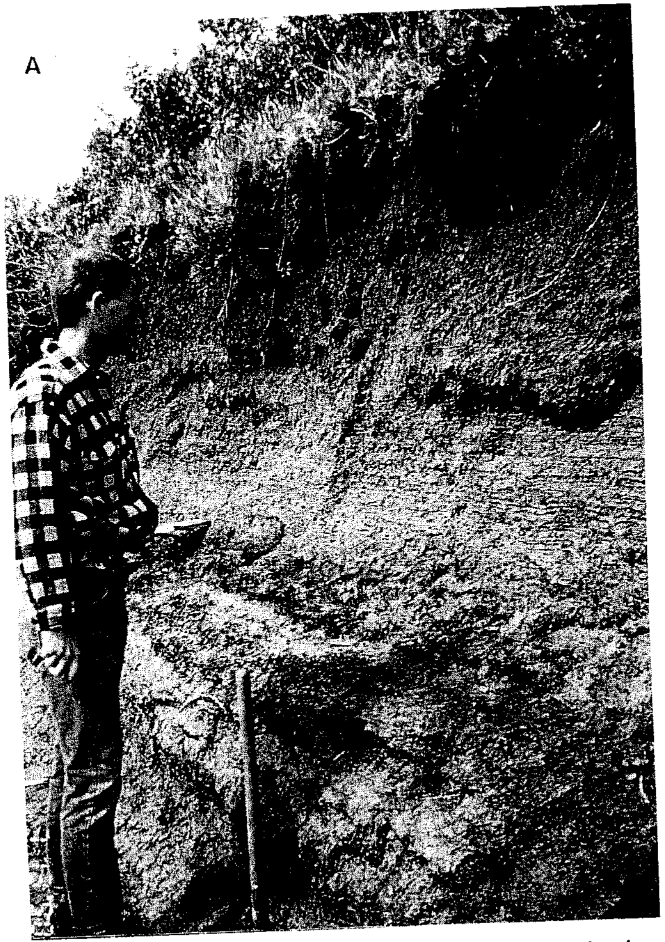

Figure 5.34 (A) Stratigraphy exposed in a channel bank in Alaganak slough on the Copper River delta, Alaska. This area was a tidal mud flat prior to about 2 m of uplift during the 1964 earthquake. The modern vegetation is growing on about 2 m of thinly laminated estuarine mud that buries a 50-cm-thick peat layer (dark layer near the shovel at the bottom of the exposure). The buried peat is composed of remains of the same species that presently grows at the site. Additional peat–mud sequences underlay the exposed section. The peats formed postseismically after emergence such as in 1964. Rapid postseismic subsidence and a rise in sea level have resulted in submergence of the postseismic subaerial peats and burial by intertidal silt, probably as annual couplets averaging about 1 to 2 cm thick. (B) Stratigraphy and displacement history for the Copper River delta assuming coseismic uplift events comparable to the 1964 uplift and linear interseismic submergence at a rate of about 6 mm/yr. Coseismic uplifts indicated by vertical lines (A–B, A′–B′, A″–B″). Peat accumulation occurs during the interval from coseismic uplift to resubmergence below extreme high tide (post-B, B′–C′, B″–C″), and accumulation of intertidal deposits occurs during the remainder of the interseismic interval (C′–D′, C″–D″). The inset diagram shows three possible nonlinear interseismic subsidence paths. [From Plafker *et al.* (1992); reprinted with permisssion of Springer-Verlag Publishers].

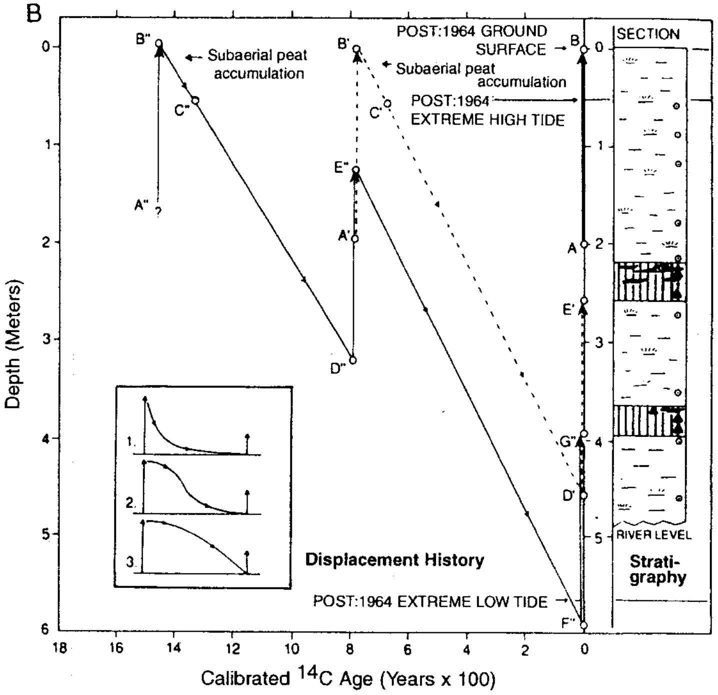

Figure 5.34 (*Continued*)

(Clarke and Carver, 1992; Merritts, 1996). The highest terraces are localized along the crests of thrust anticlines above major faults in the fold and thrust belt. At Cape Mendocino several raised terraces between ~300 and ~6000 years old are present and have been interpreted to have been elevated by interplate earthquakes at the southern tip of the subduction zone (Merritts, 1996). Support for this interpretation comes from the 1992 Cape Mendocino earthquake which was accompanied by as much as 1.4 m of uplift along a 25-km-long section of the coast between Punta Gorda and Cape Mendocino (Carver *et al.*, 1994b; Prose, 1994a). The location and mechanism for the main shock (M_w = 7.1) and the pattern of aftershocks indicate the causative fault was a low-angle east dipping thrust located at or very close to the plate interface (Oppenheimer *et al.*, 1993).

Raised late Holocene terraces have also been described in northern California at Clam Beach (Clarke and Carver, 1992; Carver and Aalto, 1992). The broad raised terrace is covered with an upper sequence of dunes that overlie a buried soil with rooted fossil spruce and fir trees (Fig 5.36A). The buried paleosol is developed into a lower sequence of dunes that overlie beach sand

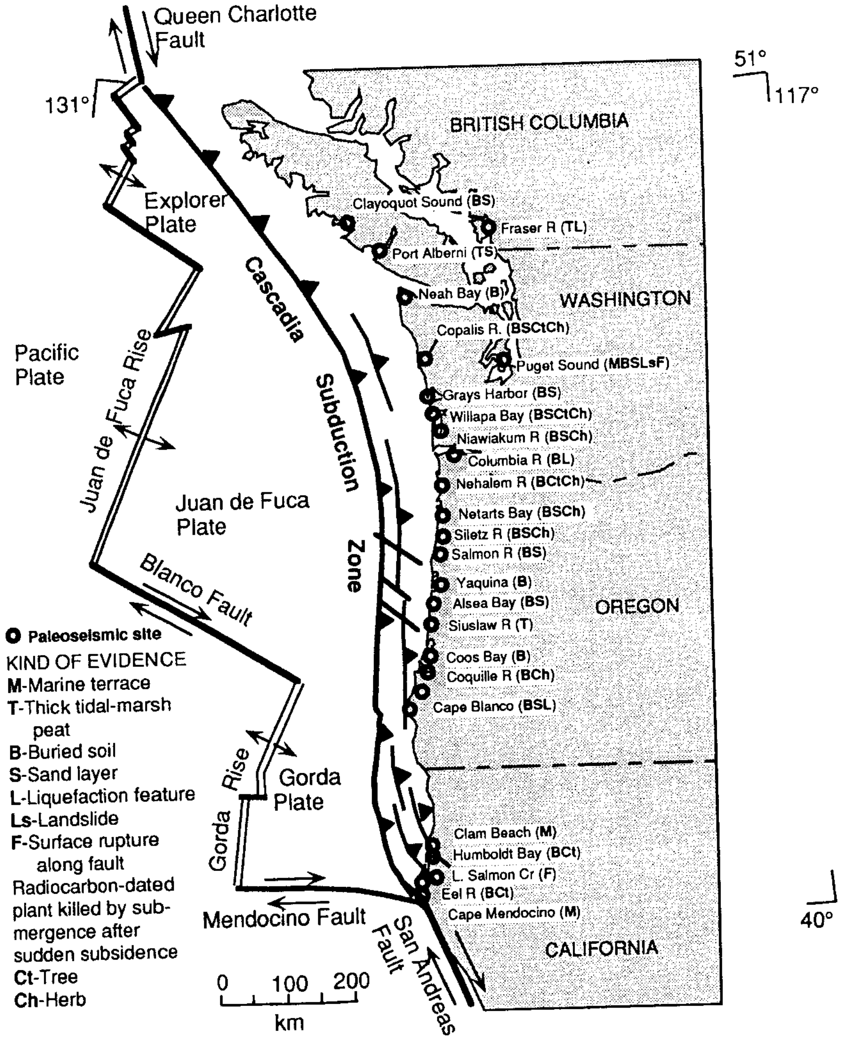

Figure 5.35 Map of the Cascadia subduction zone showing locations of principal sites of paleoseismic evidence for the last event(s) about 300 years ago. Modified from Atwater, *et al.* (1995).

containing driftwood. The ^{14}C age for the driftwood is about 1100 yr, and the age of the buried trees and soil is about 300 yr. The terrace is cut into highly faulted and folded mid-Pleistocene marine sands and muds and the abrasion platform is presently several meters above high tide level. The terrace and cover sediments are interpreted to contain a record of two coseismic uplift events (Fig. 5.36B). Each raised the coast enough to regress the shoreline and expose a wide strip of sandy seafloor to strong onshore winds, nourishing dunes along the landward edge of the elevated shoreline. Following each uplift event the supply of sand was diminished by sea-level transgression, and the dunes stabilized. Vegetation was established on the dunes and soil developed during the interseismic intervals.

The occurrence of raised late Holocene terraces along the southern part of the Cascadia subduction zone where the deformation front is closest to the coast indicates that this part of the coast is located above the locked part of the plate interface. In this respect it may be similar to the Prince William Sound region of Alaska. An important aspect of the coastal geomorphology of Prince William Sound is the position in the strain cycle that is considered; the pre-1964 geomorphology was a drowned coastline almost completely lacking Holocene terraces except at the seaward tip of the upper plate very close to the deformation front. The northern California and southern Oregon coast also have raised terraces nearest to the deformation front and a drowned shoreline further inland. This geomorphic pattern may be indicative of a preseismic position in the strain cycle for the Cascadia subduction zone as well.

5.10 PALEOSEISMIC EVIDENCE OF COSEISMIC SUBSIDENCE

Stratigraphic evidence of coseismic subsidence has been reported from dozens of sites along the Alaskan coast and bays and estuaries in northern California, Oregon, Washington, and Vancouver Island, British Colombia (Atwater, 1987; Combellick, 1991, 1993; Atwater *et al.,* 1995; Gilpin, 1995). At most sites intertidal mud overlies salt marsh peats. At a few sites in both Alaska and Cascadia intertidal mud containing salt marsh macrofossils and marine and brackish diatoms cover subaerial soils, forest litter mats, and rooted trees, and this unconformity is interpreted as an event horizon.

5.10.1 Alaska

Cook Inlet—Turnagain and Knik Arms: Paleosubduction earthquakes have been interpreted from stratigraphic evidence of relative sea levels during several pre-1964 strain cycles at several sites along the shores of Turnagain and Knik Arms, two large shallow drowned glacial valleys at the upper end of Cook Inlet. The near-shore processes in the parts of the arms are very dynamic and driven by extreme tidal ranges reaching 15 m in some places. Very large amounts of sediment from many glacial melt water rivers drain into the head of Cook Inlet. At low tide large parts of upper Cook Inlet consist of exposed mud flats and extensive salt marshes.

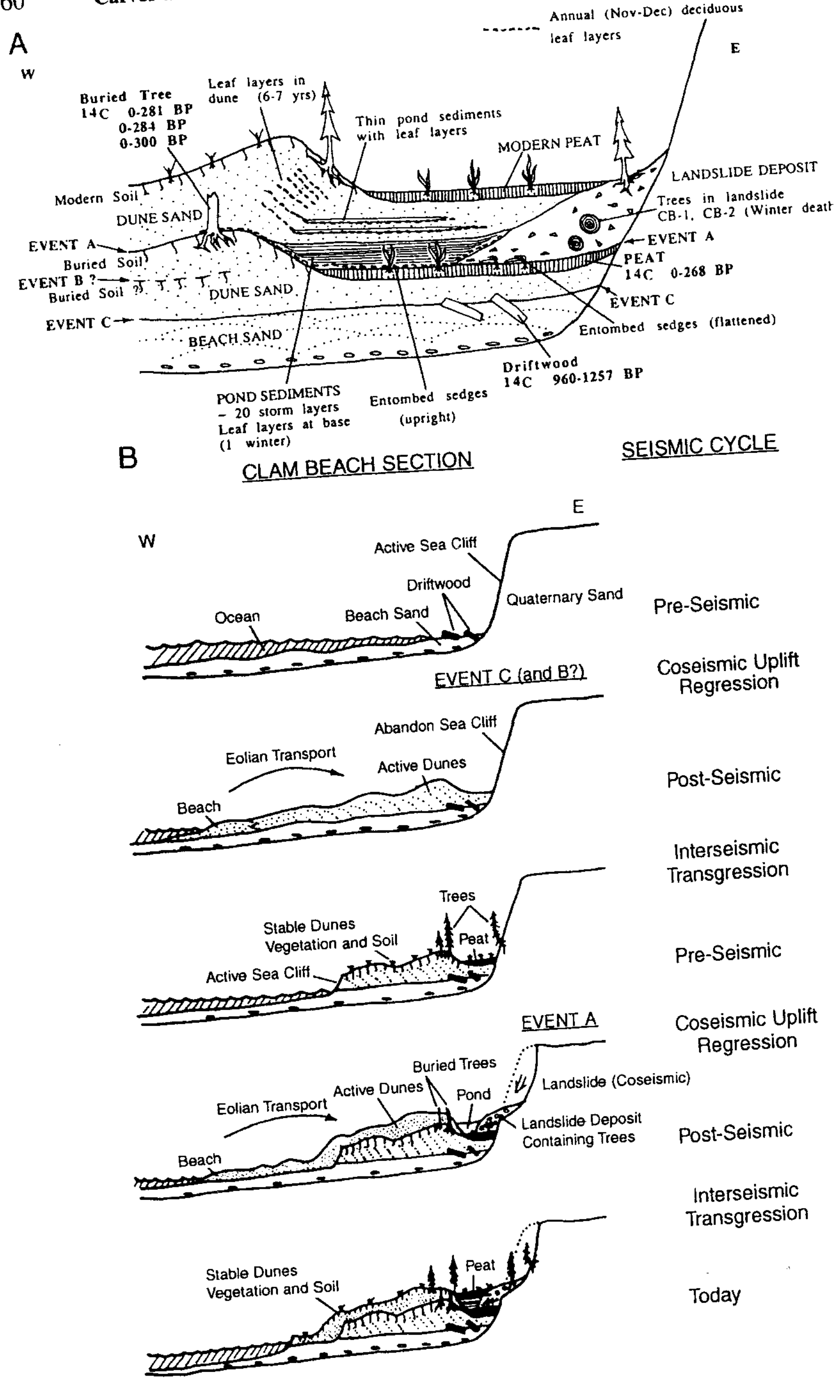

The paleoseismic sites are located along the shoreline in salt marshes and low shoreline areas that were submerged during the 1964 earthquake (Fig. 5.37). Prior to the 1964 submergence the vegetated subaerial surfaces were accumulating peat and organic soils. Spruce and willow trees grew around the edges of the marshes. Coseismic submergence initiated rapid sedimentation in places where the former emergent and vegetated surfaces were submerged by postearthquake high tides. At some places the sedimentation was rapid enough to bury the former surface and entomb many of the organic components of the surface (Bartsch-Winkler and Schmoll, 1987).

The composite stratigraphy suggests six to eight subsidence events are recorded in the stratigraphy of the upper Cook Inlet region during the past 5000 years. The age of the penultimate event has been estimated from conventional ^{14}C dating of the outer rings of fossil spruce roots and the upper 2 to 3 cm of peat from the first buried pre-1964 surface. The ages suggest the event prior to 1964 was about 750 to 950 years ago (Combellick, 1993). Tide gage and geodetic measurements show the upper Cook Inlet region has been undergoing rapid uplift since the 1964 earthquake (Savage and Plafker, 1991).

Kodiak Archipelago: Stratigraphy reflecting several cycles of submergence and emergence has been described from tidal marshes and shoreline deposits on Kodiak and nearby Afognak and Shuyak Islands near the southwest end of the 1964 rupture (Gilpin, 1995). The sites delineate a transect across the region that underwent coseismic subsidence and the zero isobase in 1964. The axis of maximum subsidence extended along the eastern side of Kodiak Island and amounted to about 2 m. The downwarped region was highly asymmetrical, with the amount of subsidence gradually decreasing to the west across the Kodiak archipelago for nearly 150 km. The downwarp was highly asymmetrical with the axis of maximum subsidence located along the eastern part of the downwarped region. The eastern limb of the downwarp was much steeper, the zero isobase located on the eastern shoreline of Kodiak Island about 20 to 25 km from the axis of maximum subsidence.

Remeasurement of tidal bench marks and tide gauge records since the earthquake show that the region that subsided during the earthquake has

Figure 5.36 (A) Cross section of the shoreline angle and cover sediments on Clam Beach, northern California. The abrasion platform of the raised terrace is presently about 1 m above highest tide level and is covered by a sequence of beach and dune sand containing a buried soil with trees in growth position, and landslide and pond sediments that bury and entomb sedges. (B) The evolution of the terrace stratigraphy is interpreted as resulting from two cycles of coseismic uplift that regressed the shoreline and exposed the seafloor to onshore wind that deposited sand dunes. The landslide was probably seismically triggered and filled the back-dune hollow to create the pond. Leaf layers in the dune above the pond sediments probably reflect annual layers.

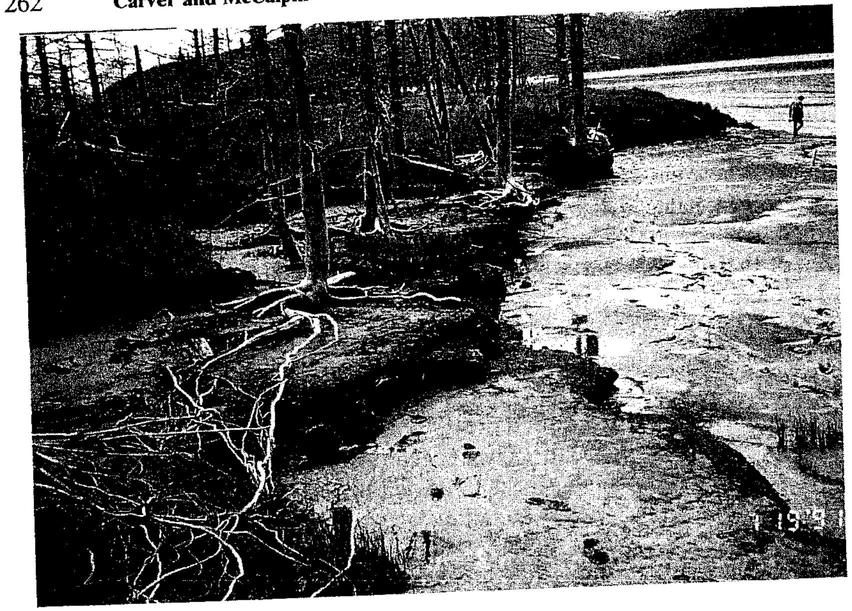

Figure 5.37 An earthquake-killed forest at Girdwood on Turnagain Arm, Alaska, records the 1964 earthquake. This locality experienced about 2 m of subsidence in 1964, flooding the forest marginal to the bay and depositing mud over the former forest floor. The prominent bench extending from beneath the buried 1964 soil to the lower right corner of the photograph is the subsided peat layer and soil resulting from the penultimate event about 800 years ago. Another older buried land surface and associated peat form a subtle bench in the intertidal mud flat along the right side of the photograph near the person in the far upper right corner. Postseismic rebound and sedimentation have raised the subsided land surface into the upper intertidal zone and salt marsh plants have replaced the spruce forest.

been uplifting at a rapid rate during the 30 years since the earthquake (Gilpin *et al.*, 1994b). The tide gauge at Kodiak City, which subsided about 2 m during the earthquake, has shown average postseismic uplift of 17.5 ± 0.8 mm/yr (Savage and Plafker, 1991). Other tidal benchmarks in the region of subsidence on Kodiak, Afognak, and Shuyak Islands also have been uplifted since the earthquake in 1964. The recovery during the 30-year postseismic interval averaged about 60% of the coseismic subsidence, and at the southern edge of the 1964 subsidence region the uplift has exceeded the subsidence.

Intertidal deposits in sheltered bays and fjords along the ragged coastline of the Kodiak islands contain sediments that record the 1964 earthquake and several prehistoric subduction earthquakes (Gilpin, 1995). The sites are mostly small salt marshes and delta fronts at the mouths of small rivers and streams. Postsubsidence deposits include thin and discontinuous layers of silt, sand, and gravel that lie on the presubsidence sphagnum peat or soil layer. At many places salt marsh vegetation has become established and is depositing estuarine peat. In contrast to the sediment-rich depositional environments at the Cook Inlet and Copper River, the bays and estuaries on Kodiak Island are typically sediment poor. The resulting stratigraphy is dominated by peat, both estuarine and subaerial. Upper intertidal environments deposit salt marsh peat characterized by the predominance of *Carix lynbgei* with *Triglochin maritima* also common. When the marsh and delta front sites are the upper reach of highest tides, as they were prior to the 1964 subsidence, sphagnum peat is deposited. Volcanic ashes from the Alaska Peninsula volcanoes are interbedded with the peats in the sections.

The stratigraphic record of at least three paleosubduction earthquakes has been interpreted from the marsh stratigraphy in the Kodiak archipelago (Fig. 5.38). Carbon-14 age estimates place the penultimate event near 400 to 500 yr B.P., and the previous two subduction earthquakes at about 800 and 1300 yr B.P. At most sites the event horizons representing three earthquakes are closely spaced, only 10 to 20 cm apart. The close spacing, when considered in light of the rise in sea level over the age of the sediments, indicates that the region experiences more interseismic uplift than coseismic subsidence. Average interseismic uplift rates are as much as 2 m/ka, with much of that occurring in the postseismic interval over a few decades.

5.10.2 Cascadia Subduction Zone

The most widespread and compelling evidence of prehistoric interplate earthquakes originating on the Cascadia subduction zone is found in late Holocene stratigraphy in many bays and estuaries from northern California to central Vancouver Island (Atwater, 1987, 1992; Grant and McLaren, 1987; Vick, 1988; Darienzo and Peterson, 1990; Clarke and Carver, 1992; Nelson, 1992a; Clague and Bobrowsky, 1994a). The stratigraphy consists of layers of peat that are interbedded with estuarine sand, silt, and mud (Fig. 5.39). The sediments are found along the margins of bays and estuaries where low energy intertidal environments have persisted during the last several thousand years and salt marshes have formed and deposited layers of peat. The peat layers are usually 10 to 30 cm thick and separated by 0.5 to 1 m of mud (Fig. 5.39A). At many places the upper contact of the peat with the overlying mud records an abrupt change in local depositional environment marked by the submergence of the marsh into the lower intertidal zone and rapid formation of tidal mud flats. In contrast, the change from mud to peat usually appears gradually over many centimeters and is interpreted to reflect the gradual establishment of vegetation on the tidal mud flats as clastic deposition raises the sediment surface into the low-marsh environment.

The peat is composed of the remains of herbaceous plants that indicate the highest tide level to within a few tens of centimeters. Along the Pacific

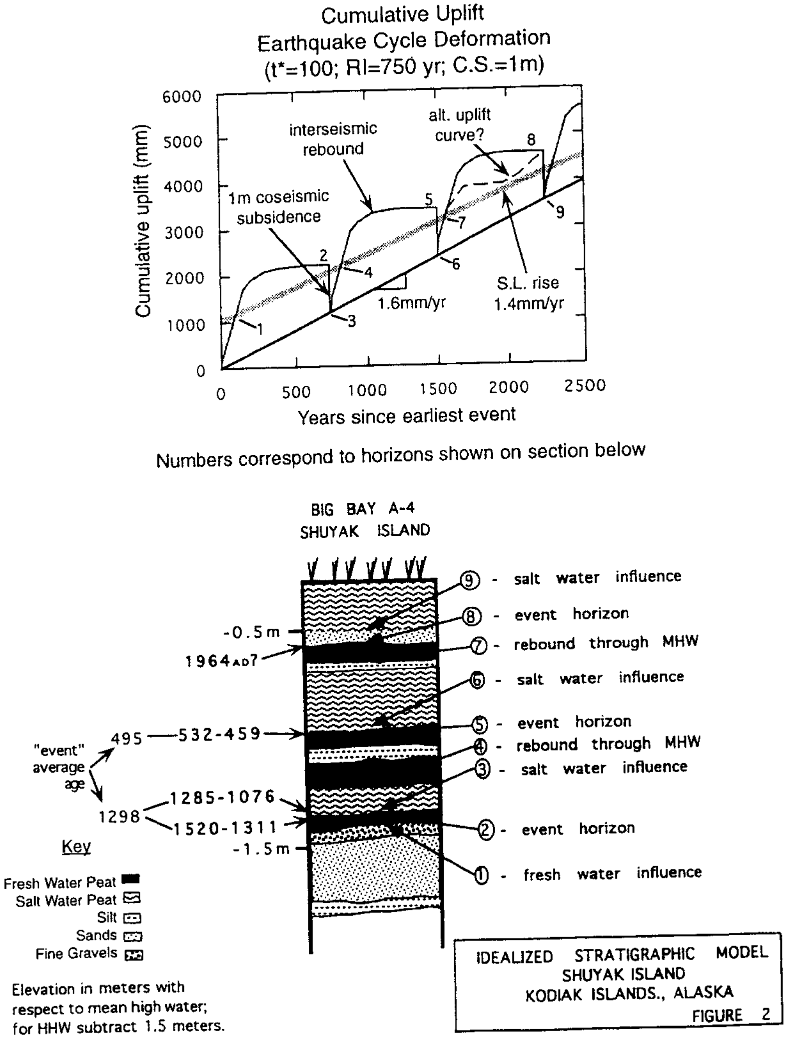

Figure 5.38 Paleoseismic interpretation of late Holocene stratigraphy along Skiff Passage on Big Bay, Shuyak Island, Alaska. The sediments consist of terrestrial or fresh water peat alternating with layers of marine silts, sand, and gravel. The upper contacts of the peats are sharp and appear to reflect sudden submergence. The cumulative uplift diagram shows a possible relative sea-level model for the origin of the stratigraphy. From Gilpin *et al.* (1994c).

Northwest coast native salt marsh plants that have been used to define this upper intertidal position include *Triglochin meritimum, Salicornia virginica, Jaymea carnosa, Distichlis spicata,* and *Grindelia stricta.* These plants dominate the flora within a meter or less of the elevation of highest tidal inundation where there is little competition with other plants that are not adapted to the saline conditions. Assemblages of these plants are sometimes indicative of vertical subdivisions of the upper inter tidal zone. *S. virginica, T. meritimun, and J. carnosa* are common low and middle marsh species, while *D. spicata* and *G. stricta* are usually restricted to the high marsh (Fig 5.27). The fossilized rhizomes and stem bases of many of the salt marsh plants can be identified in the field. *T. meritimum,* for example, produces distinctive V-shaped rhizomes and large sheathed stem bases that are frequently preserved and easily identified. *G. stricta* has large reddish woody roots that are also easily identified in the sediments. The presence of fossil salt marsh plants allows estimation of the elevation of deposition of the buried peats relative to the elevation of modern marshes. This elevation difference is the total relative sea-level change since formation of the peat, and includes the primary and secondary coseismic subsidence, tectonic and nontectonic postseismic vertical motions, and eustatic sea-level changes.

Rooted stems, branches, and leaves of the herbaceous marsh plants have been found entombed in growth position in the basal part of the overlying mud in some bays along the Cascadia subduction zone (Fig 5.39B). The rooted marsh plant stems and leaves extend upward into the overlying mud a few centimeters where many are broken off or have decayed away. However, some are bent over and preserved along bedding surfaces in the mud. The dead leaves and stems of the herbaceous plants are fragile, and if exposed to weathering most decay in a year or less. The preservation of the fragile plant remains in growth position reflects sudden submergence and rapid burial. Where dense marsh vegetation has been buried quickly the peat-mud contact may be gradational over several centimeters. This stratigraphy is inferred to result from coseismic subsidence caused by slip on the Cascadia megathrust landward of the downdip limit of rupture.

Layers of sand interpreted as tsunami deposits directly overlie some of the buried peats at many of the buried marsh sites from northern California to Vancouver Island. The deposits are composed of very well sorted sand, generally fine to medium grain size, and range from a few millimeters to tens of centimeters thick. At Willapa Bay (Fig 5.40) on the southern Washington coast the mineralogy and distribution of the sand indicates it was transported from the barrier bars and beaches fronting the estuary landward into the head of the bay (Reinhart and Bourgeois, 1987, 1989). The sand sheets in other bays also appear to have been derived from beaches and barrier bars seaward of the marsh sites, suggesting that landward transport occurred as large tsunamis overtopped the barrier bars.

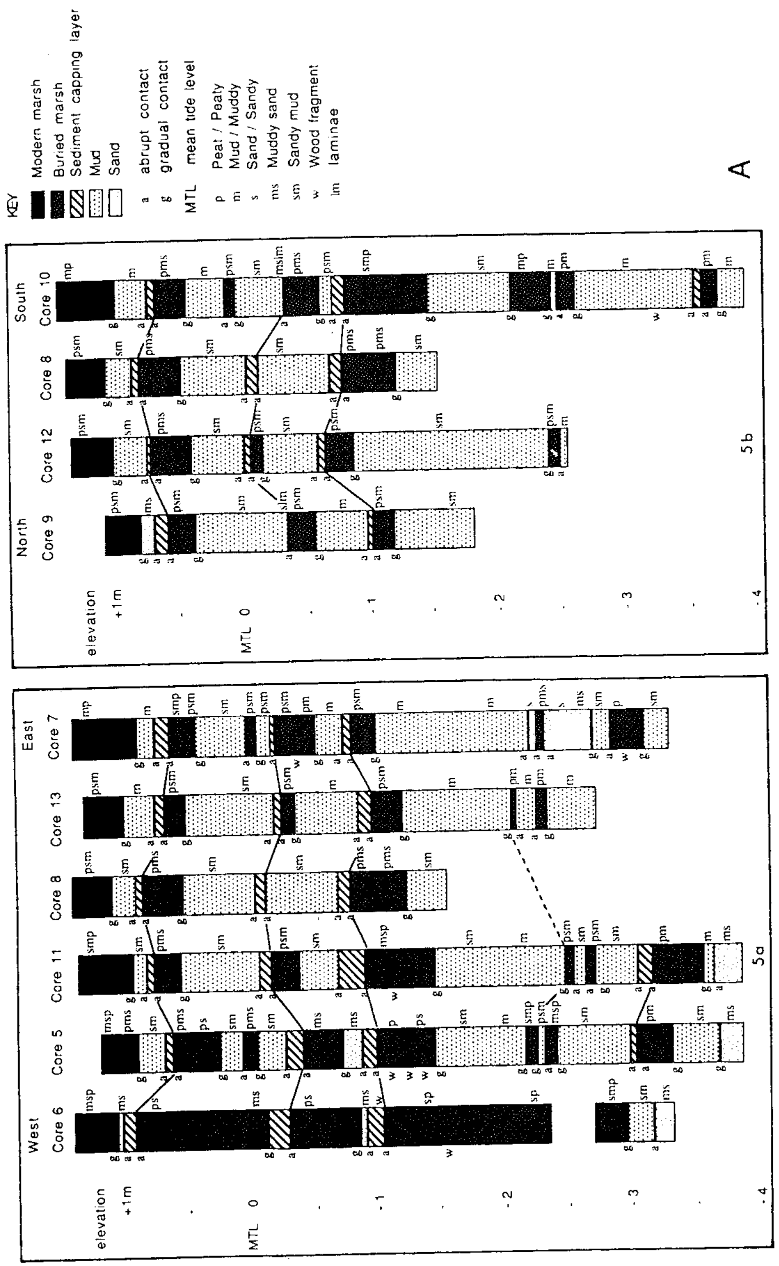

Figure 5.39 (A) Core logs and stratigraphic correlations between core sites at Netarts Bay marsh in northern Oregon. Up to seven sudden submergence events are reflected by the peat–mud couplets. Sand interpreted to have been deposited by large local tsunamis lies on the submerged peat surfaces in many cores. The stratigraphy shows local variation from core to core. [From Peterson and Darienzo (1988); reprinted with permission of the Oregon Dept. of Geol. and Min. Industries.] (B) Photograph of the upper buried peat and overlying mud–peat couplet at Mad River Slough in Humboldt Bay, California. (C) Diagram of the upper peat-mud couplet at Mad River Slough in Humboldt Bay, northern California. The sharp upper contact of the peat includes above-ground stems and leaves of salt marsh herbs entombed in the overlying intertidal mud. The upper part of the mud layer contains fossils of pioneer marsh plants and grades upward into the overlying modern peat. The present salt marsh plant assemblege is the same as that preserved in the buried horizon. [From Jacoby and *et al.* (1995); reprinted with permission of the Geol. Soc. of Am.]

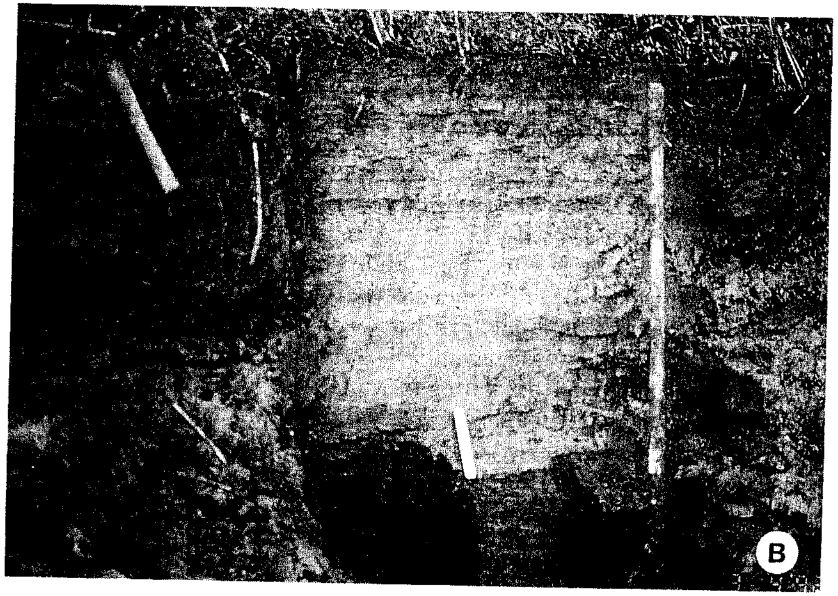

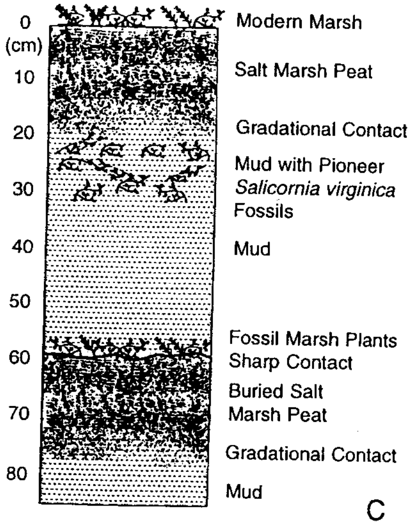

Figure 5.39 (*Continued*)

The late Holocene buried marsh sediments around several Pacific Northwest bays and estuaries contain layers of salt marsh peat that grade laterally landward into organic rich buried soils. These soils were formed above the reach of the highest tides and supported spruce and on the Washington coast, cedar forests. These forests were submerged into the upper intertidal zone during the paleosubsidence events, and fossil stumps and roots of large trees are entombed in growth position in the overlying estuarine mud at the heads of the estuaries (Fig. 5.28). Most of the trees are deeply decayed and missing their outermost rings, but a few have well-preserved annual ring sequences that extend to the bark. The record of growth recorded by these trees indicates that submergence was rapid and synchronous over a large area (Yamaguchi *et al.*, 1989; Atwater and Yamaguchi, 1991). At the south end of the subduction zone dendrochronologic cross-dating of roots from eight stumps in a buried forest exposed in channel banks of the Mad River slough on the north end of Humboldt Bay shows all died during a four-year period (Jacoby *et al.*, 1995).

The age estimated for the last subduction earthquake, based on high-precision ^{14}C analysis of earthquake-killed trees at the Copalis River and Willapa Bay in southern Washington (Fig. 5.40), is about A.D. 1700 with a 2σ uncertainty of about ±20 years (Atwater *et al.*, 1991). Similar analysis of trees interpreted to have been killed by the last subduction earthquake at the Nehaliem River in Oregon (Nelson and Atwater, 1993), and Humboldt Bay in northern California (Carver *et al.*, 1992) also result in a calibrated age of about A.D. 1700. These estimates are in agreement with the results of mass AMS ^{14}C dating for entombed herbaceous plants from seven bays and estuaries along the Oregon and southern Washington coast (Nelson and Atwater, 1993). The similar ages for the last large earthquake at sites along at least the southern 750 km of the subduction zone leave open the possibility that it was a single giant earthquake in the magnitude range of $M_w = 9$. Alternatively, the paleoseismic evidence may have been produced by a sequence of several great ($M_w > 8$) subduction zone earthquakes that occurred during a few decades or less about A.D. 1700. Both of these types of rupture sequences have occurred on other subduction zones that are similar to Cascadia (e.g., Fig. 5.23).

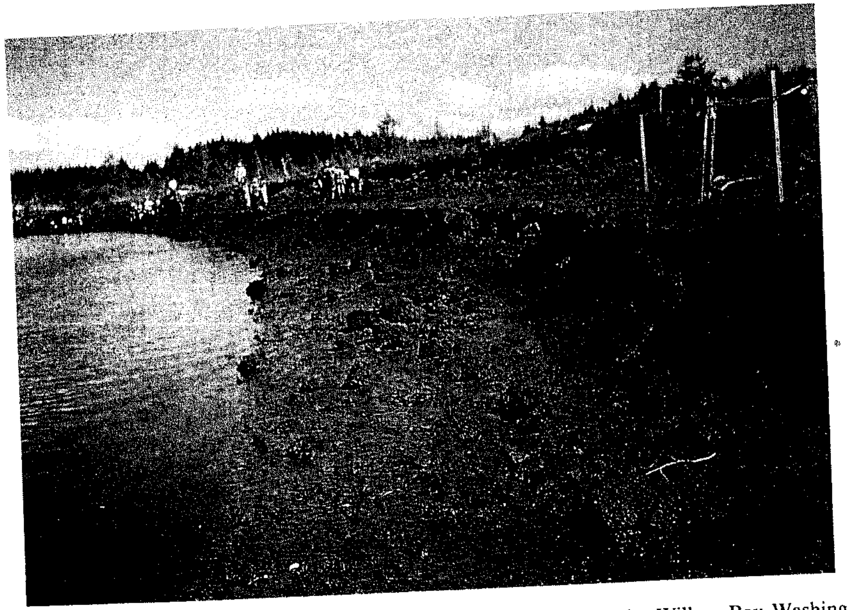

Figure 5.40 Prominent ledge of peat buried beneath intertidal mud at Willapa Bay, Washington. This submerged peat layer is locally covered by a thin sand sheet that entombs the above-ground parts of salt marsh herbs rooted in the peat. The sand was probably deposited by a tsunami immediately after the submergence.

Conventional ^{14}C ages for earlier paleoearthquakes have been estimated at some sites along the subduction zone (Grant *et al.*, 1989; Vick, 1988; Darienzo and Peterson, 1990; Atwater, 1992; Clarke and Carver, 1992; Nelson, 1992a, c). Samples used for age dating have included bulk peat, rhizomes and stem bases of selected marsh plants including *T. meritimum* and *G. stricta,* and twigs, wood, and charcoal contained in the peat or in the overlying mud. The age estimates suggest between two and five subsidence events have taken place along much of the length of the subduction zone during the last 2 ka. At many sites the conventional ^{14}C ages suggest that, prior to the earthquake ~300 years ago, large earthquakes also occurred about 700, 1100, and 1600 years ago. The assessment of the number and age of separate paleoearthquakes at different places along the Pacific Northwest coast depends on which evidence is accepted as coseismic and how the paleoseismic event horizons are correlated to define individual rupture segments. Subdivision of the subduction zone into more shorter segments, and acceptance of more of the evidence as coseismic, increases the number of earthquakes but reduces their magnitudes, whereas interpretation of longer segments and fewer events results in larger, less frequent, subduction earthquakes.

5.10.3 Ambiguities in Characterizing Subduction Paleoearthquakes

Ambiguities in characterizing subduction earthquakes arise mainly because the dominant evidence is regional geodetic deformation, rather than measurements on the causative fault trace itself (as with on-land faults). Nonseismic mechanisms can cause changes in relative sea level on coasts that mimic those created by all but the largest ($M > 8.5$) subduction earthquakes. Thus, there is a high threshold of detection for subduction paleoearthquakes. In addition, there are uncertainties about the lateral extent of paleoearthquakes, due to difficulties in correlating subsidence events between isolated sites where good evidence is preserved, and due to the lack of dating precision. Finally, even those well-documented changes in coastal relative sea level that are almost certainly coseismic could have resulted from either "blind" M > 7 earthquakes on local upper plate faults, from short M > 8 megathrust earthquakes, or from long M > 9 megathrust earthquakes. At a single site, the evidence from all three would appear identical. These ambiguities create major limitations to estimating paleoearthquake magnitude (see Chapter 9).

Chapter 6 Paleoseismology of Strike-Slip Tectonic Environments

Ray J. Weldon II, James P. McCalpin, and Thomas K. Rockwell

6.1 INTRODUCTION

Strike-slip faults have played a critical role in the development of paleoseismology for several reasons. First, strike-slip faults are often the longest faults on continental landmasses and typically have conspicuous geomorphic expression. Second, many of these faults have long records of seismicity because they pass through populated continental regions and have experienced surface ruptures during large and great historical earthquakes. Third, because coseismic deformation along strike-slip faults is horizontal, subsequent earthquakes (and related interseismic sedimentation and erosion) do not deeply bury, or expose to erosion, traces of earlier events.

Major strike-slip faults that have been assessed for paleoseismicity are typically associated with plate boundaries, such as the San Andreas fault and Queen Charlotte–Fairweather faults (North American/Pacific plates); the Motagua fault, Guatemala (Caribbean/North American plates); the Alpine fault, New Zealand (Pacific/Indian plates); the North Anatolian fault (Turkish/Eurasian plates); and the Dead Sea transform zone (African/Arabian plates). Other active strike-slip faults are located within the major lithospheric plates and define the boundaries of continental microplates (e.g., central Asia, Mongolia, and China). A final major class of faults, as yet unstudied for paleoseismology, is the numerous submarine transform faults (fracture zones) associated with oceanic spreading centers.

Strike-slip faults by definition displace geologic markers approximately parallel to the earth's surface. Because most young deposits and geomorphic surfaces are planar and form parallel to the earth's surface, this style of displacement poses special problems that are not typically encountered in studying dip-slip faults, which displace deposits and surfaces orthogonal to their original orientation. This chapter focuses on how to overcome this fundamental problem. The geometry of deposits and surfaces being displaced parallel to the earth's surface does provide some advantages, however. Longer records of paleoearthquakes lie closer to the surface of the earth than for dip-slip faults, where evidence of older earthquakes is deeply buried and therefore less accessible to investigation. Also, because strike-slip faults typically produce less relief than dip-slip faults they are less likely to destroy the record by uplift or erosion, or to disrupt sedimentation, erosion, or other surficial processes that produce stratigraphic and geomorphic markers and preserve the record of events.

We divide this chapter into geomorphic and stratigraphic sections. Geomorphic studies commonly yield the size of paleoearthquakes, and stratigraphic studies are most likely to yield the timing of paleoearthquakes. While it is possible to determine the size of a paleoearthquake through stratigraphic studies (several attempts are discussed later), it is extremely difficult. When one considers how variable displacement along the principal strand of a fault can be (e.g., Ambraseys and Tchalenko, 1969), one must conclude that the stratigraphic approach to determining individual paleoearthquake offset is not extremely productive, because it is difficult to carry out and is unlikely to be representative of the fault. Similarly, the difficulty in dating geomorphic features makes geomorphic studies to determine the timing of paleoearthquakes difficult and unproductive.

When looking for sites to carry out paleoseismic investigations, we look for different things depending on whether we wish to date earthquakes or determine their size. The best stratigraphic sites involve rapid deposition, which quickly obscures geomorphic markers, and distributed deformation so that evidence of individual paleoearthquakes is spread out and should be attributable to its component paleoearthquakes (see Sec. 6.3.1). The best sites for measuring the size of paleoearthquakes are regions where many small geomorphic features (gullies, ridges) are constantly being formed, so one may see many examples of offset due to a paleoearthquake, determine its true offset, and distinguish that displacement from those caused by other paleoearthquakes.

Finally, the philosophical theme that we carry throughout this chapter is that one must never rely on a few observations. A single trench, a few geomorphic offsets, or a single numerical age estimate is almost always uninterpretable. Multiple trenches, many geomorphic offsets, and a large number of related dates are necessary to understand paleoearthquakes. We choose our examples in this chapter to illustrate specifically how one combines many observations, rather than interpreting them individually, and to show how one may go astray by not rigorously examining all of the data at hand.

6.1.1 General Style of Deformation on Strike-Slip Faults

The main seismogenic structure in strike-slip or transform tectonic environments is the *strike-slip fault*. The general characteristics of strike-slip (or wrench) faults are reviewed by Sylvester (1988). Where fault strike is parallel

to the slip vector, strike-slip faults tend to concentrate deformation along a single linear fault strand (Fig. 6.1) that may extend for tens or hundreds of kilometers with only minor changes in strike. If fault strike locally diverges from the slip vector, the dip-slip component of slip on the fault plane increases, resulting in *oblique slip*. Bilham and King (1989) term this degree of strike

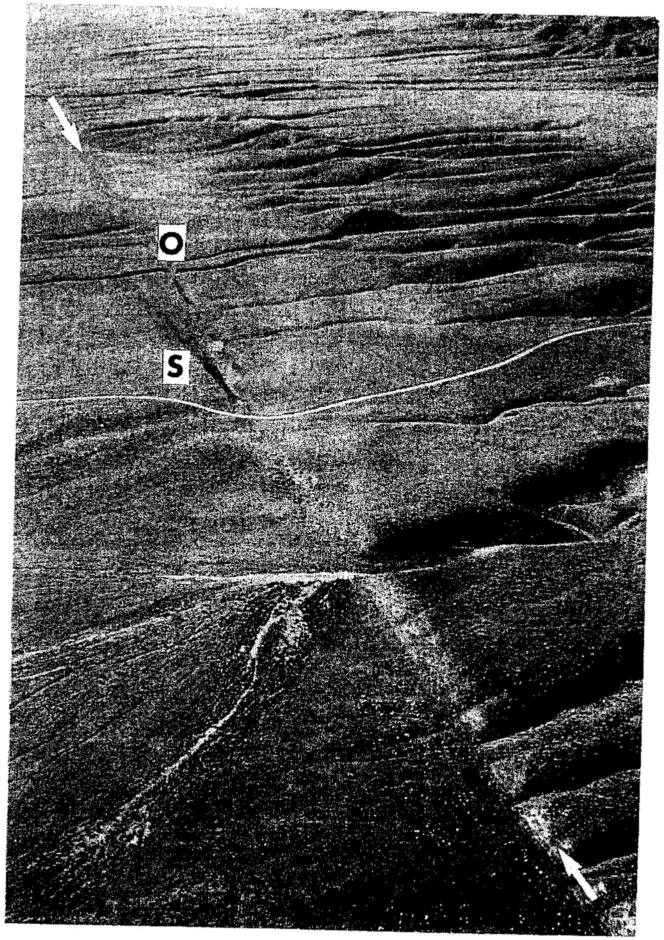

Figure 6.1 Aerial photograph of the San Andreas fault (between arrows) across the Carizzo Plain, California. The linear trace and lack of vertical relief across the fault are typical of many plate-boundary strike-slip faults. Note dextrally offset stream (below "O") and sag pond (to right of "S"). Some strike-slip faults are less linear at this scale, and are composed of alternating tension gashes and pressure ridges oriented obliquely to the main trace (e.g., Baljinnyam *et al.*, 1993). [Photograph courtesy of R. E. Wallace and the U.S. Geological Survey; from Wallace, (1990).]

divergence *segment obliquity*. Although normal (Chapter 3) and reverse (Chapter 5) ruptures commonly have a component of oblique slip, we have deferred the formal discussion of oblique slip to the next section, based on its importance in strike-slip environments.

On right-lateral faults a bend or stepover to the right induces local extension (*dilation*) and a bend or stepover to the left induces local compression (*antidilation*). Crowell (1974) noted that *double bends* (a pair of bends outside of which fault strike is the same) are common along strike-slip faults. On a right-lateral fault *releasing double bends* (such as a bend to the right and then to the left) or stepovers to the right (termed *dilational jogs*), tend to create *transtensional* features such as normal faults, monoclinal folds, rhomboidal grabens, and pull-apart basins. Bends and stepovers of the opposite symmetry (*restraining double bends* and *antidilational jogs*) induce *transpressive structures* such as pressure ridges, thrust faults, and folds. An oblique component of displacement can also be revealed by *en-echelon* fault segments, with (for example) a right-stepping pattern usually indicating left-lateral movement and vice versa. Secondary dip-slip faults and folds may form parallel to straight fault segments or perpendicular near en-echelon steps.

6.1.1.1 Defining Slip Components

Minor changes in strike on a strike-slip fault often cause major changes in the geomorphic expression of the fault trace, for reasons explained later. Figure 6.2 shows the slip components, and the trigonometric relations among them, for the general case of oblique slip on a nonvertical fault plane. The net slip displacement vector (Δu) in this example represents right-lateral faulting with a reverse component. The three-dimensional slip vector can be partitioned into a *horizontal component* (Δu_h) and a *vertical component* (Δu_v). The horizontal component can be further partitioned into a *strike-slip component* (Δu_{ss}) and an orthogonal *convergent component* (Δu_c). In addition to the three equations in Fig. 6.2 at upper right, Baljinnyam *et al.* (1993, p. 29) make the approximation that, for segment obliquity ($\Delta\Theta$)<20°, $\Delta u_{ss} = \Delta u_h$. For larger angles of obliquity the correct relation should be used:

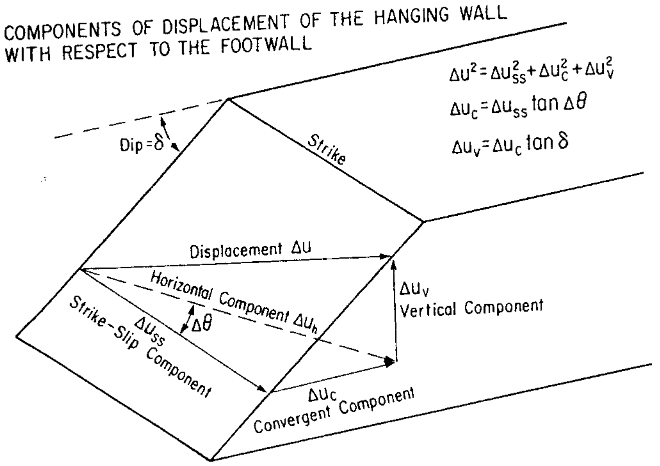

Figure 6-2. Block diagram showing the relationships of horizontal and vertical components of displacement to the slip vector and local strike of the fault. Terms are defined and discussed in the text. [From Baljinnyam *et al.* (1993); reprinted with permission of the Geological Society of America.]

$$\Delta u_{ss} = \cos \Delta\Theta \, (\Delta u_h) \tag{6.1}$$

Baljinnyam *et al.* (1993) quantitatively describe how segment obliquity ($\Delta\Theta$ in Fig. 6.2) can result in creation of vertical relief on a strike-slip fault. In their example, the slip vector azimuth is 85°, horizontal slip component (Δu_h) is 6 m, and the fault dips (β) is 55°. For fault segment strikes of 85° (i.e. parallel to the slip vector) $\Delta\Theta = 0$, and thus $\Delta u_c = 0$ and no vertical component results; the result, across low-relief terrain, would be a fault trace such as that shown in Fig. 6.1. For fault segment strikes of 95° and 105°, Δu_c is calculated as 1.04 and 1.75 m, corresponding to vertical displacements (Δu_v) of 1.4 and 2.5 m, respectively, from reverse-oblique faulting. If the latter case was expressed across a low-relief plain with few streams, the lateral component of offset may go unnoticed, and the 2.5-m-high fault scarp could be attributed to pure reverse faulting. For fault segments with the opposite obliquity, for example, an azimuth of 80° compared to a slip vector azimuth of 85°, the equations in Fig. 6.2 predict normal-oblique faulting with a vertical component of 0.75 m.

This simple analysis assumes that the earth materials in contact across the fault act as rigid bodies and do not internally deform as the component of convergence increases. For most unconsolidated surficial deposits this assumption is probably unfounded. For example, Thatcher and Lisowski (1987) report that at many locations less than 70% of the 1906 coseismic slip occurred on the San Andreas fault trace itself, the remainder of the slip appearing as distributed deformation (intergranular shear, subsidiary faulting, and perhaps folding) within 600 m of the fault. McCalpin (1996) compared segment obliquity at 31 sites along a 55-km-long section of the Awatere fault (New Zealand) to the ratio of (prehistoric) horizontal:vertical offset, and found that about one-third of measurements did not obey the relations predicted in Fig. 6.2. He concluded that inelastic deformation was probably responsible.

6.1.2 Historical Strike-Slip Earthquakes as Modern Analogs for Paleoearthquakes

Historical strike-slip surface ruptures are well documented on interplate and intraplate faults (Table 6-1). These coseismic ruptures accompanied great

Table 6-1

Well-Studied Historical Strike-Slip Fault Surface Ruptures

Date and magnitude	Area/fault	Maximum displacement (m)	Length of rupture (km)	Reference
a. Ruptures Studied Immediately after the Earthquake				
1906, M_s 7.8	San Andreas, California	6.1	432	Lawson *et al.* (1908)
1957, M_s 7.9	Gobi-Altai, Mongolia	9.4	245	Florensov and Solonenko (1963)
1966, M_s 6.8	Anatolia, Turkey	0.4	30	Ambraseys and Zatopek (1968); Wallace (1968b)
1967, M_s 7.4	West Anatolia, Turkey	2.6	83	Ambraseys and Zatopek (1969)
1968, M_s 6.8	Borrego Mountain, California	0.4	31	Clark (1972)[a]
1968, M_s 7.1	Dasht-e-Bayaz, Iran	5.2	80	Tchalenko and Ambraseys (1970)[a]
1972, M_s 6.2	Managua, Nicaragua	0.7	15	Brown *et al.* (1973)
1979, M_s 6.7	Imperial Valley, California	0.8	31	Sharp (1982); Sharp *et al.* (1982)
1987, M_s 6.6	Superstition Hills, California	0.9	27	Sharp *et al.* (1989)
1992, M_s 7.6	Landers, California[b]	6.1	85	Ebersold (1992); Sieh *et al.* (1993)
1994, M_{JMA} 7.2	Kobe, Japan	2.3	9	Awata *et al.* (1996)
b. Ruptures Studied Decades after the Earthquake				
1857, M_s 8.3	San Andreas, California	9.4	297	Sieh (1978b)
1905, M 8.7	Bulnay, Mongolia	11	375	Khil'ko *et al.* (1985); Baljinnyam *et al.* (1993)
1920, M_s 8.5	Haiyun, China	10.0	220	Zhang *et al.* (1987)
1931, M 8	Fu-Yun, China	14.6	180	Baljinnyam *et al.* (1993)

[a] Graphs of displacement along strike are also shown in Thatcher and Bonilla (1989, p. 389–391).
[b] Surface rupture is shown on videotape (Prose, 1994b).

earthquakes as large as M 8.6 with up to 14.6 m of displacement over lengths of >400 km, to smaller earthquakes near the threshold of surface rupture (<0.5-m maximum displacement, <10-km rupture length). Several historical ruptures traversed populated areas where lateral offsets of cultural features (roads, fences) permitted precise measurements of horizontal displacement (e.g., 1906 San Francisco; 1972 Managua; 1979 Imperial Valley; 1992 Landers). Figure 6.3 shows two ruptures where multiple precise measurements of horizontal slip were made. Like normal- and reverse-fault ruptures, slip tends to maintain high levels in the central part of the rupture, with near-maximum slip in very short sections. Slip either decreases rapidly at the end of rupture

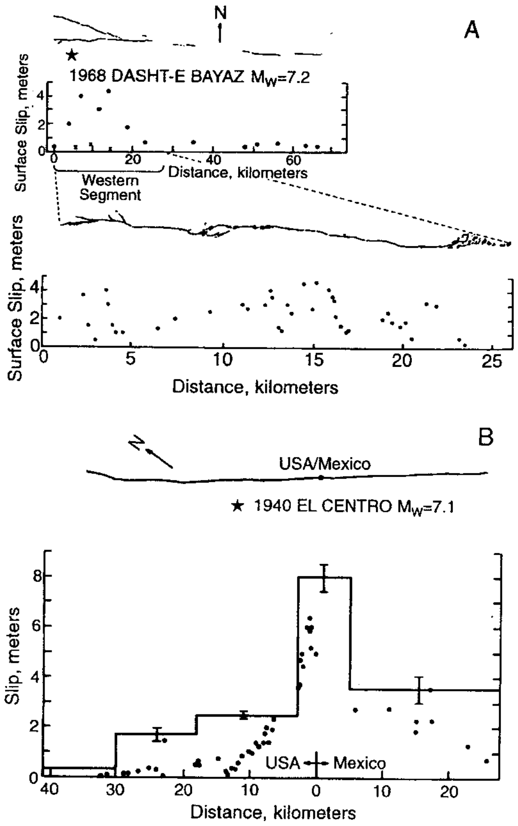

Figure 6-3. Patterns of horizontal slip along strike in two historical strike-slip surface ruptures. Map views show detail of rupture traces; stars indicate epicenters. (A) 1968 Dasht-e-Bayaz (Iran) earthquake. (B) 1940 El Centro, California, earthquake; geodetic estimates of slip are shown by straight lines with one-stranded deviation error bars. From Thatcher and Bonilla, (1989).

(left side of Fig. 6.3A) or trails off in a long, low-slip tail (Figs. 6.3 A and B). Preearthquake and postearthquake geodetic surveys (e.g., Thatcher and Lisowski, 1987) demonstrate that strike-slip deformation often extends hundreds of meters away from the prominent surface rupture trace, a phenomenon that may explain some of the short-wavelength variability in slip shown in Fig. 6.3.

Measurements on historical strike-slip ruptures also document the rate at which slip varies along strike during a single earthquake (Ambraseys and Tchalenko, 1969; Ambraseys and Zatopek, 1969; Sieh, 1978b; Sharp *et al.*, 1982). This rate is termed *slip gradient* and is dimensionless. Slip gradients can be large, for example, the decrease from 4.2 to 1.6 m within 330 m along strike (2.6m/330m, or 0.008) in the 1968 Dasht-e-Bayaz earthquake (Ambraseys and Tchalenko, 1969), or the decrease from 6.1 to 3.6 m within 1.4 km along strike in the 1940 El Centro, California, earthquake (Sharp, 1982). The recent detailed measurements on the 1992 Landers, California, rupture have revealed even more extreme slip gradients (McGill and Rubin, 1994). The maximum slip gradient along the Emerson fault was 2×10^{-1}, between two features offset 250 and 535 cm, respectively, located only 12 to 20 m apart. Maximum slip gradients on the other faults that ruptured in the Landers earthquake were on the order of 10^{-2}, as were the maximum slip gradients for the 1979 Imperial Valley earthquake (Sharp *et al.*, 1982) and the 1987 Superstition Hills earthquake (Sharp *et al.*, 1989), which had smaller maximum and average slip than did Landers (Table 6-1). These slip gradients could be due to changes in the amount of slip across the rupture, or caused by a change from concentrated to distributed deformation. In the latter case the lateral offset along the main surface rupture trace may appear to decrease, even though the net offset across a broad zone centered on the trace may remain constant.

Great (M > 8) strike-slip earthquakes in the late 1800s and early 1900s also provided incontrovertible evidence linking fault displacement and earthquakes (e.g., 1855 West Wairarapa, New Zealand; 1872 Owens Valley, California; 1891 Nobi, Japan; 1906 San Francisco, California). The latter gave rise to the elastic rebound theory (Reid, 1910) and to the perfectly periodic model of earthquake behavior (see Chapter 9).

6.2 GEOMORPHIC EVIDENCE OF PALEOEARTHQUAKES

Active strike-slip faulting produces a characteristic assemblage of landforms (Fig. 6.4) including *linear valleys, offset or deflected streams, shutter ridges, sag ponds, pressure ridges, benches, scarps, and small horsts and grabens* (Keller, 1986). In many cases the fault trace is composed of a wide zone of alternating *tension gashes* (extensional) and *moletracks* (compressional) that trend obliquely with respect to overall fault strike. Baljinnyam *et al.* (1993, p. 46) attributed such a wide zone of surface deformation in Mongolia to coseismic rupturing of permafrost in valley bottoms, and noted that the same rupture trace across hills not underlain by permafrost was much narrower.

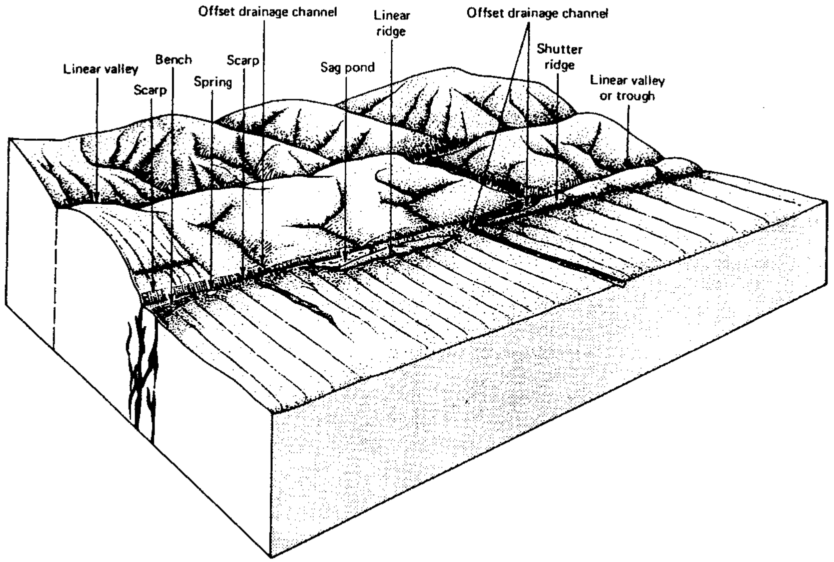

Figure 6-4. Assemblage of landforms associated with strike-slip faulting. [From Surficial Geology-Building with the Earth; Costa and Baker (1981). Copyright© 1981 John Wiley and Sons. Reprinted by permission of John Wiley and Sons, Inc.]

Strike-slip faults also transport nontectonic landforms laterally, while the erosional and depositional processes forming them continue to operate. This lateral transport causes the most obvious geomorphic effects when faults strike perpendicular to the direction of stream transport. Three landforms are typically used to reconstruct paleoseismic offset histories: fluvial terraces, stream channels, and alluvial fans.

6.2.1 Landforms Used as Piercing Points

In paleoseismology the main goal of geomorphic analysis is to measure lateral (or oblique) displacements that can be attributed to individual paleoearthquakes. These displacements are then used to estimate paleomagnitude or seismic moment (Chapter 9). Quaternary displacements across strike-slip faults are typically measured from displaced landforms such as terraces, channels, or fans. Due to the possible oblique nature of the slip vector, field workers need to identify landform elements that intersect the fault plane as *piercing* *points* on either side of the fault. On gently sloping or flat terrain the most common piercing point landforms are linear features such as the axes or thalwegs of stream channels, narrow erosional ridges such as interfluves between gullies, bases or crests of terrace risers, or narrow constructional ridges such as debris-flow levees or gravel bars (Fig. 6.5). If comparable points on such well-defined landforms can be located in the field and traced to the fault, it is possible to measure the net slip vector directly. In special cases (Sec. 6.2.1.4) lateral offset can be measured from large landforms even if piercing points cannot be located.

6.2.1.1 *Offset Terraces*

The initial methods for measuring and interpreting laterally and obliquely displaced fluvial terraces were proposed by Suggate (1960), Lensen (1964a), and Sugimura and Matsuda (1965). Multiple offsets of Holocene river terraces have been extensively documented in New Zealand (Lensen, 1964b, 1968, 1973; Lensen and Vella, 1971; map in Suggate *et al.,* 1978) and in Japan (summarized by Okada, 1980). Lensen (1968) suggests the following field technique for measuring terrace riser offsets. If offset risers are the same height across the fault, equivalent points of the riser profile (e.g., crests or toes) can be used as piercing points. However, on oblique-slip faults, terrace risers on the upthrown side of the fault are typically higher (and, thus, broader) than risers on the downthrown side. In this case, the riser crest and toe on the higher scarp have probably retreated and advanced (laterally) farther from their original positions than have equivalent points on the lower riser. Lensen (1968) thus suggests using the riser midpoint as the piercing point for measuring lateral offset, based on the assumption that risers erode by slope decline rather than by slope retreat. Knuepfer (1988) argues that even the midpoint may have retreated or advanced, and suggests averaging the lateral offsets between the crests and toes of the offset risers.

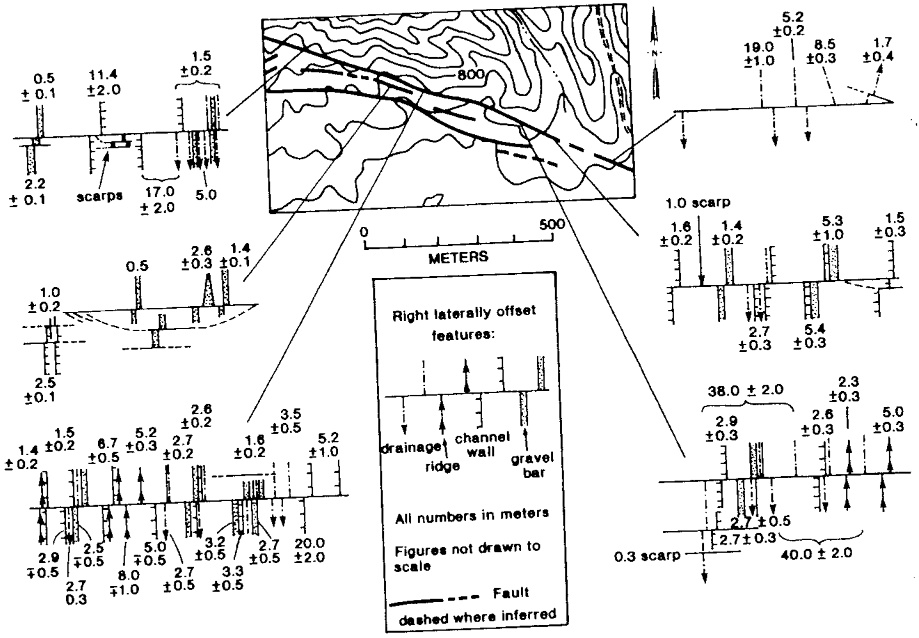

Figure 6-5. Example of an inventory of horizontal offsets for four types of landforms (drainages, channel walls, ridges, gravel bars) typically found in semiarid regions. These measurements can be statistically analyzed to deduce the number of paleoearthquake displacements. [From Rockwell and Pinault (1986); reprinted with permission of the Geological Society of America.]

The interplay between fluvial processes and strike-slip faulting often produces unique landforms from which one can reconstruct the history of paleoearthquakes, as described in this chapter. Consider the typical geometry (Fig. 6.6A) of an active river, riverbank, two terraces (the lower of which, T1, preserves an abandoned channel on its *tread*), and one *terrace riser* crossed by a strike-slip fault. In Fig. 6.6B all landforms are dextrally offset by a constant amount. After faulting (Fig. 6.6C) the stream erodes the lateral offset of the riverbank, but the offset is preserved on the abandoned channel and upper riser (R1). Eventually the stream migrates farther to the left and incises (Fig. 6.6D), leaving the former floodplain as a new terrace (T2), complete with an abandoned channel. Renewed faulting (Fig. 6.6E) dextrally offsets all landforms by the same amount, but on T1 and R1 this new offset adds to the prior offset that occurred in Fig. 6.6B. After faulting, the stream once again erodes the lateral offset of the riverbank. This alternation of faulting and terrace formation can continue for many cycles.

This hypothetical scenario emphasizes several critical points in interpreting offset terrace flights. First, terrace treads and their abandoned channels preserve the vertical and lateral components of offset; terrace risers can only record the lateral component of offset. Second, lateral offset of riverbanks is routinely removed by stream erosion after faulting, especially where the riverbank is laterally displaced toward the active channel. In this regard, Bull (1991, p. 238) distinguished the *leading edge* of a terrace flight, where terraces and risers are laterally displaced into the stream's path and the traces of offset destroyed, from the *trailing edge* of a terrace flight, where offset terraces and riverbanks are laterally displaced away from the active channel, and offsets are more likely to be preserved. Third, a terrace riser is abandoned by the river contemporaneously with the abandonment of the terrace *below* the riser (Knuepfer, 1988), not the terrace above the riser as supposed by Lensen (1968). Therefore, the age of a riser, and its offset, correlate with that of the terrace tread below the riser. Knuepfer (1988) also cites several instances where abandoned channels on a terrace tread are offset much less than the

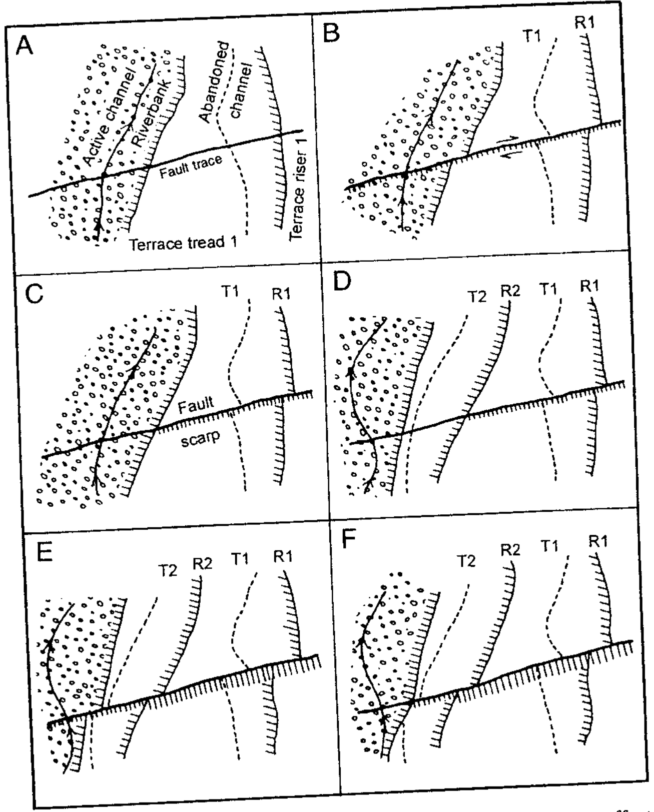

Figure 6-6. Hypothetical plan view of development of a terrace sequence offset by a dextral-oblique fault, upthrown toward the top of each figure. Hachures on terrace risers and fault scarps point to lower surface. (A) Prefaulting geometry. (B) First faulting event dextrally offsets all landforms. (C) Lateral erosion after first faulting event trims the offset riser between T1 and the active channel (patterned). (D) Incision of the active channel and creation of terrace T2. (E) Second faulting event. (F) Lateral erosion after second faulting event. See text for detailed discussion. From Knuepfer (1988).

terrace riser below the tread. This geometry indicates that the channel is considerably younger than the terrace tread, and must have been created by tributary flow on the terrace after its abandonment.

From the above points, it follows that scoured terrace risers (usually found on leading edges) record only offsets made after abandonment of the terrace surface below them. On unscoured risers (often found on trailing edges) these offsets, which were eroded from leading edge risers, may be partially or totally preserved. Thus, the difference between lateral offsets of contemporaneous risers on the leading versus the trailing edges comprises a minimum estimate of the incremental (single-event?) offset that occurred before their abandonment.

Offset terrace flights are only interpretable in terms of individual paleoearthquakes if each earthquake is separated from the next by an episode of incision and terrace formation (e.g., the scenario in Fig. 6.6). Where this fortunate alternation of faulting and downcutting has occurred, the offsets of successively older terraces would be simple multiples of the single-event offset. Such offsets are recorded by the two youngest terraces at the Saxton River (New Zealand) of 7.5 m (one event) and 15 m (two events; Knuepfer, 1992; McCalpin, 1996), and on the Wellington Fault (see example later). To create such a geometry, the recurrence interval between earthquakes must be approximately the same, or less than, the interval between terrace formation. Stated another way, the number of terraces must be equal to or greater than the number of earthquakes.

Where terrace formation occurs more often than faulting, multiple terraces are formed between earthquakes. In this case two or more successive terrace treads and risers in the flight may record identical offsets (e.g., the classic Branch River terraces, Lensen, 1968). In the opposite case, where faulting occurs more often than terrace formation, each terrace tread and riser is offset by multiple events before it is abandoned. In this case, the difference in offset between successive terrace risers records multiple events. Where such a sequence of events has occurred in New Zealand (at the Branch River terraces, among other places), the difference in offset between successive terraces is on the order of 20 to 30 m, rather than the 6 to 8 m associated with individual events. In these cases, where earthquakes recur more often than terraces are formed, the number, displacement, and timing of individual paleoearthquakes cannot be uniquely deduced from geomorphic evidence.

Figure 6.7 shows examples of both cases just described, from a single site along the Wellington Fault, New Zealand. Channels on the youngest faulted terrace (T2) are offset 3.7 and 4.7 m, whereas the riser above this terrace shows apparent offset of 7.4 m. Van Dissen *et al.* (1992) conclude that T2 has been offset once and the T2/T3 riser twice, with the 7.4-m offset of the latter representing a minimum value after some (unknown) amount of riser erosion. Thus, subsequent to the cutting of the T2/T3 riser, two faulting events occurred but only one terrace surface preserves evidence of those offsets. The opposite sequence is shown by the consistent offsets (18.0 and 19.0 m) of the two risers between T3/T4 and T4/T5. This geometry indicates that terraces were being created more frequently than were faulting events. Such an irregular alternation of terrace formation and faulting events is probably to be expected at most locations, rather than the more idealized sequence of one faulting event following the formation of each terrace. Further details on this site in New Zealand are given in Berryman (1990).

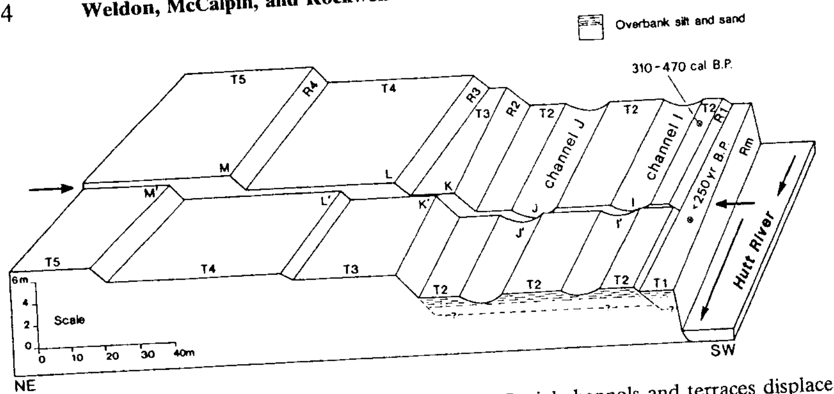

Figure 6-7. Perspective scale drawing of Holocene fluvial channels and terraces displaced by the dextral Wellington fault (between arrows) at Te Marua, North Island, New Zealand. Offsets I–I′, J–J′, K–K′, L–L′ and M–M′, are 3.7, 4.7, 7.4, 18.0, and 19.0 m, respectively. [From Van Dissen *et al.*, (1992); reprinted with permission of the Royal Society of New Zealand.]

6.2.1.2 Offset Stream Channels

Laterally offset streams were used in early descriptions of active strike-slip faults to document recurrent movement. A classic locality in the United States is the Carizzo Plain segment of the San Andreas fault (Fig. 6.1; Wallace, 1968a; Sieh, 1978b; Sieh and Jahns, 1984; Grant and Sieh, 1993, 1994). Wallace (1968a, 1990) recognized that the drainage patterns across the fault zone may have a complex relationship to fault offset. He makes a useful distinction between *stream misalignment* (a purely descriptive term for stream segments that do not align across the fault), *stream diversion* (streams forced to flow parallel to the fault by capture or blockage; also termed *deflection* by others), and *stream offset* (tectonic translation of a stream channel). It is often difficult to determine from surface observations alone whether stream misalignment is caused by diversion, offset, or a combination of both. Human alteration of stream channels can also influence estimates of stream offset. For example, Sieh and Jahns (1984) measured 3.5 ± 0.5 m of lateral offset on the San Andreas fault near Cholame, California, (attributed to the A. D. 1857 earthquake), whereas Lienkaemper and Sturm (1989) measured 5.7 ± 0.7 m offset at the same site. The difference was caused by 2 m of post-A.D. 1966 agriculturally induced slopewash deposition in the offset channel, which was not recognized by the earlier workers. The uncertainties introduced by the variable (usually unknown) contribution of diversion and offset to total misalignment can be represented by a quality modifier (good, fair, poor) attached to the lateral offset measurements, as done by Sieh (1978b).

Offsets of stream channels can be interpreted in terms of individual paleoearthquakes only if the stream reestablishes its course across the fault

between each earthquake. Given the tendency of streams (especially intermittent or ephemeral streams) to be diverted laterally along the fault zone, such reestablishment is unlikely to occur after every offset event. Thus, the differences between lateral offsets recorded by adjacent stream channels often reflect multiple faulting events, and amount to tens or hundreds of meters, rather than single-event amounts. For example, the modern channel of Wallace Creek (California) is offset 130 m dextrally by the San Andreas fault, whereas the next (abandoned) channel along strike is offset 380 m dextrally. Both the 130- and 380-m offsets obviously represent many paleoearthquakes, in light of the 9.5-m offset experienced there during the last major earthquake (1857 Ft. Tejon earthquake, M ca. 8). Sieh and Jahns (1984) conclude that Wallace Creek has only reestablished its course straight across the fault twice in the past 13,000 years. The latter reestablishment occurred after the channel section within the fault zone filled up with alluvium, and water was able to spill straight across the fault. The reason for such severe aggradation is unknown, but may have resulted from fault-induced changes is stream gradient, as explained in Sec. 6.3.1.

The geomorphology of large perennial streams where they cross strike-slip faults is more complex than for ephemeral streams, because streams are responding to climate changes (resulting in aggradation and degradation) as well as to tectonic transport. The landforms resulting from this interplay of tectonic and climatic forces (channels, fans, and terraces) are typically unique to each site, based on the timing and severity of Quaternary climate changes and the rate of lateral slip. An excellent case history is described by Bull and Knuepfer (1987) and Bull (1991, Chapter 5) from the Charwell River and Hope Fault in New Zealand. However, at this site most landforms were offset by tens of meters (i.e., from multiple faulting events), so only slip rates, and not parameters of individual paleoearthquakes, could be deduced.

6.2.1.3 Offset Alluvial Fans

A third landform that is commonly translocated away from its source is that of alluvial fans. Due to the poor resolution in defining the axis of a fan, this technique is not usually useful for measuring offsets of less than 10 to 20 m, so individual paleoearthquakes often cannot be detected. Sieh and Jahns (1984) describe a 13-ka alluvial fan at Wallace Creek on the San Andreas fault that has been displaced 475 m right-laterally from its source gullies. Matching of the alluvial fan apex (a broad feature) with the suspected source gullies (narrow features) was accomplished by making an isopach map of the alluvial fan, and matching the areas of greatest fan thickness with the mouths of suspected source gullies (Sieh and Jahns, 1984, p. 892). Similar fan offsets are described by Bull and Knuepfer (1987) and Bull (1991, p. 237) in New Zealand. This technique works best when the fault zone is coincident with the heads of alluvial fans.

6.2.1.4 *Offset Ridges and Valleys*

Strike-slip faults that displace high-relief terrain create fault scarps by lateral offset of ridge and valley walls (Fig. 6.8). In a general sense, lateral displacement of a ridge will create scarps that face in opposite directions if the net slip vector is inclined closer to horizontal than are the sideslopes of the ridge. This geometry is reflected in Fig. 6.8 where the net slip vector is nearly horizontal and ridge sideslopes have a gradient of ca. 30°. If the net slip vector has a large vertical component, such that it is more steeply inclined than the ridge sideslopes, scarps on opposite sides of the ridge will face in the same direction but will have different heights (Fig. 6.9).

Where ridge sideslopes are relatively planar and the fault trace is roughly perpendicular to the ridge crest, the net slip vector can be measured graphically even if sharp piercing points cannot be found. Figure 6.9 shows the reconstruction of right-lateral/normal displacement of an erosional ridge along the 1954 Fairview Peak, Nevada, fault scarp. This ridge has planar sideslopes of 23° but its crest is too broad to comprise a precise piercing point. Oblique displacement resulted in a valley-facing fault scarp with vertical surface offset of 1.3 m on the left (south) flank of the ridge but with 4.0 m of valley-facing vertical offset on the right (north) flank. There is only one unique net displacement vector that will result in these two scarp heights on a ridge with 23° sideslopes. That vector can be found by drawing a topographic profile of the ridge parallel to the fault on paper, and on a transparent overlay. One then shifts the profile on the overlay with respect to the profile on the underlying paper (in the same direction as inferred fault slip, without any rotation) until the apparent height of fault scarps on both ridge flanks is equal to that observed in the field. This graphical technique, applied to the profile in Fig. 6.9, results in an estimated horizontal slip component of 3.0 m and a vertical slip component of 2.3 m (Fig. 6.9C). The estimated vertical component should match that measured from a standard topographic scarp profile perpendicular to the fault

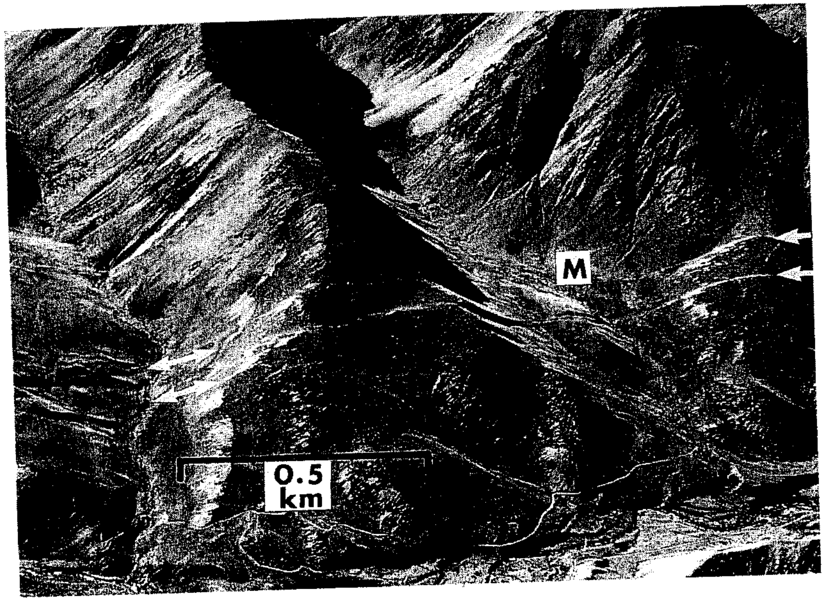

Figure 6-8. Oblique aerial photograph of fault scarps along the right-lateral Awatere fault, New Zealand. Two glaciated valleys are at left and right center. Fault scarps formed by dextral offset of valley sideslopes face toward the mountains (away from viewer) on the right side of each valley wall (light tones), and away from the mountains (toward the viewer) on the left side of each valley wall (shadowed scarps). Note the general lack of vertical relief where the faults cross the flat valley floors, and the dextral offset of the elongated hill of ground moraine below "M."

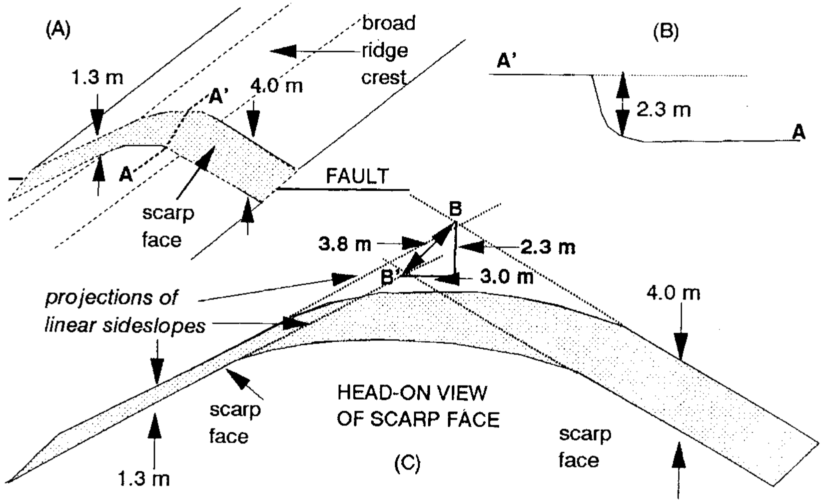

Figure 6-9. Diagrams showing an obliqely offset ridge and a crude method of measuring slip components, based on an example from the 1954 Fairview Peak, Nevada, fault scarp. (A) Perspective drawing of a broad-crested ridge offset in a dextral-normal sense. Scarp height on the left side of ridge = 1.3 m, scarp height on right side = 4.0 m. Ridge sides are linear and slope at 23°. (B) Topographic profile along the ridge crest perpendicular to the fault scarp. Scarp height = vertical surface offset = 2.3 m. (C) Head-on view of scarp face. The lines defining the crest and base of the fault scarp have identical shape, and are shifted laterally and vertically with respect to one another until the observed scarp heights on ridge sideslopes are attained. Graphical projections of linear sideslopes above and below the fault scarp define points B and B′, respectively. The vertical offset between B and B′ is measured graphically as 2.3 m, the same as the field measurement (see part B). The projection method further indicates a lateral offset of 3.0 m and a net slip (double-headed arrow) of 3.8 m at this site. Uncertainties in this method arise from the variable ridge cross-sectional shape above and below the fault, and errors from line projection.

scarp along the crest of the ridge (Fig. 6.9B). In this example the oblique slip vector was inclined more steeply than the 23° ridge sideslopes, so scarps on opposite sides of the ridge face in the same direction.

6.2.2 Measuring Lateral Offsets from Landforms

Measuring the lateral offsets caused by paleoearthquakes on strike-slip faults differs in many ways from measuring displacements on dip-slip faults (Chapters 3, 4, and 5). On the latter structures, displacement could be estimated from fault scarp height or from thickness of scarp-derived colluvium. Strike-slip faulting, in contrast, displaces the landscape horizontally, and vertical relief along the fault trace (if it exists) is commonly the result of differential erosion or local variations in strike that are not relevant to the regional rupture. Horizontal displacements can only create vertical relief under two conditions: (1) If fault strike varies sufficiently from net slip direction to form transtensive or transpressive structures or (2) if the fault trace laterally shifts topography with considerable relief.

Due to erosional smoothing in and near the fault zone it is usually impossible to trace a linear landform right to the fault trace itself. Instead, the landform will be traced as close as possible to the fault and then projected to the fault plane from either side. The uncertainty in measuring lateral displacements thus has two components, the first arising from the preservation of the landform and its correlation across the fault (qualitative), the second from locating correlative points on the landform and then projecting them to the fault trace (quantitative). [Sieh (1978b) used a rating system (excellent, good, fair, poor) to indicate the uncertainty of the first type.] Excellent and good designations reflect the absence of complicating secondary faults, little or no lateral warping, sharp offset expression, and clearly interpretable geologic and geomorphic features. Uncertainties of the second type are expressed by assigning a plus-or-minus value to every measurement, reflecting the probable bounds of error. To support measurements of lateral offset made with tape measures, Sieh (1978b), McGill and Sieh (1991) and Grant and Sieh (1994) advocate compiling large-scale topographic maps of the displaced landforms with contour intervals as small as 10 cm (see Chapter 2).

6.2.3 Reconstructing Individual Earthquake Displacements

Horizontal separations measured between piercing point landforms could be the result of one or many paleoearthquakes, depending on the age of the landforms and the recurrence time of the fault. Numerous workers (e.g. Wallace, 1968a; Sieh, 1977; Rockwell and Pinault, 1986; Rockwell, 1989; McGill and Sieh, 1991; Trifonov *et al.*, 1992) have suggested that individual paleoearthquakes can be identified from a *frequency histogram* of lateral offsets. Such histograms commonly show clusters or groups of similar displacements (e.g., 3, 6, 9, and 12 m), which are then interpreted to be the cumulative slip associated with a discrete number of paleoearthquakes. McGill and Sieh (1991) contend that such an interpretation rests on two assumptions. First, new geomorphic features must form during every interseismic period and some of these must survive up to the period of observations. If earthquakes and erosional processes are scattered in time, this assumption is reasonable. However, if earthquakes or erosional events are clustered in time, no interearthquake landforms may be formed and the combined displacements of two paleoearthquakes may appear as one large displacement in the geomorphic record. Second, one must assume that observed displacements are coseismic (or closely postseismic) rather than the result of continuous creep. Both of these assumptions can be validated on many faults by historical observations and other paleoseismic studies.

McGill and Sieh (1991) also used slip gradients as an indirect criterion to distinguish between landforms offset by one versus two paleoearthquakes. For example, two terrace risers laterally offset 2.7 ± 0.7 and 5.6 ± 0.7 m, respectively, were only 10 m apart, equating to a slip gradient of 3×10^{-1}. Another pair of risers offset 3.4 ± 0.5 and 5.3 ± 0.3 m are also 10 m apart (slip gradient of 2×10^{-1}). They argued that the ca. 5-m offsets must represent two displacements and the ca. 3-m offsets only one displacement, because nowhere have slip gradients as large as 2×10^{-1} been observed in historical ruptures. However, prior to the 1992 Landers, California, earthquake very few offset measurements had been measured on historical strike-slip ruptures closer than about 50 m to each other, and this lack of data predetermined that calculated slip gradients could not exceed a certain value. With the documentation of slip gradients at Landers as high as 3×10^{-1}, it is much harder to justify the use of slip gradients as a method for distinguishing the number of displacements that have affected a landform.

6.2.3.1 Quantitative Analysis of Multiple Lateral Offsets

McGill and Sieh (1991) measured 74 offset geomorphic features over a distance of 27 km along the Garlock fault in Pilot Knob Valley, California. This study is distinctive because it not only involves a large number of offsets which are rated for quality, but also includes quantitative uncertainties associated with each offset measurement and therefore permits a reasonably rigorous statistical analysis. The values of the offsets appear to be clustered, suggesting multiple ruptures, and all of the proposed clusters span the area of coverage. While this uniformity does not rule out possible segment boundaries within the study area, the simplest interpretation is that the entire 27-km reach moves during each earthquake; for simplicity we adopt this assumption in the following analysis. In addition, individual offsets within each cluster show little trend with position, so slip gradients appear to be minimal. (The method of quantitative analysis described next could equally well be applied to normal or reverse faults, if many high-quality measurements of fault scarp height are available.)

Figure 6.10A shows the probability density function for 62 offsets (excluding offsets that yield only limiting values). This probability density function was

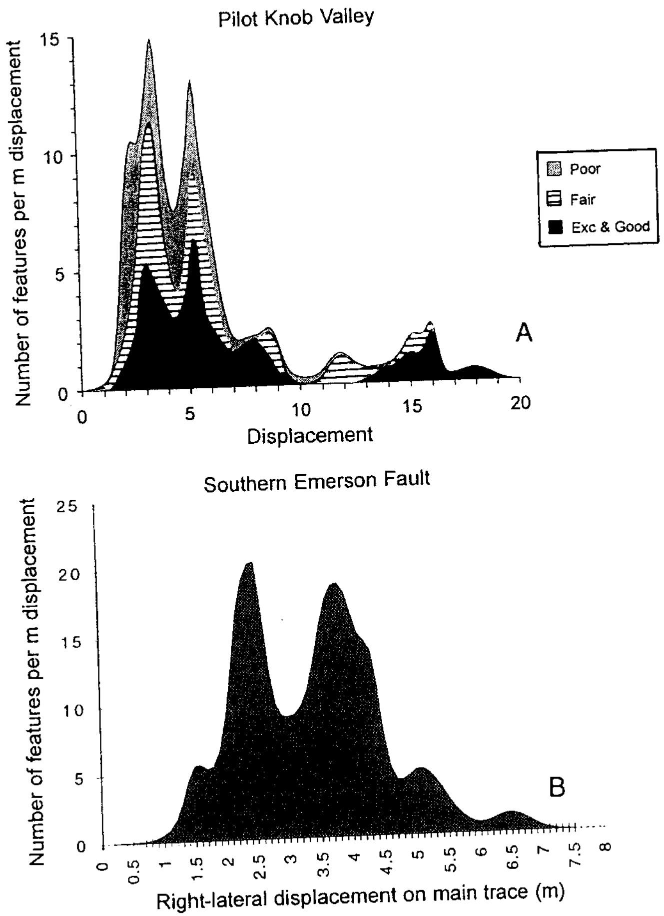

Figure 6-10. (A) Summed Gaussian probability density functions for 62 geomorphic offsets across the Garlock fault zone in Pilot Knob Valley, California. Shading indicates the quality of offset estimates used. The six peaks were interpreted by McGill and Sieh (1991) to represent the cumulative slip associated with six paleoearthquakes. [From McGill and Sieh (1991); reprinted with permission of the American Geophysical Union.] (B) Summed Gaussian probability distributions of lateral offsets along a 5-km length of the Emerson fault created during the 1992 Landers, California, earthquake. Note the bimodal distribution resulting from a single faulting event. From McGill and Rubin (1994).

constructed as follows. Each of the 62 offsets was represented by a Gaussian probability density function with a mean at the best estimate of the offset and with a standard deviation equal to one-half of the uncertainty (i.e., the uncertainties were assumed to be ±2 standard deviations). The probability density functions for all 62 offsets were then summed to produce Fig. 6.10A. [One could as well have parameterized the data differently, e.g., using an asymmetrical triangular function (Humphreys and Weldon, 1994), but the sum of a large number of centrally weighted distribution functions will approach the sum of Gaussians.] It is important to note that this combined density function includes both scatter arising from the natural variability in offset along a rupture (*intrinsic variability*) as well as uncertainty due to the inherent difficulty of measuring offsets hundreds to thousands of years after their formation (*measurement uncertainty*).

Total variability of offset (σ_T) can be thought of as containing both measurement (σ_m) and intrinsic (σ_i) components. The measurement error (σ_m) reflects how precisely one can measure the offset, and could be inferred from repeated measurements of offset features, preferably by different people at different times to minimize bias. In this example we infer σ_m by examining the stated uncertainties assigned by McGill and Sieh (1991) to many individual measurements of offset. The intrinsic variability (σ_i) reflects how variable displacement is along the length of the rupture (or along the fraction of its length studied), and can be calculated from the variability of data or, if no data are available, inferred from data on other large strike-slip ruptures.

Total variability can be defined as:

$$\sigma_T = (\sigma_m^2 + \sigma_i^2)^{1/2}. \qquad (6.2)$$

Since σ_m and σ_T can be directly determined from field measurements and the Gaussian grouping procedure, respectively, one can solve for the intrinsic variability:

$$\sigma_i = (\sigma_T^2 - \sigma_m^2)^{1/2}. \qquad (6.3)$$

The intrinsic variability of offset is of interest for several reasons. For individual ruptures it gives us a measure of the variability in displacement, relatively independent of our ability to measure displacement with real markers in the field. Also, if we are to interpret multiple clusters of offsets as the results of multiple paleoearthquakes, we must be certain that we can distinguish these clusters from the results of simple statistical fluctuation or observer bias.

The intrinsic variability of landform offsets depends on how many displacement events (paleoearthquakes) are recorded by a set of landforms. For example, assume that a rupture has 2 ± 1 m of offset, with a simple triangular function representing the intrinsic variability of offset (peak on the left, Fig. 6.11A). If one then simply superimposes this same offset on itself, assuming a *strictly characteristic repeating event*, one gets the second peak from the left

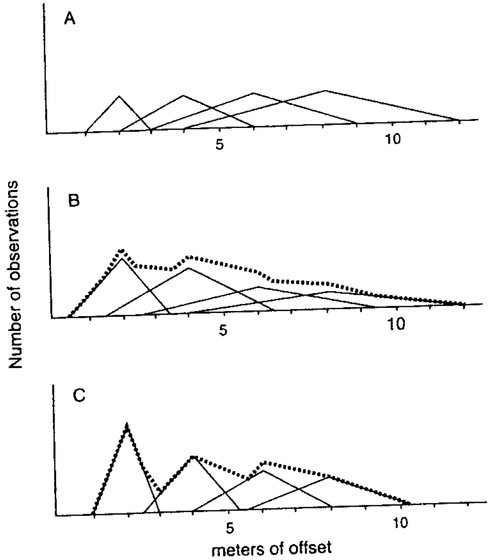

Figure 6-11. Hypothetical diagrams showing the effects of intrinsic variability and measurement uncertainty on histograms of lateral offset. (A) Distribution of lateral offsets produced by one earthquake (triangle on left), two earthquakes (second triangle from left), three, and four earthquakes with displacement of 2 ± 1 m each that repeat identically along strike. (B) A more realistic portrayal of part (A), in which the total number of offset measurements (markers) is the same for each number of earthquakes. (C) Same data as part (B), but assuming four earthquakes with a 2 ± 0.5 m offset each. Dotted lines in parts (B) and (C) show the cumulative distribution of lateral offsets after four earthquakes.

in Fig. 6.11A. The peak of the two-event distribution is 4 m, but the uncertainty has broadened because small offsets (e.g., 1 m + 1 m = 2 m) and large offsets (e.g., 3 m + 3 m = 6 m) will superimpose in places. As more and more ruptures are added, the peaks broaden further. [Since the geomorphic feature is only measured once (today) measurement uncertainty does not compound as does intrinsic variability, and measurement uncertainty mostly affects the smaller offsets because for them it is a relatively large fraction of total offset.] In Fig. 6.11A the peaks are plotted with equal heights so the growth of the uncertainty can be easily seen. If the peaks are plotted with equal weights (Fig. 6.11C), as if there were an equal number of offsets measured for each peak, we see a more realistic view. When a cumulative curve is constructed from these peaks (heavy dotted line) it becomes difficult to identify individual peaks. A very large number of observations would be required to resolve the subtle inflections that overlie the individual peaks. If there were fewer large offsets than small (a likely possibility given the fact that offsets are progressively destroyed by erosion), the older peaks would have less weight and would be further obscured. Even if the assumed intrinsic variability is reduced to half (i.e., to 2 ± 0.5 m per event; Fig. 6.11C) it would still be difficult to locate the second peak from the left accurately, and the third and fourth peaks would not be distinguishable without an extremely well-resolved distribution function.

If a *less characteristic* view of ruptures is taken (i.e., successive earthquakes have similar, but not identical, patterns of slip along strike), the growth of the intrinsic variability would be somewhat lessened, because small or large offsets would not be as likely to be superimposed, and the result would be more centrally located. In this case σ_i increases with each successive event, but not as rapidly as for strict characteristic behavior. Assuming standard distributions (as did McGill and Sieh, 1991) the intrinsic variability of the *i*'th offset becomes:

$$\sigma_{ix} = [\Sigma\sigma_{i(x-n+1)}{}^2]^{1/2} \tag{6.4}$$

where $n = 1$ to x, and x is the number of offset events.

It should be noted that the cumulative intrinsic variability can also *decrease* in successive events if small offsets at a point on the fault are succeeded by large offsets, such that slip rate along the fault tends to be constant (i.e., the variable slip model described in Sec. 9.5.1). However, the limited data on strike-slip faults indicates that characteristic or uniform slip behavior is more typical than variable slip behavior (Schwartz and Coppersmith, 1984; Lindvall *et al.,* 1989). In our analysis of the Garlock data set we thus assume that weak characteristic behavior causes growth in the intrinsic uncertainty. Our conclusions about the lack of resolution to distinguish rupture events would be even stronger with strict characteristic behavior, such as that illustrated by the example in Fig. 6.11.

McGill and Sieh (1991) interpreted each of the six peaks in Fig. 6.10A as resulting from six separate paleoearthquakes, and give their best estimates of the cumulative offsets as 3.4, 5.3, 8.6, 11.8, 15.9, and 18.0 m. This inference is supported by the approximately integral increase in each peak's offset, that is, 3.4, 5.3 (3.4 + 1.9), 8.6 (5.3 + 3.3), 11.8 (8.6 + 3.2), and 15.9 m (11.8 m + 4.1 m). From these displacements and Eqs. (6.2) through (6.4) we calculate the uncertainties that should accompany these offsets (Table 6-2).

It is clear that there is disagreement between the data in Table 6-2 and the interpretation that each of the six peaks represents an earthquake. Equation (6.3) requires that the peaks be wider than the measurement error, and Eq. (6.4) requires that each peak be broader than the previous one. Examination of Fig. 6.10A indicates that both of these tenets are violated by the field data. The second peak from the left in Fig. 6.10A (at 5.3 m) is clearly narrower than the peak at 3.4 m. Peaks 3 through 6 appear to be even narrower, but due to the limited number of measurements in each of those peaks their total

Table 6-2

Calculated Offsets and Uncertainties for the Pilot Knob Valley Section of the Garlock Fault

Event displacement (m)	$\sigma_T{}^a$ (m)	$\sigma_m{}^b$ (m)	$\sigma_i{}^c$ (m)	σ_T(if $\sigma_i = 1$)
3.4 (latest)	1.2	0.9	0.8	1.3
1.9	0.9	1.1	[d]	1.8
3.3	1.4	1.4	[d]	2.2
3.2	1.2	1.8	[d]	2.7
4.1	1.7	2.3	[d]	3.2
2.1	1.1	2.5	[d]	3.5

[a] σ_T measured from the probability plots, by assuming the cumulative curve is composed of six Gaussian peaks centered approximately where proposed by McGill and Sieh (1991).

[b] σ_m determined from the regression of the stated uncertainties versus offset and the mean event displacement.

[c] σ_i calculated from Eq. (6.3).

[d] Indicates a calculated intrinsic uncertainty of less than 0, which is not physically possible.

uncertainty is poorly resolved. This poor resolution also implies that their mean offset is unresolved, so the peak centers cannot be taken to represent the mean rupture offset, even if the peaks are produced by individual events. There are several possible solutions to this inconsistency between the predicted versus the observed uncertainties of various histogram peaks: (1) The measurement error is greatly overestimated, (2) there is systematic bias in picking the offsets, and (3) individual peaks on the histogram do not represent individual earthquakes. Although we strongly suspect that the last explanation is correct, we discuss the others in some detail for pedantic purposes.

First, given the uncertainties in the reconstruction of features like small streams, terrace risers, and ridges across the fault, it seems unlikely to us that the measurement errors are significantly overestimated. However, even if the measurement error is overestimated, the histogram peaks must still broaden with increasing number of events due to the compounding of intrinsic variability. If there were no measurement error, for example, the last earthquake would have had 1.2 m of intrinsic variability. Even if the previous event had no variability (unlikely) the second peak in the offset distribution would have to contain at least as much variability as did the last event, because offsets are the sum of these two events. If each earthquake had only 1 m of variability, the peaks would broaden as indicated in the last column of Table 6-2. By the time one had superimposed six offset events, each with 1 m of intrinsic variability and the measurement error calculated from the data, the 1σ uncertainty of the sixth peak would be 3.5 m; this value is much greater than that indicated by the field data in Fig. 6.10A.

The second possibility, bias of the data, is supported by the unlikely fact that the peaks are better resolved than the raw measurement errors indicates is possible. This bias could be derived from the unconscious choice of a best match of uncertain features that is consistent with previous choices. This statement is not meant to suggest any impropriety in the data collection, but to acknowledge that it is extremely difficult to avoid bias where measurements of "matches" involves interpretation of the exact location of the feature being measured. From experience we know that after one finds several convincing offsets, one's eye is keyed to looking for matches in that range, so that one will often overlook or misinterpret offsets that are unexpected, thus biasing the sample. Without suggesting that this was the case here, any time a data set is more precise than one's measurement error, bias must be considered.

The third possibility is that not every peak on the histogram represents an individual paleoearthquake, or that paleoearthquake displacements may be multimodal, or appear to be so with limited data. Determining the most likely number of paleoearthquakes might be accomplished in a progressive fashion, by starting with one earthquake, and then adding additional earthquakes until the field data are adequately described. This approach could be formalized by comparing the improvement of model fit as additional earthquakes are added, but we simply offer qualitative arguments here. If there was just one earthquake (i.e., one true peak in the data), the mean offset is about 5 m and the total, measurement, and intrinsic uncertainties are 3.9, 1.2, and 3.7, respectively. This interpretation can be challenged both on the poor fit of the data to the model, and the plausibility of the results. First, the density function is very asymmetrical, with a few very large offsets greater than 10 m. This suggests the addition of at least one more earthquake peak, to reduce the extreme asymmetry. Visual inspection of the Fig. 6.10A histogram supports at least a bimodal distribution. Second, the 1σ range of the intrinsic uncertainty is very large, essentially equal to the mean offset, which seems unlikely given historical ruptures, where variability is typically less than half of the mean. Finally, from a physical point of view, a one-event model would require that the rupture had significant offset up to 15 m, which is implausibly large for the Garlock fault.

Adding a second peak produces the following values:

Event displacement	σ_T	σ_m	σ_i
5.0	2.3	1.0	2.1
9.8	3.2	2.2	2.3

This scenario produces two rather centrally located peaks with reasonable, and similar, intrinsic uncertainties (note that the greater total uncertainty is due to the slightly larger measurement uncertainty and the compounding effect of the intrinsic uncertainty). However, the previous event would be almost twice as large as the most recent, suggesting very noncharacteristic behavior.

One could add one more peak, but the relatively slight improvement in the fit of the data to a model distribution caused by three paleoearthquakes is probably not justified. However, it is worth considering a three-event scenario because it implies characteristic behavior. If there have been three displacement events, and we assume symmetrically distributed peaks, they would be at 5, 10 and 16 m and would thus have, within the limits of the data's ability to locate the mean of the multiple ruptures, the same offset of 5 m, a very reasonable value for the Garlock fault. It is also interesting that each of the peaks would be composed of two subpeaks, rather than a centrally located peak, which would be very difficult to generate three separate times simply by chance. This may mean that each rupture is essentially bimodal in displacement along the fault. Bimodality has been proposed by McGill and Rubin (1994) for the 1992 Landers rupture (Fig. 6.10B). Bimodal slip along strike can be plausibly explained if the rupture trace is composed of sections where a significant proportion of net slip occurs on secondary structures (and is too subtle to be measured in reconnaissance studies), alternating with sections where essentially all of the offset occurs on the main fault trace and is easily captured by field measurements. Thus, this apparent bimodality of slip may reflect complex responses of surficial deposits to faulting (distributed versus discrete rupture), rather than a bimodal distribution of slip at depth.

6.3 STRATIGRAPHIC EVIDENCE OF PALEOEARTHQUAKES

The stratigraphy and deformation of unconsolidated sediments in strike-slip fault zones provides the best evidence for determining the number of and age of paleoearthquakes, and in some cases (Sec. 6.3.4) the offset in individual events. Much of the progress in reconstructing paleoseismic histories from stratigraphic evidence followed Sieh's (1978a) widely read paper on fault-zone stratigraphy and numerical dating on the San Andreas fault. These microstratigraphic techniques, coupled with fault-zone trenching technology, have permitted far more detailed paleoseismic analyses than could have been performed from geomorphic measurements. However, the success of stratigraphic investigations depends heavily on the choice of sites for excavation, as explained later. In addition, stratigraphic features produced outside of the fault zone, mainly from ground failure, are also useful for identifying paleoearthquakes and are discussed in Chapters 7 and 8.

6.3.1 Sedimentation and Weathering in Strike-Slip Fault Zones

Previous paleoseismic investigations (e.g., Sieh, 1978a; Fumal *et al.*, 1993) have emphasized the importance of sedimentation and weathering in strike-slip fault zones for reconstructing paleoearthquake histories. The best sites for distinguishing individual paleoearthquakes are where (1) essentially continuous deposition has occurred in the fault zone throughout the time period of interest, concomitant with faulting, and (2) multiple fault strands occur in a wide zone. The second phenomenon cannot always be inferred from surface evidence, but sediment traps are relatively easy to locate from fault-zone geomorphology. In these traps, deposits often continue to accumulate after each displacement event, creating the multiple unconformities and cross-cutting relationships from which each displacement event may be distinguished. In the semi-arid terrain of the western United States, Holocene sediments typically accumulate in two geomorphic settings along strike-slip faults: sag ponds and intermittent stream channels.

6.3.1.1 The Sag Pond Environment

The best depositional environments for preserving paleoearthquake evidence are relatively low-energy environments where sediments accumulate episodically in thin strata, separated by weathering profiles, organic soils, or peats (e.g., the Pallett Creek site: Sieh, 1978a; the Wrightwood site: Fumal *et al.,* 1993; the Glen Ivy Marsh site: Rockwell *et. al.,* 1986). Along strike-slip faults in California, these conditions are often found in sag ponds fed by unconcentrated slopewash, minor rillwash, or small ephemeral streams. Alternating subaqueous (fluvial/lacustrine) deposition and subaerial exposure typically give rise to a stratigraphic sequence of finely stratified sand, silt, and clay (in beds a few centimeters to tens of centimeters thick), interbedded with soil A horizons or thin peats. The organic content of peats and soils is maximized if the sag pond does not completely dry out during normal dry seasons. Trenching has been successful in very wet marshes that were drained by dewatering wells (Rockwell *et al.,* 1986). Alternatively, recent stream incision from natural or man-made causes can dewater sag ponds (e.g., Sieh, 1978a). Thus, paleoseismologists should search for sag ponds that fill with water and receive fine-grained, distal fluvial deposition from small catchment areas in the infrequent very wet years, but exist as marshes or swamps the rest of the time.

Not every sag pond meets these criteria. Tectonic depressions occupied by larger, through-flowing gullies are often subject to channel scour and lateral erosion (see next section), and may be too well drained and dry between rare depositional events to develop peat or rich organic soils. Sag ponds fed by streams subject to debris flow may fill with thick debris containing minimal organic material. At the opposite extreme, perennial sag ponds are typically sites of continuous fine-grained lacustrine deposition. Trenches in such settings (which are possible only if the sag pond has been drained) have revealed massive deposits of dark gray clay with few stratigraphic markers (Rockwell *et al.*, 1986). When in doubt about the sedimentology of a sag pond, one should attempt to "think like a stream" to infer the depositional processes operative at each site (J. D. Sims, personal communication, 1995).

Sag ponds along strike-slip faults typically occupy structural depressions created by transtension and normal faulting, which are found in minor releasing steps or bends (e.g., the Pallett Creek and Glen Ivy Marsh sites on the San Andreas fault, California). Such features are readily observed on aerial photographs. More rarely, sediments are trapped when shutter ridges partially or completely block ephemeral drainages that flow perpendicular to fault strike, creating marshes or swamps (e.g., Hall, 1984). Alluvial fan deposition in the fault zone can also block fault-parallel drainage and create marshes.

6.3.1.2 The Intermittent Stream Environment

Several workers (Wallace, 1990; J. D. Sims., personal communication) have speculated that the complex stratigraphy of nested cut-and-fill channels in streams that cross strike-slip faults are caused by predictable geomorphic processes, and might be related to individual paleoearthquakes. For example, Wallace (1990, pp. 17–19) describes the hypothetical evolution of a straight channel that formerly crossed the fault at right angles, and was later offset by right-lateral strike-slip (Fig. 6.12):

> *The strike slip partly or temporarily dams the stream, causing upstream alluviation at C. A fresh fault scarp is formed in the vicinity of A, and successive offsets expose new scarp areas to the left of A. The dam at B is eroded, and the alluvium deposited earlier at C is dissected. As offset progresses further, the channel segment along the fault line between B and A continually elongates, thus lowering the channel gradient more and more. Because of this decreasing gradient, alluvium is deposited upstream from A to and beyond C, and eventually the stream, having difficulty maintaining a channel along that elongate course, spills across the fault trace and creates a new channel more nearly in alignment with the segment upstream from the fault.*

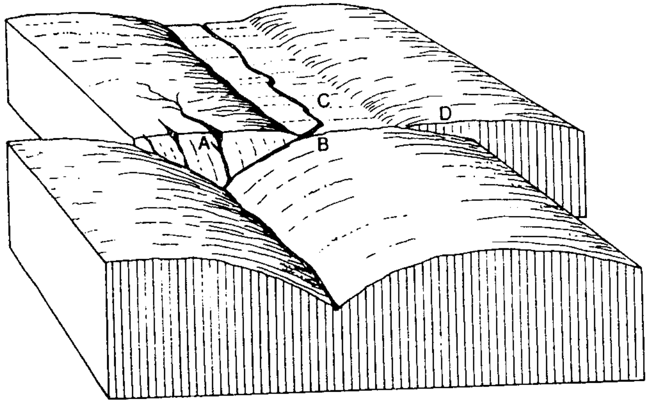

Figure 6-12. Schematic block diagram showing general features and conditions produced where a stream channel is offset by dextral fault slip. See text for discussion of points A-D. From Wallace (1990).

J. D. Sims refined Wallace's idea into a "*tectono-sedimentological process–response model*" (Fig. 6.13) and tested the model at the Phelan Creek site on the San Andreas fault, California. They divide streams crossing the fault

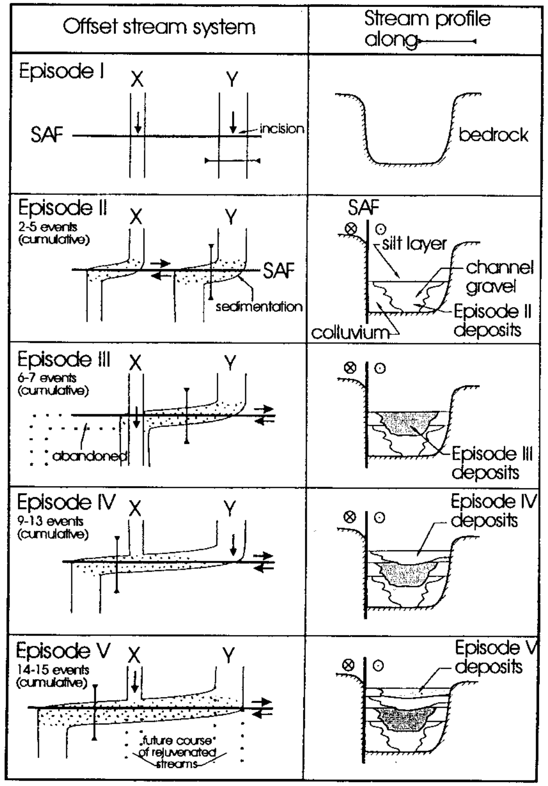

Figure 6-13. Schematic diagrams illustrating the tectono-sedimentological process-response model for strike-slip faults. Left side shows plan views of two intermittent streams successively offset dextrally in multiple faulting events. Right side shows cross sections through the along-fault reach of the stream (except in episode I). Time progresses from top to bottom (i.e., from episode I to episode V). Deposits related to each multiple-event episode are shaded in the right-side diagrams. At Phelan Creek, subunits within deposits of a given episode were assumed to represent individual paleoearthquakes, based on the coincidence of radiocarbon ages with other trench sites. From J.D. Sims, U.S. Geological Survey, Reston, VA, personal communication, 1995.

into an *upstream reach* (upstream of the fault), an *along-fault reach* (essentially parallels the fault), and a *downstream reach* (downstream of the fault). The nearly right-angle bends between the upstream, along-fault, and downstream reaches are termed the *upstream* and *downstream bends*, respectively. According to their model, each faulting event lengthens the along-fault reach and decreases its gradient. In response, the stream aggrades in the along-fault reach in an attempt to increase its gradient back to its prefaulting gradient. Deposition begins at the upstream bend, due to partial damming. The extent of damming can be assessed by comparing the ratio of the average channel width to the average lateral offset per earthquake. For example, a 9-m coseismic offset would completely dam any stream channel <9 m wide, creating a topographic depression and causing ponding and marsh or lacustrine deposition. The same 9-m offset of a ≫9-m-wide channel would only create channel diversion, inducing fluvial aggradation due to gradient decrease but no ponding.

Each faulting episode forces the along-fault reach to readjust its slope abruptly and a new depositional cycle is initiated (Fig. 6.13). The offset history would thus be represented by a sequence of stacked channel fills, in a geometry similar to that of stacked colluvial wedges against normal fault scarps. Eventually, successive depositional episodes fill the along-fault channel to nearly bankfull, reducing the freeboard and leading to channel overtopping during seasonal flooding. The overtopped channel spills straight across the fault, becomes incised, and a new cycle is initiated.

J. D. Sims and coworkers document that stacked channel fills do exist in along-fault reaches at Phelan Creek. However, it is difficult to prove that every one of these fills is offset induced (rather than climatically induced) at this site because few subsidiary faults exist that would give an independent confirmation (via upward terminations or other structural indicators) that each channel fill formed soon after a paleoearthquake. Instead, Sims notes that the age of each channel fill unit or subunit closely matches the ages of paleoearthquakes dated elsewhere on the same fault segment (e.g., Prentice and Sieh, 1989; Sieh *et al.*, 1989; Fumal *et al.*, 1993; Grant and Sieh, 1994) by the use of more traditional structural indicators such as upward terminations (Sec. 6.3.3). At this point their model cannot be accepted as proven, but further research is certainly warranted to determine the conditions under which stacked channel fills consistently replicate paleoearthquake sequences.

As a cautionary note, we acknowledge that multiple episodes of sedimentation and erosion from nontectonic causes (storms, fires, stream capture) certainly affect fault zones. For example, 70 cm of fan sediments containing six soil horizons have accumulated in the San Andreas fault zone at the Bidart fan, California, since the last surface-rupturing earthquake (A.D. 1857). The latest episode of deposition is clearly associated with storms (Grant and Sieh, 1994), and by analogy the six soils and five intervening deposits are all storm related. Thus, workers should be cautious in inferring paleoearthquakes based solely on the complex record of erosion and deposition within strike-slip fault zones (similar caveats were made for normal fault grabens in Sec. 3.3.2.2).

6.3.2 Trenching Techniques

There are basically three approaches used to generate the necessary three-dimensional data to characterize strike-slip paleoseismic events. They are (1) to excavate *multiple, closely spaced trenches* orthogonal to the fault, generally one at a time and (usually) backfilling to avoid collapse, (2) to *excavate progressively* a volume of the fault zone by digging successive exposures orthogonal to the fault, and (3) to excavate a few trenches *perpendicular to the fault* and then to excavate two trenches *parallel to and on each side of the fault.* The case histories that we discuss later include all of these techniques, but we briefly describe each approach here, discuss some of the advantages and disadvantages of each technique, and suggest what problems are best addressed with each approach. In every case, the strategy must evolve as the excavation develops, to incorporate what is learned as work progresses.

In all three approaches, one or more trenches perpendicular to the fault (*locator trenches*) are excavated to locate the fault precisely and to guide future excavations. We summarize the sequence of excavations at Wrightwood, California (Fig. 6.14) to show how the approach evolved as we learned from each excavation. First, natural streambank exposures of the fault (at Swarthout Creek) were cleaned and peat and wood were dated to confirm the age of local deposits. Trench 1 (a locator trench) was excavated to span the entire fault zone. It was clear that there were at least two fault traces, defined by lush vegetation and subtle scarps (subsequently named the main and secondary fault zones). Numerous small, previously unsuspected, structures were revealed in the secondary fault zone. Because the main fault strand displaced only sediments that were several thousand years old in trench 1, and displayed very complex repetitive deformation, we excavated trench 2 in the hope of exposing a younger (and less complexly deformed) section. The younger section was found, but the secondary fault zone did not extend to trench 2. Trenches 1 and 2 were later connected by trench 10 (Fig. 6.14) and, once connected, the results were subsequently integrated and published (Fumal *et al.*, 1993).

Part of the site, involving the secondary fault zone, was excavated using *multiple parallel trenches.* First, trench 3 was excavated perpendicular to trench 1, away from obvious deformation, to establish the lateral extent of the young stratigraphic section; next, two trenches (4 and 5) were excavated parallel to trench 1, across the fault zone, to establish the continuity of the structure. All of these trenches were mapped (both walls) and individual units could be carried through the entire "fork-shaped" network of trenches. Finally trenches

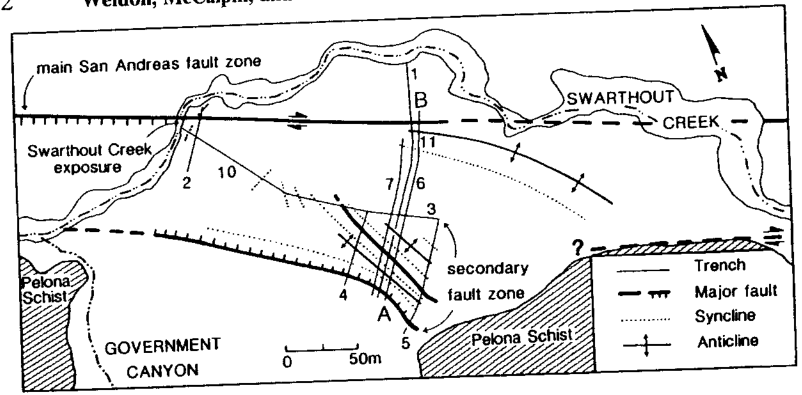

Figure 6-14. Map of the Wrightwood paleoseismic site on the San Andreas fault zone, California, showing location of trenches (numbered), major fault zones (thick lines), and associated folds. From Fumal *et al.*, (1993), modified by the addition of new trench locations.

6 and 7 were excavated, successively to avoid collapse, 1 m from and on each side of trench 1. Thus, we had 10 exposures across the fault zone (2 from each of trenches 4–7, and 1), and 6 exposures in a 5-m stretch (involving trenches 1, 6, and 7). Each trench was logged and then carefully buried after logging to preserve the grid, marker flags, and nails, for future reference.

The greatest advantage of the multiple parallel trench approach is the preservation of mapped surfaces (though a later, deep excavation destroyed a portion of four exposures). Overall, about 90% of the mapped exposures at Wrightwood can be reexcavated and checked; in fact, we have often reexposed surfaces to check relationships or simply to tie in the reference grid to new trenches. We feel that it is very important to allow future critical investigators the ability to reinterpret the structures or resample the section. This approach is also quite safe, because one always can work in shored trenches, which is commonly not possible with progressive excavations or fault parallel excavations. Disadvantages include the inability to have more than one trench open at a time, the time involved in cutting and refilling trenches, the space it takes, and the fact that the exposures must be at least a meter apart, which makes measuring small lateral offsets difficult. However, as discussed elsewhere, it is very unlikely that a single site will yield both recurrence and slip data, so we recommend this approach when seeking recurrence data at a suitable site.

Another approach is to *excavate progressively* a volume of sediment, usually by repeatedly cutting back and mapping a free face that progresses orthogonally to the fault. While we have employed this technique on the Elsinore fault and the main fault strand at Wrightwood at Swarthout Creek (Fumal *et al.*, 1993), the results are not documented in detail in the literature, so we use an example from Pallett Creek (Sieh, 1984); it is, in our opinion, an excellent example of this approach. A 50-m-long section, 5 m deep, and 15 m wide was progressively excavated with walls mapped on average every meter; additional vertical and subhorizontal exposures were also mapped, where critical relationships were found. An upper 2.5-m exposure was first excavated orthogonal to the fault and extended progressively. After suitable room was established, a second, lower, 2.5-m exposure was excavated that progressively "followed" the first, as excavation continued, leaving a bench between the two exposures. Exposures were surveyed, gridded, and photographed; critical units and relationships were labeled and mapped, and then a new wall was cut. From these data, isopach and structure contour maps were constructed (Sieh, 1984). A similar progressive excavation study by Wesnousky *et al.* (1991) is described in Sec. 6.3.4.

The major advantage associated with this approach is the rapidity with which the data are collected, making such three-dimensional reconstructions possible. An additional advantage is seeing the units and structures evolve as the exposure is cut back; one may stop at any place, such as where key information is preserved, and map horizontal surfaces; to locate exact piercing points. The major drawback is the destruction of the volume excavated and thus the impossibility of rechecking or reinterpreting the results. While Sieh (1984) only excavated a small fraction of the young section deformed by the fault, the exposures recorded and interpreted now only exist on photographs and maps. In our experience, photographs are often difficult to interpret, especially by individuals unfamiliar with the site, and with time photographs become progressively more difficult to interpret even by the original investigator, as first-hand knowledge of the site fades. However, in situations where one wishes to recover the deformation associated with individual earthquakes, which was the goal of the Sieh (1984) study, this is probably the best approach. Note, however, that the events characterized by Sieh (1984) had already been discovered in multiple trenches and natural exposures (Sieh, 1978a), and that the deformation determined by the 3-D trenching is only about one-third of the total deformation across the fault (Salyards *et al.*, 1992).

The third approach is *trenching parallel to and on each side* of the fault. Typically two or more locator trenches are cut across the fault to establish its exact position, and then trenches subparallel to the fault are cut some distance away from the fault to locate potential markers to trace to the fault. Subsequent trenches are cut close to the fault on each side, leaving a thin *septum* containing the fault (see Fig. 6.30). Piercing lines can be located on each side of the fault on the thin septum, and their trends estimated from the two walls of the trench parallel to the fault and, if available, additional trenches farther away from the fault. Because this technique provides relatively few exposures of the fault, it is best suited for measuring offset (Sec. 6.3.5), rather than determining the stratigraphic horizon or age of the earthquake. However, discrete increases in the downward displacement can be recognized this way, providing information about the stratigraphic level of earthquakes.

A variation of this approach, which is most commonly applied in Japan, is to make a U-shaped, T-shaped (Tsukuda and Yamazaki, 1984), or *rectangular excavation (open pit)* that provides exposures both parallel to and perpendicular to the fault (see Fig. 2.11). Typically the Japanese slope the walls, so that they have a 45° exposure. The advantages of this approach include the ability to project onto both vertical and horizontal views (Fig. 6.15); the walls are more stable than in a narrow and deep "California-style" trench, especially in soft and wet sediments (Yoshioka *et al.*, 1993), one does not need shoring, and because the walls often meet at the bottom of the excavation one has a continuous 3-D exposure, rather than a floor. The major disadvantage is the greatly increased amount of material that must be removed; these exposures are very expensive and time consuming to create, and a large volume of the critical material near the fault is lost. In addition, trench logs as drawn often have different vertical and horizontal scales (e.g., Sato *et al.*, 1992, pp. 562–563) which must be rectified by projecting onto a vertical plane.

In summary, we recommend multiple parallel trenches for the recognition and dating of paleoseismic events. As discussed elsewhere, we do not recommend trying to determine both the timing and offset at a single site, but if that is the goal of the project, the second technique, progressive excavation of the fault zone is probably the best. If one is most interested in the offset of one or a few features, the final method, fault parallel trenching, is the best approach. There are, of course, many possible modifications and hybrids of these three basic strategies that could be adapted to particular projects; one should remain flexible and modify the approach as one learns more about the specific case with each excavation.

6.3.3 Stratigraphic Indicators of Paleoearthquakes

Paleoearthquakes are typically recognized in exposures of strike-slip faults from six general types of evidence: (1) upward termination of fault displacement, (2) abrupt changes in vertical separation of strata as faults are traced upsection or downsection, (3) abrupt changes in thickness of strata or of facies across a fault, (4) fissures and sand blows in the stratigraphic sequence, (5) angular unconformities produced by folding and tilting, and (6) colluvial wedges shed from small scarps (Fig. 6.16). In section, strike-slip faults tend to define narrower deformation zones than do dip-slip faults (mean widths of 5.5 and 12.1 m, respectively; Bonilla and Lienkaemper, 1991). Fissures and voids are common (58% of trenches inventoried), similar to normal faults but unlike reverse faults, which is indicative of transtension or of low confining pressures at shallow depths. Conversely, features indicating strong compres-

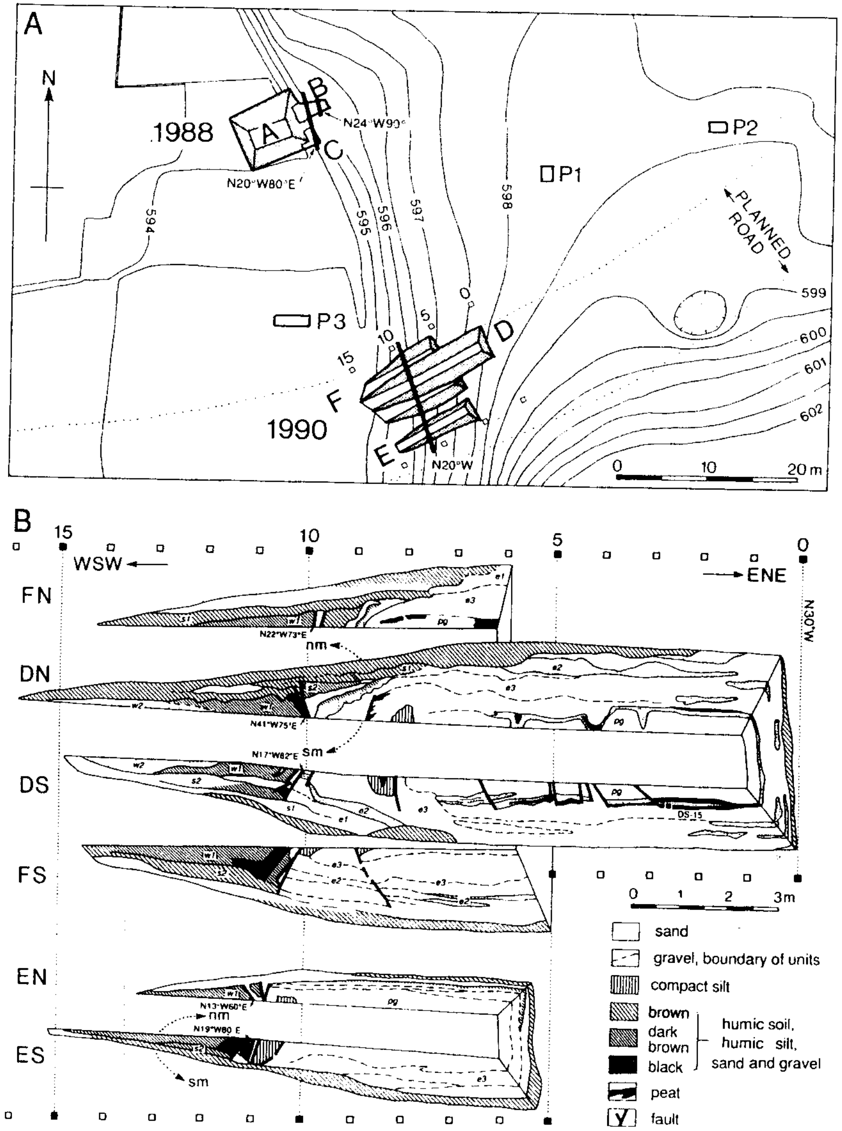

Figure 6-15. Examples of Japanese open-pit trenches and logs made from them. (A) Detailed topography and geometry of trenches across the Gofukuji fault. Fault planes are shown by heavy lines. Shaded areas are the sloping sidewalls of the trench. Elevations are in meters. (B) Simplified plan views of walls of trenches, D, E, and F. Trench D is inset within wider trench F. Each wall is named after the trench name (D,E,F) plus north (N) or south (S). [From Okumura *et al.*, (1994); reprinted with permission of the Seismological Society of Japan.]

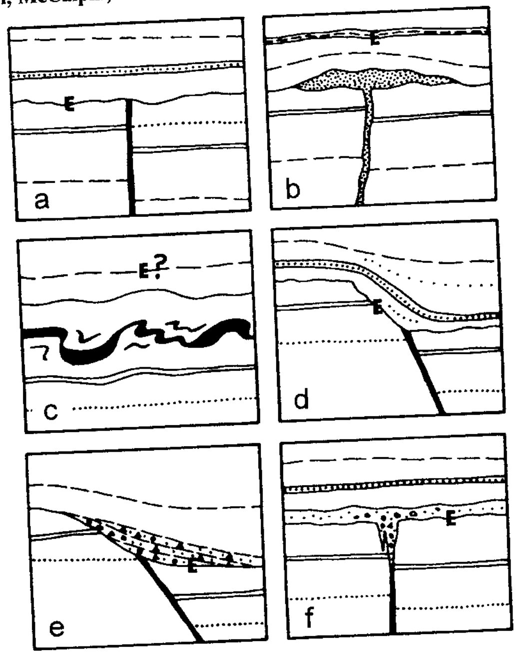

Figure 6-16. Schematic diagrams of typical stratigraphic indicators of paleoearthquakes in strike-slip environments. In all examples strata have been offset by a single event, either along faults (thick black lines) or sand dikes (stippled pattern). The event horizon (E) most closely approximates the time of faulting. (A) Fault terminates upward against an unconformity (the event horizon). This abrupt termination contrasts with gradual dieout up (see Chapter 2). (B) Sand dike feeds an injected sill of sand that has folded overlying strata (dashed line). The event horizon is at the contact of the folded and unfolded strata, *not* at the top of the sill. (C) Deformed horizon overlain and underlain by undeformed strata. Identification of the event horizon is complicated by ambiguity in the position of the ground surface at the time of soft-sediment deformation (see Chapters 7 and 8). (D) Fault underlies an eroded scarp and is overlain by unconformable strata; the unconformity is the event horizon. (E) Fault underlies a scarp that has been buried by scarp-derived colluvium. This is the typical geometry encountered on normal or normal-oblique faults (see Chapter 3). (F) Fault grades upward into a fissure that has been filled with material from an overlying unit (dots and circles). The fissure may have opened prior to the deposition of the dotted/circled unit, in which case the event horizon is the basal contact of that unit. Alternatively, the lower part of the dotted/circled unit may have existed at the time of fissuring and pieces may have fallen into the fissure, after which deposition of the unit continued. In that case, the event horizon is within the dotted/circled unit. [From C.R. Allen (1986). Reprinted with permission from Active Tectonics. Copyright© 1986 by the National Academy of Sciences. Courtesy of the National Academy Press, Washington, D.C.]

sion in the near-surface environment (gouge, breccia, slickensides) are less common on strike-slip faults (observed in 4 to 15% of trenches inventoried; Bonilla and Lienkaemper, 1991, Table 17).

6.3.3.1 Upward Fault Terminations

Upward fault terminations (Fig. 6.16A) are probably the most commonly-cited evidence for paleoearthquakes (e.g., Sieh, 1978a). Upward terminations are generally most effective in identifying the latest faulting event, because subsequent ruptures often follow the same plane. However, a single upward termination at a given stratigraphic level is tenuous evidence for a displacement event (Grant and Sieh, 1994), for reasons given next.

First, Bonilla and Lienkaemper (1991) record that, where the ground surface at the time of rupture is known, 73% of principal and secondary strike-slip faults *die out upward* and do not reach the ground surface at the time of the earthquake (see Chapter 2). The depth below the ground surface at which faults *dieout up* varies from a few centimeters to >2 m, with a mode at 15 to 30 cm (i.e., an asymmetrical distribution; Bonilla and Lienkaemper, 1991, Fig. 15, Table 10). Thus, about three-quarters of strike-slip fault strands die out before they reach the ground surface at the time of the earthquake, but the depth of dieout up may be predictable only in statistical terms. Second, strike-slip ruptures are often composed of a series of en-echelon steps (Fig. 6.17), where slip is being transferred from one fault to another. Faults often dieout up in the step and terminate at different stratigraphic levels from exposure to exposure, even though the faults were all formed at the same time.

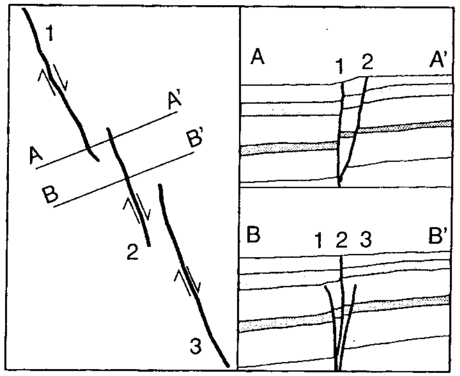

Figure 6-17. Schematic diagrams showing how transfer of strike-slip displacement across en-echelon steps leads to upward terminations of fault strands at different stratigraphic levels. Plan view at left, cross sections at right. In section A-A′, fault strands 1 and 2 are expressed at the surface. In section B-B′, only fault strand 2 reaches the surface. The projections of flanking faults 1 and 3 exist in the subsurface, but die out upward before reaching the ground surface. Faults 1 and 3 formed at the same time as fault 2, but they might be misinterpreted as being older if the principle of upward termination is too strictly applied. For a discussion of the "dieout up" phenomenon, see Sec. 2.3.2.5.1. From Rockwell (1987).

Third, shaking, *freeze–thaw*, and *wet–dry cycling* commonly make fractures propagate above the event horizon after faulting. It is very common to see small, hairline cracks propagating up into what were probably previously unfaulted units.

In summary, upward terminations of rupture must be interpreted carefully and should only be used when the termination is consistent at many locations or in association with other indicators, like scarp colluvium or fissures. To be confident of a distinct paleoearthquake, upward terminations must exist at the same stratigraphic horizon at several locations in the trench and on both walls.

6.3.3.2 Downward Growth in Displacement

Abrupt *downward increases in displacement* on a fault often indicate multiple faulting events, as described in Sec. 2.2.2.5 for dip-slip faults. However, these increases can also result during a single faulting event if certain conditions are met. First, the vertical component of slip on a strike-slip fault may decrease naturally upsection, in a manner similar to dieout up. Second, if faulted strata are lenticular (i.e., they thicken and thin along strike), lateral displacement will result in variable vertical separations of contacts at the fault plane. Depending on the shape of lenticular (or previously folded) strata, vertical separations may either increase or decrease upsection, or do both at different stratigraphic levels. *When faulted strata are neither horizontal or planar, changes in vertical stratigraphic separation do not prove changes in strike-slip displacement.* If sufficient 3-D data exist, the shape and offsets of individual stratigraphic units can be traced, and can permit recognition of the stratigraphic horizon of individual earthquakes. Third, discrete downward increases in offset can also be caused by faults merging, rather than from cumulative displacement events. From struggling with many examples like this, we conclude that working on zones where the deformation is localized to a few meters for thousands of years (at least for a fault as active as the San Andreas) is a waste of time. One should look for places where the deformation from individual events is separated as widely as possible.

6.3.3.3 Downward Increase in Thickness/Facies Contrasts

Another line of evidence for multiple events is a *downward increase in thickness or facies contrasts* across the fault. Such reconstruction can be done in principle by finding the facies transition or the same thickness of a given unit on each side of the fault, usually accomplished by the progressive excavation technique described in Sec. 6.3.3 (e.g., Sieh, 1978a, 1984). However, even this technique becomes difficult where strata have been deformed in multiple events or faulted by multiple intersecting strands.

6.3.3.4 Fissures and Sand Blows

We consider *fissures,* either filled with overlying material (Fig. 6.16F) or with extruded sand (*sand blow*), to be very good indicators of the stratigraphic position of an earthquake. Although many are quick to point out that liquefaction can be caused by other distant faults and therefore be misleading, we are aware of few (if any real) examples of sand blows in paleoseismic excavations being clearly related to earthquakes on some other fault. In every case at the Wrightwood trench site, fissures are associated with fault ruptures. At the Pallett Creek site, Sieh (1978a) identified most of the earthquakes by the stratigraphic position of sand blows and subsequently (Sieh, 1984) showed that those horizons were associated with discrete increases in deformation.

The best cases are when fissures or sand blows are associated with actual fault displacement, such as is shown in the particularly good example of Fig. 6.18. In that figure one can see where we cut into the fault revealing a fissure, partially filled with well sorted sand that was probably extruded as a sand blow, but little if any sand flowed onto the surface. The vertical separation across the fault can be seen by the white sand layer within darker peat.

Sand blow deposits that were vented, and thus lay upon the ground surface at the time of rupture, must not be confused with *sills,* which are injected below the ground surface (Fig. 6.16B). In the former case the event horizon lies beneath the extruded sand (see Chapter 7), whereas in the latter case (Fig. 6.16B) the event horizon (E) lies at some distance above the sill, where strata deformed upward by sand intrusion are unconformably overlain by undeformed strata. Detailed descriptions of sills are given in Chapter 7. While caution should be exercised, as in interpreting any data, sand blows and fissures appear to be one of the most reliable indicators of paleoearthquakes in strike-slip fault zones.

6.3.3.5 Angular Unconformities

Angular unconformities produced by folding or tilting constitute relatively unambiguous paleoseismic indicators (Figs. 6.16D and 6.16E). When poorly consolidated sediments are folded during coseismic strike-slip displacement, an angular unconformity (i.e. an event horizon) is formed when sedimentation resumes. Angular unconformities, typically having wide areal extent, do not suffer from the complications (induced by merging fault traces) that affect paleoseismic indicators restricted to fault planes. In addition, there are few nontectonic processes that can create angular unconformities. The main source of ambiguity associated with angular unconformities is whether folding can be caused by aseismic creep. However, if creep is operative during sedimentation, each successively lower stratigraphic unit will be incrementally more folded. In most exposures (e.g., the Wrightwood trenches, see Figs. 6.23 and 6.24), strata are folded in discrete packages, and discrete periods of folding can be inferred from the technique of "unfolding" the folds.

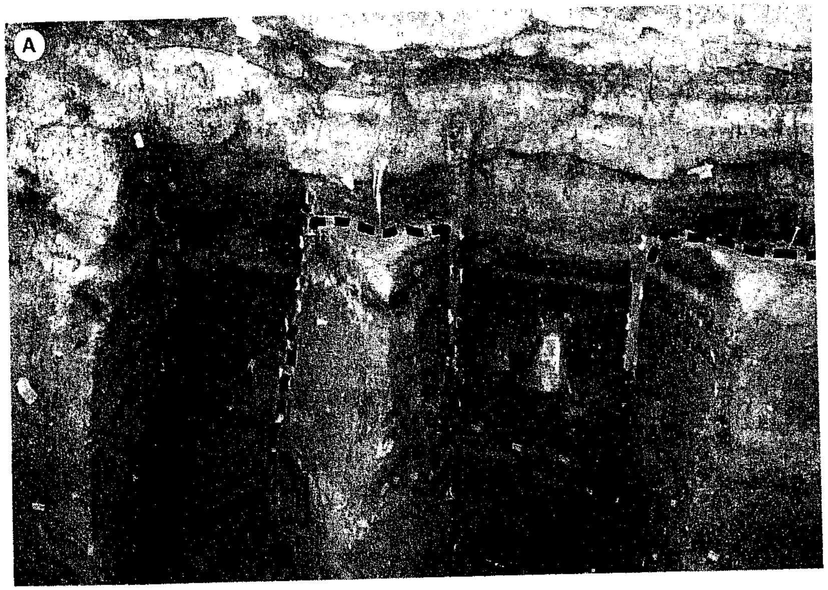

Figure 6-18. Photograph of a filled fissure along a fault plane in the Swarthout Creek exposure at the Wrightwood, California, trench site. The fissure (dashed line), which strikes approximately parallel to the plane of the photograph, is exposed on five excavated surfaces and is associated with event 4 shown in Fig. 6.21 (see also Fumal *et al.,* 1993).

6.3.3.6 Colluvial Wedges

The final stratigraphic indicator of paleoearthquakes is the *colluvial wedge* (Fig. 6.16E). Production of colluvial wedges in a strike-slip environment requires the creation of a fault scarp containing a free face, typically the result of segment obliquity and the accompanying vertical component of displacement (Sec. 6.1.1.1). The evolution and sedimentology of colluvial wedges is discussed in detail in Sec. 3.3.2.1. Due to the small height of most oblique-slip or secondary dip-slip fault scarps in strike-slip fault zones, colluvial wedges are generally thin and colluvial facies are poorly differentiated.

6.3.3.7 Example from the San Andreas Fault at Wrightwood, California

In this section we describe, via trench logs and photographs, the appearance and significance of all six types of stratigraphic indicators at a single trench site. The two main traces and numerous smaller structures at the Wrightwood site make it an ideal site for paleoseimic study, because the deformation is so widely dispersed it is possible to find many types of stratigraphic indicators of paleoearthquakes. If all of the deformation were limited to a simple trace or zone, it would be difficult to identify deformation associated with individual displacement events. For example, in Fig. 6.19 fault displacement has been restricted to a narrow zone for several thousand years, making resolution of the individual events extremely difficult. Figure 6.20 shows a photograph of obvious thickness mismatches across a fault.

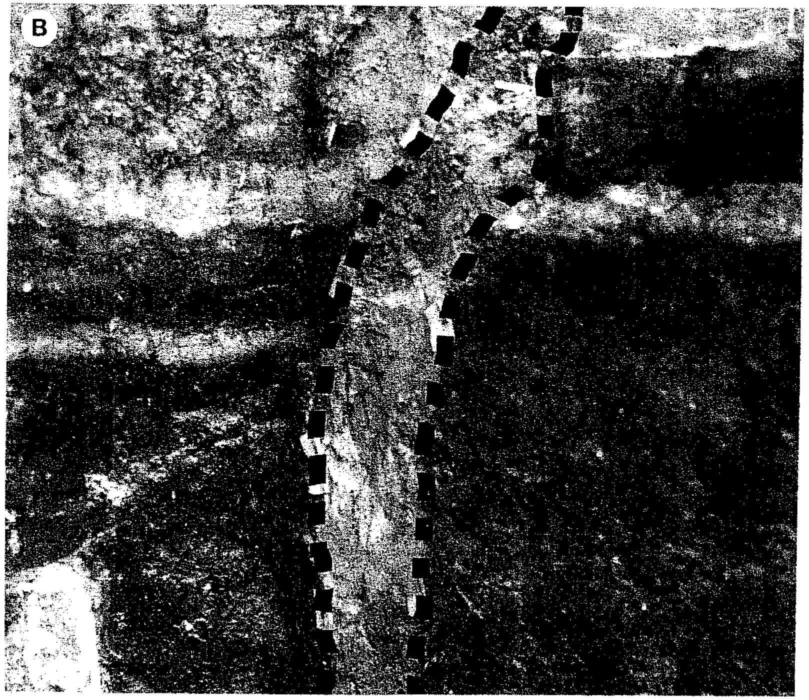

Figure 6-18 Continued

Figure 6.21A shows a composite trench log where three types of stratigraphic indicators (upward terminations, sand dikes/fissures, and angular unconformities) reveal evidence for five displacement events. The following reconstruction of events is after Fumal *et al.* (1993). Evidence for the youngest rupture is a large fissure (at 1.8 m) that formed above a fault and was subsequently filled in by a debris flow (unit 148) dated at A.D. 1890 ± 20. A sand dike also cuts all units below unit 148. The fissure and dike are attributed to the 1857 Ft. Tejon earthquake (M ca. 8). The next earlier event is not expressed by discrete fault traces, but by the angular unconformity between units 142 and 144; Fumal *et al.* (1993) assign this deformation to the A.D. 1812 San Juan Capistrano earthquake. If surface faulting occurred at this exposure during this event, all such fault traces must have been rejuvenated by the 1857 earthquake, which obscured the earlier displacements.

The next earlier event (event 3) produced rupture on at least two faults (at 2.4 and 4.1 m) that affect only units older than peat 135f. The fault at

Figure 6-19. (A) Log of the northern end of trench 11 at Wrightwood, illustrating the complexity of deformation caused by repeated rupture in a narrow zone. Black units are peat. Trench location is shown on Fig. 6.14. Box shows location of part B. (B) Close-up of deformation.

2.4 m evidently produced a small scarp that was subsequently buried by colluvium (labeled in Fig. 6.21A) largely derived from units 136e and 138. This displacement event predates peat 135g, which was later folded by the A.D. 1812 earthquake; Fumal *et al.* (1993) date Event 3 at about A.D. 1700.

The next earlier event (event 4) is indicated by several upward fault terminations at peat 135d (at 3.0 m and 4.8 m), a sand dike (at 4.0 m), and tightly folded beds between ca. 2 and 5 m. This event is dated at ca. A.D. 1610. The oldest event (event 5) is represented by a series of faults that displace and rotate strata between 4 and 7 m and displace peat 130, but do not displace overlying units. Based on the upward termination, this event is dated about A.D. 1470. Units below unit 127 may have been deformed by additional displacement events, but limited exposure prevents resolving all of the events. The pattern of older faults to the right (southwest) and younger faults to the left (northeast) indicates that ruptures have progressively moved to the northeast through time, thus separating the deformation and making it easier for us to interpret.

Fault dieout up in a stepover can be seen in successive trenches at Wrightwood. In the first trench (Fig. 6.22D) there is one north-dipping trace. In the second (Fig. 6.22C) there are two, which appear to reach separate stratigraphic levels and which could be interpreted as two separate events. In the third trench (Fig. 6.22B) there is only the south-dipping trace, this time at the same stratigraphic level as the north-dipping trace in Fig. 6.22D. In map view, one

Figure 6-19 Continued

could infer that this is an en-echelon step, and that there has been just one faulting event. It would be possible to trench across an en-echelon step and interpret the stratigraphy as the result of either one event, two events (if there are two traces that are traced to different levels), or perhaps no events, if the two faults of the en-echelon trace do not overlap and the trench falls between them. Young rupture can also jump from place to place without obviously being part of en-echelon steps, as shown by slightly different patterns of faulting in close exposures such as trenches 6, 7, and 11 in Fig. 6.14.

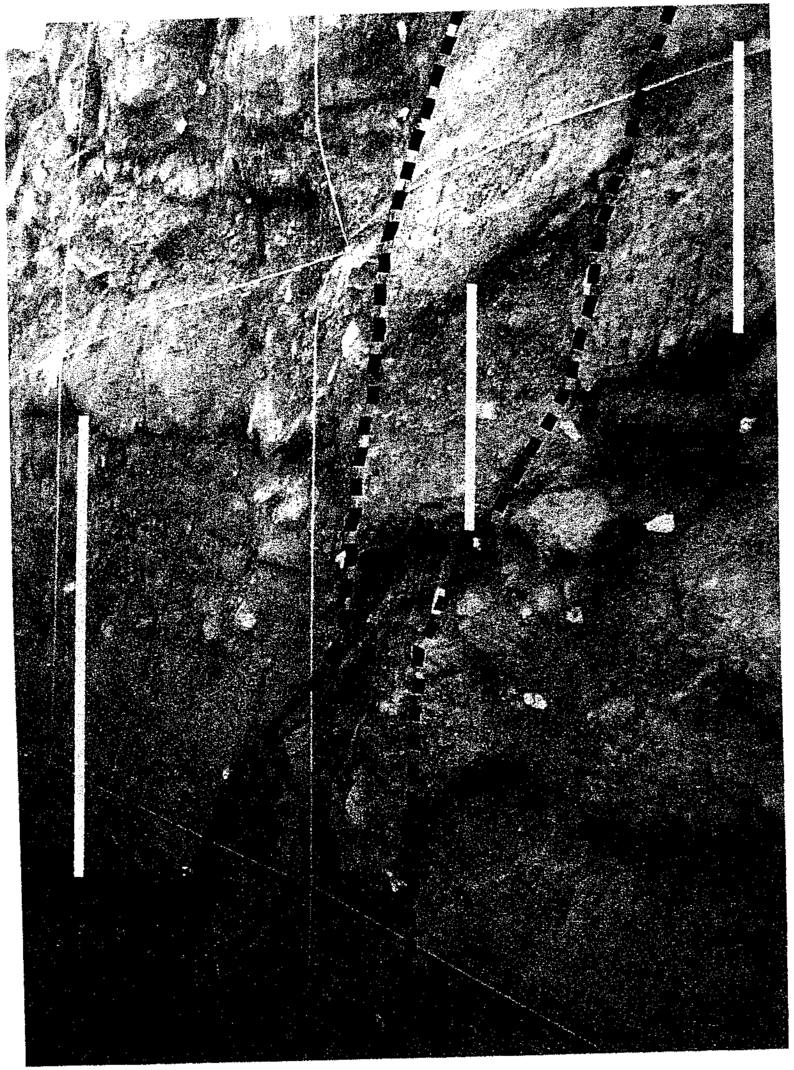

Figure 6-20. Photograph showing thickness changes across two faults (dashed lines). To the left of the faults units 41 through 44 are ca. 1 m thick (white bar); in the fault zone they are 30 cm thick (white bar); and to the right of the fault zone they are 40 cm thick (white bar). These thickness variations are caused by strike-slip displacement of lenticular strata.

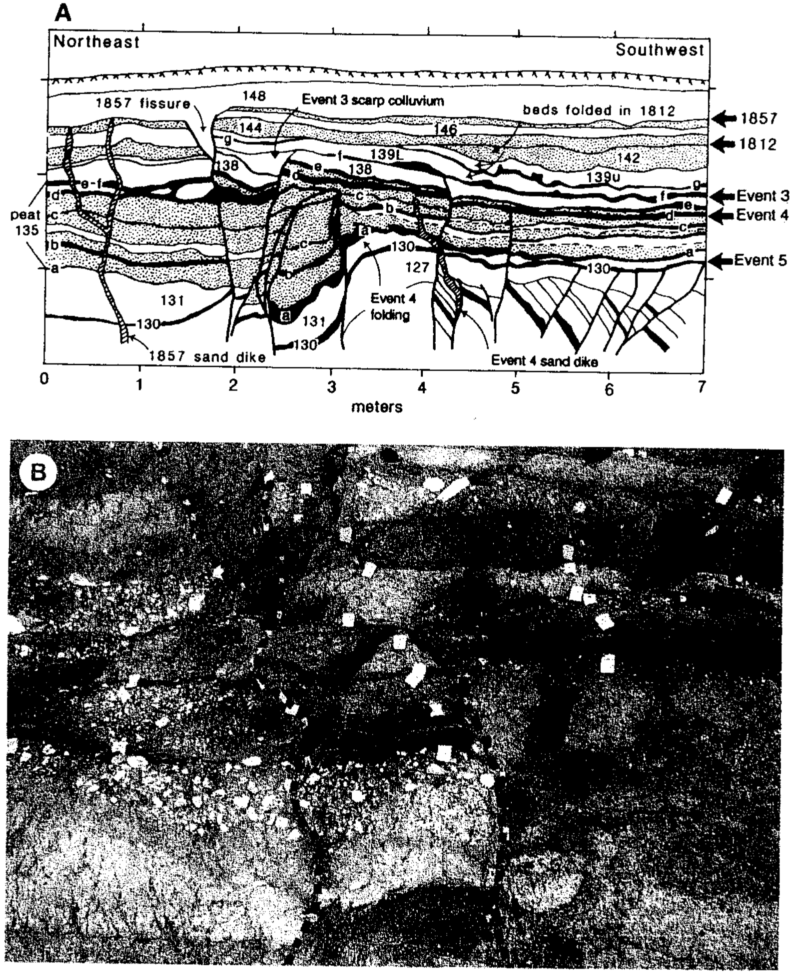

Figure 6-21. Composite log of Swarthout Creek exposures at the northeastern corner of the Wrightwood trench site, showing deformation of the main fault zone associated with the past five earthquakes. Fault strands are shown by heavy lines. Peat layers are black, stippled layers are granitic alluvial deposits. All other units are debris flows composed of schist debris. Numbers refer to unit designations of Fumal *et al.* (1993). [From Fumal *et al.*, (1993); reprinted with permission of the American Association for the Advancement of Science.]

A colluvial wedge was produced by oblique-normal faulting on the secondary fault zone (Fig. 6.14) at Wrightwood. In Fig. 6.23, units 139u through 148 are obviously wedge-shaped. Figure 6.24 shows an example of folding from near the northeast end of trench 11 (anticline on Fig. 6.14). By sighting down

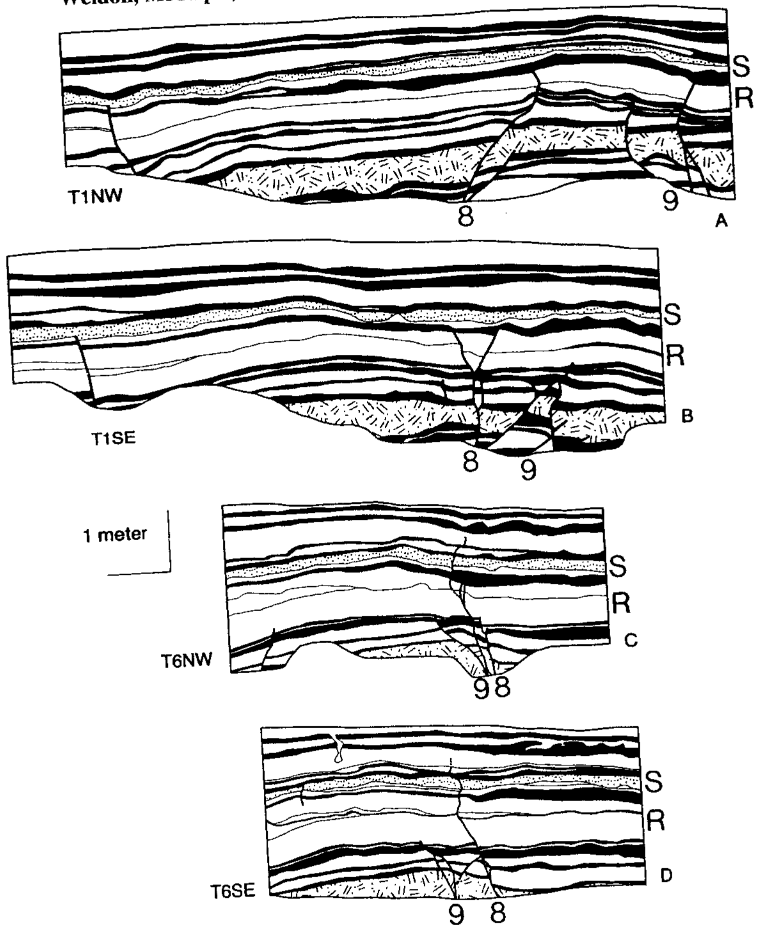

Figure 6-22. Logs of successive trench walls at the Wrightwood site showing how the same faults in a stepover die out upward at different stratigraphic levels. The four logs (A-D) are identified by trench number (e.g., T1, located on Fig. 6.14) and by the wall logged (NW or SE). Horizontal distance between A and B is 1 m, between B and C is 0.8 m, between C and D is 1 m. An older fault zone (9) displaces all units below unit R (thickest white unit) on trench walls B, C, and D, but on wall A one fault in this zone extends up through bed R. A younger fault zone (8) appears to die out upward at a thick peat (black) between R and S (stippled unit) in T1NW and T1SE, yet it can be traced into beds stratigraphically above unit S on trench walls C and D. Fault zones 8 and 9 cross each other between walls B and C because fault zone 9 strikes more northerly than does fault zone 8.

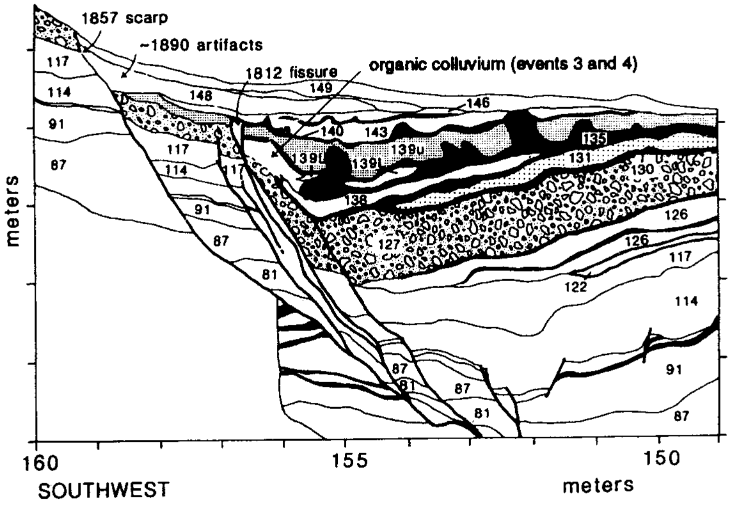

Figure 6-23. Composite log of the southwest end of trench 6 at Wrightwood showing a colluvial wedge and back-tilted strata near the scarp-forming normal-oblique fault. Minor features from trenches 1, 4, 5, and 7 have been added. Numbers refer to the unit designations of Fumal *et al.* (1993). Black units are peat, patterned units are coarse alluvium, white units are debris flows. [From Fumal *et al.*, (1993); reprinted with permission of the American Association for the Advancement of Science.]

the horizontal string (center), one can see the broad folding. In some cases, such as Fig. 6.24, the subsequent unconformity is easy to see. In other cases it is more subtle. Figure 6.25 shows an example of a syncline from near the northeast end of trench 4 (Fig. 6.14). Because it appeared that unit S was more folded than unit T, we progressively "unfolded" the section to see if we could argue for an event between the two units. Unfolding is done by digitizing the contacts, calculating the elevation difference between the youngest folded contact and a horizontal line, then subtracting that elevation difference from all the underlying contacts. Figure 6.26 shows the results; when unfolded on top of unit T, it is clear that unit S is folded, because both bottom and top contacts share relief not shared by unit T. Subsequent unfolding on the top of unit S produces a smooth depression that is not found in lower units, so it represents the first folding of this syncline (this conclusion is not based simply on this one example, but is shown to illustrate how one can analyze subtle folds).

It appears that in transtensive environments these folds are common, which suggests that trenching fault steps and pull-aparts will often be successful. In some cases one can see the causative faults; for example, in Fig. 6.19 weak

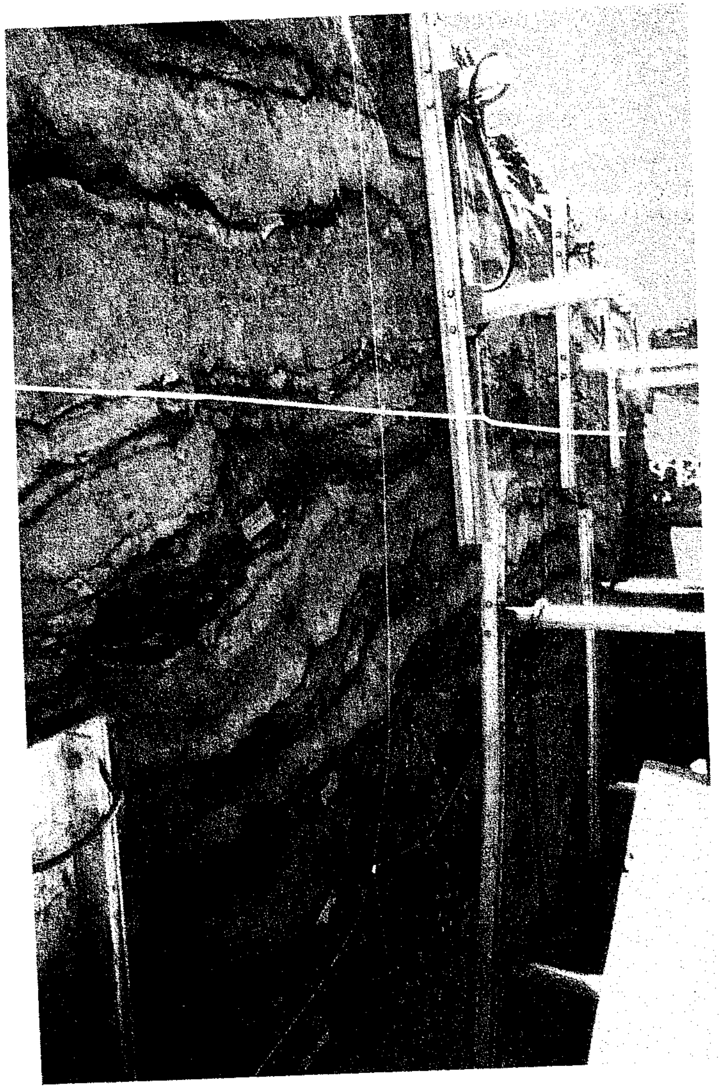

Figure 6-24. Photograph of a broad anticline at the northeast end of trench 11 at Wrightwood (covers the left half of Fig. 6.19).

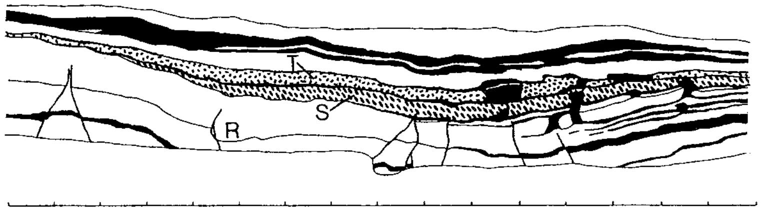

Trench #4

Figure 6-25. Log of the northeast end of trench 4 at Wrightwood. The wall contains subtle unconformities between units R, S, and T that can only be recognized by the unfolding technique described in Fig. 6.26. Tick marks on scale (bottom) are 1 m apart.

layers (generally thinly bedded silts and peats) are occupied by dip-slip (listric) faults, producing rotation of the overlying beds. To test this hypothesis for the larger folds we see at Wrightwood, we dug a deep excavation beneath a particularly well-developed syncline (Fig. 6.27). The half graben is clearly related to the faults following a very weak, thinly bedded series of layered silts and peats. It is clear that the section was undeformed until unit W was deposited, when a fault trace off the figure began to follow the weak units and to surface (or come close to the surface) at this fold. Subsequent deposition caused thicker deposits (units X, Y, and Z) to be laid down in the resulting depression.

In summary, the best resolved paleoearthquakes at the Wrightwood and Pallett Creek sites (e.g., event V of Sieh, 1984) are those associated with highly curved faults. These faults produce the greatest vertical deformation of the ground surface, which is subsequently preserved as thickness variations in younger sedimentary units.

6.3.4 Measuring Lateral Displacements from Stratigraphic Data

The most commonly used stratigraphic markers for measuring displacement across strike-slip faults are buried stream channels. For example, Sieh (1984) used gravel stringers and filled channels extensively to reconstruct the lateral offset of individual events at Pallett Creek, California. Difficulties arise when the size of the feature is comparable (or greater) than the offset associated with a single event, there are multiple fault traces, and there is relief near the fault (such as a scarp), which makes it very difficult to know the original geometry of likely stratigraphic markers. In addition, the spacing of the excavations makes it very difficult to see exactly what happens at the fault, where the streams may have been diverted. To illustrate this issue more clearly, we discuss three recent three-dimensional trenching projects across strike-slip faults, in which misalignment of a buried stream channel was due wholly, partly, or not at all to lateral offset by single or multiple earthquakes.

6.3.4.1 Whittier Fault Example (Most of Misalignment Caused by Diversion)

The Whittier fault zone near Los Angeles, California, crosses a stream with about 50 m of right-lateral misalignment. Trenches were initially excavated across the fault to determine the width and characteristics of the fault as well

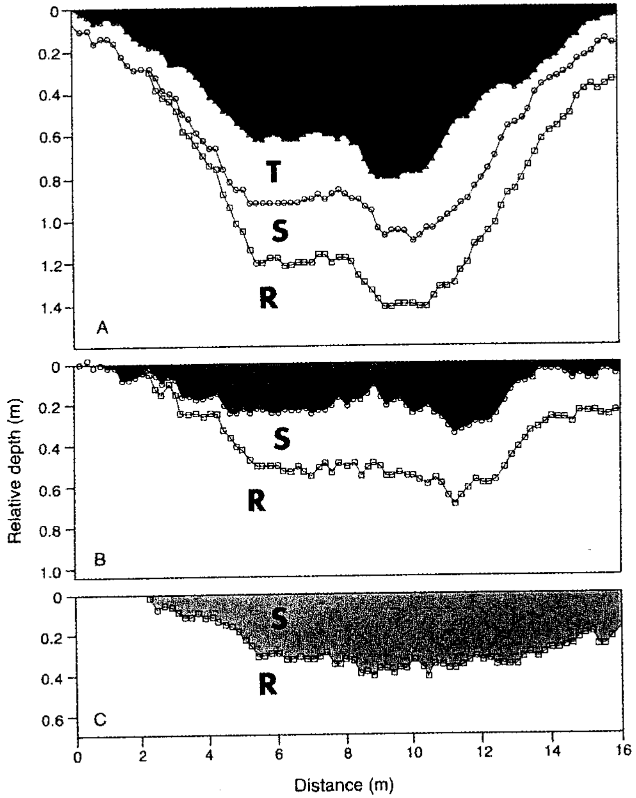

Figure 6-26. Results of the unfolding technique on two strata from the northeast end of trench 4. A vertical exaggeration of 6.5x is used to accentuate the subtle unconformities. Boundaries of strata are represented by squares, circles, and triangles (digitized at a constant horizontal interval) joined by thin lines. (A) Present configuration of the two strata. (B) Geometry of the lower two contacts after unfolding to restore the upper contact of unit T to horizontal. (C) Geometry of the lower contact after unfolding to restore the upper contact of unit S to horizontal. After step C, the lower contact of unit S still has a synclinal shape, suggesting that underlying unit R was also folded.

as the general stratigraphy of the channel environment (Fig. 6.28). Five buried alluvial channels were identified in the subsurface, and range in age from historical (complete with rusted iron pipes and wire) to early Holocene. Channels were differentiated based on their stratigraphic position and composition. One channel (Q4) in the middle of the sequence contains abundant, distinctive tar clasts (a natural tar seep occurs just upstream) that allowed for a unique correlation across the fault. All channels were traced into and across the fault zone to resolve slip. Excavations close to the fault were carried out by hand to avoid obscuring important relationships.

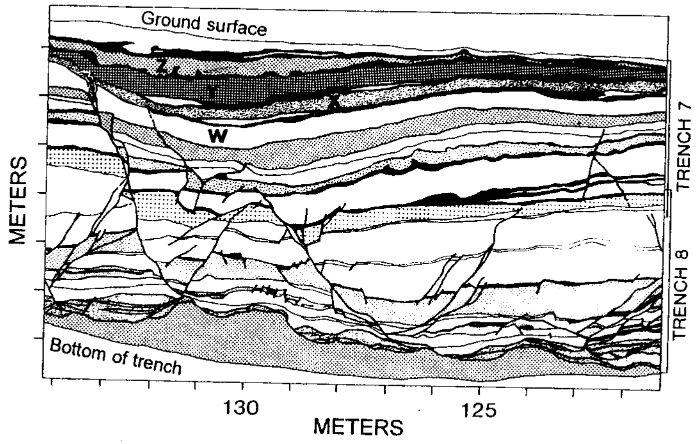

Figure 6-27. Log of stacked trenches 7 and 8 beneath a broad syncline, mapped in trenches 1, 4–9, 12, and 17. Black units are peats, other units are alluvium and debris flows. Patterns have no textural significance, but only serve to distinguish strata. The main structure is a normal-oblique fault (at left) that defines a broad syncline and half-graben tilted toward the fault. Units W and below predate folding, units X–Z postdate folding. Note the many subsidiary faults that die out upward and die out downward at different stratigraphic levels.

Channel Q4 was exposed in the initial trenches (T4, T17) with a trend at a high angle to the fault. We believed that channel Q4 would directly intercept the fault, and it would be a simple matter to measure its offset across the fault. However, as is clear in Fig. 6.28, the channel flowed along a paleoscarp within centimeters of the fault, and where the channel crossed the fault, only about 1.9 m of slip was resolved. If two trenches had been placed parallel to the fault, even as close as 1 m upstream and downstream from the fault zone, the channel would have been projected into the fault to estimate slip of nearly 20 m, an order of magnitude greater than the true displacement of the Q4 channel.

In a similar example Wesnousky *et al.* (1991) used the progressive excavation technique to log 39 consecutive face positions when tracing a subsurface channel that was misaligned 12 m across the San Jacinto fault, California. Their structure contour map drawn on the base of the buried channel identified three pairs of piercing points which yielded lateral offsets of 4.5, 4.2 ± 0.7, and 5.4 ± 0.6 m, respectively. Thus, only about half (ca. 5 m) of the 12 m of apparent right-lateral misalignment of the 2-ka channel can be attributed to faulting; the remainder was due to diversion of the stream parallel to the fault.

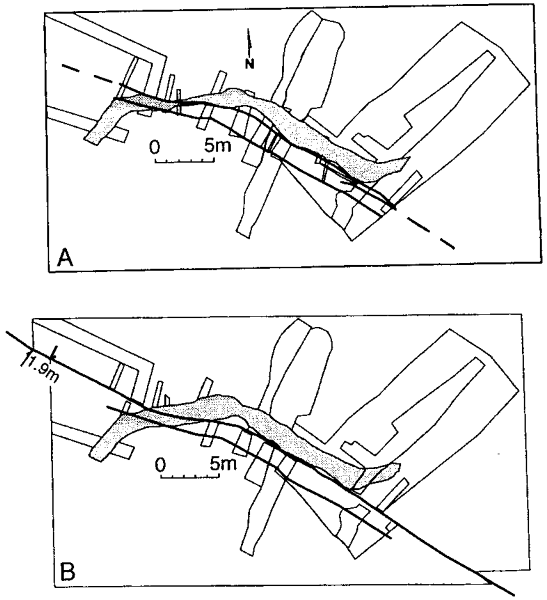

Figure 6-28. Plan view of faults (thick lines), buried channel Q4 (stippled pattern), and trenches (outlined by thin lines) across the Whittier fault, California. (A) Present geometry of the buried channel Q4. The channel is only offset at far left. (B) Restored geometry of buried channel Q4 before the latest fault displacement, based on channel margins as piercing points. Total restored slip is 1.9 m dextral.

This study is one of the most detailed published examples of the incremental trenching technique and is highly recommended to interested readers.

6.3.4.2 *Rose Canyon Example (Most of Misalignment Caused by Tectonic Offset)*

On the Rose Canyon fault (San Diego, California), most of the geomorphology associated with active faulting was destroyed by urban development in the 1960s. Based on predevelopment aerial photographs, the site of greatest potential for preserving the most recent offset now lay beneath a parking lot. Three borings were first conducted to determine the depth of artificial fill beneath the parking lot (about 2 m) and the depth to the water table (about 4.5 m), providing a 2.5-m unsaturated zone in which to trench (Lindvall and Rockwell, 1995).

After a locator trench (T1 on Fig. 6.29) determined the precise location and width of the fault zone and the general stratigraphy and age relations, two fault-parallel trenches (T2, T3) were emplaced about 5 m away from the fault to search for buried channels that could be traced into and across the fault. Only one distinct, gravel-filled channel was located east of the fault in trench 2. The trend of the channel was determined to be roughly perpendicular to the fault and was therefore a potentially useful slip indicator.

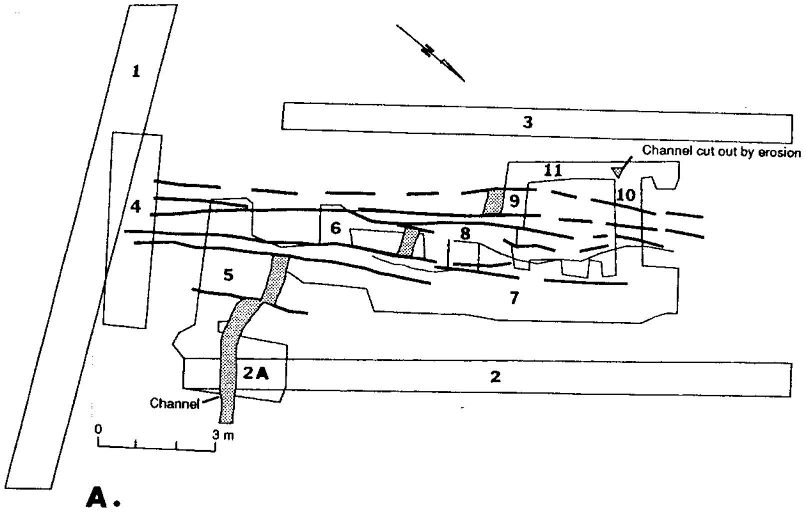

Figure 6-29. Plan view of trenches (thin lines), faults (thick lines), and buried channel (stippled pattern) across the Rose Canyon fault, San Diego, California. Trenches 1–3 were excavated from the surface of a parking lot, whereas trenches 4–11 were hand dug from the floor of a large excavation (not shown) that removed 2 m of artificial fill from beneath the parking lot.

The artificial fill was then removed to the top of the original ground surface. Because the channel was small, about 0.5 m across, all subsequent excavations were performed by hand to avoid destroying critical relationships; a photograph of the excavation is included as Fig. 6.30. The channel was sequentially exposed in numerous exposures into and through the fault zone (Fig. 6.29). All channel exposures as well as important stratigraphic horizons were surveyed as they were exposed to avoid loss of spatial data. The channel was preserved in each fault block in such a way that when the excavations were completed, geologists could walk through the excavations and see the displaced channel segments.

Figure 6.31 shows the inferred reconstruction across the many fault traces. Unfortunately, the stratigraphic unit containing the channel in the northwesternmost corner of the excavation had been graded out when the site was developed in 1960. Consequently, only a minimum slip was determined, and therefore a minimum slip rate was calculated. Nevertheless, it was shown in this case that the channel maintained a relatively straight course across the entire fault zone and true slip could be determined.

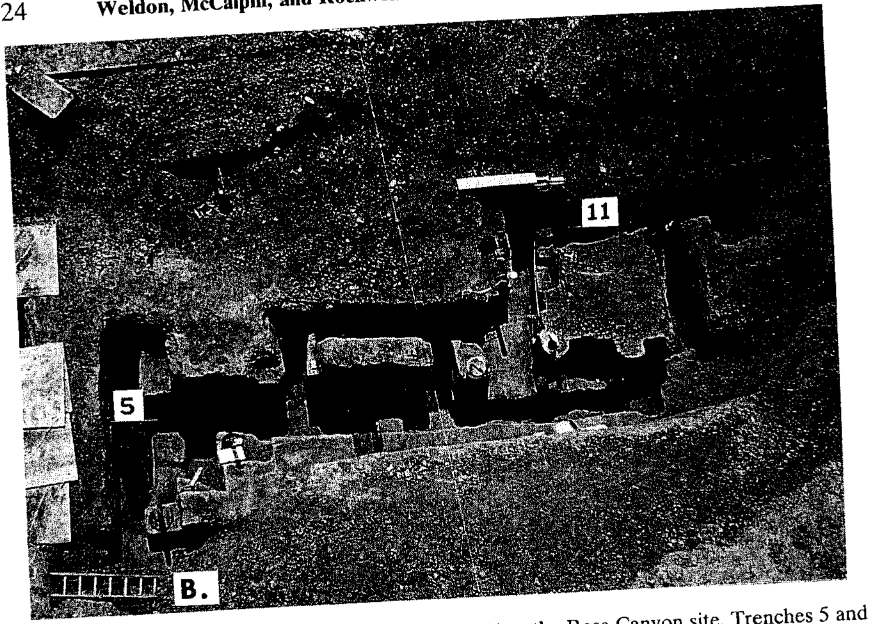

Figure 6-30. Vertical photograph of trenches 5-11 at the Rose Canyon site. Trenches 5 and 11 are labeled for reference. Note aluminum hydraulic shore (light-colored object above and left of "11") for scale; its total length is 2.8 m. North is to lower right corner. Note numerous benches within excavation. For further details, see Lindvall and Rockwell (1995).

The three field examples described emphasize the necessity to resolve completely the channel geometry into and across a fault in order to resolve slip, either for a slip rate or as an estimate of earthquake slip in discrete events. Projection of linear features only a few meters distant into the fault zone can produce substantial errors in slip estimation, if the geometry of the features within the fault zone itself is not known. The preceding examples required substantial amounts of field time to allow for careful tracing of linear features into the faults without their destruction or loss of data. This final point is brought forward because, in most cases, not all structural and stratigraphic relationships are immediately apparent during the early phases of a trench project and fault exposures may be logged without fully understanding them. It is recommended to proceed cautiously when laterally excavating a strike-slip fault because many relationships may be lost during the excavations. Trenching, by its very nature, is destructive. Many sites are unique along a particular section of a fault and there may be only one opportunity to collect the data. Careful work will require time, and the work is not complete until every stratigraphic unit and structural relationship is understood.

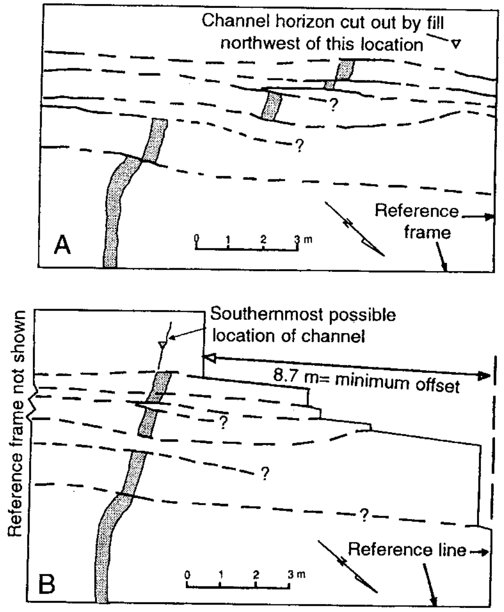

Figure 6-31. Retrodeformation of the buried channel across the multiple strands of the Rose Canyon fault. (A) Present configuration of the buried channel exposed by trenching. The open triangle represents the farthest position to the NW that the unit containing the channel is preserved. (B) Restoration of the channel by 8.7 m. This restoration assumes only brittle slip along five fault strands and therefore represents a minimum (dextral) offset. For further details, see Lindvall and Rickwell (1995).

6.4 DATING PALEOEARTHQUAKES

The usual approach to dating earthquakes (e.g., C. R. Allen, 1986) is to bracket the earthquake by dating the youngest datable stratum deformed by the quake and the oldest datable stratum that overlies the event horizon. In other cases, one attempts actually to date the event horizon, such as by shaving off the few millimeters of peat that formed immediately prior to or after the earthquake, and dating the samples very precisely (e.g., Sieh *et al.*, 1989).We have shown (Biasi and Weldon, 1994a) that neither of these techniques are optimal because they make little or no use of the information in the age of all the super- and subjacent horizons and are sensitive to potential contamination. We briefly describe here our approach for using more of the available data and apply it to an example of a strike-slip fault; however, the technique could be applied to paleoearthquakes on any type of structure.

The ^{14}C age of a carbon-bearing sample is an approximately Gaussian measurement in radiocarbon years before present. One converts ^{14}C age to a calendric date distribution using a dendrochronologic calibration (e.g. Stuiver

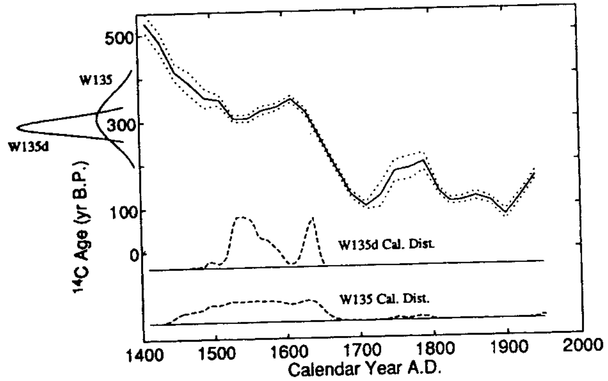

Figure 6-32. Relationship between calendar years (horizontal axis) and radiocarbon years (vertical axis) for the period A.D. 1400 to present, showing possible calendric ages for samples W135 and W135d (dashed lines at bottom) from the Wrightwood trench site. Solid line indicates mean age relation, dotted lines show 1σ confidence intervals. The W135 distribution of ^{14}C ages is based on standard counting, W135d distribution on extended counting. [From Biasi and Weldon (1994a); reprinted with permission of the University of Washington.]

and Reimer, 1993). For a given sample the only way to improve precision is to count ^{14}C decays for a longer period of time (or more atoms); however, the calibration often frustrates such attempts. As shown in Fig. 6.32, sample W135d is a high-precision ^{14}C sample but shows only limited improvement in calendric precision over the low-precision W135 sample. The width of the calendric distributions is controlled by the intersection of the ^{14}C age distribution with the calibration curve, so multiple intercepts yield wide, multipeaked distributions of calendar age. While one can often qualitatively argue for one peak or another (e.g., Sieh, *et al.,* 1989; Fumal *et al.,* 1993) the merit of these arguments is hard for others to assess and their uncertainties hard to quantify.

Our approach to solving this problem is best introduced by an analogy. If one rolls a fair die, there is an equal chance that the result will be any number between 1 and 6. If, however, the die is rolled twice, and we are told that the second roll is greater than the first, we would reconsider our estimate of each roll. Clearly the second roll cannot be 1, nor the first roll 6, because each would violate the knowledge that the second roll is greater. The additional knowledge means smaller numbers for the first roll and larger numbers for the second are more likely to have actually occurred. This intuitive process is formalized by Baye's theorem:

$$px\,(X1 \mid X2 < X1) = 1/C\, pX1(x)\, \mathrm{P}(x < X2), \qquad (6.5)$$

where $X1$ and $X2$ represent the random outcomes of rolls 1 and 2, $pX1(x)$ is the initial (prior) distribution (uniform from 1 to 6 inclusive), x is a particular number of spots, $P(x < X2)$ is the probability that $X2$ is larger than x, and C is found by summing the rightmost two terms over all possible x. Read from left to right, this equation states that our refined distribution of the first roll, given that the second must be greater, is proportional to our initial (prior) distribution of $X1$ times the likelihood that the second is larger than x. The exact result may be calculated by tabulating the 15 cases satisfying $X1 < X2$. This example can be translated into date refinement by asserting that the true age of a stratigraphic layer must be older than the layer that overlies it, and by viewing their calendar age histograms as prior probability distributions.

The dice analogy makes it easy to imagine extending this scheme to any number of layers. If there were six dice lined up on the table, and we were told that each one had a higher value than the previous, we would know exactly the value of each die (1, 2, 3, 4, 5, 6, in order) because no other combination allows the knowledge of their order to be true. In stratigraphic terms, this means that the more layers we know the "age" of, the more we know about each individual layer's age. In essence this is why a Bayesian analysis yields greater precision on the age of a single horizon than does repeated high-precision ^{14}C dating of that same horizon. In addition, the process is less susceptible to contamination or poor data near the event horizon, so more accurate results can be expected. One should date as many distinct layers as possible, whether or not they directly bound events, to refine the distributions bounding the event. Note, however, that this Bayesian approach only results in increased precision if the calendar age probability distributions overlap in a vertical sequence. For many sites the only datable material will yield ages many hundreds or thousands of calendar years apart. The multiple thin peat layers found at the Wrightwood and Pallett Creek sites on the San Andreas fault zone, for which this method was developed, are thus not representative of most trench sites, but finding such stratigraphy should obviously be a goal in trench siting.

To illustrate the Bayesian approach, we take an example from Pallett Creek (Sieh, 1978a, 1984; Sieh *et al.,* 1989; additional examples from Wrightwood and Pallett Creek, California, are found in Biasi and Weldon, 1994a, b). Figure 6.33 shows the youngest one-third of the stratigraphically ordered dating information at Pallett Creek; the dashed lines represent the output from dendro calibration (our prior distributions) and the solid show the posterior distributions, taking into account the calendric distributions and growth order of all super- and subjacent layers. One can immediately see that there is a substantial decrease in the variance; average variance reduction for the entire section was 59%. Note that in cases with two peaks, such as P88u and P68ll, the process essentially picks the peak that is consistent with all of the available information. Broad peaks, like P68u2 or P68l2, are "trimmed" by the constraints supplied by the more narrow overlying and underlying distributions.

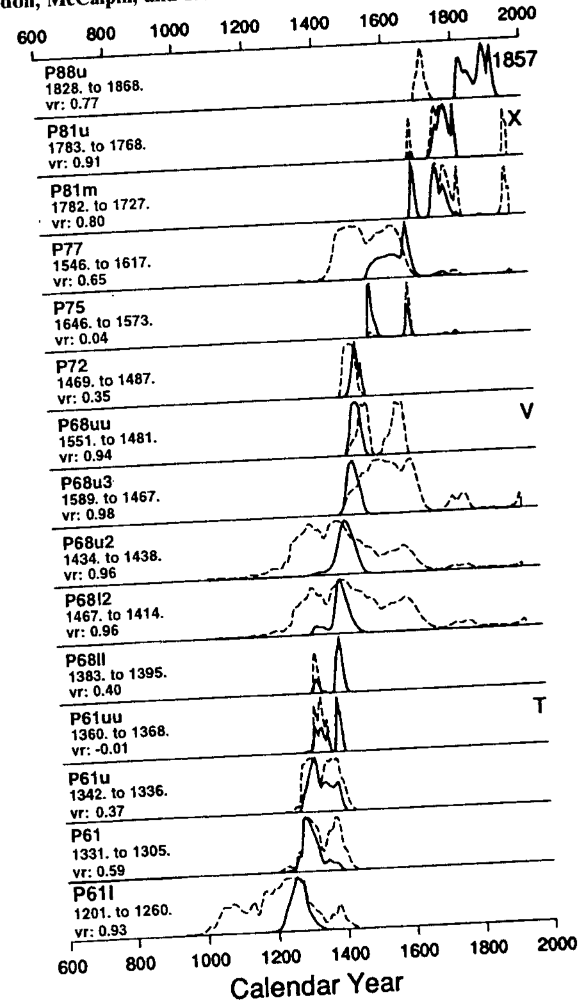

Figure 6-33. Calendar year age distributions of 16 upper dated units from the Pallett Creek site along the San Andreas fault zone. Dashed lines represent histograms of possible calendar years from dedro-corrected ^{14}C dates. Solid lines represent ages using the Bayesian technique (stratigraphic order and growth rate constraints) of Biasi and Weldon (1994a). [From Biasi and Weldon (1994a); reprinted with permission of the University of Washington.]

One may add information other than stratigraphic order, such as known growth or sedimentation rates. The solid lines of Fig. 6.33 reflect constraint by both ordering and by the amount of peat separating distinct units. At both Pallett Creek and Wrightwood peat grows at a reasonably constant rate of 0.054 to 0.057 cm/yr (Biasi and Weldon, 1994a); therefore, the samples separated by a significant thickness of peat must not only have formed in the correct stratigraphic order, but sufficient time must have passed in between to grow the peat. The formalization of ordering plus a minimum time separation can be found in Biasi and Weldon (1994a).

In some cases, such as P75, P72, and P68uu, the analysis generates peaks that are in very unlikely portions of the prior distributions. This suggests that one or more of the samples are inconsistent and are distorting nearby distributions. All three samples derive from high-precision ^{14}C age determinations by a leading laboratory, and P68uu and P72 were replicated, so analytic errors are not likely. We argue (Biasi and Weldon, 1994c) that sample P72 is the source of the inconsistency. This could be inferred from a stratigraphic plot (like Fig. 6.33), because the mean prior ages of P68uu and P72 are stratigraphically inverted by almost 100 years, and P75, which stratigraphically appears to have formed very soon after P72, has a mean prior age almost 200 years younger. Thus, the fact that P72 has been multiply dated at high precision does not preclude it from being out of formation order, probably because the peat incorporated older carbon. Further, as discussed in detail by Biasi and Weldon (1994c), removing P72 from the record changes the estimated age of event V, which it brackets, by more than 50 years, and significantly weakens the evidence for clustering of the events; so the implications of incorporating the age of even a single contaminated layer can be quite significant.

In addition to refined layer age estimates, the Bayesian approach yields probability distributions that can be used formally to yield an age range and uncertainty for earthquakes or the time intervals between them. If one arbitrarily picks a peak of the bounding layer date distribution (e.g., Sieh *et al.*, 1989; Fumal *et al.*, 1993), or chooses one date over another (e.g., Sieh *et al.*, 1989), one cannot formalize the resulting uncertainty because the uncertainty introduced by the reasonable inferences are unquantifiable. For further development of these concepts, see Biasi and Weldon (1994c). The key features of the layer, event, and interval distributions are that they follow from systematic and uniform treatment of all available data.

In summary, as increasing precision and formal estimates of uncertainty are required of paleoseismic studies, we must develop ways to formalize the information, such as stratigraphic superposition, that we instinctively apply in the field.One should not simply accept an analysis, such as a ^{14}C age, without incorporating all of the available information with it. From a ^{14}C sampling point of view, it is generally better to date another nearby layer (especially if its age distribution is likely to overlap that of the horizon of interest) than to date repeatedly or date with very high precision the horizon closest to the event horizon. Thus when a single piece of information lacks necessary precision, or can be misleading or in error, one must analyze suites of related data. Placing a date within its context, such as by dating and analyzing together many horizons, is the temporal equivalent of not interpreting a single trench relationship or geomorphic offset.

Chapter 7 Using Liquefaction-Induced Features for Paleoseismic Analysis

Stephen F. Obermeier

7.1 INTRODUCTION

This chapter focuses on the methodology for determining whether observed sediment deformation had a seismic shaking origin or a nonseismic origin. Emphasis is placed on the process of *liquefaction,* which is the transformation of a granular material from a solid state into a liquefied state as a consequence of increased *pore-water pressure* (Youd, 1973). The discussion encompasses various manifestations of liquefaction-induced deformation in fluvial and near-shore marine deposits, and the application of criteria for establishing an earthquake origin.

The systematic study of paleoliquefaction is a young discipline. Accordingly, some of the physical parameters that control effects of liquefaction in the field are not completely understood. Still, the principles and methodology for conducting paleoliquefaction studies are sufficiently advanced to warrant their routine application in paleoseismic studies. The method in this text for conducting paleoliquefaction studies was developed largely out of necessity in the United States, where the historic seismic record is particularly short.

Paleoliquefaction studies are useful to engineers and planners because of the *high shaking threshold* required to develop liquefaction features. The threshold is a horizontal acceleration on the order of 0.1 g for strong earthquakes, even in highly susceptible sediment (National Research Council, 1985, p. 34; Ishihara, 1985, p. 352). Worldwide data on historical earthquakes show that features having a liquefaction origin can be developed at earthquake magnitudes as low as about 5, but that a magnitude of about 5.5 to 6 is the lower limit at which liquefaction effects become relatively common (Ambraseys, 1988). (Earthquake magnitude, M, is used rather loosely as either moment magnitude or surface-wave magnitude, whichever is larger.)

Liquefaction has been severe and widespread in many worldwide earthquakes and has many manifestations. Some noteworthy reports discuss the effects in the region of the 1811–12 New Madrid, Missouri, earthquakes (Fuller, 1912); in the region of the 1886 Charleston, South Carolina, earthquake

(Dutton, 1889); in northern California (Youd and Hoose, 1978); in the vicinity of the 1964 Alaska earthquake (U. S. Geological Survey Professional Papers 542 through 545), various earthquakes in Japan (O'Rourke and Hamada, 1989) and Italy (Galli and Ferreli, 1995); and the earthquake of 1897 in India (Oldham, 1899). However, the deformational effects of liquefaction have rarely been illustrated and discussed in vertical section, the view most useful for paleoliquefaction studies and to which this chapter is devoted. Noteworthy accounts of the vertical view are reported by Sieh (1978a), Amick *et al.* (1990), Audemard and de Santis (1991), Tuttle and Seeber (1991), Clague *et al.* (1992), Wesnousky and Leffler (1992, 1994), Tuttle (1994), and Sims and Garvin (1995). Findings of exceptional interest in these reports are discussed herein where appropriate. The principal basis for this text is the author's observations of liquefaction effects at widely diverse geologic and geographic settings.

Seismic liquefaction effects described in this text are caused mainly by *cyclic shaking* of level or nearly level ground. Primary seismological factors contributing to liquefaction are the *amplitude of the cyclic shear stresses* and the *number of applications* of the shear stresses (Seed, 1979b). These factors, respectively, are related to field conditions of shaking amplitude (i.e., *peak acceleration*) and *duration* of strong shaking. Both peak acceleration and duration generally correlate with the earthquake magnitude. Analytical engineering methods for evaluating variable and irregular cyclic stress applications typical of real earthquakes are well developed and yield results acceptable for engineering analysis (Seed *et al.*, 1983), providing that shaking amplitude–time records can be reasonably bracketed. In this chapter there is also a brief discussion of how to set limits for the strength of prehistoric shaking.

Pseudonodules and other such features caused by the *plastic deformation* or *flowage* of very soft muds and freshly deposited cohesionless sediments (often referred to as *syndepositional features* or *soft-sediment deformations*) are discussed briefly. Liquefaction is not required to deform muds and extremely loose, freshly deposited cohesionless sediments, although a high pore-water pressure can be involved. The geologic literature is replete with articles attributing an earthquake origin to deformed muds and convoluted sands (see discussion by Lucchi, 1995). Keep in mind, however, that very weak sediments also are commonly deformed as a result of other geologic processes such as loading during rapid sedimentation, localized artesian conditions, or slumping. In addition, soft-sediment deformations often form at such low levels of seismic shaking that the shaking poses no hazard. Thus the usefulness of these features for hazard assessment normally is more limited, and interpretations of origin often are equivocal. Interpretation of the origin of suspected liquefaction features is usually much more straightforward and reliable than for soft-sediment deformations. Still, in field situations where it can be proven that the soft-sediment structures formed synchronously at widespread locations, an earthquake origin can sometimes be attributed.

This chapter also contains discussion of features formed by chemical weathering and of features deformed by a periglacial environment, which can mimic those of earthquake origin. Tests are suggested for interpretation of origin.

This chapter is intended primarily for geologists and to a lesser extent for engineers. Some few terms, though, are used in their geotechnical engineering context because of the lack of geologic equivalents for semiquantitative description of certain sediment properties. Most of these terms are given in Table 7-1, which relates the state of compactness (i.e., relative density) of sand to descriptors such as "very loose" to "very dense." In a similar sense, the term "clean" sand refers to a sand with no silt or clay, or any bonding matter. The term *liquefaction susceptibility* refers to the ease with which a saturated sediment liquefies and is described with qualifiers such as "very low" or "very high" (Youd and Perkins, 1978).

7.2 OVERVIEW OF THE FORMATION OF LIQUEFACTION-INDUCED FEATURES

It is the application of shear stresses that causes a buildup of pore-water pressure, which in turn leads to liquefaction of saturated *cohesionless sediment.* For seismically induced liquefaction, these shear stresses are due primarily to the upward propagation of *cyclic shear waves.* Cohesionless sediments that are loosely packed tend to become more compact when sheared. Continued cyclic shearing can cause the pore-water pressure to increase suddenly to the static confining pressure, leading to large strains and flowage of the water and sediment. No appreciable change in volume of the deposit is required for this change in state from a solid-like to a viscous, liquid-like material (i.e.,

Table 7-1

Relative Density of Sand as Related to Standard Penetration Test Blow Counts[a]

No. of blows	Relative density
0–4	Very loose
4–10	Loose
10–30	Medium or moderate
30–50	Dense
>50	Very dense

[a] From Terzaghi and Peck (1967).

liquefaction). The process is driven by breakdown of the packing arrangement of grains.

Liquefaction during earthquake shaking most commonly originates at a depth ranging from a few meters to about 10 m. Liquefaction takes place only where the sediment is completely saturated. The zone of liquefaction during shaking depends on the relationship between the cyclic shear stresses generated by the earthquake and the stress required to initiate liquefaction in the sediment (Fig. 7.1). Development of liquefaction is increasingly difficult with depth, because the higher static vertical effective stress (total overburden pressure minus pore-water pressure) applied by the overburden greatly increases the shearing and deformation resistance of sediment.

Sediment *vented* to the ground surface is the most conspicuous evidence of liquefaction at depth. Water from the zone of high pore-water pressure must escape upward to cause venting. A water–sediment mixture typically erupts suddenly and violently to the surface, through preexisting holes or through fractures opened in the capping material in response to liquefaction. In exceptional situations the mixture spouts as high as 6 to 7 m, especially where flow is concentrated into holes and cracks through an overlying *finer grained cap* (Dutton, 1889; Fuller, 1912; Housner, 1958). Water, sand, and silt can continue to flow to the surface as *sand volcanoes* for hours after earthquake shaking has stopped. Sediment is left behind on the ground surface in the form of cones, often called *sand blows* or *sand boils* (Fig. 7.2). The cones of sand can be as much as a meter in height and tens of meters in width.

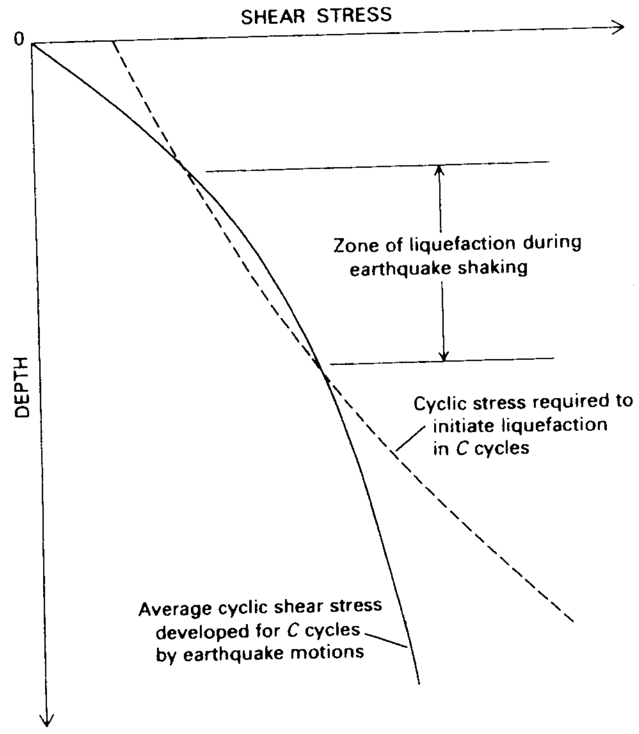

Figure 7.1 Schematic depiction illustrating location of the zone of liquefaction that is induced during earthquake shaking. *C*, number of shaking cycles. [From Seed and Idriss (1971); reprinted with permission of the American Society of Civil Engineers.]

The increased pore-water pressure during ground shaking can be manifested in other ways. The high pore-water pressure decreases the shear strength of granular strata at depth. These strata can then fail in shear even where the ground surface is inclined as gently as 0.1 to 5% (Youd, 1978; Youd and Bartlett, 1991). Huge masses of overlying soil can shift horizontally in the form of laterally moving landslides (called *lateral spreads;* Fig. 7.3). Separation between individual blocks is commonly as much as 2 to 3 m where shaking has been especially strong. This separation tends to be largest near stream banks or scarps in alluvium, even if only a few meters in height, because these breaks in slope are where there is less resistance to lateral movements. Figure 7.4 illustrates a variation of lateral spreading that takes place on level ground far from breaks in slope. Here, oscillation of the ground above the liquefied zone forms blocks separated by fissures.

Liquefaction of granular deposits normally leads to surface cracking and formation of localized depressions because of densification of liquefied sedi-

Figure 7.2 Small sand blows near the town of El Centro from the 1979 Imperial Valley, California, earthquake. The sand blows were produced by a mixture of sand and water that spouted to the surface; they provide evidence of extensive liquefaction at depth. White scale in foreground is 20 cm long. (Photograph courtesy of R. F. Scott.)

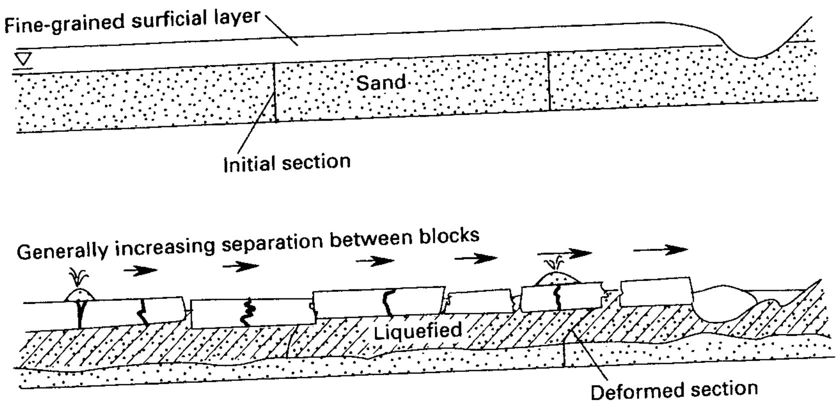

Figure 7.3 Vertical section of lateral spread before and after failure. Liquefaction occurs in the cross-hatched zone. The surface layer then moves laterally down the gentle slope, breaking into blocks bounded by fissures. Sand is vented to the surface through some fissures, but other fissures are only partly filled. The blocks can tilt and settle differentially with respect to one another. (From Youd, 1984a.)

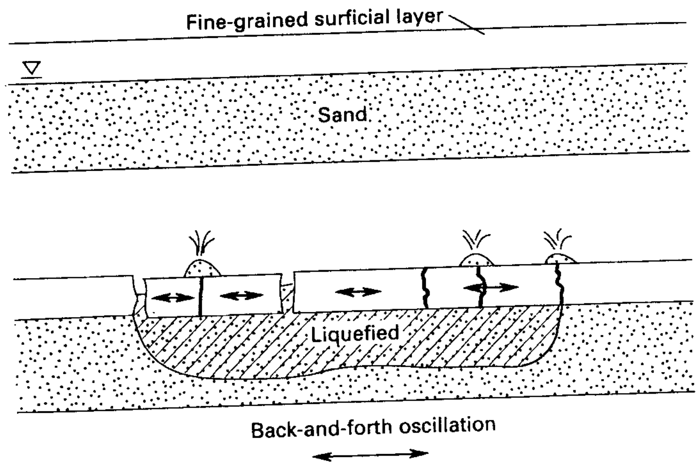

Figure 7.4 Vertical section showing fissures and blocks resulting from oscillation of level ground far from breaks in slope (figure from Youd, 1984a). Ground oscillation can result from fundamentally different mechanisms driven by surface waves (Youd, 1984a) or body waves (Pease and O'Rourke, 1995). In the mechanism driven by surface waves, liquefaction in the zone marked by diagonal lines decouples the surface layer from the underlying liquefied layer. The decoupled layer vibrates at a different frequency than the underlying liquefied layer; as a result, fissures form between oscillating blocks. In the mechanism driven by body waves, ground oscillation becomes severe in response to a resonant frequency effect in which horizontal displacement in the cap is amplified with respect to that of the underlying liquefied sand.

ment after expulsion of water, even where there is no evidence of venting of sand and water to the surface. These settlements can be as much as 0.25 to 0.5 m where thick sands liquefy severely (Tokimatsu and Seed, 1987).

On slopes that exceed about 5%, severely liquefied sediments can cause huge landslides (sometimes called *flow failures*) that can flow as much as tens to hundreds of meters (Seed, 1968). Ground disruption can be so severe that it is difficult to establish what the surface geometry was prior to failure (Chapter 8). Strength properties of materials in the failure zone can be changed greatly. Flow failures along banks of streams and hillsides can also originate by static (nonearthquake) mechanisms, however. Determination that prehistoric landslide movement on a steep slope was seismically triggered generally requires complex engineering testing and analysis difficult to perform in the best of circumstances, irrespective of whether liquefaction was involved (Chapter 8). Therefore, sites on level ground are best for distinguishing a seismic from a nonseismic origin.

Clastic dikes on level to nearly level ground are the primary source of data used for paleoseismic interpretations. Very important factors controlling the development and density of dikes include not only the compactness and thickness of sediment that liquefied but also cap thickness. Such dikes almost certainly form solely in response to *hydraulic fracturing* of the cap in a great many field situations, but dike development can be enhanced greatly by the cap simply being *pulled apart in tension at sites of lateral spreading as well as by strong oscillatory shaking at the surface.*

7.2.1 Process of Liquefaction and Fluidization

The process of seismically induced liquefaction of saturated granular sediments has been studied extensively and is reasonably well understood (Seed, 1979b; National Research Council, 1985; Castro, 1987; Dobry, 1989). Figure 7.5 illustrates the typical field situation on level ground. A liquefiable sand layer is overlain by a thin, nonliquefiable stratum, and the groundwater table is shallow. Earthquake-induced shear stresses propagate through the sand and cause shear strain of the sediment structure. (Shear strain is the angle in radians, γ, shown in Fig. 7.5.) Because grains attempt to move into a denser packing arrangement relatively quickly during back-and-forth shear straining, water in the voids does not have time to escape. The pore-water pressure can thereby increase. In loose deposits, stresses at the grain contacts can approach zero, and concurrently the pore-water pressure carries the weight of the overburden. The first time this occurs is often referred to as *initial liquefaction* (National Research Council, 1985, p. 42). A large loss of strength can take place once this condition is reached. In very loosely packed sand, the strain can increase suddenly, and blocks on slopes can move large distances. The combination of elevated pore pressure with large loss of strength is sometimes referred to

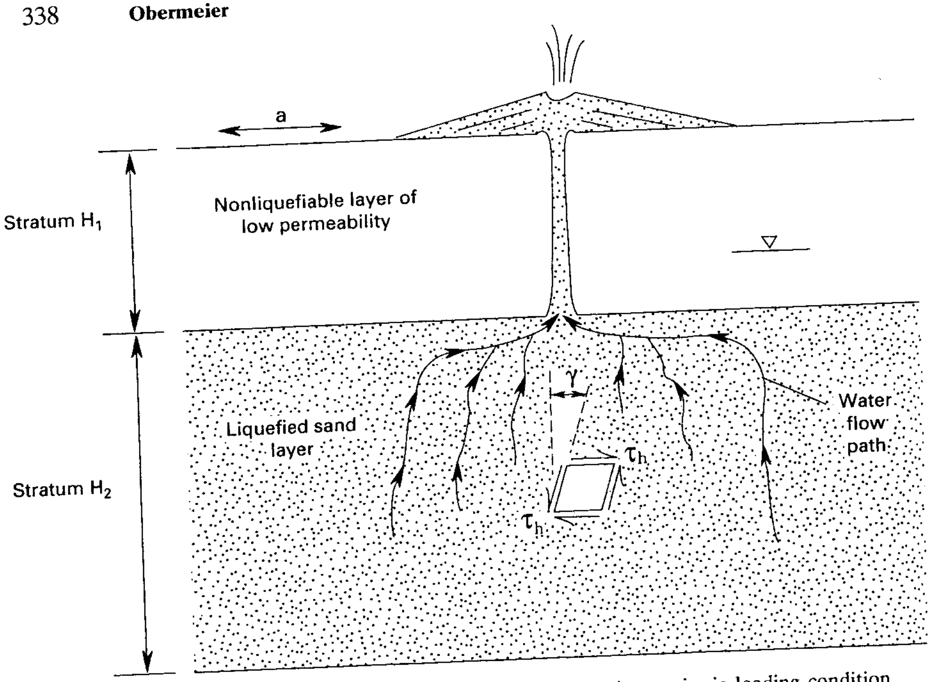

Figure 7.5 Vertical section showing typical sediment relations, seismic loading condition, and water flow paths involved in formation of sand blows; γ, shear strain (angle in radians); a, horizontal acceleration; τ_h, shear stress induced by horizontal acceleration.

as *complete liquefaction* (Youd, 1973). In more densely packed sand the pore pressure rise is less sudden, and the strength loss is less severe; thus, any increase in strain is less dramatic and is limited. Very densely packed sands may not develop pore-water pressures high enough to cause liquefaction. For the purpose of this text, the condition of highly elevated pore-water pressure with a significant loss of strength is referred to simply as "liquefaction." When the term "initial liquefaction" is used, emphasis is on the elevated pore-water pressure rather than loss of strength.

The cyclic strain in sands that is required to induce liquefaction is usually very small. Ten cycles of back-and-forth shearing generally suffice if the shear strain exceeds 0.3%. For earthquakes having long durations and many cycles, the *critical shear strain* can be as low as 0.04% (Dobry, 1989). Following liquefaction, *densification* can occur after water is expelled from the sediment. The vertical settlement caused by sediment densification often is quite small, being less than 2 to 3% of the height of the stratum that liquefied (Castro, 1987, p. 175).

Only minor disturbance to original stratification may take place in that portion of the stratum where only initial liquefaction has occurred. The effects to bedding are often virtually indistinguishable to the unaided eye. Closer inspection may show that platy minerals such as mica and clay are reoriented from their original flat-lying position (and can form structures known as *dishes,* shown later in Fig. 7.24), and thin laminations of finest constituents are warped. Small, steeply inclined, flame-like sand-rich structures known as *pillars* (see Fig. 7.24) can form where water collects beneath a slightly less permeable lamina and then locally penetrates through the lamina to winnow out silt and other very fine constituents. This winnowing takes place by a process often referred to as *fluidization.*

Fluidization occurs when flowing water exerts sufficient drag or lift to momentarily suspend grains of sediment. When a fluid is forced vertically through a layer of cohesionless sediment at a rate sufficient to cause fluidization, the layer expands rapidly, porosity increases, and the sediment ceases to be grain supported and becomes fluid supported. Fluidized flow typically destroys original bedding and structures, at least locally. Fluidization can result from a number of mechanisms, including seepage caused by compaction of underlying sediments, seepage from springs, or seepage from deposits liquefied either from static or earthquake forces (Sec. 7.5).

Reoriented minerals and small deformation structures similar to those caused by liquefaction-induced fluidization occur as syndepositional features in many environments (e.g., Lowe and LoPiccolo, 1974; Lowe, 1975; van Loon, 1992), which makes interpretation of a seismic or nonseismic origin uncertain. In contrast, larger features caused by fluidization from seismic liquefaction are easier to interpret because, in many field situations, sand-filled dikes whose widths exceed several centimeters and whose heights exceed a meter or so cut weathering horizons or other strata that are obviously much younger than the source zone for the dikes. This relation generally eliminates syndepositional processes from the list of possible causes for formation of the dikes.

Many variables control the formation of large fluidization features caused by seismic liquefaction. The influence of some of the most important variables is fairly well understood. The main elements are illustrated in Fig. 7.5. Assume stratum H_2 liquefies. Water tends to flow upward by two mechanisms, relief of the high pore-water pressure and reconsolidation. Reconsolidation tends to cause densification as it progresses from the bottom of stratum H_2 upward (Scott and Zuckerman, 1973; Scott, 1986). Water expelled from the zone that liquefied during shaking tends to accumulate beneath a low-permeability capping layer to form a *water-rich zone* (Liu and Qiao, 1984; Elgamal *et al.,* 1989; Fiegel and Kutter, 1994); this zone in turn probably supplies much of the water and sand that vents to the surface through breaks in the cap. Sediment may also be vented to the surface from greater depth, where liquefaction first developed. Venting can occur during the time of strong shaking or be delayed by as much as a few minutes following very strong shaking (Kawakami and Asada, 1966). Where the cap is thin (<1 to 2 m) is where the increased pore-water pressure in the underlying sand–water mixture can most easily break through to the surface. Characteristics of the lower layer that enhance the liquefaction-fluidization process are (1) a thick, loose sand that, once liquefied, provides a large volume of water available for upward flow, and (2) a permeability that is high enough to allow water to flow quickly to the base of the cap but that is not so high as to dissipate excess pore pressures between seismic cycles of shearing (Castro, 1987, pp.177–179; Dobry, 1989). This simple model fully explains most field observations. However, seemingly contradictory and unexplained manifestations of the liquefaction and fluidization process also are encountered in the field. For example, sand dikes cutting gravel layers much more permeable than the sand dikes have been reported by Tuttle *et al.* (1992).

7.2.2 Factors Affecting Liquefaction Susceptibility and Effects of Fluidization

The most important factors controlling development of dikes and sills are (1) grain size, (2) relative density (i.e., degree of compactness), (3) depth and thickness of strata, (4) age of sediments, (5) characteristics of the fine-grained cap, (6) topography and nature of seismic shaking, (7) depth to water table, and (8) seismic history. The following discussion is condensed from Obermeier (1994b). Not discussed here are secondary factors affecting liquefaction susceptibility such as grain shape, sediment fabric, weak grain-to-grain bonding in sediment, and static horizontal stress conditions; those factors are summarized in articles by Seed (1979b) and Mitchell (1976, p. 244).

Liquefaction-induced features often form readily in sand and silty sand. Even though large liquefaction-induced dikes have been documented in gravel (Andrus *et al.*, 1991; Meier, 1993), the threshold magnitude ($M \sim 7$) is much higher than for sand (Valera *et al.*, 1994). Exceptionally loose silt deposits can form sizable sand blows (Youd *et al.*, 1989), but a small amount of clay greatly diminishes the ability of sediment to liquefy and flow. Liquefaction is unusual in sediments containing more than 15% clay (Seed *et al.*, 1983). Criteria for evaluating liquefaction of clay-bearing sediments are given in Finn *et al.* (1994).

The state of *relative density* of cohesionless sediment has a very large influence on liquefaction and flow. Materials of low to moderate relative density (Table 7-1 shows the commonly used engineering measure) are most susceptible to liquefaction. Susceptible sediments are usually late- to mid-Holocene in age (Youd and Perkins, 1978), although sediments as old as 200,000 to 240,000 yr B.P. have liquefied (Obermeier *et al.*, 1990).

Liquefaction generally originates in strata located a few meters to 10 m beneath the surface, but reported depths range from a few tenths of a meter (Sims, 1973; Audemard and de Santis, 1991) to greater than 20 m (Seed, 1979b). Susceptible beds are usually ≥0.3 to 1.0 m in thickness, but Tuttle and Seeber (1991) describe an 8- to 10-cm-thick sand bed that liquefied and formed a dike exceeding 2.5 m in height. Whether sand vents to the surface is normally determined by the ratio of cap thickness (H_2 in Fig. 7.5) to thickness of the source stratum (H_1 in Fig. 7.5; see Ishihara, 1985). Dikes generally do not extend to the surface when the cap thickness exceeds 10 m and often are severely restricted for thicknesses of more than 5 m. Dikes also may not cut to the surface where roots have greatly enhanced the tensile strength of the cap; here, *sills* can form abundantly beneath the root mat (Clague *et al.*, 1992; Obermeier, 1994b).

Effects of seismic shaking typically are topographically amplified near abrupt relief such as stream banks, leading to greatly increased ground breakage with venting (Fuller, 1912; McCulloch and Bonilla, 1970). Still, far from any topographic declivities, dikes can form in response to very strong surface oscillations (T. L. Youd, Brigham Young University, Provo, UT, written communication, 1994).

Liquefaction susceptibility is influenced strongly by depth to the water table. For example, increasing the depth from the surface to 5 m or less commonly reduces susceptibility from high to moderate, and increasing the depth to 10 m reduces susceptibility to nil.

The seismic history of sediment can influence its ability to reliquefy during earthquakes many years later. An occurrence of severe liquefaction can cause significant densification of source sediment (Castro, 1987), except possibly within a thin zone just beneath a fine-grained cap. This thin, loose zone is thought to form by water and sediment flowing up from the liquefied zone (Elgamal *et al.*, 1989; Dobry and Liu, 1992). In subsequent earthquakes, severity of liquefaction may be diminished because of densification of most of the source stratum. Worldwide observations show, though, that liquefaction from widely timed earthquakes commonly recurs at the same site even to the extent of using the same dike for venting (Kuribayashi and Tatsuoka, 1975; Youd and Hoose, 1978; Youd, 1984b; Obermeier *et al.*, 1990; Tuttle *et al.*, 1992).

Field observations of the influence of the preceding factors are discussed throughout this chapter, as case history examples.

7.3 CRITERIA FOR AN EARTHQUAKE-INDUCED LIQUEFACTION ORIGIN

The following set of criteria can establish whether observed sediment deformation was caused by seismically induced liquefaction:

1. The features have sedimentary characteristics that are consistent with an earthquake-induced liquefaction origin; namely, there is evidence of an

upward-directed hydraulic force that was suddenly applied and was of short duration.

2. The features preferably have sedimentary characteristics consistent with historically documented observations of the earthquake-induced liquefaction processes, in a similar physical setting. In addition, preferably there is more than one type of feature commonly caused by seismically induced liquefaction. Such features include dikes, sills, vented sediment, lateral spreads, and some types of soft-sediment deformations.

3. The features occur in ground water settings where suddenly applied, strong hydraulic forces of short duration could not be reasonably expected except from earthquake-induced liquefaction. In particular, the possibility of an origin from artesian conditions or nonseismic landsliding must be ruled out.

4. Similar features occur at multiple locations, preferably at least within a few kilometers of one another, in similar geologic and ground water settings. The regional pattern of size and abundance of features should be consistent with a pattern of shaking associated with an earthquake.

5. The evidence for age of the features supports the interpretation that they formed in one or more discrete, short episodes that individually affected a large area and that the episodes were separated by relatively long time periods during which no such features formed.

Determination of the regional pattern of size and abundance of the suspected liquefaction features may be critical to interpretation of origin. Preferably at least 20 to 30 km of cumulative fresh exposure is examined. Such a regional approach to a paleoliquefaction study helps eliminate the possibility that nonseismic processes (Sec. 7.5) are responsible for creating the features, and it helps to develop a sense of the various processes that deform sediments. The next section illustrates application of the five criteria and presents examples of how an understanding of the local geologic setting is critical to interpretations.

7.4 HISTORIC AND PREHISTORIC LIQUEFACTION—SELECTED STUDIES

In this section, I describe earthquake-induced liquefaction features in four geologic–geographic settings: coastal South Carolina, the New Madrid seismic zone of Missouri, the Wabash Valley seismic zone of Indiana and Illinois, and coastal Washington State (all in the United States). The two latter areas have not had historic liquefaction. The discussion emphasizes the role of the local geologic setting in deducing an earthquake origin. Special consideration is given to elimination of artesian springs and nonseismic landsliding as possible sources of observed deformations. Where possible, the magnitudes of the prehistoric earthquakes are estimated by comparison with historical liquefaction-producing earthquakes in the region.

7.4.1 Coastal South Carolina

The strongest historical earthquake in the southeastern United States took place in 1886 near Charleston, South Carolina [moment magnitude about 7.5 (Johnston, 1994)]. Clear evidence of seismotectonic conditions in the region is lacking, which prompted searches for prehistoric liquefaction features. Liquefaction evidence has since been found for many strong prehistoric earthquakes (Obermeier *et al.,* 1987; Amick *et al.,* 1990). Results of the searches are shown in Fig. 7.6. The figure shows the approximate boundary of the 1886 earthquake meisoseismal zone, shows the sites where in 1886 swarms of liquefaction features described as *craterlets* were formed (Dutton, 1889; see Fig. 7.7), and shows the sites where liquefaction features predating 1886 were found. The prehistoric liquefaction-induced features are mainly ancient craterlets that are now filled.

None of the pre-1886 *craters* found has an expression on the ground surface that is discernible by on-site surface examination or on aerial photographs. These features are seen only in walls of excavations. At most sites shown on Fig. 7.6, at least three or four pre-1886 craters are exposed within a few hundred meters of one another.

The physical setting of the region within 50 km of the South Carolina coast is conducive to widespread liquefaction. That region is known locally as the "low country" because it has low local relief (1 to 3 m) and low elevation (0 to 30 m), and because vast expanses are under water much of the year. Most of the Carolina low country is covered by a 5- to 15-m-thick blanket of unconsolidated Quaternary marine and fluvial deposits, which lies on semilithified Tertiary sediment. The Quaternary deposits primarily occur as a series of well-defined, temporally discrete, interglacial beaches and associated back-barrier and shelf deposits that form belts subparallel to the present shoreline. Increasingly older beach deposits are progressively farther inland and at higher altitudes. Most beach deposits consist of clean, medium- to fine-grained sand.

Most of the craters discovered were on the ancient beach deposits. The search for liquefaction features was generally restricted to the beach deposits younger than about 250,000 years and older than about 80,000 years (Fig. 7.6). Sand in these deposits is loose at many places. Normal depth to the ground water table in these sediments is about 1 to 2 m, even in topographically elevated regions. Deposits older than about 250,000 years have such a low susceptibility to liquefaction (due to effects of chemical weathering) that the likelihood of their liquefying has been extremely low during the late Pleistocene and Holocene. Deposits younger than about 80,000 years generally have such a high ground water table that exposures are very limited.

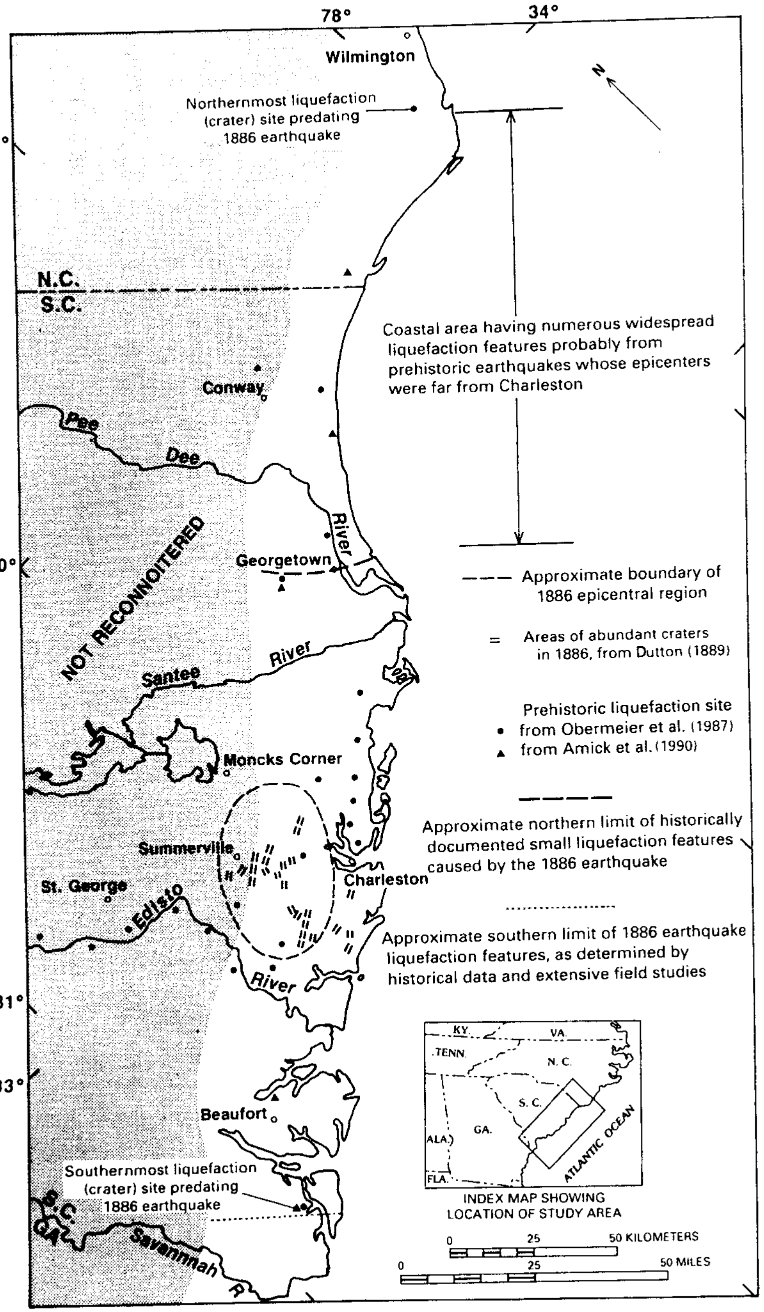

Tabular sand dikes were discovered in fluvial terraces and in back-barrier environments where the cap is much richer in clay. Sills were observed only rarely. The following discussion concentrates on the craters, because the section below discussing liquefaction effects in the New Madrid seismic zone adequately deals with characteristics of tabular sand dikes and sills, which are the types of liquefaction-induced features most often encountered where there is a thick clay-rich cap.

7.4.1.1 Characterization of Craters

Figure 7.8 is a schematic cross section through a typical crater site on a beach ridge. According to eyewitness observations in 1886, "craterlets are found in greatest abundance in belts parallel with (beach) ridges and along their anticlines" (Peters and Herrmann, 1986). Thus the locations of crater sites we discovered are consistent with historical observations.

Almost all craters that predate 1886 have a morphology and size comparable to the 1886 craters of Fig. 7.7 except that the craters are now filled with sediment. Figure 7.7 shows moderate to large craters produced by the 1886 earthquake. Examination of photographs taken in 1886 shows that surficial sheets of vented sand around crater rims normally had thicknesses of about 15 to 20 cm. The maximum reported thickness of vented sand was 1 m, and the maximum crater diameter was about 6 m (Dutton, 1889).

The crater sites are located where weathering has imposed a strong soil profile on the ancient beaches (Fig. 7.9). Near the surface, a thin A horizon (organic matter and several percent sand) overlies a thin very light gray E (eluviated) horizon; the E horizon overlies a thick, weakly cemented, black Bh horizon (humate-enriched sand containing a few percent clay) that grades down rather sharply into a variably thick, light-colored B–C horizon (transition zone between B and C horizons). The B–C unit grades down into C horizon sands (parent material). The craters cut the solum and the C horizon. Within the filled crater are well-defined zones of sediment. The fill materials are fine- to medium-grained sand and clasts from the Bh, B–C, and C horizons of the host, and there is sand from depths much below the exposed C horizon. The walls of the crater are commonly smooth and sharply defined when viewed closely, especially in the lower part.

Figure 7.6 Coastal portion of South and North Carolina containing liquefaction sites. Unshaded onshore region is predominantly marine deposits younger than about 240,000 years. Numerous ancient beach ridges lie in this unshaded region. Shading denotes region of older marine deposits that was not reconnoitered, except locally. Younger fluvial sediments occur locally. All liquefaction sites along the Edisto River are in fluvial sediments. Almost every liquefaction site shown represents an area where numerous liquefaction features are exposed in a network of drainage ditches several kilometers in length. Index map shows coastal region searched.

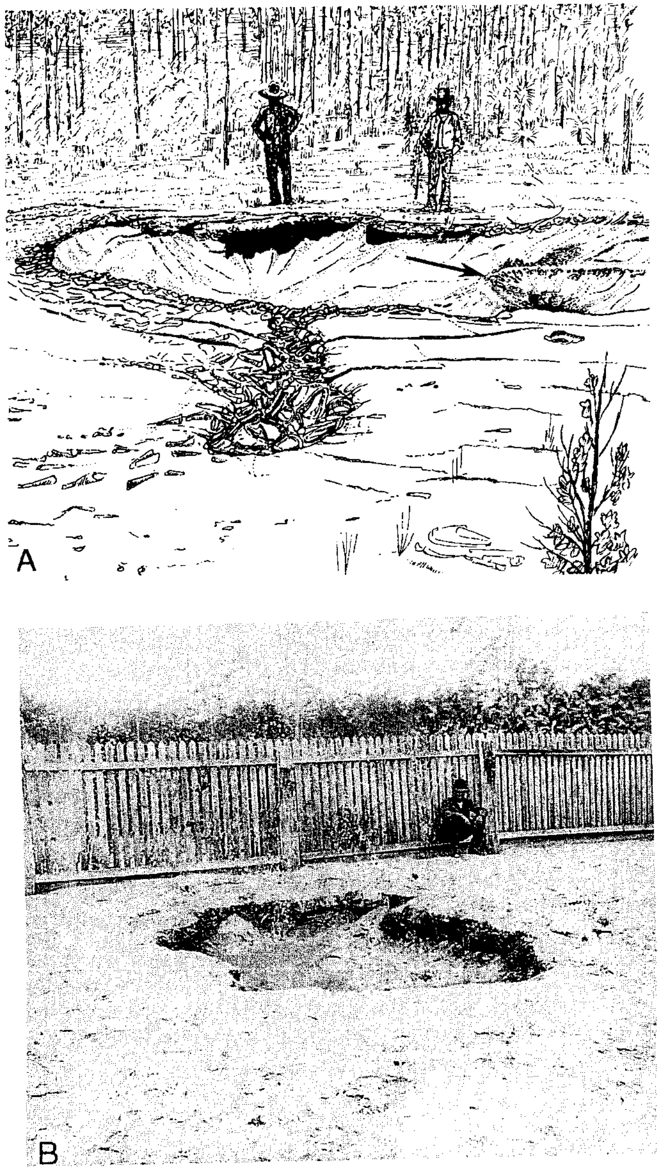

Figure 7.7 Craters produced by the 1886 Charleston, South Carolina, earthquake. (A) Sketch from a photograph of an 1886 crater (sand blow at Ten Mile Hill, near the present Charleston airport). Note that the crater contains sand sloughing toward the lowest parts and that there is a constructional sand volcano located in the right part of the crater (at arrow). The crater is surrounded by a thin blanket of sand partly veneered with cracked mud. (B) Photograph of typical crater produced by the 1886 earthquake. Note the thin blanket of ejected sand around the crater and sand and clasts of dark soil within the crater. (Photograph from the archives of the Charleston Museum.)

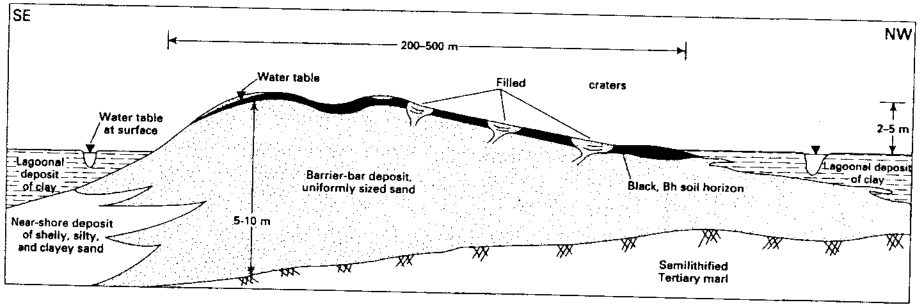

Figure 7.8 Schematic vertical section of representative barrier showing sediment types, groundwater table locations, filled craters, and Bh (humate-rich) soil horizons. Modern shoreline is located southeastward. Lagoonal clay deposit at left is younger and lower in elevation than the barrier-bar deposit.

The Bh horizon of the laterally adjoining undisturbed host generally is abruptly thicker than the Bh horizon on the filling in the crater. With increasing age, the Bh horizon of the filled crater is thicker, more clay rich, and has better developed soil structure. Craters older than about 5000 years have Bh

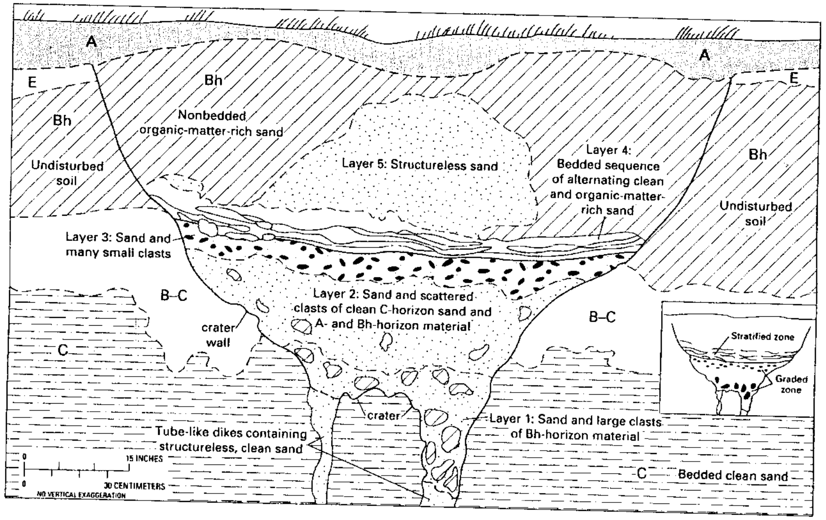

Figure 7.9 Schematic vertical section of filled liquefaction crater that forms a bowl in three dimensions. Letters correspond to soil horizons. The filled crater in this figure long predates the 1886 Charleston earthquake, on the basis of thickness of Bh horizon in the filled crater. Inset shows zonation within the crater.

horizons that approach having the thickness and development in host sediment enclosing the craters.

The filled craters are characterized by a *sequence* of five layers. Layer 5 (Fig. 7.9) is a structureless, gray, humate-enriched and cemented sand, which overlies a thinly (2- to 3-mm) laminated sequence of alternating light- and dark-colored sands (layer 4). The lamina typically are discontinuous and irregular in thickness. The dark color is due to humate staining. The basal bed sharply overlies a medium-gray structureless sand (layer 3), which contains many small clasts of Bh material and wood. Layer 3 grades down into a structureless sand zone (layer 2) containing many intermediate-sized clasts (1 to 5 cm in diameter). Layer 2 grades down into layer 1, which contains densely packed intermediate-sized (1- to 5-cm) and large-sized (>5-cm) clasts of Bh material in a structureless sand matrix; the large clasts have diameters exceeding 25 cm in many filled craters. Beneath the bowl are dikes containing clean sand. The dikes are tube-like in plan view.

The filled craters are interpreted to have formed in the following phases: (1) A large hole is excavated at the surface by the violent upward discharge of the liquefied mixture of sand and water; (2) a sand rim accumulates around the hole by continued expulsion of liquefied sand and water; (3) sand, soil clasts, and water are churned briefly in the lower part of the bowl, followed by settling of the larger clasts and formation of the graded-fill sequence of sediment (layers 1-3); and (4) the crater is intermittently filled by adjacent surface materials to form the thin stratified-fill sequence (layer 4) during the weeks to years after the eruption. Layer 5 is in the strongly bioturbated zone and thus has no stratification. The sand blanket ejected from the crater is indistinguishable in the field from the surface and near-surface (A, E, and Bh) soil horizons, because the blanket has been incorporated within these soil horizons.

The presence of friable, angular clasts of B–C, C, and Bh horizon material in the graded-fill portion (layers 1–3) is consistent with a short-lived, churning type of upwelling from the vent. Water commonly flows for a day or so from vents, on the basis of worldwide observations. The violent, boiling phase is much shorter in duration. Hence, the presence of friable clasts argues against a long-term artesian spring origin; such a spring would abrade, round, and disaggregate the clasts. In addition, springs are very unlikely to form in the topographic-geologic setting at some of the crater sites (Fig. 7.8).

An earthquake origin for the craters is also supported by the presence of sand-filled tabular fissures, whose overall shape and dimensions strongly suggest that they are *incipient craters.* Fissures such as those shown in Fig. 7.10 are rather common in the epicentral zone of the 1886 earthquake. The figure shows a V-shaped fissure connecting to a tube-like dike with sand transported upward from depth. The tabular fissures in the V-portion widen with depth until they connect to a single, near-vertical, large, sand-filled tube. The V-shaped fissures probably represent the early phase of development of craters; upward forces, however, were too weak to excavate the overlying material.

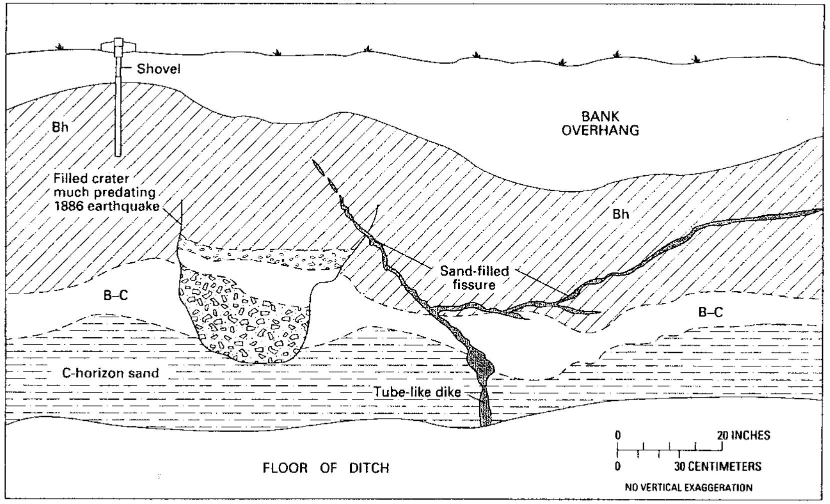

Figure 7.10 Schematic vertical section showing V-shaped, sand-filled fissures interpreted as resulting from liquefaction during the 1886 Charleston earthquake. Sand in the fissures came from a depth of 6 m, on the basis of grain size and mineralogy. Fissure cuts soil horizon developed on filled crater predating 1886.

It is possible that liquefaction produced craters because of a fortuitous combination of sediment properties. The source beds that liquefied were exceptionally susceptible to liquefaction; they are loose (engineering sense), fine-grained, uniformly sized, and free of clay (Martin and Clough, 1990). These properties would cause the source beds to liquefy abruptly and, once liquefied, the sand–water mixture would flow readily. I suspect that the liquefied sand strata quickly migrated laterally to a hole such as that left by a decayed root. The sudden application of an upward force around the hole caused the formation of a V-shaped crack. The liquefied sand violently vented because of its exceptional ability to flow. The V-shaped cracks developed because overlying sediment is isotropically cemented with humate, has no pronounced planes of weakness, and is very brittle; the process is similar to formation of a conchoidal fracture in an isotropic, brittle medium such as glass, when struck by a rock.

Liquefaction-induced craters are common during earthquakes worldwide. Good examples for various earthquakes in Japan are shown in articles by Kawakami and Asada (1966) and by Iwasaki (1986). Craters were especially prevalent during the M 7.5 Niigata earthquake of 1964; soils around Niigata typically are sand rich all the way to the ground surface (Katayama *et al.*, 1966), much as for the Charleston crater region. For the northeastern United States, sketches of prehistoric seismically induced craters in host sand deposits are to be found in Tuttle (1994).

Craters can also form in a clay-rich cap. In Alaska during the great earthquake of 1964, craters having a relatively small diameter (many ~1 m) formed at sites of violent venting, which apparently eroded deep holes (the craters) through a clay-rich cap; some "craters" (actually surface depressions) as much as 10 m in diameter and extremely shallow (25 to 40 cm) also formed (Reimnitz and Marshall, 1965). These very large "craters" apparently formed as sand vented to the surface and undermined a clay-rich cap, thereby making a swale. In Argentina, Youd and Keefer (1994, pp. 227–229) have shown that preexisting holes through a clay-rich cap later led to erosion of large craters in response to liquefaction during a M 7.4 earthquake. Craters also formed in a clay-rich cap in the Nile River Valley during the M 5.9 Dahshure, Egypt, earthquake of 1992 (Elgamal *et al.*, 1993). No mechanism for formation of the craters in Egypt can be demonstrated because of the lack of geologic and geotechnical data at the crater sites. However, the regularity of alignment of the craters suggests that man-made holes led to formation of the craters.

7.4.1.2 Prehistoric Seismicity

Many filled craters in South Carolina contained small twigs and bark from trees. This woody matter is concentrated along the contact between layers 3 and 4 (Fig. 7.9) and obviously fell into the open pits soon after they formed. Twigs and bark from various craters yield radiocarbon ages of approximately 600, 1250, 3200, 5150, and older than 5150 years, documenting five prehistoric earthquakes in the Charleston area (Amick and Gelinas, 1991).

An estimate of the magnitude of prehistoric South Carolina earthquakes is provided by comparison of their liquefaction effects with worldwide observations, and also by comparison with observations of liquefaction in South Carolina in 1886. Data from the 1886 earthquake furnish a database for the regional development of craters, as well as their size and abundance. Worldwide data show that features having a liquefaction origin can be developed at magnitudes as low as M ~ 5 but that a magnitude of about 5.5 is the lower limit at which liquefaction effects are relatively common (Ambraseys, 1988). The source sands that produced craters in coastal South Carolina commonly are highly susceptible to liquefaction and flow; because of this susceptibility one might suggest that a low-magnitude earthquake could have produced the prehistoric craters. However, numerous prehistoric craters in the Charleston area, many having diameters in excess of 3 m, clearly are too large to have been the result of marginal liquefaction. Such large diameters suggest that the earthquake that produced them was much stronger than M 5 to 5.5. In addition, the prehistoric craters that formed 600 and 1250 years ago extend along the coast at least as far as the craters produced by the M 7.5 earthquake of 1886.

Interpretations of prehistoric earthquake magnitudes must account for liquefaction susceptibility. Principal variables are water table depth and the compactness of the source sands. The water table is presently very shallow, being less than 1 to 2 m below the ground surface. Almost certainly the water table has been essentially unchanged for the past few thousand years at many of the crater sites (Amick *et al.*, 1990). Just prior to the 1886 earthquake, the Charleston area was experiencing an extraordinarily wet period, so water table conditions were optimal for production of liquefaction features (Taber, 1914, p. 126). *Standard penetration test (SPT)* data also show that the source sands are so loose as to liquefy readily. It is not unusual that the sand deposits at the liquefaction sites have SPT blow counts as low as 10 or less (Martin and Clough, 1990). It is difficult to conceive of any mechanism that would have made the sands much more compact when the prehistoric earthquakes occurred. In summary, the liquefaction susceptibility was high at many places when the 1886 earthquake struck.

We noted previously that craters having ages of 600 and 1250 years extend along the coast at least as far as craters of the 1886 earthquake extend. A comparison of the size (diameter) of the craters shows that those formed 600 years and 1250 years ago are larger than the 1886 craters, both in the vicinity of Charleston and far away. Consideration of all factors suggests that these prehistoric earthquakes were at least on the order of the M 7.5 event in 1886. Paleoliquefaction evidence for the event that took place 3200 years ago has been found only in the vicinity of Charleston. The existence of abundant, exceptionally large craters for this event might suggest that the earthquake was exceptionally large, but the limited size of the affected area suggests otherwise. The absence of craters far from Charleston might be explained alternatively by a lower sea level and thus a lower water table level, and by a generally drier climate during this part of the Holocene (Amick *et. al.*, 1990). Absence of the 3200-year-old craters far from Charleston might also be explained by an exceptionally shallow earthquake, in which energy attenuates rapidly within a short distance. For craters having an age of 5000 years or older, there is a greatly diminished chance for preservation of organic material that can be dated with accuracy, so it is difficult to evaluate the magnitude of such old events.

Some of the craters far to the north of the Charleston area, in the vicinity of the South Carolina-North Carolina border (Fig. 7.6), have ages different from those of craters to the south. This difference suggests another epicentral region in the vicinity of the state boundary.

7.4.2 New Madrid Seismic Zone

The 1811–12 sequence of earthquakes in the central United States consisted of four very strong earthquakes (M ~ 7.8 to 8.3) within a three-month period. Six aftershocks had magnitudes of 6 to 7 (Hamilton and Johnston, 1990).

Epicenters of the strongest 1811–12 earthquakes probably were distributed along a fault zone exceeding 100 km in length (McKeown *et al.*, 1990). These epicenters, in combination with continuing seismicity, define the New Madrid seismic zone (Fig. 7.11).

The meisoseismal region for the 1811–12 earthquakes was centered in a huge area of alluvial lowlands. Prominent effects of liquefaction extended over an area of 10,000 km^2 in the lowlands and are plainly visible on the ground today (Figs. 7.12 and 7.13). Large areas have more than 25% of the surface covered with vented sand more than a meter thick (Obermeier, 1989).

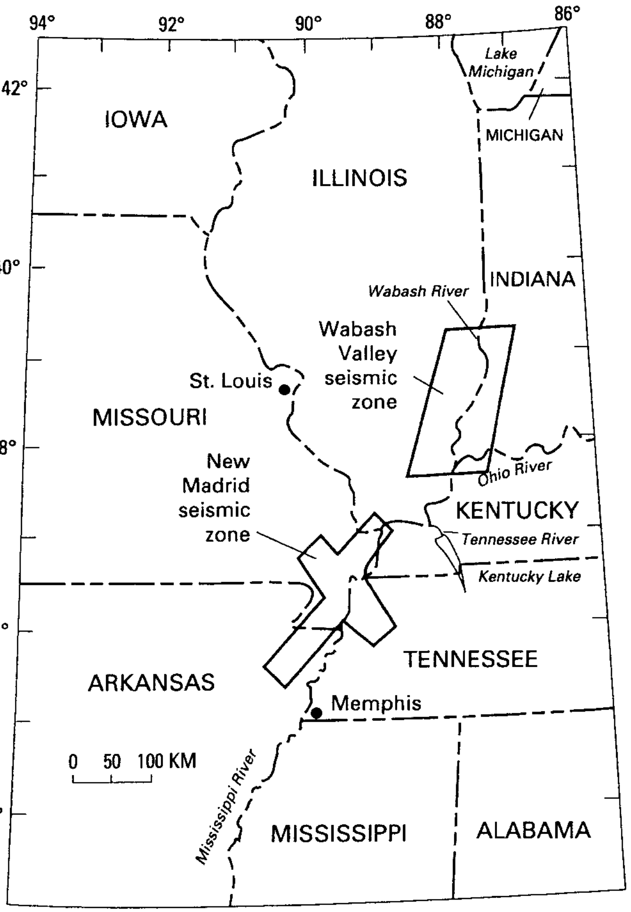

Figure 7.11 Approximate limits of New Madrid seismic zone and Wabash Valley seismic zone. New Madrid seismic zone is the source area of the 1811–12 earthquakes and continues to have many small earthquakes and a few slightly damaging earthquakes. The Wabash Valley seismic zone is a weakly defined zone of seismicity having infrequent small to slightly damaging earthquakes.

The alluvial lowlands is an area of very low relief, thick strata of fine and medium sand at shallow depth, a very high water table, and a clay-rich cap. The sand strata generally are moderately compact. The lowland is made up largely of late Wisconsinan braid-bar terraces that formed in floods of glacial meltwater carrying great quantities of sand. Thickness of sand beneath the terraces generally exceeds 30 m, and at most places the sands are capped with clay-rich strata interbedded with thin sand and silt strata having a total cap thickness of a few meters. Much of the alluvial lowland also is occupied by large areas of Mississippi River meander-belt deposits, which were laid down during Holocene time as insets into the braid-bar terraces. Most of the meander-belt deposits consists of point-bar accretion topography of arcuate ridges and swales, abandoned channels, and natural levees. Many abandoned channels are filled with as much as 30 m of soft clay and silt. A cap of montmorillonite-rich clay at least a few meters thick lies on meander-belt sediments at most places. Overall, the alluvial lowland region is quite susceptible to the formation of earthquake-induced liquefaction effects during strong shaking.

Reports made shortly after the 1811–12 earthquakes noted great multitudes of sand blows, linear fissures as deep as 6 m and hundreds of meters long, craters many meters in diameter, and lateral spreads as long as hundreds of meters (Penick, 1976). Individual and coalesced sand blows and some long linear fissures through which sand vented are the only features that are still readily visible on the ground surface. Great numbers of intruded dikes and sills can be seen in walls of deep (>3- to 4-m) drainage ditches.

Also within the 1811–12 earthquakes meisoseismal region are many sedimentary features of unknown or nonseismic origin. Mainly, the features formed as nonseismic sand boils, mima mounds, or deformed mud.

7.4.2.1 Characterization of Venting and Fracturing at the Ground Surface

Even though sand that was vented to the surface by the earthquakes of 1811–12 is still visible today, most evidence of venting has been obliterated by agricultural practices. However, even small features were abundant at the time of a field study by Fuller (1912). Individual sand blows induced by the 1811–12 earthquakes typically are dome-like accumulations of clean sand on the ground surface. Fuller (1912, p. 79) noted that "the normal blow is a patch of sand nearly circular in shape, from 8 to 15 feet across, and 3 to 6 inches high." Such small sand blows as Fuller described can rarely be found at present. The sand blows now obvious range from about 0.3 to 0.7 m in height at the center and thin to a feather edge at a distance of 5 to 20 m from the center.

Sand vented to the surface by the 1811–12 earthquakes is obvious on aerial photographs, where the sand vented onto the dark clay-rich cap. The vented

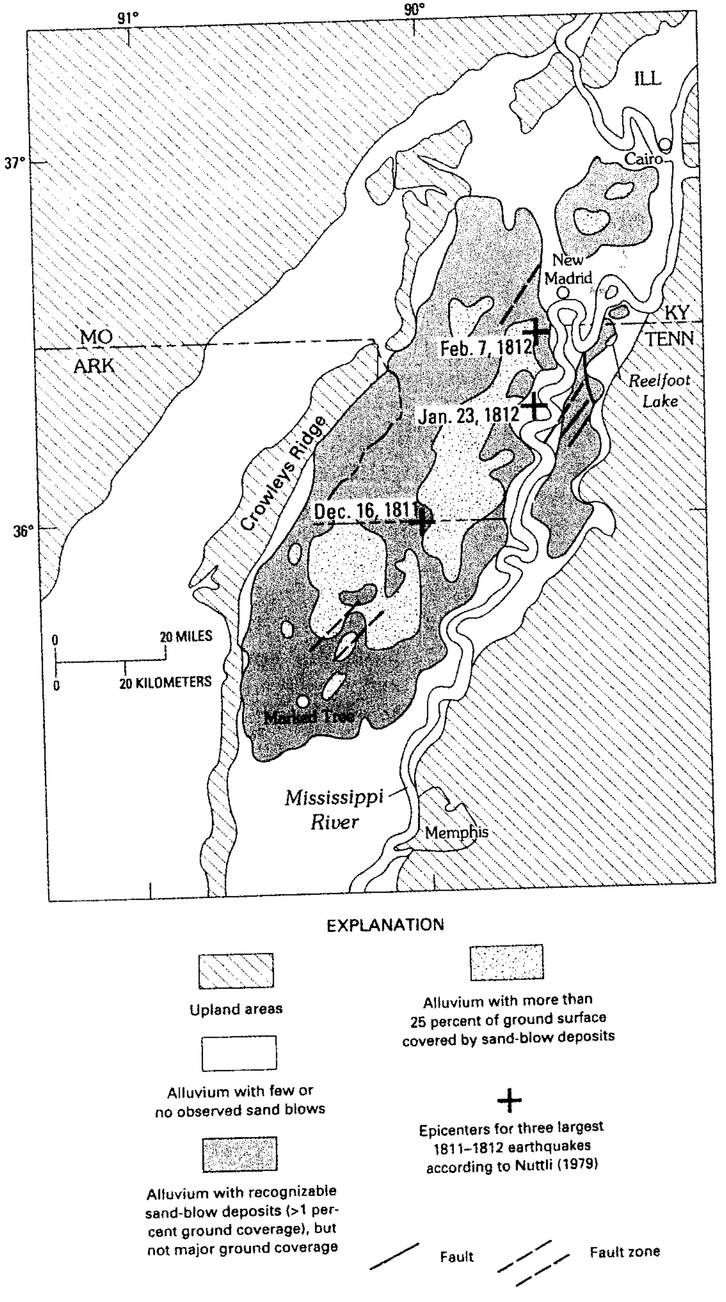

sand dries more rapidly than clay during seasonal drying, making a tonal contrast on the photograph. Figures 7.13A and B illustrate the contrast and also illustrate how venting has taken place at irregular and somewhat erratically spaced intervals. The photographs also show that extensive venting took place through approximately linear dikes that are more or less parallel. These patterns of erratic spacing and parallelism generally reflect small differences in site characteristics. One of the most obvious is cap thickness. Typically, venting in point-bar deposits has taken place along the highest, thinnest part of the meander scroll. Where the cap is thicker, sand blows tend to be less abundant but larger. The wider spacing between dikes apparently causes more concentrated flow to the surface.

Long, linear dikes, commonly with exceptionally large quantities of vented sand, also tend to develop parallel to topographic declivities along streams and scarps. Dikes here have formed in response to lateral spreading movements, which generally take place more readily near the declivities (Fig. 7.13A). Wide (>1-m) dikes having lengths of many hundreds of meters are not unusual. Whereas the widest dikes tend to be close to the declivities, they also may develop many hundreds of meters away. Fuller (1912, p. 49), for example, states: "In the sand-blow districts the spacing of (lateral spreading) fissures varies from several hundred feet down to less than 10 feet. . . . In the case of the large (several meters wide) fault-block (lateral spread) fissures the spacing is greater, several hundred feet often intervening between the cracks, while the space between them may be half a mile or more. Isolated cracks of this type are not uncommon."

The direction of shaking during the earthquake probably had a very secondary influence on orientation of the largest dikes at most places in the meisoseismal region of the 1811–12 earthquakes (Obermeier, 1989). It is the local geologic-topographic setting that is of predominant influence. Cap thickness and proximity to stream banks and abandoned meanders are most important. Such important influence of the local setting has also been shown in a report about the 1964 Alaskan earthquake (M 9.2) by McCulloch and Bonilla (1970, Fig. 46) and is emphasized by Oldham (1899) for the great earthquake of 1987 in India, so the observed effects in the meisoseismal region of the 1811–12 earthquakes seem typical. Still, localized extension and compression of the

Figure 7.12 Regions having abundant vented sand, excluding modern floodplains, in the New Madrid seismic zone. (From Obermeier *et al.*, 1990.) Sand was presumably vented in response to the 1811–12 earthquakes. Severe liquefaction also occurred locally beyond the areas shown on the map, especially along streams west of Crowley's Ridge (Fuller, 1912). Also shown are the approximate epicenters for the three strongest 1811–12 earthquakes and major faults and fault zones.

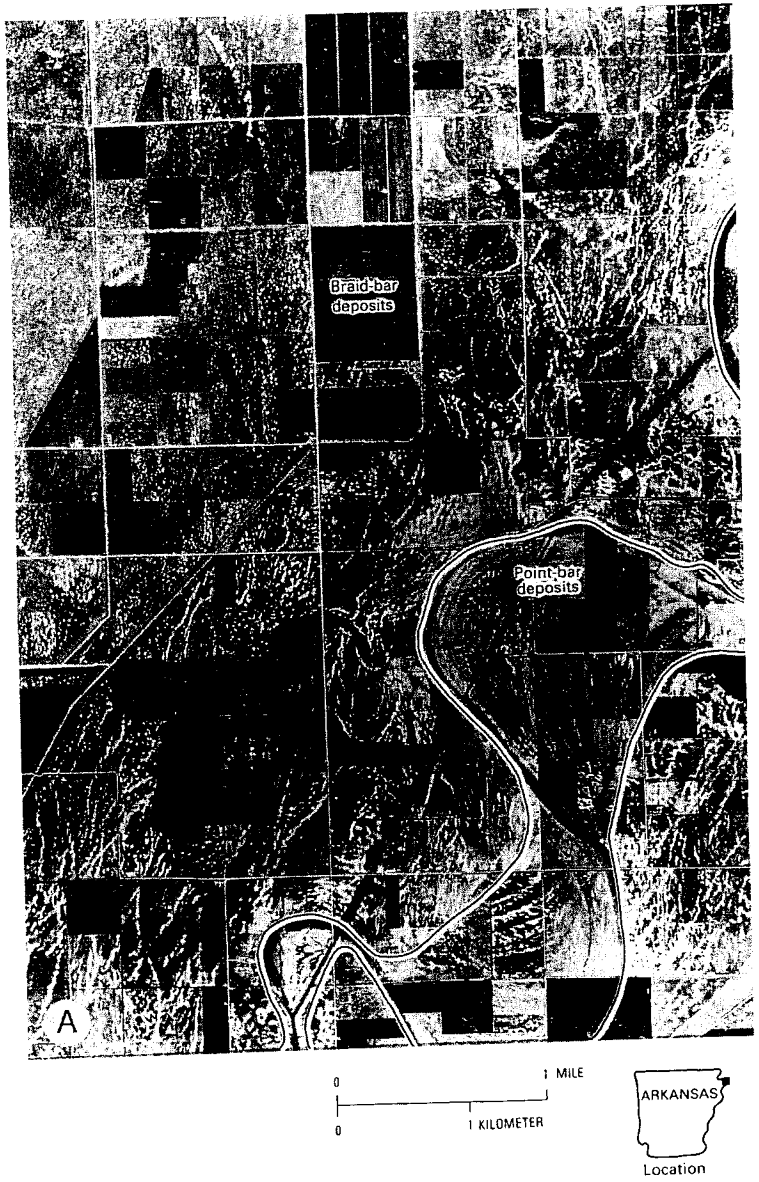

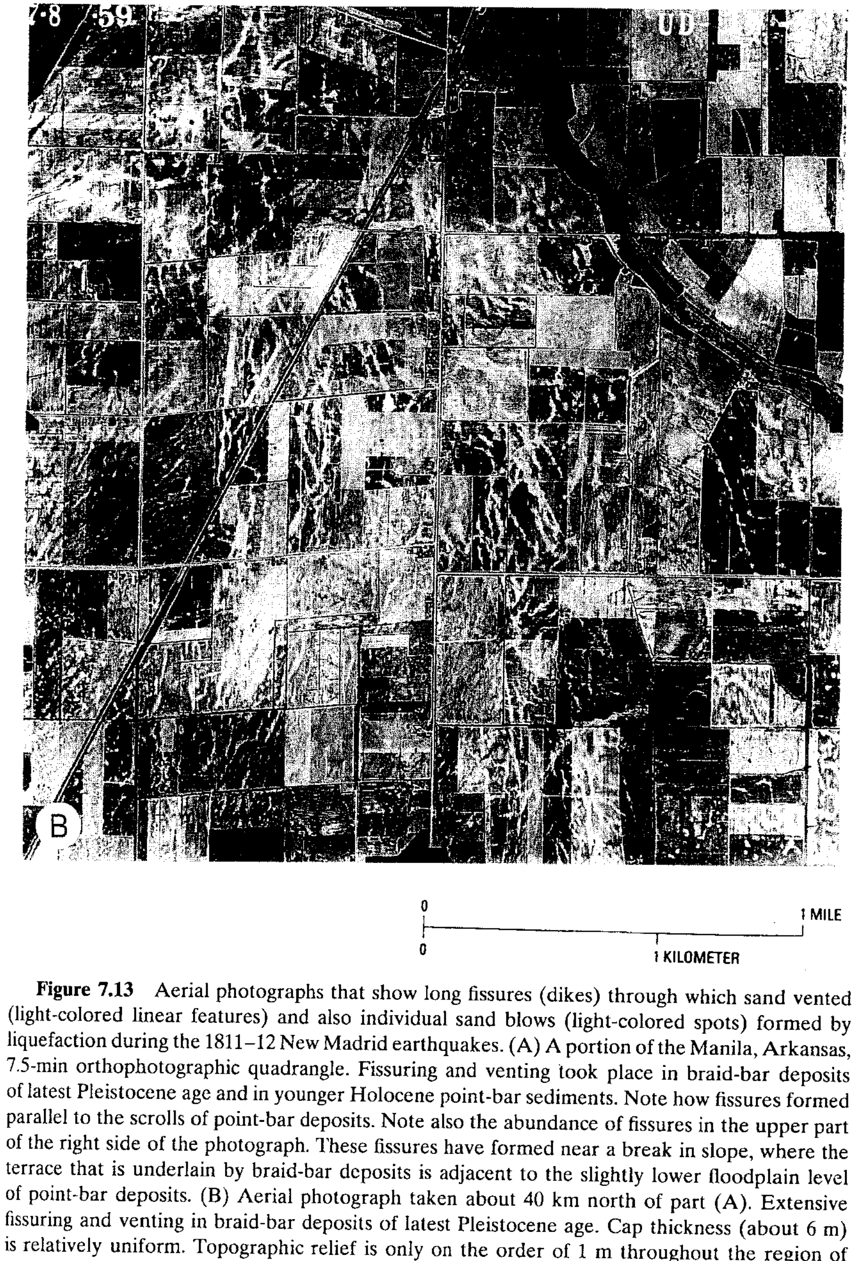

Figure 7.13 Aerial photographs that show long fissures (dikes) through which sand vented (light-colored linear features) and also individual sand blows (light-colored spots) formed by liquefaction during the 1811–12 New Madrid earthquakes. (A) A portion of the Manila, Arkansas, 7.5-min orthophotographic quadrangle. Fissuring and venting took place in braid-bar deposits of latest Pleistocene age and in younger Holocene point-bar sediments. Note how fissures formed parallel to the scrolls of point-bar deposits. Note also the abundance of fissures in the upper part of the right side of the photograph. These fissures have formed near a break in slope, where the terrace that is underlain by braid-bar deposits is adjacent to the slightly lower floodplain level of point-bar deposits. (B) Aerial photograph taken about 40 km north of part (A). Extensive fissuring and venting in braid-bar deposits of latest Pleistocene age. Cap thickness (about 6 m) is relatively uniform. Topographic relief is only on the order of 1 m throughout the region of extensive fissuring. Note severe fissuring over a width of at least 3 km.

ground surface, which may relate to the direction of strong surface shaking, may be relatively common at places (Oldham, 1899, p. 99).

The aerial photograph in Fig. 7.13 indicates enough randomness in dike orientation that most vertical exposures will intersect many dikes. This is especially relevant because searches for paleoliquefaction features are often made in banks of ditches or rivers, which may not be oriented optimally to intersect dikes.

7.4.2.2 *Characterization of Sand Blows and Dikes in Sectional View*

Most sand blows of the 1811–12 earthquake have a well-defined set of internal relations and stratigraphy, shown in a somewhat idealized version in Fig. 7.14. The main *feeder dike* is beneath the central part of the dome. The basal few centimeters of sediment that vented onto the original ground are generally a fine to medium sand with a slight to moderate amount of silt, containing scattered centimeter-long round to irregular clasts derived from the underlying clay-rich strata cut by the dike. Sediment along the basal few centimeters grades up within a few centimeters to coarser sand with less silt containing numerous irregular 1- to 5-cm-long clay-rich clasts. The clasts are encased in clean, medium- to coarse-grained sand. The clasts are largest and most plentiful near the feeder dike. The basal part of the sand-blow deposit also contains numerous 1- to 3-cm long rounded lignite fragments and other low-density materials vented to the surface. These low-density materials originated from the source sand. Clasts from the cap occur almost exclusively in the lowermost quarter of vented material. Above this in the larger sand blows, away from the vent, is a much thicker zone (tens of centimeters) of very clean, generally medium- to coarse-grained sand that is nearly structureless except for suggestions of laminations of sediment. Higher yet, the sand grades upward to a mainly medium-sized sand. Here there are weakly to moderately developed planar to wavy laminations of fines and sand generally a few millimeters in thickness, which gently dip down and away from the central part of the sand volcano (Fig. 7.14A). Where sediment vented into swales on the ground surface, this sequence may be capped by a silt-rich stratum with organic debris, 0.5 to several centimeters thick; this cap may also contain multiple very thin (1-mm-thick) clay-rich layers (Saucier, 1989). The organic matter in the cap consists of small pieces of charcoal and wood. The organic debris and thin clay-rich layers formed in swales located both above the vent (Fig. 7.14A) and in depressions far from the mound of vented sediment.

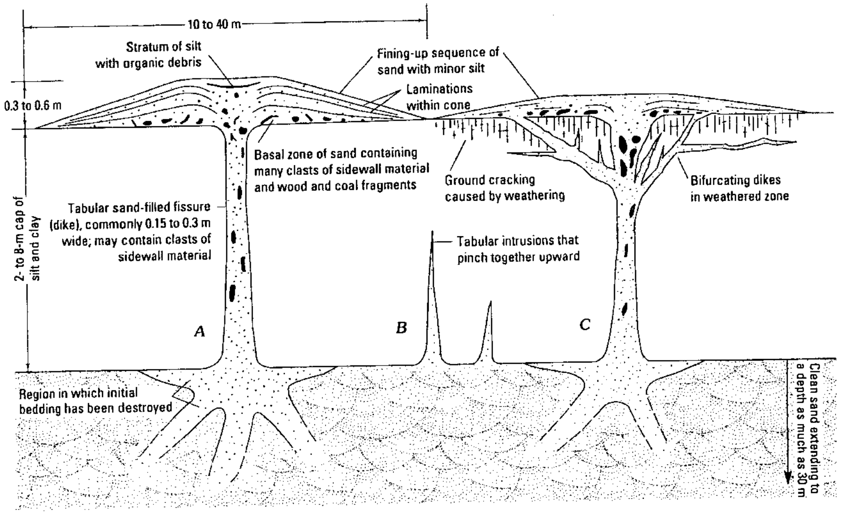

Figure 7.14 Schematic vertical section showing dikes cutting through overbank silt and clay strata and the overlying sand-blow deposits. (A) Stratigraphic details of sediment vented to the surface. (B) Dikes that pinch together as they ascend. (C) Characteristics of dikes in fractured zone of weathering, in highly plastic clays. Situations shown are encountered in many places in meisoseismal zone of the 1811–12 New Madrid earthquakes.

Closest to where dikes vented onto the ground surface, are well-defined strata that dip steeply into the dike (Fig. 7.14A). These strata typically contain the coarsest sediment vented. Next to these strata, in the lower and central part of the sand blow, there may be evidence of shearing and disruption caused by the forceful expulsion and boiling of sediment and water.

The overall *upward-fining sequence* of vented sediment, from the basal clast-bearing sand to the uppermost organic-matter-bearing stratum, represents the transition from the turbulent violent eruption very shortly after initial venting to the final ebbing flow to the ground surface. The planar and wavy laminations probably represent weak variations in flow from the dike.

Dikes that formed in the clay-rich cap of the 1811–12 earthquakes, meisoseismal region typically are sand-filled fissures that are steeply dipping (60° to 90°) and are mainly planar. In vertical section, dikes having widths exceeding several centimeters commonly are spaced from several meters to hundreds of meters apart.

Dike widths range from millimeters to several meters. Many of the widest "dikes" are sand-filled fissures that were almost certainly caused by lateral spreading. Figure 7.15 shows a feature probably having such an origin; the lignitic, silty clay stratum in the sand indicates the location of the top of the sand (S_1) that flowed into the opening of the lateral spread. The upper sand (S_2) probably was vented later during a following earthquake. (In contrast, often little or no sand vents to the ground surface from the large space between blocks opened by lateral spreading.) The tendency of sidewalls of many of the larger sand dikes throughout the 1811–12 earthquakes' meisoseismal zone to be parallel to one another in vertical section also indicates a pulling-apart origin during lateral spreading.

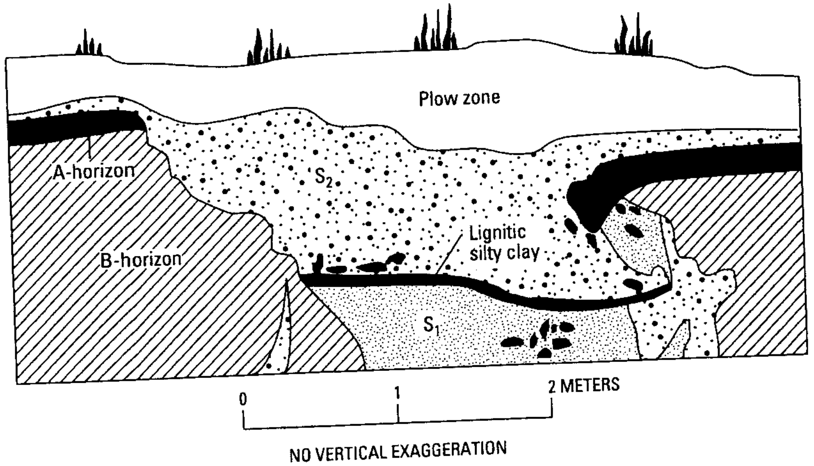

Figure 7.15 Sketch of vertical exposure in a ditch in the meisoseismal zone of the 1811–12 New Madrid earthquakes showing evidence for about 1.5 m of lateral spreading. The S_1 sand was emplaced during lateral spreading. The lignitic, silty clay layer next was laid down on S_1 sand. Later, S_2 sand was vented to the surface, burying the lignitic silty clay and S_1 sand. Note that the sidewalls are approximately parallel. [From Wesnousky and Leffler (1992); reprinted with permission of the Seismological Society of America.]

Dikes about 15 cm or less in width are very common. Dikes in this width range normally become more narrow upward as illustrated in Fig. 7.14A. The tapering may represent downwarping of the ground surface in response to sand at depth having been vented to the surface. At almost all places, even isolated sand blows have vented through small, vertically planar dikes. The smallest dikes pinch together as illustrated in Fig. 7.14B.

Within the uppermost meter or so, dikes cutting through the weathered portion of the clay-rich cap may branch irregularly upward into many smaller segments (Fig. 7.14C). Possibly, preexisting weathering planes of weakness cause a single large dike to branch into many small members. The clay cap typically contains a large proportion of montmorillonite. During dry years, desiccation cracks extend a meter or more in depth. Pedogenesis has also developed a strong soil structure (pedons) in a thick B horizon near the surface.

Where larger dikes branch extensively (Fig. 7.14C), there may be only minor evidence of venting onto the ground surface. Apparently this network is effective in dissipating the energy of the flow. Locally though, venting has excavated the highly fractured zone, leaving behind a widened dike at the top. This excavated zone may contain many clay clasts mixed irregularly in a matrix of sand.

Dikes that cut through the fine-grained cap generally are filled with a loose mixture of fine and medium sand and a minor amount of silt. Clasts of clay, some as long as 20 cm, may also occur but generally are not abundant. Elongate clasts tend to be parallel to sidewalls. The clasts were derived from the sidewalls and transported up the dike. The mixture of sand, silt, and clasts has a sharply defined contact with the sidewalls. Weak laminations within the sand and silt may parallel the sidewalls. Cross-cutting, vertically oriented zones of sand and silt within the dike are also commonplace. These probably represent episodes of venting during separate pulses or venting from different source zones at depth.

The finest constituents (fine sand and silt) have been winnowed from dike fillings at some sites of venting. *Winnowed zones* within the dike are commonly tubular and as much as several centimeters in width. Locally, winnowing extends several meters down into the dike. This winnowing probably took place by water flowing up through the dike during final phases of expulsion of water, following initial emplacement of the sand in the dike.

Many dikes that pinch together upward have a large proportion of silt and clay mixed with the sand near the top. Often it is unclear whether the silt and clay have invaded the dike by pedogenesis or whether the silt and clay were constituents of the originally intruded sediment. Dikes that taper upward are generally of limited usefulness for paleoliquefaction studies, owing to difficulties in determining when the dikes formed.

Many variations of the relations shown in Fig. 7.14 exist. One of the most common is a large amount of *downwarping* of the cap toward the dike. This downwarping tends to be most pronounced where a large amount of sand has been vented to the surface. It is not unusual that the cap be downdropped by more than 0.5 m on one or both sides of the dike and that the cap be otherwise faulted or severely deformed near the dike (e.g., Wesnousky and Leffler, 1992, Figs. 9, 12, and 14). Some scattered small tubular dikes can also be found in clay caps of the 1811–12 earthquakes' meisoseismal region. Holes that originated from decay of tree roots or from excavation by crayfish are ubiquitous and doubtlessly were used as the conduits for small tubular dikes. These tubular holes through the cap had a very minor role as conduits for venting, though, as compared to steeply dipping planar dikes. However, these holes possibly were preferred paths during the early phase of venting, and thereby controlled where hydraulic fracturing developed planar dikes. Small holes whose walls are defined by angular breaks, and which have a tortuous upward path, also are commonly observed conduits for sand venting during the 1811–12 earthquakes. Another field example, in Venezuela, of where venting was localized in tubular (crab) burrows is reported by Audemard and de Santis (1991); this venting occurred in response to limited liquefaction during moderate earthquakes.

The preceding discussion has focused on characteristics of dikes that cut through a clay-rich cap that varies in consistency from very soft to brittle. Excellent descriptions and detailed drawings of tabular dikes that cut interbedded clay and sand strata during the 1989 Loma Prieta, California, earthquake (M 7) are in Sims and Garvin (1995). The dikes and sand blows that they describe generally are much smaller and represent less forceful venting than those of the 1811–12 earthquakes, yet the sediment relations in the dikes and sand blows in both regions are quite similar.

Locally, the cap in the 1811–12 earthquakes' meisoseismal region is a very weakly cemented sand containing only a minor amount of silt and clay, with some slight bonding from oxides of iron and manganese. The liquefaction features in the areas of weakly cemented sand caps appear to have been mainly large open craters, similar to those of the 1886 Charleston, South Carolina, earthquake. In contrast to the filled craters in South Carolina, very large clasts of host sediment generally are not present in the crater (see sketches in Tuttle, 1994). Apparently the host sand is too friable.

7.4.2.3 Characterization of Sills in Sectional View

Combinations of dikes and sills are also common within the nonliquefiable cap. Where sills are abundant, dikes generally are also plentiful. Sills form preferentially at three locales: (1) along the base of the cap, (2) along bedding planes and other horizontal planes of weakness in the cap, and (3) beneath exceptionally dense, strong root mats. These three locales are illustrated in Fig. 7.16.

Laterally extensive sills as thick as 0.5 m are commonplace along the base of the cap. An intruding sill can dome up an overlying flexible, clay-rich cap having a thickness of as much as a few meters. Sills are also common within the cap where original horizontal sedimentary structures and planes of weakness have not been destroyed by weathering. Sills especially tend to form irregularly within thin beds of silt or sand sandwiched between clay-rich beds. Small branches from the main sill commonly intrude into the overlying clayey stratum, forming more sills and dikes. Clay-rich clasts can abound within the sill. The clasts have been transported many meters horizontally at many places, but clasts that have simply been detached and foundered vertically several centimeters are also very common (see Fig. 7.16). The shape of clay-rich clasts in the sills, generally angular, suggests a brittle or shattering mode of fracturing of the stratum from which the clasts were derived. Despite this pattern of fracturing, the clay-rich clasts and their source beds commonly have such a soft consistency as to permit very easy penetration of several centimeters by thumb pressure.

Sills at a depth of about a meter or less in a clay-rich cap can be quite wavy in vertical section. These sills can thin and thicken dramatically within a horizontal distance of a meter or less and produce blister-like bulges on the surface. In plan view, these bulges can range from circular to very elongate. Sills can be as thick as 0.7 m near the surface. Such large thicknesses are less common at greater depths, except locally along the base of the cap. Sills very close to the ground surface generally seem to have formed beneath root mats of grass and trees.

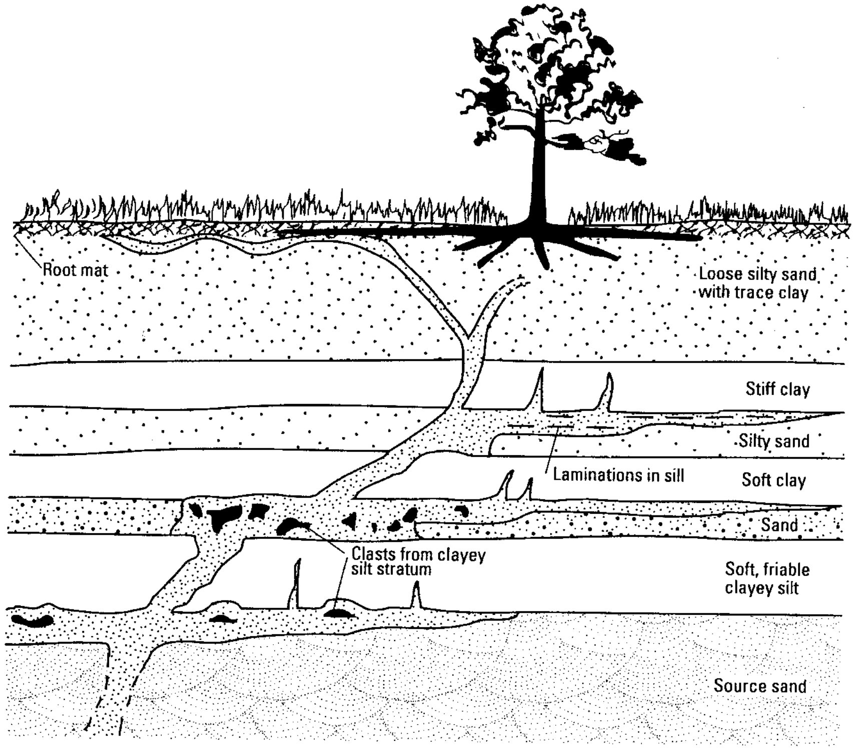

Figure 7.16 Schematic vertical section showing where sills form preferentially. Note that thin sills can extend great distances horizontally, especially where the overlying cap is thin. Such severe sill development as shown in the figure is typically accompanied by large sand blows.

Figure 7.17A shows a commonly observed field example in which near-vertical dikes are connected to a laterally extensive sill. The sill has formed within a clay cap that has only incipient horizons of weakness. The sill is at least 25 m long but is only 10 cm thick. The sill more or less follows a single horizon in sectional view. The type of internal layering seen in this sill is commonplace. Individual laminae are composed of small pieces of lignite or fine-grained sand and silt (Figs. 17B and 17C). Also common at this site and elsewhere are structureless sills containing many *clay clasts* in a sand matrix, as well as sand with graded bedding of clay clasts concentrated along the base.

Laterally extensive sills also tend to form in the upslope direction along the base of a cap, where the base dips appreciably. Such sills especially occur along the base of a clay-filled abandoned channel; here a sill typically extends

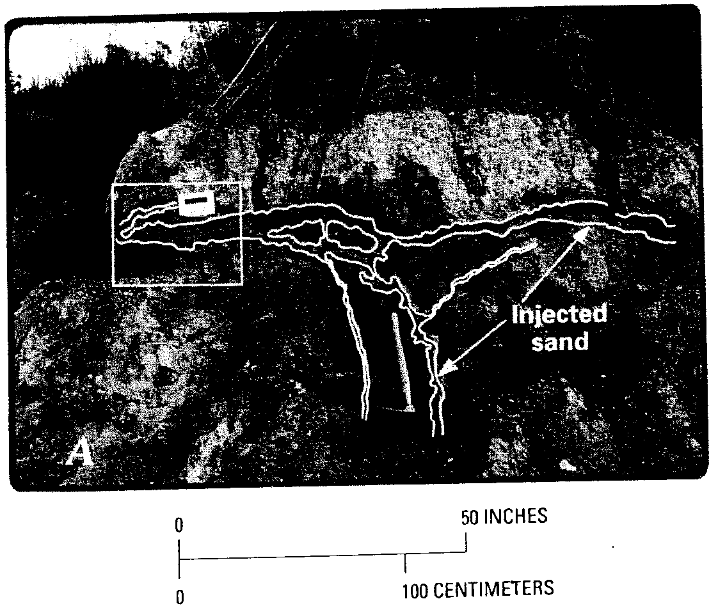

Figure 7.17 Sand dikes and sills exposed in a nonliquefiable cap of silt and clay; the dikes and sills are interpreted as having originated by liquefaction during the 1811–12 New Madrid earthquakes. Outcrop is the bank of a ditch in the meisoseismal area of the 1811–12 earthquakes. (A) Overview and line drawing of typical small dikes and small sills. The sill extends far beyond the photograph and is at least 25 m long. Rectangle shows area of part (B). (B) View showing details of layering in sills. (C) Very close view showing details of layering in sill. Sill is made up of fine- and medium-grained sand with some silt- and sand-sized lignite. Black bands are lamina of small pieces of lignite.

upslope to where the cap is thinner, and the sill feeds into a steeply dipping dike which has vented onto the surface (M. P. Tuttle, University of Maryland, College Park, written communications, 1993).

The exposure illustrated in Fig. 7.18 shows another common type of field example in which sand dikes and sills cut the upper liquefied sands and the lower portion of the nonliquefiable cap. In the upper part of the liquefied sand (bed A, Fig. 7.18A), small dikes branch out from a large dike (feature 1), cut through the basal bed of the cap (bed B) at horizontal intervals of 0.5 to 1 m, and extend upward about 0.5 to 1 m. A few dikes and sills intrude to much higher levels (features 2, 3, and 4). At exposures nearby (not shown), dikes extend to the surface. Sand has vented to the surface to produce many large sand blows in the field adjoining the outcrop of Fig. 7.18.

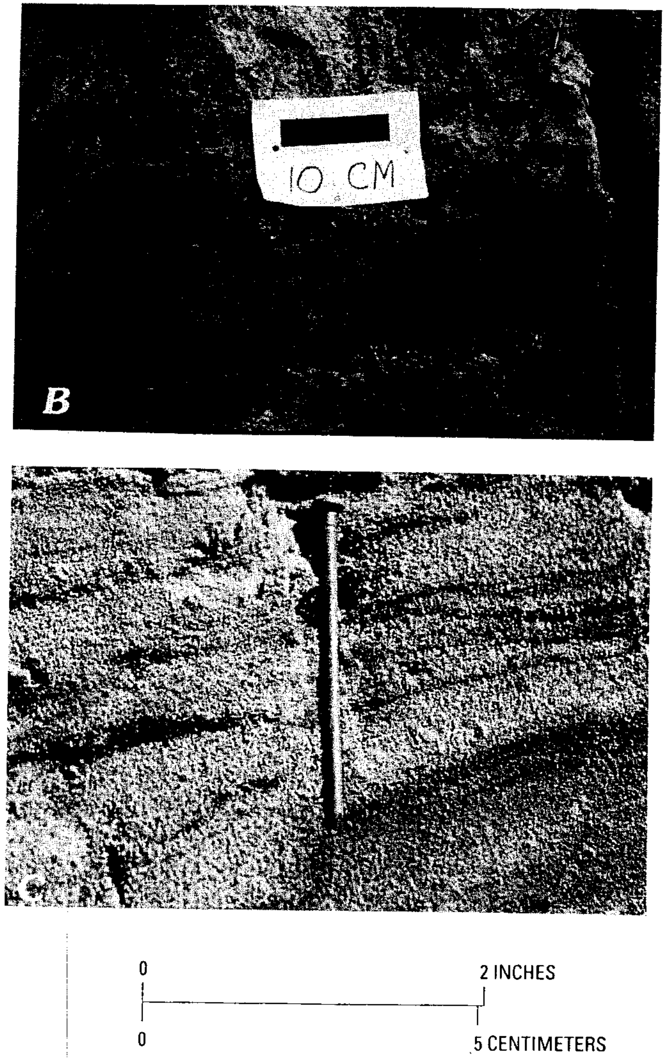

Figure 7-17 Continued

The dikes and sills shown in Fig. 7.18A as features 1 through 4 contain clean, medium-grained sand. The edges of the intrusions are sharp in clay-rich beds such as beds C, D, and G. Locally, intrusions puncture the very soft clay with sharp angular turns and breaks that follow a haphazard path (features 2 through 3). Edges of intrusions are generally less distinct in beds of clean, permeable sand. Dikes commonly widen and terminate upward as flame-shaped structures (feature 4) in a permeable sand bed (bed H). Clay clasts may be present in lower portions of the structures.

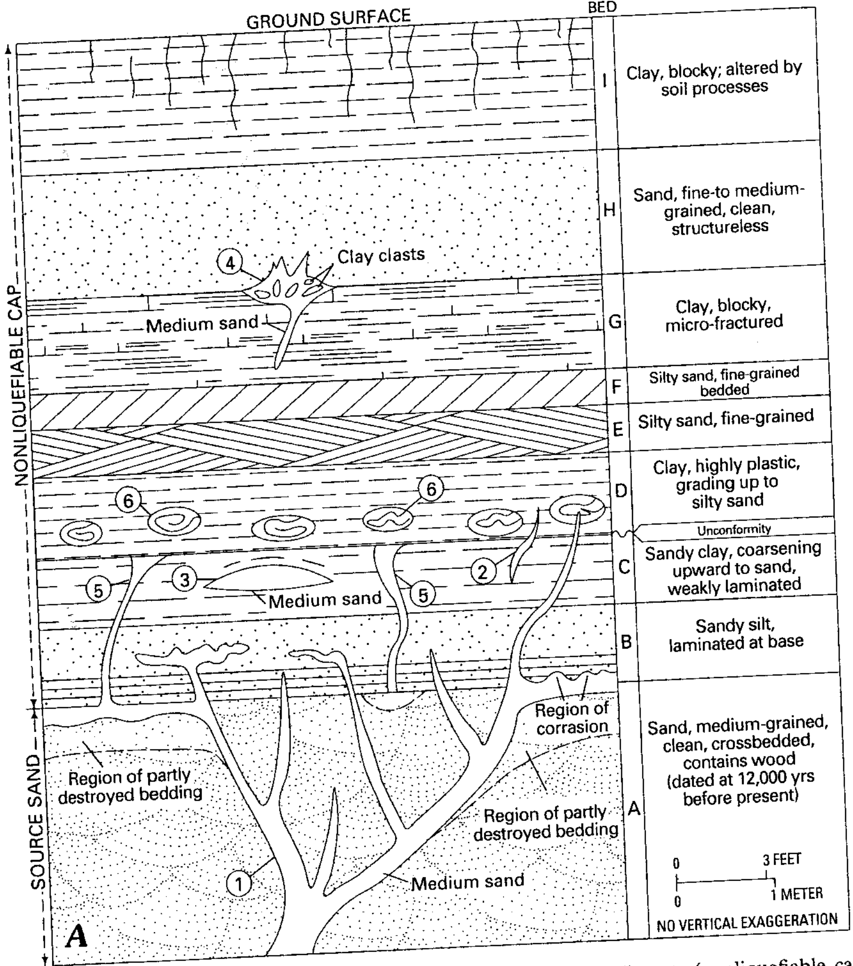

Figure 7.18 Schematic vertical section showing Holocene sediments (nonliquefiable cap) and underlying Wisconsinan age source sand that liquefied. Exposure is in a ditch in the meisoseismal region of the 1811–12 New Madrid earthquakes. Earthquake-induced intrusions cut section at many places. (A) Schematic diagram of stratigraphic relations and liquefaction-induced features (numbered 1–5). Feature 1, dikes of medium-grained sand that cut cap and source sand; features 2 and 3, intruded dikes and sills of massive, clean, medium-grained sand; feature 4, dike and flame structures of medium-grained sand containing and large clasts from bed G; feature 5, dikes of medium-grained sand, truncated unconformably; feature 6, pseudonodules collapsed in bed D. (B) Photograph of beds A–D showing sand intrusion (feature 3). Knife is 12 cm long (B–E). (C) Photograph of dikes (feature 1) cutting source (bed A) and bed B. (D) Photograph of plan view of bed B showing intrusion structures caused by feature 1; the plan view is in the area of the knife that is oriented vertically in part (B). (E) Photograph of part of feature 4, showing clay clasts in sand matrix intruded into bed H.

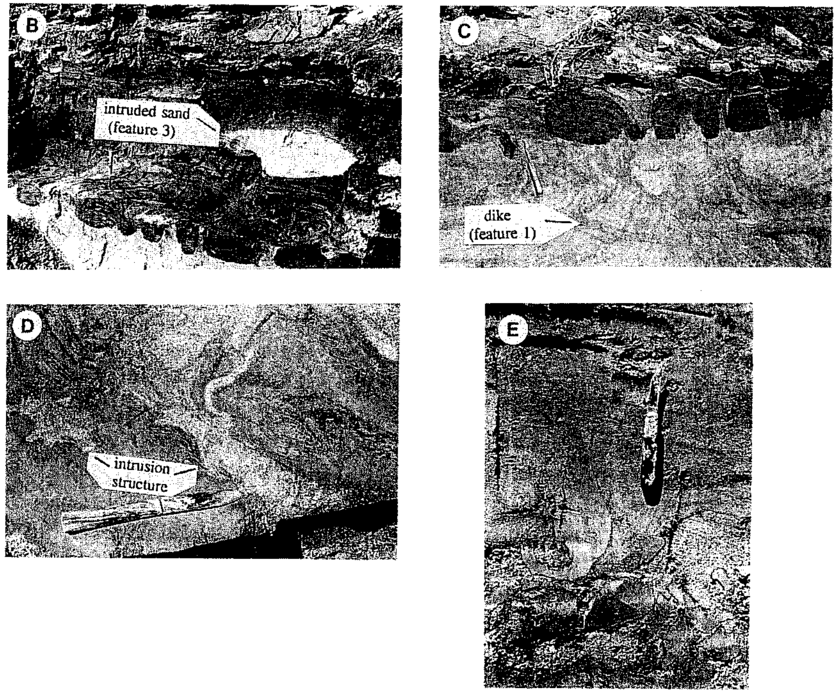

Figure 7-18 Continued

The sill at the base of bed B, at the extreme right side of the figure, has an irregular contact along the top. Here the sill has *corraded* the base of the friable bed B. Small intact pieces of bed B have sunk into the sill, probably attesting to a very water-rich condition in the sill at the time of its intrusion. Such destruction of friable beds by sills is commonplace throughout the meisoseismal region, especially along the base of the cap. In regions of only marginal development of small dikes, sills along the base of the cap and within the cap are not observed at many places, but where present may help to serve as independent evidence for a seismic liquefaction origin.

Features labeled 1 through 4 in Fig. 7.18 are interpreted to be earthquake-induced because (1) they are widely distributed over tens of kilometers, (2) they contain dikes and sills commonly as wide as 15 cm that suggest intrusion by large volumes of water-saturated sediment, (3) they contain clean, medium-sized sand containing large angular clay clasts (which is evidence of forceful intrusion), and (4) artesian conditions are unlikely at these sites.

The dike shown as feature 5 has an uncertain origin (Fig. 7.18A). Three small dikes that were truncated at the contact of beds C and D were exposed in a 25-m section along the ditch but were not found in other nearby exposures of beds C and D. The dikes may represent seismic liquefaction that occurred prior to the 1811-12 earthquakes. They contain, however, a large proportion of silty fine-grained sand, which does not suggest forceful intrusion at this site. Possibly they resulted from springs that formed near the base of a stream bank or as slump-related features that formed soon after initial deposition of the host sediments. Feature 6 (pseudonodules) is discussed in a following section.

Flame-shaped structures such as those of feature 4 have developed at many places within thick sand beds in the meisoseismal region of the 1811–12 earthquakes. Flame-shaped structures commonly have widths ranging from millimeters to about a third of a meter. Apparently the upper sand beds do not liquefy and, because of their relatively high permeability, perhaps in combination with an unsaturated condition, permit the energy of the pressurized water from beneath to dissipate within the large volume.

A form of a rather uncommon deformation feature (not shown) probably related to seismic liquefaction involves plastic deformation of silt and clay along the base of the cap. The lowermost 10 to 20 cm of the cap contains a convoluted mixture of severely disturbed, plastically deformed silt and clay, intruded by sand. Such *convolutions* probably take place only where extremely soft silt and clay lie directly on liquefied sand.

7.4.2.4 Paleoliquefaction Studies

Systematic paleoliquefaction studies were undertaken only recently throughout the meisoseismal region of the 1811–12 earthquakes. This region has large terraces of late Wisconsinan and early Holocene age where the water table appears to have been very shallow since the terraces were formed (Wesnousky and Leffler, 1992, 1994). Thus, if very strong earthquakes occurred since early Holocene time, liquefaction features should be present in the geologic record. Definitive evidence for liquefaction predating 1811–12 has been found in the northern part of the New Madrid seismic zone (see Figs. 7.11 and 7.12) near Reelfoot Lake (Russ, 1979) and at a site about 30 km northeast of Reelfoot Lake (Saucier, 1991b). Russ found that three earthquakes have induced liquefaction during the past 2000 years and, on that basis, suggested a recurrence interval of 600 years for liquefaction-producing events. Saucier (1991b) estimated an average recurrence interval of 470 years for liquefaction-producing events in the past 1300 years. Farther south, in the southern half of the seismic zone, field work has discovered effects of three prehistoric liquefaction-producing events during the past 2000 years (Tuttle and Schweig, 1995). Whether or not these more southern episodes are correlative with those farther north has not yet been resolved. Therefore, the upper limits for the magnitudes of these prehistoric earthquakes cannot yet be determined. Only the lower limits can be estimated, and these are the threshold values. The threshold magnitude is about M 6.4 to 6.8 on the basis of historical observations of liquefaction-producing events in the New Madrid seismic zone (Obermeier, 1988).

7.4.3 Wabash Valley Seismic Zone

Many small to slightly damaging earthquakes have occurred throughout the region of the Wabash River valley of Indiana and Illinois in the past 200 years. Seismologists have long suspected that the weakly defined Wabash Valley seismic zone (Fig. 7.11) could be capable of producing earthquakes stronger than the largest of record (M ~ 5.5; Hamilton and Johnston, 1990). A search for paleoliquefaction features has resulted in discovery of very large prehistoric, Holocene earthquakes.

The main search was in the Wabash River valley along the central axis of the Wabash Valley seismic zone. Alluvium generally as thick as 10 to 30 m lies on bedrock. The valley contains expanses of low glaciofluvial terraces of late Pleistocene age. These terraces are mainly braid-bar deposits of gravel and gravelly sand. Inset into the Pleistocene terraces are slightly lower Holocene floodplains of finer point-bar sediment. The sand-gravel deposits of both braid bars and point bars typically are overlain by a 2- to 5-m-thick alluvial cap of sandy silt to clayey silt. Bordering the valley are extensive plains of silt and clay that contain patches of clean sand, laid down in slackwater areas during glaciofluvial alluviation. The water table is presently shallow (<3 m) and appears to have been shallow over large areas much of the time following glaciofluvial alluviation, on the basis of depth of carbonate leaching and B horizon soil development in sandy and silty alluvium. This combination of a relatively shallow water table and widespread sand-rich deposits with an overlying fine-grained cap has provided an excellent opportunity for liquefaction features to form throughout much of the Holocene.

7.4.3.1 Characterization of Features

Hundreds of dikes have been found. Sills within the cap are sparse, even where thick sills occur along the base of the cap. Dikes and sills occur both in Holocene point-bar deposits and in the late Pleistocene glacial outwash and slackwater deposits. Figure 7.19 shows the locations searched, sites where dikes were discovered, and sites of exceptionally large (widest) dikes. Virtually all sites shown on the figure have more than one dike, and many sites have more than 10. Almost all the liquefaction sites are in actively eroding banks of rivers, which were about the only areas searched. The dikes are steeply dipping, tabular, and connect to a sediment source at depth. Many smaller dikes pinch together as they go up. Dikes filled with sand containing some gravel and silt are very common. Mainly sand was vented, though commonly with large quantities of gravel (Fig. 7.20). Within many dikes is an upward-fining sequence of coarsest material. Also within many dikes are sharply defined, vertically intertwined and intersecting zones containing distinctly different grain sizes, which in places can be traced to different source strata at depth. Where dikes cut through a thick clay cap without pronounced horizontal planes of weakness, it is not unusual that the dike width does not exceed a centimeter throughout a height of as much as 4 to 5 m. Widths as much as 15 cm or more throughout the height of the dike are very common and widespread in the region. Locally, though, in what is interpreted as meisoseismal regions of the prehistoric earthquakes, dikes have widths ranging from 0.7 to 2.5 m.

Sediment vented to the surface extends as much as 40 m in width. Thicknesses of vented sediment of 0.15 to 0.2 m are not unusual. Most vented sediment fines upward and laterally, especially if gravel was vented. The vented sediment at sites bordering the Wabash River generally lies on a paleosol and is buried beneath a 1- to 3-m thickness of overbank deposits, as illustrated in Fig. 7.20. On slightly elevated terraces, where flooding has been rare, the vented sediment has been incorporated into the surface soil.

At some sites there is good evidence for more than one pulse of venting. This evidence is best shown at sites near Vincennes (Fig. 7.19), where both sand blows and their dikes are largest for the event of 6100 yr B.P. The vented sediment is manifest as two upward-fining sequences. The lower pulse of vented sand fines upward to a thin silt layer; the upper pulse has abundant sand and gravel that also fines upward. There is no evidence of a significant hiatus between pulses.

The interpretation that sediments were vented from the dikes onto the ground surface rather than intruded as sills is based on several lines of evidence. Sills would cut irregularly across sedimentary horizons at some places (see Figs. 7.16 and 7.17), rather than always being confined to a single horizontal layer as in the Wabash Valley. Sills also would tend to follow the contact

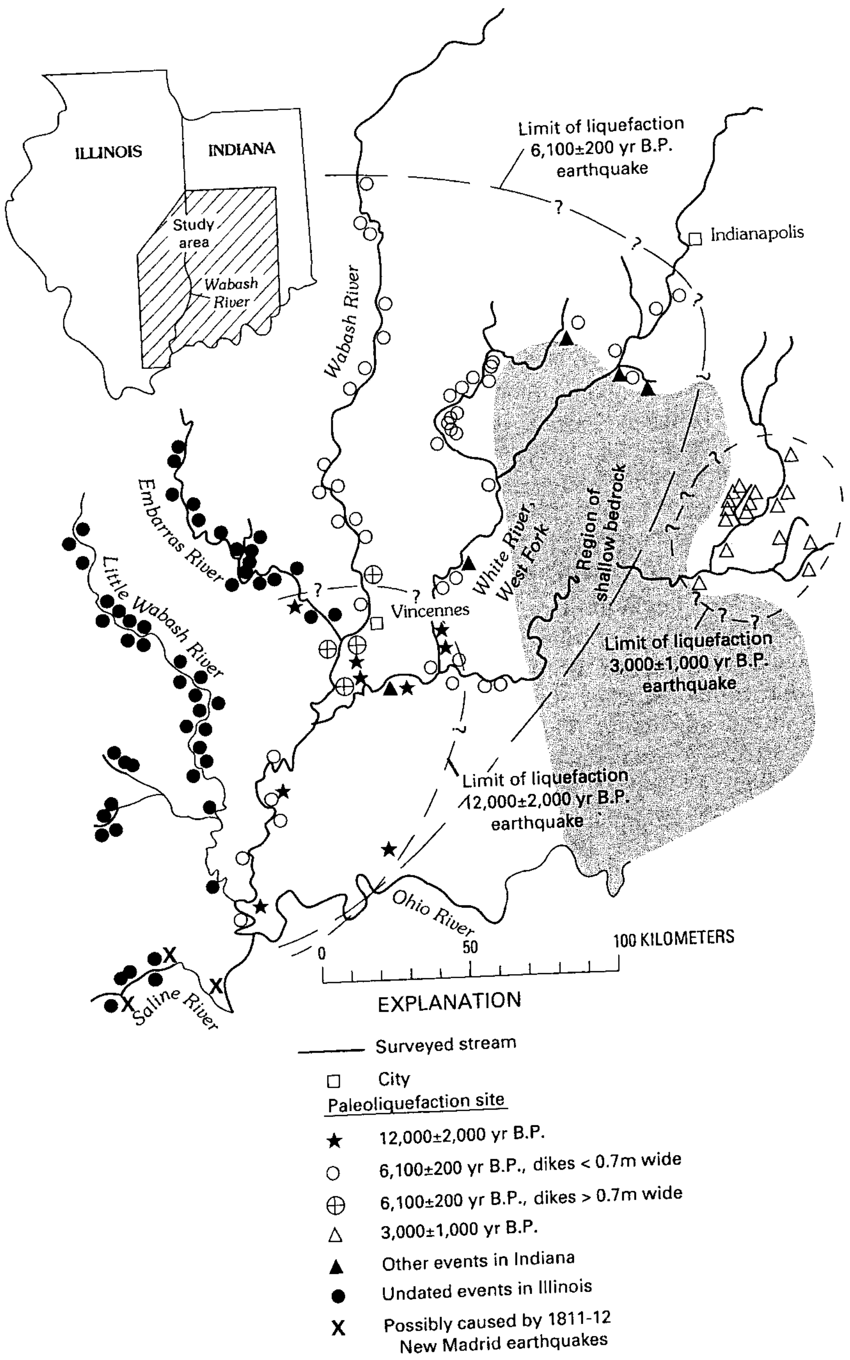

Figure 7.19 Map showing area searched for liquefaction features, showing sites where paleoliquefaction features (mainly dikes) were discovered, and showing regional limits of liquefaction for different earthquakes. About 10 percent of the length of the rivers searched has freshly eroded exposures. Only exceptionally are there no fresh exposures of mid-Holocene or older sediments within a 20-km length of river; no suitable exposures are in the region of shallow bedrock on the map. Liquefaction sites on the map generally denote exposures with numerous dikes. Some sites in the southern part of the study area have unweathered dikes near the surface, probably induced by the 1811–12 New Madrid earthquakes. Dike widths on the figure were measured at least 1 m above the base of the dike. Sites with dikes having a width >0.7 m are shown for the 6100-yr-B.P. earthquake. Note the core region of exceptionally large dikes around Vincennes. (Modified from Munson *et al.* (1994) and Obermeier *et al.* (1993).)

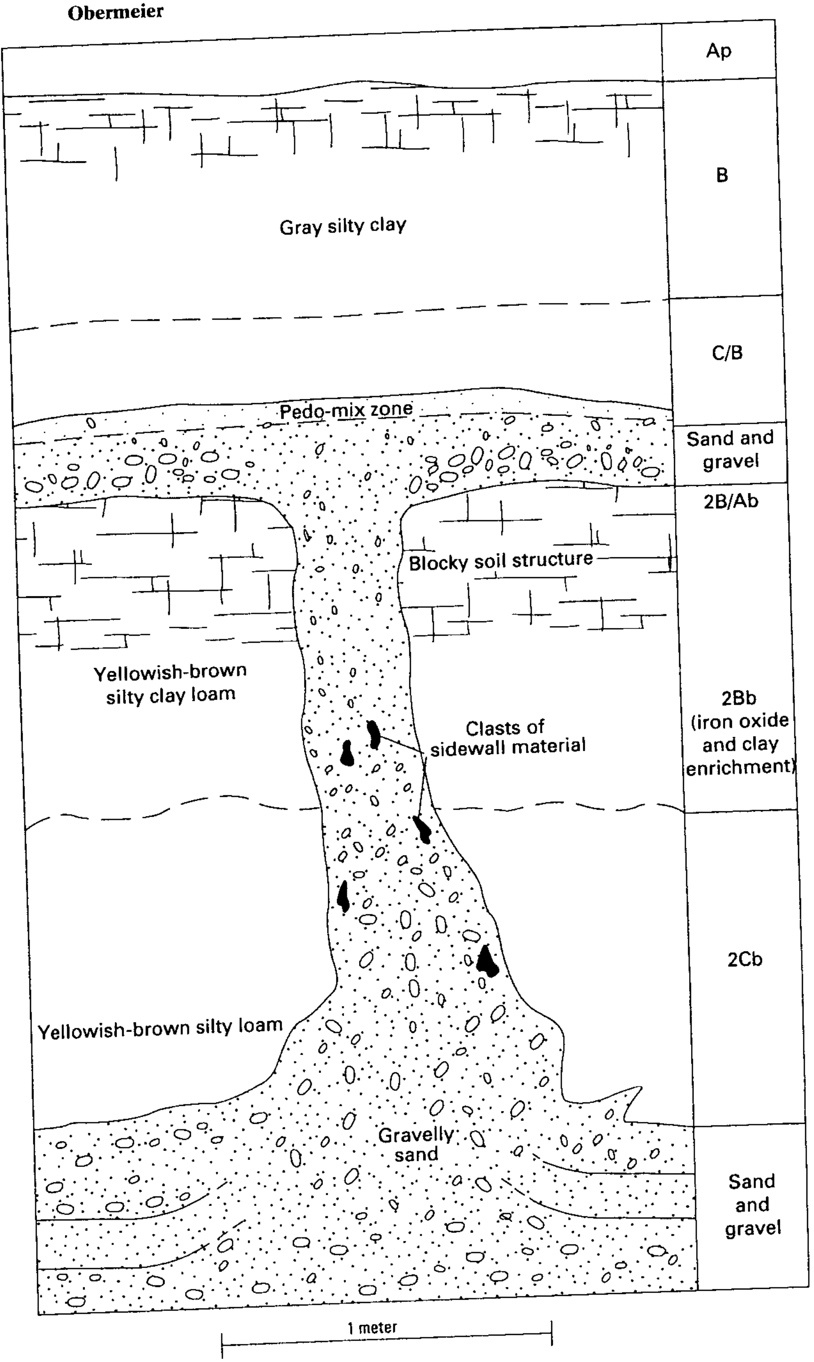

between sand and clay strata rather than lie on a paleosol, and sills probably would have some dikes branching up.

7.4.3.2 Ages of Dikes

Radiocarbon dating and archeological evidence at widespread sites show that most of the liquefaction features in Fig. 7.19 resulted from a single earthquake 6100 ± 200 years ago (Munson *et al.*, 1992, 1994). Very large dikes with extensive sand blows from this earthquake are centered about Vincennes, implying a nearby epicenter. The evidence for two pulses of venting admits the possibility of more than one strong earthquake spaced very closely in time. Such close spacing of strong earthquakes happened in the nearby 1811-12 New Madrid earthquakes.

The next strongest earthquake in the Wabash Valley took place about 12,000 years ago. Again the largest dikes appear approximately central to the regional distribution. A smaller event occurred about 3000 years ago. Other earthquakes are represented by scattered dikes of late Pleistocene age, but the paucity of exposures in Pleistocene deposits precludes determination of a regional pattern of sizes.

Bracketing of the time when the dikes west of the Wabash River formed has not yet been done. However, the severity of weathering of vented material and in dikes shows that almost all the dikes have ages of thousands of years.

7.4.3.3 Evidence for Seismic Origin

All aspects of the Wabash Valley dikes can also be observed in the 1811–12 New Madrid earthquakes' meisoseismal region, which has a physical setting generally similar to that of the Wabash Valley. An earthquake-induced liquefaction origin is interpreted for the dikes of the Wabash Valley for the following reasons, considered in combination: (1) The dikes widen downward, or else have walls that are parallel (agreeing with a lateral spreading origin); (2) dikes are approximately linear in plan view and exhibit strong parallel alignment in local areas; (3) the dikes vented large quantities of sandy sediment to the surface; (4) material in the dikes fines upward and was transported upward; 5) bedding in some source beds is homogeneous, and the contact of source beds with overlying fine-grained sediment is highly disturbed in some places;

Figure 7.20 Diagrammatic vertical section showing general characteristics of buried sand- and gravel-filled dikes along the Wabash River. Source beds are Holocene point-bar deposits or late Wisconsinan age braid-bar deposits overlain by much finer overbank sediment. Sediment in source beds beneath dikes shows evidence of flow into dikes. Gravel content and size decrease upward in dikes at many places. The column on the right side of the figure contains pedological descriptions of host materials.

(6) flow structures project upward from the source zones into the bottom of the dike; (7) many dike sites are in flat and topographically elevated landforms, located at least several kilometers from any high, steep slopes that might have existed at the time of formation of the dikes, and therefore could not have been induced by nonseismic landsliding; (8) other nonseismic mechanisms such as artesian springs that could produce similar features are not plausible at many dike sites because of the lack of topographic relief and the local geologic setting; (9) the size and abundance of the dikes along the Wabash River, the area where data are most complete, generally decreases with increasing distance from a core region of largest dikes (Fig. 7.19); and (10) large regions in the same geological setting, with liquefiable sediment, have been searched far north of the Wabash Valley seismic zone and have no dikes (Munson *et al.*, 1994). Detailed discussion of these factors is given in Obermeier *et al.* (1993).

Sills within the cap such as those illustrated in Fig. 7.17 are sparse in the Wabash Valley region. I have observed elsewhere a similar lack of sill development in the cap. For example, in the banks of the Chehalis River, near Centralia, Washington, there are many dikes exposed that doubtlessly were induced by the M 7.1 earthquake of Olympia, Washington, in 1949 (Obermeier, 1994a). The field setting is that of a thick (6- to 8-m) cap of stiff clay without pronounced horizontal planes of weakness that overlie medium sand. The dikes along the Chehalis River have a tabular morphology that strongly resembles that seen in the Wabash Valley, because very thin (1-cm) dikes commonly extend upward several meters or more before pinching together.

7.4.3.4 *Paleoseismic Implications*

Historical earthquakes in the Wabash Valley, with magnitudes as high as M ~ 5.5, have not been reported as having caused liquefaction. Undoubtedly the paleoearthquakes in the Wabash Valley far exceeded the magnitude of any historic events because of the large areal distribution of liquefaction effects and the large size of some of the dikes. The magnitude of the 6100-year-old event is estimated to be M ~ 7.5 (Obermeier *et al.*, 1993).

7.4.4 Coastal Washington State

Tidal marshes buried in coastal Washington and nearby coastal Oregon record episodes of sudden submergence accompanied by tsunamis during late Holocene time; these episodes have been ascribed to great (M ~ 8 to 9) earthquakes on the basis of the large region along the coast that appears to have submerged simultaneously (Atwater, 1987, 1992; Darienzo and Peterson, 1990; Nelson, 1992a). No direct evidence of strong shaking had been discovered to corroborate that seismic shaking accompanied the episodes of submergence, however.

These inferred earthquakes are interpreted to have originated by rupture along the thrust fault where the oceanic (Juan de Fuca) plate is being subducted beneath the continental (North America) plate-the Cascadia subduction zone (Fig. 7.21B). However, no strong Cascadia earthquake has occurred during the time of written history in the Pacific Northwest, some 200 years. Modern seismicity on the subduction zone is limited to scattered, small earthquakes, none with thrust mechanisms in the region of sudden submergence.

Atwater (1992) inferred at least two occurrences of coseismic subsidence when great earthquakes struck the coast of Washington, including the region around the Columbia River valley, during the past 2000 years. Strong evidence indicates that one event was about 300 years ago, and less widespread evidence indicates that another event occurred between 1400 and 1900 years ago. The portion of the thrust fault that ruptured and provided energy for seismic shaking was most likely a small distance offshore (a few tens of kilometers), on the basis of the location of the subsided zone (Atwater, 1987), heat-flow data (Hyndman and Wang, 1993), and strain data (Savage and Lisowski, 1991).

The inferred earthquakes would be expected to have caused such strong shaking as to have produced abundant liquefaction features near the coast, even in sediments having moderate to low susceptibility. To verify occurrence of strong shaking, I initiated a search for liquefaction features in cutbanks of islands in the Columbia River.

7.4.4.1 *Columbia River Features*

Many large islands were searched between the towns of Astoria and Portland (Fig. 7.21). These islands originated as braid bars on a grand scale. The islands are flat, poorly drained, and swampy. Large portions are submerged during the highest tides. Strong currents and wave pounding are severely eroding many islands and as a result have sculpted clean, vertical banks as high as 2 m, which extend from water level to the top of the banks. Significant areas are also being cleaned in plan view by tides.

The banks of the islands between Astoria and Longview expose mainly soft clay-rich silt deposits (Fig. 7.22). Age at the base of the exposed clay-rich cap is less than 1000 and more than 600 years on most islands, on the basis of radiocarbon ages of fossil marsh plants (genus *Scirpus*) found in growth position and now just above the level of low tide.

Regional stratigraphic control of sediments exposed on the islands is excellent. About 1.5 m below the top of the banks is a tan horizon with a thickness of a few centimeters. This horizon is exceptionally rich in volcanic ash. About 10 to 15 cm lower is a blue-gray horizon, generally several centimeters thick, also rich in ash. Very locally, rounded pumice clasts as large as 5 cm in diameter occur in the lower ash horizon. Chemical analysis shows that the ash and pumice have minerals and elements identical with those of an eruption from Mount St. Helens in A.D. 1480–82 (C. D. Peterson, Portland State

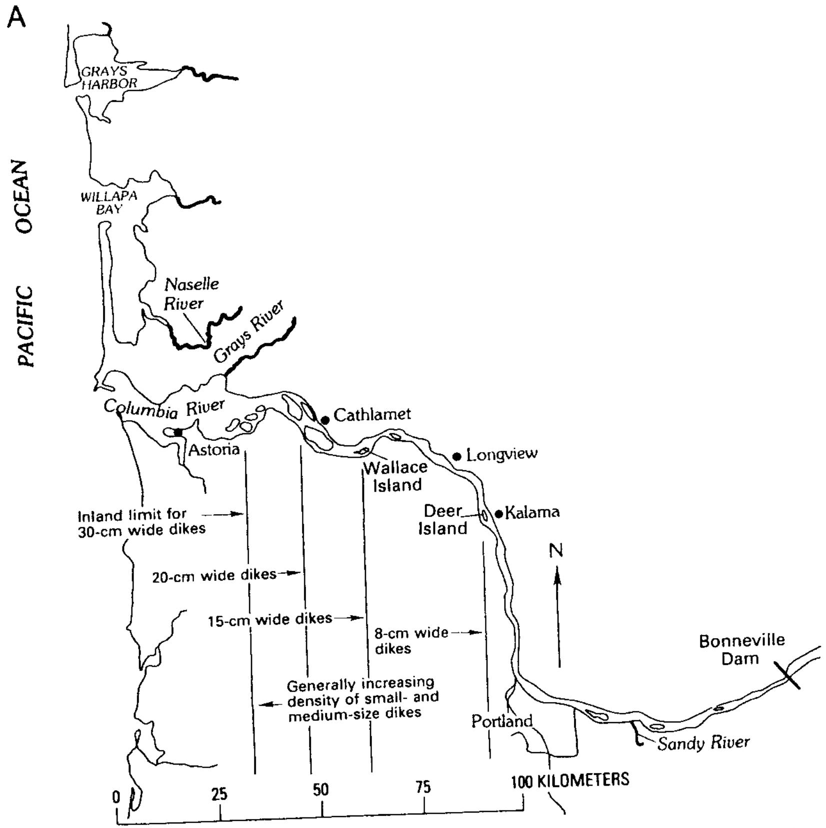

Figure 7.21 (A) Map showing that part of the Columbia River where banks of islands were searched for paleoliquefaction features. These islands have ages between 600 and 1000 years at most places. Sands beneath islands are fine to medium grained and generally are at least moderately susceptible to liquefaction. Maximum dike width is measured at least 1 m above the base of the dike. (B) Index map on next page shows Cascadia subduction zone.

University, Portland, OR, written communication, 1992). Therefore, the radiocarbon ages on fossil marsh plants and the ash data show that the sediments are old enough to record liquefaction associated with the 300-year-old down-dropping event but probably are not old enough for the event of 1400 to 1900 years ago.

At many places sand is exposed immediately beneath the clay cap. Alluvium that makes up the islands, generally thick, fine- to medium-grained sand, probably typically exceeds 100 m in thickness. Conditions on many islands are nearly ideal for formation of large liquefaction-induced features. Not only

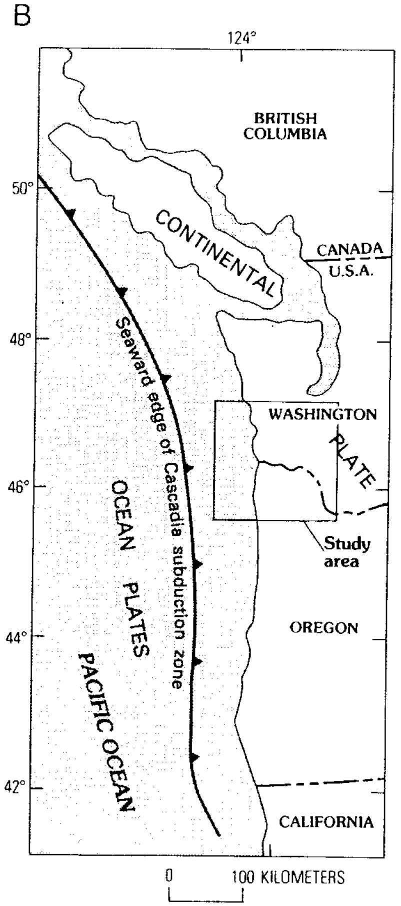

Figure 7-21 Continued

is the cap thin, but the ground water table has almost certainly been within a meter or so of the ground surface since the islands formed. The tidal range at these islands is about 2 to 2.5 m, and high tides inundate parts of the islands and doubtlessly have done so for at least several hundred years.

Hundreds of dikes have been found along 9 km of vertical banks in scattered islands upstream as far as Deer Island (Figure 7.21A). At some places the tabular nature of the dikes is exposed in plan view. Maximum dike widths and abundance of dikes tend to decrease in the upstream direction. Fig. 7.22 illustrates relations observed at many islands. A thin sand sheet lies on a weakly developed, very soft soil that is about 1 m below the present

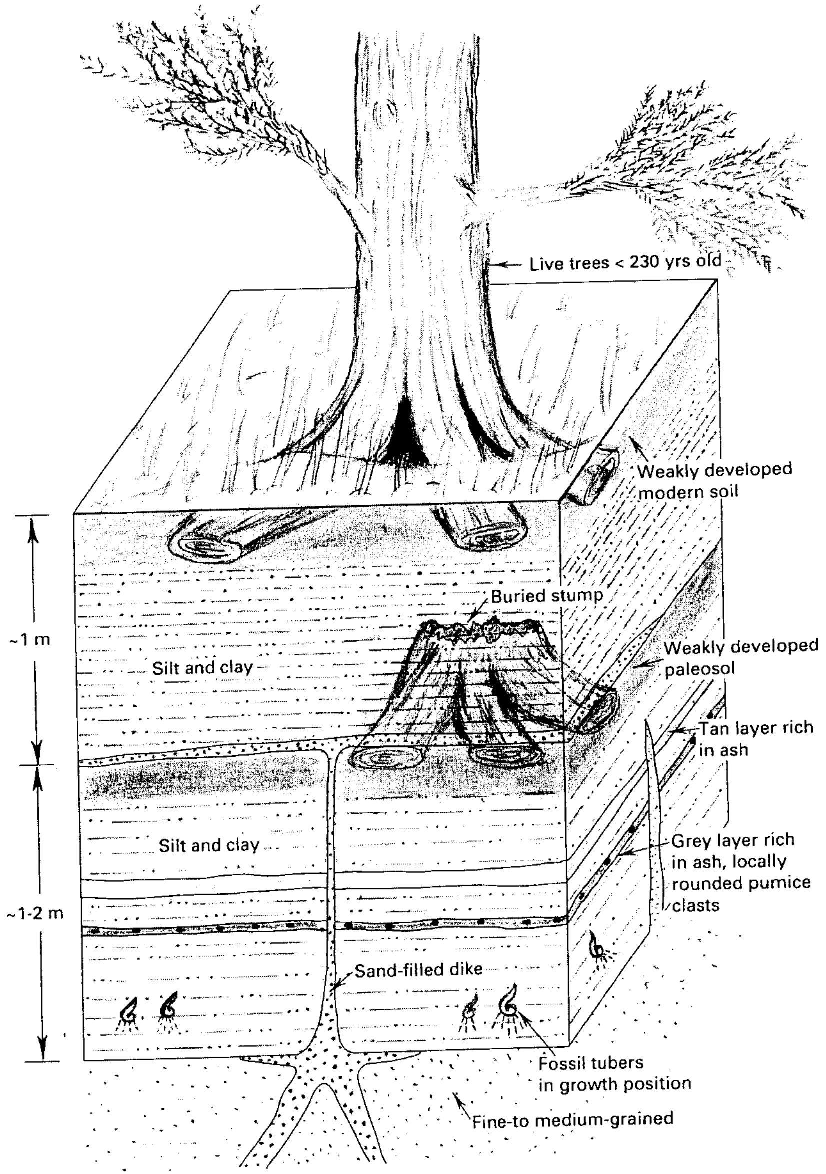

Figure 7.22 Block diagram showing typical field relations at liquefaction sites in the Columbia River islands. A sand-filled dike cuts through a 1- to 2-m thickness of soft silt and clay with a weakly developed soil at the top. The dike connects to a thin sand sheet on the soil horizon that is buried by a 1-m thickness of silt and clay. Tubers at widespread sites collected in their growth position near the base of the stratum cut by dikes have radiocarbon ages ranging between 600 and 1000 years. Widths of top of dikes are only several millimeters at most places.

surface. Locally, the upper few centimeters of the soil are contorted by small (centimeter-sized) folds and other soft-sediment deformations. The sand sheet is 1 to 4 cm in thickness and is as wide as 10 m. The sheet connects to a nearly vertical, narrow planar dike that widens downward markedly and connects to sand beneath the clayey cap. The width of the uppermost 5 to 15 cm of almost all dikes is only several millimeters or less. The width near the base of the cap is generally less than a few centimeters. Where pits were dug along the bottom of the cap, flow structures in the sand could be observed going into the base of the dikes. Pits also exposed sills as thick as 0.1 m running along the base of the cap. Rarely were sills observed to have intruded into the cap.

All dikes are interpreted to have been caused by the coastal downdropping earthquake event about 300 years ago for the following reasons: (1) The radiocarbon ages of sticks along the surface of venting agree with the 300-year-old downdropping event; (2) ages of trees (determined from tree rings) rooted in sediment above vented sand have maximum age values (about 200 years) that are reasonable for the 300-year-old downdropping event; (3) dikes generally increase in abundance toward the coast; and (4) maximum dike sizes (widths) increase toward the coast. The 1-m thickness of silt and clay above vented sand is interpreted to have been deposited following the regional downdropping from the subduction zone earthquake 300 years ago. This 1-m thickness agrees well with the estimates of coastal tectonic submergence (Atwater, 1987; 1992; Darienzo and Peterson, 1990).

The 1- to 4-cm-thick sheet of vented sand may be exceptionally thin because of the tidewater action or because of subaqueous venting. The surface of venting is submerged at high tide. Tidewater flows relatively fast in this area, so any large cones of sand initially vented to the surface could have been beveled off and the sand scattered over a large area.

Many dikes are so narrow at the top as to be hardly distinguishable. This same relation can also be observed infrequently in dikes in the Wabash Valley and in dikes in the meisoseismal region of the 1811–12 New Madrid earthquakes. The cause for this pinching is not known but may represent venting of a very water-rich mixture of sand and water through a very soft cap that closes partially after venting. The widest dikes (as much as 30 cm) on the Columbia River islands are interpreted to have formed by lateral spreading, because the sidewalls appear to be parallel.

Others have suggested that the properties of the soft silt cap on the islands may have prevented dikes from forming far inland; they suggest, instead, that only sills formed as a result of severe liquefaction over large regions. This suggestion is based on thin sills and sill-like features along the base of the cap that have been observed in samples collected in 8-cm-diameter tubes. I believe that such an interpretation is unlikely for two reasons: (1) I have never observed in other geographic–tectonic regions that extensive formation of sills in a soft cap was not accompanied by dikes, and (2) the mechanics of forming sills by severe liquefaction over a large region, without also forming dikes, does not seem plausible. In order for sills to form over a large area, the cap must be lifted to provide space for the intrusion. The force required to lift the cap must equal the weight of the cap. The simplest of calculations shows that the uplift hydraulic pressure to counteract the weight of a 1- to 2-m cap is much higher than the tensile strength of a soft cap. Therefore, dikes should develop. I can envision other mechanisms whereby small sills would form without liquefaction, however, as a result of seismic shaking.

7.4.4.2 Strength of Prehistoric Shaking

Subduction earthquakes can have very large variations in shaking characteristics, offering the possibility of an especially long duration of shaking at very low frequencies. Such uncertainties cause difficulty in interpretations of the strength of prehistoric shaking. Still, significant conclusions can be drawn for the earthquake of 300 years ago. Small dikes possibly with venting in the Columbia River islands appear to go inland as far as 90 km. These dikes very likely formed at an acceleration level on the order of 0.1 to 0.2 g (Obermeier, 1994a). These accelerations accord with both theoretically and statistically derived accelerations from seismological models for the scenario of an M ~ 8 subduction earthquake slightly offshore (Geomatrix, 1995), although the uncertainties are significant.

The lack of abundant very wide dikes throughout islands of the lower Columbia River valley also supports the seismological models noted earlier, which predict that exceptionally strong shaking should not extend very far onshore. Even though severe erosion of some islands has probably removed evidence of dikes wider than 30 cm at some places, there are many locales where erosion probably has been slight. (The widest observed dikes, 30 cm, are quite small in comparison to the width of dikes commonly found in the meisoseismal region of the 1811–12 New Madrid earthquakes or in the Wabash Valley.) Another plausible model consistent with observed liquefaction effects in the Columbia River islands is a subduction earthquake having a long duration of shaking at moderate to low peak accelerations and at an exceptionally low dominant vibration frequency (perhaps exceeding a few hertz). The fine sands that underlie the Columbia River islands are so thick and have such a low permeability that pore pressures would not dissipate between cycles of shaking, even at an extremely low frequency. In addition, the thick alluvial deposits of the Columbia River valley probably strongly amplify bedrock accelerations, irrespective of vibration frequency (Dickenson *et al.*, 1994). Therefore the sand deposits of the Columbia River should be especially susceptible to forming liquefaction features during a long duration of shaking, even at low to moderate accelerations and exceptionally low frequencies.

7.4.4.3 Ancient Marine-Terrace Features

Many ancient fluidization features have been identified in late Pleistocene marine-terrace deposits. The fluidization features can be seen for a span of 500 km in cliffs along the coast from central Washington to near the California–Oregon boundary (Peterson *et al.*, 1991; Peterson, 1992). The features are of particular interest because they admit the possibility of a long continuing record of subduction-zone earthquake shaking near the coast. The methodology for interpretation of an earthquake liquefaction origin is instructive.

Source beds for the fluidization features include beach sands and sandy gravels, and lagoonal sands. Clastic dikes are as much as 5 m in height. Dikes are filled with clean sand or gravelly sand at almost all places. Dikes are as wide as a meter in scattered locales. Some dikes have penetrated upward into dune sands or have cut through lagoonal muds and peat. Sills are particularly abundant. Sills commonly extend beneath lagoonal muds and peats; small, steeply dipping dikes branch off from these sills at many places and cut up into thin (less than 0.5 m) strata of low permeability at the surface. The largest sills are as much as a meter in thickness. Even thin sills can extend far laterally.

The possibility that the fluidization features were caused by wave action that induced liquefaction must be considered because the terrace deposits were laid down under shallow marine or shoreline conditions. Storm waves can impose significant shear stresses on the ocean-bottom sediments, even where the water depth exceeds 60 to 70 m (E. C. Clukey, Exxon Corp., Houston, TX, written communication, 1992). Wave-induced cyclic shear stresses are thought to cause liquefaction in sands and granular deposits in a manner analogous to seismically induced liquefaction (Nataraja and Gill, 1983). The action of storm waves pounding on beaches also seems plausible as a mechanism for forming fluidization features. For the fluidization features in the marine terraces of coastal Oregon and Washington, though, the mechanism of wave-related liquefaction probably can be eliminated at some sites because dikes extend up into dune sands where wave action seems unlikely. Additionally, some dikes and sills cut lagoonal deposits at places that probably would have been protected from wave action. Significant artesian pressures at these lagoonal sites also are implausible. Thus a seismic liquefaction origin seems probable for some of the features along the coast.

7.5 FEATURES GENERALLY OF NONSEISMIC OR UNKNOWN ORIGIN

Deformation features in unconsolidated sediments can form by many nonseismic processes (Sims, 1978; van Loon, 1992). Figure 7.23 provides a graphical overview of how various seismic and nonseismic processes can create certain features. Note that some features are never produced seismically, whereas others (e.g., warped and folded bedding) can be induced from either seismic or nonseismic mechanisms. In the following section I briefly survey the voluminous literature of soft-sediment deformation, making special note of common

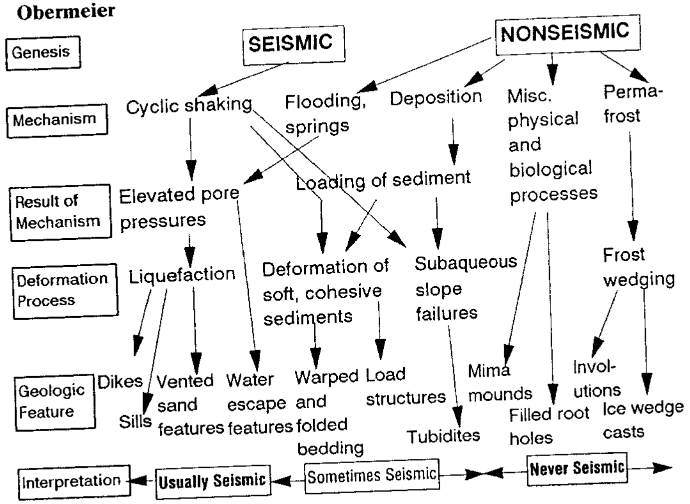

Figure 7.23 Graphical explanation of how various geological features of sediment deformation can be caused by either seismic or nonseismic causes. Much of the ambiguity in genesis arises because a given *deformation process* or *result of mechanism* can be caused by either seismic or nonseismic mechanisms. Features at the left side of the diagram are usually caused by earthquakes, whereas features on the right side are never caused by earthquakes.

features that might be confused as resulting from seismic shaking. Assignment of unambiguous origin to isolated occurrences of such features may be impossible without determining their regional pattern.

7.5.1 Terrestrial Disturbance Features

Artesian conditions cause abundant nonseismic sand boils (vented sand volcanoes) to form in lowlands near the levees of the Mississippi River, USA, every few years (Kolb, 1976). The sand boils are typically restricted to a belt within 0.5 to 1 km of the levees, which aids in interpretation of origin. The cone-shaped, external form of the sand vented to the surface by these sand boils generally is very similar to that of a solitary sand blow caused by earthquake-induced liquefaction. Internally though, there can be significant differences, especially for the larger vented features. Going upward in sand boils are rythmic, planar strata of silty sand to clean sand that dip away from the central part of the sand boil; the individual strata are almost invariably much more sharply defined, more uniform in thickness (typically about 1 cm), and have a more narrow range of grain sizes than sediment vented in response to seismic liquefaction. Especially relevant for paleoseismic studies is that the sand boils have vented through dikes that are almost always more or less circular. Their diameters are commonly a few decimeters, but can be as much as a meter.

Fortunately for paleoseismic studies, the regional pattern of occurrence of seismically induced liquefaction features generally should become evident as earthquake magnitude increases, which reduces the likelihood of confusion with nonseismic sand boils.

Slumps along stream banks are commonplace in both seismic and nonseismic conditions. Sliding blocks (of dominantly horizontal movement) can develop in special nonseismic field settings and can resemble seismically induced lateral spreads. I believe that generally it is not worthwhile to attempt to assign seismic or nonseismic origin to prehistoric slumps along actively eroding stream banks; there are too many uncertainties about the physical setting when such an ancient slump formed. For example, questions crucial to interpretation include the initial ground slope and the possibility of a stream bank having been undercut by an eroding stream. These questions are virtually impossible to resolve. Slumps in loose, fine sands are especially difficult to interpret because they may be prone to static liquefaction even on relatively gentle slopes (Lade, 1992). Methods to interpret the seismic or nonseismic origin of landslides in geologic settings other than eroding stream banks are discussed in Chapter 8.

Thrown trees can excavate pits that resemble liquefaction-induced craters. Sediment filling in these pits typically does not have the orderly progression of clasts found in liquefaction-induced craters. Pits excavated by thrown trees sometimes can be distinguished from liquefaction-induced craters by the absence of feeder dikes or sediment from depth. Thrown trees can also form tabular breaks as roots are pulled through a fine-grained cap. The breaks can be filled with sand, gravel, or other sediment dragged into the break. However, the dragged sediment tends to be arranged haphazardly and have a much larger range of grain sizes than an intrusion formed by seismic liquefaction.

Mima mounds (also called prairie mounds or pimple mounds) have had many origins attributed to them, most commonly to animal burrowing, but also to seismicity (Berg, 1990). Mima mounds in the meisoseismal region of the 1811–12 earthquakes are domes less than 30 m in diameter and 1 m high. In many upland areas, though, the mima mounds are formed on nonliquefiable deposits and therefore are not of earthquake origin (Saucier, 1991a). Mounds on alluvial lowlands can be identified as not resulting from earthquake liquefaction if excavation shows an absence of vents to connect the mounds to underlying source beds (Fuller, 1912, p. 80).

7.5.2 Features Formed in Subaqueous Environments

It is not possible in this chapter to describe and discuss a great number of features, mainly syndepositional in origin, that can also be triggered by seismic shaking. Four types of features, however, are considered: (1) load structures in muds; (2) water-escape structures; (3) sheet slumps, warped bedding, and recumbent folding; and (4) bedding caused by turbidity flow. For an overview of the myriad possibilities, the reader is referred to Lowe and LoPiccolo (1974), Lowe (1975), Reineck and Singh (1980), Allen (1982), Mills (1983), Jones and Preston (1987), and Einsele *et al.* (1991).

Load structures are bulbous bodies of sandy or silty material that intrude downward into underlying weaker, finer grained muddy sediment. *Pseudonodules* form when overlying sandy or silty sediments become detached and sink to become isolated kidney-shaped bodies encased in the underlying mud. In *load-casted ripples,* sandy or silty intrusions form because of the unequal loading of migrating ripples of sand on a mud substratum. Load-casted ripples show progressively deformed radial internal lamination caused by the rotation of the ripple cross-laminations as the ripples sink (Dzulynski and Walton, 1965, pp. 146–149). *Convolute bedding* is manifested as more-or-less regular folds which are developed either throughout or confined to the upper part of a single sedimentary unit (Allen, 1982). Similar to load structures in mud are *ball-and-pillow structures* in which kidney-shaped bodies of sand, locally slightly silty, have foundered into a cleaner sand (see Pettijohn and Potter, 1964, Plate 100A). Ball-and-pillow structures are abundant in many glaciofluvial deltas, where huge volumes of sand were quickly deposited.

Water-escape features include *dish structures, pillars,* and *convolute laminations* (Pettijohn and Potter, 1964; Lowe and LoPiccolo, 1974). Dishes appear to form as upward-moving water locally flows beneath laminations of lower permeability and escapes by horizontal flow. Pillars are circular columns or sheet-like zones of structureless or swirled sand, sometimes bounded by dark laminations, that cut steeply through sand ranging from structureless to laminated. Note that water escape only requires elevated pore pressure, which can be seismic or nonseismic in origin. Figure 7.24 shows field relations commonly observed between dish structures, pillars, and convolute bedding. I have observed all these features and relations in proximity to dikes at sites of earthquake-induced liquefaction.

Features such as *sheet slumps, warped beds* (Allen, 1982), and *recumbent folds* (Allen and Banks, 1972; Sims, 1973; Owen, 1987) are well represented in the geologic record. Audemard and de Santis (1991) observed that during a moderate earthquake, warping developed within the uppermost 0.2 m of sediment, where mud overlaid a thin sand stratum. Sims (1973) observed low-amplitude folds in the uppermost 4 to 5 cm of lake sediments (mud with very fine sandy laminae and partings) and interpreted that the folds developed in response to a nearby magnitude 6.5 earthquake. Thus, deformation of very soft, cohesive sediments can result from either cyclic shaking or from loading of sediment (Fig. 7.23).

Widespread *turbidites* are very common in marine sediments (see numerous articles in the journal edited by Cita and Lucchi, 1984). It is often tacitly assumed that such a distribution strongly suggests a seismic origin to turbidites and warrants the name *seismites.* Although a widespread synchronous distribution is suggestive of seismicity, other mechanisms such as storm-induced wave trains or tsunamis can be responsible. An excellent example of how turbidites can be used in conjunction with other evidence for tectonism (regional downdropping) is given in Adams (1990).

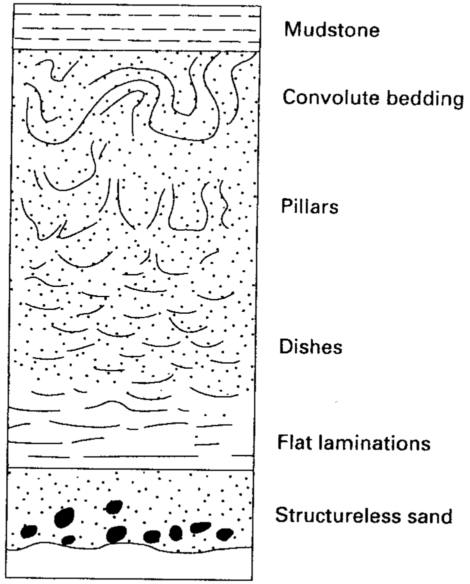

Figure 7.24 Schematic vertical section showing commonly observed vertical sequence of the sedimentary structures of convolute bedding, pillars, and dishes. Example shown is in thick sandstone beds. [From Lowe and LoPiccolo (1974); reprinted with permission of the Society for Sedimentary Geology.] I have observed this sequence of structures in sediments exposed in the banks of a river near the meisoseismal zone of the 1886 Charleston earthquake.

7.5.2.1 *Paleoseismic Examples*

Proving a regional, coeval deformation of sediment in fluvial deposits is extremely difficult; proving such development in lakes, especially deep lakes, can be much more tractable. An illustrative example is given by Ringrose (1989a). Features of probable seismic shaking origin were found at widespread exposures in sediments of a late Quaternary glacial lake, located in Scotland. The sediments consist mostly of laminated silt and sand. Deformation features developed in two episodes about 10,000 years ago. The features are restricted to well-defined horizons of very large areal extent. Figure 7.25 shows how the styles vary from most severe (Fig. 7.25A) to marginal (Fig. 7.25D). The most severe deformations are centrally located in a geographic sense and are charac-

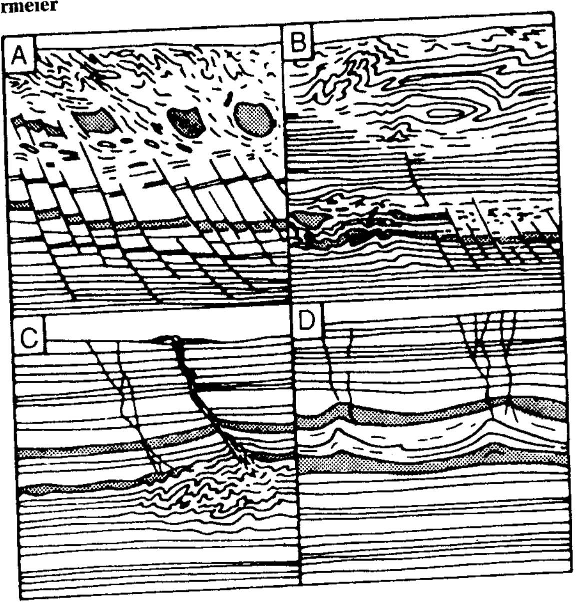

Figure 7.25 Schematic depiction of sediment deformation structures observed by Ringrose (1989a) in late Quaternary lake sediments. Sediment consists of laminated silts and sands (stippled). (A) through (D) represent change from most severe deformations to slightly distinguishable deformations. Each box is about 2 m across.

terized with the *fault-grading stratigraphy* of Seilacher (1969). This stratigraphy refers to a fourfold sequence, going from the top down: (1) completely fluidized sediment, (2) partially coherent sediment layers, (3) faulted layers, and (4) undeformed sediment. Evidence of deformation in Fig. 7.25D is so slight that beds are only gently warped, and there is very minor evidence for fluidization.

In eastern Canada, Adams (1982) has reported the presence of thin contorted zones within silt and clay *varves* of early Holocene age. Synchronous contortions occur at widely scattered glacial lake sites, and there is a crude regional pattern with greatest deformations at the center. Thus, a paleoseismic origin was interpreted. Morner (1985) has reported a similar type of finding in glacial lake varves of early Holocene age in Sweden; association of deformed varves with tectonic faulting, fracturing, and slumping led to a seismic interpretation.

7.5.3 Features Formed by Weathering

Distinguishing liquefaction-induced features can be difficult where weathering effects are severe. A wide variety of features produced by chemical weathering

in the southeastern United States mimics those caused by earthquake liquefaction (Obermeier *et al.,* 1990). The boundary between the E (eluviated, or bleached) and B soil horizons is commonly abrupt and irregular and is characterized by narrow, near-vertical *pedogenic tongues* of the white E horizon that penetrate downward into the B horizon. Locally, tongues of E horizon sand extend more than a meter into a thick, red to brown, clayey B horizon. Tongues of this size and shape can give the impression of fractured and brecciated ground and might be mistaken for liquefaction features unless examined carefully. Pedogenic tongues can range in morphology from tubular (Gamble, 1965) to planar (defining B horizon polygons; Nettleton *et al.,* 1968a).

Another category of pedogenic feature that might be confused with earthquake-induced liquefaction is the BE′ horizon, which forms from the progressive chemical destruction of a clay-rich Bt (argillic) horizon (Daniels *et al.,* 1966; Nettleton *et al.,* 1968a,b; Steele *et al.,* 1969). Sharp contacts between the leached quartz sand areas and the much more clayey material may suggest to the uninitiated that this feature formed by some type of ground disruption, possibly ancient liquefaction. Examples of both phenomena just described are diagrammed in Obermeier (1994b, Figs. 36, 37).

7.5.4 Features Formed in a Periglacial Environment

Two classes of features produced in a periglacial (freezing–melting) environment, loosely defined as (1) *involutions* and (2) *ice-wedge casts,* can resemble features that have an earthquake-induced origin. Involutions are surficial manifestations of frost-related stirring (*cryoturbation*) and are often characterized by distortion and mixing of the uppermost meter or so of the ground. Ice-wedge casts are downward-pinching, planar, nearly vertical features that originated by thermal contraction of frozen ground.

Vandenberghe (1988, p. 182) lists six types of involutions in terms of symmetry, amplitude-wavelength ratio, and pattern of occurrence. The features range from individual folds of small amplitude and large wavelengths (resembling slightly warped bedding caused by earthquake shaking) to intensely convoluted forms having amplitudes generally between 0.6 and 2 m (again resembling earthquake-induced convoluted bedding); load structures, diapirs, and dikes are also common. The genesis of involutions is probably related to three main process categories: load casting during melting, pressures in water trapped between freezing fronts, and pressures and heaving caused during freezing (Vandenberghe, 1988). Involutions are associated with ground patterned by freezing (*patterned ground*) and ice-wedge casts at many places, however, which helps in interpretation.

Ice-wedge casts (Black, 1976), also called *ground-wedge pseudomorphs* (Harry and Gozdik, 1988), result from ground cracking caused by contraction of frozen ground. Wedges of ice then form in the cracked ground. Later, when permafrost melts, host sediment slowly replaces the melting ice and forms an ice-wedge cast. An earthquake-induced origin can be incorrectly deduced for ice-wedge casts, especially in clean granular host deposits. Strong vertical alignment of infilling sediment commonly takes place, especially in narrow casts. This vertical alignment superficially resembles the effects of upward-flowing water such as winnowing out of fine grain sizes and fluidization. However, a liquefaction origin is almost unequivocally eliminated if there are no feeder dikes going from the host to sediments in the cast. Field studies in the northeastern United States (Stone and Ashley, 1992) have shown that the uppermost meter of a cast is often composed of fine sand and silt, including pebbles polished by wind abrasion, rather than sediment from depth vented to the surface. Stone and Ashley also found that air photographs can reveal a well-developed polygonal network of wedge structures, thereby demonstrating an almost certain permafrost origin.

7.6 ESTIMATION OF STRENGTH OF PALEOEARTHQUAKES

Interpretations of the strength of paleoearthquakes can be made using several independent techniques. First, a very crude association exists between severity of shaking, as measured by the Modified Mercalli intensity scale, and the threshold for formation of liquefaction effects and soft-sediment deformations such as pseudonodules and small recumbent folds. In a second approach (magnitude bound method) applicable to field situations where the regional extent of liquefaction from a paleoearthquake can be estimated, a probable minimum magnitude can be determined. In a third method (the engineering-based method of Seed *et al.*, 1983), limits can be placed on accelerations that formed the liquefaction features in many field situations; these accelerations can then be compared with estimates of accelerations, determined from seismological models or statistical analysis, for assessing magnitude. Yet another engineering-based method with great promise uses an energy method for assessing the likelihood of liquefaction at a site (Law *et al.*, 1990). A more geologically based method with much promise would make use of dike width as a measure of the severity of lateral spreading, and thereby the strength of shaking. Such a method would be a variation of the Liquefaction Severity Index of Youd and Perkins (1987) and its updated version (Bartlett and Youd, 1992), which is a quantitative method for estimating the maximum amount of lateral spreading as a function of earthquake magnitude and distance from the seismic energy source.

The methods discussed next for estimating prehistoric earthquake magnitude require locating the epicentral region. I suggest using the regional pattern of maximum dike widths as an easy means to approximate this region. Where field data are adequate, a preferable measure is the sum of dike widths normalized to the amount of outcrop (P. J. Munson, Indiana University, Bloomington, IN, oral communication, 1994). Maximum dike width is used rather than density of dikes because the density generally is highly sensitive to cap thickness (Ishihara, 1985; Obermeier, 1989). Lateral spreading, alternatively, is so insensitive to cap thickness as to not even be used as a parameter for the Liquefaction Severity Index (Bartlett and Youd, 1992).

7.6.1 Association with Modified Mercalli Intensity

The Modified Mercalli intensity (MMI) value is a qualitative measure of earthquake-induced damage (Wood and Neumann, 1931). The scale ranges from I to XII, with I representing the level at which shaking may be felt slightly and XII representing total destruction. MMI of about VI is the threshold for widespread development of small-scale soft-sediment deformation features such as folds, pseudonodules, contorted laminations, and recumbent folds (Sims, 1975).

Although liquefaction effects have occurred at MMI values as low as V and VI (Keefer, 1984), the lowest intensity at which liquefaction-induced features can become common is a value of VII, where highly susceptible deposits are present (National Research Council, 1985, p. 34). Values of VIII to IX are generally required before liquefaction-induced ground failure becomes severe enough to cause damage to buildings. A serious shortcoming of use of MMI values as a measure of the strength of shaking of prehistoric earthquakes is caused by the very crude association with ground failure effects. Still, associating intensity effects with distance from the energy source offers the ability to place crude limits on earthquake magnitude (Galli and Ferreli, 1995).

7.6.2 Magnitude Bound

Figure 7.26 shows the distance from the epicenter to the farthest observed liquefaction effect at the ground surface (plan view), such as venting of sand or ground fissuring. The data are from worldwide earthquakes in a wide variation of tectonic and alluvial settings. The sites of liquefaction range from having thin to thick alluvium. Amplification of bedrock accelerations is probably small for thin alluvium, whereas for thick alluvium the amplification is undoubtedly as high as 2 to 2.5 at many places (Idriss, 1990). Liquefaction susceptibility is also doubtlessly very high at many of the farthest sites. Therefore, using the bound in the figure should provide a minimum estimate of magnitude of paleoearthquakes, especially in regions where conditions are less than optimal for forming liquefaction effects.

The farthest sites of liquefaction effects on the ground surface (in plan view) often cannot be determined in a paleoliquefaction search (normally in

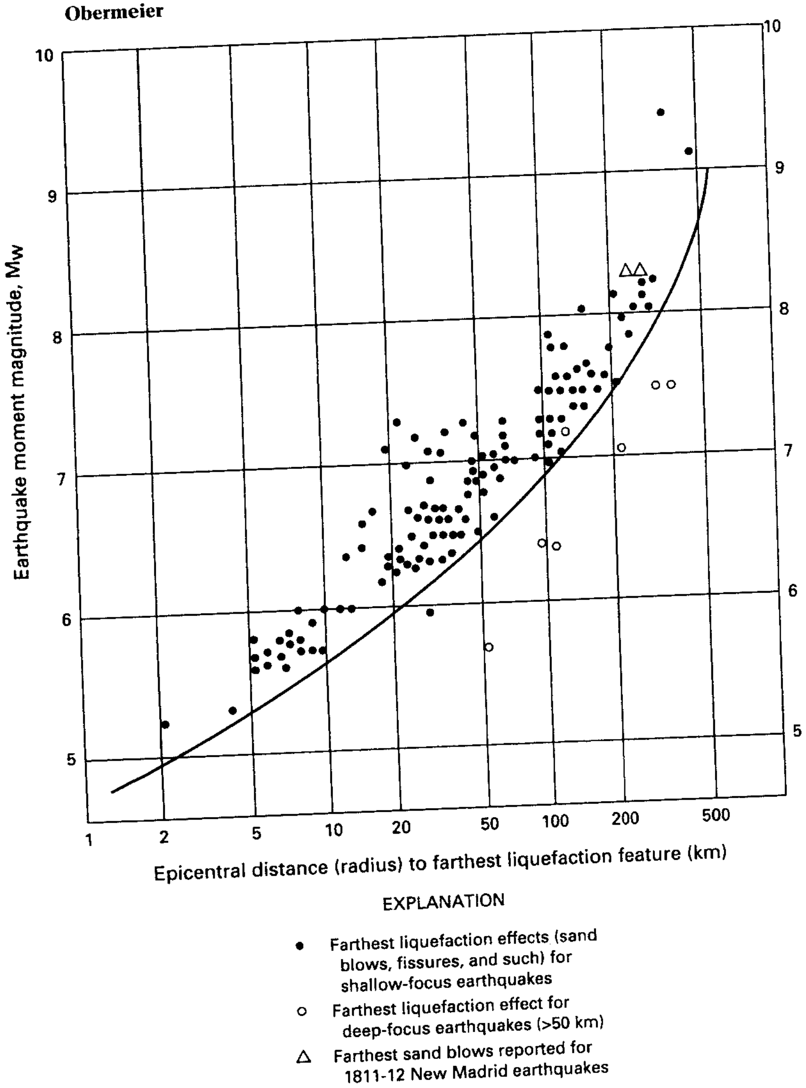

Figure 7.26 Relationship between earthquake moment magnitude (M_w) and distance from earthquake epicenter to the farthest liquefaction effect (venting to the surface or ground fracturing), with bound suggested by Ambraseys (1988). Curve separates data from earthquakes worldwide that had focal depths <50 km from those having depths >50 km.

sectional view). However, it has been my experience that this farthest distance can be reasonably approximated if a very large amount of exposure is searched in sectional view. A lower limit magnitude thus can be established by using the plot in Fig. 7.26. Two illustrative examples are given on the basis of my field experience, one for the Charleston earthquake of 1886 and the other for the New Madrid earthquakes of 1811–12. Both examples are regions of widespread moderate to high liquefaction susceptibility and probably at least moderate amplification of bedrock accelerations. Using the farthest liquefaction effects observed (90 to 100 km) at the time of the 1886 Charleston earthquake as a point on the outer bound of Fig. 7.26 yields an estimated minimum magnitude of about M 6.8; actual magnitude was M ~ 7.5. I have found small liquefaction features (unweathered dikes extending almost to the surface) as far as 100 km from the epicenter of the 1886 earthquake that were almost certainly caused by that earthquake. In a similar vein for the 1811–12 New Madrid earthquakes, I have found liquefaction features (unweathered dikes extending nearly to the surface) in widely spaced regions as far as 250 to 275 km from the epicenter of the M ~ 8.3 event. Farthest effects observed in 1811–12 were the same distances in these widely spaced regions. Using Fig. 7.26 yields a magnitude of 7.5 to 7.7. What these findings suggest is that if effects of liquefaction are observed at the surface at the time of the earthquake, in the same region there should be an abundance of dikes that pinch together only slightly below the ground surface—and that some could be found in a search for liquefaction features. (Keep in mind though, that small, pinching-up dikes that do not approach the surface may extend much farther from the meisoseismal region.) In summary, my experience for the two earthquakes above, based on farthest discovered paleoliquefaction features that approach the ground surface (within 1 to 2 m), indicates that the estimates of magnitude using Fig. 7.26 are not outrageously lower than actual values, providing field conditions are favorable for liquefaction.

The outer bound line in Fig. 7.26 can sometimes be adjusted, in regions of historic liquefaction, to account for influence of the local setting on farthest development of liquefaction effects. Such an example is given in Obermeier *et al.* (1993).

7.6.3 Method of Seed *et al.*

A means to circumvent the problem of not being able to locate the distal effects of liquefaction, for the magnitude bound method above, is provided by the method of Seed *et al.* (1983, 1985). This method was developed to provide engineers with an estimate of the shaking threshold required to produce surface manifestations of liquefaction during future earthquakes (Fig. 7.27). The method can be adapted to paleoseismologic studies. The method is based on worldwide observations following many earthquakes, supple-

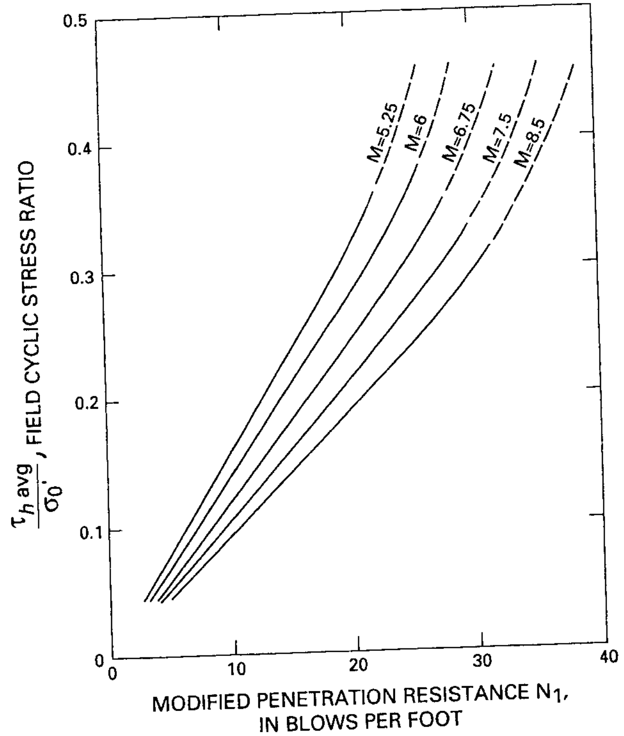

EXPLANATION

$\tau_{h\,avg}$	Average earthquake-induced horizontal cyclic shear stress
σ_0'	Vertical effective stress
N_1	Standard Penetration Test blow count measured in field, modified to blow count resistance at vertical effective stress of 1 ton/ft² (kg/cm²)

Figure 7.27 Curves for the method of Seed *et al.* (1983) used to evaluate the potential occurrence of liquefaction with accompanying venting of sand on appreciable ground cracks at a site on level ground. Curves are for clean sand deposits (average diameter >0.25 mm) and for different earthquake magnitudes (5.25 to 8.5). Points above and to the left of curves show conditions having high potential for liquefaction.

mented by extensive laboratory studies. The curves of Fig. 7.27 are not intended to indicate whether any very minor liquefaction at depth occurs (such as the liquefaction of an isolated thin sand bed); rather, the curves predict where liquefaction is sufficiently severe to produce scattered occurrences of limited venting or small ground openings (several centimeters) at the surface.

The method applies to level ground conditions. Sites of wide lateral spreads, especially near free faces, should be excluded because of the possibility of enhanced ground breakage with copious venting.

To use Fig. 7.27, the relative density of the source deposits is evaluated *in situ* by the standard penetration test (SPT) blow count method (Table 7-1). An adjusted SPT blow count value (the N_1 value of Fig. 7.27), which is the value corrected for site conditions of depth of the water table and static stress conditions of the source stratum, is then related to the shaking required to cause venting. Figure 7.27 shows the boundary curves for different earthquake magnitudes. The curves relate the N_1 value in clean sands to the field cyclic stress ratio. This is the ratio, on an element in the sand layer, of the average earthquake-induced horizontal cyclic shear stress ($\tau_{h\,\mathrm{avg}}$) to the static vertical effective stress (σ_0'). The field cyclic stress ratio due to earthquake shaking is computed from the following equation (Seed *et al.*, 1983):

$$\tau_{h\,\mathrm{avg}}/\sigma_0' = (0.65A_{\max}\,\sigma_0\,r_d)/(\sigma_0'g), \tag{7.1}$$

where $A_{\max}$ is the peak horizontal acceleration at the ground surface, σ_0 is the total overburden stress on the sand under consideration, σ_0' is the initial effective overburden stress (total stress minus pore-water pressure) on the sand layer under consideration, r_d is the stress reduction factor ranging from a value of 1 at the ground surface to a value near 0.9 at a depth of about 10 m, and g is the acceleration of gravity. The curves of Fig. 7.27 for various magnitudes are based on the premise that the expected duration (i.e., number of cycles) of strong shaking is longer for increasingly higher magnitudes.

The locations of the curves of Fig. 7.27 were picked partly by judgment. Liao *et al.* (1988) have used statistical regression methods to assess the probability of liquefaction based on the Seed *et al.* curves. Their results are shown in Fig. 7.28, normalized in terms of magnitude. Although the Liao *et al.* results basically agree with the trend of the Seed *et al.* curve, Fig. 7.28 shows some noteworthy differences. For clean sand deposits, the Liao *et al.* curve at 50% probability lies almost everywhere above the Seed *et al.* curve. This difference is understandable in terms of the original intent of the Seed *et al.* curve for engineering design. If, however, the intent is to reverse the process to backcalculate the maximum ground acceleration that probably occurred at a paleoliquefaction site, then the engineering conservatism in the Seed *et al.* curve could lead to a value that may be too low. Whether or not the Seed *et al.* value is too low depends on the constraints on liquefaction and venting at the site; these constraints depend very much on factors such as cap thickness, strength of the cap, and depth to the water table. If all factors are favorable, the Seed *et al.* curves probably provide a good assessment for backcalculations at sites where only minor venting or ground breakage occurred. Favorable conditions would include a cap thickness of less than a few meters (Ishihara, 1985; Obermeier, 1989), a water table within a few meters of the surface, and

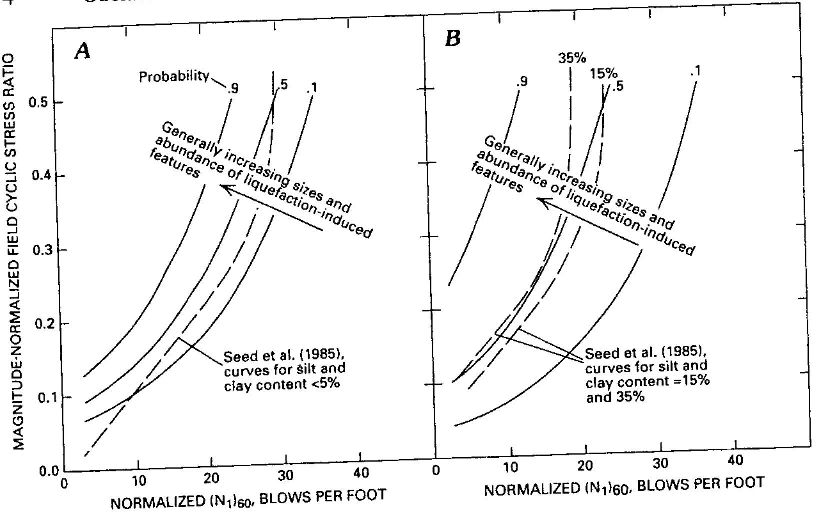

Correction factor for magnitude-normalized cyclic stress ratio (Seed et al., 1985)

Earthquake magnitude	Correction factor
8-1/2	0.89
7-1/2	1.0
6-3/4	1.13
6	1.32
5-1/4	1.5

Figure 7.28 Probability of liquefaction with accompanying venting or appreciable ground cracking, normalized to blow count value, magnitude, and field cyclic stress ratio. (A) curves for silt and clay content ≤5%. (B) Curves for silt and clay contents of 15 and 35%. [From Liao *et al.* (1988); reprinted with permission of the American Society of Civil Engineers.]

a cap that is not greatly strengthened by a mat of roots. Sites of marginal liquefaction offer a good likelihood that the blow count *N*-values of the source bed have not changed substantially by the occurrence of liquefaction. Paleoliquefaction sites where severe liquefaction took place should be avoided for backcalculations, because these sites can yield only estimates of minimum shaking levels. Severe liquefaction can be indicated by large sand blows or strong warping of the cap. Sites of wide lateral spreads, especially near free faces, should be avoided because these sites can yield backcalculated values that are too low.

The curves of Fig. 7.27 do not fully account for field conditions that are not conducive to venting, such as the presence of a very thick cap or a mat of peat in the cap. Elimination of sites having these unfavorable conditions would likely increase the probability. A misconception among many geologists is that the strength of clay in the cap has a major bearing on whether or not venting occurs. However, the pore-water pressure that develops by an occurrence of liquefaction along the base of the cap normally greatly exceeds the tensile strength of the sediment in the cap; any extensive liquefaction should be adequate for hydraulic fracturing of the cap with formation of dikes. Even where the cap is very soft, field observations show that a brittle mode of fracturing almost always occurs rather than formation of plastic intrusions.

To use the method of Seed *et al.* for estimating the strength of paleoseismic shaking, bounds must be placed on depth of the water table at the time of the earthquake. Maximum depth to the water table sometimes can be bracketed by observing the highest regional level at which dikes cut the base of the cap. The water level almost certainly was at least this high; if the water level had been much lower, the excess pore-water pressure probably would have been dissipated into granular, permeable sediment along the base of the cap.

7.6.4 Overview of Estimates of Magnitude

It is obvious that the curves in Figs. 7.27 and 7.28 do not yield a unique solution to both acceleration and magnitude. Only possible combinations can be determined. The estimate of magnitude preferably should be based on estimates of accelerations from seismological models and statistical analysis, in conjunction with an estimate of magnitude based on the observed areal distribution of the paleoliquefaction features.

Factors that control the regional extent (span) of liquefaction features and sizes of liquefaction features include liquefaction susceptibility and amplification of bedrock shaking, as well as seismological factors of focal depth and shaking frequency of the earthquake, and stress change (drop) in the rock of the rupture zone at the time of the earthquake. Possible shaking characteristics are myriad. A shallow hypocentral depth can result in more severe shaking in the meisoseismal area than that caused by a deeper earthquake. Far from the meisoseismal area, however, shaking may be less severe for the more shallow earthquake than for a deeper one. A higher stress drop should cause accelerations to be higher both in the meisoseismal area and far away. Clearly, any interpretation of prehistoric magnitude needs to be calibrated as much as possible to the local tectonic setting in order to select the most reasonable parameters.

An accounting for all the factors above was implicit in the analysis of prehistoric liquefaction features centered about Charleston, South Carolina, discussed previously. There I concluded that some prehistoric earthquakes were at least equal in strength to the 1886 earthquake (M ~ 7.5). Seismological factors were indirectly considered by showing that the size and span of features predating 1886 exceeded those of the 1886 event, both in the meisoseismal region of the 1886 earthquake and far away. In addition, near Charleston, the fact that features that predate 1886 are more abundant and larger than elsewhere helped to define the region of strongest shaking.

The South Carolina example, for which one can compare historical and prehistoric liquefaction effects to estimate past earthquake magnitudes, is exceptional. At most places such extensive historic liquefaction data from a very strong earthquake do not exist for the same seismotectonic setting. Estimates of magnitude elsewhere must be based on a more numerical analysis. Such an approach was used for analysis of liquefaction features in the Wabash Valley (Obermeier *et al.*, 1993). Here historic liquefaction-producing earthquakes in the years 1811–12 and 1895 occurred in the New Madrid seismic zone, some 100 km southwest of the Wabash Valley. The seismotectonic setting of the two areas is likely similar. Thus the factors of hypocentral depth, stress drop, and frequency characteristics can be assumed to be similar as a first approximation. The geologic and ground water settings (i.e., liquefaction settings) are also similar between the sites of historic liquefaction and the Wabash Valley. Accounting for differences in amplification of bedrock shaking permitted definition of a curve parallel to the bound in Fig. 7.26, and thereby an estimate of magnitude.

7.6.5 Negative Evidence

The absence of liquefaction features (negative evidence) also plays an important role in assessing prehistoric earthquakes. Where depth of the water table can be bounded through time, and the susceptibility of potential source deposits can be estimated, the lack of liquefaction effects can be used to place limits on the maximum levels of prehistoric ground shaking. There is no well-defined procedure for determining the amount of outcrop that must be searched for liquefaction features to support such a negative conclusion. Some uncertainty arises because strong shaking probably attenuates from the energy source as a somewhat variable (stochastic) function rather than in a smooth manner. Many observations of ground failure effects and damage to buildings show that large variations in ground response probably are commonplace within both short and long distances from the meisoseismal area. These variations often have no readily identifiable basis. Similarly, both the size and abundance of liquefaction-induced features can have large variations within a local area. For example, in the meisoseismal area of the 1811–12 New Madrid earthquakes, within a given length of outcrop there may be hundreds of dikes and sills of all sizes. Yet, in an outcrop of the same length nearby, where conditions for liquefaction appear to be about the same, an order of magnitude fewer features can be found.

I suggest that where there is any doubt that the source sediments have been at least moderately susceptible to liquefaction through time, 10 or more kilometers of fresh exposure should be searched in order to find effects of accelerations as low as 0.1 to 0.2 g. Preferably the contact of the base of a fine-grained cap with potentially liquefiable sand can be observed at many places, in order to search for even small dikes and sills. The search is best conducted when the water table is very low.

Chapter 8 | Using Landslides for Paleoseismic Analysis

Randall W. Jibson

8.1 INTRODUCTION

Most moderate to large earthquakes trigger landslides (Fig. 8.1). In many environments, landslides preserved in the geologic record can be analyzed to determine the likelihood of seismic triggering. If evidence indicates that a seismic origin is likely for a landslide or group of landslides, and if the landslides can be dated, then a paleoearthquake can be inferred and some of its characteristics can be estimated. Such paleoseismic landslide studies thus can help reconstruct the seismic shaking history of a site or region.

Paleoseismic landslide studies differ fundamentally from paleoseismic fault studies. Whereas fault studies seek to characterize the movement history of a specific fault, landslide studies characterize the shaking history of a site or region irrespective of the earthquake source. In regions that contain multiple seismic sources and in regions where surface faulting is absent, paleoseismic ground-failure studies thus can be valuable tools in hazard and risk studies that are more concerned with shaking hazards than with interpretation of the movement histories of individual faults. In some countries, such as Russia (Solonenko, 1977; Nikonov, 1988a) paleoseismic studies typically rely more on landslides and sackungen than on surface fault ruptures.

As discussed in this chapter, the practical lowerbound earthquake that can be interpreted from paleoseismic landslide investigations is about magnitude 5 to 6. This range is comparable or perhaps slightly lower than that for paleoseismic fault studies. Obviously, however, larger earthquakes tend to leave much more abundant and widespread evidence of landsliding than smaller earthquakes; thus, available evidence and confidence in interpretation increase with earthquake size.

Paleoseismic landslide analysis involves three steps: (1) identify a feature as a landslide, (2) date the landslide, and (3) show that the landslide was triggered by earthquake shaking. This chapter addresses each of these steps and discusses methods for interpreting the results of such studies by reviewing the current state of knowledge of paleoseismic landslide analysis.

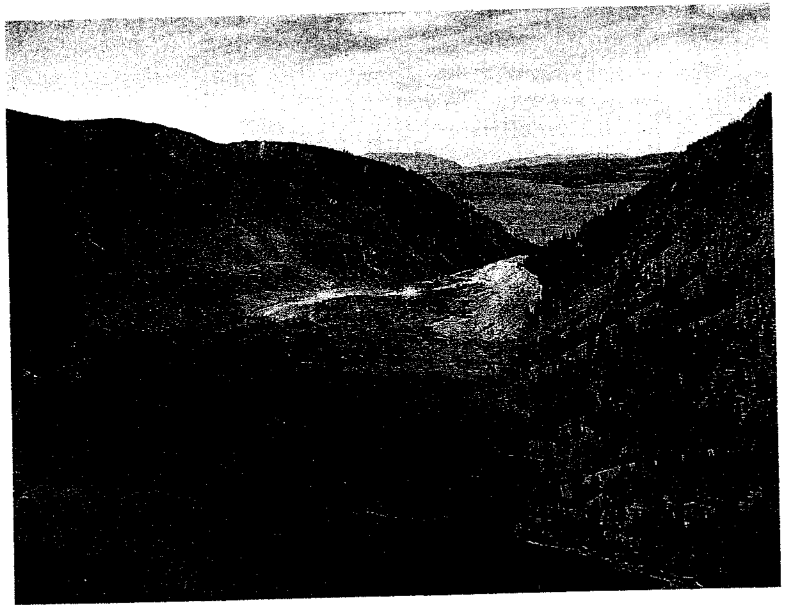

Figure 8.1 Madison Canyon landslide, triggered by the 1959 Hebgen Lake, Montana, earthquake (**M** 7.1). Strong shaking caused 28 × 10^6 m^3 of rock to slide into the canyon, which dammed the river and created a lake more than 60 m deep (see Hadley, 1964). Slide scar at left is 400 m high, debris is as much as 67 m thick in valley axis, and slide debris travelled 130 m up right valley wall. [Photograph courtesy of J. R. Stacy, U. S. Geological Survey Photographic Library (photo no. 209a).]

8.2 IDENTIFYING LANDSLIDES

Landslides include many types of movement of earth materials. In this chapter, the classification system of Varnes (1978) is used, which categorizes landslides by the type of material involved (soil or rock) and by the type of movement (*falls, topples, slides, slumps, flows,* or *spreads*). Other modifiers commonly are used to indicate velocity of movement, degree of internal disruption, state of activity, and moisture content (Varnes, 1978).

Identifying surface features as landslides can be relatively easy for fairly recent, well developed, simple landslides. Older, more degraded landslides or slides having complex or unusual morphologies are more difficult to identify. Several excellent summaries of approaches to landslide identification and investigation have been published (Schuster and Krizek, 1978; Záruba and Mencl, 1982; Brunsden and Prior, 1984; McCalpin, 1984), and the details need not be repeated here. In general, landslides are identified by anomalous topography, including arcuate or linear scarps, backward-rotated masses, benched or hummocky topography, bulging toes, and ponded or deranged drainage. Abnormal vegetation type or age also are common. Submarine landslides can be identified with the aid of marine remote-sensing techniques (Field *et al.*, 1982).

Earthquakes can trigger all types of landslides, and all types of landslides triggered by earthquakes also can occur without seismic triggering. Therefore, an earthquake origin cannot be determined solely on the basis of landslide type. However, some types of landslides tend to be much more abundant in earthquakes than other types. For example, Solonenko (1977) described some common characteristics of landslides triggered by earthquakes in the former Soviet Union. In a more comprehensive study, Keefer (1984) ranked the relative abundance of various types of landslides from 40 major earthquakes throughout the world (Table 8-1). Overall, the more *disrupted types* of landslides are much more abundant than the more *coherent types* of landslides. The relative rarity of *subaqueous landslides* stems, in part, from difficulties in observation. Keefer (1984) also observed that most earthquake-induced landslides occur in intact materials rather than in preexisting landslide deposits; thus, the number of *reactivated landslides* is small compared to the total number of landslides triggered by earthquakes. Keefer (1984) described typical properties of source areas of various types of earthquake-triggered landslides.

Table 8-1.
Relative Abundance of Earthquake-Induced Landslides

Abundance	Landslide type
Very abundant	Rock falls Disrupted soil slides Rock slides
Abundant	Soil lateral spreads Soil slumps Soil block slides Soil avalanches
Moderately common	Soil falls Rapid soil flows Rock slumps
Uncommon	Subaqueous landslides Slow earth flows Rock block slides Rock avalanches

Note: Data from Keefer (1984). Landslide types use nomenclature of Varnes (1978) and are listed in decreasing order of abundance.

In general, slope materials that are weathered, sheared, intensely fractured or jointed, or saturated are particularly susceptible to landsliding during earthquakes.

Sackungen (ridge-crest troughs) are a somewhat controversial type of ground failure that some investigators claim may be related to seismic shaking. Sackungen are identified by one or more of the following: (1) grabens or troughs near and parallel to ridge crests of high mountains, (2) uphill-facing scarps a few meters high that parallel the topography, (3) double-crested ridges, and (4) bulging lower parts of slopes (Varnes *et al.,* 1989).

8.3 DETERMINING LANDSLIDE AGES

Paleoseismic interpretation requires establishing the numerical age of a paleoearthquake. In the case of earthquake-triggered landslides, this means that dating landslide movement is required. Several methods for dating landslide movement can be used; some are similar or identical to those used for dating fault scarps (as discussed in other chapters), while others are unique to landslides. Most of the methods discussed here are simply applications of numerical dating techniques discussed in Chapter 1, which contains general descriptions of sampling and testing procedures.

Different types of landslides may be datable by different methods, depending on a variety of factors such as distance of movement, degree of internal disruption, landslide geometry, type of landslide material, type and density of vegetation, and local climate. Ideally, multiple, independent dating methods should be used to increase the level of certainty of the age of landslide movement (Johnson, 1987).

8.3.1 Historical Methods

Some old landslides may have been noted by local inhabitants or may have damaged or destroyed human works or natural features (e.g., Whitehouse and Griffiths, 1983). In some parts of the world, potentially useful historical records or human works may extend back several hundreds or thousands of years. For example, a prehistoric encampment at Mam Tor, in Derbyshire, England, was partly destroyed by a landslide (Johnson, 1987). The encampment was first occupied about 3000 yr B.P. according to archaeological studies (Jones and Thompson, 1965); this date provides an approximate maximum age of the landslide. In the United States, few historical records exceed 200 yr in length, but some of these may still be useful. In a paleoseismic investigation of landslides possibly triggered by the 1811–12 New Madrid earthquakes, Jibson and Keefer (1988) reported that oral accounts of local inhabitants helped establish minimum landslide ages in the 1850s, which helped bracket absolute ages. Also, grave markers on landslide masses, datable roads and trails whose locations clearly show that they either postdated or predated landslide movement, disturbed stone fences or other property markers, and other human works can potentially bracket or definitively date landslide movement (e.g., Jibson and Keefer, 1988).

For fairly recent events, comparing successive generations of topographic maps or aerial photographs can bracket the time period in which mappable landslides first appeared.

8.3.2 Dendrochronology

Dendrochronology can be applied to date landslide movement in several ways (Hupp *et al.,* 1987). At the simplest level, the oldest undisturbed trees on disrupted or rotated parts of landslides should yield reasonable minimum ages for movement (Jibson and Keefer, 1988; Logan and Schuster, 1991; Williams *et al.,* 1992). On rotational slides that remained fairly coherent, preexisting trees that survived the sliding will have been tilted because of headward rotation of the ground surface; if both tilted and straight trees are present on such landslides, the age of slide movement is bracketed between the age of the oldest straight trees and the youngest tilted trees (Fuller, 1912). Using this simple application of dendrochronology to date coherent translational slides is more difficult because trees can remain upright and intact even after landslide movement. On all types of landslides, trees growing from the surface of the scarp will yield minimum ages of scarp formation, from which the age of slide movement can be interpreted.

In some cases, trees killed by landslide movement will be preserved and can thus yield the exact date of movement. For example, Jacoby *et al.* (1992) dated trees beneath the surface of Lake Washington near Seattle that were drowned by landsliding into the lake. They were able to date the landslide movement from the preserved tree-ring records and from radiocarbon dating of the outermost wood.

A more sophisticated application of dendrochronology involves quantitative analysis of growth rings. For trees that have survived one or more episodes of landslide movement, such analysis can be used to identify and date *reaction wood* (eccentric growth rings), growth suppression, and corrosion scars, which may be evidence of landslide movement (Hupp *et al.,* 1987). Reconstruction of movement histories by such dendrochronologic analysis has been documented successfully in several areas (e.g., Terasmae, 1975; Reeder, 1979; Jensen, 1983; Bégin and Filion, 1985; Hupp *et al.,* 1987; Osterkamp and Hupp, 1987). Some landslides block stream drainages and form dams that impound ponds or lakes. Inundation of areas upstream from landslide dams can drown trees that can be dated dendrochronologically (Logan and Schuster, 1991).

8.3.3 Radiocarbon Dating

Radiocarbon dating can be used in a variety of ways to date organic material buried by landslide movement, as discussed by Stout (1977). Landslide scarps degrade similarly to fault scarps, so colluvial wedges at the bases of landslide scarps may contain organic material that can be retrieved by trenching or coring and dated radiometrically. Fissures on the body of a landslide, particularly near the head where extension may take place, also may trap and preserve organic matter. If the landslide mass is highly disrupted, as in rock or soil falls or avalanches, then some vegetation from the original ground surface may have become mixed with the slide debris; such organic material excavated from slide debris can be dated radiometrically (Burrows, 1975; Whitehouse and Griffiths, 1983; McCalpin, 1989c, 1992). At the toes of landslides, slide material commonly is deposited onto undisturbed ground; if this original ground surface can be excavated beneath the toe of a slide, buried organic material from this surface can be dated to indicate the age of initial movement.

Sag ponds commonly form on landslides, and organic material deposited in such ponds can be dated radiometrically. Organics at the base of the pond deposits should yield reliable dates of pond formation (Stout, 1969, 1977; McCalpin, 1989c).

Vegetation submerged from inundation of areas upstream from landslide dams also can be dated radiometrically. Schuster *et al.* (1992) dated the emplacement of rock-avalanche dams by radiocarbon dating the outer few rings of drowned trees protruding from landslide-dammed lakes and detrital wood and charcoal in lacustrine deposits that formed behind a landslide dam. Similarly, landslides into lakes can submerge and kill vegetation that can be dated radiometrically (Jacoby *et al.*, 1992).

8.3.4 Lichenometry

Lichenometry—analysis of the age of lichens based on their size—has been used successfully to date rock-fall and rock-avalanche deposits (Nikonov and Shebalina, 1979; Oelfke and Butler, 1985; Nikonov, 1988a; Smirnova and Nikonov, 1990; Bull *et al.*, 1994; Bull, 1996). By measuring lichen diameters on rock faces freshly exposed at the time of failure, numerical ages can be roughly estimated by assuming that lichens colonized the rock face in the first year after exposure. Because rock-fall and rock-avalanche deposits typically include abundant rocks having freshly exposed faces, numerous samples generally can be taken to create a database for the statistical analysis required by lichenometry. Lichenometric ages must be calibrated at sites of known historical age or by comparison with other numerical dating techniques. Lichenometric dating is subject to considerable uncertainty, however, because several

decades may elapse before lichens colonize a fresh rock exposure, and lichens may never colonize unstable landslide deposits on very steep slopes (Oelfke and Butler, 1985).

8.3.5 Weathering Rinds

For a given climate and rock type, measuring the thickness of weathering rinds can be used to date when rocks were first exposed at the ground surface (Chinn, 1981; Knuepfer, 1988). For rock falls and rock avalanches and for other landslides whose movement exposed rock fragments at the ground surface, measuring the thickness of weathering rinds can be used to date landslide movement (Whitehouse and Griffiths, 1983; McCalpin, 1989c, 1992). Determining which rock surfaces were initially exposed at the time of landsliding can be difficult, but if a sufficiently large number of samples can be measured, consistent statistical results of predominant ages that relate to landslide movement can be obtained.

8.3.6 Pollen Analysis

Analysis of pollen in deposits filling depressions on landslides can yield both an estimated age of initial movement and, in some cases, a movement history through time (Franks and Johnson, 1964; Adam, 1975; Tallis and Johnson, 1980; Dietrich and Dorn, 1984; Johnson, 1987). Such analyses assume that sediment deposition and incorporation of pollen occur immediately following landslide movement and that local climatic and vegetation variations can be accounted for. Pollen samples from the buried ground surface beneath the toes of landslides also have potential for use in dating landslide movement.

8.3.7 Geomorphic Analysis

Landslides are disequilibrium landforms that will change through time more rapidly than surrounding terrain. By analyzing the degree of degradation of landslide features such as scarps, ridges, sags, and toes, relative ages can be assigned to various landslides (Schroder, 1970; McCalpin, 1986; Crozier, 1992). For example, McCalpin and Rice (1987) analyzed 1200 landslides in the Rocky Mountains and assigned each of them to one of four relative age groups based on morphology. Numerical age ranges for these groups were estimated based on correlation with other landslides in the Rocky Mountains that have similar morphologies and surface-clast weathering and for which ^{14}C dates were available. Although the classification scheme of McCalpin and Rice (1987) was developed for the Rocky Mountains, similar schemes could be developed for other areas (Wieczorek, 1984).

Another example of relative dating by geomorphic analysis was developed in New Zealand by Crozier (1992), who identified distinct age groups of landslides based on degree of definition of landslide features, soil development, tephra cover, stream dissection, preservation of vegetation killed by movement, and drainage integration. Ranges of numerical ages for these groups were estimated by dating organic material retrieved from representative landslides from each group.

Jibson and Keefer (1988) concluded that since a large group of landslides in the New Madrid seismic zone all appeared to have the same degree of geomorphic degradation, these landslides were contemporaneous. Other types of evidence (Jibson and Keefer, 1988, 1989, 1993) were then used to link the synchronous ages of these landslides to triggering by the 1811–12 New Madrid earthquakes.

Models of fault-scarp degradation also have potential application in landslide dating because landslide scarps should behave similarly to fault scarps. Several approaches to morphologic fault-scarp dating have been proposed (e.g., Bucknam and Anderson, 1979; Nash, 1980; Mayer, 1984), all of which require calibration for various parameters such as climate and scarp material. Scarp degradation commonly is modeled as a diffusion process (Colman and Watson, 1983; Andrews and Hanks, 1985; Andrews and Bucknam, 1987), in which degradation rate varies in time and is a function of slope angle, which represents the degree to which the scarp is out of equilibrium with the surrounding landscape.

Christiansen (1983) used sedimentation rates to date landslide age. An ancient landslide moved over alluvium deposited by the North Saskatchewan River, Canada, and part of the landslide was buried by continued deposition. The rate of alluvial deposition was determined by radiocarbon dating to be fairly uniform at about 2.4 mm/yr. By measuring the depth of the landslide shear zone below the present surface of the alluvium, an age of about 4,000 yr B.P. was estimated.

Johnson (1987) discusses some other geomorphic methods to date landslide movement, including correlation of landsliding with specific periods of fluvial downcutting or aggradation and correlation with known limits of ice sheets.

Analysis of soil-profile development also is a potential tool for dating landslides. New soil profiles will begin to develop on disrupted landslide surfaces. If such surfaces can be identified, dating the newly developed soil profile will indicate the age of movement (Small and Clark, 1982; Birkeland, 1984; Knuepfer, 1988; Birkeland *et al.,* 1991).

8.4 INTERPRETING AN EARTHQUAKE ORIGIN FOR LANDSLIDES

Interpreting an earthquake origin for a landslide or group of landslides is by far the most difficult step in the process, and methods and levels of confidence in the resulting interpretation vary widely. Because paleoseismology is a relatively new field of study, analysis of landslides within that field is, in many respects, embryonic. Only a handful of studies have been published to date that explicitly use landslides to identify and date paleoearthquakes, although several others develop methods that can be applied in paleoseismic investigations. This section summarizes several basic approaches that have been documented to interpret the seismic origin of landslides.

8.4.1 Regional Analysis of Landslides

Most paleoseismic landslide studies involve analysis of large groups of landslides rather than individual features. The premise of these regional analyses is that a group of landslides of the same age, scattered across a discrete area, was triggered by a single event of regional extent. In an active seismic zone, that event commonly is inferred to be an earthquake. Such an interpretation may be justified in areas where landslide types and distribution from historical earthquakes have been documented and can be used as a standard. In areas where such historical observations are absent, assuming an earthquake origin for landslides of synchronous age is much more tenuous, primarily because large storms can trigger widespread landslides having identical ages and spatial distribution.

Crozier (1992) cited six criteria to support a seismic origin for some landslides in New Zealand; these criteria can be applied generally: (1) ongoing seismicity in the region, which has triggered landslides, (2) coincidence of landslide distribution with an active fault or seismic zone, (3) geotechnical slope-stability analyses showing that earthquake shaking would have been required to induce slope failure, (4) large size of landslides, (5) presence of liquefaction features associated with the landslides, and (6) landslide distribution that cannot be explained solely on the basis of geological or geomorphic conditions. Obviously, the more of these criteria that are satisfied, the stronger the case for seismic origin.

Russian scientists were the first to analyze the distribution and ages of landslides in seismic zones for paleoseismic analysis. Several papers in Russian deal with the development and application of such studies in Central Asia, but these papers are not readily available outside Russia. A few papers by Russian authors written in English that reference this body of Russian literature are discussed next.

Nikonov (1988a) estimated that analysis of landslides in a region can detect earthquakes having magnitudes greater than 6.5 and that epicentral zones can be located within about 10 km. Analysis of fault features is considered preferable for epicentral location and magnitude estimates; analysis of landslides is preferable for age determination (Nikonov, 1988a). The method developed by the Russians (Nikonov, 1988a) involves complementary studies of fault-related features and shaking-induced features in a known seismic zone. The premise of the approach is that large earthquakes in mountainous areas trigger many landslides, and that the number, size, and areal extent of the landslides are proportional to the size of the earthquake (Solonenko, 1977). Many landslides in a seismic zone are dated either by the radiocarbon method or lichenometry; if one or more groups of landslides cluster in both space and time, then an earthquake origin is inferred (Nikonov, 1988a). Each age cluster is interpreted to define a different paleoearthquake. Generally, no criteria other than synchronous age are used, so the seismic origin of these landslides is, to a great degree, simply assumed. An earthquake origin is more certain in cases where landslide ages match ages of local fault features and where the types of landslides correspond to those documented in previous earthquakes (Solonenko, 1977). Based on historical observations that large, deep-seated landslides are triggered only within Modified Mercalli intensity (MMI) isoseismals VII–IX, only large earthquakes that triggered large, well-preserved landslides have been interpreted from such landslide studies (Nikonov, 1988a). This method was applied to rock-avalanche deposits in the epicentral region of the 1907 Karatog and 1949 Khait earthquakes (both **M** $\approx$ 7.4) in Tadjikistan (Nikonov and Shebalina, 1979). Lichenometric ages from young-looking deposits near the epicenter of these two earthquakes correlate with the 1907 and 1949 earthquakes, respectively. Lichenometric dates from the older parts of the deposits suggest an earlier earthquake about 200 yr before the study.

Tibaldi *et al.* (1995) analyzed the distribution of landslides triggered by the 1987 Ecuador earthquakes ($M = 6.9, 6.1$) and compared this distribution with locations of known faults and recent earthquake epicenters. They found good correlation between the elongation of the landslide distribution and the location and dimensions of the seismogenic faults in the area; thus, they concluded that this method could be used to reconstruct the geometry of seismogenic faults in other areas where synchronous landslide distributions can be mapped.

Bull *et al.* (1994) also used lichenometry to date numerous rock-fall deposits and rock-fall scarps near the Hope fault on South Island, New Zealand. Recent ages of deposits were linked to historical earthquakes, and older deposits were interpreted to have been triggered by previous earthquakes.

Adams (1981a) used landslide-dammed lakes in New Zealand to identify paleoearthquakes. He examined 17 historical landslide-dammed lakes and found that 15 of them formed during earthquakes; he therefore concluded that a seismic origin reasonably can be inferred if several synchronous prehistoric landslide dams cluster in an area. Perrin and Hancox (1992) later confirmed that most landslide dams in parts of New Zealand were, indeed, seismically triggered. Adams (1981a) estimated magnitudes of prehistoric earthquakes by comparing the areal extents of landslide dams of a given age with areal extents of landslide dams in historical earthquakes. He dated a group of prehistoric landslide-dammed lakes on South Island, New Zealand, using three

types of samples: (1) woody detritus in the debris of the landslide dams, (2) standing trees drowned by the lakes, and (3) submerged soil horizons cored beneath lake sediment. His results indicate an earthquake of magnitude 7.4 in about A.D. 1650. Adams (1981a) indicated that such analyses could identify earthquakes of **M** $\geq$ 6.75 that occurred within the past few hundred or thousand years.

Schuster *et al.* (1992) used a similar approach to date prehistoric rock avalanches that dammed streams in the Olympic Mountains in Washington State. Synchronous dates for several such avalanches indicate a common triggering event at about 1,100 yr B.P., which they argued was a large earthquake. Several lines of evidence for seismic triggering were cited: (1) The rock that failed is not known to have failed historically either during large storms or in moderate earthquakes; (2) more than 40 percent of a recent inventory of worldwide rock avalanches that formed landslide dams were formed by earthquake shaking (Costa and Schuster, 1991); and (3) in New Zealand, the distribution of landslide-dammed lakes approximates the distribution of shallow earthquakes having magnitudes 6.5 or greater (Perrin and Hancox, 1992).

Jacoby *et al.* (1992) used dendrochronology to date prehistoric landslides that moved into Lake Washington near Seattle. They were able to correlate the tree-ring records from these landslides directly with a tree buried in a tsunami deposit elsewhere in the region. Thus, they inferred an earthquake origin for the Lake Washington landsliding since it was synchronous with a deposit of more certain seismic origin.

Jibson and Keefer (1989) used a regional analysis based on both spatial distribution and synchronous age. They used discriminant analysis and multivariate regression to analyze the geographic distribution of three distinct types of landslides along bluffs that extend more than 300 km through the New Madrid seismic zone. Field evidence indicated that landslides of two of the three types (old coherent slides and earth flows) were synchronous and could have ages consistent with triggering in the 1811–12 earthquakes there; landslides of the third type (young rotational slumps) appeared much younger and unrelated to seismic activity. The bluffs were divided into segments 762 m (2500 ft) long, and the percentage of the length of each segment covered by landslides of the three types was measured for use as the dependent variable in the statistical analyses. Independent variables measured for each segment included slope height, slope angle, stratigraphic thicknesses of various units, slope aspect, and proximity to the estimated hypocenters of the 1811–12 New Madrid earthquakes. Discriminant analysis showed that bluffs having old coherent slides and earth flows are significantly closer to the estimated hypocenters of the 1811–12 earthquakes than bluffs without these types of slides (Jibson and Keefer, 1989). Bluffs having young slumps showed no such correlation. Multiple regression analysis, which simultaneously combined all factors, showed that the distribution of old coherent slides and earth flows correlates strongly with proximity to the hypocenters of the 1811–12 earthquakes, as well as with slope height and aspect (Jibson and Keefer, 1989). Again, young slumps showed no such correlation with earthquake-related independent variables. The results of these statistical analyses thus showed that old coherent slides and earth flows in the New Madrid seismic zone are spatially related to the 1811–12 earthquake hypocenters and thus probably formed in those earthquakes. This type of analysis can be used only in areas where landslide locations can be correlated with well-defined seismic source zones.

8.4.2 Submarine Landslides and Turbidites

The classic paper by Heezen and Ewing (1952) demonstrated that large offshore earthquakes can trigger huge turbidity currents having regional extent. They described the Grand Banks turbidity current, which was triggered in the epicentral area of a magnitude 7.2 earthquake on 28 November 1929. The Grand Banks turbidity current involved detachment and downslope movement of submarine sediment along 240 km of the continental shelf; after traveling 650 km from its source, the turbidity current was still moving faster than 20 km/h and therefore probably continued to move for additional hundreds of kilometers. Heezen and Ewing (1952) postulated that the earthquake triggered submarine slumps along an extensive length of the continental shelf corresponding to the epicentral zone of the earthquake and that these slumps transformed into turbidity currents that moved as rapidly as 100 km/h down slopes averaging only about 1.5°.

More recently, several studies have confirmed the triggering of large submarine landslides and turbidity currents by earthquakes. Perissoratis *et al.* (1984) documented a slump covering 15 to 20 km^2 in the eastern Korintiakos Gulf along the coast of Greece triggered by a series of earthquakes ($M = 6.4$ to 6.7) from 24 February to 4 March 1981. Field *et al.* (1982) documented a sediment flow/lateral spread on a 0.25° slope on the submarine Klamath River delta off the coast of northern California; the feature extends along 20 km of the delta front and is about 1 km long (from scarp to toe). The very low slope and the presence of liquefaction features on the surface both suggest seismic triggering, and repeated bottom surveys before and after the $M = 6.5$ to 7.2 offshore earthquake of 8 November 1980 conclusively linked the landslide to the earthquake. Lee and Edwards (1986) analyzed the stability of four submarine landslides off the coasts of California and Alaska and concluded that three of them required seismic shaking to have triggered failure. These studies provide the basis for interpreting older submarine landslides and turbidite deposits in terms of seismic triggering.

Several investigators have studied turbidites for paleoseismic interpretation. Kastens (1984) studied submarine debris flows and turbidites from the Calabrian Ridge off the coast of Italy and was able to correlate temporally deposits across several basins. This correlation is inconsistent with a mechanism of gradual oversteepening and slope failure from long-term sedimentation, which would produce temporally independent deposits in different basins. Thus, a seismic origin is postulated because of regional extent and proximity to the seismically active Aegean and Appenine–Sicily arcs. Kastens (1984) identified four debris-flow/turbidite events between 8000 and 14,000 yr B.P. and thus estimated a 1500-yr recurrence interval between postulated seismic triggering events during that period. She also compared estimates of peak ground accelerations having return periods of 1500 yr in the region with estimated ground accelerations required to trigger the submarine debris flows to show that seismic triggering is a reasonable interpretation.

Adams (1990) conducted a similar study along the Cascadia subduction zone off the coast of Washington and Oregon. He collected bottom core samples over a broad region and documented deposits from 13 turbidity currents having regional extent. He postulated triggering by very large earthquakes because each of these deposits originated in multiple independent channels 50 to 150 km apart and merged to form one large turbidity current. Synchronous, independent triggering by local endogenic processes (such as local oversteepening from long-term sedimentation) is highly unlikely. The relatively regular time interval between deposits likewise implies triggering by earthquakes having regular recurrence intervals. The mean recurrence interval between the 13 turbidites was 590 ± 50 yr, and the very broad regional extent suggests triggering earthquakes in the $\mathbf{M} = 9$ range. Using current sedimentation rates, Adams (1990) argued that the most recent turbidite likely occurred about 300 yr B.P., which agrees with independent paleoseismic evidence of a great Cascadia earthquake at about that time (Atwater, 1987).

Analysis of turbidites also provides an opportunity to make paleoseismic interpretations much farther back in the geologic record. Mutti *et al.* (1984) studied Cretaceous and Tertiary flysch sequences in Italy for paleoseismic interpretation. They used the term *seismoturbidite* for turbidites interpreted as being triggered by earthquake shaking. Primary criteria for this interpretation include (1) exceptional volumes ($\sim$100 km^3) and thicknesses ($\geq$100 m) that are one to two orders of magnitude greater than the largest "normal" turbidites in the region; (2) basinwide extent of distinct, synchronous, sheet-like deposits that are easily mappable over large areas; (3) lack of vertical and lateral facies associations with long-lived channel-lobe turbidite systems; and (4) proximity to seismic source zones. Additional criteria include irregular vertical spacing (indicating erratic occurrence), ages and repeat times proportional to the volume of the deposit, and inability to explain the deposits in terms of meteorological or eustatic processes. Using these criteria, Mutti *et al.* (1984) interpreted repeat intervals for large earthquakes triggering seismoturbidites in ancient rock sequences: an Upper Cretaceous sequence yielded repeat times of about

200,000 yr, an Eocene sequence repeat times of 500,000 to 1,000,000 yr, and a Miocene sequence repeat times of 2000 to 45,000 yr. Obviously, such interpretations are of little use for modern seismic hazard assessment, but they do provide potentially valuable tools for reconstructing the paleoseismic history of a region.

Seguret *et al.* (1984) used a similar approach to interpret Eocene turbidite sequences of the South Pyrenean basin in Spain. They used the term *megaturbidite* in the same sense as seismoturbidite (defined earlier). Using diagnostic criteria similar to those of Mutti *et al.* (1984), they interpreted several megaturbidite deposits to have been seismically triggered. Based on the size and regional extent of these deposits, they postulated triggering earthquakes having magnitudes of 7.0 to 7.5. Average recurrence intervals for these Eocene events is about 500,000 yr.

8.4.3 Landslide Morphology

Some landslides have morphologies that strongly suggest triggering by earthquake shaking. For example, stability analyses of landslides on low-angle basal shear surfaces show that they generally form much more readily under the influence of earthquake shaking than in other conditions (Hansen, 1965; Jibson and Keefer, 1988, 1993). Landslides that formed as a result of liquefaction of subsurface layers also are much more likely to have formed seismically than aseismically (Seed, 1968). Perrin and Hancox (1992) indicated that slides that form as a result of intense rainfall are more fluid and tend to spread out more across a depositional area, whereas seismically induced landslides may have a blockier appearance and a more limited depositional extent in some cases. None of these criteria is definitive, but the types and characteristics of landslides described previously do suggest seismic triggering and can be used as corroborative evidence of earthquake triggering.

Solonenko (1977) described several types of earthquake-triggered landslides documented in the Soviet Union, some of which have morphologies that he argued may be unique to seismic origin. His descriptions of such landslides can be condensed into six types: (1) subsidence of areas tens of square kilometers in extent by the opening of fracture systems in very large ($M > 8$) earthquakes; (2) collapse of slopes and mountain spurs crossed by active faults; (3) toppling of steep mountain peaks; (4) translational or rotational sliding of topographic benches covering several square kilometers; (5) rock falls and rock avalanches having abnormally long runout distances, including extreme runout events that may have moved on an air cushion; and (6) "ground avalanches and flows," where thick deposits of weak sediment, such as loess, collapse and flow large distances even on nearly level ground.

Landslide size also is cited widely as evidence of seismic triggering (for example, Whitehouse and Griffiths, 1983; Nikonov, 1988a; Crozier, 1992). In

the case of turbidites, large size is a definitive factor because of the criteria of multiple, independently triggered sources over a large area. For terrestrial landslides, use of size to demonstrate seismic origin is more tenuous. Size commonly is inferred to be a factor because of observations of large landslides in past earthquakes (Solonenko, 1977; Whitehouse and Griffiths, 1983; Nikonov, 1988a). In areas where large landslides have been documented in historical time to occur only during earthquakes, the large size of prehistoric landslides may suggest seismic origin and may even be used to infer the relative size of the triggering earthquake (Nikonov, 1988a). Remember, however, that landslides of all sizes form in the absence of earthquake shaking in a wide variety of environments. And Naumann and Savigny (1992) reached an opposite conclusion from their analysis of the stability of several rock avalanches in British Columbia, Canada. They showed that the larger slides analyzed were more susceptible to failure from increased pore-water pressure than from earthquake shaking and that earthquakes are more likely to trigger smaller rock falls (Naumann and Savigny, 1992).

In summary, landslide morphology and size can, in some circumstances, be used as corroborative evidence for seismic triggering, but only when a clear link between a specific morphology or size and earthquake triggering is observed.

Although earthquake-induced landslides generally fail during seismic shaking, some earthflows and debris slides/debris flows show *delayed response* and only begin movement 3 to 5 days after the earthquake. Jibson *et al.* (1994) list six known instances of such activity: three involved slow-moving earthflows and three involved fast-moving debris slides/debris flows. The three earthflows—the Kirkwood earthflow, following the 1959 **M** 7.1 Hebgen Lake, Montana, earthquake (Hadley, 1964), and the Chordi and Zhashkva landslides, following the 1991 M_s 7.0 Racha, Republic of Georgia, earthquake (Jibson *et al.,* 1994)—were similar in size (250 to 500 m wide, 1000 m long), began moving 3 to 5 days after the earthquake, and moved 30 to 70 m in the three to four weeks following the earthquake. Large (0.2 to 2.5 × 10^6 m^3) debris slides/debris flows occurred 13 days after the 1906 **M** 8.25 San Francisco, California earthquake; 3 days after the 1949 m_b 7.1 Tacoma, Washington, earthquake; and 2 days after the 1983 M_s 7.3 Borah Peak, Idaho, earthquake (Jibson *et al.,* 1994). Several investigators (e.g. Keefer *et al.,* 1985; Wood, 1985; Rojstaczer and Wolf, 1992) have speculated that delayed landslide movement is caused by increased groundwater flow arising from either locally increased permeability (due to coseismic fracturing) or increased pore pressure. The length of the delay may represent the time needed for groundwater levels in the slide (or pore pressures on the slide plane) to lower the factor of safety below 1.0. In addition, Chleborad (1994) states that a small upper-slope failure loaded the head of the Tacoma Narrows, Washington, debris slide, leading to massive failure 3 days later after the 1949 earthquake. Because most delayed landslides are initiated by groundwater changes that could just as well have been induced over a longer period of time, they are not unambiguous indicators of paleoseismicity.

8.4.4 Sackungen

Several different interpretations of the origin of sackungen have been proposed. Clearly, topography controls the ridge-parallel geometry of sackungen, and gravity is the principal driving force. But whether initiation of movement is by long-term creep, faulting, strong shaking, or a combination of factors has been debated. Bovis (1982) and Varnes *et al.* (1989), who studied sackungen in western North America, argued that movement stems from long-term, gravity-driven creep, although both studies mention tectonism as a possible contributor in some cases. Tabor (1971) indicated that earthquake shaking might play a minor role in sackung formation in the Olympic Mountains of Washington. Recent trenching studies of sackungen in Colorado and British Columbia, both relatively aseismic areas, reveal progressive fold deformation supportive of a creep mode of failure (McCalpin and Irvine, 1995; J. Psutka, BC Hydro, Vancouver, Canada, personal communication, 1994).

On the other hand, Beck's (1968) investigations of sackungen in New Zealand concluded that earthquake shaking was the most likely trigger of movement, primarily because the sackung topography appeared stable over long periods of seismic quiescence and because sackung were abundant in seismically active areas there. Jahn (1964) likewise surmised that sackungen in the Tatra Mountains of Czechoslovakia were triggered by earthquakes. Russian workers have long believed that most, if not all, sackungen are created during earthquakes (Solonenko, 1977; Nikonov, 1988a; see photographs in Khromovskikh, 1989, pp. 270–271), and that some are actual fault scarps. Using sackungen for paleoseismic analysis appears tenuous, at best, and should require independent evidence of seismic triggering. McCalpin and Irvine (in 1995) propose criteria for establishing the seismic origin of sackungen, principally stratigraphic evidence of abrupt displacement such as colluvial wedges, fissures, and subsidiary fault traces.

8.4.5 Interpretation of Sedimentary Structures

Some sedimentary structures have been interpreted as being seismically generated and thus could be used for paleoseismic interpretation. Although such structures (commonly called *seismites*) are not landslides, they do involve seismic disturbance of surficial earth material. Among the first such studies was that by Seilacher (1969), in which he describes *fault-graded bedding* and argues that seismic shaking is the most likely origin of this type of structure. Fault-graded bedding consists of a sequence, perhaps several decimeters thick,

that includes (from top down) (1) a liquefied zone, (2) a rubble zone, and (3) a step-faulted zone, all in gradational contact. His observation of three such sequences in a 10-m-thick section of Miocene Monterey shale in coastal California led him to conclude that such structures result from very rare, very strong earthquakes. A subsequent study (Seilacher, 1984) identified pleated lamination, convex-down stacking of bowl-shaped shells, and current orientation in starved shell ripples as additional sedimentary structures that may have seismic origin.

Spalletta and Vai (1984) examined Upper Devonian turbidites in the Carnic region of northern Italy and interpreted a seismic origin on the basis of sedimentologic structures as well as the geometries of the deposits. Their diagnostic sedimentologic criteria for seismic triggering is the presence of "intraclast parabreccias," described as being caused by "shallow earthquakes generat[ing] in-situ (autoclastic) brecciation of the early lithified, centimeters-thick, surficial pelagic carbonate layer" (Spalletta and Vai, 1984, p. 135). This brecciation is followed within seconds to hours by a sandy turbidity current triggered upslope by the same earthquake. Repeated sections containing such structures were discovered, but no recurrence intervals were estimated.

Several other such studies have interpreted various types of soft-sediment deformation features as being seismically induced and have drawn tentative conclusions about the paleoseismic history of different regions (El-Isa and Mustafa, 1986; Plaziat *et al.,* 1990; Pratt, 1992, 1994). In an interesting attempt to model the effects of seismicity on sedimentary basins, J. R. L. Allen (1986) combined empirical equations describing earthquake-magnitude recurrence intervals and maximum distances at which liquefaction-induced ground failure can occur for a given earthquake magnitude to model the potential frequency and spatial distribution of earthquake-triggered sediment deformation in sedimentary basins.

Large rock avalanches commonly are triggered by large earthquakes (Keefer, 1984). Sedimentologic criteria for identifying rock-avalanche deposits in the geologic record have been developed (Yarnold and Lombard, 1989) and could potentially be applied to paleoseismic studies if diagnostic criteria for seismic triggering were developed.

Studies of in-place deformation of lake-bottom sediment by seismically induced liquefaction have identified criteria by which lacustrine sedimentary structures can be attributed to earthquake shaking (Sims, 1973, 1975; Hempton and Dewey, 1983). Such liquefaction structures are discussed in Chapter 7.

8.4.6 Lacustrine Sediment Pulses Caused by Landslides

Adams (1980) measured sediment loads of rivers in New Zealand immediately following earthquakes and observed an order-of-magnitude increase in load for a period of several months. He correlated increases in load in different areas with the density of earthquake-triggered landslides in those areas and concluded that seismically induced landslides cause large increases in fluvial sediment load, which, in turn, cause increases in sedimentation rates in lakes and oceans. These observations have been corroborated with published observations from earthquakes elsewhere (Adams, 1981b).

On the premise of these observations, Doig (1986) analyzed organic-free silt layers 0.3 to 2.0 cm thick in otherwise organic-rich lake sediment in eastern Canada. Using sedimentation rates and radiometric methods, three of these layers were correlated with known earthquakes of A.D. 1663, 1791, and 1860 + 1870 (two events combined). Two older silt layers were likewise dated and attributed to paleoearthquakes in A.D. 1060 and 600. Doig (1986) stated that cores from deep lakes likely will yield the best cores for this type of analysis because of lack of bioturbation. He also warned that dating young (a few hundred years) silt layers characterized by lack of organic material can be difficult; he suggested that lead-210 and cesium-137 are the ideal radiometric methods for this type of analysis (see details of dating techniques in Chapter 3).

8.4.7 Landslides That Straddle Faults

In some areas, landslides have formed on slopes immediately above fault traces, and the slide mass has extended across the trace (Hunt, 1975; Morton and Sadler, 1989). Subsequent surface movement of such a fault would offset the landslide mass and allow estimation of fault slip rates if the slide could be dated. This approach does not require that the landslide be seismically triggered, because the paleoseismic interpretation is based on post-landslide fault offset of the landslide mass. However, landslides triggered in the immediate vicinity of active faults commonly are seismically triggered (Burrows, 1975).

8.4.8 Precariously Balanced Rocks

Recent work by Brune (1996) has attempted to use *precariously balanced rocks* as crude paleoseismoscopes. He used theoretical modeling, numerical simulation, physical modeling, and field experiments to estimate threshold accelerations needed to topple various configurations of balanced rocks. In general, horizontal accelerations of about 0.2 to 0.3 g were found to be needed to topple most configurations studied. Brune studied several areas around epicenters of historical earthquakes in California and Nevada and found few or no precariously balanced rocks; he concluded that such rocks had been toppled by previous earthquakes.

Brune also investigated areas of unknown seismic potential and concluded that those areas where balanced rocks were present had not experienced ground shaking exceeding about 0.2 g in the past several hundred or thousand years, the estimated time needed to form the balanced rocks.

Although this approach is still being developed and has some obvious drawbacks, it may prove useful in determining if an area has experienced a certain threshold level of ground shaking in the past few thousand years.

8.4.9 Speleothems

Forti and Postpischl (1984) detailed a method for analyzing the toppling of stalagmites for paleoseismic interpretation. By measuring and dating tilting and collapse of many stalagmites in a region, they differentiated sudden (seismic) versus gradual movements and local versus regional causes. Tilting and collapse events are dated by analysis of radiometrically determined speleothem growth rates, which allows interpretation for about the last 100,000 yr. Because stalagmites are inverted pendulums, the minimum ground shaking necessary to cause collapse can be estimated fairly easily by pseudostatic engineering analysis. Although the method has some promise, it has not, thus far, been applied successfully to identify and date specific paleoearthquakes.

8.4.10 Summary

A wide variety of methods for interpreting the seismic origin of landslides has been developed and, in some cases, successfully applied to paleoseismic analysis. Virtually all of the methods summarized in this section have one aspect in common, which is stated explicitly in most papers: the seismic origin of the features being interpreted remains tentative and cannot be proven, because in each case a nonseismic process could have produced the observed features. Circumstantial evidence for seismic triggering ranges from very strong to extremely tenuous. Indeed, on the latter end of the spectrum, the reasoning can be rather circular: an earthquake origin for a feature is assumed and then an earthquake origin is interpreted and concluded from analysis of that feature. Any paleoseismic interpretation of a feature is limited primarily by the certainty with which seismic triggering can be established. The following section addresses this dilemma by describing an approach to assess directly the conditions leading to failure of individual landslides.

8.5 ANALYSIS OF THE SEISMIC ORIGIN OF A LANDSLIDE

The most direct way to assess the relative likelihood of seismic versus aseismic triggering of an individual landslide is to apply established methods of static and dynamic slope-stability analysis (Lee and Edwards, 1986; Crozier, 1992; Jibson and Keefer, 1993). The first step in such an analysis involves constructing a detailed slope-stability model of static conditions to determine if failure is likely to have occurred in any reasonable set of groundwater and shear-strength conditions in the absence of earthquake shaking. All potential nonseismic factors must be considered; these might include processes such as fluvial or coastal erosion that oversteepens the slope or undrained failure resulting from rapid drawdown (for slopes subject to submersion). If aseismic failure can reasonably be excluded even in worst-case conditions (minimum shear strength, maximum piezometric head), then an earthquake origin can be inferred. Dynamic slope-stability analyses can then be used to estimate the minimum shaking conditions that would have been required to cause failure. In the sections that follow, a method for conducting such an analysis is described using an example from the New Madrid seismic zone summarized from Jibson and Keefer (1993).

8.5.1 Physical Setting of Landslides in the New Madrid Seismic Zone

The New Madrid earthquakes of 1811–1812 (Fuller, 1912) triggered many large landslides along the bluffs that form the eastern edge of the Mississippi River alluvial plain in Tennessee and Kentucky (Fig. 8.2). Many landslide features currently are visible along these bluffs, and one of these landslides is analyzed next to determine if a seismic versus nonseismic origin can be established with a reasonable level of confidence.

The bluffs in the study area are not, for the most part, active river banks and thus are subject to landsliding from fluvial erosion in only a few locations. The bluffs stand as high as 70 m above the alluvial plain of the Mississippi River and therefore are not subject to landsliding from conditions such as rapid drawdown because the bluff is never inundated by flooding to a significant height. The average height of the bluffs in this area is 35 m, and slope angles range from a few degrees to almost vertical, but typically are 15 to 25°.

The base of the bluffs throughout most of the area is formed by as much as 45 m of shallow-marine clays and silts of the Eocene Jackson Formation (Conrad, 1856). Lying unconformably on the Jackson Formation is as much as 20 m of Pliocene alluvial gravel and sand of the Lafayette Gravel (McGee, 1891; Potter, 1955). The bluffs are capped by 5 to 50 m of Pleistocene loess lying unconformably on the Jackson Formation and Lafayette Gravel. The average thickness of the loess in the area is about 15 m.

A translational block slide about 11 km north of Dyersburg, Tennessee, referred to as the Stewart landslide, was chosen for detailed analysis (Fig. 8.2). This landslide is representative of coherent block slides in the area, which previous research (Jibson and Keefer, 1988, 1989) indicated were probably triggered by the 1811–12 earthquakes. Figure 8.3 shows a profile of the Stewart slide; subsurface data were derived from drilling along the line of profile.

8.5.2 Geotechnical Investigation

Four rotary drill holes were placed along the line of profile to determine the bluff stratigraphy and to procure soil samples for geotechnical testing (Fig. 8.3). The standard penetration test (SPT) yielded split-spoon samples, which typically were heavily disturbed by the sampling process and were used primarily for determining index properties, such as grain size, plasticity, water content, and color. Several 13-cm-diameter undisturbed piston cores were procured to measure soil unit weight and shear strength, both needed for limit-equilibrium stability analysis. Jibson (1985) described the sampling methods in detail.

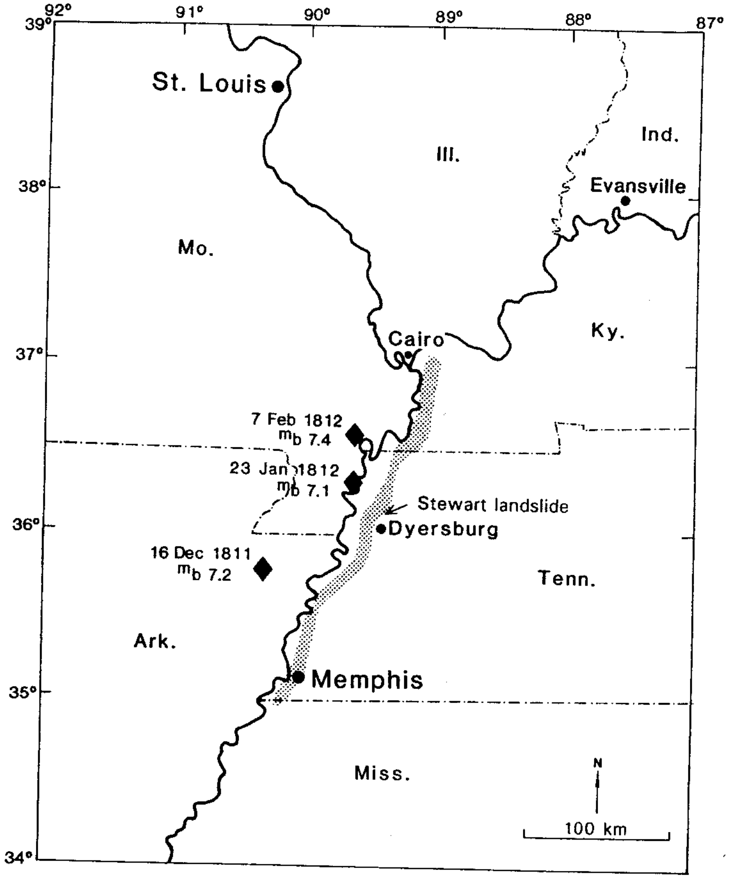

Figure 8.2 Map showing estimated epicenters (diamonds), dates, and body-wave magnitudes (m_b) of the three largest earthquakes in the 1811–12 New Madrid sequence (from Nuttli, 1973); bluffs (shaded) containing landslides triggered in 1811–12; and the location of the Stewart landslide. [From Jibson and Keefer (1993); reprinted with permission of the Geological Society of America.]

Drained shear strengths, for use in static stability analyses, were measured using two methods: (1) direct shear in which the rate of strain was slow enough to allow full drainage and (2) consolidated-undrained triaxial (CUTX) shear in

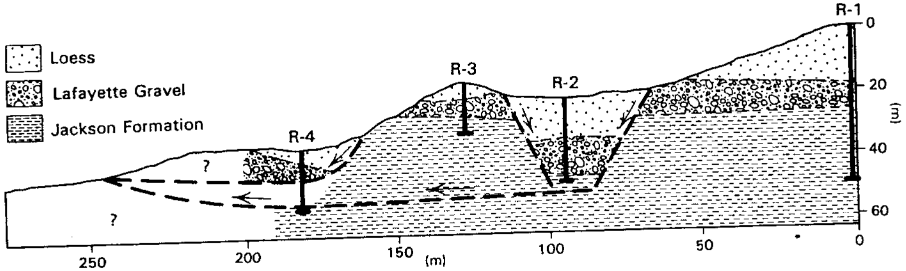

Figure 8.3 Cross section of Stewart landslide showing subsurface stratigraphy (identified from drill holes designated R-1 through R-4) and diagrammatic representation of failure surfaces. Undisturbed stratigraphy is shown at R-1. [From Jibson and Keefer (1993); reprinted with permission of the Geological Society of America.]

which pore pressures were measured to allow modeling of drained conditions (Jibson, 1985). Undrained shear strengths, for use in dynamic analysis, were measured primarily by CUTX tests. CUTX test results were supplemented by vane-shear and penetrometer data and correlation with SPT blow counts where undisturbed samples were unavailable.

8.5.3 Static (Aseismic) Slope-Stability Analysis

Figure 8.4 shows an idealized model of the pre-landslide bluff in drained conditions, appropriate for modeling static (aseismic) stability. The bluff is

Layer	Unit Weight (kN/m^3)	Drained Friction Angle	Drained Cohesion (kPa)
1	19.3	34°	0.25
2	19.6	35°	0.50
3	19.8	30°	0.43
4	22.0	32°	0.32
5	18.1	15°	2.06
6	18.1	20°	1.81
7	17.3	12°	0.71
8	18.1	20°	2.27
9	18.1	15°	2.06
10	18.1	12°	2.52

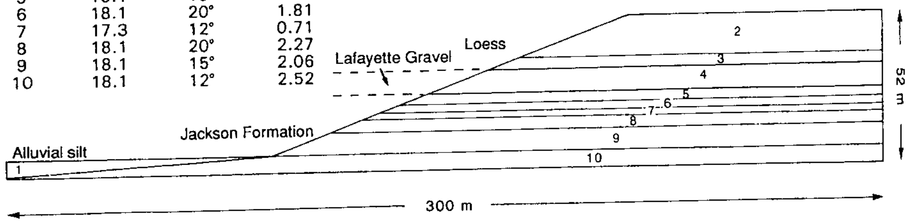

Figure 8.4 Idealized model of pre-landslide bluff at Stewart site in drained conditions. Soil properties are shown for each designated layer in the computer model. [From Jibson and Keefer (1993); reprinted with permission of the Geological Society of America.]

45 m high as measured from the profile (Fig. 8.3). Undisturbed bluffs adjacent to the Stewart slide have slopes of about 20° and have simple, uniformly sloping faces. Geotechnical properties of the stratigraphic layers in the model were assigned using the results of the shear-strength tests; layers where no shear-strength tests were performed were assigned strengths based on stratigraphic and index-property correlation with layers where strengths were measured (Jibson, 1985).

Lack of published data made modeling groundwater conditions along the bluffs difficult. Therefore, several potential groundwater conditions were modeled (Fig. 8.5) that effectively bracket the most and least critical conditions that are physically possible. Because of the local topography and hydraulic properties of the bluff materials, the most critical condition modeled (Fig. 8.5, condition 1) is a more critical situation than can realistically exist in the bluffs and thus provides a worst-case bounding condition. The most likely groundwater condition also was modeled: a water table sloping upward from the base of the bluffs to the top of the Jackson Formation, and a second water table perched on the relatively impermeable Jackson that saturates the Lafayette Gravel.

The STABL computer program (Siegel, 1978) was used to determine the stability of the modeled bluff in aseismic conditions. STABL searches for the most critical failure surface by randomly generating circular, wedge, and

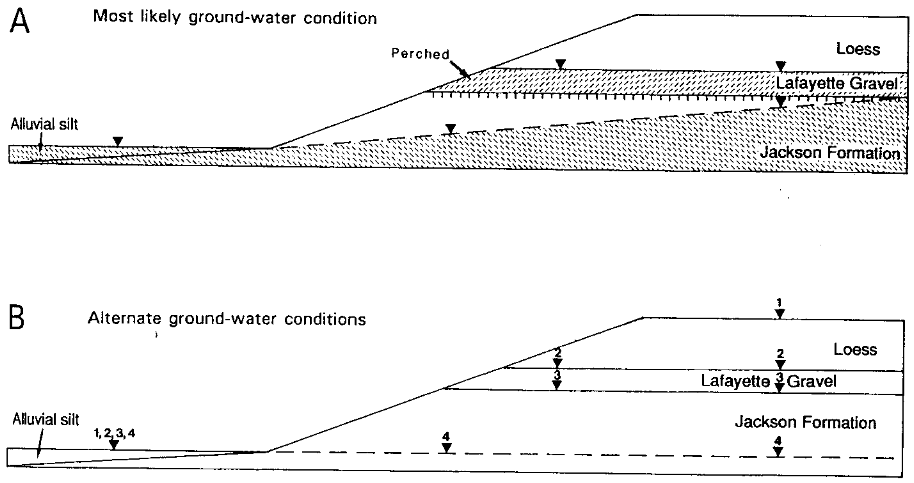

Figure 8.5 Groundwater conditions modeled in the slope-stability analyses. (A) Most likely groundwater condition; saturated zones are shown by cross-hatched pattern. (B) Piezometric surfaces of four alternate groundwater conditions are shown by inverted triangles numbered 1–4. [From Jibson and Keefer (1993); reprinted with permission of the Geological Society of America.]

irregular slip surfaces and calculating the factor of safety[1] for each generated surface. The program plots the 10 most critical surfaces of each type and their factors of safety. The geometry of the actual failure surface (shown diagrammatically in Fig. 8.3) was determined by locating weak or disturbed layers by drilling and by analysis of the surface geometry of the landslide. The safety factor for this surface was calculated using the simplified Janbu method (Siegel, 1978) for each groundwater condition.

Determining the stability of the bluffs from the factor of safety requires judgment. Gedney and Weber (1978) recommended that engineered slopes have safety factors between 1.25 and 1.50 for the type of analysis used. Because of the high density of good-quality geotechnical data, this range is used as the criterion to evaluate slope stability: Between FS 1.00 and 1.25, slopes are considered to be marginally stable; between FS 1.25 and 1.50, slopes are considered to be stable; and above FS 1.50, slopes are considered to be very stable.

The results of the stability analyses are summarized in Table 8-2. The lowest factor of safety in the most critical groundwater condition is 1.32, which indicates that the bluff at the Stewart site is stable in aseismic conditions even in the most critical groundwater condition. In the most likely groundwater condition (sloped and perched), the minimum factor of safety is 1.82, indicating a very stable bluff. The factor of safety of the actual failure surface in the most likely groundwater condition is 1.88.

Our analysis shows that an artesian piezometric surface tens of meters above ground level at the top of the bluff would be needed to reduce the factor of safety to 1.0. Such an artesian condition is impossible because (1) the regional geology and topography preclude such a condition because the top of the bluff is 30 to 70 m above the alluvial plain, and no topographically higher artesian recharge area exists, and (2) a piezometric surface high above the bluff-top that dips steeply to the base of the bluff is physically unrealistic.

Figure 8.6 shows the locations of the most critical slip surfaces of various shapes and of the actual slip surface. All the surfaces have grossly similar shapes, but the most critical computer-generated surfaces all lie well above the actual failure surface. This disparity suggests that the sliding did not take place under drained, static conditions.

The rather high factors of safety, even in unrealistically high groundwater conditions, and the disparity between the most critical computer-generated slip surfaces and the actual surface indicate that it is extremely unlikely that the existing landslide at the Stewart site formed in aseismic, drained conditions.

---

[1] The factor of safety (FS) is the ratio of the sum of the resisting forces that act to inhibit slope movement to the sum of the driving forces that tend to cause movement. Slopes having factors of safety greater than 1.0 are thus stable; those having factors of safety less than 1.0 should move.

Table 8-2.

Static Factors of Safety from Stability Analyses of the Stewart Landslide in Drained and Undrained Conditions

Type of failure surface	Location of piezometric surface				
	Base of bluff[a]	Top of Jackson[b] Formation	Top of Lafayette[c] Gravel	Top of bluff[d]	Most likely[e]
		Drained stability analyses			
Circular	**1.90**	**1.66**	**1.61**	1.35	**1.82**
Irregular	1.95	1.69	1.64	**1.32**	1.87
Wedge, layer 5	4.06	3.98	3.76	2.83	4.03
Wedge, layer 6	4.24	4.03	3.80	2.79	4.23
Wedge, layer 7	2.46	2.28	2.14	1.47	2.45
Wedge, layer 8	3.81	3.39	3.23	2.51	3.72
Wedge, layer 9	2.83	2.48	2.38	1.88	2.71
Wedge, layer 10	2.40	2.10	2.03	1.68	2.25
Actual Surface	1.96	1.73	1.67	1.40	1.88
		Undrained stability analysis			
Circular	1.72	1.72	1.64	**1.99**	1.62
Irregular	**1.64**	**1.64**	**1.55**	2.16	**1.53**
Wedge, layer 5	2.81	2.81	2.50	3.59	2.49
Wedge, layer 6	3.23	3.23	2.96	3.84	2.93
Wedge, layer 7	2.19	2.19	1.99	2.81	1.97
Wedge, layer 8	3.18	3.18	3.05	3.57	3.02
Wedge, layer 9	2.00	2.00	1.89	2.41	1.87
Wedge, layer 10	1.99	1.99	1.88	2.25	1.87
Actual surface	1.74	1.74	1.66	2.12	1.65

Note: Most critical surface for each groundwater condition shown in **bold** type.

[a] Fig. 8.5B, piezometric surface 4.

[b] Fig. 8.5B, piezometric surface 3.

[c] Fig. 8.5B, piezometric surface 2.

[d] Fig. 8.5B, piezometric surface 1.

[e] Fig. 8.5A.

8.5.4 Dynamic (Seismic) Slope-Stability Analysis

Jibson and Keefer (1993) used the dynamic displacement analysis developed by Newmark (1965), now used widely in engineering practice (Seed, 1979a), to evaluate the seismic stability of the bluff. In the *Newmark method* a landslide is modeled as a rigid friction block that begins to move when a given critical

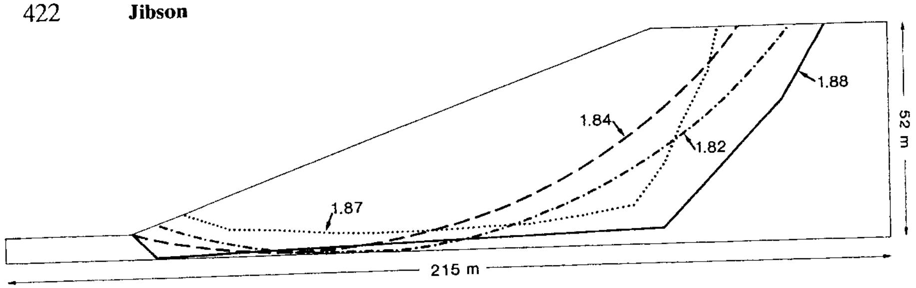

Figure 8.6 The three most critical slip surfaces and their factors of safety (FS = 1.82, 1.84, 1.87) for static, drained conditions at the Stewart site in the most likely groundwater condition. Heavy, solid line shows location of actual failure surface (FS = 1.88). [From Jibson and Keefer (1993); reprinted with permission of the Geological Society of America.]

acceleration is exceeded; *critical acceleration* is defined as the acceleration required to overcome frictional resistance and initiate sliding on an inclined plane. The analysis calculates the cumulative permanent displacement of the block as it is subjected to the effects of an earthquake *acceleration-time (strong-motion) history,* and the user judges the significance of the displacement. Laboratory model tests (Goodman and Seed, 1966) and analysis of actual earthquake-induced landslides (Wilson and Keefer, 1983) have confirmed that Newmark's method can fairly accurately predict landslide displacements if slope geometry and soil properties are known accurately and if earthquake ground accelerations can be estimated using real or artificial acceleration-time histories. I have provided a detailed treatment elsewhere of how to conduct a Newmark analysis on landslides in natural slopes (Jibson, 1993).

Newmark (1965) showed that the critical acceleration is a simple function of the static factor of safety and the landslide geometry; it can be expressed as

$$a_c = (\mathrm{FS} - 1)g \sin \alpha, \tag{8.1}$$

where a_c is the critical acceleration in terms of a ratio to g, the acceleration of Earth's gravity; FS is the static factor of safety; and α is the angle from the horizontal (hereafter called the *thrust angle*) at which the center of mass of the potential landslide block first moves.

The algorithm developed by Wilson and Keefer (1983) is used to apply Newmark's method, which simply consists of double-integrating the portions of the selected acceleration-time history that lie above the critical acceleration of the landslide block. This double integration of the acceleration record yields the cumulative permanent displacement of the block (also termed the *Newmark displacement*).

Conducting a Newmark analysis requires three pieces of information: (1) the static factor of safety and (2) the thrust angle of the potential landslide (both needed to calculate the critical acceleration), and (3) an earthquake acceleration-time history.

8.5.4.1 Static Factor of Safety

During earthquakes, soils behave in a so-called undrained manner because excess pore pressures induced by the transient ground deformation cannot dissipate during the brief duration of the shaking; therefore, a layered model of the bluff in *undrained conditions* was constructed (Fig. 8.7). *Undrained shear strength* is treated as a single numerical quantity that is represented in the analysis as cohesion, and the friction angle is taken to be zero (Lambe and Whitman, 1969). Undrained shear strengths used in the model (Fig. 8.7) were measured directly in the laboratory, as described previously. Because undrained strength depends in large part on consolidation stress, layers of roughly similar thickness were constructed that reflect the increase in shear strength with depth even for relatively homogeneous materials.

STABL was used to generate potential failure surfaces and to determine the most critical failure surface in the same manner as described above for the aseismic stability analysis in drained conditions. Table 8-2 summarizes the results of the undrained slope stability analyses using this model. The lowest factor of safety is 1.53, which shows that the bluff is statically stable in undrained conditions. Figure 8.8 shows the locations of the most critical slip surfaces for the most likely groundwater condition. All the slip surfaces, including the actual failure surface, plot very close to one another and have similar factors of safety. Both circular surfaces have large radii and approxi-

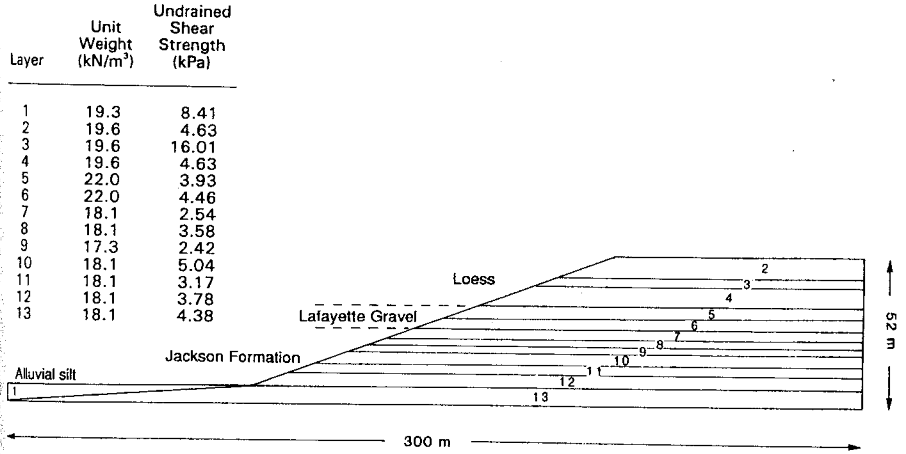

Layer	Unit Weight (kN/m³)	Undrained Shear Strength (kPa)
1	19.3	8.41
2	19.6	4.63
3	19.6	16.01
4	19.6	4.63
5	22.0	3.93
6	22.0	4.46
7	18.1	2.54
8	18.1	3.58
9	17.3	2.42
10	18.1	5.04
11	18.1	3.17
12	18.1	3.78
13	18.1	4.38

Figure 8.7 Idealized model of pre-landslide bluff at Stewart site in undrained conditions. Soil properties are shown for each designated layer in the computer model. [From Jibson and Keefer (1993); reprinted with permission of the Geological Society of America.]

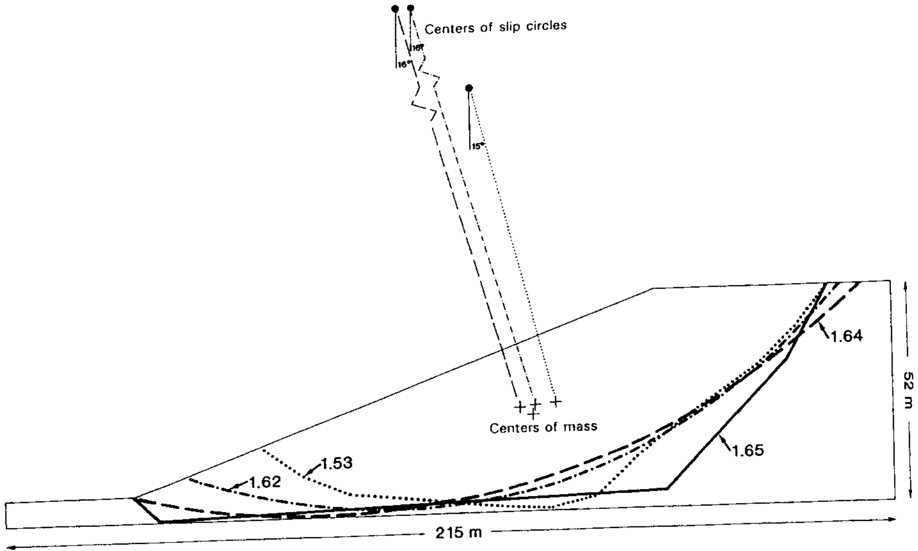

Figure 8.8 The three most critical slip surfaces and their factors of safety (FS = 1.53, 1.62, 1.64) for static, undrained conditions at the Stewart site in the most likely groundwater condition. Heavy, solid line shows location of actual failure surface (FS = 1.65). Geometric construction to determine thrust angle also shown. [From Jibson and Keefer (1993); reprinted with permission of the Geological Society of America.]

mate planar basal shear surfaces, as is expected from the shape of the actual shear surface (Fig. 8.3). The fact that the most critical computer-generated surfaces closely parallel the actual failure surface indicates that the model of the bluffs is reasonable and that slope failure is more likely to have occurred in undrained conditions than in drained conditions.

8.5.4.2 Thrust Angle

The thrust angle (α) is the direction in which the center of gravity of the slide mass moves when displacement first occurs. For a planar slip surface parallel to the slope face (an infinite slope), the thrust angle is the slope angle. For rotational movement on a circular surface, Newmark (1965) showed that the thrust angle is the angle between the vertical and a line segment connecting the center of gravity of the landslide mass and the center of the slip circle.

Figure 8.8 shows geometric constructions of the thrust angles for the two circular failure surfaces and the circular approximation of the irregular surface. Thrust angles for these surfaces all are 15 to 16°. The thrust angle of the actual surface is difficult to estimate because of its irregular shape and consequent complex movement. An average inclination of the actual failure surface can be calculated by weighting the inclinations of the line segments forming the actual surface by their relative lengths. This yields an average inclination of 16°, consistent with the other generated surfaces.

8.5.4.3 Earthquake Acceleration-Time History

The hypothesis being tested is that the Stewart landslide was triggered by the 1811–12 earthquakes; therefore, earthquake acceleration-time histories must be selected to approximate the shaking conditions from the 1811–12 earthquakes at the Stewart site. Choosing strong-motion records to represent the ground motions from the 1811–12 earthquakes is difficult because most available records are from California earthquakes, which probably differ in many respects from large earthquakes in the central United States (e.g., Nuttli, 1983). Differences in the propagation of strong ground motion due to regional differences in attenuation, however, may not be as great as previously believed, and they appear to be significant only at great epicentral distances (>150 km) for very large earthquakes (Hanks and Johnston, 1992). The Stewart site is only 20 to 70 km from the three estimated epicenters of the 1811–12 earthquakes.

Estimating various ground-motion characteristics of the 1811–12 earthquakes at the Stewart site and comparing these estimated characteristics with those of existing earthquake records provides a basis for choosing an input ground motion. Peak ground acceleration (PGA), duration, and shaking intensity are used for this comparison, and these parameters can be estimated by several methods, as described by Jibson and Keefer (1993). Although PGA is the most commonly used index of strong shaking, it is a rather crude single measure of earthquake shaking intensity because it measures only a single point in an acceleration-time history. A more quantitative measure of total shaking intensity developed by Arias (1970) is useful in seismic hazard analysis and correlates well with distributions of earthquake-induced landslides (Harp and Wilson, 1995). *Arias intensity* is the integral over time of the square of the acceleration, expressed as

$$I_a = \pi/2g \int [a(t)]^2 \, dt, \qquad (8.2)$$

where I_a is the Arias intensity, expressed in units of velocity, and $a(t)$ is the ground acceleration as a function of time. Arias intensity is used as the primary characteristic for comparison in selecting strong-motion records.

Although strong motion has not been recorded for earthquakes in the magnitude range of the 1811–12 events, several existing strong-motion records have shaking characteristics similar enough to the estimated shaking characteristics of the 1811–12 events to be useful. An extensive catalog of digitized strong-motion records was examined, primarily from California earthquakes, and two records for each of the three 1811–12 earthquakes were selected. Records were chosen to match, as closely as possible, the estimated range of Arias intensities and PGA's from the 1811–12 events so as to bracket the likely ranges of shaking conditions that actually occurred. None of the available strong-motion records have Arias intensities greater than 10 m/s; therefore, where estimated Arias intensities exceeded this level, the available record having the greatest Arias intensity was used. Table 8-3 shows the records selected and compares some of their characteristics with those estimated by Jibson and Keefer (1993) for the Stewart site from the 1811–12 earthquakes.

Table 8-3

Strong-Motion Records Used to Model Ground Shaking from the 1811–12 Earthquakes at the Stewart Landslide

Earthquake recording site, component	**M**	R (km)	$\hat{a}$ (g)	T (s)	I_a (m/s)	D_N (cm)
16 Dec 1881 New Madrid, MO, Stewart landslide site (estimated)	8.2	68	0.39	20–40	2.7^a $2.7–5.5^b$	
• 15 Oct 1979 Imperial Valley, CA, El Centro differential array, 360°	6.5	7	0.49	6.6	2.1	6–8
• 24 Nov 1987 Superstition Hills, CA, Superstition Mountain site 8, 135°	6.5	6	0.90	12.2	6.8	23–25
23 January 1812 New Madrid, MO, Stewart landslide site (estimated)	8.1	24	0.74	18–40	17.4^a $8.9–19.7^b$	
• 9 Feb 1971 San Fernando, CA, Pacoima Dam, 164°	6.6	3	1.22	6.7	9.1	50–55
• 16 Sep 1978 Tabas, Iran, 74°	7.4	3	0.71	16.1	10.0	39–44
7 Feb 1812 New Madrid, MO, Stewart landslide site (estimated)	8.3	44	0.71	25–40	8.2^a $11.3–18.1^b$	
• 24 Nov 1987 Superstition Hills, CA, Superstition Mountain site 8, 135°	6.5	6	0.90	12.2	6.8	23–25
• 16 Sep 1978 Tabas, Iran, 74°	7.4	3	0.71	16.1	10.0	39–44

Note: Characteristics of the 1811–12 earthquakes estimated as described in text. All strong-motion records are from U.S. Geological Survey recording stations except for the Tabas, Iran, record (Hadley *et al.*, 1983). **M**, moment magnitude (estimates for the 1811–12 earthquakes from Hamilton and Johnston, 1990); *R*, earthquake source distance; $\hat{a}$, peak ground acceleration; *T*, duration of strong shaking as defined by Dobry *et al.* (1978); I_a, Arias (1970) intensity; D_N, Newmark (1965) displacement (range shown covers range of critical accelerations discussed in text).

[a] Estimated using Eq. (4) of Jibson and Keefer (1992).

[b] Estimated using Eq. (5) of Jibson and Keefer (1992).

8.5.4.4 Calculation of the Newmark Landslide Displacement

Critical accelerations were calculated based on a thrust angle of 16° and on the factors of safety (FS 1.62, 1.64) of the two circular slip surfaces in the perched and sloped groundwater conditions. These slip surfaces most closely coincide with the actual surface and have the lowest factors of safety. Equation (8.1) yields critical accelerations of 0.17 to 0.18 g for these input values. These critical accelerations are specified in the computer program that double integrates the strong-motion record to calculate the Newmark displacement.

The significance of the Newmark displacements must be judged in terms of the probable effect on the potential landslide mass. For example, Wieczorek *et al.* (1985) used 5 cm as the *critical displacement* leading to failure of landslides in San Mateo County, California; Keefer and Wilson (1989) used 10 cm as the critical displacement for coherent slides in southern California. When displacements in this range occur, previously undisturbed soils can lose some of their strength and be in a residual-strength condition. Static factors of safety using *residual shear strengths* can then be calculated to determine the stability of the landslide after earthquake shaking (and consequent inertial landslide displacement) ceases.

Table 8-3 shows Newmark displacements calculated for the two critical accelerations using the six strong-motion records listed. Displacements are 6 to 55 cm and thus fall on both sides of the critical 5- to 10-cm range. Displacements generated by the model earthquakes of the 16 December 1811 event are 6 to 8 cm; in this range, the likelihood of catastrophic failure is uncertain. The soils sampled and tested at the Stewart site all showed significant strength reductions during strain in both drained and undrained conditions (Jibson, 1985); residual strength generally was reached after shear displacements of about 0.5 cm (for silts and sands) to 6 cm (for clayey silts). Therefore, even modest displacements would have at least partially reduced the soil shear strength and thus would have reduced the critical acceleration of the landslide in future earthquakes. The model earthquakes for the 23 January and 7 February 1812 events generated Newmark displacements of 23 to 55 cm, which undoubtedly would have reduced soil shear strengths to residual levels.

For all groundwater conditions, all static factors of safety for the Stewart slide calculated using residual shear strengths in both drained and undrained conditions (Jibson, 1985) were less than 0.8 and in most cases were less than 0.4. Therefore, if the bluff materials reach residual strength, catastrophic failure almost certainly will occur. Displacements of 20 to 50 cm thus would reduce the shear strength of the bluff materials to a residual-strength condition and probably would lead to catastrophic failure. The repeated shaking of the bluffs by three large earthquakes (and the far more numerous moderate earthquakes) and the reduction of the critical acceleration of the partially failed landslide mass leave little doubt that the very large displacements of the Stewart slide would have occurred during the entire 1811–12 earthquake sequence.

8.5.4.5 Summary

In summary, static stability analyses of drained conditions indicate that failure of the Stewart landslide in aseismic conditions is extremely unlikely. Dynamic analysis shows that shaking conditions similar to those in 1811–12 would have induced large displacements that probably would lead to catastrophic failure. Further analysis (Jibson and Keefer, 1993) showed that no earthquakes since 1812 could have triggered the observed landslide movement. The results of these analyses are consistent with results from field and regional studies (Jibson and Keefer, 1988, 1989), which indicated that the ages and regional distribution of landslides similar to the Stewart slide are consistent with triggering in 1811–12. Datable material needed to determine the precise age of landsliding at the Stewart site could not be recovered, so the analytical approach outlined here was crucial in linking the landslide to the 1811–12 earthquakes. Considered together, these studies strongly support such a conclusion.

The reliability of results of the analyses such as this obviously depends on the amount and quality of input data and the appropriateness and accuracy of the modeling approach used. As Clark and Cole (1992) pointed out, obtaining samples that accurately reflect the shear strength along a failure plane is very difficult, particularly in cases where reactivated landslides having well-formed basal shear surfaces are being analyzed. In such cases, using minimum shear-strength estimates is generally appropriate because the material along the preexisting shear surface is probably at residual level (Clark and Cole, 1992).

8.5.5 Analysis of Unknown Seismic Conditions

The procedure described in the last section was used to test the hypothesis that an individual landslide was triggered by an historical earthquake whose magnitude and location have already been estimated. The goal of most paleoseismic investigations, by contrast, is to detect and characterize prehistoric or undocumented earthquakes whose effects are recorded in the geologic record. Therefore, a more general procedure for paleoseismic landslide analysis is required.

If static stability analyses clearly indicate that failure in aseismic conditions is highly unlikely, then an earthquake origin can be hypothesized on that basis alone. A dynamic analysis can then be used to estimate the minimum shaking intensities necessary to have caused failure. Such an approach requires a general relationship between critical acceleration, shaking intensity, and Newmark displacement; a relationship developed by Jibson and Keefer (1993) is reiterated here.

Jibson and Keefer (1993) selected 11 strong-motion records having Arias intensities between 0.2 and 10.0 m/s, which span the range between the smallest shaking intensities that might cause landslide movement and the largest shaking intensities ever recorded. For each strong-motion record, they calculated the Newmark displacement for several critical accelerations between 0.02 and 0.40 g, the range of practical interest for most earthquake-induced landslides. Analysis of the resulting data set indicated that a multivariate model of the following form would fit the data well:

$$\log D_N = \mathrm{A}\,\log I_a + \mathrm{B}a_c + \mathrm{C} \pm \sigma, \tag{8.3}$$

where D_N is Newmark displacement in centimeters; I_a is Arias intensity in meters per second; a_c is critical acceleration in g's; σ is the estimated standard deviation of the model; and A, B, and C are the regression coefficients. The resulting model has an R^2 of 0.87, and the coefficients all are significant above the 99.9% confidence level:

$$\log D_N = 1.460\,\log I_a - 6.642a_c + 1.546 \pm 0.409. \tag{8.4}$$

This model yields the mean value of Newmark displacement when σ is ignored; the variation about this mean represented by σ results from the stochastic nature of earthquake ground shaking. Thus, even two strong-motion records having identical Arias intensities can produce significantly different Newmark displacements for slopes having identical critical accelerations. Therefore, Eq. (8.4) yields a range of displacement values that must be interpreted with considerable judgment. Figure 8.9 shows critical acceleration lines defined by Eq. (8.4). The model underestimates Newmark displacement at low levels of Arias intensity (less than 0.5 m/s) for very small critical accelerations (0.02 g), but otherwise the model fits the data well.

In the case of the Stewart landslide, if we knew nothing of the shaking history of the site, the minimum earthquake shaking intensity could be estimated using Eq. (8.4). This requires us to judge the amount of Newmark displacement (the critical displacement) that would reduce shear strength on the failure surface to residual levels and lead to catastrophic failure. As discussed previously, critical displacements of about 10 cm are probably realistic for this type of slide, based on previous studies (Wieczorek *et al.*, 1985; Wilson and Keefer, 1985; Keefer and Wilson, 1989), laboratory shear-strength testing of soil samples from the site (Jibson, 1985), and field studies of landslides in the region (Jibson and Keefer, 1988). Insertion of a displacement value of 10 cm and the range of critical accelerations of the Stewart landslide (0.17 to 0.18 g) into Eq (8.4) yields a lower bound Arias intensity of about 2.6 m/s to trigger the Stewart slide.

Wilson and Keefer (1985) developed an empirical relationship between Arias intensity, earthquake magnitude, and source distance:

$$\log I_a = \mathbf{M} - 2\,\log R - 4.1, \tag{8.5}$$

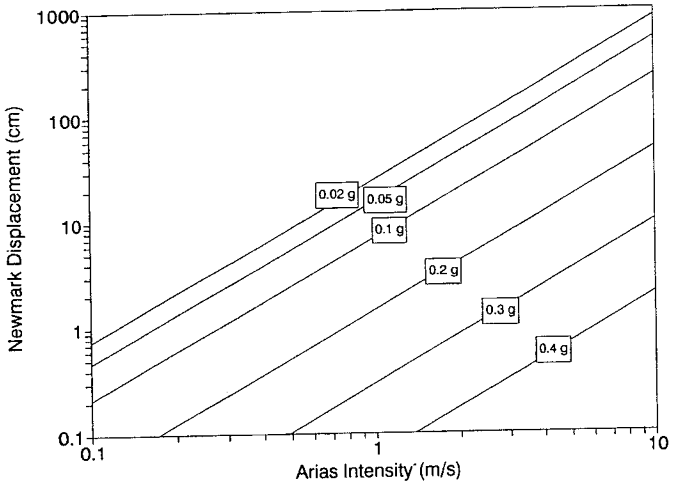

Figure 8.9 Newmark displacement as a function of Arias intensity for several values of critical acceleration as modeled by the regression equation, Eq. (8.4). [From Jibson and Keefer (1993); reprinted with permission of the Geological Society of America.]

where I_a is Arias intensity in meters per second, **M** is moment magnitude, and R is earthquake source distance in kilometers. For a minimum source distance of 5 km (focal depth at the epicenter), the Arias intensity of 2.6 m/s estimated above yields **M** = 5.9 as the minimum threshold earthquake magnitude required to have caused slope failure. Although this magnitude is considerably lower than those estimated to have been generated by the 1811–12 earthquakes, it provides a reasonable lower bound in the absence of any other information. If more than one landslide of identical age were similarly analyzed in an area, magnitude and location estimates can be optimized by using the larger required source distances between two or more separate sites.

8.6 INTERPRETING RESULTS OF PALEOSEISMIC LANDSLIDE STUDIES

Once a landslide or group of landslides has been identified, dated, and linked to earthquake shaking, what can we learn about the magnitude and location of the triggering earthquake? Several approaches to this last level of paleoseismic interpretation are possible, and, in most cases, multiple lines of evidence will be required to make reasonable estimates of magnitude and location. Perhaps the most important aspect of such interpretation is a thorough understanding

of the characteristics of landslides triggered by recent, well-documented earthquakes.

8.6.1 Some Characteristics of Landslides Triggered by Earthquakes

Keefer (1984) conducted by far the most comprehensive study of landslides caused by historical earthquakes. He documented minimum earthquake magnitudes and intensities that have triggered landslides of various types, average and maximum areas affected by landslides as a function of magnitude, and maximum distances of landslides from earthquake sources as a function of magnitude. For these comparisons, he grouped different types of landslides into three categories: *disrupted slides and falls* (defined as falls, slides, and avalanches in rock and soil); *coherent slides* (defined as slumps and block slides in rock and soil and slow earth flows); and *lateral spreads and flows* (defined as lateral spreads and rapid flows in soil and subaqueous landslides).

8.6.1.1 Minimum Earthquake Magnitudes That Trigger Landslides

In a review of intensity reports from 300 earthquakes, Keefer (1984) found that the smallest earthquake reported to have caused landslides had a magnitude of 4.0. Landslides of various types have threshold magnitudes ranging from 4.0 to 6.5 (Table 8-4); disrupted landslides have lower threshold magnitudes than coherent slides. Although smaller earthquakes could conceivably trigger landslides, such triggering by very weak shaking probably would occur on slopes where failure was imminent before the earthquake.

8.6.1.2 Minimum Shaking Intensities That Trigger Landslides

Keefer (1984) also compared landslide initiation to Modified Mercalli intensity (MMI). Table 8-5 shows the lowest MMI values and the predominant

Table 8-4
Minimum Earthquake Magnitude Required to Trigger Landslides

Earthquake magnitude	Type of landslide
4.0	Rock falls, rock slides, soil falls, disrupted soil slides
4.5	Soil slumps, soil block slides
5.0	Rock slumps, rock block slides, slow earth flows, soil lateral spreads, rapid soil flows, subaqueous landslides
6.0	Rock avalanches
6.5	Soil avalanches

Note: Data from Keefer (1984).

Table 8-5.

Minimum Modified Mercalli Intensity Required to Trigger Landslides

Landslide type	Lowest Modified Mercalli intensity	Predominant Modified Mercalli intensity
Disrupted slides and falls	IV	VI
Coherent slides	V	VII
Lateral spreads and flows	V	VII

Note: Data from Keefer (1984).

minimum MMI values reported where the three categories of landslides occurred. Keefer's (1984) data show that landslides of various types are triggered one to five levels lower than indicated in the current language of the MMI scale.

Nikonov (1988a) and Solonenko (1977) correlated landslide initiation with threshold shaking levels using the Russian MSK intensity scale. Their observations indicated that small landslides are initiated at intensities IV through VII, large landslides at intensities VIII through IX, and "large landslides in basement rocks" at intensities of IX or greater.

8.6.1.3 Areas Affected by Earthquake-Triggered Landslides

For 30 historical earthquakes, Keefer (1984) drew boundaries around all reported landslide locations and calculated the areas enclosed. His plot of area versus earthquake magnitude (Fig. 8.10) shows a well-defined upper bound curve representing the maximum area that can be affected for a given magnitude. Also shown is a regression line showing average area, the equation of which is

$$\log A = M_s - 3.46, \tag{8.6}$$

where A is area affected by landslides in square kilometers and M_s is surface-wave magnitude (Keefer and Wilson, 1989).

Keefer (1984) noted that the area affected by landslides will be influenced, in part, by the geologic conditions that control the distribution of susceptible slopes. Also, he noted that earthquakes having focal depths greater than about 30 km plot on or near the upper bound (Fig. 8.10), which indicates that deeper earthquakes can trigger landslides over larger areas. Surprisingly, he found no differences in the areas affected by landsliding that could be attributed to regional differences in seismic attenuation.

8.6.1.4 Maximum Distance of Landslides from Earthquake Sources

Keefer (1984) related earthquake magnitude to the maximum distance of the three categories of landslides from the earthquake epicenter and from the closest point on the fault-rupture surface (Fig. 8.11). Again, upper bound curves are well defined and are constrained to pass through the minimum threshold magnitudes shown in Table 8-4 as distance approaches zero.

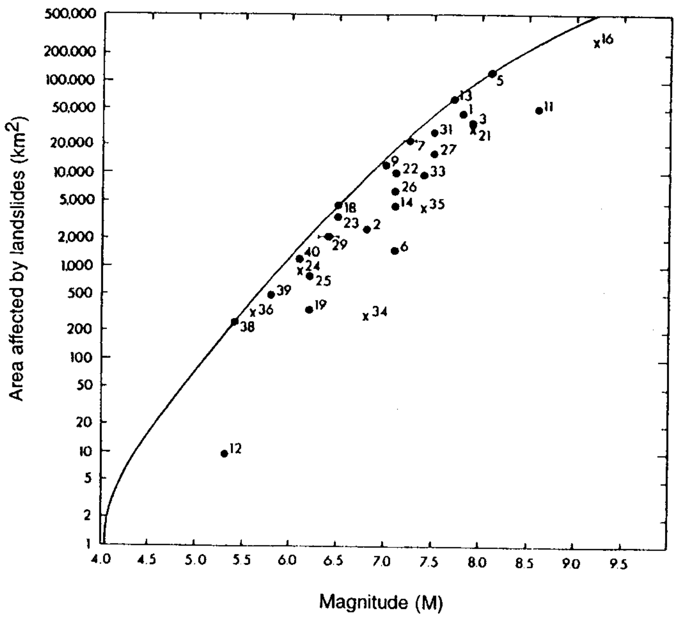

Figure 8.10 Area affected by landslides in earthquakes having different (generally M_s) magnitudes. Solid line is upper bound; numbers beside data points refer to earthquakes analyzed by Keefer (1984); dots denote onshore earthquakes; ×'s denote offshore earthquakes. [From Keefer (1984); reprinted with permission of the Geological Society of America.]

Figure 8.11 indicates that disrupted slides and falls have the lowest shaking threshold and that lateral spreads and flows have the highest shaking threshold. As with area, earthquakes having focal depths greater than 30 km generally triggered landslides at greater distances than shallower earthquakes of similar magnitude.

8.6.2 Interpreting Earthquake Magnitude and Location

Keefer's (1984) results allow interpretation of earthquake magnitude and location in a variety of ways. If a single landslide is identified as being seismically triggered, then a minimum magnitude and MMI can be estimated based on the landslide type. For example, Schuster *et al.* (1992) used Keefer's (1984) magnitude of 6.5 as a lower bound estimate for triggering of rock avalanches that formed dams. If several landslides in an area are identified as being seismically induced, then application of Keefer's (1984) magnitude–area and magnitude–distance relationships can yield minimum magnitude estimates. As the area in which landslides documented to have been triggered by the same earthquake increases, the estimated magnitude will increase toward the actual magnitude of the triggering earthquake. Therefore, documentation and analysis of landslides over a large area will produce more accurate magnitude estimates. If seismic source zones are well documented, then the distance from the closest source zone to the farthest landslide will yield a reasonable minimum magnitude estimate. The observation that greater source depth relates to greater areas affected and source distances for landslides of all types (Keefer, 1984) further complicates estimation of earthquake magnitude.

For a specific region, earthquake magnitude can be estimated based on comparison of paleoseismic landslide distribution with landslide distributions from recent, well-documented earthquakes in the region. This approach has been applied to landslide dams in New Zealand (Adams, 1981a) and to landslides in central Asia (Nikonov, 1988a).

Several types of interpretations from seismically triggered turbidites are possible. The linear extent of synchronous turbidites triggered from the edges of continental shelves can be used to estimate fault rupture length and, hence, earthquake magnitude (Adams, 1990). The extreme size and very long recurrence intervals (10^4 to 10^6 yr) for lithified turbidites preserved in the older geologic record argue that they formed in very rare, large-magnitude earthquakes (Mutti *et al.,* 1984; Spalletta and Vai, 1984). The paucity of seismically induced sedimentary structures in some older, lithified deposits likewise suggests long recurrence intervals and consequent large earthquake magnitudes (Seilacher, 1969).

Static and dynamic slope-stability analyses facilitate direct estimation of the minimum ground shaking, and hence magnitude, required to have caused failure of individual landslides (Jibson and Keefer, 1992, 1993), as described in detail previously. If the critical acceleration of a landslide can be determined by stability analysis, and if a reasonable amount of displacement (such as 10 cm) leading to catastrophic failure can be estimated, then Eq. (8.4) can be used to estimate the threshold Arias intensity required to initiate failure. Equation (8.5) (from Wilson and Keefer, 1985) can then be used to estimate the minimum magnitude of the triggering earthquake.

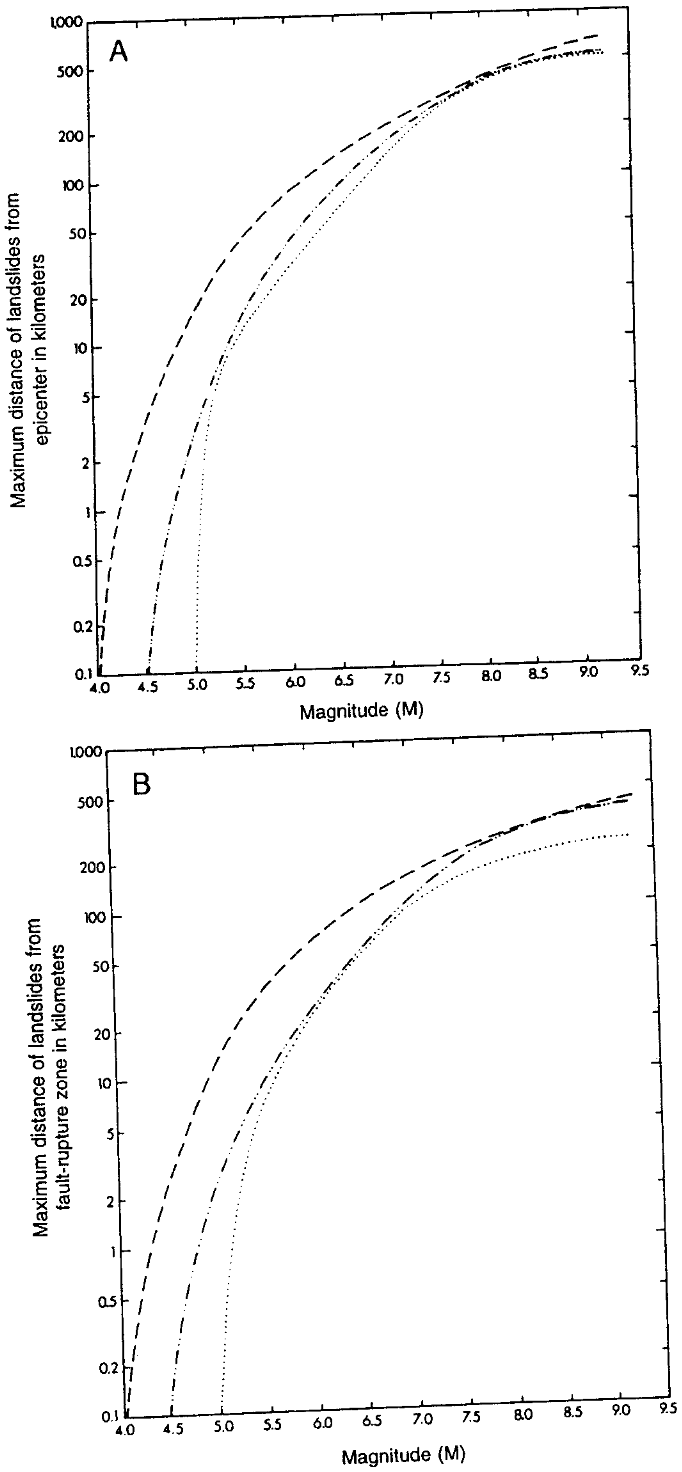

Figure 8.11 Maximum distance to landslides from (A) epicenter and (B) fault-rupture zone for earthquakes of different magnitudes. Dashed line is upper bound for disrupted slides and falls; dash-double-dot line is upper bound for coherent slides; and dotted line is upper bound for lateral spreads and flows. [From Keefer (1984); reprinted with permission of the Geological Society of America.]

A similar approach for estimating earthquake magnitude from the results of slope-stability analyses was outlined by Crozier (1992) and is based on the work of Wilson and Keefer (1985). They defined a quantity referred to as $(A_c)_{10}$, which is the critical acceleration of a landslide that will yield 10 cm of displacement (the estimated critical displacement leading to catastrophic failure) in a given level of earthquake shaking. They selected 10 strong motion records that spanned a range of Arias intensities and iteratively determined $(A_c)_{10}$ for each record. From these values, they developed a regression model relating Arias intensity to $(A_c)_{10}$:

$$\log(A_c)_{10} = 0.79 \log I_a - 1.095, \tag{8.7}$$

where $(A_c)_{10}$ is in g's and I_a is in meters per second. If the critical acceleration of a landslide can be determined, then this value can be used as the threshold value of $(A_c)_{10}$ in Eq. (8.7), and the Arias intensity that would trigger the critical displacement of 10 cm can be calculated. Magnitude can then be estimated from Eq. (8.5).

Stability analysis also could possibly be applied to speleothemes, whose dynamic stability can easily be modeled, to estimate the ground shaking required to cause failure.

Earthquake locations generally are estimated based on the distribution of synchronous landslides attributed to a single seismic event. In a broad area of roughly similar susceptibility to landsliding, the earthquake epicenter probably will coincide fairly closely with the centroid of the landslide distribution. In areas of highly variable or asymmetrical landslide susceptibility, epicenter estimation is much more difficult and subject to error. In areas where seismic source zones are well defined, the epicentral location is best defined as the point in a known seismic source zone (or along a known seismogenic fault) closest to the centroid of the landslide distribution.

8.7 SOME FINAL COMMENTS

The use of landslides as paleoseismic indicators is a fairly recent development that is beginning to expand in scope and complexity. A few final comments on the advantages and limitations of paleoseismic landslide analysis are in order.

The primary limitation of paleoseismic analysis of landslides is the inherent uncertainty in interpreting a seismic origin. Unlike liquefaction, which can occur aseismically only in relatively rare conditions, landslides of all types form readily in the absence of earthquake shaking as a result of many different triggering mechanisms. In many cases, ruling out aseismic triggering will be impossible, and the level of confidence in any resulting paleoseismic interpretation will be limited. For this reason, paleoseismic landslide analysis should include, so far as possible, multiple lines of evidence to constrain a seismic origin. In this way, a strong case can be built for seismic triggering of one or more landslides, even if no single line of evidence is unequivocal. Where independent paleoseismic evidence from fault or liquefaction studies is available, paleoseismic landslide evidence can provide useful corroboration.

Detailed slope-stability analyses generally can be performed only on certain types of landslides. Failure conditions of falls, avalanches, and disrupted slides cannot easily be modeled using Newmark's (1965) method, and even static stability analyses of these types of slides can be very problematic. Also, the pre-landslide geometry of slides in very steep terrain can be difficult or impossible to reconstruct. Thus, the analytical method described herein generally can be applied only to fairly coherent landslides where pre-landslide geometry can be reconstructed with confidence, where groundwater conditions can be modeled reasonably, and where the geotechnical properties of the materials can be accurately measured.

Even allowing for these limitations, paleoseismic landslide studies have been extremely useful where applied successfully, and they hold great potential in the field of paleoseismology. Dating landslide deposits is, in many cases, easier than dating movement along faults because many different dating methods can be used on the same slide to produce redundant results. In addition, landslides have the potential for preserving large amounts of datable material in the various parts of the slide (scarp, body, toe, etc.). In areas containing multiple or poorly defined seismic sources, paleoseismic ground-failure analysis may be preferable to fault studies because landslides preserve a record of the shaking history of a site or region from all seismic sources. Knowing the frequency of strong shaking events may, in many cases, be more critical than knowing the behavior of any individual fault.

Paleoseismic landslide analysis may have greatest utility in assessing earthquake hazards in stable continental interiors, such as the eastern and central United States, where fault exposures are rare or absent but where earthquakes are known to have occurred. In such areas, analysis of earthquake-triggered ground failure, both landslides and liquefaction, may be one of the few paleoseismic tools available.

Another advantage of paleoseismic landslide analysis is that it gets directly at the effects of the earthquakes being studied. Ultimately, most paleoseismic studies are aimed at assessing earthquake hazards. Fault studies can be used to estimate slip rates, recurrence intervals, and, indirectly, magnitudes. From these findings, we extrapolate the effects of a possible earthquake on such a fault. In paleoseismic landslide studies, we observe the effects directly. Thus, if a seismic origin can be established, a landslide shows directly what the effects of some previous earthquake were. Even if magnitude and location are poorly constrained, at least we have a partial picture of the actual effects of seismic shaking in a locale or region. Thus, for example, a map of the distribution of landslides triggered by the 1811–12 earthquakes in the New

Madrid seismic zone (Jibson and Keefer, 1988) yields a very useful picture of the likely distribution of landslides in future earthquakes there.

In conclusion, paleoseismic landslide analysis can be applied in a variety of ways and can yield many different types of results. Although interpretations are limited by the certainty with which a seismic origin can be established, paleoseismic landslide studies can play a vital role in the paleoseismic interpretation of many areas, particularly those lacking fault exposures.

Chapter 9

Application of Paleoseismic Data to Seismic Hazard Assessment and Neotectonic Research

James P. McCalpin

9.1 INTRODUCTION

The original justification for paleoseismic investigations was that they allowed analysis of a longer history of large earthquakes than was possible from the short historic record (Wallace, 1981; Sieh, 1981). This desire to reconstruct long earthquake histories for faults or regions was often driven by practical rather than research considerations. Of course, paleoseismic data can be used in research neotectonic investigations and can provide relatively short-term geologic data that complements longer term geological, geophysical, and seismological data on regional fault behavior and deformation style (e.g., Wesnousky *et al.*, 1984; Wesnousky, 1986). However, most paleoseismic studies to date have been undertaken to provide input for *seismic hazard assessments* (SHAs; Reiter, 1990).

Beginning in the 1960s, government regulations in several industrialized countries mandated SHAs for construction of new critical facilities (nuclear and other power plants, dams, hospitals, and schools). A key element of an SHA is *seismic source characterization,* i.e., the assignment of magnitudes and recurrence rates for large, potentially damaging earthquakes that could be generated by active faults near a site. An SHA is required to describe the largest earthquake that could occur within each identified seismic source zone. If a time interval or exposure time for the occurrence of such an earthquake is specified, the earthquake is termed the *maximum earthquake* (dePolo and Slemmons, 1990, p. 3). If no time limit is specified, then the *maximum credible earthquake* (MCE) is the largest earthquake that appears capable of occurring in an area or along a fault. In many parts of the world there have been few or no large earthquakes on active (i.e., late Quaternary) faults, much less an occurrence of the MCE. Accordingly, the task of identifying active faults, characterizing them for SHAs, and estimating the magnitude of the MCE falls largely to geologists utilizing geologic data (Fig. 9.1), rather than to seismologists using historic or instrumental data.

The preceding chapters described techniques needed to reconstruct the locations, displacements, and ages of paleoearthquakes in a region. Such a

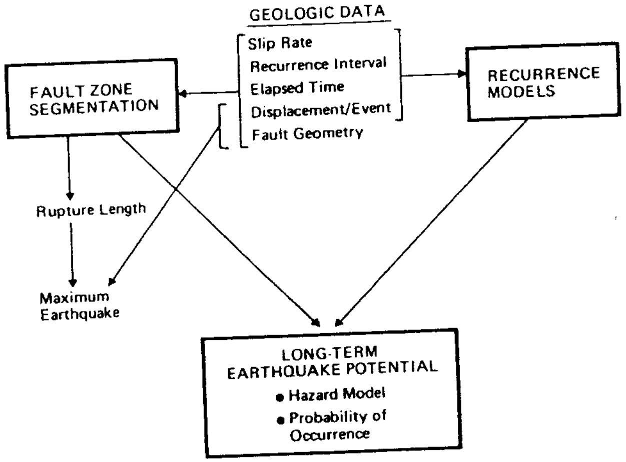

Figure 9.1 Relationship between geologic (mainly paleoseismic) data and stages of seismic hazard evaluation. Fault segmentation and recurrence models are discussed in Secs. 9.4 and 9.6, respectively. [From Schwartz and Coppersmith (1986). Reprinted with permission from Active Tectonics. Copyright© 1986 by the National Academy of Sciences. Courtesy of the National Academy Press, Washington, D.C.]

chronology is often adequate for the rather narrowly defined purposes of SHAs, and represents a considerable body of scientific knowledge that can stand alone. However, paleoseismic data by themselves cannot be fully integrated into more research-oriented neotectonic studies unless they can be explained by general models of fault behavior, and understood in the context of the present-day tectonic environment and stress field (Schwartz and Coppersmith, 1986). To contribute to the expanding field of neotectonic research, paleoseismic data must be synthesized with other data on historical seismicity, moment rates, geodetic strain rates, and stress fields to create a seismotectonic synthesis.

Within each of the major tectonic environments described in this book (extensional, compressive, strike-slip) the contribution of paleoseismic data to SHAs and to neotectonic research varies in importance. For faults with abundant historic seismicity, large historic surface ruptures (near to or equal to the maximum earthquake), and carefully monitored strain rates (e.g., the San Andreas fault zone, California), paleoseismic data mainly supplement the historic record by providing a longer history of large earthquakes. In contrast, for historically quiescent faults (such as the Wasatch fault zone, Utah) paleoseismic data provide the majority of information on the location, size, and recurrence of large earthquakes that is critical for seismic source characterization.

This chapter is mainly concerned with how the paleoseismic field measurements described in Chapters 3 through 8 are interpreted in terms of paleomagnitude and recurrence, and then applied to SHAs and integrated into larger studies of neotectonics. The next two sections (9.2, and 9.3) describe how to estimate paleoearthquake magnitude and recurrence from field measurements of displacement and earthquake age, respectively; such estimates are directly applied to SHAs. Sections 9.4 through 9.6 describe the important seismotectonic concepts of fault segmentation, fault behavior models, and earthquake recurrence models. Although such models were originally based on seismic or structural data, many of the critical tests involving large earthquakes can only be made based on paleoseismic data. The final section (9.7) discusses future prospects of the field of paleoseismology, what topics are inadequately addressed at present, and what steps might be taken to solve current problems in the field. For an overview of SHAs and how paleoseismic data are viewed by the hazards community, see Reiter (1990, 1995).

9.2 ESTIMATING PALEOEARTHQUAKE MAGNITUDE

Although various types of primary evidence have been used to infer magnitudes for paleoearthquakes, the length of surface rupture and the maximum displacement on continental fault traces are by far the most commonly used parameters (Bonilla *et al.,* 1984; Wells and Coppersmith, 1994). The inferred rupture length and slip for paleoearthquakes are compared to worldwide data on rupture length and slip during historic earthquakes (of known magnitude) to estimate a probable paleoearthquake magnitude.

Additional methods involve estimating magnitude from the area of the fault plane that slipped during past ruptures (Wells and Coppersmith, 1994) or the seismic moment, that is, the total energy released during the earthquake (Kanamori, 1977; Wyss, 1979). In some of largest plate-boundary earthquakes, for example, the 1960 southern Chile and 1964 southern Alaska earthquakes, there is little or no surface faulting, so the length or area of the zone of coseismic deformation as measured by permanent land-level change can be used to estimate earthquake magnitude. Although these additional methods may have a stronger theoretical basis than the empirical correlations between fault length and magnitude, the additional errors in estimating fault width and coseismic displacement may make the resulting estimates of magnitude no more accurate than those based only on a single parameter, such as fault length. As with the dating of paleoearthquakes, the best approach is to estimate paleomagnitudes using several methods.

Dating precision and the accuracy of stratigraphic and geomorphic correlations have an important bearing on magnitude estimates, because paleoearthquakes closely spaced in time may have created surface features that, after several hundred or thousand years, appear to be the product of one large paleoearthquake. The Dixie Valley–Fairview Peak earthquakes of 1954 (M_L 7.1 and M_L 6.8) created two zones of fault scarps 123 km in length in the span of 4 min. If the entire zone of scarps were attributed to a single earthquake, empirical relations would suggest a magnitude (M_s) 7.8 earthquake. Many historic surface-rupturing earthquakes in the western United States were probably composed of multiple events (Doser and Smith, 1989), thus the surface scarps visible today along many faults may not have formed simultaneously. Multiple great subduction earthquakes ($M_w > 7.8$) have also uplifted or submerged many tens of kilometers of coast as little as a few minutes to a few days apart (e.g., Ando, 1975; Plafker and Savage, 1970). Modern subduction zone earthquakes that produce such easily misinterpreted evidence continue to fuel debate as to whether similar marine terraces meters apart (such as on the east side of Tokyo Bay or on the Huon Penisula of New Guinea), were formed by single large earthquakes thousands of years apart or by many small, much more frequent earthquakes (e.g., Pandolfi *et al.*, 1992, versus Ota *et al.*, 1993). Thus, even with significant improvments in dating precision and accuracy, paleoseismological methods may never be able to distinguish multiple large earthquakes less than a few years or decades apart.

Another complexity that affects magnitude estimates for paleoearthquakes, the opposite of the problem described in the previous paragraph, is that of multiple simultaneous ruptures on different faults due to strain partitioning. Oblique strain in the lower crust can be relieved by simultaneous dip-slip and strike-slip displacement on separate surface faults during the same earthquake (e.g., Lettis and Hanson, 1991). In a different type of plate-boundary setting, shallow crustal faults in a subduction zone that are independent of the main plate-boundary megathrust commonly slip during megathrust earthquakes (e.g., Clarke and Carver, 1992; Chapter 5). The separate surface ruptures during such earthquakes may be difficult to recognize as simultaneous and might be ascribed to two smaller paleoearthquakes, each of which would be considerably smaller than the earthquake that actually occurred.

Having mentioned these important caveats, we now describe in some detail how paleoearthquake magnitudes are typically estimated for SHAs. Within the description of each method we refer to the physical processes that are thought to control the parameter of interest, and how variability in those processes induces corresponding uncertainties in the empirical relationships.

9.2.1 Methods Using Primary Evidence

In an exhaustive review, dePolo and Slemmons (1990) list five methods for estimating the maximum (or maximum credible) earthquake on a fault or in a region: historical, paleoseismic, source characterization, regional, and relative comparison. The somewhat self-explanatory labels for each method indicate that most approaches make magnitude estimates based on observed historical or theoretical/tectonic data, rather than on inferred prehistoric data. In this section we describe only the *paleoseismic approach,* which is based on deducing the magnitudes of specific prehistoric earthquakes, rather than on predicting the magnitudes of future earthquakes. For an explanation of how paleoseismic magnitude estimates are combined with estimates using the other four approaches, the reader is referred to dePolo and Slemmons (1990).

Paleoearthquake magnitudes have traditionally been estimated from primary fault-zone evidence (surface-rupture length or displacement), rather than from secondary ground-shaking evidence. The earliest approach was to compare the inferred rupture length (L) or maximum displacement (D) from a paleoearthquake with the corresponding measurements from historic earthquakes of known magnitude. While this approach used easily obtained field data, correlations of earthquake magnitude with single fault parameters contained considerable variance. This variance is not surprising because a correlation based on either L or D alone cannot account for variations in depth of the earthquake, shape of the rupture surface, relation of the rupture surface to the earth's surface, the stress drop, the shear modulus, and many other factors that may vary between earthquakes of the same magnitude (Bonilla *et al.,* 1984, p. 2384). Next, multiple parameter correlations (magnitude versus LD or LD^2; magnitude versus fault area) were tried, in the hope that a physically more complete representation of earthquake geometry would decrease the variance in correlation; however, variance still remained.

The most recent approach correlates magnitude to the estimated seismic moment, which requires estimates of the rupture area, rock strength, and average displacement during paleoearthquakes. The more recent approaches thus have a sounder physical basis for estimating paleoearthquake magnitude, but require parameters that are difficult to estimate accurately for paleoearthquakes. The spectrum of approaches to paleomagnitude estimation thus ranges from the early simplistic models relying on measured data, to more sophisticated models relying on data that are increasingly inferred by indirect means; all models contain some uncertainty. In the following sections, we briefly describe the most common paleomagnitude estimation techniques, and consider the strong and weak points of each method.

One area of current ambiguity is whether the empirical relationships between magnitude and fault parameters vary significantly with seismotectonic region. Previous authors have suggested that different relations hold for stable continental interiors versus mobile belts [Johnston, 1994; Electric Power Research Institute (EPRI), 1994], for plate boundaries versus nonplate boundaries (Bonilla *et al.,* 1984), or for other subdivisions of the earth's regions (Acharya, 1979; Khromovskikh, 1989). In contrast, the recent comprehensive survey of fault parameters by Wells and Coppersmith (1994) indicates no significant differences in regressions between plate-boundary and other tectonic regions. In light of this ambiguity, investigators will have to decide if the advantage of using a regional (as opposed to global) regression analysis outweighs the disadvantage of fewer observations and (possibly) lower correlation coefficients.

9.2.1.1 *Surface-Rupture Length Method*

This method of paleomagnitude estimation involves estimating the length of prehistoric surface rupture, and comparing its length to the *surface rupture lengths* (*SRLs*) of historic earthquakes of known magnitude. The most recently analyzed historic data set for this comparison (Fig. 9.2) is that of Wells and Coppersmith (1994), although similar plots are presented by Slemmons (1982), Bonilla *et al.* (1984), Heaton *et al.* (1986), and Khromovskikh (1989). The historical data range from moment magnitude (**M**) 5.8 to 8.1. To estimate paleomagnitude from an inferred paleorupture length, one uses a regression of **M** on *SRL* (length, measured as a straight-line distance between the rupture endpoints).

Two sources of uncertainties exist in this method: (1) deficiencies in the lengths cited in the historic data set and (2) difficulties in accurately measuring the length of prehistoric ruptures. For the first source, Bonilla *et al.* (1984, p. 2380) list 10 sources of error in relating historic earthquake magnitude to a surface rupture length. The error sources are listed in Table 9-1, with a notation of whether the error is likely to lead to an overestimate (O) or underestimate (U) of rupture length, or whether it introduces a random error (R). Of these 10 sources of error, three would lead to an underestimate of the true surface rupture length, while the other seven could lead to underestimates or overestimates (i.e., random error).

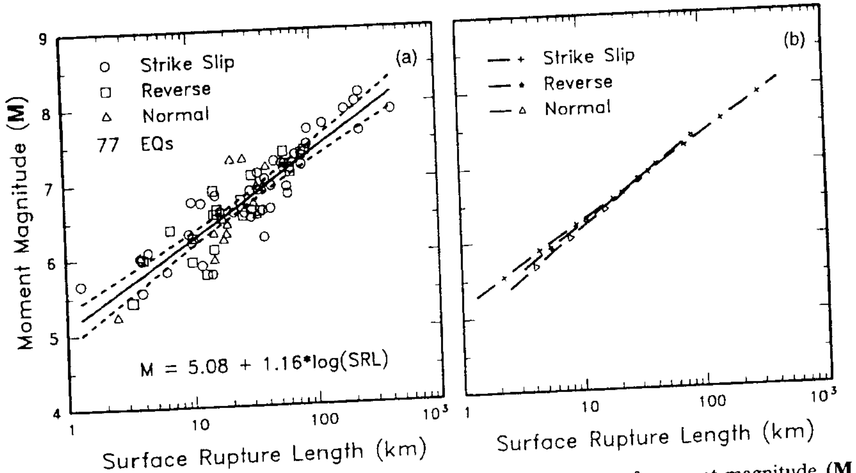

Figure 9.2 Surface rupture length (*SRL*, in km) as a function of moment magnitude (**M**) for 77 earthquakes in the historical data set of Wells and Coppersmith (1994). Equation at bottom lists regression of **M** on log *SRL* for all fault types. Note that in part (B) there is little difference between the relationships for the three fault types. [From Wells and Coppersmith (1994); reprinted with permission of the Seismological Society of America.]

When considering prehistoric surface ruptures, some of the error sources cited in Table 9-1 apply directly (such as number 1). A corollary to error 1 is the situation in which a prominent fault scarp traversing an older geomorphic surface abruptly stops at the contact with a younger surface. The obvious inference is that the scarp originally extended farther, but was eroded or buried by younger deposits. In such a case, the rupture length mappable today is a minimum estimate of the original rupture length. The along-strike width of the younger covering unit determines the uncertainty in estimating the original rupture length; the maximum possible paleo-*SRL* is that of the preserved scarp plus the entire width of the younger surface. Other error sources

Table 9-1

Sources of Uncertainty in Measuring Surface-Rupture Length for Historic Surface Ruptures

Source of uncertainty	Sense of probable error[a]	Also applies to prehistoric ruptures?
1. Fault enters water and no subaqueous observations were made.	U	Y
2. Ends of rupture areas were not examined thoroughly.	R	Y
3. End points obscured by landslides, dessication cracks, vegetation, or other materials that could absorb and conceal fault ruptures.	U	Y
4. Displacement dies out gradually and ends are indefinite.	R	Y
5. Local decrease in displacement along fault is incorrectly interpreted as dying out at the end of the faults.	U	Y
6. Difficulty in distinguishing between main fault and subsidiary faults.	R	Y
7. Inclusion or exclusion of irregularities in fault geometry such as curves, jogs, and overlaps.	R	Y
8. Text of source report gives different length than distance scaled on map.	R	N
9. Map scale not correctly determined (e.g. bar scale different from actual map scale).	R	N
10. Mistakes in making map measurements.	R	N

[a] O, overestimate; R, random error; U, underestimate.

for historic ruptures also have analogs for paleoruptures. Error sources 3, 4, 5, and 6 in Table 9-1 all relate to defining the endpoints of rupture, which is generally more difficult for paleoearthquakes than for historic earthquakes, for the reasons given later.

The detectability of surface rupture decreases with increasing age. Displacements of less than 30 cm can be obscured relatively rapidly by the surficial processes of weathering and erosion. Therefore, the accuracy of a paleorupture length estimate depends on the original amount of surface displacement, the time since the event, and the rate of local geomorphic processes. For large paleoearthquakes ($M_s > 7$), which typically have maximum displacements near 1 to 3 m in the center (see next section), the main difficulty in estimating paleo-*SRL* arises from erosional obscuring of the small-displacement ends of the rupture. For example, of the 35 km of surface rupture produced by the 1983 M_s 7.3 Borah Peak, United States, earthquake (Fig. 3.6), 10 km was composed of fissures and small scarps less than 30 cm high at both rupture ends (Crone *et al.,* 1987). These small features will be obscured by surface processes long before the 1- to 3-m-high scarps of the central section disappear. Similar small displacements on the ends of historic ruptures are documented for normal (Figs. 3.5, and 3.6), reverse/thrust (Fig. 5.3), and strike-slip (Fig. 6.3) ruptures. Rupture preservation also depends on local geomorphic process rates, as affected by topography, climate, and material resistance to erosion. Fault scarps in arid and semi-arid climates may persist much longer than those in humid or tropical environments. Scarps that displace low-gradient geomorphic surfaces (such as river terraces and the distal parts of alluvial fans) are preserved longer than similar-size features that form on steep topography such as range-front facets (McCalpin, 1983). Scarps in noncohesive, fine materials (eolian sand, grus, loose colluvium) may disappear within a few weeks or months after they form. All of these phenomena make it relatively easy to underestimate the original length of surface rupture.

A different type of problem is differentiating surface ruptures caused by different events. Most long seismogenic faults display prehistoric scarps of various ages along most of their length. If scarps resulting from more than one rupture are mistakenly assigned to a single paleoevent, the rupture length, and thus paleomagnitude, will be overestimated. This is particularly problematic on multiple-segment faults where individual segments have ruptured with short recurrence times, creating abutting fault scarps of similar size and steepness. Recent studies on strike-slip faults (Fumal *et al.,* 1993) and on normal faults (Machette *et al.,* 1992a, b) have attempted to locate the boundaries of individual paleoearthquake ruptures by trenching and numerical dating, but such efforts are time consuming and expensive, and are hampered in proving rupture contemporaneity by the precision of dating techniques. However, it is sometimes possible to prove that rupture did *not* occur at one location during the same time span that rupture did occur at another location, and this negative evidence can be used to bound the maximum length of past rupture segments.

Finally, the practice of using straight-line measurements of *SRL*, as opposed to fault-trace measurements, may lead to unrealistically small *SRL* values for many large historic earthquakes. For example, the two overlapping ruptures in the 1959 M_s 7.5 Hebgen Lake, Montana, earthquake have a straight-line length of only 27 km, compared to a fault-trace length of at least 42 km. The surface-wave magnitude of this earthquake, as calculated by the equations of Bonilla *et al.* (1984) using a rupture length of 27 km, thus underestimates the observed magnitude by 0.6 magnitude units. As rupture sinuosity increases, so does the difference between straight-line and fault-trace lengths. To overcome this problem, Mason (1992) proposed using the average of the straight-line and fault trace lengths, based on the assumption that most faults are right-cylindrical in shape (see diagram in Mason, 1992, p. 25). Despite the appeal of such an approach, Mason's regressions of **M** on log *SRL* actually possess slightly smaller correlation coefficients than do Bonilla *et al.*'s (1984).

Like many single-parameter correlations, the correlation between historic earthquake magnitude and surface rupture length contains considerable variance (Bonilla *et al.,* 1984; Wells and Coppersmith, 1994). Bonilla *et al.* reasoned that some of this variance may be introduced by uncertainties in the magnitude and *SRL* measurements themselves, rather than by stochastic (earthquake-to-earthquake) variations. If measurement errors dominate the overall variance in a regression, then a weighted least-squares regression (WLS, in which more weight is given to better defined points) should have less variance than an ordinary (unweighted) least-squares regression (OLS). Bonilla *et al.* (1984) found that the OLS and WLS variances were very similar, and thus concluded that most of the variance in empirical regressions of earthquake magnitude with length or displacement arises from stochastic errors. As a result, Wells and Coppersmith (1994) do not even cite the errors associated with their measurements of **M,** *SRL,* and *D,* and use only an OLS regression. However, paleoseismologists should still try to estimate the uncertainty in their field estimates of *SRL* in order to provide a range of estimates for probable paleomagnitude.

9.2.1.2 Maximum Displacement Method

The maximum displacement method involves determining the *maximum displacement* (*MD*) associated with a paleoearthquake, and comparing that value to the maximum displacement measured in historic earthquakes. *MD* is commonly used in compilations of historic earthquakes (Bonilla *et al.,* 1984; Wells and Coppersmith, 1994) (Fig. 9.3) because it is easier to determine from historic accounts than is average displacement. Historical data sets for displacement are affected by at least nine sources of error (Bonilla *et al.,* 1984, p. 2380), which might lead to underestimates (U), overestimates (O),

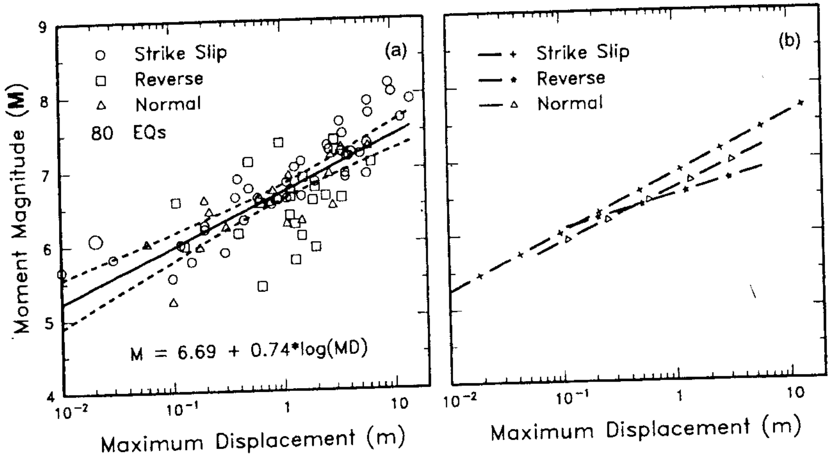

Figure 9.3 Maximum fault displacement (*MD*, in meters) as a function of moment magnitude (M) for 80 earthquakes in the historical data set of Wells and Coppersmith (1994). Equation at bottom lists regression of **M** on log *MD* for all fault types. Note differences among fault types in part (B); for reverse faults displacement does not increase with magnitude as rapidly as for other type faults. [From Wells and Coppersmith (1994); reprinted with permission of the Seismological Society of America.]

or random errors (R) in the displacement measurement (Table 9-2). Four of the errors will lead to underestimation of the true maximum displacement, one to an overestimate, and four to random errors. Paleoseismologists should try to assess how severely these uncertainty sources affect their estimates of *MD*.

When making field measurements of the inferred maximum paleoseismic displacement on a fault, additional uncertainties arise. If displacement is measured only from fault scarp height, then postfaulting erosion and deposition may have increased or decreased the relief. On dip-slip faults, surface relief usually decreases with time as erosion strips material from the upthrown block, deposition occurs on the downthrown block, or both. On strike-slip faults, apparent lateral offsets of river terraces, for example, can be decreased by erosional trimming (Chapter 6).

While few geomorphic processes overaccentuate the size of surface displacements, it is still possible to overestimate the original fault displacement from surface features. The most common cause of overestimation is misinterpretation of the cumulative displacement of two or more paleoearthquakes for the effect of a single event. This problem is acute where successive paleoearthquakes have ruptured along the same individual traces in a fault zone. The only foolproof way to determine if surface features represent one or

Table 9-2

Sources of Uncertainty in Estimating the Maximum Displacement of a Historic Surface Rupture

Source of uncertainty	Sense of error[a]	Has application to prehistoric ruptures?
1. Entire rupture trace was not examined and therefore maximum displacement may have been missed.	U	Y
2. Maximum displacement may have occurred where good measurements could not be made (e.g., no reference lines for measurement of strike-slip).	U	Y
3. Maximum displacement may be obscured by landslides, vegetation, local bodies of water, or other entities.	U	Y
4. Surface offset, scarp height, or throw (defined in Sec. 3.2.3) may have been reported instead of net slip.	R	Y
5. Nontectonic effects such as local slope movements are not separated from tectonic effects.	R	Y
6. Displacement was partly absorbed by distributed fracturing, flexing, intergranular movements, and other processes.	U	Y
7. Afterslip of unknown amount increased the displacement.	O	Y
8. Field investigator rounded off measurements.	R	Y
9. Mistakes occurred when making and recording measurements.	R	Y

[a] O, overestimate; R, random error; U, underestimate.

many events is to examine subsurface exposures. However, use of these exposures also has its limitations, as discussed in detail in Chapters 3 through 6.

9.2.1.3 Average Displacement Method

Recently more estimates have been made on the *average surface displacement* (*AD*) in historic earthquakes, and these estimates may provide a sounder basis for estimating paleoearthquake magnitude. From a theoretical standpoint, Kanamori (1977) showed that seismic moment (and, thus, magnitude) is a linear function of *average subsurface displacement* (*ASD*) on the fault plane, not maximum surface displacement (*MD*). The relation between *MD*, *AD*, and *ASD* is complex (Thatcher and Bonilla, 1989) and this complexity explains why correlations of magnitude and displacement contain so much variation. Figure 9.4 shows how the true earthquake slip distribution differs from that inferred from surface geologic and geodetic data. In most historic dip-slip earthquakes, *MD* underestimates geodetic slip (Fig. 9.4), probably because surface slip was measured across relatively short fault-scarp profiles, which neglected a subtle component of far-field deformation. Geodetic slip

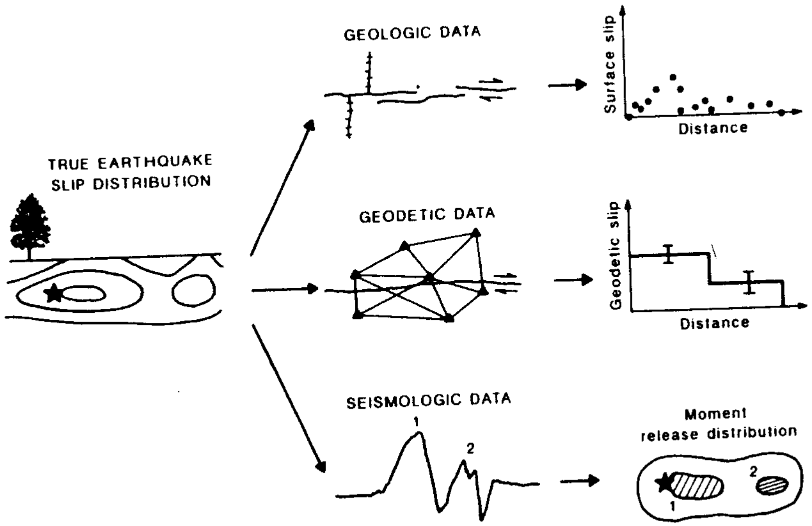

Figure 9.4 Schematic diagram showing the relation of the true earthquake slip distribution on a fault plane (far left), to surface deformation measurements (geologic data, geodetic data) and moment release distribution. The three field data sources represent different manifestations of the true slip distribution. In paleoseismic studies only one of these data types (geologic data) is commonly available for study, so the inference of true slip distribution (from which average slip could be calculated) carries large uncertainties. From Thatcher and Bonilla (1989).

is probably a better surface estimator of slip at depth, but even geodetic slip may suffer from attenuation as the displacement propagates upward from seismogenic depths. Thus, the variable relation between maximum slip at the surface and average slip on the causative fault plane is probably responsible for much of the scatter in bivariate plots such as those shown in Fig. 9.3.

Wells and Coppersmith (1994) state that, where *ASD* can be computed from seismic moments, *ASD* averages 76% of *MD,* and *ASD* averages 132% of *AD*. Thus, the average subsurface displacement on a fault plane evidently attenuates before reaching the surface on the 32 faults examined by Wells and Coppersmith. Such attenuation may result from strain absorption by intergranular shear in near-surface unconsolidated deposits in the fault zone. The maximum surface displacement, being on average 32% larger than the *ASD,* represents either (1) the attenuated surface expression of maximum subsurface displacement (a quantity not tabulated by Bonilla *et al.* or Wells and Coppersmith) or (2) an exaggerated response of surficial deposits to faulting, such as graben formation or back-tilting (Chapter 3).

Average surface displacement on historic surface ruptures may be calculated by several graphical methods, depending on the number of displacement measurements along strike and the degree of accuracy desired (compare the slip along strike patterns among Figs. 3.5, 3.6, 5.3, and 6.3). Choices include a linear point-to-point function, a running three-point average, or an enveloping function that minimizes the effects of anomalously high or low displacements (D. B. Slemmons, Las Vegas, Nevada, personal communication, 1994). Wells and Coppersmith (1994, pp. 986–987) computed *AD* for 57 historic earthquakes between **M** 5.7 and 8.1 where at least 10 displacement measurements were distributed along the rupture. The ratio of *AD*/*MD* averages about 0.5 with a range of 0.2 to 0.8; the ratio is not dependent on earthquake magnitude. Despite good theoretical reasons for expecting *AD* to correlate better with magnitude than *MD,* the correlation coefficients are actually slightly lower for the former (Table 9-3; Wells and Coppersmith, 1994, Table 2B). Mason (1992) analyzed a subset of five well-studied normal surface ruptures and found the *AD*/*MD* ratio to range from 0.31 to 0.56, with a mean of 0.40.

Mason also proposes that displacements measured in randomly located trenches along a fault scarp should be assumed to be closer to the mean than to the maximum displacement. (This contention could be supported by a statistical analysis of surface displacement patterns, but few have been attempted.) Therefore, he suggests that (for normal faults in the Basin and Range Province) these "average" trench displacement measurements could be multiplied by 2.5 (the reciprocal of 0.40) to estimate the *MD,* and that *MD* value could then be used in the many regression equations of **M** or M_s against *MD*. This procedure is quite different from that used in the past, where displacement measurements from trenches were often assumed to be equal to *MD,* especially if the trench was located in the center of a fault segment where surface displacements tend to be large (albeit variable). Mason's procedure leads to very large displacement estimates, and thus large (conservative?) magnitude estimates; however, his suggestion does point out a need to quantify the statistical relationships between *AD* and *MD* for faults of different types and in different regions.

A simple test of Mason's assumption can be made by examining the statistics of slip along strike for a well-measured event, such as the 35-km-long 1983 Borah Peak, Idaho, normal fault rupture. Within two weeks after the earthquake, throw was measured at 62 locations roughly equally spaced along strike. Throw values are first normalized by dividing them by the maximum throw (2.7 m), and then the incremental and cumulative frequency distributions of normalized throws are plotted (Fig. 9.5). Plots for the whole rupture (bars, and dashed cumulative curve) show the effects of many small throws (10 to 30 cm) measured in the northern 10 km of the rupture. Because of these small throws, the median and mean normalized throws are less than half the maximum throw. Because most trenches are placed in the central half of fault segments (where displacements are large), the cumulative frequency distribution of throws in the central half of the rupture is also plotted in Fig.

Table 9-3

Empirical Relationships between Moment Magnitude (**M**) and Surface-Wave Magnitude (M_s), and fault Parameters

Equation[a]	Slip type[b]	Number of events	Coefficients and standard errors		Standard deviation (σ)	Correlation coefficient (r)
			a(sa)	b(sb)		
M = a + b*log(SRL)	SS	43	5.16(0.13)	1.12(0.08)	0.28	0.91
	R	19	5.00(0.22)	1.22(0.16)	0.28	0.88
	N	15	4.86(0.34)	1.32(0.26)	0.34	0.81
	all	77	5.08(0.10)	1.16(0.07)	0.28	0.89
M = a + b*log(MD)	SS	43	6.81(0.05)	0.78(0.06)	0.29	0.90
	R[c]	21	6.52(0.11)	0.44(0.26)	0.52	0.36
	N	16	6.61(0.09)	0.71(0.15)	0.34	0.80
	all	80	6.69(0.04)	0.74(0.07)	0.40	0.78
M = a + b*log(AD)	SS	29	7.04(0.05)	0.89(0.09)	0.28	0.89
	R[c]	15	6.64(0.16)	0.13(0.36)	0.50	0.10
	N	12	6.78(0.12)	0.65(0.25)	0.33	0.64
	all	56	6.93(0.05)	0.82(0.10)	0.39	0.75
Ms = a + b*log(SRL)	SS	23	6.24(0.26)	0.62(0.14)	0.29	0.71
	R	12	5.71(0.52)	0.92(0.32)	0.27	0.68
	N			No relationships calculated		
	all	45	6.04(0.22)	0.71(0.12)	0.31	0.66
Ms = a + b*log(MD)	SS	18	7.00(0.14)	0.78(0.25)	0.33	0.61
	R			No relationships calculated		
	N	9	6.81(0.07)	0.74(0.13)	0.19	0.91
	all	39	6.95(0.08)	0.72(0.15)	0.32	0.63

[a] Equations based on moment magnitude (**M**) from Wells and Coppersmith (1994); equations based on surface-wave magnitude (M_s) from Bonilla *et al.* (1984). *SRL*, surface rupture length, measured as a straight-line distance between rupture ends, in km; *MD*, maximum surface displacement, in meters; *AD*, average surface displacement, in meters.

[b] SS, strike-slip; R, reverse; N, normal; all, all fault types.

[c] Relationship not significant at the 95% confidence level.

9.5 (solid curve). This curve shows the effect of removing the very small throws, and has a median (50th percentile) value equal to 50% of the maximum throw.

There is a 50% chance that a throw measured at a randomly located point on such a rupture will be either larger or smaller than the median; this statistical property presumably underlies Mason's speculations. The median normalized throws for the whole rupture and central half are 0.367 and 0.50, respectively. If the median is the most likely value to measure in a randomly sited trench, then the maximum throw for a given paleoearthquake could be most likely estimated by multiplying the median throw by the inverse of those two numbers (2.7 and 2.0, respectively). Thus, Mason's suggestion to multiply randomly measured throw values on normal faults by about 2.5 to approximate *MD* has

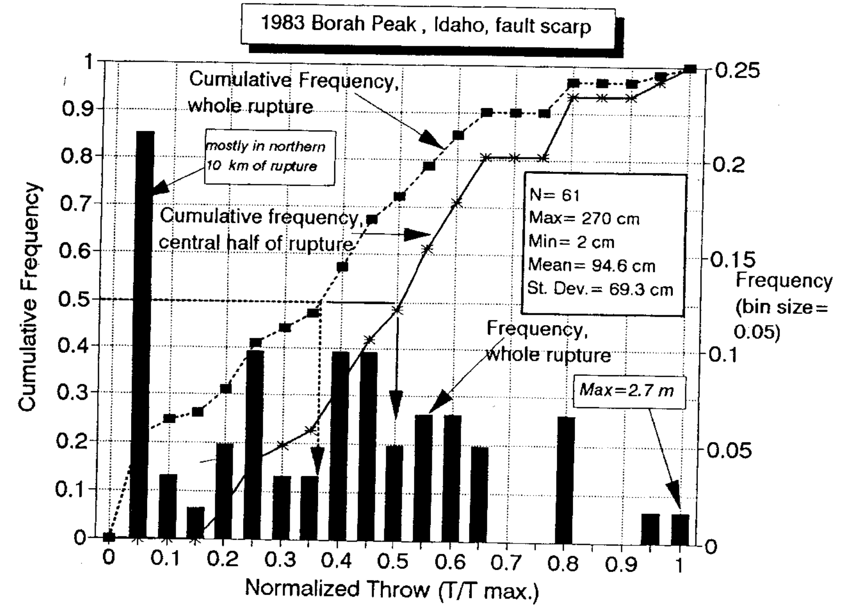

Figure 9.5 Frequency distributions of normalized throws from the 1983 Borah Peak surface rupture, central Idaho. Black bars at bottom show frequency of normalized throws for entire rupture trace; dashed curve shows corresponding cumulative frequency. Solid line shows cumulative frequency of normalized throws for the central half of the rupture only. Throw statistics (in box at right) refer to the entire rupture trace.

some statistical justification. Conversely, the cumulative frequency curves also demonstrate that the probability of randomly measuring a throw near to the maximum is quite small. For example, in Fig. 9.5 throws greater than or equal to 90% of the maximum throw comprise only 3 to 6% of the entire distribution. Thus, by randomly locating a trench on a fault trace, one has only a 3 to 6% chance of measuring a throw that is within 90% of the maximum throw. Although the foregoing analysis is based on only a single (normal-fault) rupture, the results strongly suggest that throws measured in randomly located trenches are unlikely to approach the maximum displacement in each paleoearthquake.

9.2.1.4 Length Times Displacement Method

Empirical relations between magnitude and log *LD* or log *LD*^{2} have been developed by numerous authors (see multiple citations in dePolo and Slemmons, 1990, p. 12). The use of both *L* and *D* is thought to incorporate more physical information about an earthquake than using either parameter individually. Several workers (Slemmons, 1982; Bonilla *et al.*, 1984) showed that regressions of M_s against log *LD* have higher correlation coefficients than regressions using either L or D individually (Table 9-3, bottom row). Mason (1992, p. 50) suggested that the improved fit of LD regressions resulted from the fact that rupture lengths tend to underrepresent magnitude systematically, whereas displacements systematically overrepresent magnitude; thus multiplying L times D would cancel these tendencies. For the particular data set under study (16 normal earthquakes), Mason (1992) pointed out that use of the straight-line method of SRL measurement tended to *underestimate* true fault dimensions, whereas maximum displacements on normal faults tended to be exaggerrated by graben formation and back-tilting in small areas and *overestimated* the pattern of displacement of the entire fault. These counterbalancing tendencies may not necessarily hold true for all fault types. However, comparing the all-fault-type regressions of Bonilla *et al.* (1984; my Table 9-3) we note that the LD regression has a higher correlation coefficient, but also a slightly higher standard deviation, than regressions based on L or D alone. Unfortunately, Wells and Coppersmith (1994) did not compute a regression of moment magnitude (**M**) on log LD.

9.2.1.5 Rupture-Area Method

The rupture-area method uses an empirical correlation between historic earthquake magnitude and rupture area, as determined from the spatial distribution of aftershocks (Wyss, 1979; Wells and Coppersmith, 1994). Using this method for paleoearthquakes involves substituting estimates of subsurface rupture length and width for aftershock areas. The rupture area method is most useful for paleoearthquakes that occurred on structures that did not produce a discrete surface rupture, such as subduction zone megathrust earthquakes or blind thrust earthquakes that occurred beneath Quaternary folds. Obviously, magnitudes should not be estimated by this method if good data exist on surface rupture length or displacement. For those peculiar situations where such data are not available, we may estimate subsurface rupture length based on the dimensions of the underlying fault, as inferred from deeper geological or geophysical investigations. In the absence of surface rupture evidence it may be difficult to decide if the entire fault-plane area, or only a portion of it, ruptured in a paleoearthquake. We defer the detailed discussion of fault segmentation to sec. 9.4, but point out that it would be much more difficult to identify earthquake segments on a concealed fault than on a surface fault.

The paleorupture area to apply would be calculated by multiplying inferred rupture length (with the associated errors previously described) times the down-dip dimension of the fault plane in the brittle zone of the earth's crust. Rupture length estimates for subduction zones have been based on the spatial extent of crustal subsidence and uplift determined from geomorphic studies (e.g., Nelson and Personius, 1995), whereas length estimates for blind thrusts are based on the length of surface folds (e.g. Hummon *et al.*, 1994). In both of these cases the length of paleoseismic deformation probably exceeds the length of subsurface rupture, and inverse elastic dislocation modeling may be necessary to deduce the dimensions of the concealed fault that would produce the observed surface deformation (e.g., Hummon *et al.*, 1994, for blind thrusts; Barrientos and Ward, 1990, for subduction megathrusts). Rupture width estimates reflect the down-dip dimension of the fault. Sibson (1986) suggests that, in addition to the depth of the rheologically brittle zone of the crust, an underlying "transition zone" atop the truly ductile (aseismic) zone of the crust should be included in rupture width estimates. The depth of the brittle/ductile transition at the time of prehistoric faulting must be estimated, along with the dip of the fault plane between the surface and the transition zone. The estimates of rupture length and width obviously require a detailed knowledge of local crustal structure, which may be lacking in many areas. This method should only be used where high-quality geological and geophysical data are available to determine the subsurface geometry of the fault.

9.2.1.6 Seismic-Moment Method

The seismic moment of a paleoearthquake can be calculated if the area of the rupture, *ASD,* and shear rigidity of rocks are accurately known [Appendix 1, Eq. (A.1)]. If we assume that shear rigidity has been essentially constant at modern values, then the method is similar to the rupture area method just outlined, but requires an additional estimate of *ASD*. *ASD* can be estimated in two ways. If the fault has surface rupture expression, then *ASD* might be estimated as either 0.76 *MD* or 1.32 *AD,* based on the empirical relations of Wells and Coppersmith (1994, pp. 987–988). However, both of these empirical relations have considerable variance. For faults that do not break the surface, *ASD* may be estimated in two ways: (1) for blind thrusts, by analogy to historic earthquakes (Hummon *et al.*, 1994), and (2) for subduction zones, mean long-term slip rate (from plate motion studies) divided by the mean recurrence interval between morphogenic earthquakes (e.g., Geomatrix, 1995). Once seismic moment is computed, the moment magnitude (M_w) of the paleoearthquake can be calculated by Eq. A.2, and Fig. A.1.1 (Appendix 1) can be used to convert that M_w value to any other magnitude scale.

The seismic moment method is the most physically robust method of paleomagnitude estimation, and it does not incorporate the stochastic variations that are incorporated in an empirical data set. However, the method requires input values for both paleorupture area and *ASD,* the latter of which (as previously described) can be especially difficult to estimate for paleoearthquakes, particularly on subduction zones.

9.2.2 Methods Using Secondary Evidence

Methods of estimating paleomagnitude from secondary evidence, such as liquefaction or landslides, are still in the process of development and testing.

At present, estimates are based primarily on a semiquantitative comparison of the areal extent of secondary features with the results of historic earthquakes of known magnitude. A critical component of these methods is the location of the epicenter of the paleoearthquake, which is not an important consideration for the methods previously described based on direct paleoseismic evidence. Methods based on liquefaction features are described in Chapter 7 and those based on landslides are described in Chapter 8.

9.3 PALEOSEISMIC SLIP RATES AND RECURRENCE

Slip rate and recurrence interval are two fundamental descriptors of paleoseismicity, and both are critical components of SHAs. *Slip rates* are calculated from the cumulative displacement of dated landforms or deposits. Calculation of slip rate does not require recognition or dating of any individual paleoearthquakes, so the topic is more a part of neotectonics than of paleoseismology. However, one method of calculating the recurrence interval uses slip rate (see discussion later), so we briefly review slip rate estimation. At the end of this section, we describe how slip rates derived from paleoseismic data can be applied to SHAs.

Recurrence interval (the time span between any two paleoearthquakes) can be estimated in two fundamentally different ways. The first method used in neotectonic studies calculated an *average* recurrence interval that incorporated multiple paleoearthquakes and, thus, averaged the time spans among the events (see *direct method,* later). The method preferred at present involves dating each separate paleoearthquake directly (the *geologic method*). The strengths and weaknesses of each approach are outlined in the following sections. The time span that has passed since the latest earthquake on a given fault is referred to as the *elapsed time.* The elapsed time is not a recurrence interval, because it does not bound the occurrence of two earthquakes, but rather one earthquake and the present time. The elapsed time is a *minimum value* for the latest recurrence interval, even if the next earthquake were to occur tomorrow.

9.3.1 Recurrence Estimation Using Slip Rates

The earliest method for estimating paleoearthquake recurrence used averaged (or long-term) slip rates, divided into assumed values of slip per event, to calculate an average recurrence interval (Wallace, 1970). This method has been termed the *direct method* of recurrence estimation (e.g., Working Group, 1988), although that modifier may mislead people into thinking that earthquakes are being dated directly. The estimate of long-term slip rate is based on the cumulative displacement of a dated feature or deposit that had been

offset by multiple earthquake ruptures. The slip per event is more difficult to estimate from reconnaissance studies, but can be estimated from the maximum or average slip observed during large historic earthquakes, or from the smallest consistent offsets of geomorphic features.

In general, slip rate may be calculated (after Wallace, 1970) as:

$$\mathrm{RI} = D/\,(S - C), \tag{9.1}$$

where

RI = mean recurrence interval
D = displacement during a single, typical faulting event
S = coseismic slip rate
C = creep slip rate (assumed to be zero for most faults unless historic creep has been documented).

Estimates of displacement per event and slip rate will contain uncertainties that arise from (1) the field measurements of paleoseismic offset and (2) errors in dating offset landforms and deposits, as described in Chapters 3, 5, and 6. It is critical that these uncertainties be carried throughout any computation of slip rate (e.g., Niemi and Hall, 1992). For example, a landform may be offset 50 ± 5 m and be bracketed by limiting ages of 15 and 23 ka. Uncertainties in net offset are often presumed to follow a Gaussian distribution (Sec. 6.2.3), with (in our example) 50 m representing a "best estimate" of offset and 5 m presumed to capture most (95%) of the measurement uncertainty (i.e., 2σ). Uncertainties in landform age likewise arise from the (typically) limited number of numerical ages, and uncertainty about how tightly those ages bracket true landform age. For example, if we deem it unlikely that true landform age is outside of the bracketing ages, we may presume that bracketing ages define $\pm 2\sigma$ limits on the probability distribution of age. In the example cited above, such an assumption implies mean age $\mu = 19$ ka and $\sigma = 2$ ka. In contrast, if we consider the ages as not so closely bracketing, we may consider them to constitute $\pm 1\sigma$ limits on the age distribution, in which case our example values would be $\mu = 19$ ka and $\sigma = 4$ ka.

In the less closely bracketed scenario above, slip rate is calculated as:

$$\frac{\text{Net offset}}{\text{Landform age}} = \frac{50 \pm 5\ \text{m}}{19 \pm 4\ \text{ka}}. \tag{9.2}$$

According to the division rule for values with unequal standard deviations (Geyh and Schliecher, 1990):

$$t^* \pm \sigma^* = \frac{t_1}{t_2} \pm t^* \sqrt{\left(\frac{\sigma_1^2}{t_1^2}\right) + \left(\frac{\sigma_2^2}{t_2^2}\right)} \tag{9.3}$$

Substituting the values from Eq. (9.2) into Eq. (9.3); we obtain:

$$\frac{50 \pm 5 \text{ m}}{19 \pm 4 \text{ ka}} = 2.63 \pm 0.61 \text{ m/ka} \quad \text{or} \quad 2.63 \pm 0.61 \text{ mm/yr.} \qquad (9.4)$$

The slip rate calculated in Eq. (9.4) thus retains the elements of uncertainty associated with the input variables. The 2-σ limits on slip rate from Eq. 9.4 (1.41 to 3.85 m/ka) bound 95% of the probability distribution and are similar to the minimum and maximum cross-quotients derived from the values in Eq. (9.2) (1.96 to 3.67 m/ka).

In a similar manner, estimates of displacement per event carry uncertainties based on the field measurements of landforms or strata offset in individual paleoearthquakes. To continue with our example, suppose our hypothetical fault had a typical (characteristic) displacement of 5.5 ± 1.5 m per event, which we assume to be normally distributed. Recurrence interval is then calculated via Eq. (9.1) as:

$$\text{RI} = \frac{5.5 \pm 1.5 \text{ m}}{2.63 \pm 0.61 \text{ m/ka}} = 2.09 \pm 0.75 \text{ ka} \quad \text{or} \quad 2090 \pm 750 \text{ yr.} \qquad (9.5)$$

This recurrence interval incorporates the uncertainties in net offset, landform age, and slip per event, making the assumption that each of those variables is normally distributed. The 2-σ limits on the recurrence interval from Eq. (9.5) (590 to 3590 yr) are somewhat greater than the minimum and maximum cross-quotients (1234 to 3465 yr).

The paleoseismic input variables of net offset, landform age, and slip per event may also be assumed to follow other probability distributions. An obvious distribution is the discrete uniform distribution, in which all values between the bracketing (field) values are assumed to have equal probability. This distribution might be appropriate, for example, if only two field measurements of a parameter can be collected (such as the landform ages cited in our example) and they both seem equally likely. The mean (μ) and variance (σ^2) of a discrete uniform probability distribution can be calculated from the field data and the equations:

$$\mu = \frac{\sum_{i=1}^{k} x_i}{k} \qquad (9.6)$$

and

$$\sigma^2 = \frac{\sum_{i=1}^{k} (x_i - \mu)^2}{k} \qquad (9.7)$$

Calculations of slip rates and recurrence intervals based on the assumption of a uniform parameter distribution would be done in the same manner as above, using Eqs. (9.1) through (9.3). Calculations are obviously simplified if input parameters can be assumed to obey the same type of probability distribution.

Recurrence intervals calculated by the direct method are mean values, and average the actual recurrence intervals between all of the earthquakes that have displaced the dated datum. The direct method does have have one small advantage, however, in that failure to identify any individual paleoearthquake (as in a trench) does not adversely affect the calculated recurrence interval. A recurrence estimate based on the direct method is better than no estimate at all, but like all averages, it tells us little about the time variation in time intervals between events. We know from a decade of detailed paleoseismic work that recurrence intervals between paleoearthquakes are commonly irregular, and that the pattern of irregularity may be a key element in understanding the earthquake dynamics of individual faults and their seismic slip cycle (Scholz, 1990). Thus, while the direct method is useful in a reconnaissance sense, the preferred method of recurrence estimation would involve actual dating of individual paleoearthquakes.

9.3.2 Recurrence Estimation Using Numerical Dating of Paleoearthquakes

Since the early 1970s, geologists have been conducting detailed mapping and trenching investigations to identify and numerically date individual paleoseismic events (Sec. 1.4). This approach to recurrence estimation is termed the *geologic method* (Working Group, 1988). The task involves a multidisciplinary application of stratigraphy, sedimentology, structural geology, geomorphology, and geochronology, as described in detail for various tectonic settings in Chapters 3 through 6. Geochronologic techniques in particular have been pushed to their resolution limits in this effort to date individual prehistoric events. The overall goal of dating prehistoric earthquakes is to bracket the time of faulting as tightly as possible, by dating the youngest faulted deposit and the oldest unfaulted deposit that are stratigraphically related to a single paleoearthquake. Rarely can the exact date of an event be determined: instead, numerical ages are obtained that predate and postdate the event by some time interval. Section 1.4 describes the suite of current dating techniques that can be used in paleoseismology, and the applications and limitations of each method. Chapters 3 though 8 describe how and where to collect dating samples in various paleoseismic settings in order to most closely bracket the age of faulting. The resulting recurrence intervals then become major factors in deducing the type of earthquake recurrence model (Sec. 9.6) for individual faults or regions.

The precision with which recurrence can be calculated depends on how paleoearthquake age is bracketed by age control. For example, the constraint that the earthquake is younger or older than a given datum, without any indication of how much younger or older, is not a very tight constraint. In contrast, if numerical ages tightly bracket the event horizon from a paleoearthquake we can consider the earthquake date approximately known. Figure 9.6 shows graphically how these two kinds of "loose" and "tight" age constraints can combine to result in various estimates of average recurrence. Four general cases may be envisioned for the simple situation of two paleoearthquakes, which have produced a one-event fault scarp across a geomorphic surface dated 10 ka and a two-event scarp across a higher (30-ka) surface. In case 1 (not shown in Fig. 9.6), the age of each earthquake is known (e.g., from stratigraphic studies), so the actual recurrence is determined by merely subtracting their ages. In case 2, the age of the later earthquake is known rather exactly but the earlier earthquake is only known to be have occurrred between the formation of the two datums (Fig. 9.6, case 2). If we further require recurrence to be uniform through time, recurrence intervals ranging from 10 to 20 ka (mean, 15 ka) will satisfy the stipulated timing constraints, depending on when the earlier earthquake occurrred. Uniform recurrences longer than 20 ka are not permissible because the earlier event would not have displaced the older datum, and uniform recurrences shorter than 10 ka are not permissible because they would require more than one event between 10 to 30 ka, and also an additional event between 0 to 10 ka.

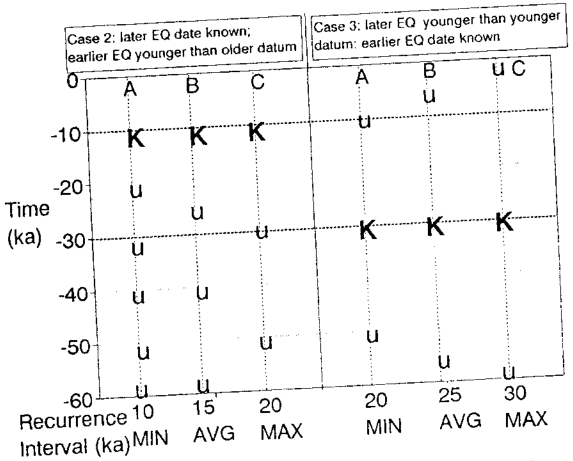

Figure 9.6 Schematic diagram showing six hypothetical series of earthquakes on time lines (vertical dashed lines) for several general cases of age control. *K,* earthquake of known age; u, earthquake constrained only to be younger than a dated datum (heavy dashed lines at 10 and 30 ka). Case 2: General case where the age of the later of two paleoearthquakes is well known, but the earlier earthquake is only known to be younger than a 30-ka datum. With uniform recurrence, the shortest recurrence interval is 10 ka, the longest 20 ka, and the average 15 ka. Case 3: General case where the age of the earlier of two paleoearthquakes is well known, but the later earthquake is only know to be younger than 10 ka. With uniform recurrence, the shortest recurrence interval is 20 ka, the longest 30 ka, and the average 25 ka. In this example only the earthquake series that result in minimum, average, and maximum recurrence are shown for each case; many other intermediate series exist.

Similar reasoning can be made in the other cases. In general case 3, we know the age of the earlier earthquake, but only know that the later earthquake is younger than the younger datum (Fig. 9.6, case 3). Only uniform recurrences of 20 to 30 ka (mean, 25 ka) will satisfy the stipulations. Finally, if we do not know the exact age of either earthquake (Fig. 9.7), but only know that they occurred sometime before and after formation of the younger datum, allowable uniform recurrences range from 10 to 30 ka (mean, 20 ka). If we relax the condition that recurrence must be uniform, then recurrences could be as short as one year (scenario 7) or as long as infinity, and little can be concluded about recurrence. The practical implication of this exercise is to show that "loose" age constraints, such as those derived from dating displaced landforms, do not permit very precise estimates of even average recurrence interval. Instead, we can only compute a mean recurrence and range of permissible recurrences, in a manner similar to that achieved with the so-called "direct" method using slip rates and average displacements per event.

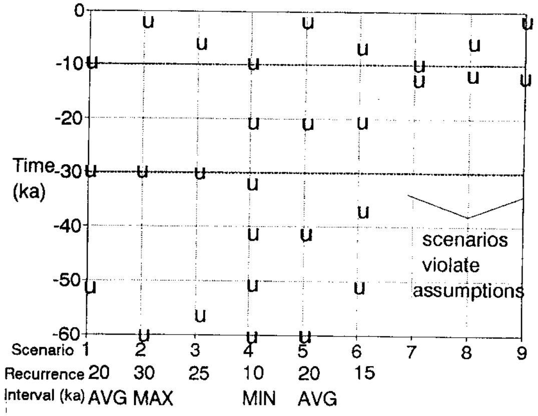

Figure 9.7 Schematic diagram showing nine hypothetical series of earthquakes on time lines (vertical dashed lines); in each case the 10-ka datum has been faulted once, and the 30-ka datum has been faulted twice. u, earthquake constrained only to be younger than a dated datum (heavy dashed lines at 10 and 30 ka). Scenarios 1–6 show results of uniform recurrence. In scenario 1, faulting occurred just after the formation of each surface; RI = 20 ka. In scenario 2, faulting occurred just after 30 ka, and yesterday; RI = 30 ka, the maximum uniform recurrence. In scenario 3, faulting occurred just after 30 ka, and at 5 ka. The minimum uniform recurrence (10 ka) is shown in scenario 4, where faulting occurred just before 30 ka, at 20 ka, and just after 10 ka. Scenarios 5 and 6 show examples of the many other intermediate scenarios; these define an average (uniform) recurrence of 20 ka. Scenarios 7, 8, and 9 show the results of nonuniform recurrence; the minimum allowable recurrence becomes one year (just before 10 ka, and just after 10 ka), whereas the maximum recurrence remains unchanged at 30 ka.

9.3.3 Testing for Contemporaneity of Paleoearthquakes

An increasing need in paleoseismology is to test the contemporaneity of paleoearthquakes between study sites on a fault zone or between nearby fault zones. Such testing has practical and academic implications. For example, if paleoearthquake ages on adjacent fault segments are found to be nearly identical, they may represent a single multiple-segment rupture with anomalously large source dimensions and magnitude. Many models of fault segmentation (Sec. 9.4) and behavior (Sec. 9.5) could be validated if we could test whether paleoearthquakes identified at different locations were the same event. For understanding the kinematics of complex faults, it would be helpful to know if main faults and their subsidiary faults always rupture at the same time.

In general, we may test whether two numerical ages (or suites of ages) can be considered the same based on how much their probability distributions overlap (Geyh and Schliecher, 1990). For example, if we presume that numerical ages on a given event horizon follow a Gaussian distribution, then we can utilize the "Z statistic" (e.g. Sheppard, 1975) to compare the overlap of the two ages given their means and standard deviations.

$$Z = T1 - T2/\sqrt{\sigma_1^2 + \sigma_2^2}, \tag{9.8}$$

where

$T1$ = mean age of the older earthquake
$T2$ = mean age of the younger earthquake
σ_1 = standard deviation of $T1$
σ_2 = standard deviation of $T2$.

As the difference between mean ages (the numerator) becomes smaller in relation to the averaged standard deviation (the denominator), the probabilty of the ages being drawn from the same population increases. Figure 9.8 shows a graph of probability of contemporaneity as a function of the Z statistic, with example radiocarbon ages from two sites on the Wasatch fault zone, Utah (McCalpin *et al.*, 1994). In that study the mean radiocarbon age of the most recent paleoearthquake at sites located 25 km apart in the same fault segment was 827 ± 169 yr B.P. and 669 ± 156 yr B.P., respectively. The Z statistic computed for these two ages is 0.69, yielding a 50% probability that the earthquakes at the two sites were the same event. In contrast, a similar comparison of earlier event ages between the two sites indicated a very low probability of contemporaneity, leading McCalpin *et al.* (1994) to conclude that those ruptures had not spanned the entire length of the fault segment.

9.3.4 Constructing Space–Time Diagrams

The space–time distribution of paleoearthquakes on fault segments or adjacent faults is often represented on a *space-time plot* or *diagram* (Schwartz, 1988a, p. 8). Space–time diagrams were used as early as 1975 to represent the distribution of historic earthquakes on subduction zone segments (e.g., Yonekura, 1975). On early paleoseismic space–time diagrams time was plotted on the horizontal axis, fault segments formed the vertical axis, and the estimated age range for paleoearthquakes on each segment was represented by a box (Fig. 9.9; also see Schwartz, 1988a, pp. 9, 12; Machette *et al.*, 1989, p. 240; 1991, p. 144; 1992a, p. A49; 1992b, p. 36). Later space–time diagrams (e.g., McCalpin, 1993a, p. 151) adopted the convention of placing time on the vertical axis (after Yonekura, 1975) with age increasing downward. The age limits of the box were defined by bracketing numerical ages, with the "most probable time of faulting" shown by symbols within the box. A more recent style of representing age constraints is to plot all of the closely constraining numerical ages directly (Fig. 9.10). This style has the advantage of showing the spread and central tendencies of the constraining ages for each paleoearthquake. In Fig. 9.10 only close maximum age limits on paleoearthquakes are plotted, because they compose the majority of limiting ages. However, the boxes on a space–time diagram of this style should not be confused with those of the earlier styles, in which box dimensions represent bracketing ages. Because overlapping boxes on adjacent segments might be interpreted as multisegment ruptures, it is important that workers explain exactly how the limits of their boxes are defined.

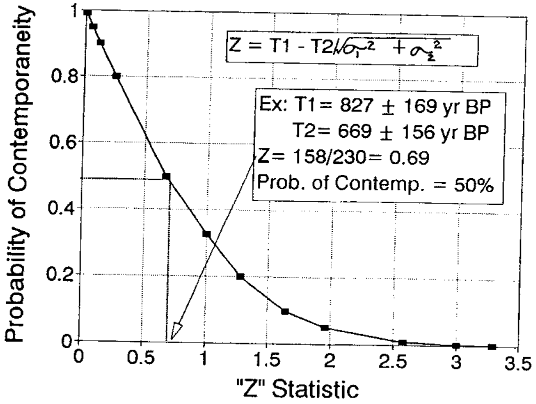

Figure 9.8 Probability of contemporaneity of numerical ages as a function of the Z statistic (equation in upper box). Numerical ages *T1* and *T2* in the lower (example) box at right are weighted mean limiting ages of the latest two paleoearthquakes, at two trench sites 25 km apart, on the Weber segment of the Wasatch fault zone, Utah (McCalpin *et al.*, 1994). Assuming that the limiting ages on each paleoearthquake obey a Gaussian distribution, there is a 50% probability that the two paleoearthquakes are the same event. Graph constructed from data in Sheppard (1975).

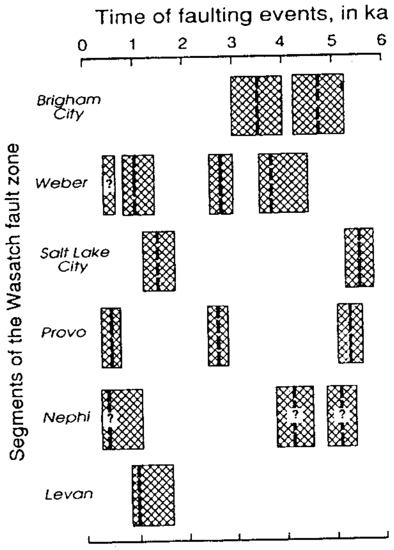

Figure 9.9 Example of a space–time diagram; estimated timing of major paleoearthquakes on the Wasatch fault zone (Utah) in the past 6 ka. Dashed vertical lines indicate estimates of the most probable time of faulting (queried or missing where timing is uncertain). Cross-hachure patterns indicate permissible limits for faulting events as determined from a combination of calibrated ^{14}C and thermoluminescence age estimates. [From Machette *et al.*, (1992b); reprinted with permission from *Annales Tectonicae.*]

The symbols representing earthquakes in a space–time diagram can also represent temporal probabilities of occurrence. If an earthquake is bracketed by only two numerical ages, these ages define the limits of a box (time span) within which the probability of earthquake occurrence must be assumed to be uniform. If an earthquake is bracketed by multiple ages, a box may be defined by the extremes of age (i.e., the youngest minimum and oldest maximum age limit). The "most probable time of faulting" might then be represented within the box, perhaps as defined by the oldest minimum and youngest maximum limiting ages, or as the mean or weighted mean of the limiting ages. Addition of such a symbol to the box indicates that the probability of earthquake occurrence within the box is not uniform, but is higher near the symbol. Finally, if earthquakes are constrained by close one-sided age constraints (such as in Fig. 9.10) the ages themselves can be plotted. From these ages a mean age and standard deviation can be calculated for each paleoearthquake. These ages can then be compared, via the Z statistic, to assess quantitatively the contemporaneity of earthquakes on different fault segments.

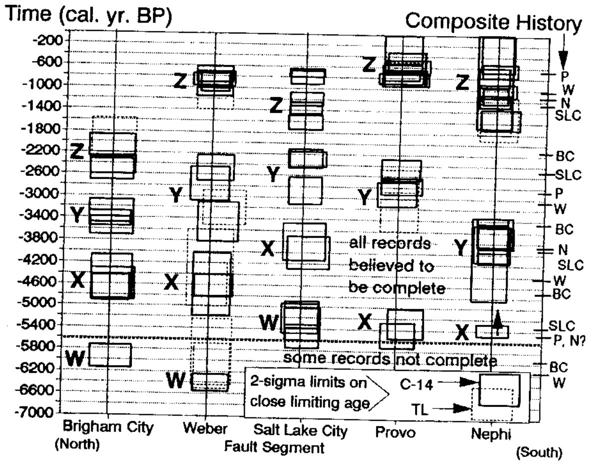

Figure 9.10 Space–time diagram of the Wasatch fault zone (same segments and time span as in Fig. 9.9), but with axes transposed and all of the close limiting numerical ages plotted instead of the permissible limits for faulting. Vertical dimensions of each box span the 2-σ age limits. Most limiting ages are from similar stratigraphic positions immediately beneath event horizons and are thought to date each earthquake closely (see Sec. 3.4.5). The composite paleoseismic history (right margin) shows the mean of limiting ages for each paleoearthquake, identified by segment. This diagram includes three paleoearthquakes (event Z on Brigham City, events X and Y on Salt Lake City) that were identified after Fig. 9.9 was published. [From McCalpin and Nishenko (1996); reprinted with permission of the American Geophysical Union.]

9.3.5 Slip Rates

Slip rates can be calculated from the cumulative displacement of dated landforms or deposits, even if individual paleoearthquakes cannot be identified. Many neotectonic studies cite slip rates on this basis, but slip rate may also be calculated in paleoseismic studies by dividing measured displacement per event by recurrence interval. The small number of paleoearthquakes that can be characterized on a single fault limits our ability to assess the variability of slip rates over geologic time for that fault. However, by making the *ergodic substitution* (see Sec. 9.7.4) we can examine slip rate variability for certain types of faults, and apply those patterns to individual faults with short records.

An example is the case of the Pajarito fault of northern New Mexico (McCalpin, 1995). Due to the geologic setting, slip rate on this normal fault could only be calculated from the large displacements on a 1.1 million yr-old (Ma) datum; no younger deposits were present in the fault zone. A mean, long-term slip rate of 0.12 mm/yr was thus calculated for the past 1.2 million years, but it was not possible to estimate how much faster slip rates could be over the shorter time periods (hundreds or thousands of years) relevant to an SHA. Using the ergodic approach, McCalpin (1995) inventoried slip rates in 27 normal faults in the western United States over time intervals ranging from a few thousand years to a few million years. All data were derived from fault-scarp heights across dated landforms. Interval slip rates were normalized by adjusting each fault's long-term slip rate to 0.12 mm/yr. The empirical distribution function (EDF; Fig. 9.11) shows that most interval slip rates in the normalized data set are less than the mean (long-term) rate, with slip rates progressively greater than the mean becoming increasingly rare. This pattern implies that in a "staircase-type" representation of variable slip over time (e.g., Fig. 1.2), "treads" are more abundant than "risers". For the SHA, rapid slip rates with low probabilities (e.g., 5 and 10% probabilities of exceedance) are of special interest for estimating hazard. Based on the EDF, the initial slip rate estimates and associated probabilities adopted by experts for the SHA logic tree (Fig. 9.12A) were modified considerably (Figs. 9.12B and C). There is little difference between the mean slip rates and associated probabilities in these three logic tree scenarios, but the fastest rates and associated probabilities differ significantly, especially between parts Figs. 9.12A and C. This example provides another demonstration of the utility of the ergodic substitution for solving applied problems.

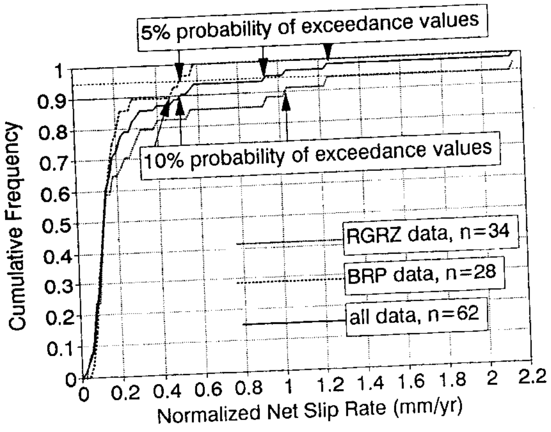

Figure 9.11 Empirical distribution function (EDF) of normalized slip rates from normal faults in the western United States. RGRZ, Rio Grande rift; BRP, Basin and Range Province. The 62 slip rates in the data set cover time periods ranging from 2000 to 2,000,000 years and were normalized by the factor required to make each fault's long-term slip rate = 0.12 mm/yr. Normalized slip rates at 5 and 10% probability of exceedance are shown for each data set and the grouped data set. [From McCalpin (1995); reprinted with permission of the Seismological Society of America.]

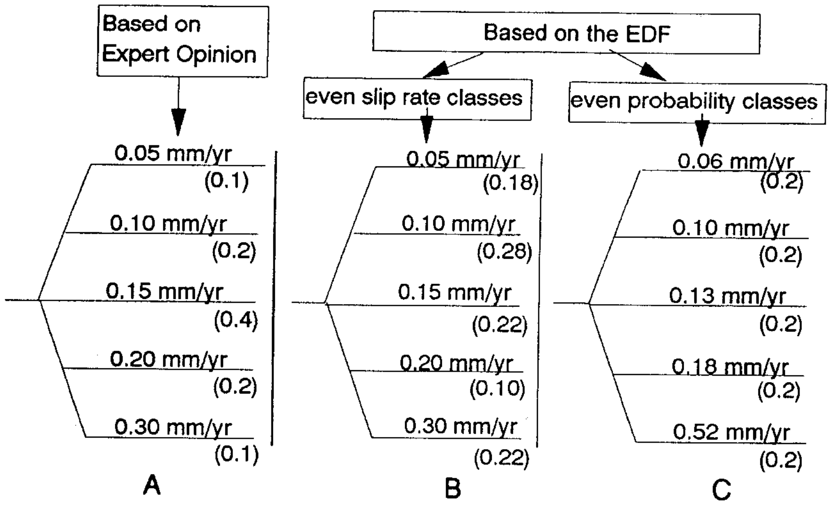

Figure 9.12 Comparison of logic tree branches describing probable slip rates for the Pajarito fault, New Mexico. (A) Slip rates and probabilities based on expert opinion. (B) Slip rates and probabilities based on the EDF (Fig. 9.11), using the same slip rate classes as in part A. (C) Slip rates and probabilities based on the EDF, using five classes of equal probability. Note the difference in extreme slip rates between the expert opinion tree (0.30 mm/yr at 0.1 probability) and the even probability tree (0.52 mm/yr at 0.2 probability). [From McCalpin (1995); reprinted with permission of the Seismological Society of America.]

9.4 FAULT SEGMENTATION

Most long active faults have historically ruptured over only a part of their total length in large earthquakes. Surface rupture often terminated at geometric or structural changes in the fault zone, leading early workers (e.g. Allen, 1968) to speculate that faults may be partitioned into consistent *rupture segments.* Under this hypothesis, an earthquake rupture on a long fault zone would always be restricted to the individual segment in which it began; segments would thus be *persistent.* With the later advent of the characteristic earthquake model (Sec. 9.5) workers further hypothesized that these surface-rupturing earthquakes, restricted as they were to segments of finite length, would be limited to a narrow magnitude range. This simple yet elegant model had instant appeal to workers in the seismic hazards field. If true, the model implied that the extent of rupture length could be predicted (i.e., it would be limited to the segment), and thus the maximum magnitude of earthquakes could be estimated (via the methods in Sec. 9.2) even in the absence of historic large earthquakes. The model also implied that, since each large characteristic paleoearthquake would have ruptured the entire fault segment, the recurrence history could be deciphered from only a single study site within each segment. In view of the usefulness of such simplifying assumptions to seismic hazard studies, the segmentation model was embraced with understandable enthusiasm.

Accordingly, workers from the late 1970s to present have striven to identify the component segments of many faults. In the absence of historic ruptures on these faults, they have used numerous types of "static" (i.e., time-invariant) geometric, structural, geophysical, and geologic criteria to define their "segments." Two problems have arisen from this practice. The first is purely terminological. The term "segment" was originally based on observed historic surface ruptures, such as the 1857 and 1906 ruptures on the San Andreas fault, USA. In contrast, most "segments" defined in later studies were defined based on static geologic or structural criteria, in the hope that such features might serve to arrest a future earthquake rupture. For example, the San Andreas fault zone has been divided into "segments" by at least four authors (Table 9-4). The number of "segments" identified for this one fault ranges from 4 to 784, with corresponding mean lengths of 245 and 1.2 km. The causes of such terminological ambiguity are described by Schwartz and Sibson (1989b, p. iii), who state "faults are geometrically and mechanicially segmented at a variety of scales. Segments may represent the repeated coseismic rupture during a single event on a long fault and may be tens to hundreds of kilometers long, they may represent a part of a rupture associated with an individual faulting event and only a few kilometers long, or they may represent local inhomogeneities along a fault plane and be only a few tens or hundreds of meters in length." From a paleoseismic perspective our main interest is in segments that rupture during large earthquakes. The question thus arises, do these shorter "segments" link to form earthquake rupture segments and, if so, how? The second problem is that the basis for fault segmentation schemes is not always described in publications, or if it is, an insufficient number of characteristics, or inappropriate characteristics, is used for segment definition. Because of the terminological confusion arising from a decade of rather loose usage of the term "segment," these matters are discussed in detail next.

9.4.1 Earthquake Segments

Discrete portions of faults that have demonstrably ruptured to the surface two or more times can legitimately be termed *earthquake segments* (dePolo *et al.*, 1989, 1991). Previous authors have also used the synonymous terms *earthquake rupture segment* and *rupture segment.* The criteria for the use of this term are fairly strict, only two types of evidence being admissible. The first is that documented historic surface ruptures have repeatedly been limited to the segment. The second type of evidence is that multiple prehistoric ruptures were limited to the segment. This type of evidence is more ambiguous than historic rupture evidence, because it depends on the degree to which details are known of local paleoseismic history. For example, the spatial extent

Table 9-4

Fault Segment Lengths Proposed for Active Faults by Various Authors

Fault name	Type[a]	Number of segments	Total fault length (km)	Mean segment length (km)	Modal segment length (km)	Criteria used for recognition[b]
1. Wasatch fault zone[c]	N	10	343	33	35	B,P,S,G,M
2. NE Basin and Range, >100 km[c]	N	10	—	25	20–25	B,P,S,G,M
3. NE Basin and Range, <100 km long[c]	N	20	—	20	10–20	B,P,S,G,M
4. Idaho[d]	N	20	280	22	20–25	B,P,S,G,M
5. North-central Nevada[e]	N	70	—	10	10	M
6. San Andreas[f]	S	4	980	245	15–175?	B,S,G,M
6. San Andreas[g]	S	7	980	140	300?	B,P,S,M
6. San Andreas[h]	S	784	980	1.2	1	M
6. San Andreas[i]	S	68	980	14	12	M
7. San Jacinto[j]	S	20	250	12	10–15	M
8. Elsinore[k]	S	7	337	48	—	M,P
9. Xianshuihe[l]	S	1	220	220	—	M
10. Transverse Ranges[m]	R	—	—	20–30	—	M
11. Oued Fodda, Algeria[n]	R	3	32	11	11–12	B,P,S,M

[a] N, normal; S, strike-slip; R, reverse.
[b] B, behavioral; P, paleoseismic; S, structural; G, geological; M, geometric.
[c] Machette *et al.* (1992a).
[d] Crone and Haller (1991).
[e] Wallace (1989).
[f] Allen (1968).
[g] Wallace (1970).
[h] Wallace (1973).
[i] Bilham and King (1989).
[j] Sanders (1989).
[k] Rockwell (1989).
[l] Allen *et al.* (1989).
[m] Ziony and Yerkes (1985).
[n] King and Yielding (1983).

of a single-event fault scarp can be taken as the minimum (preserved) extent of that surface rupture. Where only multiple-event fault scarps are present, it may be difficult to determine the length of any of the contributing component paleoruptures. Only in the past 10 years have multiple trenches been sited along multisegment faults in the United States to confirm that "segments" inferred from static geologic criteria have indeed functioned as "earthquake segments" (e.g. Machette *et al.*, 1992a; Fumal *et al.*, 1993). Fewer yet are studies of multiple trench sites within a single, statically defined segment, that could detect whether each paleorupture completely traversed the length of the segment, as predicted by the model. For example, an initial study on the Wasatch fault zone (USA), based on three trench sites (eight trenches) within a single segment, showed that the latest two paleoearthquakes can be confidently correlated over most of the segment. An earlier paleoearthquake does not appear to have ruptured the complete segment (McCalpin *et al.*, 1994). Similar partial-segment ruptures have been inferred for the southern San Andreas fault based on paleoseismic trench data (Fumal *et al.*, 1993). In identifying rupture terminations via trenching, the precision is limited by the horizontal spacing between the trenches. Searching for paleoseismic rupture terminations via trenching can naturally be very time consuming and expensive.

9.4.2 Fault Segments

In the absence of observed, or deduced, surface rupture evidence, faults can be subdivided into portions based on a variety of static geometric or geologic criteria (Table 9-5). If these portions are to be termed "segments," it must be clearly stated what type of segments they are and on what basis they are defined. The term *fault segment* may therefore be used as a general term for portions of the fault distinguished on static geologic criteria, as distinctive from "earthquake segments". For purely descriptive purposes, the term *fault section* might be even more preferable for these portions, with a later discussion of how the descriptive sections might interact to constitute earthquake segments (M. N. Machette, personal communication, 1993).

The subdivision of segment types in Table 9-5 follows a crude order from those most likely to coincide with earthquake segments (at top) to least likely (at bottom). The category of behavioral evidence, for example, includes the extent of inferred individual paleoearthquakes (type 1), and less, but still relevant, details on paleoseismic behavior (type 2). These measures are more likely to correlate well with extent of earthquake rupture than the more static, indirect parameters listed lower in the table. Wheeler (1989), speaking of normal faults, suggested that a segment boundary is probably persistent if a single Holocene or late Pleistocene rupture zone satisfies two conditions: (1) the rupture spanned a fault segment adjacent to the boundary and (2) the rupture did not cross the boundary. Verifying these two conditions is difficult in practice because one cannot ususally determine whether all fault scarps in a rupture zone formed in the same earthquake. However, one can infer some degree of contemporaneity by correlating the fault scarps. "A convincing demonstration that the correlated scarps satisfy the first condition includes showing that (vertical) separations on several correlated scarps are largest in the middle of the segment and smallest at both ends. A convincing demonstration that scarps satisfy the second condition includes showing that the correlated scarps on one segment differ in age from scarps on adjacent segments" (Wheeler, 1989, pp. 438-439). Field testing this second condition is limited by the resolution of fault-scarp dating methods (Chapter 3).

Among the static parameters, those most often found to control rupture termination are those that reflect most closely the characteristics of the seismogenic fault plane. Progressively more indirect static measures, which may not directly reflect barriers to rupture propagation, less commonly define true

Table 9-5

Types of Fault Segments and the Characteristics Used to Define Them

Type of segment[a]	Characteristics used to define the segment[a]	Likelihood of being an earthquake segment[b]
1. Earthquake	Historic rupture limits.	By definition, 100%[c]
2. Behavioral	1) Prehistoric rupture limits defined by multiple, well-dated paleoearthquakes.	High
	2) Segment bounded by changes in slip rates, recurrence intervals, elapsed times, sense of displacement, creeping versus locked behavior, fault complexity.	Mod. (26%)
3. Structural	Segment bounded by fault branches, or intersections with other faults, folds, or cross-structures.	Mod.–High (31%)
4. Geologic	1) Bounded by Quaternary basins or volcanic fields. 2) Restricted to a single basement or rheologic terrain. 3) Bounded by geophysical anomalies. 4) Geomorphic indicators such as range-front morphology, crest elevation	Variable[d] (39%)
5. Geometric	Segments defined by changes in fault orientation, stepovers, separations, or gaps in faulting.	Low–Mod. (18%)

[a] Classification follows the segment boundary types of dePolo *et al.* (1989, 1991) and Knuepfer (1989).

[b] Percentages = percent of cases where historic ruptures have ended at this type of boundary, as opposed to rupturing through it (Knuepfer, 1989, Table 3).

[c] However, restriction of a single historic rupture to the segment does not mean that all future ruptures will be similarly restricted.

[d] Small number of observations, accuracy questionable (Knuepfer, 1989, Table 3).

rupture segments. According to the analysis of Knuepfer (1989), the family of geometric discontinuities in fault zones (bends, stepovers, and gaps) as a group is least likely to bound earthquake segments. However, some of the seven types of geometric features defined by Knuepfer (1989, Table 3) have a much higher frequency as rupture endpoints than others. Unfortunately, many published fault segmentation schemes rely heavily on geometric evidence, perhaps because it is easy to gather.

9.4.3 Segment Boundaries

A *segment boundary* is defined as "a portion of a fault where at least two (preferably successive) rupture zones have ends" (Wheeler, 1989). Although a complete description of segment boundary types is beyond the scope of this book, a brief description is warranted for these fundamental features. In practice, fault segments defined on static criteria (structural, geologic, or geometric evidence) are usually recognized by the spatial discontinuities that separate them. These discontinuities form the segment boundaries between the descriptive fault segments. On small-scale maps segment boundaries are often indicated as points, but in fact they are domains of complex structure that may have significant along-strike dimensions, up to 20 to 40% of the length of adjacent fault segments.

Knuepfer (1989) identified 20 types of fault-related features that occurred at the ends of historic surface ruptures. These features should be the basis for any segmentation scheme, according to their observed frequency as rupture termination points. For strike-slip faults, releasing bends and steps, restraining bends, branch and cross-cutting structures, and changes in sense of slip were the most common characteristics of rupture endpoints. Larger bends and stepovers were more likely to stop rupture than smaller bends. The pattern on dip-slip faults is less clear. On reverse faults, mapped fault terminations, branching and cross-structures tend to be most associated with rupture endpoints. Finally, most structural and geometric features on normal faults appear little more likely to be rupture endpoints than to be ruptured through. The most likely structures to occur at rupture endpoints are cross-structures, but even they are ruptured through in 60% of observed ruptures.

9.4.4 Behavior of Segment Boundaries

The mechanical role of a segment boundary in accommodating slip should theoretically indicate something about its persistence as an initiator or terminator of rupture. King and Yielding (1984) divided geometric discontinuities along faults into two types. *Conservative discontinuities* transfer slip smoothly, because the vector of slip lies within the fault planes on either side of the discontinuity. Even though the fault may change orientation, no volume change or new faults must be created in the bend to accommodate slip (Fig. 9.13A). *Nonconservative discontinuities* require, from the interplay of the fault slip vector with the bend, volume changes or subsidiary faulting to conserve mass (Fig. 9.13B). The required volume change may disrupt a propagating rupture and terminate it.

If the segmentation model as originally conceived is valid, and the preceding mechanical discussion sound, then certain types of fault discontinuities should persistently define rupture terminations. A persistent segment boundary can therefore be defined as one which forms a consistent, long-term barrier to the propagation of rupture. Persistent boundaries thus control most large ruptures during much of the evolution of the fault (Wheeler, 1989). In contrast, a nonpersistent segment boundary would cause rupture termination only part of the time, with some ruptures propagating through the boundary. Nonpersistent boundaries control only a few successive ruptures during a short part of the fault's evolution, but none before or after it (Wheeler, 1989). Inherent in the concept of segmentation is the idea of persistent barriers (Aki, 1979, 1984) that control rupture propagation (Schwartz and Coppersmith, 1986, p. 218).

Unfortunately, the historic record of surface ruptures is insufficient to test whether most fault segment boundaries are persistent. Few fault segments anywhere in the world have experienced two very similar surface-rupturing earthquakes in historic time. On those faults with the longest, well-documented record of major surface ruptures, such as strike-slip faults in China (e.g., Allen *et al.,* 1989) or Turkey (Ambraseys, 1978), historic ruptures on adjacent parts of the faults have overlapped. Given the limited data set, Schwartz (1989) argued that paleoseismic data are the most reliable source for determining the long-term persistence of segments. In contrast, Wheeler (1989) states that, because paleoseismologists have studied only the last few paleoearthquakes on any fault, even that record is insufficiently long to determine segment persistence, and static geological criteria must be used.

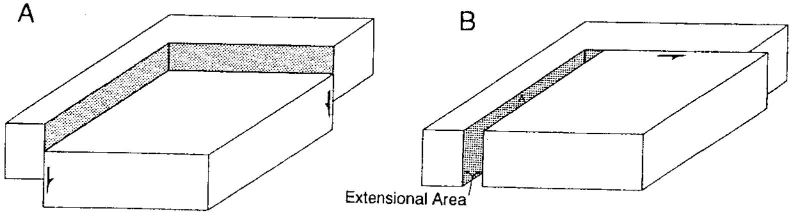

Conservative Displacement - No volume change or new faults created along the two faults with different orientations.

Nonconservative Displacement - A volume increase occurs along fault A.

Figure 9.13 Block diagrams showing (A) conservative and (B) nonconservative discontinuities along faults. [Adapted from King and Yielding (1983) by DePolo and Slemmons (1990); reprinted with permission of the Geological Society of America.]

Even when high-quality paleoseismic data are available, care must be taken to avoid circular reasoning in defining segment persistence. For example, on normal faults in the western United States, fault segments have been proposed based mainly on static, and to a lesser degree behavioral, characteristics (Schwartz and Coppersmith, 1984; Machette *et al.*, 1992a). Within each segment thus defined, as few as one detailed trenching investigation was performed to reconstruct the paleoseismic history. The occurrence of paleoearthquakes was then plotted on a space-time diagram to see if the timing of events was similar or different on adjacent segments. If the timing appeared different, as was often the case, it was concluded that each segment ruptured fully up to the segment boundary in each event. However, such a conclusion is not justified without trench data from the ends of the segments as well as the middle. Without such data, it cannot be proven that a rupture observed in the middle of a fault segment extended as far as the segment boundaries, or if ruptures may have crossed the segment boundary but stopped just short of the trench sites in the middle of the adjacent segments. In fact, the spatial/temporal patterns that have been used to support these behavioral segmentation schemes could just as well be reproduced by randomly occurring earthquakes unrestricted to segments of any kind! As mentioned in Sec. 9.7.2, the key localities for paleoseismic data that would prove or disprove the persistence of segmentation occur in the segment boundaries, not in the middle of segments.

9.4.5 Segmentation of Historic Surface Ruptures

If the segmentation theory is valid, then historic surface ruptures should have been restricted to fault segments that are recognizable on structural, geologic, or geometric grounds. While the worldwide data set of historic ruptures has not been rigorously examined in this light, smaller data sets have been examined. One such data set includes 17 historic earthquakes (1869–1986 A.D.) in the Basin and Range Province, western USA, ranging from M_L 5.6 to M_W 7.8 to 8.0 (dePolo *et al.*, 1989, 1991; Slemmons, 1995). Thirteen of these 17 earthquakes were of normal or normal-oblique displacement, whereas the remainder were strike-slip.

The moderate magnitude ($\mathbf{M} < 7$) earthquakes ruptured individual geometric or structural segments, and half of them were accompanied by sympathetic or secondary surface faulting. *All of the earthquakes with* $\mathbf{M} > 7$ *ruptured multiple geometric or structural segments.* Only half of the surface rupture endpoints coincided with fault-zone discontinuities that might have been identifiable based on static geologic criteria. The results of dePolo *et al.* (1991) suggest that inferred geometric or structural segments do not always represent earthquake segments, especially in regions of normal faulting. Furthermore, some earthquake rupture discontinuities may be difficult to identify from surface evidence, and significant faulting may occur beyond the identifiable static fault-zone discontinuities. It should be assumed that multiple geometric or structural segments will rupture in $\mathrm{M} > 7$ earthquakes. Accordingly, behavioral evidence, especially that contributed by paleoseismic studies of individual events, is essential for constraining the reasonableness of multisegment rupture scenarios.

9.4.6 Is the Segmentation Concept Useful?

At present there is undeniable confusion about the usefulness of the fault segmentation concept. The first step in alleviating this confusion is to standardize the definitions of various types of segments. One suggested outline is presented in Table 9-5. Second, authors must explicitly state what parameters were used to characterize their segments or segment boundaries, and state whether any quantitative tests (e.g. Wheeler and Krystinik, 1992) on the strengths of segment boundaries were performed. These two steps pertain only to standardization of terms, and do not address the basic question of whether persistent earthquake segments actually exist and, if so, whether they bear any consistent spatial relation to statically defined fault segments. Addressing those questions will require more comparisons of historic surface rupture traces with the statically defined fault segments of those same faults, as has been done for smaller data sets (dePolo *et al.*, 1991). Paleoseismologists should hope that some consistent relation will be found relating earthquake segments to fault segments. The existence of such a relationship would greatly simplify the reconstruction of paleoseismic histories on multisegment faults, as well as the prediction of seismic hazard on such structures. Conversely, if persistent earthquake segments do not exist, or bear no relation to fault geometry, then paleoseismic studies will require much more closely spaced data along a fault zone before the zone's behavior can be characterized.

9.5 MODELS OF FAULT BEHAVIOR

Fault behavior models seek to categorize how coseismic displacement on a fault varies with time, both at a single location, and along the trace of the fault. Fault behavior has both spatial and temporal aspects. The underlying spatial assumption of fault behavior models is that the pattern of surface deformation during earthquakes is linked to the pattern of strain release on the underlying fault plane. If fault segments, asperities, barriers, and areas of localized strain accumulation exist, they should reveal themselves in the pattern of surface deformation. The temporal assumption of the models is that there is some linkage between the time between major strain-release events (earthquakes) and the amount of strain released in each event (see Scholz, 1990, for further details). Fault behavior models thus provide a useful conceptual framework in which to interpret paleoseismic data.

The earliest fault behavior models described how fault displacement varied through time at a single location along a fault, without regard to the pattern of slip along strike. The simplest model is the *perfectly periodic model* conceived by Reid (1910) based on observations of the 1906 San Francisco, California, earthquake (Fig. 9.14A). In this model earthquakes occur whenever stress builds up to a given level (T1), and the stress drop and magnitude of each earthquake are identical. With the additional assumption of constant stress buildup through time (note uniform time between T1 and T2), the earthquakes become perfectly periodic.

Shimazaki and Nakata (1980) proposed two variations on this perfectly periodic model, based on observations of subduction zone earthquakes in Japan over several hundred years. In the first model, termed *time predictable* (Fig. 9.14B), earthquakes occur at a constant critical stress level (T1), but the stress drop and magnitude vary. Thus the time of the next earthquake in the series can be predicted based on the slip in the previous earthquake, if we assume a constant slip rate through time. The second model makes a contrary assertion, that earthquakes fail back to a given stress level (T2) regardless of their size, and thus slip in the next earthquake can be predicted from the time since the previous earthquake; this is termed the *slip-predictable model.*

The discovery that slip varies along strike during earthquakes necessitated expanding these one-dimensional models to include a second dimension along fault strike. Two-dimensional behavior models were initially formulated based on along-strike slip patterns in historic earthquakes (see examples in Chapters 3 and 6), and were later expanded to include slip patterns for paleoearthquakes based on geomorphic offsets (e.g. Schwartz and Coppersmith, 1984). Models can be classified into two broad groups, the variable slip models and the uniform slip models.

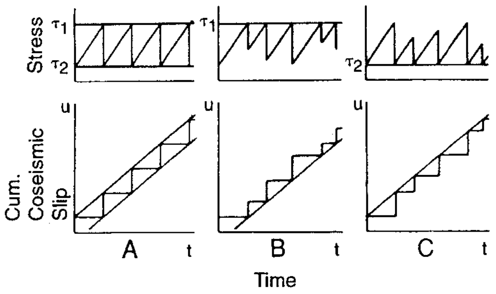

Figure 9.14 Diagram contrasting (A) the perfectly periodic model, (B) the time-predictable model, and (C) the slip-predictable model of earthquake recurrence. Upper figures show patterns of stress drop with time, lower figures show patterns of fault slip through time. [From Scholz (1990); reprinted with permission of Cambridge University Press.]

9.5.1 Variable Slip Models

Variable slip models predict that slip rate along strike is constant, but that displacement per event at a point is variable, and thus earthquake size is variable. The pattern of cumulative displacements along strike is not regular, and rupture in individual events is not limited to fault segments. The relation between displacement per event and time between events can be either time- or slip-predictable (Fig. 9.14).

9.5.2 Uniform Slip Models

The family of uniform slip models has in common that displacement per event at a point on the fault is constant, but differs in that slip rate along strike may be constant or variable (Figs. 9.15B, C, D, and E). Three of the four uniform slip models (characteristic earthquake, overlap, and coupled) implicitly assume that fault segments exist that are reasonably persistent.

9.5.2.1 Uniform Slip Model

The simplest uniform sip model assumes that displacement per event at a point is constant, slip rate along strike is constant, and strain is released by both rare large earthquakes and more frequent smaller earthquakes (Fig. 9.15B). Neither the large nor moderate earthquakes are necessarily limited to fault segments. The contribution of slip from moderate magnitude (**M** 6 to 7) earthquakes in this model is large. If these moderate earthquakes are near the thresholds of recognition for surface rupture or ground shaking, they may not be recognized in the paleoseismic record. Few paleoseismic studies have inferred a simple uniform slip model, probably due to the difficulty in detecting small rupture events associated with moderate magnitude earthquakes.

9.5.2.2 Coupled Model

The coupled model is similar to the uniform slip model, but it recognizes that individual rupture events are restricted to persistent fault segments (Fig. 9.15E). In the idealized drawing, segment boundaries are very narrow, and slip in a single event decreases from a constant intrasegment value to zero in a short span. Such rapid decreases in slip at rupture ends are not typical of historic ruptures (however, see Fig. 5.2). Although long-term slip rates along strike are constant, at any given moment the cumulative amount of slip along strike may show considerable variation (for example, after event 3, or after event 10). In this respect the pattern can be very similar to that of the characteristic earthquake model (discussed next).

9.5.2.3 Characteristic Earthquake Model

The characteristic earthquake model (Fig. 9.15C) assumes that most strain is released in large earthquakes within a narrow, "characteristic" magnitude

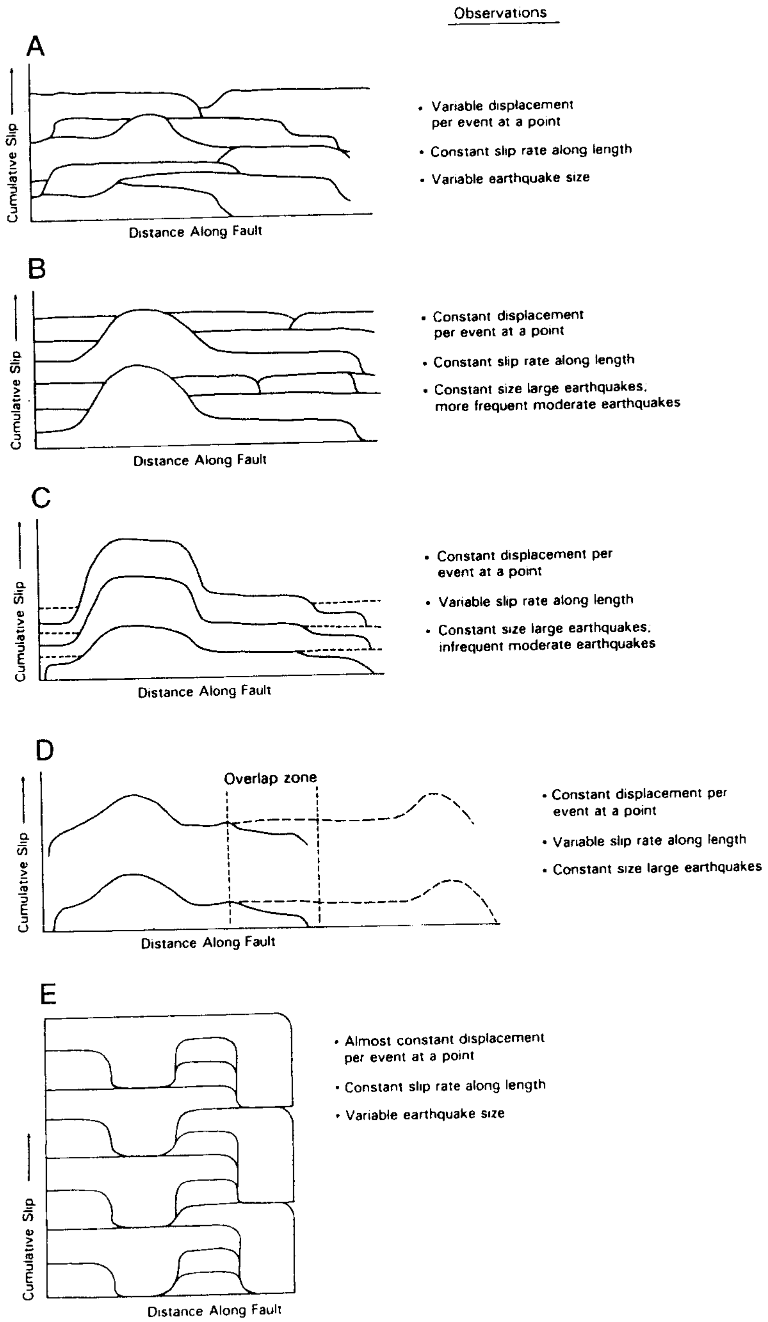

range (Schwartz and Coppersmith, 1984). Moderate earthquakes within a one-magnitude range below the characteristic earthquake may be rare, if not entirely absent. [In the more extreme *maximum moment model* of Wesnousky *et al.* (1984) *all* strain is released in large characteristic earthquakes.] The characteristic model implicitly assumes that ruptures are limited to persistent segments, that displacement per event at a point is constant, and that slip rate along strike is variable; the model makes no assumptions about recurrence. This model was based mainly on paleoseismic observations of large displacements at trench sites, with no evidence of smaller displacement events, plus a decrease in structural relief at segment boundaries.

This model differs fundamentally from preceding models by stating that slip deficits at the ends of major ruptures are never "filled in" by slip from smaller earthquakes. Thus the pattern of variable slip along strike in a single event persists and grows with each successive event. The long-term effect of this variable slip rate on dip-slip faults is the creation of variable tectonic relief along strike. This relief may be manifested as variations in (1) elevation of structural levels in the mountain block, (2) depth to basement in the downthrown block, (3) bedrock blocks stranded at intermediate structural levels between fault strands, or (4) a combination of these three variations.

The physical basis for the characteristic earthquake model is elucidated by Schwartz and Coppermith (1984, pp. 5696-5697) as follows: " rupture segments, barriers to fault rupture, and the distribution of slip appear to persist through repeated earthquakes. . . it can be argued that the constitution and strength of fault zone materials as well as the style of stress application can be considered essentially constant through several seismic cycles. Given that this set of conditions remains relatively constant, we would expect generally uniform behavior of the fault with respect to the size of the characteristic earthquake that it produces."

Hecker and Schwartz (1994) compiled measurements of slip at single locations in successive (paleo)earthquakes, and concluded that most of the 27 faults in their data set displayed characteristic behavior. D. P. Schwartz (personal communication, 1995) states that, of the nearly 50 faults studied to date, the coefficient of variation (COV) of slip (standard deviation/mean) for successive morphogenic paleoearthquakes at individual sites is ≤0.3 for 80% of the faults. Thus, for a site with a mean displacement of 2 m, 67% of slip events would display slip between 1.4 and 2.6 m.

Figure 9.15 Diagrams showing patterns of along-strike slip for various models of fault behavior. (A) Variable slip model. (B) Uniform slip model. (C) Characteristic earthquake model. (D) Overlap model. (E) Coupled model. [From Berryman and Beanland (1991); reprinted with permission of Pergamon Press.]

9.5.2.4 *Overlap Model*

The overlap model is a refinement of models that assumes rupture is limited to segments (i.e., characteristic earthquake and coupled models). The overlap model conceives a segment boundary as a zone of some finite along-strike length. Ruptures originating in adjacent segments extend into the segment boundary with diminished displacement, and "overlap" so that their sum is similar to the single-event displacement just outside the segment boundary. Paleoseismic data from the Wasatch fault zone indicate that overlap ruptures have occupied the segment boundary between the Provo and Nephi segments (Ostenaa, 1990). Trenches in the segment boundary revealed evidence for four small-displacement events, whereas trenches in the interiors of adjacent segments revealed evidence for two large-displacement events on each segment. It has been suggested that trenching in segment boundaries can distinguish between ruptures that propagated completely through a segment boundary, and thus involved two segments, and ruptures that died out within a segment boundary. This matter of rupture length is critical for estimating paleoearthquake magnitude (Sec. 9.2).

9.6 MODELS OF EARTHQUAKE RECURRENCE

We consider models of the variation of recurrence through time, herein termed *earthquake recurrence models,* as a subset of the more general fault behavior models just described. In particular these recurrence models describe the frequency distribution of recurrence intervals between large (morphogenic) earthquakes. For example, the recurrence intervals in Reid's perfectly periodic model show no variation through time, although both historic (Ando, 1975) and prehistoric (Sieh *et al.,* 1989; Machette *et al.,* 1992a) data show variance in recurrence intervals between large earthquakes. Characterizing the frequency distribution of recurrence for large earthquakes has two practical applications. First, we cannot make forecasts of future earthquake probability on faults unless we can define the mean, variation, and distribution type of recurrence intervals (e.g., Working Group, 1988, 1990). The type of recurrence distribution has a profound impact on future earthquake probability (Fig. 9.16; see also McCalpin and Nishenko, 1996). Second, we cannot assess whether an earthquake on one fault has triggered an earthquake on a second fault unless we can prove that the perturbation of recurrence on the second fault is beyond that which might have arisen by statistical chance.

Early models assumed that the distribution of recurrence intervals between large earthquakes was *Gaussian* and could be described by a mean and standard deviation (e.g., Sykes and Nishenko, 1984; Bakun and Lindh, 1985). However, examination of sets of historic and prehistoric recurrence data soon proved otherwise. Nishenko and Buland (1987) combined a set of recurrence

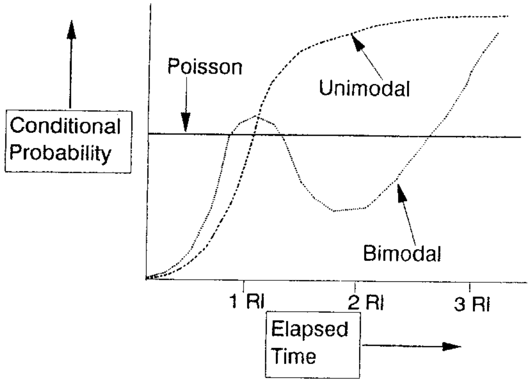

Figure 9.16 Conceptual diagram showing how recurrence distribution controls the increase of conditional probability of future faulting as elapsed time increases. The horizontal axis is approximately calibrated in units of mean recurrence interval (RI). For Poisson (random) recurrence between large earthquakes, elapsed time has no effect on conditional probability. For unimodal recurrence distributions, conditional probability increases as elapsed time increases, with a maximum rate of increase at 1 RI. For a bimodal recurrence distribution with an intercluster recurrence of three times the intracluster recurrence (or 3 RI), conditional probability increases until the mean intracluster recurrence is reached. As elapsed time increases beyond 1 RI and the earthquake has still not occurred, conditional probability decreases because it is more likely that we are entering a seismic gap, rather than a cluster. However, as elapsed time continues to increase and approaches the mean intercluster recurrence, the conditional probability rises to very high levels.

data from many fault zones (the ergodic substitution) and concluded that recurrence between large subduction-zone earthquakes followed a *lognormal distribution* where ln T/T_{avg} equaled 0.2 (T is a recurrence interval for a fault, T_{avg} is the average recurrence for that fault). Sieh *et al.* (1989) examined a series of 12 paleoearthquakes at a single site on the San Andreas fault zone and concluded that recurrence followed a *Weibull distribution* with a shape factor (β) of 1.5. They also argued, based on failure theory, why earthquake recurrence intervals should follow a Weibull distribution. Nishenko (1985) found that a Weibull distribution with $\beta = 4.8$ best fit recurrence data from the Chilean subduction zone. Finally, several paleoearthquake histories seem to indicate a bimodal distribution of recurrence (Sieh *et al.,* 1989; Nishenko and Schwartz, 1990; McCalpin and Nishenko, 1996). *Bimodal recurrence* implies a series of earthquakes that occur in clusters and gaps, with a short mode of recurrence within the clusters and a long mode of recurrence between the clusters (forming gaps). Bimodal recurrence has generally not been observed in the historic earthquake record due to the small number of large earthquakes that have occurred on any given fault. Thus, if temporal clustering of large earthquakes is a widespread phenomenon, the critical evidence will have to come from paleoseismic chronologies.

Although there is still uncertainty as to which frequency distributions are appropriate for recurrence, or whether different types of faults obey different distributions, the concept of recurrence distributions has become useful in generating synthetic seismic histories (e.g., Ward and Goes, 1993). In the following sections, we describe the use of synthetic paleoseismic histories to test whether paleoearthquakes on one fault segment have triggered paleoearthquakes on adjacent segments.

9.6.1 Temporal Clustering, Contagion, and Synthetic Histories

Space–time diagrams of paleoearthquakes (Figs. 9.9 and 9.10) often reveal paleoearthquakes on adjacent segments or faults that occurred anomalously close in time. Perkins (1987) proposed that such earthquakes may represent fault *contagion,* a term he coined to represent the process of one large earthquake influencing the occurrence of another large earthquake on an adjacent or nearby fault. Contagion would be caused by the transmittal of post-earthquake stress changes between adjacent crustal blocks, and would have a lag time of years to centuries. In a fault system where contagion is strong, the space-time diagram of activity would reveal short time periods in which paleoearthquakes occurred on all segments, separated by time gaps in which no earthquakes occurred on any segment. This pattern produces a type of *temporal cluster* of paleoearthquakes across fault segments, which is different than the type of temporal cluster described earlier on a single fault segment. This type of *multisegment clustering* can exist even if the recurrence on all individual segments is uniform (Fig. 9.17A).

Perkins (1987) noted that multisegment temporal clustering was best expressed on the *composite earthquake history,* that is, on a time line that contains all of the earthquakes on each segment (see Table 9.6 for definitions of terms relating to earthquake histories). When independently generated (i.e., noncontagious) individual recurrence histories are transferred to a single composite history, the resulting frequency distribution of recurrence intervals in the composite history is always exponential. This conclusion holds regardless of the values or the type of frequency distributions of recurrence in the individual histories. However, when contagion is acting between individual fault histories, the composite history begins to display temporal clusters and gaps, and thus the distribution of recurrence becomes bimodal. The stronger the contagion effect, the more bimodal the composite recurrence distribution becomes. In the most extreme case of contagion, earthquakes on all fault segments would occur within the same year, and the composite history would thus contain only two recurrence values (one value equal to less than one year within a temporal cluster, and a second value representing the length of time gaps between the clusters). The presence of fault contagion can be assessed by comparing the observed composite paleoseismic history (from a space–time diagram) with synthetic composite histories generated with or without contagion. We give two examples in the following subsections.

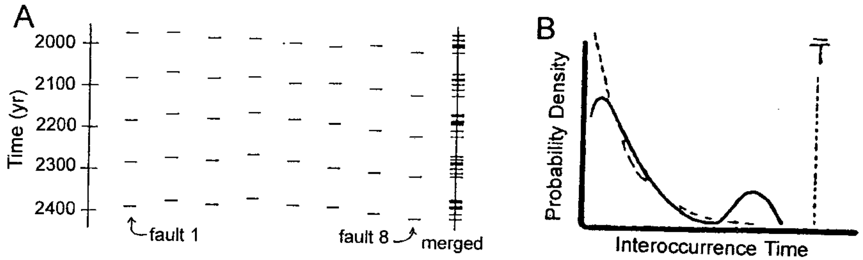

Figure 9.17 (A) Hypothetical space–time diagram showing the occurrence of earthquakes (short dashes) through time (vertical axis) on eight adjacent faults (or fault segments). Each fault has the same mean recurrence interval recurrence and, in this simplified case, recurrence is perfectly periodic on each fault. The merged (composite) earthquake history for all eight faults is shown at right. This space–time diagram was designed to represent a highly contagious system of faults, and accordingly the composite history is composed of clusters of earthquake events separated by time gaps. (B) Probability density function of interoccurrence time (recurrence interval) for the merged time line in part (A). Solid line shows the observed (bimodal) distribution of recurrence, with the short mode (at left) representing recurrence intervals within the clusters, and the long mode (at right) representing recurrence intervals between clusters. Dashed line shows the exponential distribution of recurrence intervals that is typical of noncontagious behavior. $\bar{T}$ is the interoccurrence time on each segment. From Perkins (1987).

9.6.2 Testing for Contagion in Paleoseismic Histories

"Earthquake ruptures are termed contagious if the occurrence of the rupture of one fault or fault segment increases the likelihood of the occurrence of rupture on an adjacent fault or fault segment" (Perkins, 1987, p. 428). Contagion should result in a temporal clustering of paleoearthquakes within the fault system, as rupture on one segment induces (after some time) rupture on the adjacent segment. Any temporal clustering of paleoearthquakes in a multisegment system will also create time gaps in which no faulting occurs. The reconstructed paleoseismic histories of adjacent fault segments or faults can be plotted as adjacent time lines (e.g., Figs. 9.9 and 9.10) in a space–time diagram that can be visually inspected for effects of contagion.

Visual inspection of a space–time diagram does not constitute a rigorous test for the presence of contagion. To prove that contagion has occurred, one must demonstrate that the observed clustering of paleoearthquakes across segments was unlikely to have arisen soley by chance. Thus, all tests for contagion must be framed in terms of probabilities. In the following section we briefly review several quantitative and semiquantitative tests designed to identify contagious (i.e., nonrandom) influences between faults or fault segments.

Table 9-6

Definitions and Abbreviations of Terms Used in Analyzing Paleoseismic Chronologies for Contagion

Term	Abbreviation	Definition
Field paleoseismic history	FPH	The inferred spatial/temporal history of paleoearthquakes on two or more adjacent faults or fault segments, based on field data.
Synthetic paleoseismic history	SPH	A spatial/temporal history of paleoearthquakes on two or more adjacent faults or fault segments, generated by Monte Carlo simulation. This requires assumption of a frequency distribution for the recurrence intervals on each fault. Events are plotted as points along parallel time lines.
Composite paleoseismic history	CPH	The result of transferring all paleoseismic events on multiple faults (time lines) onto a single time line. The events can be from a field or synthetic paleoseismic history.
Temporal cluster	TC	An abnormally high incidence of paleoearthquakes in a short time period, compared to the rest of the paleoseismic history. Is usually identified subjectively. Example: on a six-fault system with RI = 7 kyr[a], five paleoearthquakes in 2 kyr.
Time gap	TG	An abnormally low incidence of paleoearthquakes in a long time period, compared to the rest of the paleoseismic history. Usually identified subjectively. Example: on a six-fault system, with RI = 7 kyr, no paleoearthquakes in the past 4 ka. Time gaps usually occur before and after temporal clusters.
Contagion	C	Earthquake ruptures are termed contagious if the occurrence of the rupture of one fault or fault segment increases the likelihood of the occurrence of rupture on an adjacent fault or fault segment.
Mean recurrence interval	T	Mean of measured recurrence intervals, or, long-term slip rate divided into the mean slip per event.
Standard deviation of the recurrence intervals	σ	The standard deviation of all the measured individual recurrence intervals, assuming a normal distribution.
Normalized standard deviation of the recurrence intervals	σ'	σ/T
Contagion time	t_c	The time within which an earthquake on one fault or fault segment will cause an earthquake on a nearby fault or an adjacent fault segment.
Normalized contagion time	t_c'	t_c/T
Number of faults	n	The number of faults or fault segments represented in a space–time diagram.

[a] kyr = kiloyears = 1000 years; ka = kiloannum = 1000 years before present.

9.6.2.1 *The Moving Window Method*

The moving window test compares the pattern of earthquakes in the observed composite paleoseismic history to patterns in many randomly chosen time windows of the same length in synthetic composite paleoseismic histories (McCalpin, 1993b; McCalpin and Nishenko, 1996). Because the synthetic composite histories were created by adding independently created individual histories (Fig. 9.18), the composite histories contain no contagion effects, and show only temporal patterns created by random interactions between fault segments. As such, synthetic composite histories form a "random baseline case" or null hypothesis against which to compare observed histories. We can thus ask, "How often does the pattern of clusters and gaps in the observed composite paleoseismic history occur in a synthetic composite history that we know was generated randomly?" If the observed pattern appears frequently in the synthetic record, we may conclude that a contagion mechanism is not

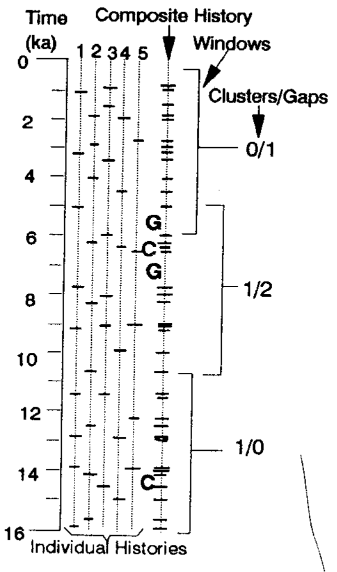

Figure 9.18 Space–time diagram composed of five individual synthetic paleoseismic histories. Earthquakes are shown as short thick lines on individual synthetic histories of each segment (numbered 1-5). All earthquakes are merged onto the composite history (at right). C, temporal cluster (≥4 events in ≤560 years); G, gap (no events in ≥1015 years) (both definitions derived from the Wasatch fault zone, Fig. 9.10). Each individual synthetic history was generated independently, by randomly selecting recurrence intervals drawn from a Gaussian distribution with mean = 2000 yr and σ = 600 yr. This example shows the first 16 ka of the 380-ka simulation run. Three window positions (5.6 ky long, see text) are shown, with the composition of clusters and gaps (as defined earlier) noted. [From McCalpin and Nishenko (1996); reprinted with permission of the American Geophysical Union.]

necessary to explain the record, and thus not rule out the null hypothesis. However, if the pattern of clusters and gaps in the observed record rarely, or never, appears in the synthetic histories, we may conclude that the observed clustering is so unusual that it must be the result of intersegment contagion.

Using the Wasatch fault zone (WFZ) as an example (Fig. 9.10), we define a temporal cluster as $\geq$4 earthquakes among the five central segments in $\leq$560 yr. The longest time gap between earthquakes on all five segments is that immediately preceding the four-earthquake cluster (1015 yr), so we define a gap as 0 earthquakes in $\geq$1015 yr. The remainder of the observed WFZ space–time diagram contains no obvious clusters or gaps tighter than those defined previosly.

Having now defined what constitutes a cluster and gap, we examine successive 5.6 ky time windows (the length of the complete WFZ record) on composite paleoseismic histories generated with different assumed recurrence distributions to see how often one cluster and one gap appear. At each window position, we record the number of clusters and gaps as previously defined (Fig. 9.18). A window may contain as few as zero clusters and zero gaps (the least clustered combination) or as many as three clusters and three gaps (the most clustered combination observed). In the 12 models generated by McCalpin and Nishenko (1996), they observed 19 different combinations of clusters and gaps (some possible permutations were never observed). The observed WFZ history contains one cluster and one gap, so combinations that are even more clustered than the observed WFZ history may represent contagion effects.

9.6.2.1.1 Results of the Moving Window Test

The most common cluster/gap combination observed in 4 of the 12 synthetic models of McCalpin and Nishenko (1996) was one cluster and one gap (10 to 26% of all windows had this combination), which is the pattern in the observed WFZ record (Figs. 9.9 and 9.10). Therefore, one could say that the earthquake pattern in the observed WFZ record has a 10 to 26% chance of representing a composite history created only by random interactions among five segments (rather than by contagion). However, the randomly generated composite histories often contained combinations *more* clustered than that observed for the WFZ. By including the frequency of occurrence of these more clustered combinations, we can state that there is an 18 to 69% chance (depending on the recurrence distributions assumed for individual fault segments) of obtaining a composite history *as clustered or more clustered than* the observed WFZ history by superposition of purely random events across five independent fault segments.

9.6.2.2 The Perkins Method

The Perkins method, named after its originator (Perkins, 1987), evaluates contagion by examining the composite paleoseismic history. The frequency distribution of recurrence intervals in a purely random, Poissonian system is exponential, with abundant short recurrence intervals, and progressively rarer long intervals. The frequency distribution of recurrence intervals in a composite paleoseismic history should obey this exponetial relationship, if there is no contagion operating. Perkins (1987) noticed that, in a composite record of idealized contagious faults, the frequency distribution of recurrence intervals becomes bimodal (Fig. 9.17B). The temporal clusters in the composite record contain an exponential distribution of short recurrence intervals within them, and the next common recurrence interval is much longer, representing the time gaps (Fig. 9.17). As the contagion effect strengthens, this bimodality is increased; as contagion weakens, the bimodality disappears and the distribution approaches an exponential one.

Perkins (1987) proposed that bimodal (contagious) behavior becomes apparent when the product

$$\sigma' \times n \times t_c' \leq 0.05$$

(terms defined in Table 9-6). Therefore, if the frequency distribution of recurrence times is bimodal, and σ' and n are known, t_c' can be estimated. In a hypothetical example based on the Wasatch fault zone, USA, Perkins (1987) calculated contagion times of 80 to 100 years. Such short contagion times may be responsible for the observed pulse of historic faulting elsewhere, for example, in the central Nevada seismic belt (Wallace and Whitney, 1984), which succeeded a long period of seismic quiescence.

The thought-provoking concepts proposed by Perkins (1987) have not yet been applied to many observed paleoseismic histories, partly due to the scarcity of multifault or multisegment histories, and partly due to the limited distribution of the original paper. As more high-quality paleoseismic histories are reconstructed, they should be subjected to a contagion analysis such as Perkins'.

9.7 CURRENT ISSUES AND FUTURE PROSPECTS IN PALEOSEISMOLOGY

As the areal and topical scope of paleoseismology expands, debate continues about some central issues in paleoseismology that have developed during the past two decades (Crone, 1987). These issues impact the interpretation of paleoseismic evidence in diverse geomorphic, climatic, and tectonic settings; for this reason many are of critical importance in seismic hazard assessment. Finding ways of resolving these issues is a major challenge to the paleoseismic community as we approach the next millenium.

We hope to have demonstrated in previous chapters that paleoseismology covers a wide range of subtopics and techniques, but progress in those subtopics has not been equal. Those subtopics that address questions posed by SHAs, for example, concerning the location, displacement, and magnitude of the most recent paleoearthquake in areas of high slip rates, are the most developed. This situation can be expected because most funding to perform paleoseismic studies, at least in industrialized countries, is directly tied to SHAs. In contrast, the more research-oriented subtopics dealing with stable continental interiors, offshore faults, recurrence models, longer term fault behavior, and the interseismic part of the earthquake deformation cycle are less developed, although that situation is rapidly changing. In this section we make some (admittedly arbitrary) speculations about the critical issues and shortcomings of paleoeseismology. These issues can be grouped into five broad categories: (1) recognizing paleoearthquakes, (2) estimating displacement/magnitude, (3) estimating age/recurrence, (4) testing fault behavior models, and (5) scientific policy.

9.7.1 Recognizing Paleoearthquakes

To a large extent, our understanding of postfaulting geomorphic processes in fault zones is based on what we expect might form, rather than on what has been observed to form after historic earthquakes or in controlled experiments. Many of the commonly accepted stratigraphic indicators of paleoearthquakes (e.g., colluvial wedges and soils) are based on conceptual models of fault-zone erosion, deposition, and weathering, yet few studies have carefully documented the development of such features following historic earthquakes, despite the promising early work of Wallace (1977, 1980a). Programs of *repeated terrestrial photogrammetry,* such as that begun by Machette (1985) on the Borah Peak, USA, fault scarp, should be instituted at every future large surface rupture to confirm our conceptual models. Stratigraphic indicators of paleoearthquakes should also be confirmed by *trenching historic surface ruptures,* accompanied by the type of statistical analysis performed by Bonilla and Lienkaemper (1991). Small-scale features could also be reproduced in experiments that allow us, under controlled conditions, to study the three-dimensional geometry and statistical properties of faults, folds, and plastic deformation in unconsolidated sediments.

The *threshold of recognizing* coseismic slip depends on displacement type, rates of weathering/erosion, and the rheology of surface material (Bonilla, 1988). For example, millimeters of coseismic displacement have been recognized where man-made objects such as roads have been displaced, whereas decimeters of displacement across natural terrain are sometimes difficult to see only days after a rupture. Conceptual models of relative rates (Fig. 1.4) suggest that, as time passes in different erosional environments, the threshold of slip recognition becomes larger. However, we have little data at present to quantify how recognition thresholds change with time, in various surficial deposits, for different types of slip.

A recent development in paleoseismology is the study of large earthquakes that occur on *blind faults* (usually reverse faults), without accompanying surface fault rupture (Stein and Yeats, 1989). In such earthquakes (and presumably in similar paleoearthquakes) the major effects are landslides, liquefaction (if susceptible materials exist), and broad areas of subtle vertical displacement. The *landscape response to this vertical displacement* may appear similar to the response to nontectonic forces, such as eustatic sea-level changes, climate change (Bull, 1991), and complex response of landscapes to gradual change (e.g., Schumm, 1986). Unless the landscape response to coseismic elevation changes and tilting can be differentiated from responses to other nontectonic causes, we may never detect many of the paleoearthquakes on "blind" faults. We need to develop geomorphic and depositional models for active folds that parallel the models developed for dip-slip and strike-slip faults.

The techniques described in this book were developed for paleoseismic studies on land, but many more earthquakes occur offshore than onshore. *Underwater faults* pose a hazard to many areas, but their inaccessibility generally limits studies of their paleoseismic histories. As noted by Wesnousky (1986), the earthquake hazard in California has probably been underestimated because offshore seismogenic faults are not well studied. At present, studies of offshore crustal faults generally do not yield information about individual paleoearthquakes, but they can provide estimates of slip rates, average recurrence intervals, fault segmentation, and paleoearthquake magnitudes (estimated fault length). What kind of techniques need to be developed so that offshore studies can yield data comparable to that from onshore studies?

We need to define the criteria for distinguishing between *seismic* versus *nonseismic soft-sediment deformation.* At present there is a divergence of opinion on this subject, with European authors interpreting many deformation features as seismic with no independent evidence of seismicity, while U. S. authors tend to interpret many deformation features even in seismic areas as aseismic in origin (Chapter 7). The refinement process will require both field studies of future earthquakes and laboratory simulations. A parallel effort is needed to characterize *seismic* versus *nonseismic landslides.* The present technique (Chapter 8) is expensive and time consuming, and a short-cut would be very appealing.

Recognizing earthquakes in *stable continental interiors* will require the increasing development of recognition methods that use secondary paleoseismic evidence such as liquefaction and landslides. Many recently studied faults in continental interiors (Meers fault, USA: Crone and Luza, 1990; "Ungava fault", Canada: Adams *et al.,* 1991, 1992; Lake Surprise fault, Australia: Crone *et al.,* 1992) have long recurrence intervals (tens of thousands to hundreds of thousands of years). The elapsed times for these seismogeneic faults may be so long that traces of the latest prehistoric earthquake have been obscured by erosion or deposition. For example, much of the north-central United

States is mantled with glacial deposits less than 18,000 years old, so paleoearthquakes that occurred before that date would not be visible today. In the humid eastern states of the United States, deep saprolitic weathering, combined with forest cover, may have obscured traces of paleoearthquakes that occurred in the past several tens of thousands of years, on structures that are now seismically queiscent.

9.7.2 Estimating Displacement/Magnitude

While many post-earthquake surveys have measured coseismic slip, only a few have monitored for *afterslip,* mainly on strike-slip faults. We thus know very little about afterslip on normal and reverse faults, and almost nothing about nonseismic slip that might occur before or between large earthquakes. The implication for paleoseismology is that an unknown portion of offset measured on landforms or in deposits may not be coseismic. To establish the proportions of afterslip, *postfaulting geodetic monitoring* should become standard practice after historic surface-faulting earthquakes.

To estimate the magnitude of *paleoearthquakes on blind faults,* we need to relate the broad geodetic changes at the surface to the amount of slip on the underlying fault. Paleoseismologists should collaborate with structural modelers to devise elastic dislocation models that faithfully reproduce the inferred paleoseismic surface deformation while maintaining believable subsurface geometries.

9.7.3 Estimating Age/Recurrence

Although *numerical dating techniques* have greatly improved in the past two decades, the evolving demands of paleoseismology will require continuing improvement. For example, dating large infrequent earthquakes in stable continental interiors will require improved dating techniques that span many tens to hundreds of thousands of years. The main challenge of dating is to test current (and future) recurrence and segmentation models. Verification of these models with field observations requires paleoseismic records that contain multiple, well-dated earthquakes. At present, most paleoseismic chronologies contain too few events to compare with model predictions, and/or the age limits on each event are too broad to justify rigorous statistical comparison. Part of the solution to this problem is to collect more samples from each exposure, apply Bayesian statistics to the dates if appropriate (Sec. 6.4), and increase the analytical accuracy of the dating techniques. Those steps alone will not solve the problem, however, unless an equally important issue is addressed: How do we quantitatively associate the numerical age from a sediment to the exact time of the paleoearthquake (i.e., quantify sample context, or "provenance" errors)?

Another application of improved dating precision is *complex fault zones.* Many fault zones are composed of more than one parallel or overlapping individual fault strands. These fault strands may rupture in a complex spatial and temporal pattern to accommodate coseismic strain release over many recurrence cycles (e.g., the 1992 Landers earthquake in the central Mojave shear zone). From a practical perspective, the complete paleoseismic chronology of a fault zone can only be determined if every fault strand at a given point on the zone is investigated. In some past studies in zones of complex faulting not every parallel fault strand was trenched, so some paleoearthquakes may have gone undetected. Other faults systems bound relatively intact small *crustal blocks that are mechanically interconnected,* such that movement on one block should alter the stress field in adjacent blocks. Theoretically there should be some pattern in the spatial/temporal distribution of paleoearthquakes in such interconnected blocks. A *space–time diagram* of well-dated paleoearthquakes could thus provide tectonic modelers with a powerful tool for investigating the structural dynamics of such regions.

9.7.4 Testing Fault Models

Fault segments have been defined for large normal, reverse, and strike-slip faults over scales varying from hundreds of meters to hundreds of kilometers. At which scale do these segments define repeatable seismogenic rupture zones, if they do at all? This question can be answered partly by documentation of future surface ruptures. At the same time, paleoseismic studies at many sites along segmented faults should also be able to detect if paleoruptures were confined to *persistent segments.* Early studies on large faults generally investigated in detail only one or two sites per fault segment, usually located in the center of the segment where slip rates were highest. A second generation of studies is now needed elsewhere within these segments, especially toward segment ends and within *segment boundaries.* The critical evidence for multisegment ruptures, for example, can either be found by tracing ruptures through segment boundaries (a direct approach, which has seldom been tried), or by correlating numerically dated paleoearthquakes from the centers of adjacent segments (an indirect approach, with large uncertainties).

A more fundamental problem of using paleoseismic data to test models is the *limited number of paleoearthquakes* that can be recognized and characterized on a given fault. The typical paleoseismic record for a well-studied fault may contain 2 to 4 paleoearthquakes, and even the longest records usually contain fewer than 10 events. These small numbers are insufficient for statistical testing of behavioral models such as the characteristic earthquake model or for determining the frequency distribution of recurrence intervals needed for earthquake forecasting. One way to overcome this inherent limitation of paleoseismology is to make an *ergodic substitution of space for time* that is widely used in geology, seismology, geomorphology, and hydrology (e.g. Hunter and Mann, 1992). The ergodic hypothesis states that "under certain circumstances sampling in space can be equivalent to sampling through time, and that space-time transformations are permissible as a working tool" (Chorley *et al.,* 1984, p. 32). In paleoseismology, this substitution would involve combining the data on displacement, recurrence, or segmentation for groups of similar faults in similar tectonic environments, and then assuming that the long-term behavior of any one fault is similar to the grouped behavior of all the faults (e.g., Nishenko and Buland, 1987; McCalpin, 1995). We may never be able to extend the paleoseismic history of a single fault to include more than 10 paleoearthquakes, but we can certainly inventory the past 2 to 4 paleoearthquakes on, say, 20 similar faults to form a data set of 40 to 80 paleoearthquakes that form a composite data set.

In practical terms, the ergodic substitution (if justified) implies that our limited resources in paleoseismology would be just as well spent studying the easily accessible, recent paleoseismic history of many faults, rather than the elusive long-term record of any one fault. Alternatively, if each active fault on the earth displays unique behavior with regard to displacement, magnitude, and segmentation, then the ergodic substitution is not warranted. In this case the hazard potential of any seismic source can only be assessed based on paleoseismic data from that source, which means that paleoseismologists should devote their resources to reconstructing long paleoseismic histories on those faults closest to urban areas or critical facilities.

9.7.5 Scientific Policy

Should more paleoseismic resources be devoted to studies of moderate magnitude paleoearthquakes in highly populated regions, even though evidence of such earthquakes is harder to find and date and more ambiguous than evidence of large earthquakes in less densely populated regions? The relevance of this question is underlined by the occurrence of numerous damaging earthquakes in the 1980s and 1990s (Loma Prieta, California, 1989; Northridge, California, 1994) that produced little or no primary or secondary permanent deformation. Earthquakes in this moderate magnitude range (**M** 6.0 to 7.0) cannot be detected by current paleoseismic techniques except in exceptional circumstances.

Geologists understandably concentrated their early paleoseismic studies on paleoearthquakes of **M** > 7 because the primary and secondary evidence is large, well expressed, and relatively unambiguous. This focus on unambiguous paleoseismic evidence was necessary when field techniques and interpretive models were being developed. However, the principles of paleoearthquake recognition are now fairly well established, as we hope to have shown. Paleoseismologists can tell hazard investigators where and how often large (**M** > 7) earthquakes have occurred in a populated region, but not where and how often potentially damaging **M** 6 to 7 earthquakes have occurred. These more frequent, smaller earthquakes may pose more hazard to populations than the less frequent, larger, and more distant earthquakes.

Paleoseismic data form the only basis on which to test many long-term models of fault behavior. In the past, neotectonicists have formulated and tested models of fault behavior based on the available paleoseismic data, *data generally acquired for other purposes* than model testing (e.g., for an SHA). As a result, the data often covered an insufficient length of time, or have been too imprecise, or covered too small an area to support rigorous tests of models such as segmentation, characteristic behavior, etc. To solve this problem, neotectonic modelers need to tell field paleoseismologists what type of field data are necessary to test their models, and how precise it must be. Most field paleoseismologists would be willing to collect additional field data at a site if such an effort permitted the validation of a behavioral model that they could use in seismic hazard characterization.

Appendix 1
Earthquake Magnitude Scales

Several magnitude scales are widely used and each is based on measuring of a specific type of seismic wave, in a specified frequency range, with a certain instrument. The scales commonly used in western countries, in chronological order of development, are: local (or Richter) magnitude (M_L), surface-wave magnitude (M_s), body-wave magnitude (m_b for short period, m_B for long period), and moment magnitude (M_w or $\mathbf{M}$). Reviews of these magnitude scales are given by Bath (1981), Kanamori (1983), and dePolo and Slemmons (1990); their interrelations are shown in Fig. A.1.1.

A.1.1. LOCAL (RICHTER) MAGNITUDE (M_L)

Richter magnitude was the first widely-used instrumental magnitude scale to be applied in the USA (Richter, 1935). The scale is based on the amplitude (in mm) of the largest seismogram wave trace on a Wood–Anderson seismograph (free period 0.8 sec), normalized to a standard epicentral distance of 100 km. Richter defined his magnitude 0 earthquake as that which produced a maximum amplitude of 0.001 mm at a distance of 100 km. Each successively larger magnitude was defined as a ten-fold increase in amplitude beyond the base level. Thus, a maximum seismogram amplitude (at a distance of 100 km) of 0.01 mm represents M_L 1.0, 0.1 mm equals M_L 2.0, 1 mm equals M_L 3.0, and so on. Richter (1935) devised a nomograph to normalize the amplitudes for earthquakes closer or farther away than 100 km, based on the attenuation of seismic energy in California.

The Richter magnitude scale accurately reflects the amount of seismic energy released by an earthquake up to about M_L 6.5, but for increasingly larger earthquakes, the Richter scale progressively underestimates the actual energy release. The scale has been said to "saturate" above M_L 6.5, from a combination of instrument characteristics and reliance on measuring only a single, short-period peak height (see details in Kanamori, 1983).

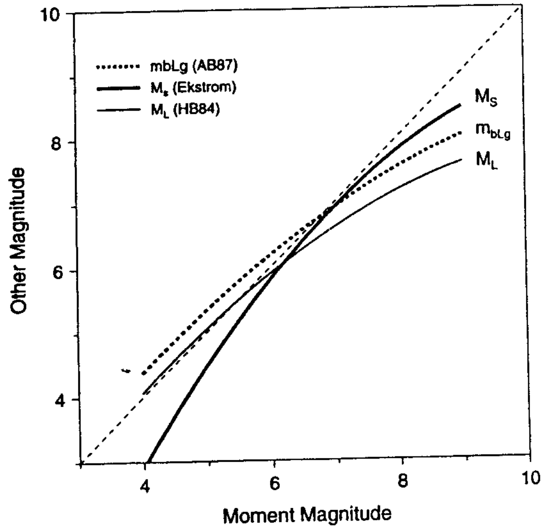

Figure A.1.1 Graph showing the relationship of various magnitudes to moment magnitude. Relation for m_{bLg} is from Atkinson and Boore (1987). For M_s and M_L the relations come from fitting a quadratic to the data compiled by Ekström (1987) and Hanks and Boore (1984), respectively. [From Boore and Joyner (1994); reprinted with permission of the Applied Technology Council.]

A.1.2. SURFACE-WAVE MAGNITUDE (M_s)

The surface-wave magnitude scale was developed to solve the "saturation" problem of Richter magnitude above M_L 6.5. The measurement procedure is similar to measuring the Richter magnitude, except that the peak wave amplitude is measured for surface waves that have periods of 20 sec, from long-period seismographs at teleseismic distances (Gutenberg, 1945). The surface-wave magnitude calculation does not require a seismograph record within 100 km (or nearby) of the epicenter, so the teleseismic records of many large-to-moderate magnitude earthquakes worldwide have been assigned surface-wave magnitudes. Because of this large data set, M_s is the typical magnitude used in empirical comparisons of magnitude versus earthquake rupture length or displacement (e.g. Bonilla *et al.*, 1984). However, the surface-wave magnitude scale also saturates, at about $M_s > 8$.

A.1.3. BODY-WAVE MAGNITUDE (M_{bLg})

The short-period body-wave magnitude (m_{bLg}) is the principal magnitude used in the tectonically "stable" eastern part of North America and Canada. This magnitude is measured from peak motions recorded at distances up to 1000 km on instruments with a passband in the range 1 to 10 Hz. Peak motions usually correspond to the Lg wave. This magnitude scale is little used in paleoseismology because it saturates at magnitude levels below that of M_s. However, it is possible to convert m_{bLg} values to other magnitude scales, and vice versa (Kanamori, 1983).

A.1.4. MOMENT MAGNITUDE (M_W OR M)

The moment magnitude scale is the most recent scale (Kanamori, 1977; Hanks and Kanamori, 1979) and is fundamentally different from the earlier scales. Rather than relying on measured seismogram peaks, the M_w scale is tied to the seismic moment (M_0) of an earthquake. The seismic moment is defined as

$$M_0 = D\,A\,\mu \qquad \text{(A.1.1)}$$

where D is the average displacement over the entire fault surface, A is the area of the fault surface, and μ is the average shear rigidity of the faulted rocks. The value of D is estimated from observed surface displacements or from displacements on the fault plane reconstructed from instrumental or geodetic modeling. A is derived from the length multiplied by the estimated depth of the ruptured fault plane, as revealed by surface rupture, aftershock patterns, or geodetic data. The method thus assumes that the rupture area is rectangular. The shear rigidity of typical crustal rocks is assumed to be about 3.0 to 3.5×10^{11} dyne/cm^2 (Aki, 1966; dePolo and Slemmons, 1990).

The seismic moment thus more directly represents the amount of energy released at the source, rather than relying on the effects of that energy on one or more seismographs at some distance from the source. Moment magnitude is calculated from seismic moment using the relation of Hanks and Kanamori (1979) for southern California

$$M_w = 2/3 \log M_O - 10.7 \qquad \text{(A.1.2)}$$

where M_W is the moment magnitude, and M_o is the seismic moment.

The seismic moment scale was developed to circumvent the problem of saturation in other magnitude scales, and is typically used to describe great earthquakes (i.e., $M_s > 8$). Kanamori (1983) composed a graph relating M_w to M_L, M_s, m_b and m_B (Fig.A.1.1). In the interest of standardization, paleoearthquake magnitude should be estimated on the M_W scale; if not, then the magnitude scale used should be clearly noted.

Appendix 2
Radiocarbon Sampling Techniques

A.2.1 HOW MUCH TO SAMPLE

For conventional radiocarbon dating, suggested minimum and optimum dry weights are given in Table A.2.1. For AMS, dating samples containing as little as a few milligrams of carbon can be dated.

A.2.2 SAMPLE PRETREATMENT

Pretreatment procedures strongly influence the radiocarbon ages of samples that contain multiple organic compounds, such as soils. Styles of pretreatment seem to vary from region to region and between laboratories, which makes

Table A.2.1

Suggested Sample Weights for Radiocarbon Dating[a]

Material	Typical carbon content (%)	Optimum dry weight (g)	Minimum dry weight (g)
Clean charcoal	25–75	10–20	3
Dirty charcoal	10–25	20–50	5
Wood	20–30	30–100	5
Cloth	20–30	30–100	5
Shells	8–12	50–100	15
Limestone	5–10	100–200	25
Bone	0.5–4	200–500	150
Peat	5–20	100–200	70
Humus soil or sediment	0.2–4	200–800	150

[a] Adapted from Beta Analytic, Miami, Florida, and Taylor, 1987.

comparison of radiocarbon ages between distant regions often difficult. In the western USA the fine (< 125-μm) organic fraction is thought to be least susceptible to contamination by younger carbon, so it is physically concentrated from coarse-grained A horizons (Kihl, 1975). Rinses with HCl and NaOH then follow.

References

Abdallah, A., Courtillot, V., Kasser, M., Le Dain, A. Y., Lepine, J. C., Robineau, B., Ruegg, J. C., Tapponnier, P., and Tarantola, A., (1979). Relevance of Afar seismicity and volcanism to the mechanics of accreting plate boundaries. *Nature (London)* **282,** 17–23.

Abe, K. (1992). Seismicity of the caldera-making eruption of Mount Katmai, Alaska in 1912. *Bull. Seismol. Soc. Amer.* **82,** 175–191.

Acharya, H. K. (1979). Regional variations in the rupture-length magnitude relationships and their dynamical significance. *Bull. Seismol. Soc. Amer.* **69,** 2063–2084.

Adam, D. P. (1975). A late Holocene pollen record from Pearson's Pond, Weeks Creek landslides, San Francisco Peninsula, California. *J. Res. U.S. Geol. Surv.* **3,** 721–731.

Adams, J. (1980). Contemporary uplift and erosion of the Southern Alps, New Zealand: Summary. *Geol. Soc. Am. Bull., Part I* **91,** 2–4.

Adams, J. (1981a). Earthquake-dammed lakes in New Zealand. *Geology* **9,** 215–219.

Adams, J. (1981b). Earthquakes, landslides, and large dams in New Zealand. *Bull. N. Z. Nat. Soc. Earthquake Eng.* **14,** 93–95.

Adams, J. (1982). Deformed lake sediments record prehistoric earthquakes during the deglaciation of the Canadian Shield. *EOS, Trans. Am. Geophys. Union* **63**(18), 436 (abstr.).

Adams, J. (1990). Paleoseismicity of the Cascadia subduction zone: Evidence from turbidites off the Oregon–Washington margin. *Tectonics* **9,** 569–583.

Adams, J. (1992). Paleoseismology-A search for ancient earthquakes in Puget Sound. *Science* **258,** 1592–1593.

Adams, J. (1994). Paleoseismology studies in Canada- a dozen years of progress. *U.S. Geol. Surv. Open File Rept.* **94-568,** 3–4.

Adams, J., Wetmiller, R. J., Hasegawa, H. S. and Drysdale, J. (1991). The first surface faulting from a historic intraplate earthquake in North America. *Nature (London)* **352,** 617–619.

Adams, J., Percival, J. A., Wetmiller, R. J., Drysdale, J. A. and Robertson, P. B. (1992). Geological controls on the 1988 Ungava surface rupture; a preliminary interpretation. *Geol. Surv. Pap. (Geol. Surv. Can.)*, **92-1C,** 147–155.

Ager, D. V. (1993). *The Nature of the Stratigraphical Record,* 3rd ed., Wiley, New York.

Ager, T. A., and Sims, J. D. (1981). Holocene pollen and sediment record from the Tangle Lakes area, Alaska. *Palynology* **5,** 85–98.

Aki, K. (1966). Generation and propagation of G waves from the Niigata earthquake of June 16, 1964; Part 2, Estimation of earthquake moment, released energy, and stress-strain drop from the G wave spectrum. *Bull. Earthquake Res. Instit.* Vol.**44,** pp. 73–88.

Aki, K. (1979). Characterization of barriers on an earthquake fault. *J. Geophys. Res.* **84,** 6140–6148.

Aki, K. (1984). Asperities, barriers, characteristic earthquakes, and strong motion prediction. *J. Geophys. Res.* **89,** 5681–5698.

Algermissen, S. T., and Perkins, D. M. (1976). A probabilistic estimate of maximum acceleration in rock in the contiguous United States. *U.S. Geol. Surv. Open File Rept.* **76-416,** 1–45.

Algermissen, S. T., Perkins, D. M., Thenhaus, P. C., Hanson, S. L., and Bender, B. L. (1982). Probabilistic estimates of maximum acceleration and velocity in rock in the contiguous United States. *U.S. Geol. Surv. Open File Rep.* **82-1033,** 1–107.

Algermissen, S. T., Perkins, D. M., Thenhaus, P. C., Hanson, S. L., and Bender, B. L. (1990). Probabilistic earthquake acceleration and velocity maps for the United States and Puerto Rico. *U.S. Geol. Surv. Misc. Field Stud. Map* **MF-2120**.

Allen, C. R. (1968). The tectonic environments of seismically active and inactive areas along the San Andreas fault system. In *Conference on Geologic Problems of San Andreas Fault System.* W. R. Dickinson and A. Grantz, (eds.),. *Stanford Univ. Pub., Geol. Sci.* **11,** 70–80.

Allen, C. R. (1975). Geological criteria for evaluating seismicity. *Geol. Soc. Am. Bull.* **86,** 1041–1057.

Allen, C. R. (1986). Seismological and paleoseismological techniques of research in active tectonics. In *Active Tectonics*: Studies in Geophysics (R. E. Wallace, chairman), pp. 148–154. Natl. Acad. Press, Washington, DC.

Allen, C. R., Zhouli, L., Hong, Q., Xueze, W., Huawei, Z. and Weishi, H. (1989). Segmentation and recent rupture history of the Xianshuihe fault, southwestern China. In *Fault Segmentation and Controls of Rupture Initiation and Termination.* D. P. Schwartz, and R. H. Sibson, (eds.), *U.S. Geol. Surv. Open File Rept.* 89-315, 10–30.

Allen, J. R. L. (1982). Sedimentary structures—Their character and physical basis. In *Dev. in Sedimentol.* **30B,** (2), 1–663.

Allen, J. R. L. (1986). Earthquake magnitude-frequency, epicentral distance, and soft-sediment deformation in sedimentary basins. *Sediment. Geol.* **46,** 67–75.

Allen, J. R. L., and Banks, N. L. (1972). An interpretation and analysis of recumbent-folded deformed cross-bedding. *Sedimentolology* **19,** 257–283.

Ambraseys, N. N. (1978). Studies in historical seismicity and tectonics. In *The Environmental History of the Near and Middle East* (W. C. Brice, ed.), pp. 185–210. Academic Press, New York.

Ambraseys, N. N. (1988). Engineering seismology; earthquake engineering and structural dynamics. *J. Int. Assoc. Earthquake Eng.* **17,** 1–105.

Ambraseys, N. N., and Melville, C. P. (1982). *A History of Persian Earthquakes.* Cambridge Univ. Press, New York.

Ambraseys, N. N., and Tchalenko, J. S. (1969). The Dasht-e-Bayaz (Iran) earthquake of August 31, 1968; a field report. *Bull. Seismol. Soc. Am.* **59,** 1751–1792.

Ambraseys, N. N., and Zatopek, A. (1968). The Varto Usturkan (Anatolia) earthquake of 19 August 1966; summary of a field report. *Bull. Seismol. Soc. Am.* **58,** 47–102.

Ambraseys, N. N., and Zatopek, A. (1969). The Mudurnu Valley, West Anatolia, Turkey earthquake of 22 July 1967 *Bull. Seismol. Soc. Am.* **59,** 521–589.

Amick, D., and Gelinas, R. (1991). The search for evidence of large prehistoric earthquakes along the Atlantic coast. *Science* **251,** 655–658.

Amick, D., Gelinas, R., Maurath, G., Cannon, R., Moore, D., Billington, E., and Kemppinen, H. (1990). Paleoliquefaction features along the Atlantic seaboard. *U.S. Nucl. Regul. Comm., [Rep]. NUREG/CR* **NUREG/CR-5613,** 1–146.

Ando, M. (1975). Source mechanisms and tectonic significance of historical earthquakes along the Nankai Trough, Japan. *Tectonophysics* **27,** 119–140.

Andrews, D. J., and Bucknam, R. C. (1987). Fitting degradation of shoreline scarps by a model with nonlinear diffusion. *J. Geophys. Res.* **92,** 12,857–12,867.

Andrews, D. J., and Hanks, T. C. (1985). Scarps degraded by linear diffusion: Inverse solution for age. *J. Geophys. Res.* **90,** 10,193–10,208.

Andrus, R. D., Stokoe, K. H., and Roesset, J. M. (1991). Liquefaction of gravelly soil at Pence Ranch during the 1983 Borah Peak, Idaho earthquake. *Proc. Int. Conf. Soil Dyn. Earthquake Eng. 5th,* Karlsruhe, Germany, pp. 251–262.

Andrus, R. D., and Youd, T. L. (1987). Subsurface investigation of a liquefaction-induced lateral spread, Thousand Springs Valley, Idaho. *U.S. Army Waterways Exp. Stn. Misc. Pap.* **GL-87-8,** 106 pp.

Appelgate, B., Goldfinger, C., MacKay, M. E., Kulm, L. D., Fox, C. G., Embley, R. W. and Meis, P. J. (1992). A left-lateral strike-slip fault seaward of the Oregon convergent margin. *Tectonics* **11,** 465–477.

Arabasz, W. J., Pechmann, J. C., and Brown, E. D. (1992). Observational seismology and evaluation of earthquake hazards and risk in the Wasatch Front area, Utah. In Assessment of Regional and Earthquake Hazards and Risk Along the Wasatch Front, Utah P. L. Gori, and W. W. Hays, (eds.), *U.S. Geol. Surv. Prof. Pap.* **1500-D,** D1–D36.

Arias, A. (1970). A measure of earthquake intensity. In *Seismic Design for Nuclear Power Plants* (R. J. Hansen, ed.), pp. 438–483. MIT Press, Cambridge, MA.

Asquith, D. O. (1985). Characteristics and alternative mechanisms of late Quaternary faulting, proposed LNG terminal site, Point Conception, California. *Bull. Assoc. Eng. Geol.* **22,** 171–192.

Astaras, T., and Soulakellis, N. (1991). LANDSAT-TM data processing techniques for mapping geological and geomorphological features in the central Macedonian area, N. Greece. *Proc. Int. Earth Sci. Congr. Aegean Reg.,* Izmir, Turkey, Vol. **2,** pp. 76–91.

Atkinson, G. M., and Boore, D. M. (1987). On the m_N, **M** relation for eastern North American earthquakes. *Seismol. Res. Lett.* **58,** 119–124.

Atwater, B. F. (1987). Evidence of great Holocene earthquakes along the outer coast of Washington State. *Science* **236,** 942–944.

Atwater, B. F. (1992) Geologic evidence for earthquakes during the past 2,000 years along the Copalis River, southern coastal Washington. *J. Geophys. Res.* **97,** 1901–1919.

Atwater, B. F., and Moore, A. L. (1992). A tsunami about 1000 years ago in Puget Sound, Washington. *Science* **258,** 1614–1617.

Atwater, B. F., and Yamaguchi, D. K. (1991). Sudden, probably coseismic submergence of Holocene trees and grass in coastal Washington State. *Geology* **19,** 706–709.

Atwater, B. F., Nunez, H. J., and Vita-Finzi, C. (1992). Net late Holocene emergence despite earthquake-induced submergence, south-central Chile. *Quat. Int.* **15/16,** 77–85.

Atwater, B. F., Stuiver, M., and Yamaguchi, D. K. (1991). Radiocarbon test of earthquake magnitude at the Cascadia subduction zone. *Nature* (*London*) **353,** 156–158.

Atwater, B. F., Trumm, D. A., Tinsley, J. C., III, Stein, R. S., Tucker, A. B., Donahue, D. J., Jull, A. J. T., and Payen, L. A. (1990). Alluvial plains and earthquake recurrence at the Coalinga anticline. In the Coalinga, California, Earthquake of May 2, 1983. M. J. Rymer, and W. L. Ellsworth, (eds.), *U.S. Geol. Surv. Prof. Pap.* **1487,** 273–298.

Atwater, B. F., Nelson, A. R., Clague, J. J., Carver, G. A., Bobrowsky, P. T., Bourgeois, J., Darienzo, M. E., Grant, W. C., Hemphill-Haley, E., Kelsey, H. M., Jacoby, G. C., Nishenko, S. P., Palmer, S. P., Peterson, C. D., Reinhart, M. A., and Yamaguchi, D. K. (1995). Summary of coastal geologic evidence for past great earthquakes at the Cascadia subduction zone. *Earthquake Spectra* **11,** 1–18.

Audemard, A., and de Santis, F. (1991). Survey of liquefaction structures induced by recent moderate earthquakes. *Bull. Int. Assoc. Eng. Geol.* **44,** 5–16.

Awata, Y., Mizuno, K., Sugiyama, Y., Imura, R., Shimokawa, K., Okumura, K., Tsukuda, E., and Kimura, K. (1996). Surface Fault Ruptures on the Northwest Coast of the Awaji Island, Associated with the Hygo-ken Nanbu Earthquake of 1995, Japan. *"Zisin" J. Seismol. Soc. Jap.* **49,** (in press).

Bailey, A. D. (1974). Near-surface fault detection by magnetometer. *Calif. Geol.* **27,** 274.

Bakun, W. H., and Lindh, A. G. (1985). The Parkfield, California earthquake prediction experiment. *Science* **229,** 619–624.

Baljinnyam, I., Bayasgalan, A., Borisov, B. A., Cisternas, A., Dem'yanovich, M. G., Ganbaatar, L., Kochetkov, V. M., Kurushin, R. A., Molnar, P., Philip, H., and Vashchilov, Y. Y. (1993).

Ruptures of major earthquakes and active deformation in Mongolia and its surroundings. *Geol. Soc. Amer. Mem.* **181,** 1–62.

Barberi, F., Bertagnini, A., and Landi, P., (eds.) (1990), *Mt. Etna: The 1989 Eruption.* Giannini, Pisa.

Barrientos, S. E., and Acevedo-Aranguiz, P. S. (1992). Seismological aspects of the 1988–1989 Lonquimay (Chile) volcanic eruption. *J. Volcanol. Geotherm. Res.* **53,** 73–87.

Barrientos, S. E., and Ward, S. N. (1990). The 1960 Chile earthquake—Inversion for slip distribution from surface deformation. *Geophys. J. Int.* **103,** 589–598.

Barrientos, S. E., Plafker, G., and Lorca, E. (1992). Postseismic coastal uplift in southern Chile. *Geophys. Res. Lett.* **19,** 701–704.

Bartlett, S. F., and Youd, T. L. (1992). Empirical Analysis of Horizontal Ground Displacement Generated by Liquefaction-Induced Lateral Spreads, Tech. Rep. NCEER-92-0021. State University of New York, Buffalo.

Bartsch-Winkler, S., and Schmoll, H. R. (1987). Earthquake caused sedimentary couplets in the Upper Cook Inlet Region. In Geologic Studies in Alaska by the U.S. Geological Survey during 1986 (T. D. Hamilton, and J. P. Galloway, eds.), *Geol. Surv. Circ. U.S.* **998,** 92–95.

Bartsch-Winkler, S., and Schmoll, H. R. (1993). Evidence for Late Holocene sea level fall from reconnaissance stratigraphic studies in an area of earthquake-subsided intertidal deposits, Isla Chiloe southern Chile. In Sedimentation and Tectonics (R. Steel et al., eds.). *Spec. Pub Int. Assoc. Sedimentol.* **20,** 91–108.

Bath, M. (1981). Earthquake magnitude; recent research and current trends. *Earth Sci. Rev.,* **17,** pp. 315–398.

Beanland, S., and Barrow-Hurlbert, S. A. (1988). The Nevis-Cardrona fault system, central Otago, New Zealand; late Quaternary tectonics and structural development. *N. Z. J. Geol. Geophys.* **31,** 337–352.

Beanland, S., Berryman, K. R., Hull, A. G. and Wood, P. R. (1986). Late Quaternary deformation at the Dunstan Fault, central Otago, New Zealand. *Bull.- R. Soc. N. Z.* **24,** 293–306.

Beanland, S., Berryman, K. R., and Blick, G. H. (1989). Geological investigations of the 1987 Edgecumbe earthquake, New Zealand. *N. Z. J. Geol. Geophys.* **32,** 73–91.

Beanland, S., Blick, G. H., and Darby, D. J. (1990). Normal faulting in a back arc basin; geological and geodetic characteristics of the 1987 Edgecumbe earthquake, New Zealand. *J. Geophys. Res.* **95,** 4693–4707.

Beck, A. C. (1968). Gravity faulting as a mechanism of topographic adjustment: *N. Z. J. Geol. Geophys.* **11,** 191–199.

Bégin, C., and Filion, L. (1985). Analyse dendrochronologique d'un glissement de terrain de la région du Lac à l'Eau Claire (Québec nordique). *Can. J. Earth Sci.* **22,** 175–182 (in French).

Begin, Z. B. (1993) Application of quantitative morphologic dating to paleo-seismicity of the northern Negev, Israel. *Isr. J. Earth Sci.* **41,** 95–103.

Beloussov, V. V. (1980). *Geotectonics.* Springer-Verlag, Berlin.

Ben-Menaham, A. (1981). Variation of slip and creep along the Levant Rift over the past 4500 years. *Tectonophysics* **80,** 183–197.

Benson, A. K., and Baer, J. L. (1987). Close order gravity surveys—A means of fault definition in valley fill sediments. *Proc. Symp. Eng. Geol. Soils Eng., 23rd,* Logan, UT, *1987,* pp. 219–240.

Benson, A. K., and Mustoe, N. B. (1991). Delineating concealed faults and shallow subsurface geology along the Wasatch Front, Utah, USA, by integrating geophysical and trench data. *Q. J. Eng. Geol.* **24,** 375–387.

Berberian, M. (1979). Earthquake faulting and bedding thrust associated with the Tabas e Goldshan (Iran) earthquake of December 16, 1978. *Bull. Seismol. Soc. Am.* **69,** 1861–1887.

Berberian, M., and Qorashi, M. (1994). Coseismic fault-related folding during the South Golbaf earthquake of November 20, 1989, in southeast Iran. *Geology* **22,** 531–534.

Berg, A. W. (1990). Formation of mima mounds: A seismic hypothesis. *Geology* **18,** 281–284.

Bergman, E. A., and Solomon, S. C. (1990). Earthquake swarms on the Mid-Atlantic Ridge: Products of magmatism or extensional tectonics? *J. Geophys. Res.* **95,** 4943–4965.

Berry, M. E. (1990). Soil catena development on fault-scarp slopes, Sierra Nevada, California. *Geomorphology* **3,** 333–350.

Berryman, K. R. (1990). Late Quaternary movement on the Wellington Fault in the Upper Hutt area, New Zealand. *N. Z. J. Geol. Geophys.* **33,** 257–270.

Berryman, K. R., and Beanland, S. (1991). Variation in fault behavior in different tectonic provinces of New Zealand. *J. Struct. Geol.* **13,** 177–189.

Berryman, K. R., Ota, Y., and Hull, A. G. (1989). Holocene paleoseismicity in the fold and thrust belt of the Hikurangi subduction zone, eastern North Island, New Zealand. *Tectonophysics* **163,** 185–195.

Betancourt, J. L., Van Devender T. R., and Martin P. S. (1991). *Packrat Middens: The Last 40,000 Years of Biotic Change.* Univ. of Arizona Press, Tucson.

Biasi, G. P., and Weldon, R. J., II (1994a). Quantitative refinement of C-14 distributions. *Quat. Res.* **41,** 1–18.

Biasi, G. P., and Weldon, R. J., II (1994c). Quantitative approaches to event dating and constraint. *U.S. Geol. Surv. Open File Rep.* **94-568,** 18–20.

Bilham, R. (1985). Subsurface radar imagery of near-surface fractures associated with the Borah Peak earthquake. *U.S. Geol. Surv. Open File Rep.* **85-290-A,** 182–194.

Bilham, R., and King, G. C. P. (1989). Slip distribution and oblique segments of the San Andreas fault, California; observations and theory. In *Fault Segmentation and Controls of Rupture Initiation and Termination* (D. P. Schwartz, and R. H. Sibson, eds.), *U.S. Geol. Surv. Open File Rept.* **89-315,** 80–93.

Bilham, R., and Seeber, L. (1985). Paleoseismic studies using subsurface radar profiling: Summaries of Technical Reports, vol. XIX. *U.S. Geol. Surv. Open File Rept.* **85-22,** 47.

Birkeland, P. W. (1984). *Soils and Geomorphology.* Oxford Univ. Press, Oxford, UK.

Birkeland, P. W., Machette, M. N., and Haller, K. M. (1991). Soils as a tool for applied Quaternary geology. *Utah Geol. Surv. Misc. Publ.* **91-3,** 1–63.

Bjornsson, A., Johnsen, G., Sigurdsson, S., Thorbergsson, G., and Tryggvason, E. (1979). Rifting of a plate boundary in north Iceland 1975–1978. *J. Geophys. Res.* **84,** 3029–3038.

Bjornsson, A., Saemundsson K., Einarsson P., Tryggvason, E., and Gronvald, K. (1977). Current rifting episode in north Iceland. *Nature (London)* **266,** 318–323.

Black, R. F. (1976). Periglacial features indicative of permafrost; ice and soil wedges. *Quat. Res.* **6,** 3–26.

Blakely, R. J., and Jachens, R. C. (1991). Regional study of mineral resources in Nevada: Insights from 3-D analysis of gravity and magnetic anomalies. *Geol. Soc. Am. Bull.* **103,** 795–803.

Bleil, U., Hall, J. M., Johnson, H. P., Levy, S., and Schoenharting, G. (1982). The natural magnetization of a 3-kilometer section of Icelandic crust. *J. Geophys. Res.* **87,** 6569–6589.

Bloom, A. L. (1970). Holocene submergence in Micronesia as the standard for eustatic sea-level changes. *Geol. Soc. Am. Bull.* **81,** 145–154.

Bloom, A. L. (1977). *Atlas of Sea-Level Curves: IGCP Project 61 Sea Level Project.* UNESCO, Paris.

Blumetti, A. M. (1995). Neotectonic investigations and evidence of paleoseismicity in the epicentral area of the January–February 1703, central Italy, earthquakes. In Perspectives in Paleoseismology (L. Serva, and D. B. Slemmons, eds.), *Assoc. Eng. Geol. Spec. Publ.* **6,** 83–100.

Bodin, P., and Klinger, T. (1986). Coastal uplift and mortality of intertidal organisms caused by the September 1985 Mexico earthquakes. *Science* **233,** 1071–1073.

Bonaccorso, A., and Davis, P. M. (1993). Dislocation modelling of the 1989 dike intrusion into the flank of Mount Etna, Sicily. *J. Geophys. Res.* **98,** 4261–4268.

Bonilla, M. G. (1970). Surface faulting and related effects. In *Earthquake Engineering* (R. L. Wiegel, ed.), pp. 47–74. Prentice-Hall, New York.

Bonilla, M. G. (1973). Trench exposures across surface fault ruptures associated with the San Fernando earthquake. In Geological and Geophysical Studies, Vol. 3, pp 173–182. U.S. Dep. Comm., Natl. Ocean. Atmos. Admin., Washington D.C.

Bonilla, M. G. (1982). Evaluation of potential surface faulting and other tectonic deformation *U.S. Geol. Surv. Open File Rept.* **82-0732,** 1–91.

Bonilla, M. G. (1988). Minimum earthquake magnitude associated with coseismic surface faulting. *Bull. Assoc. Eng. Geol.* **25,** 17–29.

Bonilla, M. G. (1991). Faulting and seismic activity. In The Heritage of Engineering Geology; The First Hundred Years (G. A. Kiersch, ed.), *Centennial Special Vol. 3,* pp. 251–264. Geol. Soc. Am., Boulder, CO.

Bonilla, M. G., and Lienkaemper, J. J. (1991). Factors affecting the recognition of faults exposed in exploratory trenches. *U.S. Geol. Surv. Bull.* **1947,** 54.

Bonilla, M. G., Mark, R. K., and Lienkaemper, J. J. (1984). Statistical relations among earthquake magnitude, surface rupture length, and surface fault displacement. *Bull. Seismol. Soc. Am.* **74,** 2379–2411.

Boore, D. M. and Joyner, W. B. (1994). Prediction of ground motion in North America. In *Proceedings of the ATC-35 Seminar on New Developments on Earthquake Ground Motion Estimates and Implications for Engineering Design Practice,* pp. 6-1 to 6-14. Appl. Tech. Counc., Redwood City, CA.

Borgia, A., Ferrari, L., and Pasquaré, G. (1992). Importance of gravitional spreading in the tectonic and volcanic evolution of Mount Etna. *Nature* (*London*) **357,** 231–235.

Bosher, R., and Duennebier, F. K. (1985). Seismicity associated with the Christmas 1965 event at Kilauea Volcano. *J. Geophys. Res.* **90,** 4529–4536.

Bourgeois, J., and Reinhart, M. A. (1989). Onshore erosion and deposition by the 1960 tsunami at Rio Lingue estuary, south-central Chile, *EOS Trans. Am. Geophys. Union* **70,** 1331.

Bourgeois, J., and Reinhart, M. A. (1993). Tsunami deposits from 1992 event; Implications for interpretation of paleotsunami deposits, Cascadia subduction zone. *EOS Trans. Am. Geophys. Union* **74,** 350.

Bovis, M. J. (1982). Uphill-facing (antislope) scarps in the Coast Mountains, southwest British Columbia. *Geol. Soc. Am. Bull.* **93,** 804–812.

Bowen, F. E. (1954). Late Pleistocene and Recent vertical movement at the Alpine Fault. *N. Z. J. Sci. Technol.,* **35,** *Sect. B,* 390–397.

Boyd, T. M., Engdahl, E. R., and Spence, W. (1992). Analysis of seismicity associated with a complete seismic cycle along the Aleutian arc: 1957 through 1989. In Proceedings of the Wadati Conference on Great Subduction Earthquakes, Fairbanks, Alaska (D. Christensen, M. Wyss, R. E. Habermann, and J. Davies Org.), pp. 43–50.

Bradley, W. C., and Griggs, G. B. (1976). Form, genesis, and deformation of central California wave-cut platforms. *Geol. Soc. Am. Bull.* **87,** 433–449.

Brandsdottir, B., and Einarsson, P. (1979). Seismic activity associated with the September 1977 deflation of the Krafla central volcano in northeastern Iceland. *J. Volcanol. Geotherm. Res.* **6,** 197–212.

Branno, A., Esposito E. G. I., Luongo, G., Marturano, A., Porfido, S., and Rinaldis, V. (1984). The October 4th, 1983 Magnitude 4 earthquake in Phlegraean Fields: Macroseismic survey. *Bull. Volcanol.* **47,** 233–246.

Brown, R. D., Jr, Ward, P. L., and Plafker, G. (1973). Geologic and seismologic aspects of the Managua, Nicaragua, earthquakes of December 23, 1972. *U.S. Geol. Surv. Prof. Pap.* **838,** 1–34.

Brune, J. N. (1996). Precariously balanced rocks and ground-motion maps for southern California. *Bull. Seismol. Soc. Am.* **86,** 43–54.

Brunsden, D., and Prior, D. B. (1984). *Slope Instability* Wiley, New York.

Bryan, C. J. (1992). A possible triggering mechanism for large Hawaiian earthquakes derived from analysis of the 26 June 1989 Kilauea south flank sequence. *Bull. Seismol. Soc. Am.* **82,** 2368–2390.

Buchanan-Banks, J. M. (1987). Structural damage and ground failures from the November 16, 1983, Kaoiki earthquake, Island of Hawaii. *U.S. Geol. Surv. Prof. Pap.* **1350,** 1187–1220.

Bucknam, R. C., and Anderson, R. E. (1979). Estimation of fault scarp ages from a scarp-height-slope-angle relationship. *Geology* **7,** 11–14.

Bucknam, R. C., Hemphill-Haley, E., and Leopold, E. B. (1992). Abrupt uplift within the past 1700 years at the southern Puget Sound, Washington. *Science* **258,** 1611–1614.

Bull, W. B. (1984). Tectonic geomorphology. *J. Geol. Educ.* **32,** 310–324.

Bull, W. B. (1985). Correlations of flights of global marine terraces. In Tectonic Geomorphology: *Binghamton Symposia in Geomorphology* (M. Morisawa and J. Hack, eds.), Vol. **15,** pp. 129–152.

Bull, W. B. (1987). Relative rates of long-term uplift of mountain fronts. In Directions in Paleoseismology (A. J. Crone, and E. M. Omdahl, eds.), *U.S. Geol. Surv. Open File Rep.* **87-673,** 192–202.

Bull, W. B. (1991). *Geomorphic Responses to Climatic Change.* Oxford Univ. Press, New York.

Bull, W. B. (1996). Prehistorical earthquakes on the Alpine fault, New Zealand. *J. Geophys. Res.* **101**(B3), 6087–6150.

Bull, W. B., Cowan, H. A., and Pettinga, J. R. (1991). New ways of dating earthquakes on two segments of the oblique-slip Hope fault, New Zealand. *Geol. Soc. Am., Abstr. Prog.* Vol. **23,** no. 5, p. A431.

Bull, W. B., King, J., Kong, F., Moutoux, T. and Phillips, W. M. (1994). Lichen dating of coseismic landslide hazards in alpine mountains. *Geomorphology* **10,** 253–264.

Bull, W. B., and Knuepfer, P. L. K. (1987). Adjustments of the Charwell River, New Zealand to uplift and climatic changes. *Geomorphology* **1,** 15–32.

Bull, W. B., and McFadden, L. D. (1977). Tectonic geomorphology, north and south of the Garlock Fault, California. In *Geomorphology in Arid Regions* (D. O. Doehring, ed.), 8th Annu. Binghampton Geomorphol. Symp., pp. 115–138. Allen & Unwin, London.

Bull, W. B., and Pearthree, P. A. (1988). Frequency and size of Quaternary surface ruptures of the Pitaycachi fault, northeastern Sonora, Mexico. *Bull. Seismol. Soc. Am.* **77,** 956–978.

Bullard, T. F., and Lettis, W. R. (1993). Quaternary fold deformation associated with blind thrusting, Los Angeles Basin, California. *J. Geophys. Res.* **98,** 8349–8369.

Bullen, K. E., and Bolt, B. A. (1985). *An Introduction to the Theory of Seismology* Cambridge Univ. Press, Cambridge, UK.

Bulletin of Volcanic Eruptions (1986). Annual Report of the World Volcanic Eruptions in 1983. *Suppl. Bull. Volcanol.* **48,** 29–32.

Bulletin of Volcanic Eruptions (1987). Annual Report of the World Volcanic Eruptions in 1984. *Suppl. Bull. Volcanol.* **49,** 37–65.

Bulletin of Volcanic Eruptions (1992). Annual Report of the World Volcanic Eruptions in 1989. *Suppl. Bull. Volcanol.* **54,** 78–80.

Burbach, G. V., and Frohlich, C. (1986). Intermediate and deep seismicity and lateral structure of subducted lithosphere in the Circum-Pacific region. *Rev. Geophys.* **24,** 8333–8374.

Burbank, D. W., and Verges, J. (1994). Reconstruction of topography and related depositional systems during active thrusting. *J. Geophys. Res.* **99,** 20,281–20,297.

Burke, R. M., and Carver, G. A. (1989). The degree of soil development from buried soils formed in fault-generated colluviums reflect interseismic time, northern California. *Geol. Soc. Am. Abstr. Prog.* **21**(5), 61.

Burrows, C. J. (1975). A 500-year-old landslide in the Acheron River valley, Canterbury (Note). *N. Z. J. Geol. Geophys.* **18,** 357–360.

Bursik, M. (1992). How to predict an eruption at Long Valley caldera. *EOS, Trans. Am. Geophys. Union* **73,** 343.

Bursik, M., and Sieh, K. (1989). Range front faulting and volcanism in the Mono Basin, eastern California. *J. Geophys. Res.* **94,** 15,587–15,609.

Buwalda, J. P., and St. Amand, P. (1955). Geological effects of the Arvin-Tehachapi earthquake. In Earthquakes in Kern County, California, during 1952 *Bull.- Calif., Div. Mines Geol.* **171,** 41–56.

Cabrera, J., Sebrier, M., and Mercier, J. L. (1987). Active normal faulting in the high plateaus of central Andes- the Cuzco region (Peru). *Ann. Tecton.* **1,** 116–138.

Calhoun, R. S., and Fletcher, C. H. (1994). Sediment deposition and implications for relative sea -level on the Hanalei coastal plain, Kauai, Hawaii. *Geol. Soc. Am. Abstr. Prog.* **26**(7), A-306.

California Department of Transportation (1977). *California Trenching and Shoring Manual* California Division of Structures, Sacramento, CA.

Caputo, R. (1993). Morphogenic earthquakes: A proposal. *Bull. INQUA Neotecton. Comm.* **16,** 24.

Carter, M. (1982). *Geotechnical Engineering Handbook.* Methuen, London.

Carver, G. A. (1987a). Late Cenozoic tectonics of the Eel River basin region, coastal northern California. In Tectonics, Sedimentation, and Evolution of the Eel River and Other Coastal Basins of Northern California (H. Schymiczek and R. Suchland, eds.), *San Joaquin Geol. Soc. Misc. Publ.* **37,** 61–72.

Carver, G. A. (1987b). Geologic criteria for recognition of individual paleoseismic events in compressional tectonic environments. *U.S. Geol. Surv. Open File Rep.* **87-673,** p.115–128.

Carver, G. A., and Aalto, K. R. (1992). Late Cenozoic tectonics and sedimentation, northern coastal California; Trip Stop Guide. In Field Guide to the Late Cenozoic Subduction Tectonics and Sedimentation of Northern Coastal California (G. A. Carver, and K. R. Aalto, eds.), *Pac. Sect., Am. Assoc. Pet. Geol.* **GB-71,** 59–74.

Carver, G. A., and Burke, R. B. (1989). Active convergent tectonics in northwestern California. In Geologic Evolution of the Northernmost Coast Ranges and Western Klamath Mountains, California (K. R. Aalto, and Harper, leaders), *28th Int. Geol. Cong. Field Trip Guidebook* **T308,** pp. 64–82.

Carver, G. A., Gilpin, L. M., and Boer, J. (1994a). Tsunami deposits from the 1964 Alaskan earthquake on N. E. Kodiak Island, Alaska. *Geol. Soc. Am. Abstr. Prog.* **26**(7), 529.

Carver, G. A., Jayko, A. S., Valentine, D. W., and Li, W. H. (1994b). Coastal uplift associated with the 1992 Cape Mendocino earthquake, northern California. *Geology* **22,** 195–198.

Carver, G. A., Stuiver, M., and Atwater, B. F. (1992). Radiocarbon ages of earthquake-killed trees at Humboldt Bay, California. *EOS, Trans. Am. Geophys. Union* **73,** 398 (abstr.).

Cass, R., and Wall, M. R. (1989). *Trench Safety Shoring Manual; Using Common Sense in the Common Trench.* Cruse Publications, San Jose, CA.

Castilla, I. C. (1988). Earthquake-caused coastal uplift and its effects on rocky intertidal kelp communities. *Science* **242,** 440–443.

Castro, G. (1987). On the behavior of soils during earthquakes. In *Developments in Geotechnical Engineering* (A. S. Cakmak, ed.), Vol. 42, pp. 169–204. Elsevier, Amsterdam.

Catt, J. A. (1988). *Quaternary Geology for Scientists and Engineers.* Halsted Press, New York.

Cerling, T. E. (1990). Dating geomorphic surfaces using cosmogenic ^{3}He. *Quat. Res.* **33,** 148–156.

Chapuis, A., and van den Berg, J. (1988). The new Kern DSR series of first order stereo plotters. *Int. Soc. Photogramm. Remote Sens. 16th Annu. Congr.,* Kyoto, Japan, Comm. II, pp. 1–8.

Chinn, T. J. H. (1981). Use of rock weathering-rind thickness for Holocene absolute age-dating in New Zealand. *Arct. Alp. Res.* **13,** 33–45.

Chleborad, A. F. (1994). Modeling and analysis of the 1949 Narrows landslide, Tacoma, Washington. *Bull. Assoc. Eng. Geol.* **31,** 305–328.

Chorley, R. J., Schumm, S. A., and Sugden, D. E. (1984). *Geomorphology.* Methuen, London.

Christiansen, E. A. (1983). The Denholm landslide, Saskatchewan. Part I: Geology. *Can. Geotech. J.* **20,** 197–207.

Cita, M. B., and Lucchi, F. R., eds. (1984). Seismicity and Sedimentation; Spec. Issue. *Mar. Geol.* **55**(1/2).

Clague, J. J., and Bobrowsky, P. T. (1994a). Evidence for a large earthquake and tsunami 100-400 years ago on western Vancouver Island, British Columbia. *Quat. Res.* **41,** 176–184.

Clague, J. J., and Bobrowsky, P. T. (1994b). Tsunami deposits beneath tidal marshes on Vancouver Island, British Columbia. *Geol. Soc. Amer. Bull.* **106,** 1293–1303.

Clague, J. J., Naesgaard, E., and Sy, A. (1992). Liquefaction features on the Fraser delta: Evidence for prehistoric earthquakes. *Can. J. Earth Sci.* **29,** 1734–1745.

Clague, J. J., Bobrowsky, P. T., and Hamilton, T. S. (1994). A sand sheet deposited by the 1964 Alaska tsunami at Port Alberni, British Columbia. *Estuarine, Coastal Shelf Sci.* **38,** 413–421.

Clark, B. R., and Cole, W. F. (1992). Importance of accurate geological characterization in the analysis of seismically triggered landslides. *Proc. 35th Annu. Meet. Assoc. Eng. Geol.,* Long Beach, CA., pp. 469–472.

Clark, M. M. (1972). Surface rupture along the Coyote Creek fault. U.S. Geol. Surv. Prof. Pap. **787,** 55–87.

Clark, M. M., Grantz, A., and Rubin, M. (1972). Holocene activity on the Coyote Creek fault as recorded in sediments of Lake Cahuilla. *U.S. Geol. Surv. Prof. Pap.* **787,** 112–130.

Clarke, J. A., Farrell, W. E., and Peltier, W. R. (1978). Global changes in post glacial sea level; a numerical calculation. *Quat. Res.* **9,** 265–287.

Clarke, S. H. (1992). Geology of the Eel River basin and adjacent regions; Implications for late Cenozoic tectonics of the southern Cascadia subduction zone and Mendocino triple junction. *Am. Assoc. Pet. Geol. Bull.* **76,** 199–224.

Clarke, S. H. and Carver, G. A. (1992). Late Holocene tectonics and paleoseismicity, southern Cascadia subduction zone. *Science* **255,** 188–192.

Clarke, S. H., Greene, H. G., and Kennedy, M. P. (1985). Identifying potentially active faults and unstable slopes offshore. In Evaluating Earthquake Hazards in the Los Angeles Region-An Earth-Science Perspective (J. I. Ziony, ed.), *U.S. Geol. Surv. Prof. Pap.* **1360,** 347–373.

Cluff, L. S., and Slemmons, D. B. (1971). Wasatch fault zone- features defined by low-sun angle photography. *Utah Geol. Assoc. Publ.* **1,** G1–G9.

Cohen, S., Holdahl, S., Caprette, D., Hilla, S., Safford, R., and Schultz, D. (1995). Uplift of the Kenai Peninsula, Alaska, since the 1964 Prince William Sound earthquake. *J. Geophys. Res.* **100,** 2031–2039.

Coe, J. A., Taylor, E. M., and Schilling, S. P. (1991). Close-range geophotogrammetric mapping of trench walls using multi-model stereo restitution software: ACSM-ASPRS Annual Convention. *Photogramm. Primary Data Acquis.* **5,** 30–43.

Cole, J. W. (1990). Structural control and origin of volcanism in the Taupo volcanic zone, New Zealand. *Bull. Volcanol.* **52,** 445–459.

Collins, T. K. (1990). New faulting and the attenuation of fault displacement. *Bull. Assoc. Eng. Geol.* **27,** 11–22.

Colman, S. M. (1986). Morphology and age of fault scarps in the Rio Grande rift, south-central Colorado. In *Contributions to Colorado Seismicity and Tectonics- A 1986 Update* (W. P. Rogers, and R. M. Kirkham, eds.), *Spec. Publ.-Colo. Geol. Surv. Spec. Pub.* **28,** 38–58.

Colman, S. M., and Watson, K. (1983). Ages estimated from a diffusion equation model for scarp degradation. *Science* **221,** 263–265.

Colman, S. M., Pierce, K. L., and Birkeland, P. W. (1987). Suggested terminology for Quaternary dating methods. *Quat. Res.* **28,** 314–319.

Comartin, C. D., Greene, M., and Tubbesing, S. K., eds. (1995). Great Hanshin earthquake disaster- Hyogo-Ken Nanbu earthquake preliminary report. *Earthquake Eng. Res. Inst., Tech. Rep.* **95-04,** 1–120.

Combillick, R. A. (1991). Paleoseismology of the Cook Inlet region, Alaska; Evidence from peat stratigraphy in Turnagain and Knik Arms. *Prof. Rep.- Alaska Div. Geol. Geophys. Surv.* **112,** 1–52.

Combellick, R. A. (1993). The penultimate great earthquake in southcentral Alaska: evidence from a buried forest near Girdwood. In Short Notes on Alaskan Geology 1993 (D. N. Solie, and F. Tannian, eds.), *Alaska Prof. Rep.- Div. Geol. Geophys.* **113,** 7–15.

Coney, P. J. (1987). The regional tectonic setting and possible causes of Cenozoic extension in the North American Cordillera. In *Continental Extensional Tectonics* (M. P. Coward, J. F. Dewey, and P. L. Hancock, eds.), *Spec. Publ- Geol. Soc. London* **28,** 177–186.

Conrad, T. A. (1856). Observations of the Eocene deposit of Jackson, Miss., with descriptions of 34 new species of shells and corals. *Proc. Acad. Nat. Sci. Philadelphia.* **7,** 257–258.

Converse, Davis and Associates (1968). Geologic report on the probability of faulting at the Paramedical Building site, San Fernando Valley Joint Union College District (unpublished report).

Costa, J. E., and Baker, V. R. (1981). Surficial geology- Building with the earth. Wiley, New York.

Costa, J. E., and Schuster, R. L. (1991). Documented historical landslide dams from around the world. *U.S. Geol. Surv. Open File Rep.* **91-239,** 1–486.

Cotton, C. A. (1950). Tectonic scarps and fault valleys. *Geol. Soc. Am. Bull.* **61,** 717–758.

Cotton, W. R., Fowler, W. L., and Hay, E. A. (1988). Late Pleistocene and Holocene Paleoseismicity of the San Gabriel Fault, Saugus/Castaic Area, Los Angeles County, California. *unpublished Final Tech. Rep., U.S. Geol. Surv. Contract No.* **14-08-0001-G1196**. Wm. Cotton & Assoc., Los Gatos, CA.

Crofts, R. S. (1981). Mapping techniques in geomorphology. In *Geomorphological Techniques* (A. Goudie, ed.), pp. 66–78. Allen & Unwin, London.

Crone, A. J., ed. (1983). Paleoseismicity along the Wasatch Front and adjacent areas, central Utah. *Spec. Stud.-Utah Geol. Miner. Surv.* **62,** 1–62.

Crone, A. J. (1987). Introduction. In *Directions in Paleoseismology* (A. J. Crone, and E. M. Omdahl, eds.), *U.S. Geol. Surv. Open File Rept.* **87-673,** 1–6.

Crone, A. J., and Haller, K. M. (1991). Segmentation and the coseismic behavior of Basin-and-Range normal faults; examples from east-central Idaho and southwestern Montana. *J. Struct. Geol.* **13,** 151–164.

Crone, A. J., and Harding, S. T. (1984a). Near-surface faulting associated with Holocene fault scarps, Wasatch fault zone, Utah. In A Workshop on Evaluation of Regional and Urban Earthquake Hazards and Risk in Utah (W. W. Hays, and P. L. Gori, eds.), *U.S. Geol. Surv. Open File Rep.* **84-763,** 241–268.

Crone, A. J., and Harding, S. T. (1984b). Relationship of late Quaternary fault scarps to subjacent faults, eastern Great Basin, Utah. *Geology* **12,** 292–295.

Crone, A. J., and Luza, K. V. (1990). Style and timing of Holocene surface faulting on the Meers fault, southwestern Oklahoma. *Geol. Soc. Am. Bull.* **102,** 1–17.

Crone, A. J., and Omdahl, E. M., eds. (1987). Directions in Paleoseismology, Proc. of Conf. XXXIX *U.S. Geol. Surv. Open File Rep.* **87-673,** 1–456.

Crone, A. J., Machette, M. N., Bonilla, M. G., Lienkaemper, J. J., Pierce, K. L., Scott, W. E., and Bucknam, R. C. (1987). Surface faulting accompanying the Borah Peak earthquake and segmentation of the Lost River fault, central Idaho. *Bull. Seismol. Soc. Am.* **77,** 739–770.

Crone, A. J., Machette, M. N., and Bowman, J. R. (1992). Geologic investigations of the 1988 Tennant Creek, Australia, earthquakes- implications for paleoseismicity in stable continetal regions. *U.S. Geol. Surv. Bull.* **2032-A,** A1–A51.

Crowell, J. C. (1974). Origin of late Cenozoic basins in southern California. In *Tectonics and Sedimentation* (W. R. Dickinson, ed.), *Spec. Pub.- Soc. Econ. Paleontol. Mineral.* **22,** 190–204.

Crozier, M. J. (1992). Determination of paleoseismicity from landslides. In *Landslides (Glissements de terrain)* (D. H. Bell, ed.), Int. Symp., 6th, Christchurch, New Zealand, 1992, Vol. **2,** pp. 1173–1180. A. A. Balkema, Rotterdam.

Daniels, R. B., Nettleton, W. D., McCracken, R. J., and Gamble, E. E. (1966). Morphology of soils with fragipans in parts of Wilson County, North Carolina. *Soil Sci. Soc. Am. Proc.* **30,** 376–380.

Darienzo, M. E., and Peterson, C. D. (1990). Episodic tectonic subsidence of Late Holocene salt marshes, northern Oregon central Cascadia margin. *Tectonics* **9,** 1–22.

Davis, D. J., Suppe, J., and Dahlen, F. A. (1983). Mechanics of fold and thrust belts and accretionary wedges. *J. Geophys. Res.* **88,** 1153–1172.

Davis, G. H. (1984). *Structural Geology of Rocks and Regions.* Wiley, New York.

Davis, T. L., and Dubendorfer, E. M. (1987). Strip map of the western big bend segment of the San Andreas fault. *Geol. Soc. Am. Map Chart Ser.* **MC-60,** Scale 1:31,682.

Dawson, A. G., Foster, I. D. L., Shi, S., Smith, D. E., and Long, D. (1991). The identification of tsunami deposits in coastal sediment sequences. *Sci. Tsunami Hazards* **9,** 73–82.

Das, S., and Scholz, C. H. (1983). Why large earthquakes do not nucleate at shallow depths. *Nature* (*London*) **305,** 621–623.

Decker, R. W. (1987). Dynamics of Hawaiian volcanoes: An overview. In Volcanism in Hawaii (R. W. Decker, T. L. Wright, and P. H. Stauffer, eds.), *U.S. Geol. Surv. Prof. Pap.* **1350,** 997–1018.

Decker, R. W., Wright, T. L., and Stauffer, P. H., eds. (1987). Volcanism in Hawaii, *U.S. Geol. Surv. Prof. Pap.* **1350.**

Demek, J., ed. (1972). *Manual of Detailed Geomorphological Mapping.* Subcommission on Geomorphological Mapping, International Geographical Union, Academia, Prague.

Demek, J., and Embleton, C., eds., (1978). *Guide to Medium-Scale Geomorphological Mapping,* Manual of the Subcommission on Geomorphological Mapping, International Geographical Union. E. Schweizerbart'sche Verlagsbuchhandlung, Stuttgart, Germany.

Demets, C., Gordon, R. G., Argus, D. F., and Stein, S. (1990). Current plate motions. *Geophys. J. Int.* **101,** 425–478.

De Natale, G., and Pingue, F. (1993). Ground deformations in collapsed caldera structures. *J. Volcanol. Geotherm Res.* **57,** 19–38.

Deng, G. D., Wang, Y., Liao, Y., Zhang, W., and Li, M. (1984). Fault scarps, colluvial wedges on the frontal fault of Mt. Helenshan and its active history during the Holocene. *Chin. Sci. Bull.* **9,** 557–564 (in Chinese).

dePolo, C. M. (1994). The maximum background earthquake for the Basin and Range province, western North America. *Bull. Seismol. Soc. Am.* **84,** 466–472.

dePolo, C. M., and Slemmons, D. B. (1990). Estimation of earthquake size for seismic hazards. In *Neotectonics in Earthquake Evaluation* (E. L. Krinitsky and D. B. Slemmons, eds.), *Geol. Soc. Am., Rev. Eng. Geol.* **8,** 1–28.

dePolo, C. M., Clark, D. G., Slemmons, D. B. and Aymand, W. H. (1989). Historical Basin and Range Province surface faulting and fault segmentation. In *Fault Segmentation and Controls of Rupture Initiation and Termination* (D. P. Schwartz and R. H. Sibson, eds.), *U.S. Geol. Surv. Open File Rep.* **89-315,** 131–162.

dePolo, C. M., Clark, D. G., Slemmons, D. B., and Ramelli, A. R. (1991). Historical surface faulting in the Basin and Range Province, western North America- implications for fault segmentation. *J. Struct. Geol.* **13,** 123–136.

Dickenson, S. E., Obermeier, S. F., and Roberts, T. H. (1994). Constraints on earthquake shaking in the lower Columbia River region of Washington and Oregon, during late Holocene time. *Proc. U.S. Natl. Conf. Earthquake Eng., 5th,* Chicago. Earthquake Engin. Res. Inst., El Cerrito, CA. **3,** 313–322.

Dietrich, W. E., and Dorn, R. (1984). Significance of thick deposits of colluvium on hillslopes: A case study involving the use of pollen analysis in the coastal mountains of northern California. *J. Geol.* **92,** 147–158.

Ding, G., ed. (1982). Active Faults in China, *Proc. 1979 Yinchuan Conf.* Seismol. Comm. Chin. Seismol. Soc., Seismol. Press, Bejiing (in Chinese).

Dobry, R. (1989). Some basic aspects of soil liquefaction during earthquakes. *Ann. N. Y. Acad. Sci.* **558,** 31–38.

Dobry, R., and Liu (1992). Centrifuge modeling of soil liquefaction. *Proc. World Conf. Earthquake Eng., 10th,* Madrid, Spain, **11,** 6801–6809.

Dobry, R., Idriss, I. M., and Ng, E. (1978). Duration characteristics of horizontal components of strong-motion earthquake records. *Bull. Seismol. Soc. Am.* **68,** 1487–1520.

Doig, R. (1986). A method for determining the frequency of large-magnitude earthquakes using lake sediments. *Can. J. Earth Sci.* **23,** 930–937.

Dorn, R. I., and Phillips, F. M. (1991). Surface exposure dating; review and critical evaluation. *Phys. Geogr.* **12,** 303–333.

Doser, D. I., and Smith, R. B. (1989). An assessment of source parameters of earthquakes in the Cordillera of the western United States. *Bull. Seismol. Soc. Am.* **79,** 1383–1409.

Douglas, B. C. (1991). Global sea level rise. *J. Geophys. Res.* **96,** 6981–6992.

Du, Y., and Aydin, A. (1992). Three-dimensional characteristics of dike intrusion along the northern Iceland rift from inversion of geodetic data. *Tectonophysics* **204,** 111–121.

Dutton, C. E. (1889). The Charleston earthquake of August 31, 1886. *U.S. Geol. Surv. 9th Annu. Rep. 1887-1888,* pp. 203–528.

Dvorak, J. J., and Okamura, A. T. (1987). Geometry of intrusions and eruptive fissures at Kilauea Volcano determined from trilateration measurements. *Hawaii Symposium on How Volcanoes Work,* Abstr. Vol., p. 58. Hilo, Hawaii.

Dzulynski, S., and Walton, E. K. (1965). Sedimentary features of flysch and greywackes. *Dev. Sedimentol.* **7,** 1–274.

Dzurisin, D., and Newhall, C. G., (1984). Recent ground deformation and seismicity at Long Valley (California), Yellowstone (Wyoming), the Phlegraean Fields (Italy), and Rabaul (Papua New Guinea). *U.S. Geol. Surv. Open File Rep.* **84–939.**

Dzurisin, D., Anderson, L. A., Eaton, G. P., Koyanagi, R. Y., Lipman, P. W., Lockwood, J. P., Okamura, R. T., Puniwai, G. S., Sato, M. K., and Yamashita, K. M. (1980). Geophysical observations of Kilauea volcano, Hawaii: 2. Constraints on the magma supply during November 1975-September 1977. *J. Volcanol. Geotherm. Res.* **7,** 241–269.

Dzurisin, D., Yamashita, K. M., and Johnson, D. J. (1986). Preliminary results of precise leveling and trilateration surveys in Yellowstone National Park, Wyoming, 1985. *U.S. Geol. Surv. Open File Rep.* **86-265-B,** 1–28.

Easterbrook, D. J. (ed.), 1988, *Dating Quaternary Sediments,* Spec. Pap. No. 227. Geol. Soc. Am., Boulder.

Eaton, G. P. (1982). The Basin and Range province: Origin and tectonic significance. *Annu. Rev. Earth Planet. Sci.* 10, 409–440.

Eaton, G. P., Christiansen, R. L., Iyer, H. M., Pitt, A. M., Mabey, D. R., Blank, H. R., Zeitz, I., and Gettings, M. E. (1975). Magma movement beneath Yellowstone National Park. *Science* **188,** 787–796.

Ebersold, D. B., ed. (1992). Landers Earthquake of June 28, 1992, San Bernadino County, California; Field Trip Guidebook, S. Calif. Sect. Assoc. Eng. Geol., 1992 Annu. Field Trip, Long Beach, CA.

Eiby, G. A. (1968). An annotated list of New Zealand earthquakes, 1460-1965. *N. Z. J. Geol. Geophys.* **11,** 630–647.

Einarsson, P. (1991). Earthquakes and present-day tectonism in Iceland. *Tectonophysics* **189,** 261–279.

Einarsson, P., and Bjornsson, A. (1979). Earthquakes in Iceland. *Jokull* **29,** 37–43.

Einarsson, P., and Brandsdottir, B. (1980). Seismological evidence for lateral magma intrusion during the July 1978 deflation of the Krafla volcano in NE-Iceland. *J. Geophys.* **47,** 160–165.

Einarsson, P., and Brandsdottir, B. (1984). Seismic activity preceding and during the 1983 volcanic eruption in Grimsvotn, Iceland. *Jokull* **34,** 13–23.

Einsele, G., Ricken, W., and Seilacher, A., eds., (1991). *Cycles and Events in Stratigraphy.* Springer-Verlag, Berlin.

Ekström, G. A. (1987). A broad band method of earthquake analysis. Ph.D. Thesis, Harvard University, Cambridge, MA.

Ekstrom, G., and Engdahl, E. R. (1989). Earthquake source parameters and stress distribution in the Adak Island region of the central Aleutian Islands, Alaska. *J. Geophys. Res.* **94,** 15499–15519.

(EPRI) (1994). *The Earthquakes of Stable Continental Regions—Assessment of Large Earthquake Potential,* Rep. TR102261, 5 vols. EPRI, Palo Alto, CA.

Elgamal, A-W. M., Dobry, R., and Adalier, K. (1989). Study of effect of clay layers on liquefaction of sand using small-scale models. In Large Ground Deformation and Their Effects on Lifelines, Tech. Rep. NCEER-89-0032, pp. 233–245. State Univ. New York, Buffalo.

Elgamal, A-W. M., Amer, M., and Adalier, K. (1993). Liquefaction during the October 12, 1992 Egyptian Dahshure earthquake. *Int. Conf. Case Hist. Geotech. Eng., 3rd,* Univ. Missouri, Rolla, 1993.

El-Isa, Z. H., and Mustafa, H. (1986). Earthquake deformations in the Lisan deposits and seismotectonic implications. *Geophys. J. R. Astron. Soc.* **86,** 413–424.

Embleton, C., ed. (1987). Neotectonics and morphotectonics. *Z. Geomorphol., Suppl.* **63,** 1–211.

Emerman, S. H., and Marrett, R. (1990). Why dikes? *Geology* **18,** 231–233.

Endo, E. T. (1985). Seismotectonic framework for the southeast flank of Mauna Loa Volcano, Hawaii. *Unpub. Ph.D. Thesis, University of Washington,* Seattle.

Endo, E. T., Malone, S. D., Noson, L. L., and Weaver, C. S. (1981). Locations, magnitudes, and statistics of the March 20-May 18 earthquake sequence: 1980 eruptions of Mount St. Helens, Washington. *U.S. Geol. Surv. Prof. Pap.* **1250,** 93–107.

Engelder, J. T. (1974). Microscopic wear grooves on slickensides-indicators of paleoseismicity. *J. Geophys. Res.* **79,** 4387–4392.

Enzel, Y., Amit, R., Harrison, J. B. J., and Porat, N. (1994). Morphologic dating of fault scarps and terrace risers in the southern Arava, Israel; comparison to other age-dating techniques and implications for paleoseismicity. *Isr. J. Earth Sci.* **43,** 91–103.

Faïn, J., Miallier, D., Aitken, M. J., Bailiff, I. K., Grün, R., Mangini, A., Mejdahl, V., Rendell, H. M., Townsend, P. D., Valladas, G., Visocekas, R., and Wintle, A. G., eds.(1992). Proceedings of the 6th international specialist seminar on thermoluminescene and electron spin resonance dating. *Quat. Sci. Rev.* **11**(1/2), 1–274.

Fairer, G. M., Whitney, J. W., and Coe, J. A. (1989). A close-range photogrammetric technique for mapping neotectonic features in trenches. *Bull. Assoc. Eng. Geol.* **26,** 521–530.

Fedotov, S. A., Gorel'chik, V. I., Stepanov, V. V., and Garbuzova, V. T. (1983). The development of the Great Tolbachik fissure eruption in 1975 from seismological data. In *The Great Tolbachik Fissure Eruption: Geological and Geophysical Data 1975-1976* (S. A. Fedotov and Y. K. Markhinin, eds.), pp. 189-203. Cambridge Univ. Press, Cambridge, UK.

Fenton, C. H. (1992). *Neotectonics in Scotland-A Field Guide.* Dep. Geol., University of Glasgow, Glasgow, Scotland.

Fenton, C. H. (1994). Postglacial faulting in Canada; an annotated bibliography. *Geol. Surv. Can. Open-File Rep.* **2774,** 1–98.

Ferrucci, F., and Patané, D. (1993). Seismic activity accompanying the outbreak of the 1991-1993 eruption of Mt. Etna (Italy). *J. Volcanol. Geotherm. Res.* **57,** 125–135.

Fiegel, G. L., and Kutter, B. L. (1994). Liquefaction mechanism for layered soils. *J. Geotech. Eng., Am. Soc. Civ. Eng. Proc.* **120,** 737–755.

Field, M. E., Gardner, J. V., Jennings, A. E., and Edwards, B. D. (1982). Earthquake-induced sediment failures on a 0.25° slope, Klamath River delta, California. *Geology* **10,** 542–546.

Filson, J., Simkin, T., and Leu, L.-K. (1973). Seismicity of a caldera collapse, Galapagos Islands 1968. *J. Geophys. Res.* **78,** 8591–8622.

Fink, J. H., and Pollard, D. D. (1983). Structural evidence for dikes beneath silicic domes, Medicine Lake Highland Volcano, California. *Geology* **11,** 458–461.

Finn, W. D. L., Ledbetter, R. H., and Wu, G. (1994). Liquefaction in silty soils: design and analysis. In Ground Failures Under Seismic Conditions (S. Prakash and Dakoulas, eds.), *Am. Soc. Civ. Eng., Geotech. Spec. Publ.* **44,** 51–76.

Flanigan, V. J., and Long, C. L. (1987). Aeromagnetic and near-surface electrical expression of the Kilauea and Mauna Loa volcanic rift systems. In Volcanism in Hawaii (R. W. Decker, T. L. Wright, and P. H. Stauffer, eds.), *U.S. Geol. Surv. Prof. Pap.* **1350,** 935–946.

Flint, R. F. (1971). *Glacial and Quaternary Geology.* Wiley, New York.

Florensov, N. A. (1960). On the neotectonics and seismicity of the Mongol-Baikal mountain area. *Geol. Geophys.* **1,** 79–90 (in Russian).

Florensov, N. A., and Solonenko, V. P. (1963). *Gobi-Altai Earthquake, 1963.* Akad. Nauk SSSR, Moscow, (in Russian).

Forman, S. L. (1989). Application and limitations of thermoluminescence to date Quaternary sediments. *Quat. Int.* **1,** 47–59.

Forman, S. L., Machette, M. N., Jackson, M. E., and Maat, P. (1989). An evaluation of thermoluminescence dating of paleoearthquakes on the American Fork segment, Wasatch fault zone, Utah. *J. Geophys. Res.* **94,** 1622–1630.

Forman, S. L., Nelson, A. R., and McCalpin, J. (1991). Thermoluminescence dating of fault scarp derived colluvium: Deciphering the timing of paleoearthquakes on the Wasatch fault zone, north-central Utah. *J. Geophys. Res.* **96,** 595–605.

Forman, S. L., Smith, R. P., Hackett, W. R., Tullis, J. A., and McDaniel, P. A. (1993). Timing of late Quaternary glaciations in the western United States based on the age of loess on the eastern Snake River Plain, Idaho. *Quat. Res.* **40,** 30–37.

Forman, S. L., Pierson, J., Smith, R. P., Hackett, W. R., Valentine, G. and Page, W. D. (1996). Assessing the accuracy of thermoluminescence to date baked sediments beneath late Quaternary lava flows. *J. Geophys. Res.* **99**(8), 15,569–15,576.

Forslund, T., and Gudmundsson, A. (1991). Crustal spreading due to dikes and faults in southwest Iceland. *J. Struct. Geol.* **13,** 443–457.

Forti, P., and Postpischl, D. (1984). Seismotectonic and paleoseismic analyses using karst sediments. *Mar. Geol.* **55,** 145–161.

Foulger, G., and Julian, B. R. (1993). Non-double-couple earthquakes at the Hengill-Grensdalur volcanic complex, Iceland: Are they artifacts of crustal heterogeneity? *Bull. Seismol. Soc. Am.* **83,** 38–52.

Foulger, G., and Long, L. E. (1984). Anomalous focal mechanisms: Tensile crack formation on an accreting plate boundary. *Nature* (*London*) **310,** 43–45.

Franks, J. W., and Johnson, R. H. (1964). Pollen analytical dating of a Derbyshire landslide. *New Phytol.* **63,** 209–216.

Frost, E. G., Baker, E. D., Lindvall, S. C., Smilo, S. A., and Rockwell, T. K. (1991). Computer-enhanced imaging of neotectonic features exposed within trench faces; techniques for seeing the unseen being developed on the Rose Canyon fault zone. In *Environmental Perils, San Diego Region* (P. L. Abbott, ed.), Annu. Meet. Geol. Soc. Am., pp. 47–60. San Diego Assoc. Geol. San Diego, CA.

Fuller, M. L. (1912). The New Madrid earthquake. *U.S. Geol. Surv. Bull.* **494,** 1–120 pp.

Fumal, T. E., Pezzopane, S. K., Weldon, R. J., II, and Schwartz, D. P. (1993). A 100-year average recurrence interval for the San Andreas fault at Wrightwood, California. *Science* **259,** 199–203.

Galli, P. and Ferreli, L. (1995). A methodological approach for historical liquefaction research. In Perspectives in Paleoseismology (L. Serva, and D. B. Slemmons, eds.), *Assoc. Eng. Geol. Spec. Publ.* **6,** 35–48.

Gamble, E. E. (1965). Origin and morphogenetic relations of sandy surficial horizons of upper Coastal Plain soils of North Carolina. Ph.D. Thesis, North Carolina State University, Raleigh.

Gans, P. B. (1987). An open-system, two-layer crustal stretching model for the eastern Great Basin. *Tectonics* **6,** 1–12.

Ganse, R. A., and Nelson, J. B. (1982). Catalog of significant earthquakes, 2000 B. C. to 1979, including quantitative casualties and damage. *Bull. Seismol. Soc. Am.,* **72,** 873–877.

Gardner, D. A., and Stahl, I. (1977). Geotechnical-seismic investigation of the proposed 330 Zone Water Storage Reservoir and water conditioning facilities site for the city of San Buenaventura, California. *Geotech. Consult. Inc., Rep.* **V77151,** 1–19.

Gardner, T. W. (1989). Neotectonism along the Atlantic passive continental margin: A review. *Geomorphology* **2,** 71–97.

Gedney, D. S., and Weber, W. G., Jr. (1978). Design and construction of soil slopes. In *Landslides—Analysis and control* (R. L. Schuster and R. J. Krizek, eds.), Spec. Rep. **176,** pp. 172-191. Transp. Res. Board., Natl. Acad. Sci., Washington D.C.

Geomatrix (1995). *Seismic Design Mapping State of Oregon,* Task 2, Ground Motion Attenuation, Final Rep. prepared for Oregon Dep. Trans., Proj. 2442, Contract 11688, pp. 2–26. Geomatrix Consultants, San Francisco.

Gerson, R., Grossman, S., Amit, R., and Greenbaum, N. (1993). Indicators of faulting events and periods of quiescence in desert alluvial fans. *Earth Surf. Processes Landforms* **18,** 181–202.

Geyh, A. A., and Schleicher, H. (1990). *Absolute Age Determination.* Springer-Verlag, Berlin.

Ghosh, S. K. (1988). *Analytical Photogrammetry,* 2nd ed. Pergamon, New York.

Gilbert, G. K. (1884). A theory of the earthquakes of the Great Basin, with a practical application: Letter to the Salt Lake Tribune, Sept. 20, 1883; repr. *J. Geol.* **27,** 49–53.

Gilbert, G. K. (1886). The inculcation of scientific method by example with an illustration drawn from the Quaternary geology of Utah. *Am. J. Sci.,* [3], **31,** 284–299.

Gilbert, G. K. (1890). Lake Bonneville. *U.S. Geol. Surv., Monogr.* **1,** 1–572.

Gilbert, G. K. (1928). Studies of Basin Range structure. *U.S. Geol. Surv. Prof. Pap.* **153,** 1–92.

Gillard, D., Wyss, M., and Nakata, J. S. (1992). A seismotectonic model for western Hawaii based on stress tensor inversion from fault plane solutions. *J. Geophys. Res.* **97,** 6629–6641.

Gilpin, L. M., (1995). Holocene paleoseismicity and coastal tectonics of the Kodiak Islands, Alaska. *PhD Dis.* University of California Santa Cruz, Santa Cruz, CA.

Gilpin, L. M., Carver, G. A., and Hemphill-Haley, E. (1994a). Paleoseismicity of the SW extent of the 1964 Alaskan rupture zone, eastern Aleutian arc, Kodiak Island, Alaska. In Proceedings of the Workshop on Paleoseismology (C. S. Prentice, D. P. Schwartz, and R. S. Yeats, eds.), *U.S. Geol. Surv. Open File Rept.* **94-568,** 70.

Gilpin, L. M., Carver, G. A., Ward, S., and Anderson, R. S. (1994b). Tidal benchmark readings and post-seismic rebound of the Kodiak Islands, SW extent of the 1964 Great Alaskan Earthquake rupture. *Seismol. Res. Lett.* **65,** 68.

Gilpin, L. M., Ward, S., Anderson, R., Moore, J. C., and Carver, G. A. (1994c). Holocene interseismic deformation and stratigraphic modeling of the earthquake cycle, Kodiak Islands. *U.S. Geol. Surv. Open File Rep.* **94-176,** 339–344.

Glass, C. E., and Slemmons, D. B. (1978). *Imagery in Earthquake Analysis,* Rep. No 11. U.S. Army Waterways Experiment Station, Vicksburg, MS.

Glazner, A. F., and Ussler, W. (1989). Crustal extension, crustal density, and the evolution of Cenozoic magmatism in the Basin and Range of the western United States. *J. Geophys. Res.* **94,** 7952–7960.

Goldfinger, C., Kulm, L. D., Yeats, R. S., Appelgate, B., MacKay, M. E., and Moore, G. F. (in press). Active strike-slip faulting and folding of the Cascadia plate boundary and forearc in central and northern Oregon. In *U.S. Geol. Surv. Prof. Pap.* **1560.**

Goodman, R. E. (1976). *Methods of Geological Engineering,* pp. 112-121. West Publishing, St. Paul, MN.

Goodman, R. E., and Seed, H. B. (1966). Earthquake-induced displacements in sand embankments. *J. Soil Mech. Found. Div., Am. Soc. Civ. Eng.* **92,** 125–146.

Gordon, F. R. (1971). Faulting during the earthquake at Meckering, western Australia--14 October 1968. *Bull.-R. Soc. N. Z.* **9,** 95–96.

Gordon, F. R., and Lewis, J. D. (1980). The Meckering and Calingiri earthquakes, October 1968 and March 1970. *Bull.-Geol. Surv. West Aust.* **126,** 1–229.

Gorel'chik, V. L. (1989). Seismological study of the Kliuchevskoi flank eruption of 1983 (Kamchatka). *J. Volcanol. Geotherm Res.* **38,** 269–280.

Goudie, A., ed. (1981). *Geomorphological Techniques.* Allen & Unwin, London.

Goy, J. L., Simon, J. L. and Zazo, C. (1988). Criterios geomorfologicos aplicados a la neotectonica. In *Perspectives en Geomorfologia* (M. Gutierrez and J. L. Pena, eds.), pp. 4–27. S. E. G. Zaragoza.

Goy, J. L., Silva, P. G., Zazo, C., Bardaji, T. and Somoza, L. (1991). Model of morphoneotectonic map and legend. *Bull. INQUA Neotecton. Comm.* **14,** 19–31.

Grant, L. B., and Sieh, K. E. (1993). Stratigraphic evidence for seven meters of dextral slip on the San Andreas fault during the 1857 earthquake in the Carizzo Plain. *Bull. Seismol. Soc. Am.* **83,** 619–635.

Grant, L. B., and Sieh, K. (1994). Paleoseismic evidence of clustered earthquakes on the San Andreas fault in the Carizzo Plain, California. *J. Geophys. Res.* **99,** 6819–6841.

Grant, W. C., and McLaren, D. D. (1987). Evidence for Holocene subduction earthquakes along the Oregon coast. *EOS, Trans. Am. Geophys. Union* **68,** 1479 (abstr.).

Grant, W. C., Atwater, B. F., Carver, G. A., Darienzo, M. E., Nelson, A. R., Peterson, C. D., and Vick, G. S. (1989). Radiocarbon dating of late Holocene coastal subsidence above the Cascadia subduction zone-compilation for Washington, Oregon, and Northern California. *EOS Suppl., Am. Geophys. Union 1989 Fall Meet.,* **73**(43), 1331 (abstr.).

Greeley, R., and King, J. S. (1977). Volcanism of the Eastern Snake River Plain, Idaho, *Contract Rep. CR-154621.* Prepared for the Office of Planetary Geology, NASA, Washington D.C.

Grindley, G. W., and Hull, A. G. (1986). Historical Taupo earthquakes and earth deformation. *Bull. R. Soc. N. Z.* **24,** 173–186.

Grossman, E. E., Fletcher, C. H., and Jones, A. T. (1994). Evidence for an emerged shoreline of mid- to late-Holocene age on Oahu, Kauai, and Molokai, Hawaii. *Geol. Soc. Am. Abstr. Prog.* **26**(7), A-306.

Gudmundsson, A. (1983). Form and dimensions of dykes in eastern Iceland. *Tectonophysics* **95,** 295–307.

Gudmundsson, A. (1984a). A study of dykes, fissures and faults in selected areas of Iceland. *Unpublished Ph.D. Thesis, University of London,* London.

Gudmundsson, A. (1984b). Tectonic aspects of dykes in northwestern Iceland. *Jokull* **34,** 81–86.

Gudmundsson, A. (1986). Formation of crustal magma chambers in Iceland. *Geology* **14,** 164–166.

Gudmundsson, A. (1987). Tectonics of the Thingvellir fissure swarm, SW Iceland. *J. Struct. Geol.* **9,** 61–69.

Gudmundsson, A., Oskarsson, N., Gronvold, K., Saemundsson, K., Sigurdsson, O., Stefansson, R., Gislason, S., Einarsson, P., Brandsdottir, B., Larsen, G., Johannesson, H., and Thordarson, T. (1992). The 1991 eruption of Hekla, Iceland. *Bull. Volcanol.* **54,** 238–246.

Guerra, I., Lo Bascio, A., Luongo, G., and Scarpa, R. (1976). Seismic activity accompanying the 1974 eruption of Mt. Etna. *J. Volcanol. Geotherm. Res.* **1,** 347–362.

Guffanti, M., and Weaver, C. S. (1988). Distribution of late Cenozic volcanic vents in the Cascadia Range; volcanic arc segmentation and regional tectonic considerations. *J. Geophys. Res.* **93,** 6513–6529.

Gutenberg, B. (1945). Magnitude determination for deep focus earthquakes. *Bull. Seismol. Soc. Am.* Vol. **35,** pp. 117–130.

Gutenberg, B., and Richter, C. F. (1954). *Seismicity of the Earth and Associated Phenomena,* 2nd ed. Princeton Univ. Press, Princeton, NJ.

Hackett, W. R., and Smith, R. P. (1992). Quaternary volcanism, tectonics, and sedimentation in the Idaho National Engineering Laboratory area. In *Field Guide to Geologic Excursions in Utah and Adjacent Areas of Nevada, Idaho, and Wyoming* (J. K. Wilson, ed.), *Utah Geol. Surv. Misc. Publ.* 92-3, 1–17.

Hadley, D. M., Hawkins, H. G., and Benuska, K. L. (1983). Strong ground motion record of the 16 September 1978 Tabas, Iran, earthquake. *Bull. Seismol. Soc. Am.* **73,** 315–320.

Hadley, J. B. (1964). Landslides and related phenomena accompanying the Hebgen Lake earthquake of August 17, 1959. *U.S. Geol. Surv. Prof. Pap.* **435,** 107–138.

Haghipour, A., Farooqui, S. M., Amidi, M. and Aghanabati, A. (1979). The destructive Tabas earthquake of September 16, 1978, east Iran- A preliminary report. *Proc. 17th Annu. Eng. Geol. Soils Engin. Symp.,* Univ. Idaho, Moscow, ID, pp. 1–12.

Hagiwara, T., ed. (1982). Paleoearthquakes, as Reconstructed from Historical and Active Fault Data (in Japanese). Univ. of Tokyo Press, Tokyo.

Hall, N. T. (1984). Holocene history of the San Andreas fault between Crystal Springs Reservoir and San Andreas Dam, San Mateo County, California. *Bull. Seismol. Soc. Am.,* **74,** 281–299.

Haller, K. M. (1988). Segmentation of the Lemhi and Beaverhead faults, east-central Idaho, and Red Rock fault, southwest Montana, during the late Quaternary. *Ph.D. Dissertation, University of Colorado,* Boulder.

Halls, H. C., Burns, K. G., Bullock, S. J., and Batterham, P. M. (1987). Mafic dyke swarms of Tanzania interpreted from aeromagnetic data. In *Mafic Dyke Swarms* (H. C. Halls and W. F. Fahrig, eds.), *Spec. Pap.-Geol. Assoc. of Can.* 34, 173–186.

Hamilton, R. M., and Johnston, A. C. (1990). Tecumseh's prophecy—Preparing for the next New Madrid earthquake. *U.S. Geol. Surv. Circ.* **1066,** 1—30.

Hammond, C. J., Sprenke, K. F., and Hammond, W. R. (1986). Ground-penetrating radar field tests in northern Idaho. *Proc. Symp. Eng. Geol. Soils Eng. 22nd,* Boise State Univ., Boise, ID, pp. 53–68.

Hanks, T. C., and Andrews, D. J. (1989). Effect of far-field slope on morphologic dating of scarplike landforms. *J. Geophys. Res.* **94,** 565–573.

Hanks, T. C., and Boore, D. M. (1984). Moment-magnitude relations in theory and practice. *J. Geophys. Res.,* **89,** 6229–6235.

Hanks, T. C., and Johnston, A. C. (1992). Common features of the excitation and propagation of strong ground motion for North American earthquakes. *Bull. Seismol. Soc. Am.,* **82,** 1–23.

Hanks, T. C., and Kanamori, H. (1979). A moment magnitude scale. *J. Geophys. Res.* **84,** 2348–2350.

Hanks, T. C., and Schwartz, D. P. (1987). Morphologic dating of the pre-1983 fault scarp on the Lost River fault at Doublespring Pass Road, Custer County, Idaho. *Bull. Seismol. Soc. Am.* **77,** 837–846.

Hansen, W. R. (1965). Effects of the earthquake of March 27, 1964, at Anchorage, Alaska. *U.S. Geol. Surv. Prof. Pap.* **542-A,** 1–68.

Harden, J. W. (1982). A quantitative index of soil development from field descriptions- Examples from a chronosequence in central California. *Geoderma* **28,** 1–28.

Harp, E. L., and Wilson, R. C. (1995). Shaking intensity thresholds for rock falls and slides; Evidence from 1987 Whittier Narrows and Superstition Hills earthquake strong-motion records. *Bull. Seismol. Soc. Am.* **85,** 1739–1757.

Harry, D. G., and Gozdzik, J. S. (1988). Ice wedges: growth, thaw transformation, and paleoenvironmental significance. *J. Quat. Sci.* **3,** 39–55.

Harry, D. L., Sawyer, D. S., and Leeman, W. P. (1993). The mechanics of continental extension in western North America: Implications for the magmatic and structural evolution of the Great Basin. *Earth Planet. Sci. Lett.* **117,** 59–71.

Hatheway, A. W. (1982). Trench, shaft, and tunnel mapping. *Bull. Assoc. Eng. Geol.* **19,** 173–180.

Hatheway, A. W., and Leighton, F. B. (1979). Exploratory trenching. *Geol. Soc. Am., Rev. Eng. Geol.* **4,** 169–195.

Hatheway, A. W., and McClure, C. R., Jr., eds. (1979). Geology in the siting of nuclear power plants. *Geol. Soc. Am. Rev. Eng. Geol.* **4,** 1–256.

Heaton, T. H. and Kanamori, H. (1984). Seismic potential associated with subduction in the northwest United States. *Bull. Seismol. Soc. Am.* **74,** 933–941.

Heaton, T. H., Tajima, F., and Mori, A. W. (1986). Estimating ground motions using recorded accelerograms. *Surv. Geophys.* **8,** 25–83.

Hecker, S., and Schwartz, D. P. (1994). The characteristic earthquake revisited: Geological evidence of the size and location of successive earthquakes on large faults. *U.S. Geol. Surv. Open File Rep.* **94-568,** 79–80.

Heezen, B. C., and Ewing, M. (1952). Turbidity currents and submarine slumps, and the 1929 Grand Banks earthquake. *Am. J. Sci.* **250,** 849–873.

Heiken, G., Wohletz, K., and Eichelberger, J. (1988). Fracture filling and intrusive pyroclasts, Inyo Domes, California. *J. Geophys. Res.* **93,** 4335–4350.

Hemphill-Haley, E. (1992). Diatom micropaleontology of Holocene intertidal sediments in coastal southwest Washington. Ph.D. Thesis, University of California, Santa Cruz.

Hemphill-Haley, E. (1995). Diatom evidence for earthquake-induced subsidence and tsunami, Washington. *Geol. Soc. Am. Bull.* **107,** 367–378.

Hempton, M. R., and Dewey, J. F. (1983). Earthquake-induced deformational structures in young lacustrine sediments, East Anatolian Fault, southeast Turkey. *Tectonophysics* **98,** 7–14.

Henderson, J. (1937). The West Nelson earthquakes of 1929. *N. Z. J. Sci. Technol., Sect. B* **B19,** 65–144.

Hermance, J. F., Slocum, W. M., and Neumann, G. A. (1984). The Long Valley/Mono Basin volcanic complex: A preliminary magnetotelluric and magnetic variation interpretation. *J. Geophys. Res.* **89,** 8325–8337.

Hildenbrand, T. G., Rosenbaum, J. G., and Kauahikaua, J. P. (1993). Aeromagnetic study of the island of Hawaii. *J. Geophys. Res.* **98,** 4099–4119.

Hokkaido Tsunami Survey Team (1993). Tsunami devastates Japanese coastal region. *EOS, Trans. Am. Geophys. Union* **74,** 417, 432.

Holcomb, R. T. (1987). Eruptive history and long-term behavior of Kilauea Volcano. In Volcanism in Hawaii (R. W. Decker, T. L. Wright, and P. H. Stauffer eds.), *U.S. Geol. Surv. Prof. Pap.* **1350,** 261–350.

Holzer, T. L., Davis, S. N., and Lofgren, B. E. (1979). Faulting caused by groundwater extraction in south-central Arizona. *J. Geophys. Res.* **84,** 603–612.

Hooke, R. L. (1967). Processes on arid region alluvial fans. *J. Geol.* **75,** 438–460.

Horsefield, W. T. (1977). An experimental approach to basement-controlled faulting. *Geol. Mijnbouw* **56,** 363–370.

Housner, G. W. (1958). The mechanism of sand blows. *Bull. Seismol. Soc. Am.* **58,** 155–161.

Hull, A. G. (1987). Paleoseismic slip at reverse faults. In Directions in Paleoseismology (A. J. Crone, and E. M. Omdahl, eds.), *U.S. Geol. Surv. Open File Rept.* **87-673,** 262–270.

Hummon, C., Schneider, C. L., Yeats, R. S., Dolan, J. F., Sieh, K. E., and Huftile, G. J. (1994). Wilshire fault; earthquakes in Hollywood? *Geology* **22,** 291–294.

Humphreys, E. D., and Weldon, R. J., II (1994). Deformation across the western United States; a local estimate of Pacific-North American transform deformation. *J. Geophys. Res.* **99,** 19,975–20,010.

Hunt, C. B. (1975). *Death Valley: Geology, Ecology, and Archeology.* Univ. of California Press, Berkeley.

Hunt, R. E. (1984). *Geotechnical Engineering Investigation Manual.* McGraw-Hill, New York.

Hunter, R. L., and Mann, C. J., eds. (1992). *Techniques for Determining Probabilities of Geologic Events and Processes.* Int. Assoc. Math. Geol., Stud. Math. Geol., No. 4. Oxford Univ. Press, Oxford, UK.

Hupp, C. R., Osterkamp, W. R., and Thornton, J. L. (1987). Dendrogeomorphic evidence and dating of recent debris flows on Mount Shasta, northern California. *U.S. Geol. Surv. Prof. Pap.* **1396-B,** 1–39.

Huzita, K., and Ota, Y. (1977). Quaternary tectonics. In *The Quaterary Period-Recent Studies in Japan,* Jpn. Assoc. Quat. Res., pp. 127–151. Univ. of Tokyo Press, Tokyo.

Hyndman, R. D., and Wang, K. (1993). Thermal constraints on the zone of major thrust earthquake failure: The Cascadia Subduction Zone. *J. Geophys. Res.* **98,** 2039–2060.

Idriss, I. M. (1990). Response of soft soil sites during earthquakes. *H. Bolton Seed Mem. Symp. Proc.* **2,** 273–289.

Ingraham, B. J., Klimberg, D. M., and Metcalf, L. A. (1980). The Fox Range fault scarp; age determinations by soil cohesion and Wallace methods. *Proc. 18th Annu. Eng. Geol. Soils Eng. Symp.,* Boise State Univ., Boise, ID, pp. 99–113.

International Study Group (1982). An inter-laboratory comparison of radiocarbon measurements in tree rings. *Nature* (*London*) **298,** 619–623.

Ishihara, K. (1985). Stability of natural soil deposits during earthquakes *Proc. Int. Conf. Soil Mech. Found. Eng. 11th,* San Francisco, Vol. 1, pp. 321–376.

Ito, K. (1993). Cutoff depth of seismicity and large earthquakes near active volcanoes in Japan. *Tectonophysics* **217,** 11–21.

Iwasaki, T. (1986). Soil liquefaction studies in Japan: State of the art. *Soil Dyn. Earthquake Eng., Comput. Mech. Publ.* **5,** 2–68.

Jachens, R. C., and Holzer, T. L. (1982). Differential compaction mechanism for earth fissures near Casa Grande, Arizona. *Geol. Soc. Am. Bull.* **93,** 998–1012.

Jackson, D. B., and Kauahikaua, J. (1987). Regional self-potential anomalies at Kilauea Volcano. In Volcanism in Hawaii (R. W. Decker, T. L. Wright, and P. H. Stauffer, eds.), *U.S. Geol. Surv. Prof. Pap.* **1350,** 947–960.

Jackson, D. B., Swanson, D. A., Koyanagi, R. Y., and Wright, T. L. (1975). The August and October 1968 East Rift eruptions of Kilauea volcano, Hawaii. *U.S. Geol. Surv. Prof. Pap.* **890,** 1–33.

Jackson, J. A., Gagnepain, J., Houseman, G., King, G. C. P., Papadimitriou, P., Soufleris, C., and Virieux, J. (1982). Seismicity, normal faulting, and the geomorphological development of the Gulf of Corinth (Greece); the Corinth earthquakes of February and March, 1981. *Earth Planet. Sci. Lett.* **57,** 377–397.

Jackson, M. (1991). The number and timing of Holocene paleoseismic events on the Nephi and Levan segments, Wasatch fault zone, Utah. *Spec. Stud.-Utah Geol. Miner. Surv.* **78,** 1–23.

Jackson, M. D., Endo, E. T., Delaney, P. T., Anadottir, T., and Rubin, A. M. (1992). Ground ruptures of the 1974 and 1983 Kaoiki earthquakes, Mauna Loa volcano, Hawaii. *J. Geophys. Res.* **97,** 8775–8796.

Jackson, S. M., Wong, I. G., Carpenter, G. S., Anderson, D. M., and Martin, S. M. (1993). Contemporary seismicity in the eastern Snake River Plain, Idaho based on microearthquake monitoring. *Bull. Seismol. Soc. Am.* **83,** 680–695.

Jacoby, G. C. (1987). Potential and limits for dating prehistoric earthquakes using tree-ring analysis. In Directions in Paleoseismology (A. J. Crone and E. M. Omdahl, eds.), *U.S. Geol. Surv. Open File Rep.* **87-673,** 18–22.

Jacoby, G. C. (1989). Application of tree-ring analysis to paleoseismology. *Geol.* **17,** 226.

Jacoby, G. C., and Ulan, L. D. (1983). Tree-ring evidence for uplift at Icy Cape, Alaska, related to 1899 earthquakes. *J. Geophys. Res.* **88,** 9305–9313.

Jacoby, G. C., Sheppard, P. R., and Sieh, K. E. (1988). Irregular recurrence of large earthquakes along the San Andreas fault; evidence from trees. *Science* **241,** 196–199.

Jacoby, G. C., Williams, P. L., and Buckley, B. M. (1992). Tree ring correlation between prehistoric landslides and abrupt tectonic events in Seattle, Washington. *Science* **258,** 1621–1623.

Jacoby, G. C., Carver, G. and Wagner, W. (1995). Trees and herbs killed by an earthquake ~300 yr ago at Humboldt Bay, California. *Geology* **23,** 77–80.

Jahn, A. (1964). Slopes morphological features resulting from gravitation. *Z. Geomorphol., Suppl.* **5,** 59–72.

Jannik, N. O., Phillips, F. M., Smith, G. I., and Elmore, D. (1991). A ^{36}Cl chronology of lacustrine sedimentation in the Pleistocene Owens River system. *Geol. Soc. Am. Bull.* **103,** 1146–1159.

Jarrard, R. D. (1986). Relations among subduction parameters: *Rev. Geophys.* **24,** 217–284.

Jennings, A. E., and Nelson, A. R. (1992). Foraminiferal assemblage zones in Oregon tidal marshes - relation to marsh floral zones and sea level. *J. Foraminiferal Res.* **22,** 13–29.

Jensen, J. M. (1983). The Upper Gros Ventre landslide of Wyoming: A dendrochronology of landslide events and the possible mechanics of failure. *Geol. Soc. Am., Abstr. Prog.* **15**(5), 387.

Jibson, R. W. (1985). Landslides caused by the 1811-12 New Madrid earthquakes. *Unpublished PhD. Dissertation,* Stanford University, Stanford, CA.

Jibson, R. W. (1993). Predicting earthquake-induced landslide displacements using Newmark's sliding block analysis. *Transp. Res. Rec.* **1411,** 9–17.

Jibson, R. W., and Keefer, D. K. (1988). Landslides triggered by earthquakes in the central Mississippi Valley, Tennessee and Kentucky. *U.S. Geol. Surv. Prof. Pap.* **1336-C,** 1–24.

Jibson, R. W., and Keefer, D. K. (1989). Statistical analysis of factors affecting landslide distribution in the New Madrid seismic zone, Tennessee and Kentucky. *Eng. Geol.* **27,** 509–542.

Jibson, R. W., and Keefer, D. K. (1992). Analysis of the seismic origin of a landslide in the New Madrid seismic zone. *Seismol. Res. Lett.* **63**(4).

Jibson, R. W., and Keefer, D. K. (1993). Analysis of the seismic origin of landslides—Examples from the New Madrid seismic zone. *Geol. Soc. Am. Bull.* **105,** 521–536.

Jibson, R. W., Prentice, C. S., Borissoff, B. A., Rogozhin, E. A., and Langer, C. J. (1994). Some observations of landslides triggered by the 29 April 1991 Racha earthquake, Republic of Georgia. *Bull. Seismol. Soc. Am.* **84,** 963–973.

Johnson, D. (1944). Problems of terrace correlation. *Geol. Soc. Am. Bull.* **55,** 793–818.

Johnson, R. H. (1987). Dating of ancient, deep-seated landslides in temperate regions, In *Slope Stability* (M. G. Anderson and K. S. Richards, eds.), pp. 561–600. Wiley, New York.

Johnson, W. H. (1990). Ice-wedge casts and relict patterned ground in central Illinois and their environmental significance. *Quat. Res.* **33,** 51–72.

Johnston, A. C. (1994). The stable-continental-region earthquake data base. In *The Earthquakes of Stable Continental Regions* (A. C. Johnston, K. J. Coppersmith, L. R. Kanter, eds.), Electric Power Research Institute, Rept. TR-102261-V1, Ch. 3, pp. 3-1 to 3-80. Palo Alto, CA.

Jones, G. D. B., and Thompson, F. H. (1965). Excavations at Mam Tor and Brough-en-Noe. *Derbyshire Archaeol. J.* **85,** 89–93.

Jones, L. C. A. (1995). Quaternary geology and neotectonics of the east side of the Greys River Valley, western Wyoming. M.S. Thesis, Utah State University, Logan.

Jones, L. C. A., and McCalpin, J. P. (1992). Quaternary faulting on the Grey's River fault, a listric normal fault in the Overthrust Belt of Wyoming. *Geol. Soc. Am., Abtsr. Prog.* **24**(6), 20.

Jones, M. E., and Preston, R. M. F., eds. (1987). Deformation of Sediments and Sedimentary Rocks, *Geol. Soc. Am. Spec. Publ.* No. **29,** Blackwell, Oxford.

Joyner, W. B., and Boore, D. M. (1988). Measurement, characterization, and prediction of strong ground motion. In Earthquake Engineering and Soil Dynamics, II. Recent Advances in Ground-Motion Evaluation (J. L. Von Thun, ed.), *Am. Soc. Civ. Eng., Geotech. Spec. Publ.* **20,** 43–103.

Julian, B. R., and S. A. Sipkin (1985). Earthquake processes in the Long Valley caldera area, California. *J. Geophys. Res.* **90,** 11,155–11,169.

Kahle, J. E. (1975). Surface effects and related geology of the Lakeview fault segment of the San Fernando fault zone. In San Fernando, California, Earthquake of 9 February 1971 (G. B. Oakeshott, ed.), *Bull.-Calif., Div. Mines Geol.* **196,** 119–135.

Kaizuka, S. (1976). History of geomorphological research. In *Geography in Japan* (S. Kiuchi, ed.), pp. 35–63. Univ. of Tokyo Press, Tokyo.

Kaizuka, S. (1993). Geomorphology in Japan. In *The Evolution of Geomorphology* (H. J. Walker, and W. E. Grabau, W. E., eds.), pp. 255–271. Wiley, New York.

Kaizuka, S., Matsuda, T., Nogami, M., and Yonekura, N. (1973). Quaternary tectonic and recent seismic crustal movements in the Aranco Peninsula and its environs, central Chile. *Geogr. Rep. Tokyo Metro. Univ.* **8,** 38.

Kanamori, H. (1977). The energy release in great earthquakes. *J. Geophys. Res.* **82,** 2981–2987.

Kanamori, H. (1983). Mechanism of the 1983 Coalinga earthquake determined from long-period surface waves. In The 1983 Coalinga, California Earthquakes (J. H. Bennett, and R. W. Sherburne, eds.), *Spec. Publ.-Calif. Div. Min. Geol.* **66,** 233–240.

Karcz, I., and Kafri, U. (1978). Evaluation of supposed archeoseismic damage in Israel. *J. Archaeol. Sci.* **5,** 237–253.

Karcz, I., and Kafri, U. (1981). Studies in archaeoseismicity of Israel- Hisham's Palace, Jericho. *Isr. J. Earth Sci.* **30,** 12–23.

Karpin, T. L., and Thurber, C. H. (1987). The relationship between earthquakes swarms and magma transport. Kilauea Volcano, Hawaii. *Pure Appl. Geophys.* **125,** 971–991.

Kastens, K. A. (1984). Earthquakes as a triggering mechanism for debris flows and turbidites on the Calabrian ridge. *Marine Geol.* **55,** 13–33.

Kastens, K. A., Ryan, W. B. F., and Fox, P. J. (1986). Structural and volcanic expression of a fast slipping ridge-transform-ridge-plate boundary; Sea MARC I and photographic surveys at the Clipperton Ridge transform fault. *J. Geophys. Res.* **91,** 3469–3488.

Katayama, S., Fujii, T., and Takahashi, Y. (1966). Damage caused by the Niigata earthquake and the geological features of National Highway in the suburbs of Niigata City. *Soils and Found., Jpn. Soc. Soil Mech. Found. Eng.* **6,** 54–70.

Kawakami, F., and Asada, A. (1966). Damage to the ground and earth structures by the Niigata earthquake of June 16, 1964. *Soils and Found., Jpn. Soc. Soil Mech. Found. Eng.* **6,** 14–30.

Keefer, D. K. (1984). Landslides caused by earthquakes. *Geol. Soc. Am. Bull.* **95,** 406–421.

Keefer, D. K., and Wilson, R. C. (1989). Predicting earthquake-induced landslides, with emphasis on arid and semi-arid environments. In *Landslides in a Semi-Arid Environment* (P. M. Sadler, and D. M. Morton, eds.), Vol. 2, pp. 118–149. Inland Geol. Soc., Riverside, CA.

Keefer, D. K., Wilson, R. C., Harp. E. L., and Lips, E. W. (1985). The Borah Peak, Idaho, earthquake of October 28, 1983- landslides. *Earthquake Spectra* **2,** 91–125.

Keller, E. A. (1986). Investigation of active tectonics; use of surficial earth processes. In *Active Tectonics*: Studies in Geophysics (R. E. Wallace, chairman), pp. 136–147. Natl. Acad. Press, Washington, DC.

Keller, G. V., and Rapolla, A. (1974). Electrical prospecting methods in volcanic and geothermal environments. In *Physical Volcanology* (L. Civetta, P. Gasparini, G. Luongo, and A. Rapolla, eds.), pp. 133–166. Elsevier, New York.

Kelsey, H. M. (1990). Late Quaternary deformation of marine terraces on the Cascadia subduction zone near Cape Blanco, Oregon. *Tectonics* **9,** 983–1014.

Kelsey, H. M., and Carver, G. A. (1988). Late Neogene and Quaternary tectonics associated with the northward growth of the San Andreas transform fault, northern California. *J. Geophys. Res.* **93,** 4797–4819.

Kelsey, H. M., Witter, R. C., Nelson, A. R., and Hemphill-Haley, E. (1994). Repeated abrupt late Holocene environmental changes in south coastal Oregon; stratigraphic evidence at Sixes River marsh and Bradley Lake. *Geol. Soc. Am. Abtsr. Prog.* **26**(7), A-524.

Khil'ko, S. D., Kurushin, R. A., Kochetov, V. M., Balzhinnyam, I., and Monkoo, D. (1985). Strong earthquakes, paleoseismological and macroseismic data. In Earthquakes and the bases for seismic zoning of Mongolia. Trans. **41,** 19–83. *The Joint Soviet-Mongolian Sci. Geol. Res. Exp.* Moscow.

Khromovskikh, V. S. (1989). Determination of magnitudes of ancient earthquakes from dimensions of observed seismodislocations. *Tectonophysics* **166,** 1–12.

Kihl, R. (1975). Appendix: Physical preparation of organic matter samples for C14 dating. Radiocarbon date list II from Cumberland Peninsula, Baffin Island, N.W.T., Canada. *Arct. Alp. Res.* **7,** 90–91.

King, G. C. P., and Stein, R. S. (1983). Surface folding, river terrace deformation rate and earthquake repeat time in a reverse faulting environment. In The 1983 Coalinga, California Earthquakes (J. H. Bennett and R. W. Sherburne, eds.), *Spec. Publ.-Calif., Div. Mines Geol.* **66,** 165–176.

King, G. C. P., and Vita-Finzi, C. (1981). Active folding in the Algerian earthquake of 10 October 1980. *Nature* (London). **292,** 22–26.

King, G. C. P., and Yielding, G. (1983). The evolution of a thrust fault system; processes of rupture initiation, propagation, and termination in the 1980 El Asnam (Algeria) earthquake. *Geophys. J. R. Astron. Soc.* **77,** 913–933.

Klein, F. W., Koyanagi, R. Y., Nakata, J. S., and Tanigawa, W. R. (1987). The seismicity of Kilauea's magma system. In Volcanism in Hawaii (R. W. Decker, T. L. Wright, and P. H. Stauffer, eds.), *U.S. Geol. Surv. Prof. Pap.* **1350,** 1019–1185.

Klein, J., Lerman, J. C., Damon, P. E., and Ralph, E. K. (1982). Calibration of radiocarbon dates; tables based on the consensus data of the Workshop on Calibrating the Radiocarbon Time Scales. *Radiocarbon* **24,** 103–150.

Klimaszewski, M., ed. (1963). *Problems of Geomorphological Mapping,* Vol. 46. Prace Geografika, Warsaw.

Klimaszewski, M., ed. (1968). Problems of the detailed geomorphological map. *Folia Geogr.-Phys.* **2,** 7–32.

Knuepfer, P. L. K. (1988). Estimating ages of late Quaternary stream terraces from analysis of weathering rinds and soils. *Geol. Soc. Am. Bull.* **100,** 1224–1236.

Knuepfer, P. L. K. (1989). Implications of the characteristics of end-points of historical surface fault ruptures for the nature of fault segmentation. In *Fault Segmentation and Controls of Rupture Initiation and Termination* (D. P. Schwartz, D. P. and R. H. Sibson, eds.), *U.S. Geol. Surv. Open File Rep.* **89-315,** 193–228.

Knuepfer, P. L. K. (1992). Temporal variations in latest Quaternary slip across the Australian-Pacific plate boundary, northeastern South Island, New Zealand. *Tectonics* **11,** 449–464.

Kolb, C. R. (1976). Geologic control of sand boils along Mississippi River levees. In *Geomorphology and Engineering* (D. R. Coats, ed.), Halsted Press, pp. 99–114. New York.

Kong, L. S. L., Solomon, S. C., and Purdy, G. M. (1992). Microearthquake characteristics of a mid-ocean ridge along-axis high. *J. Geophys. Res.* **97,** 1659–1685.

Koto, B. (1893). On the causes of the great earthquakes in central Japan, 1891. *J. Imp. Univ. Tokyo* **4-5,** 295–353.

Krinitsky, E. L. (1974). State-of-the-art for assessing earthquake hazards in the United States; Fault assessment in earthquake engineering: U.S. Army Corps of Engineers, Waterways Experiment Station, Misc. Paper S 73-1, Rep. 2, Vicksburg, MS, 82 p.

Krinitsky, E. L., and Slemmons, D. B., eds. (1990). Neotectonics in Earthquake Evaluation, *Rev. Eng. Geol.* **8,** Geol. Soc. Am., Boulder, CO.

Kuno, H. (1936). On the displacement of the Tanna fault since the Pleistocene. *Bull. Earthquake Res. Inst., Tokyo Imp. Univ.* **14,** 621–631.

Kuno, H. (1954). Geology and petrology of Omuro-yama volcano group, North Izu. *J. Fac. Sci., Univ. Tokyo, Sect. 2.* **9,** 241–265.

Kuntz, M. A., Spiker, E. C., Rubin, M., Champion, D. E., and Lefebvre, R. H. (1986). Radiocarbon studies of latest Pleistocene and Holocene lava flows of the Snake River Plain, Idaho: Data, lessons, interpretations. *Quat. Res.* **25,** 163–176.

Kuntz, M. A., Champion, D. E., Lefebvre, R. H., and Covington, H. R. (1988). Geologic map of the Craters of the Moon, Kings Bowl, Wapi lava fields and the Great Rift volcanic rift zone, south-central Idaho. *U.S. Geol. Surv. Misc. Invest. Ser. Map* **I-1632,** scale 1:100,000.

Kuntz, M. A., Skipp, B., Lanphere, M. A., Scott, W. E., Pierce, K. L., Dalrymple, G. B., Morgan, L. A., Champion, D. E., Embree, G. F., Smith, R. P., Hackett, W. R., and Rodgers, D. W. (1990). Revised geologic map of the INEL and adjoining areas, eastern Idaho. *U.S. Geol. Surv. Open File Rep.* **90-333,** Scale 1:100,000.

Kuntz, M. A., Covington, H. R., and Schorr, L. J. (1992). An overview of basaltic volcanism of the eastern Snake River Plain, Idaho. In *Regional Geology of Eastern Idaho and Western Wyoming* (P. K. Link, M. A. Kuntz, and L. B. Platt, eds.), *Mem.-Geol. Soc. Am.* **179,** 227–267.

Kuo, S. S., and Stangland, H. G. (1989). Use of ground-penetrating radar techniques to aid in the design of on-site disposal systems. In *Engineering Geology and Geotechnical Engineering* (R. J. Watters, ed.), *Proc. Symp. Eng. Geol. Geotech. Eng., 25th,* A. A. Balkema, Rotterdam, pp. 11–18.

Kuribayashi, E., and Tatsuoka, F. (1975). Brief review of liquefaction during earthquakes in Japan. *Soils and Found., Jpn. Soc. Soil Mech. Found. Eng.* **15,** 81–91.

Kurz, M. D., Colodner, D., Trull, T. W., Moore, R. B., and O'Brien, K. (1990). Cosmic ray exposure dating with in situ produced cosmogenic ^{3}He: Results from young Hawaiian lava flows. *Earth Planet. Sci. Lett.* **97,** 177–189.

Lade, P. V. (1992). Static instability and liquefaction of loose fine sandy slopes. *J. Geotech. Eng., Am. Soc. Civ. Eng.* **118,** 51–71.

Lade, P. V., Cole, D. A. Jr., and Cummings, D. (1984). Multiple failure surfaces over dip-slip faults. *J. Geotech. Eng.* **100**(GT5), 616–636.

Lagerbäck, R. (1990). Late Quaternary faulting and paleoseismicity in northern Fennoscandia, with particular reference to the Lansjärv area, northern Sweden. *Geol. Foereni. Stockholm Foerh.* **112,** 333–354.

Lagerbäck, R. (1992). Dating of late Quaternary faulting in northern Sweden. *J. Geol. Soc. London* **149,** 285–291.

Lajoie, K. R. (1986). Coastal tectonics. In *Active Tectonics:* Studies in Geophysics (R. E. Wallace, chairman), pp. 95–124. Natl. Acad. Press, Washington, DC.

LaMarche, V. C., and Wallace, R. E. (1972). Evaluation of effects on trees of past movements on the San Andreas fault, northern California. *Geol. Soc. Am. Bull.* **83,** 2665–2676.

Lambe, T. W., and Whitman, R. V. (1969). *Soil Mechanics.* Wiley, New York.

Langbein, J., Hill, D. P., Parker, T. N., and Wilkinson, S. K. (1993). An episode of reinflation of the Long Valley Caldera, eastern California: 1989-1990. *J. Geophys. Res.* **98,** 15851–15870.

Latter, J. H., ed. (1989). Volcanic Hazards: Assessment and Monitoring, *IAVCEI Proc. Volcanol.,* **Vol. 1.** Springer-Verlag, Berlin.

Law, K. T., Cao, Y. L., and He, G. N. (1990). An energy approach for assessing seismic liquefaction potential. *Can. Geotech. J.* **27,** 320–329.

Lawson, A. C. et al. (1908). *The California Earthquake of April 18, 1906,* Report of the State Earthquake Investigation Commission, 2 vols., Publ. No. 87. Carnegie Inst. Washington, DC. (reprinted 1971).

Le Dain, A.-Y., Robineau, B., and Tapponnier, P. (1979). Les effets tectoniques de l'événement sismique et volcanique de novembre 1978 dans le rift d'Asal Ghoubbet. *Bull. Soc. Geol. Fr.* **22,** 817–822.

Lee, H. J., and Edwards, B. D. (1986). Regional method to assess offshore slope stability. *J. Geotech. Eng.* **112,** 489–509.

Legg, M. R., Luyendyk, B. P., Mammerickx, J., de Moustier, C., and Tyce, R. C. (1989). Sea Beam survey of an active strike-slip fault; the San Clemente fault in the California continental borderland. *J. Geophys. Res.* **94,** 1727–1744.

Lensen, G. J. (1958). Rationalized fault interpretation. *N. Z. J. Geol. Geophys.* **1,** 307–317.

Lensen, G. J. (1964a). The general case of progressive fault displacement of flights of degradational terraces. *N. Z. J. Geol. Geophys.* **7,** 864–870.

Lensen, G. J. (1964b). The faulted terrace sequence of the Grey River, Awatere Valley, South Island, New Zealand. *N. Z. J. Geol. Geophys.* **7,** 871–876.

Lensen, G. J. (1968). Analysis of progressive fault displacement during downcutting at the Branch River terraces, South Island, New Zealand. *Geol. Soc. Am. Bull.* **79,** 545–556.

Lensen, G. J. (1973). Guidebook for Excursion A10. INQUA Conference, Christchurch, New Zealand.

Lensen, G. J. (1976). Earth deformation in relation to town planning in New Zealand. *Bull. Int. Assoc. Eng. Geol.* **14,** 241–247.

Lensen, G. J., and Otway, P. M. (1971). Earthshift and post-earthshift deformation associated with the May 1968 Inangahua earthquake, New Zealand. In Recent Crustal Movements. (B. W. Collins, and R. Fraser, eds.), *Bull.-R. Soc. N. Z.* **9,** 107–116.

Lensen, G. J., and Vella, P. (1971). The Waiohine River faulted terrace sequence. In Recent Crustal Movements (B. W. Collins and R. Fraser, eds.), *Bull.-R. Soc. N. Z.* **9,** 117–119.

Leonard, E. M., and Wehmiller, J. F. (1992). Low uplift rates and terrace reoccupation inferred from mollusc aminostratigraphy, Coquimbo Bay area, Chile. *Quat. Res.* **38,** 246–259.

Lepine, J-C., and Hirn, A. (1992). Seismotectonics in the Republic of Djibouti, linking the Afar Depression and the Gulf of Aden. *Tectonophysics* **209,** 65–86.

Lettis, W. R., and Hanson, K. L. (1991). Crustal strain partitioning-implications for seismic-hazard assessment in western California. *Geology,* **19,** 559–562.

Lewis, J. D., Daetwyler, N. A., Bunting, J. A., and Moncrieff, J. S. (1981). The Cadoux earthquake, 2 June 1979. *Rep.-Geol. Surv. West. Austr.* **11,** 1–131.

Li, J., and Zheng, L., eds. (1992). An Excursion Guide to Tanlu Active Fault in China, *2nd Organ. Meet. IGCP, No. 26,* pp. 26–30. Seismol. Bur. Shandong Prov. and Seismol. Office of Linyi, Shandong, China.

Li, W.-H. (1992). Evidence for late Holocene coseismic subsidence in the lower Eel River valley, Humboldt County, northern California. M.S. Thesis, Humboldt State University Arcata, CA.

Liao, S. S. C., Veneziano, D., and Whitman, R. V. (1988). Regression models for evaluating liquefaction probability. *J. Geotech. Eng., Am. Soc. Civ. Eng.* **114,** 389–411.

Lienkaemper, J. J., and Sturm, T. A. (1989). Reconstruction of a channel offset in 1857 (?) by the San Andreas fault near Cholame, California. *Bull. Seismol. Soc. Am.* **79,** 901–909.

Lindvall, S. C., and Rockwell, T. K. (1995). Holocene activity of the Rose Canyon fault in San Diego, California. *J. Geophys. Res.* **100,** 24,121–24,132.

Lindvall, S. C., Rockwell, T. K., and Hudnut, K. W. (1989). Evidence for prehistoric earthquakes on the Superstition Hills fault from offset geomorphic features. *Bull. Seismol. Soc. Am.* **79,** 342–361.

Linick, T. W., Damon, P. E., Donahue, D. J., and Jull, A. J. T. (1989). Accelerator mass spectrometry; the new revolution in radiocarbon dating. *Quat. Int.* **1,** 1–6.

Lipman, P. W., and Glazner, A. F. (1991). Introduction to Middle Tertiary Cordilleran Volcanism: Magma sources and relations to regional tectonics. *J. Geophys. Res.* **96,** 13193–13200.

Lipman, P. W., and Mullineaux D. R., eds. (1982). The 1980 Eruptions of Mount St. Helens, Washington. *U.S. Geol. Surv. Prof. Pap.* **1250,** 1–844.

Lipman, P. W., Lockwood, L. P., Okamura, R. T., Swanson, D. A., and Yamashita, K. M. (1985). Ground deformation associated with the 1975 magnitude-7.2 earthquake and resulting changes in activity of Kilauea volcano, Hawaii. *U.S. Geol. Surv. Prof. Pap.* **1276,** 1–45.

Lister, L. A. and Secrest, C. D. (1985). Giant dessication cracks and differential subsidence, Red Lake playa, Mojave County, California. *Bull. Assoc. Eng. Geol.* **22,** 299–314.

Liu, H., and Qiao, T. (1984). Liquefaction potential of saturated sand deposits underlying foundation of structure. *Proc. World Conf. Earthquake Eng. 8th,* San Francisco, **Vol. 3,** pp. 199–206.

Logan, R. L., and Schuster, R. L. (1991). Lakes divided: The origin of Lake Crescent and Lake Sutherland, Clallam County, Washington. *Wash., Div. Geol. Earth Resour., Washington Geol.* **19,** 38–42.

Long, D., Smith, D. E., and Dawson, A. G. (1989). A Holocene tsunami deposit in eastern Scotland. *J. Quat. Sci.* **4,** 61–66.

Lowe, D. R. (1975). Water escape structures in coarse-grained sediments. *Sedimentology* **22,** 157–204.

Lowe, D. R., and LoPiccolo, R. D. (1974). The characteristics and origins of dish and pillar structures. *J. Sediment. Petrol.* **44,** 484–501.

Lubetkin, L. K. C., and Clark, M. M. (1988). Late Quaternary activity along the Lone Pine fault, eastern California. *Geol. Soc. Am. Bull.* **100,** 755–766.

Lucchi, F. R. (1995). Sedimentological indicators of paleoseismicity. In Perspectives in Paleoseismology (L. Serva, and D. B. Slemmons, eds.), *Assoc. Eng. Geol. Spec. Publ.* **6,** 7–18.

Lund, W. R., and Euge, K. M. (1984). Detailed inspection and geologic mapping of construction excavations at Palo Verde Nuclear Generating Station, Arizona. *Bull. Assoc. Eng. Geol.* **21,** 179–189.

Lund, W. R., Schwartz, D. P., Mulvey, W. E., Budding, K. E., and Black, B. D. (1991). Fault behavior and earthquake recurrence on the Provo segment of the Wasatch fault zone at Mapleton, Utah County, Utah. *Spec. Stud.- Utah Geol. Miner. Surv.* **75,** 1–41.

Machette, M. N. (1978). Dating Quaternary faults in the southwestern United States by using buried calcareous paleosols. *J. Res. U.S. Geol. Surv.* **6,** 369–381.

Machette, M. N. (1982). Quaternary and Pliocene faults in the La Jencia and southern part of the Albuquerque-Belen basins, New Mexico. Evidence of fault history from fault-scarp morphology and Quaternary geology. *N. M. Geol. Soc., 33rd Field Conf. Guidebook,* Albuquerque Country II, pp. 161–169.

Machette, M. N. (1985). Documentation for benchmark photographs showing some effects of the 1983 Borah Peak earthquake with considerations for studies of scarp degradation. In *Proceedings of the Workshop XXVIII on the Borah Peak Earthquake, Idaho,* Vol. A (R. S. Stein, and R. E. Bucknam, eds.), *U.S. Geol. Surv. Open File Rept.* **85-290,** 97–109.

Machette, M. N. (1989). Slope-morphometric dating. In *Dating Methods Applicable to Quaternary Geologic Studies in the Western United States* (S. L. Forman, S. L. ed.), *Misc. Publ.- Utah Geol. Mineral. Surv.* **89-7,** 30–42.

Machette, M. N. (1992). Surficial geologic map of the Wasatch fault zone, eastern part of Utah Valley, Utah County and parts of Salt Lake and Juab Counties, Utah. *U.S. Geol. Surv. Misc. Invest. Map* **I-2095,** Scale 1:50,000.

Machette, M. N., and McGimsey, R. G. (1983). Quaternary and Pliocene faults in the east part of the Aztec 1° by 2° quadrangle and west part of the Raton 1° by 1° quadrangle, northern New Mexico. *U.S. Geol. Surv. Misc. Field Stud. Map* **MF-1465-B,** Scale 1:250,000.

Machette, M. N., and Scott, W. E. (1988). A brief review of research on lake cycles and neotectonics of the eastern Basin and Range Province. In In the Footsteps of G. K. Gilbert- Lake Bonneville and Neotectonics of the Eastern Basin and Range Province (M. N. Machette, ed.), *Misc. Publ.- Utah Geol. Mineral. Surv.* **88-1,** 7–16.

Machette, M. N., Personius, S. F., Nelson, A. R., Schwartz, D. P., and Lund, W. R. (1989). Segmentation models and Holocene movement history of the Wasatch fault zone, Utah. In *Fault Segmentation and Controls of Rupture Initiation and Termination* (D. P. Schwartz, and R. H. Sibson, eds.), *U.S. Geol. Surv. Open File Rep.* **89-315,** 229–245.

Machette, M. N., Personius, S. F., Nelson, A. R., Schwartz, D. P., and Lund, W. R. (1991). Segmentation and history of Holocene earthquakes, Wasatch fault zone, Utah. *J. Struct. Geol.* **13,** 137–149.

Machette, M. N., Personius, S. F., and Nelson, A. R. (1992a). Paleoseismology of the Wasatch fault zone: A summary of recent investigations, interpretations, and conclusions. In Assessment of Regional Earthquake Hazards and Risk Along the Wasatch Front, Utah (P. L. Gori, and W. W. Hays, eds.), *U.S. Geol. Surv. Prof. Pap.* **1500-A,** A1–A71.

Machette, M. N., Personius, S. F., and Nelson, A. R. (1992b). The Wasatch fault zone, U.S.A. *Ann. Tecton., Spec. Issue 6,* Suppl., 5–39.

Machette, M. N., Crone, A. J., and Bowman, J. R. (1993). Geologic investigations of the 1986 Marryat Creek, Australia, earthquakes- implications for paleoseismicity in stable continental regions. *Geol. Surv. Bull. Bull.* **2032-B,** B1–B29.

Maemoku, H. (1988). Holocene crustal movement in Muroto Peninsula, southwest Japan. *Geogr. Rev. Jpn., Ser. A* **61,** 747–769.

Maemoku, H. (1990). Holocene crustal movement in the southern part of Kii peninsula, outer zone of southwest Japan. *J. Geogr.* **99,** 349–369.

Mahaney, W. C., ed. (1984). *Quaternary Dating Methods.* Elsevier, New York.

Marquart, G., and Jacoby, W. (1985). On the mechanism of magma injection and plate divergence during the Krafla rifting episode in northeast Iceland. *J. Geophys. Res.* **90,** 10178–10192.

Marshall, G. A., Stein, R. S., and Thatcher, W. (1991). Fault geometry and slip from coseismic elevation changes; The 18 October 1989, Loma Prieta, California earthquake. *Bull. Seismol. Soc. Am.* **81,** 1660–1693.

Martin, J. R., and Clough, G. W. (1990). Implications from a Geotechnical Investigation of Liquefaction Phenomena Associated with Seismic Events in the Charleston, South Carolina Area. Virginia Polytech. Inst. State University, Blacksburg.

Mason, D. B. (1992). Earthquake magnitude potential of active faults in the Intermountain Seismic Belt from surface parameter scaling. M.S. Thesis (Geophysics), University of Utah, Salt Lake City.

Mason, O. K., and Jordan, J. W. (1994). Eustatic sea-level changes in northwest Alaska during the last 3000 years: *Geol. Soc. Am. Abtsr. Prog.* **26**(7), A-309.

Mastin, L. G., and Pollard, D. D. (1988). Surface deformation and shallow dike intrusion processes at Inyo Craters, Long Valley, California. *J. Geophys. Res.* **93,** 13221–13235.

Mathewes, R. W., and Clague, J. J. (1994). Detection of large prehistoric earthquakes in the Pacific Northwest by microfossil analysis. *Science* **264,** 688–691.

Matsuda, T., Ota, Y., Ando, M., and Yonekura, N. (1978). Fault mechanism and recurrence time of major earthquakes in southern Kanto District, Japan, as deduced from coastal terrace data. *Geol. Soc. Am. Bull.* **89,** 1610–1618.

Mayer, L. (1984). Dating Quaternary fault scarps in alluvium using morphological parameters. *Quat. Res.* **22,** 300–313.

McCalpin, J. P. (1983). Quaternary geology and neotectonics of the west flank of the northern Sangre de Cristo Mountains, south-central Colorado. *Colo. Sch. Mines Q.* **77**(3), 1–97.

McCalpin, J. P. (1984). Preliminary age classification of landslides for inventory mapping. *Proc. Eng. Geol. Soils Eng. Symp. 21st,* Univ. Idaho, Moscow, ID, *1984,* pp. 99–120.

McCalpin, J. P. (1986). Relative dating and age classification of landslides. *Assoc. Eng. Geol., Abtsr. Prog. 29th Annu. Meet.,* San Francisco, p. 56.

McCalpin, J. P. (1987a). Recommended setback distances from active normal faults. *Proc. Symp. Eng. Geol. Soils Eng. 23rd,* Logan, UT, *1987,* pp. 35–56.

McCalpin, J. P. (1987b). Recurrent Quaternary normal faulting at Major Creek, Colorado: an example of youthful tectonism on the eastern boundary of the Rio Grande Rift Zone. *Geol. Soc. Am., Centen. Field Guide, Rocky Mt. Sect.,* pp. 353–356.

McCalpin, J. P. (1989a). Quaternary geology and neotectonics of the Molesworth section of the Awatere Fault, South Island, New Zealand. *Int. Geol. Congr., 28th,* Washington, DC, Abstr., Vol. 3, p. 486.

McCalpin, J. P. (1989b). Current investigative techniques and interpretive models for trenching active dip-slip faults. In *Engineering Geology and Geotechnical Engineering* (R. C. Watters, ed.), *Proc. Symp. Eng. Geol. Geotech. Eng. 25th,* A. A. Balkema, Rotterdam, pp. 249–258.

McCalpin, J. P. (1989c). Prehistoric earthquake-induced landslides along the Awatere fault, South Island, New Zealand. *Assoc. Eng. Geol., Abtsr. Prog., 32nd Annu. Meet.,* Vail, CO, p. 94.

McCalpin, J. P. (1992). Glacial and postglacial geology near Lake Tennyson, Clarence River, New Zealand. *N. Z. J. Geol. Geophys.* **35,** 201–210.

McCalpin, J. P. (1993a). Neotectonics of the northeastern Basin and Range margin, western USA. *Z. Geomorphol., Suppl. Bd.* **94,** 137–157.

McCalpin, J. P. (1993b). Spatial/temporal patterns of Quaternary faulting in the southern limb of the Yellowstone-Snake River Plain seismic parabola, northeastern Basin and Range margin. *Geol. Soc. Am., Abtsr. Prog.* **25**(5), 117.

McCalpin, J. P. (1994). Quaternary deformation along the East Cache fault zone, Cache County, Utah. *Spec. Stud.-Utah Geol. Miner. Surv.* **83,** 1–37 pp.

McCalpin, J. P. (1995). Frequency distribution of geologically-determined slip rates for normal faults in the western USA. *Bull. Seismol. Soc. Am.* **85,** 1867–1872.

McCalpin, J. P. (1996). Tectonic geomorphology and Holocene paleoseismicity of the Molesworth section of the Awatere Fault, South Island, New Zealand. *N. Z. J. Geol. Geophys.* **39,** 33–50.

McCalpin, J. P., and Berry, M. E. (1996). Soil catenas on normal fault scarps, with an example from the Wasatch fault zone, Utah. *Catena* (in review).

McCalpin, J. P., and Forman, S. L. (1988). Chronology of paleoearthquakes on the Wasatch fault zone by thermoluminescence (TL) dating. *U.S. Geol. Surv. Open File Rept.* **88-434,** 506–511.

McCalpin, J. P., and Forman, S. L. (1991). Quaternary faulting and thermoluminescence dating of the East Cache fault zone, north-central Utah. *Bull. Seismol. Soc. Am.* **81,** 139–161.

McCalpin, J. P., and Irvine, J. R. (1995). Sackungen at Aspen Highlands Ski Area, Pitkin County, Colorado. *Environ. Eng. Geosci.* **1,** 277–290.

McCalpin, J. P., and Khromovskikh, V. S. (1995). Holocene paleoseismicity of the Tunka fault, Baikal rift, Russia. *Tectonics* **14,** 594–605.

McCalpin, J. P., and Nishenko, S. P. (1996). Holocene paleoseismicity, temporal clustering, and probabilities of future large ($M > 7$) earthquakes on the Wasatch fault zone, Utah. *J. Geophys. Res.* **101**(B3), 6233–6253.

McCalpin, J. P., and Rice, J. B., Jr. (1987). Spatial and temporal analysis of 1200 landslides in a 900 km^2 area, middle Rocky Mountains. In *Proc. Int. Conf. Field Workshop Landslides, 5th,* Christchurch, New Zealand, *1987,* pp. 137–146.

McCalpin, J. P., and Warren, G. A. (1992). Quaternary faulting on the Rock Creek fault, Overthrust Belt, western Wyoming. *Geol. Soc. Am., Abtsr. Prog.* **24**(6), 51.

McCalpin, J. P., Robison, R. M., and Garr, J. D. (1992). Neotectonics of the Hansel Valley - Pocatello Valley corridor, northern Utah and southern Idaho. In Assessment of Regional Earthquake Hazard and Risk Along the Wasatch Front, Utah (P. L. Gori and W. W. Hays, W. W. eds), *U.S. Geol. Surv. Prof. Pap.* **1500-G,** G1–G18.

McCalpin, J. P., Zuchiewicz, W., and Jones, L. C. A. (1993). Sedimentology of fault-scarp-derived colluvium from the 1983 Borah Peak rupture, central Idaho. *J. Sediment. Pet.* **63,** 120–130.

McCalpin, J. P., Forman, S. L., and Lowe, M. (1994). Reevaluation of Holocene faulting at the Kaysville trench site, Wasatch fault zone, Utah. *Tectonics* **13,** 1–16.

McClay, D. L. (1985). The use of photography to record geologic data. *Bull. Assoc. Eng. Geol.* **22,** 143–151.

McClelland, L., Simkin, T., Summers, M., Nielsen, E., and Stein, T. C., eds. (1989). *Global Volcanism 1975-1985.* Prentice Hall, Englewood Cliffs, NJ.

McCulloch, D. S., and Bonilla, M. G. (1970). Effects of the earthquake of March 27, 1964, on the Alaska Railroad. *U.S. Geol. Surv. Prof. Pap.* **545-D,** 1–161.

McGee, W. J. (1891). The Lafayette Formation. *U.S. Geol. Surv. 12th Annu. Rept.,* Part 1, pp. 387–521.

McGill, S. F., and Rubin, C. M. (1994). Variability of surficial slip in the 1992 Landers earthquake; implications for studies of prehistoric earthquakes. *U.S. Geol. Surv. Open File Rept.* **94-568,** 118–120.

McGill, S. F., and Sieh, K. (1991). Surficial offsets on the central and eastern Garlock Fault associated with prehistoric earthquakes. *J. Geophys. Res.* **96,** 21,597–21,621.

McGuire, W. J. and Pullen, A. D. (1989). Location and orientation of eruptive fissures and feeder-dykes at Mount Etna, influence of gravitational and regional tectonic stress regimes. *J. Volc. Geotherm. Res.* **38,** 325–344.

McGuire, W. J., Murray, J. B., Pullen, A. D., and Saunders, S. J. (1991). Ground deformation monitoring at Mt. Etna; evidence for dyke emplacement and slope instability. *J. Geol. Soc., London* **148,** 577–583.

McInelly, G. W., and Kelsey, H. M. (1990). Late Quaternary tectonic deformation in the Cape Arago - Bandon region of the Oregon coast as deduced from wave-cut platforms. *J. Geophys. Res.* **95,** 6699–6714.

McKay, A. (1886). On the geology of the eastern part of Marlborough Provincial District. *N. Z. Geol. Surv., Rep. Geol. Explor. 1885,* **17,** 27–136.

McKenzie, D., McKenzie, J. M., and Saunders, R. S. (1992). Dike emplacement on Venus and Earth. *J. Geophys. Res.* **97,** 15,977–15,990.

McKeown, F. A., Hamilton, R. M., Diehl, S. F., and Glick, E. E. (1990). Diapiric origin of the Blytheville and Pascola arches in the Reelfoot Rift, east-central United States: Relation to New Madrid seismicity. *Geology* **18,** 1158–1162.

McNeilan, T. W., Rockwell, T. K., and Resnick, G. S. (1996). Style and rate of Holocene slip, Palos Verdes fault, southern California. *J. Geophys. Res.* **101**(B4), (in press).

Medawar, P. (1979). *Advice To a Young Scientist.* Oxford Univ. Press, Oxford, UK.

Medina, F., Gonzalez, L., Guiterrez, G., Aguilera, R., and Espindola, J. M. (1992). Analysis of the seismic activity related to the 1982 eruption of the El Chichon Volcano, Mexico. In *Volcanic Seismology* (P. Gasparini, R. Scarpa, and K. Aki, eds.), pp. 97–108. Springer-Verlag, Berlin and Heidelberg.

Meehan, R. L. (1984). *The Atom and the Fault.* MIT Press, Cambridge, MA.

Meghraoui, M., Cisternas, A., and Philip, H. (1986). Seismotectonics of the lower Chelif Basin; Structural background of the El Asnam earthquake. *Tectonics* **5,** 809–836.

Meghraoui, M., Philip, H., Albarede, F., and Cisternas, A. (1988). Trench investigations through the trace of the 1980 El Asnam thrust fault. *Bull. Seismol. Soc. Am.* **78,** 979–999.

Meier, L. S. (1993). The susceptibility of a gravelly soil site to liquefaction. M. S. Thesis, Virginia Polytechnic Institute, Blacksburg.

Meisling, K. E., and Sieh, K. E. (1980). Disturbance of trees by the 1857 Fort Tejon earthquake, California. *J. Geophys. Res.* **85,** 3225–3238.

Menges, C. M., Wesling, J. R., Whitney, J. W., Swan, F. H., Coe, J. A., Thomas, A. P., and Oswald, J. A. (1994). Preliminary results of paleoseismic investigations of Quaternary faults on eastern Yucca Mountain, Nye County, Nevada. In *International High Level Radioactive Waste Management Conference,* **5th,** April 1994, Las Vegas, NV, pp. 2373–2390. Am. Soc. Civ. Eng. and Am. Nucl. Soc.

Mercier, J.-L., Carey-Gailhardis, E., Mouyaris, N., Simeakis, K., Roundoyannis, T., and Anghelidhis, C. (1983). Structural analysis of recent and active faults and regional state of stress in the epicentral area of the 1978 Thessaloniki earthquakes (northern Greece). *Tectonics* **2,** 577–600.

Merritts, D. J. (1996). The Mendocino triple junction: Active faults, episodic coastal emergence, and rapid uplift. *J. Geophys. Res.* **101**(B3), 6051–6070.

Merritts, D. J., and Bull, W. B. (1989). Interpreting Quaternary uplift rates at the Mendocino triple junction, northern California, from uplifted marine terraces. *Geology* **17,** 1020–1024.

Merritts, D., and Ellis, M. (1994). Introduction to special section on tectonics and topography. *J. Geophys. Res.* **99**(B6), 12,135–12,141.

Miall, A. D. (1990). *Principles of Sedimentary Basin Analysis.* Springer-Verlag, New York.

Michetti, A. M., Brunamonte, F., Serva, L., and Whitney, R. A. (1995). Seismic hazard assessment from paleoseismological evidence in the Rietti region, central Italy. In *Perspectives in Paleoseismology* (L. Serva, and D. B. Slemmons, eds.), Spec. Publ. 6, pp. 63–82. Assoc. Eng. Geol.

Miller, R. D., and Steeples, D. W. (1986). Shallow structure from a seismic-reflection profile across the Borah Peak, Idaho, fault scarp. *Geophys. Res. Lett.* **12,** 953–956.

Miller, R. D., Steeples, D. W., and Myers, P. B. (1990). Shallow seismic reflection survey across the Mears fault, Oklahoma. *Geol. Soc. Am. Bull.* **102,** 18–25.

Mills, P. C. (1983). Genesis and diagnostic value of soft-sediment deformation structures - a review. *Sediment. Geol.* **35,** 83–104.

Minakami, T. (1974). Prediction of volcanic eruptions. In *Physical Volcanology* (L. Civetta, P. Gasparini, G. Luongo, and A. Rapolla, eds.), pp. 314–333. Elsevier, Amsterdam.

Minoura, K., and Nakaya, S. (1991). Traces of tsunami preserved in inter-tidal lacustrine and marsh deposits- Some examples from northeast Japan. *J. Geol.* **99,** 265–287.

Minoura, K., Nakaya, S., and Uchida, M. (1994). Tsunami deposits in a lacustrine sequence of the Sanriku coast, northeast Japan. *Sediment. Geol.* **89,** 25–31.

Minster, J. B., and Jordan, T. H. (1987). Vector constraints on western U.S. deformation from space geodesy, neotectonics, and plate motions. *J. Geophys. Res.* **92,** 4798–4808.

Mitchell, J. K. (1976). *Fundamentals of Soil Behavior.* Wiley, New York.

Molnar, P., and Qidong, D. (1984). Faulting associated with large earthquakes and the average rate rate of deformation in central and eastern Asia. *J. Geophys. Res.* **89,** 6203–6227.

Molnar, P., Brown, E. T., Burchfiel, B. C., Qidong, D., Xianyue, F., Jun, L., Raisbeck, G. M., Jianbang, S., Zhangming, W., Yiou, F., and Huichuan, Y. (1994). Quaternary climate change and the formation of river terraces across growing anticlines on the north flank of the Tien Shan. *J. Geol.* **102,** 583–602.

Mook, W. G., and van de Plassche, O. (1986). Radiocarbon dating. In *Sea-Level Research- A Manual for the Collection and Evaluation of Data* (O. van der Plassche, ed.), pp. 525–560. Geo Books, Norwich, UK.

Moore, J. G., Clague, D. A., Holcomb, R. T., Lipman, P. W., Normark, W. R., and Thompson, M. E. (1989). Prodigous submarine landslides on the Hawwaiian Ridge. *J. Geophys. Res.* **94,** 17,465–17,484.

Mori, J., McKee, C., Itikarai, I., Lowenstein, P., de Saint Ours, P., and Tali, B. (1989). Earthquakes of the Rabaul seismo-deformational crisis September 1983 to July 1985, Seismicity on a caldera ring fault. In *Volcanic Hazards* (J. H. Latter ed.), *IAVCEI Proc. Volcanol.* **1,** 429–462.

Morisawa, M., and Hack, J. T., eds. (1985). Tectonic Geomorphology, Proc. 15th Annu. Binghampton Geomorphol. Symp. Allen & Unwin, Boston. MA.

Moriya, I. (1980). Bandaian type eruption and its geomorphology. *K. Nishimura Mem. Geomorphol. Proc.,* pp. 214–219.

Morner, N.-A. (1976). Eustasy and geoid changes. *J. Geol.* **84,** 123–151.

Morner, N.-A. (1985). Paleoseismicity and geodynamics in Sweden. *Tectonophysics* **117,** 139–153.

Mörner, N.-A., and Adams, J., eds. (1989). Paleoseismicity and neotectonics. *Tectonophysics* **163** (whole volume).

Mörner, N-A., Somi, A., and Zuchiewicz, W. (1989). Neotectonics and paleoseismicity within the Stockholm intracratonal region in Sweden. *Tectonophysics* **163,** 289–303.

Morton, D. M., and Sadler, P. M. (1989). Landslides flanking the northeastern Peninsular Ranges and in the San Gorgonio Pass area of southern California. In *Landslides in a Semi-Arid Environment* (P. M. Sadler, and D. M. Morton, eds.), **Vol. 2,** pp. 338–355. Inland Geol. Soc., Riverside, CA.

Muehlberger, W. R., Goetz, L. K., and Belcher, R. C. (1985). Analysis of Skylab and ASTP photographs of the Levantine (Dead Sea) fault zone. In *The Surveillant Science: Remote Sensing of the Environment* (R. K. Holz, ed.), pp. 114–127. Wiley, New York.

Mueller, K. J., and Rockwell, T. K. (1995). Late Quaternary activity of the Laguna Salada fault in northern Baja California, Mexico. *Geol. Soc. Am. Bull.* **107,** 8–18.

Mundorff, M. J., Crosthwaite, E. G., and Kilburn, C. (1964). Ground water for irrigation in the Snake River Basin in Idaho. *U.S. Geol. Surv. Water-Supply Pap.* **1654,** 1–224.

Munson, P. J., Munson, C. A., Bleuer, N. K., and Labitzke, M. D. (1992). Distribution and dating of prehistoric liquefaction in the Wabash Valley of the Central U.S. *Seismol. Res. Lett.* **63,** 337–342.

Munson, P. J., Munson, C. A., and Bleuer, N. K. (1994). Late Pleistocene and Holocene earthquake-induced liquefaction in the Wabash Valley of southern Indiana. *U.S. Geol. Surv. Open File Rept.* **94-176,** 553–557.

Mutti, E., Lucchi, F. R., Seguret, M., and Zanzucchi, G. (1984). Seismoturbidites: A new group of resedimented deposits. *Mar. Geol.* **55,** 103–116.

Myers, P. B., Miller, R. D., and Steeples, D. W. (1987). Shallow seismic reflection profile of the Meers fault, Comanche County, Oklahoma. *Geophys. Res. Lett.* **14,** 749–752.

Myers, W. B., and Hamilton, W. (1964). Deformation accompanying the Hebgen Lake earthquake of August 17, 1959. *U.S. Geol. Surv. Prof. Pap.* **435,** 55–98.

Nairn, I. A., and Beanland, S. (1989). Geological setting of the 1987 Edgecumbe earthquake, New Zealand. *N. Z. J. Geol. Geophys.* **32,** 1–13.

Nairn, I. A., and Cole, J. W. (1981). Basalt dikes in the 1886 Tarawera Rift. *N. Z. J. Geol. Geophys.* **24,** 585–592.

Nakamura, K., Kasahara, K., and Matsuda, T. (1964). Tilting and uplift of an island, Awashima, near the epicentre of the Niigata earthquake in 1964. *J. Geodet. Soc. Jpn.* **10,** 172–179.

Nakata, J. S., Tanigawa, W. R., and Klein, F. W. (1982). Hawaiian Volcano Observatory Summary 81. Part 1. Seismic data, January to December, 1981. *U.S. Geol. Surv. Rep.*

Nakata, T., Koba, M., Jo, W., Imaizumi, T., Matsumoto, H., and Suganuma, T. (1979). Holocene marine terraces and seismic crustal movement. *Sci. Rep. Tohoku Univ. Ser. 7* **29,** 195–204.

Nash, D. B. (1980). Morphological dating of degraded normal fault scarps. *J. Geol.* **88,** 353–360.

Nasu, N. (1935). Recent seismic activities in the Isu Peninsula (Part 2). *Bull. Earthquake Res. Inst. Univ. Tokyo* **13,** 400–415.

Nataraja, M. S., and Gill, H. S. (1983). Ocean wave-induced liquefaction analysis. *J. Geotech. Eng., Am. Soc. Civ. Eng.* **109,** 573–590.

National Earthquake Information Center (1991). *Preliminary Monthly Determinations of Epicenters,* June issue. NEIC.

National Research Council (1985). *Liquefaction of Soils During Earthquakes.* Natl. Acad. Press, Washington, DC.

Naumann, C. M., and Savigny, K. W. (1992). Large rock avalanches and seismicity in southwestern British Columbia, Canada. In *Landslides (Glissements de terrain)* (D. H. Bell, ed.), Int. Symp., 6th, Christchurch, New Zealand, 1992, **Vol. 2,** pp. 1187–1192. A. A. Balkema, Rotterdam.

Nelson, A. R. (1992a). Holocene tidal-marsh stratigraphy in south-central Oregon; evidence for localized sudden submergence in the Cascadia subduction zone. *Soc. Econ. Petrol. Mineral., Spec. Publ.* **48,** 287–301.

Nelson, A. R. (1992b). Lithofacies analysis of colluvial sediments- an aid in interpreting the recent history of Quaternary normal faults in the Basin and Range province, western United States. *J. Sediment. Pet.* **62,** 607–621.

Nelson, A. R. (1992c). Discordant 14C ages from buried tidal-marsh soils in the Cascadia subduction zone, southern Oregon coast. *Quat. Res.* **38,** 74–90.

Nelson, A. R., and Atwater, B. F. (1993). Comparison among radiocarbon ages of earthquake-killed plants along the Cascadia subduction zone. *EOS, Trans. Am. Geophys. Union* **74,** 199.

Nelson, A. R., and Kashima, K. (1993). Diatom zonation in southern Oregon tidal marshes relative to vascular plants, foraminifera, and sea level. *J. Coastal Res.* **9,** 673–697.

Nelson, A. R., and Manley, W. F. (1992). Holocene coseismic and aseismic uplift of Isla Mocha, south-central Chile. In Impacts of Tectonics on Quaternary Coastal Evolution (Y. Ota, A. R. Nelson, and K. Berryman, eds.), *Quat. Int.* **15/16,** 61–76.

Nelson, A. R., and Personius, S. F. (1988). Preliminary surficial geologic map of the Weber segment, Wasatch fault zone, Weber and Davis Counties, Utah. *U.S. Geol. Surv. Misc. Field Stud. Map* **MF-2132,** Scale 1:50,000.

Nelson, A. R., and Personius, S. F. (1996). The potential for great earthquakes in Oregon and Washington: An overview of recent coastal geologic studies and their bearing on segmentation of Holocene ruptures, central Cascadia subduction zone. In *Assessing Earthquake Hazards and Reducing Risk in the Pacific Northwest* (A. M. Rogers, T. J. Walsh, W. J. Kockleman, and G. R. Priest, eds.), *U.S. Geol. Surv. Prof. Pap.* **1560,** Vol. 1 (in press).

Nelson, A. R., and Weisser, R. R. (1985). Late Quaternary faulting on Towanta Flat, northwestern Uinta Basin, Utah. In *Geology and Energy Resources of the Uinta Basin of Utah* (D. M. Picard, ed.), pp. 147–158. Utah Geol. Assoc., Salt Lake City.

Nelson, A. R., Atwater, B. F., Bobrowsky, P. T., Bradley, L.-A., Clague, J. J., Carver, G. A., Darienzo, M. E., Grant, W. C., Krueger, H. W., Sparks, R., Stafford, T. W., and Stuiver, M. (1995). Radiocarbon evidence for extensive plate-boundary rupture about 300 years ago at the Cascadia subduction zone. *Nature* (*London*) **378,** 371–374.

Nelson, A. R., Shennan, I., and Long, A. J. (1996). Identifying coseismic subsidence in tidal-wetland stratigraphic sequences at the Cascadia subduction zone of western North America. *J. Geophys. Res.* **101**(B3), 6115–6135.

Nelson, A. R., Jennings, A. E., and Kashima, K. (1996). An earthquake history derived from stratigraphic and microfossil evidence of a relative sea-level change at Coos Bay, southern coastal Oregon. *Geol. Soc. Am. Bull.* **108**(2), 141–154.

Nettleton, W. D., McCracken, R. J., and Daniels, R. B. (1968a). Two North Carolina Coastal Plain catenas. I. Morphology and fragipan development. *Soil Sci. Soc. Am. Proc.* **32,** 577–582.

Nettleton, W. D., Daniels, R. B., and McCracken, R. J. (1968b). Two North Carolina Coastal Plain catenas. II. Micromorphology, composition, and fragipan genesis. *Soil Sci. Soc. Am. Proc.* **32,** 582–587.

Newmark, N. M. (1965). Effects of earthquakes on dams and embankments. *Geotechnique* **15,** 139–160.

Niemi, T. M. and Hall, N. T. (1992). Late Holocene slip rate and recurrence of great earthquakes on the San Andreas fault in northern California. *Geology* **20,** 195–198.

Nieto E., A. H., Brandsdottir, B., and Munoz, C. F. (1990). Seismicity associated with the reactivation of Nevado del Ruiz, Columbia, July 1985- December 1986. *J. Volcanol. Geotherm. Res.* **41,** 315–326.

Nikonov, A. A. (1988a). Reconstruction of the main parameters of old large earthquakes in Soviet Central Asia using the paleoseismogeological method. *Tectonophysics* **147,** 297–312.

Nikonov, A. A. (1988b). On the methodology of archeoseismic research into historical monuments. In *Engineering Geol. of Ancient Works, Monuments, and Historical Sites* (P. Marinos and G. Koukis, eds.), pp. 1315–1320. A. A. Balkema, Rotterdam.

Nikonov, A. A. (1995a). On the terminology and classification of earthquake-induced disturbances: State-of-the-art and some suggestions. *Bull. INQUA Neotectonics Comm.* **18,** 14–16.

Nikonov, A. A. (1995b). The stratigraphic method in the study of large past earthquakes. *Quat. Intl.* **25,** 47–55.

Nikonov, A. A., and Shebalina, T. Y. (1979). Lichenometry and earthquake age determination in central Asia. *Nature* (*London*). **280,** 675–677.

Nishenko, S. P. (1985). Seismic potential for large and great interplate earthquakes along the Chilean and southern Peruvian margins of South America; a quantitative reappraisal. *J. Geophys. Res.* **90,** 3589-3615.

Nishenko, S. P. (1989). Circum-Pacific seismic potential 1989-1999. *U.S. Geol. Surv. Open File Rep.* **89-86,** 1–126.

Nishenko, S. P., and Bollinger, G. A. (1990). Forecasting damaging earthquakes in the central and eastern United States. *Science* **249,** 1412–1416.

Nishenko, S., and Buland, R. (1987). A generic recurrence interval distribution for earthquake forecasting. *Bull. Seismol. Soc. Am.* **77,** 1382–1399.

Nishenko, S. P., and McCann, W. R. (1981). Seismic potential for the worlds major plate boundaries. In Earthquake Prediction: An International Review (D. W. Simpson and P. G. Richards, eds.), *Am. Geophys. Union, Maurice Ewing Ser.* **4,** 20–28.

Nishenko, S. P., and Schwartz, D. P. (1990). Preliminary estimates of large earthquake probabilities along the Wasatch fault zone, Utah. *EOS, Trans. Am. Geophys. Union* **71,** 1448.

Nodder, S. D. (1993). Neotectonics of the offshore Cape Egmont fault zone, Taranaki Basin, New Zealand. *N. Z. J. Geol. Geophys.* **36,** 167.

Nodder, S. D. (1994). Characterizing potential offshore seismic sources using high-resolution geophysical and seafloor sampling programs; an example from the Cape Egmont fault zone, Taranaki Shelf, New Zealand. *Tectonics* **13,** 641–658.

Noller, J. S., Lettis, W. R., and Simpson, G. D. (1994). Seismic archeology; using human prehistory to date paleoearthquakes and assess deformation rates of active fault zones. *U.S. Geol. Surv. Open File Rept.* **94-568,** 138–140.

Nuttli, O. W. (1973). The Mississippi Valley earthquakes of 1811 and 1812: Intensities, ground motion, and magnitudes. *Bull. Seismol. Soc. Am.* **63,** 227–248.

Nuttli, O. W. (1979). Seismicity of the central United States. In *Geology in the Siting of Nuclear Power Plants* (A. W. Hatheway and C. R. McClure, Jr., eds.), Rev. Eng. Geol. Vol. **4,** pp. 67–93. Geol. Soc. Am., Washington, DC.

Nuttli, O. W. (1983). Average seismic source-parameter relations for mid-plate earthquakes. *Bull. Seismol. Soc. Am.* **73,** 519–535.

Obermeier, S. F. (1988). Liquefaction potential in the central Mississippi Valley. *U.S. Geol. Surv. Bull.* **1832,** 1–21.

Obermeier, S. F. (1989). The New Madrid earthquakes: An engineering-geologic interpretation of relict liquefaction features. *U.S. Geol. Surv. Prof. Pap.* **1336-B,** 1–114.

Obermeier, S. F. (1994a). Preliminary limits for the strength of shaking in the Columbia River valley and the southern half of coastal Washington, with emphasis for a Cascadia subduction earthquake about 300 years ago. *U.S. Geol. Surv. Open File Rept.* **94-589,** 1–40.

Obermeier, S. F. (1994b). Using liquefaction-induced features for paleoseismic analysis. *U.S. Geol. Surv. Open File Rept.* **94-663,** Chapter A, 1–58.

Obermeier, S. F., Weems, R. E., and Jacobson, R. B. (1987). Earthquake-induced liquefaction features in the coastal South Carolina region. *U.S. Geol. Surv. Open File Rept.* **87-504,** 1–13.

Obermeier, S. F., Jacobson, R. B., Smoot, J. P., Weems, R. E., Gohn, G. S., Monroe, J. E., and Powars, D. S. (1990). Earthquake-induced liquefaction features in the coastal setting of South Carolina and in the fluvial setting of the New Madrid seismic zone. *U.S. Geol. Surv. Prof. Pap.* **1504,** 1–44.

Obermeier, S. F., Martin, J. R., Frankel, A. D., Youd, T. L., Munson, P. J., Munson, C. A., and Pond, E. C. (1993). Liquefaction evidence for one or more strong Holocene earthquakes in the Wabash Valley of southern Indiana and Illinois, with a preliminary estimate of magnitude. *U.S. Geol. Surv. Prof. Pap.* **1536,** 1–27.

Oelfke, J. G., and Butler, D. R. (1985). Lichenometric dating of calcareous landslide deposits, Glacier National Park, Montana. *Northwest Geol.* **17,** 7–10.

Okada, A. (1980). Quaternary faulting along the Median Tectonic Line of southwest Japan. *Mem. Geol. Soc. Jpn,* **18,** 789–108 (in Japanese with English abstr.).

Okada, A., Takeuchi, A., Tsukuda, T., Ikeda, Y., Watanabe, M., Hirano, S., Masumoto, S., Takehana, Y., Okumura, K., Kamishima (Takemura), T., Kobayashi, T., and Ando, M. (1989). Trenching study of the Atotsugawa Fault at Nokubi, Miyagawa Village, Gifu Prefecture, central Japan. *J. Geogr.* **98,** 62–85 (in Japanese with English abstr.).

Okada, A., Watanabe, M., Ando, M., Tsukuda, T., and Hirano, S. (1992). Estimation of paleoseismicity in the Nobi active fault system, central Japan- excavation study of the Umehara fault, central strand in the Nobi active fault system. *J. Geogr.* **101,** 1–18 (in Japanese with English abstr.).

Okada, Y. (1985). Surface deformation due to shear and tensile faults in a half-space. *Bull. Seismol. Soc. Am.* **75,** 1135–1154.

Okada, Y., and Yamamoto, E. (1991). Dyke intrusion model for the 1989 seismovolcanic activity off Ito, central Japan. *J. Geophys. Res.* **96,** 10361–10376.

Okumura, K., Shimokawa, K., Yamazaki, H., and Tsukuda, E. (1994). Recent surface faulting events along the middle section of the Itoigawa-Shizuoka Tectonic Line. *J. Seismol. Soc. Jpn.* **46,** 425–438.

Oldham, R. D. (1899). Report on the great earthquake of 12th June 1987. *Mem. Geol. Surv. India* **29,** 1–379.

Olesen, O. (1988). The Stuoragurra Fault, evidence of neotectonics in the precambrian of Finnmark, northern Norway. *Nors. Geol. Tidsskri.* **68,** 107–118.

Olig, S. S., Lund, W. R., and Black, B. D. (1994). Large mid-Holocene and late Pleistocene earthquakes on the Oquirrh fault zone, Utah. *Geomorphology* **10,** 285–315.

Ollier, C. (1981). *Tectonics and Landforms.* Longman, London.

O'Neill, M. W., and Van Siclen, D. C. (1984). Activation of Gulf Coast faults by depressuring of aquifers and an engineering approach to siting structures along their traces. *Bull. Assoc. Eng. Geol.* **21,** 73–87.

Opheim, J. A., and Gudmundsson, A. (1989). Formation and geometry of fractures, and related volcanism of the Krafla fissure swarm, northeast Iceland. *Geol. Soc. Am. Bull.* **101,** 1608–1622.

Oppenheimer, D., Beroza, G., Carver, G., Dengler, L., Eaton, J., Gee, L., Gonzalez, F., Jayko, A., Li, W. H., Lisowski, M., Magee, M., Marshall, G., Murray, M., McPherson, R., Romanowicz, B., Satake, K., Simpson, R., Somerville, R., Stein, R., and Valentine, D. (1993). The Cape Mendocino, California, Earthquakes of April 1992; Subduction at the triple junction. *Science* **261,** 433–438.

O'Rourke, T. D., and Hamada, M., eds. (1989). Proceedings from the Second U.S. Japan Workshop on Liquefaction Large Ground Deformation and Their Effects on Lifelines, *Tech. Rep. NCEER-89-0032.* State University of New York, Buffalo.

Ostenaa, D. A. (1984). Relationships affecting estimates of surface fault displacements based on scarp-derived colluvial deposits. *Geol. Soc. Am., Abtsr. with Prog.* **16**(5), 327.

Ostenaa, D. A. (1990). Late Holocene displacement history, Water Canyon site, Wasatch fault, Utah. *Geol. Soc. Am., Abtsr. Prog.* **22**(6), 42.

Osterkamp, W. R., and Hupp, C. R. (1987). Dating and interpretation of debris flows by geologic and botanical methods at Whitney Creek Gorge, Mount Shasta, California. In *Debris flows/ Avalanches: Process, Recognition, and Mitigation* (J. E. Costa, and G. F. Wieczorek, eds.), Rev. Eng. Geol. Vol. **7,** pp. 157–164. Geol. Soc. Am., Washington, DC.

Ota, Y. (1975). Late Quaternary vertical movement in Japan estimated from deformed shorelines. In *Quaternary Studies* (R. P. Suggate, and M. M. Creswell, ed.), pp. 231–239. R. Soc. New Zealand, Wellington.

Ota, Y., and Suzuki, I. (1979). Notes on active folding in the lower reaches of the Shinano River, central Japan. *Geogr. Rev. Jpn.* **52,** 592–601 (in Japanese).

Ota, Y., and Yoshikawa, T. (1978). Regional characteristics and their geodynamic implications of late Quaternary tectonic movement deduced from former shorelines in Japan. *J. Phys. Earth, Suppl.* **26,** 379–389.

Ota, Y., Matsuda, T., and Naganuma, K. (1976). Tilted marine terraces of the Ogi Peninsula, Sado Island, central Japan, related to the Ogi Earthquake of 1802. *J. Seismol. Soc. Jpn.* **29,** 55–70 (in Japanese with English abstract).

Ota, Y., Hull, A. G., and Berryman, K. R. (1991). Coseismic uplift of marine terraces, Pakarae River area, eastern North Island, New Zealand. *Quat. Res.* **35,** 331–346.

Ota, Y., Chappell, J., Kelley, R., Yonekura, N., Matsumoto, E., and Nishimura, T. (1993). Holocene coral reef terraces and coseismic uplift of Huon Peninsula, Papua New Guinea. *Quat. Res.* **40,** 177–188.

Otuka, Y. (1932). Post-Pliocene crustal movements in the Outer Zone of southwestern Japan and in the Fossa Magna. *Bull. Earthquake Res. Inst., Tokyo Imp. Univ.* **10,** 701–722.

Ouichi, S. (1985). Response of alluvial rivers to slow active tectonic movement. *Geol. Soc. Am. Bull.* **96,** 504–515.

Oura, A., Yoshida S., and Kudo, K. (1992). Rupture process of the Ito-Oki, Japan, earthquake of 1989 July 9 and interpretation as a trigger of volcanic eruption. *Geophys. J. Int.* **109,** 241–248.

Ouyed M., Meghraoui, M., Cisternas, A., Deschamps, A., Dorel, J., Frechet, R., Gaulon, R., Hatzfeld, D., and Philip, H. (1981). Seismotectonics of the El Asnam earthquake. *Nature (London).* **292,** 26–31.

Oviatt, C. G., Currey, D. R., and Sack, D. (1992). Radiocarbon chronology of Lake Bonneville, eastern Great Basin, USA. *Paleogeogr., Paleoclimatol., Paleoecol.* **99,** 225–241.

Owen, G. (1987). Deformation processes in unconsolidated sands. In *Deformation of Sediments and Sedimentary Rocks* (M. E. Jones and R.M. F. Preston, eds.), Geol. Soc. London Spec. Publ. No. **29,** pp. 11–24. Blackwell, Oxford.

Paces, J. B., Menges, C. M., Widman, B., Wesling, J. R., Bush, C. A., Futa. K., Millard, H. T., Maat, P. B., and Whitney, J. W. (1994). Preliminary U-series disequilibrium and thermoluminescence ages of surficial deposits and paleosols associated with Quaternary faults, eastern Yucca Mountain. In *International High Level Radioactive Waste Management Conference,* **5th,** April 1994, Las Vegas, NV, pp. 2391–2401. Am. Soc. Civ. Eng. and Am. Nucl. Soc.

Pacheco, J. F., Sykes, L. R., and Scholz, C. H. (1993). Nature of seismic coupling along simple plate boundaries of the subduction type. *J. Geophys. Res.* **98,** 14,133–14,159.

Page, R. A. (1970). Dating episodes of faulting from tree rings- effects of the 1958 rupture of the Fairweather fault on tree growth. *Geol. Soc. Am. Bull.* **81,** 3085–3094.

Page, R. A., Stephens, C. D., and Lahr, J. C. (1989). Seismicity of the Wrangell and Aleutian Wadati-Benioff zones and the North American plate along the trans-Alaska crustal transect, Chugach mountains and Copper River Basin, southern Alaska. *J. Geophys. Res.* **94,** 16059–16082.

Palmason, G. (1981). Crustal rifting, and related thermo-mechanical processes in the lithosphere beneath Iceland. *Geol. Rundsch.* **70,** 244–260.

Pandolfi, J. M., Best, M.M. R., and Murray, S. P. (1992). Coseismic event of May 15, 1992, Huon Peninsula, Papua New Guinea; comparison with Quaternary tectonic history. *Geology* **22,** 239–242.

Pantosti, D., and Valensise, G. (1990). Faulting mechanism and complexity of the November 23, 1980, Campania-Lucania earthquake, inferred from surface observations. *J. Geophys. Res.* **95,** 15,319–15,341.

Pantosti, D., and Yeats, R. S. (1993). Paleoseismology of great earthquakes of the late Holocene. *Ann. Geofis.* **36**(3–4), 237–257.

Pantosti, D., Schwartz, D. P., and Valensise, G. (1993). Paleoseismology along the 1980 surface rupture of the Irpina fault; implications for earthquake recurrence in the southern Apennines, Italy. *J. Geophys. Res.* **98,** 6561–6577.

Parsons, T., and Thompson, G. A. (1991). The role of magma overpressure in suppressing earthquakes and topography: Worldwide examples. *Science* **253,** 1399–1402.

Parsons, T., and Thompson, G. A. (1993). Does magmatism influence low-angle normal faulting? *Geology* **21,** 247–250.

Patane, G., Gresta, S., and Imposa, S. (1984). Seismic activity preceding the 1983 eruption of Mt. Etna. *Bull. Volcanol.* **47,** 941–952.

Pavlides, S. B. (1993). Active faulting in multi-fractured seismogenic areas; examples from Greece. *Z. Geomorphol. Suppl.* **94,** 57–72.

Pavlides, S., and Mountrakis, D. (1986). *Neotectonics, An Introduction to Recent Geological Structures* Univ. Studio Press, Thessaloniki, Greece, (in Greek).

Pease, J. W., and O'Rourke, T. D. (1995). Liquefaction hazards in the San Francisco Bay region; site investigation, modeling, and hazard assessment at areas most seriously affected by the 1989 Loma Prieta earthquake. *Unpublished Contract Report to U.S. Geol. Surv., Grant No. 1434-93-G-2332.* Sch. Civ. Environ. Eng., Cornell University, Ithaca, NY.

Pelton, J. R., and Smith, R. B. (1982). Contemporary vertical surface displacements in Yellowstone National Park. *J. Geophys. Res.* **87,** 2745–2761.

Pelton, J. R., Meissner, C. W., Waag, C. J., and Wood, S. H. (1985). Shallow seismic refraction studies across the Willow Creek fault rupture zone and the Chilly Buttes sand boils. *U.S. Geol. Surv. Open File Rept.* **85-290-A,** 161–181.

Penick, J., Jr. (1976). *The New Madrid Earthquakes of 1811-12.* Univ. of Missouri Press, Columbia.

Perissoratis, C., Mitropoulos, D., and Angelopoulos, I. (1984). The role of earthquakes in inducing sediment mass movements in the eastern Korinthiakos Gulf. An example from the February 24-March 4, 1981 activity. *Mar. Geol.* **55,** 35–45.

Perkins, D. M. (1987). Contagious fault rupture, probabalistic hazard, and contagion observability. In *Directions in Paleoseismology* (A. J. Crone and E. M. Omdahl, eds.), *U.S. Geol. Surv. Open File Rept.* **87-673,** 428–439.

Perkins, J. A., and Sims, J. D. (1983). Correlation of Alaskan varve thickness with climatic parameters, and use in paleoclimatic reconstruction. *Quat. Res.* **20,** 308-321.

Perrin, N. D., and Hancox, G. T. (1992). Landslide-dammed lakes in New Zealand—Preliminary studies on their distribution, causes and effects. In *Landslides (Glissements de terrain)* (D. H. Bell, ed.), Int. Symp., 6th, Christchurch, New Zealand, 1992, Vol. **2,** pp. 1457–1466. A. A. Balkema, Rotterdam.

Personius, S. F. (1991). Paleoseismic analysis of the Wasatch fault zone at the Brigham City trench site, Brigham City, and the Pole Patch trench site, Pleasant View, Utah. *Spec. Stud.- Utah Geol. Miner. Surv.* **76,** 1–39.

Peters, K. E., and Herrmann, R. B., compilers and eds. (1986). First-hand observations of the Charleston earthquakes of August 31, 1886, and other earthquake materials. *S. C. Geol. Surv., Bull.* **41,** 1–116.

Peterson, C. D. (1992). Variation in form and scale of paleoliquefaction structures in late Pleistocene deposits of the central Cascadia margin. *Geol. Soc. Am., Abtsr. with Prog.* **24**(5), 74.

Peterson, C. D., and Darienzo, M. E. (1988). Coastal neotectonics field trip guide for Netarts Bay, Oregon. *Ore. Geol.* **50,** 99–106.

Peterson, C. D., and Darienzo, M. E. (1991). Discrimination of climatic, oceanic, and tectonic forcing of marsh burial events from Alsea Bay, Oregon, USA. In Earthquake Hazards in the Pacific Northwest of the United States (A. M. Rogers, T. J. Walsh, W. J. Kockleman, and G. R. Priest, eds.), *U.S. Geol. Surv. Open File Rept.* **91-441-C,** 1–53.

Peterson, C. D., Hansen, M., and Jones, D. (1991). Widespread evidence of paleoliquefaction in late-Pleistocene marine terraces from the Oregon and Washington margins of the Cascadia subduction zone. *Am. Geophys. Union, 1991 Fall Meet., Prog. Abtsr.,* p. 313.

Peterson, C. D., Darienzo, M. E., Burns, S. F., and Burris, W. K. (1993). Field trip guide to Cascadia paleoseismic evidence along the northern Oregon coast; evidence of subduction zone seismicity in the central Cascadia margin. *Oreg. Geol.* **55,** 99–144.

Peterson, D. W., and Moore, R. B. (1987). Geologic history and evolution of geologic concepts, Island of Hawaii. In Volcanism in Hawaii (R. W. Decker, T. L. Wright, and P. H. Stauffer eds.), *U.S. Geol. Surv. Prof. Pap.* **1350,** 141–190.

Peterson, F. F., Bell, J. W., Dorn, R. I., Ramelli, A. R., and Ku, T.-L. (1995). Late Quaternary geomorphology and soils in Crater Flat, Yucca Mountain area, southern Nevada. *Geol. Soc. Am. Bull.* **107,** 1–17.

Pettijohn, F. J., and Potter, P. E. (1964). *Atlas and Glossary of Primary Sedimentary Structures.* Springer-Verlag, New York.

Pezzopane, S. K., Menges, C. M., and Whitney, J. W. (1994) Quaternary paleoseismology and Neogene tectonics at Yucca Mountain, Nevada. *U.S. Geol. Surv. Open File Rep.* **94-568,** 149–151.

Philip, H., and Meghraoui, M. (1983). Structural analysis and interpretation of the surface deformations of the El Asnam earthquake of October 10, 1980. *Tectonics* **2,** 17–49.

Philip, H., Rogozhin, E., Cisternas, A., Bousquet, J. C., Borisov, B., and Karakhanian, A. (1992). The Armenian earthquake of 1988 December 7; faulting and folding, neotectonics and paleoseismicity. *Geophys. J. Int.* **110,** 141–158.

Pierce, K. L. (1986). Dating methods. In *Active Tectonics:* Studies in Geophysics (R. E. Wallace, chairman), Natl. Acad. Press, Washington, DC, pp. 195–214.

Pierce, K. L., and Colman, S. M. (1986). Effect of height and orientation (microclimate) on geomorphic degradation rates and processes, late-glacial terrace scarps in central Idaho. *Geol. Soc. Am. Bull.* **97,** 869–885.

Pierce, K. L., and Morgan, L. A. (1992). The track of the Yellowstone hot spot, volcanism, faulting, and uplift. In *Regional Geology of Eastern Idaho and Western Wyoming* (P. K. Link, M. A. Kuntz, and L. B. Platt, eds.), *Mem.- Geol. Soc. Am.* **179,** 1–54.

Piety, L. A., Sullivan, J. T., and Anders, M. H. (1992). Segmentation and paleoseismicity of the Grand Valley fault, southeastern Idaho and western Wyoming. In *Regional Geology of Eastern Idaho and Western Wyoming* (P. K. Link, M. A. Kuntz, and L. B. Platt, eds.), *Mem.- Geol. Soc. Am.* **179,** 155–182.

Pilcher, J. R. (1991). Radiocarbon dating. In *Quaternary Dating Methods: A User's Guide,* Tech. Guide 4, pp. 16–35. Quaternary Research Association, Cambridge, UK.

Pillmore, C. L. (1989). Geologic photogrammetry in the U.S. Geological Survey. *Photogramm. Eng. Remote Sens.* **55,** 1185–1189.

Pinter, N. (1995). Faulting on the Volcanic Tableland, Owens Valley, California. *J. Geol.* **103,** 73–83.

Pipkin, B. W., and Ploessel, M. (1985). Submarine geologic investigation for Liquefied Natural Gas Facility, southern California borderland. *Bull. Assoc. Eng. Geol.* **22,** 193–200.

Pitt, A. M., Weaver, C. S., and Spence, W. (1979). The Yellowstone Park earthquake of June 30, 1975. *Bull. Seismol. Soc. Am.* **69,** 187–205.

Plafker, G. (1965). Tectonic deformation associated with the 1964 Alaska earthquake. *Science* **148,** 1675–1687.

Plafker, G. (1969a). Surface faults on Montague Island associated with the 1964 Alaska earthquake. *U.S. Geol. Surv. Prof. Pap.* **543-G,** G1–G42.

Plafker, G. (1969b). Tectonics of the March 27, 1964 Alaska Earthquake. *U.S. Geol. Surv. Prof. Pap.* **543-I,** I1–I74.

Plafker, G. (1972). Alaskan earthquake of 1964 and Chilean earthquake of 1960-Implications for arc tectonics. *J. Geophys. Res.* **77,** 901–925.

Plafker, G. (1992). "Yo-Yo" tectonics above the eastern Aleutian subduction zone; Coseismic uplift alternating with even larger interseismic submergence. In *Wadati Conference on Great Subduction Earthquakes* (D. Christensen, M. Wyss, R. E. Habermann, and J. Davies, eds.), pp. 90–91. Fairbanks, AK.

Plafker, G., and Kachadoorian, R. (1966). Geologic effects of the March 1964 earthquake and associated seismic sea waves on Kodiak and nearby islands, Alaska. *U.S. Geol. Surv. Prof. Pap.* **543-D,** D1–D46.

Plafker, G., and Rubin, M. (1978). Uplift history and earthquake recurrence as deduced from marine terraces on Middleton Island, Alaska. *U.S. Geol. Surv. Open File Rep.* **78-943,** 687–722.

Plafker, G., and Savage, J. C. (1970). Mechanism of the Chilean earthquakes of May 21 and 22, 1960. *Geol. Soc. Am. Bull.* **81,** 1001–1030.

Plafker, G., and Ward, S. N. (1992). Back-arc thrust faulting and tectonic uplift along the Caribbean sea coast during the April 22, 1991, Costa Rica earthquakes. *Tectonics* **11,** 709–718.

Plafker, G., LaJoie, K. R., and Rubin, M. (1992). Determining recurrence intervals of great subduction zone earthquakes in southern Alaska by radiocarbon dating. In *Radiocarbon After Four Decades: An Interdisciplinary Perspective* (R. E. Taylor, A. Long, and R. S. Kra, eds.), pp. 436–453. Springer-Verlag, New York.

Plaziat, J. C., Purser, B. H., and Philobbos, E. (1990). Seismic deformation structures (seismites) in the syn-rift sediments of the NW Red Sea (Egypt). *Bull. Soc. Gieol. Fr.* [8,] **6,** 419–434.

Pollard, D. D., Delaney, P. T., Duffield, W. A., Endo, E. T., and Okamura, A. T. (1983). Surface deformation in volcanic rift zones. *Tectonophysics* **94,** 541–584.

Poreda, R. J., and Cerling, T. E. (1992). Cosmogenic neon in recent lavas from the western United States. *Geophys. Res. Lett.* **19,** 1863–1866.

Potter, P. E. (1955). The petrology and origin of the Lafayette Gravel, part II, geomorphic history. *J. Geol.* **63,** 115–132.

Power, J. A., Jolly, A. D., Stihler, S. D., Page, R. A., Lahr, L. C., Stephens, C. D., Chouet, B. A., McNutt, S. R., Davies, J. N., and March, G. D. (1992). Precursory seismicity and forecasting of the 1992 eruptions of Mount Spurr, Alaska. *EOS, Trans. Am. Geophys. Union* **73,** 342.

Pratt, B. R. (1992). Shrinkage features ("molar tooth" structure) in Proterozoic limestones; new model for their origin through synsedimentary earthquake-induced dewatering. *Geol. Soc. Am. Abtsr. with Prog.* **24**(7), 53 (abstr.).

Pratt, B. R. (1994). Seismites in the Mesoproterozoic Altyn Formation (Belt Supergroup), Montana: A test for tectonic control of peritidal carbonate cyclicity. *Geology* **22,** 1091–1094.

Prentice, C. S., and Sieh, K. E. (1989). Late Holocene record of earthquakes and slip on the San Andreas fault in excavations on the Carrizo Plain, central California. *EOS, Am. Geophys. Union* **70**(43), 1349.

Prentice, C. S., Schwartz, D. P., and Yeats, R. S. (conveners) (1994). Proceedings of the Workshop on Paleoseismology, 18-22 September 1994, Marshall, California. *U.S. Geol. Surv. Open File Rept.* **94-568,** 1–210.

Proffett, J. M., Jr. (1977). Cenozoic geology of the Yerrington distruct, Nevada, and implications for the nature and origin of Basin and Range faulting. *Geol. Soc. Am. Bull.* **88,** 247–266.

Prose, D. V. (1994a). California-Mendocino seismic. *U.S. Geol. Surv. Open File Rep.* **94-0179-F,** videotape.

Prose, D. V. (1994b). California-Landers earthquake, 1992. *U.S. Geol. Surv. Open File Rep.* **94-0179-H,** videotape.

Rapp, G., Jr. (1982). Earthquakes in the Troad. In *Troy-The Archeological Geology* (G. Rapp, Jr. and J. A. Gifford, eds.), Suppl. Monograph 4, pp. 43–58. Univ. of Cincinnati Press, Cincinnati, OH.

Rapp, G. Jr., (1986). Assessing archeological evidence for seismic catastrophes. *Geoarchaeology* **1,** 365–379.

Reches, Z., and Hoexter, D. F. (1981). Holocene seismic and tectonic activity in the Dead Sea Rift. *Tectonophysics* **80,** 235–254.

Reeder, J. W. (1979). The dating of landslides in Anchorage, Alaska-A case for earthquake-triggered movements. *Geol. Soc. Am., Abtsr. Prog.* **11**(7), 501.

Reid, H. F. (1910). The mechanism of the earthquake. In *The California Earthquake of April 18, 1906,* Report of the State Earthquake Investigation Commission. Vol. **2,** pp. 1–192. Carnegie Institution, Washington, DC.

Reilly, W. I., and Harford, B. E., eds. (1986). Recent crustal movements of the Pacific region. *Bull.- R. Soc. N. Z.* **24,** Publ. 0102, 1–583.

Reimnitz, E., and Marshall, N. F. (1965). Effects of the Alaska earthquake and tsunami on recent deltaic deposits. *J. Geophys. Res.* **70,** 2363–2376.

Reineck, H. E., and Singh, I. B. (1980). *Depositional Sedimentary Environments.* Springer-Verlag, Berlin.

Reinhart, M. A. (1992). Sedimentological analysis of postulated tsunami-generated deposits from Cascadia great-earthquakes along southern coastal Washington. M. S. paper, University of Washington, Seattle.

Reinhart, M. A., and Bourgeois, J. (1987). Distribution of anomalous sand at Willapa Bay, Washington-evidence for large-scale landward-directed processes. *EOS Trans. Am. Geophys. Union* **68,** 1469.

Reinhart, M. A., and Bourgeois, J. (1989). Tsunami favored over storm or seiche for sand deposit overlying buried Holocene peat, Willapa Bay, WA. *EOS Trans. Am. Geophys. Union* **70,** 1331.

Reiter, L. (1990). *Earthquake Hazard Analysis; Issues and Insights.* Columbia Univ. Press, New York.

Reiter, L. (1995). Paleoseismology-A user's perspective. In Perspectives in Paleoseismology (L. Serva and D. B. Slemmons, eds.), *Assoc. Eng. Geol. Spec. Publ.* **6,** 3–6.

Renard, V., and Allenau, J. P. (1979). Sea Beam, multi-beam echo-sounding in "Jean Charcot." *Int. Hydrogr. Rev.* **56,** 35–67.

Reneau, S. L., and Raymond, R., Jr. (1991). Cation-ratio dating of rock varnish; why does it work? *Geology* **19,** 937–940.

Research Group for Active Faults (1980). *Active Faults in Japan- Sheet Maps and Inventories* Univ. of Tokyo Press, Tokyo. (in Japanese with English abstr.).

Research Group for Active Faults (1991). *Active Faults in Japan- Sheet maps and Inventories* (rev. ed.). Univ. of Tokyo Press, Tokyo. (in Japanese with English abstr.).

Rhoades, D. A., Van Dissen, R. J., and Dowrick, D. J. (1994). On the handling of uncertainties in estimating the hazard of ruptures on a fault segment. *J. Geophys. Res.* **99,** 13,701–13,712.

Richter, C. F. (1935). An instrumental earthquake magnitude scale. *Bull. Seismol. Soc. Am.* **25,** 1–32.

Richter, C. F. (1958). *Elementary Seismology.* Freeman, San Francisco.

Ringrose, P. S. (1989a). Recent fault movement and paleoseismicity in western Scotland. *Tectonophysics* **163,** 305–314.

Ringrose, P. S. (1989b). Paleoseismic (?) liquefaction event in late Quaternary lake sediments at Glen Roy, Scotland. *Terra Nova* **1,** 57–62.

Robison, R. M., and Burr, T. N. (1991). Fault rupture hazard analyses using trenching and borings-Warm Springs fault, Salt Lake City, Utah. *Proc. Symp. Eng. Geol. Geotech. Eng., 27th,* Logan, UT, pp. 26-1 to 26-13.

Rockwell, T. K. (1987). Recognition of individual paleoseismic events in strike-slip environments. In *Directions in Paleoseismology* (A. J. Crone and E. M. Omdahl, eds.), *U.S. Geol. Surv. Open File Rept.* **87-673,** 129–135.

Rockwell, T. K. (1988). Neotectonics of the San Cayetano Fault, Transverse ranges, California. *Geol. Soc. Am. Bull.* **100,** 500–513.

Rockwell, T. R. (1989). Behavior of individual fault segments along the Elsinore-Laguna Salada fault zone, southern California and northern Baja California; implications for the characteristic earthquake model. In *Fault Segmentation and Controls of Rupture Initiation and Termination* (D. P. Schwartz and R. H. Sibson, eds.), *U.S. Geol. Surv. Open File Rept.* **89-315,** 288–308.

Rockwell, T. K., and Pinnault, C. T. (1986). Holocene slip events on the southern Elsinore Fault, Coyote Mountains, southern California. In *Neotectonics and Faulting in Southern California* (P. Ehlig, ed.), Guidebook Cord. Sect. Meet., Los Angeles, pp. 193–196. Geol. Soc. Am., Washington, DC.

Rockwell, T. K., Keller, E. A., Clark, M. N., and Johnson, D. L. (1984). Chronology and rates of faulting of Ventura River terraces, California. *Geol. Soc. Am. Bull.* **95,** 1466–1474.

Rockwell, T. K., McElwain, R. S., Millman, D. E., and Lamar, D. L. (1986). Recurrent late Holocene faulting on the Glen Ivy North strand of the Elsinore fault at Glen Ivy Marsh. In *Guidebook and Volume on Neotectonics and Faulting in Southern California.* Cordilleran Section. pp. 167–176. *Geol. Soc. Am.*

Rockwell, T. K., Keller, E. A., and Dembroff, G. R. (1988). Quaternary rate of folding of the Ventura Avenue anticline, western Transverse Ranges, southern California. *Geol. Soc. Am. Bull.* **100,** 850–858.

Rodgers, D. W., Hackett, W. R., and Ore, H. T. (1990). Extension of the Yellowstone plateau, eastern Snake River Plain, and Owyhee plateau. *Geology* **18,** 1138–1141.

Rogers, A. M., Walsh, T. J., Kockleman, W. J., and Priest, G. R., eds. (1995). *Assessing Earthquake Hazards and Reducing Risk in the Pacific Northwest, U.S. Geol. Surv. Prof. Pap.* **1500,** Vol. 1 (in press).

Rojstaczer, S., and Wolf, S. (1992). Permeability changes associated with large earthquakes; an example from Loma Prieta, California. *Geology* **20,** 211–214.

Rose, J. (1981). Raised shorelines. In *Geomorphological Techniques* (A. Goudie, ed.), pp. 327–341. Allen & Unwin, London.

Rosholt, J. N., Colman, S. M., Stuiver, M., Damon, P. E., Naeser, C. W., Naeser, N. D., Szabo, B. J., Muhs, D. R., Liddicoat, J. C., Forman, S. L., Machette, M. N., and Pierce, K. L. (1991). Dating methods applicable to the Quaternary. In (R. B. Morrison, ed.), *Quaternary Nonglacial Geology- Conterminous US* Geol. North Am., Vol. K-2, pp. 45–74. Geol. Soc. Am., Boulder, CO.

Roth, F. (1993). Deformation in a layered crust due to a system of cracks: Modeling the effect of dike injections or dilatancy. *J. Geophys. Res.* **98,** 4543–4551.

Rout, D. J., Cassidy, J., Locke, C. A., and Smith, I. E. M. (1993). Geophysical evidence for temporal and structural relationships within the monogenetic basalt volcanoes of the Auckland volcanic field, northern New Zealand. *J. Volcanol. Geotherm. Res.* **57,** 71–83.

Rubin, A. M. (1990). A comparison of rift-zone tectonics in Iceland and Hawaii. *Bull. Volcanol.* **52,** 302–319.

Rubin, A. M. (1992). Dike-induced faulting and graben subsidence in volcanic rift zones. *J. Geophys. Res.* **97,** 1839–1858.

Rubin, A. M. (1993). Tensile fracture of rock at high confining pressure: Implications for dike propagation. *J. Geophys. Res.* **98,** 15,919–15,936.

Rubin, A. M., and Pollard, D. D. (1988). Dike-induced faulting in rift zones of Iceland and Afar. *Geology* **16,** 413–417.

Ruegg, J. C., Kasser, M., and Lepine, J. C. (1984). Strain accumulation across the Asal-Ghoubbet rift, Djibouti, East Africa. *J. Geophys. Res.* **89,** 6237–6246.

Russ, D. P. (1979). Late Holocene faulting and earthquake recurrence in the Reelfoot Lake area, northwestern Tennessee. *Geol. Soc. Am. Bull.* **90,** 1013–1018.

Rutter, N., and Cato, N., eds. (1993). Dating Methods of Quaternary Deposits, Geosci. Can. Repr. Ser. Ed. Geol. Assoc., Canada.

Rutter, N., Brigham-Grette, J., and Catto, N., eds. (1989). Applied Quaternary geochronology. *Quat. Int.* **1** (whole volume).

Ruzhich, V. V., San'kov, V. A., and Dneprovskii, Y. I. (1982). The dendrochronological dating of seismogenic ruptures in the Stanovoi Highland. *Sov. Geol. Geophys. Engl. Transl.* **23**(8), 57–63.

Ryan, H. F., and Scholl, D. W. (1989). The evolution of forearc structures along the oblique convergence margin, central Aleutian arc. *Tectonics* **8,** 497–516.

Ryan, M. P. (1987). Neutral buoyancy and the mechanical evolution of magmatic systems. In Magmatic Processes. Physiochemical Principles (B. O. Mysen, ed.), *Geochem. Soc. Spec. Publ.* **1,** 259–287.

Ryan, M. P. (1990). The physical nature of the Icelandic magma transport system. In *Magma Transport and Storage* (M. P. Ryan, ed.), pp. 175–224. Wiley, New York.

Rymer, M. J., and Sims, J. D. (1982). Lake-sediment evidence for the date of deglaciation of the Hidden Lake area, Kenai Peninsula, Alaska. *Geology* **10,** 314–316.

Sabadini, R., Doglioni, C., and Yuen, D. A. (1990). Eustatic sea level fluctuations induced by polar wander. *Nature* (*London*) **345,** 708–710.

Sabins, F. F., Jr. (1967). Infrared imagery and geologic aspects. *Photogramm. Eng.* **29,** 83–87.

Sabins, F. F., Jr. (1969). Thermal infrared imagery and its application to structural mapping in southern California. *Geol. Soc. Am. Bull.* **80,** 397–404.

Salyards, S. L. (1985). Patterns of offset associated with the 1983 Borah Peak, Idaho, earthquake and previous events. In Proceedings of Conference XXVIII on the Borah Peak, Idaho, earthquake (R. S. Stein and R. C. Bucknam, eds.), *U.S. Geol. Surv. Open File Rept.* **85-290,** pp. 59–75.

Salyards, S. L., Sieh, K. E., and Kirschvink, J. L. (1992). Paleomagnetic measurement of nonbrittle coseismic deformation across the San Andreas fault at Pallett Creek. *J. Geophys. Res.* **97,** 12,457–12,470.

Sanders, C. O. (1989). Fault segmentation and earthquake recurrence in the strike-slip San Jacinto fault zone, California. In *Fault Segmentation and Controls of Rupture Initiation and Termination* (D. P. Schwartz and R. H. Sibson, eds.), *U.S. Geol. Surv. Open File Rep.* **89-315,** 324–349.

Sangawa, A. (1986). Fault displacement of the Kondayama Tumulus caused by earthquake. *J. Seismol. Soc. Jpn.* [2] **39,** 15–24.(in Japanese with English summary and captions).

Sangawa, A. (1992). Evidences of paleoearthquakes found out in some archaeological sites along the Median Tectonic Line. *Mem. Geol. Soc. Jpn.* **40,** 171–175 (in Japanese with English abstr.).

Sangawa, A. (1993). Research on paleoearthquakes using traces discovered at archaeological sites. *Quat. Res.* **32,** 249–256 (in Japanese with English abstr.).

Sarna-Wojcicki, A. M., Williams, K. M., and Yerkes, R. F. (1976). Geology of the Ventura Fault, Ventura County, California. *U.S. Geol. Surv. Map* **MF-781**.

Sarna-Wojcicki, A. M., Lajoie, K. R., and Yerkes, R. F. (1987). Recurrent Holocene displacement on the Javon Canyon fault- A comparison of fault-movement history with calculated average recurrence intervals. *U.S. Geol. Surv. Prof. Pap.* **1339,** 125–135.

Satake, K., Bourgeois, J., Abe, K., Tsuji, Y., Imamura, F., Iio, Y., Katao, H., Noguera, E., and Estrada, F. (1993). Tsunami field survey of the 1992 Nicaragua earthquake. *EOS, Trans. Am. Geophys. Union* **74,** 156–157.

Sato, H., Okada, A., Matsuda, T., and Kumamoto, T. (1992). Geology of a trench across the Midori fault scarp, from the Nobi earthquake of 1891, central Japan. *J. Geogr.* **7,** 556–572 (in Japanese with English abstr.).

Saucier, R. T. (1989). Evidence for episodic sand-blow activity during the 1811-12 New Madrid (Missouri) earthquake series. *Geology* **17,** 103–106.

Saucier, R. T. (1991a). Comment on "Formation of mima mounds: A seismic hypothesis." *Geology* **19,** 284.

Saucier, R. T. (1991b). Geoarchaeological evidence of strong prehistoric earthquakes in the New Madrid (Missouri) seismic zone. *Geology* **19,** 296–298.

Savage, J. C. (1995). Interseismic uplift at the Nankai subduction zone, southwest Japan, 1951-1990. *J. Geophys. Res.* **100,** 6339–6350.

Savage, J. C., and Cockerham, R. S. (1984). Earthquake swarm in Long Valley caldera, California, January 1983. Evidence for dike inflation. *J. Geophys. Res.* **89,** 8315–8324.

Savage, J. C., and Hastie, L. M. (1966). Surface deformation associated with dip-slip faulting. *J. Geophys. Res.* **71,** 4897–4904.

Savage, J. C., and Hastie, L. M. (1969). A dislocation model for the Fairview Peak, Nevada, earthquake. *Bull. Seismol. Soc. Am.* **59,** 1937–1948.

Savage, J. C., and Lisowski, M. (1991). Strain measurements and the potential for a great subduction zone earthquake off the coast of Washington. *Science* **252,** 101–103.

Savage, J. C., and Plafker, G. (1991). Tide gauge measurements of uplift along the south coast of Alaska. *J. Geophys. Res.* **96,** 4325–4335.

Savage, J. C., and Thatcher, W. (1992). Interseismic deformation at the Nankai Trough, Japan, subduction zone. *J. Geophys. Res.* **97,** 11,117–11,135.

Schiffer, M. B., and Guterman, G. J., eds. (1977). *Conservation Archeology; A Guide for Cultural Resource Management Studies.* Academic Press, New York.

Schlee, J. S., Karl, H. A., and Torresan, M. E. (1995). Imaging the sea floor. *U.S. Geol. Surv. Bull.* **2079,** 1–24.

Schoenharting, G., and Palmason, G. (1982). A gravity survey of the Reydarfjordur area, eastern Iceland, with interpretation. *J. Geophys. Res.* **87,** 6419–6422.

Schofield, J. E. (1973). Post-glacial sea levels of Northland and Auckland, New Zealand. *J. Geophys. Res.* **76,** 359–366.

Scholz, C. H. (1988). The brittle-plastic transition and the depth of seismic faulting. *Geol. Rundsch.* **77,** 319–329.

Scholz, C. H. (1990). *The Mechanics of Earthquakes and Faulting.* Cambridge Univ. Press, New York.

Schroder, J. F., Jr. (1970). Landslide landforms and the concept of geomorphic age applied to landslides. *Int. Geogr. Cong. Commun.* **1**(21), 124–126.

Schumm, S. A. (1977). *The Fluvial System.* Wiley, New York.

Schumm, S. A. (1986). Alluvial river response to active tectonics. In *Active Tectonics:* Studies in Geophysics (R. E. Wallace, chairman), pp. 195–214. Natl. Acad. Press, Washington, DC.

Schumm, S. A. (1991). *To Interpret the Earth-Ten Ways to be Wrong.* Cambridge Univ. Press, Cambridge, UK.

Schuster, R. L., and Krizek, R. J., eds. (1978). *Landslides—Analysis and Control,* Spec. Rep. **176,** Transp. Res. Board, Natl. Acad. Sci., Washington, DC.

Schuster, R. L., Logan, R. L., and Pringle, P. T. (1992). Prehistoric rock avalanches in the Olympic Mountains, Washington. *Science* **258,** 1620–1621.

Schwartz, D. P. (1988a). Geologic characterization of seismic sources- moving into the 1990's. In *Recent Advances in Ground-Motion Evaluation* (J. L. Von Thun, ed.), Earthquake Eng. Soil Dyn. II, Geotech. Spec. Publ., **20,** pp. 1–42. Am. Soc. Civ. Eng., New York.

Schwartz, D. P. (1988b). Paleoseismicity and neotectonics of the Cordillera Blanca fault zone, northern Peruvian Andes. *J. Geophys. Res.* **93,** 4712–4730.

Schwartz, D. P. (1989). Paleoseismicity, persistence of segments, and temporal clustering of large earthquakes- examples from the San Andreas, Wasatch, and Lost River fault zones. In *Fault Segmentation and Controls of Rupture Initiation and Termination* (D. P. Schwartz, and R. H. Sibson, eds.), *U.S. Geol. Surv. Open File Rept.* **89-315,** 361–375.

Schwartz, D. P., and Coppersmith, K. J. (1984). Fault behavior and characteristic earthquakes-Examples from the Wasatch and San Andreas fault zones. *J. Geophys. Res.* **89,** 5681–5698.

Schwartz, D. P., and Coppersmith, K. J. (1986). Seismic hazards; new trends in analysis using geologic data. In *Active Tectonics:* Studies in Geophysics (R. E. Wallace, chairperson), pp. 215–230. Natl. Acad. Press, Washington, DC.

Schwartz, D. P., and Crone, A. J. (1985). The 1983 Borah Peak earthquake: A calibration event for quantifying earthquake recurrence and fault behavior on Great Basin normal faults. *U.S. Geol. Surv. Open File Rep.* **85-290,** 153–160.

Schwartz, D. P., and Sibson, R. H., eds. (1989a). Fault segmentation and controls of rupture initiation and termination. *U.S. Geol. Surv. Open File Rep.* **89-315,** 1–447.

Schwartz, D. P., and Sibson, R. H. (1989b). Introduction. In *Fault Segmentation and Controls of Rupture Initiation and Termination* (R. H. Sibson and D. P. Schwartz, eds.), *U.S. Geol. Surv. Open File Rep.* **89-315,** i–iv.

Schwartz, E. J., Hood, P. J., and Teskey, D. J. (1987). Magnetic expression of Canadian diabase dykes and downward modelling. In Mafic Dyke Swarms (H. C. Halls and W. F. Fahrig, eds.), *Spec. Pap- Geol. Assoc. Can.* **34,** 153–162.

Scott, E. M., Cook, G. T., Harkness, D. D., Miller, B. F., and Baxter, M. S. (1992). Further analysis of the international intercomparison study (ICS). *Radiocarbon* **34,** 520–527.

Scott, R. F. (1986). Solidification and consolidation of a liquefied sand column. *Soils and Found., Jpn. Soc. Soil Mech. Found. Eng.* **26,** 23–31.

Scott, R. F., and Zuckerman, K. A. (1973). Sandblows and liquefaction. In *The Great Alaska Earthquake of 1964- Engineering,* pp. 179–189. Natl. Acad. Sci., Washington, DC.

Searle, R. G. (1979). Side-scan sonar studies of the North Atlantic fracture zones. *J. Geol. Soc. London* **136,** 283–292.

Seed, H. B. (1968). Landslides during earthquakes due to soil liquefaction. *J. Soil Mech. Found. Div., Am. Soc. Civ. Eng.* **94,** 1055–1122.

Seed, H. B. (1979a). Considerations in the earthquake-resistant design of earth and rockfill dams. *Geotechnique* **29,** 215–263.

Seed, H. B. (1979b). Soil liquefaction and cyclic mobility for level ground during earthquakes. *J. Geotech. Eng., Am. Soc. Civ. Eng.* **105,** 201–255.

Seed, H. B., and Idriss, I. M. (1971). A simplified procedure for evaluating soil liquefaction potential. *J. Soil Mech. Found. Eng., Am. Soc. Civ. Eng.* **97,** 1249–1274.

Seed, H. B., Idriss, I. M., and Arango, I. (1983). Evaluation of liquefaction potential using field performance data. *J. Geotech. Eng., Am. Soc. Civ. Eng.* **109,** 458–482.

Seed, H. B., Tokimatsu, K., Harder, L. F., and Chung, R. M. (1985). Influence of SPT procedures in soil liquefaction resistance evaluation. *J. Geotech. Eng., Am. Soc. Civ. Eng.* **111**(12), 1425–1445.

Seguret, M., Labaume, P., and Madariaga, R. (1984). Eocene seismicity in the Pyrenees from megaturbidites on the South Pyrenean Basin, Spain. *Mar. Geol.* **55,** 117–131.

Seilacher, A. (1969). Fault-graded beds interpreted as seismites. *Sedimentology* **13,** 155–159.

Seilacher, A. (1984). Sedimentary structures tentatively attributed to seismic events. *Mar. Geol.* **55,** 1–12.

Selby, M. J. (1993). *Hillslope Materials and Processes, 2nd ed.* Oxford Univ. Press, Oxford, UK.

Serva. L., and Slemmons, D. B., eds. (1995a). *Perspectives in Paleoseismology,* Spec. Publ. 6. Assoc. Eng. Geol.

Serva. L., and Slemmons, D. B. (1995b). Introduction. In *Perspectives in Paleoseismology* (L. Serva and D. B. Slemmons, eds.), Spec. Publ., 6, p. 1. Assoc. Eng. Geol.

Sharp, R. V. (1982). Comparison of 1979 surface faulting with earlier displacements in the Imperial Valley. *U.S. Geol. Surv. Prof. Pap.* **1254,** 213–222.

Sharp, R. V., Lienkaemper, J. J., Bonilla, M. G., Burke, D. B., Fox, B. F., Herd, D. G., Miller, D. M., Morton, D. M., Ponti, D. J., Rymer, M. J., Tinsley, J. C., and Yount, J. C. (1982). Surface faulting in the central Imperial Valley. *U.S. Geol. Surv. Prof. Pap.* **1254,** 119–144.

Sharp, R. V., Budding, K. E., Ader, M. J., Bonilla, M. G., Boatwright, J., Clark, M. M., Fumal, T. E., Harms, K. K., Lienkaemper, J. J., Morton, D. M., O'Neill, B. J., Ostergren, C. L., Ponti, D. J., Rymer, M. J., Saxton, J. L., and Sims, J. D. (1989). Surface faulting associated with the Superstition Hills earthquakes of November 24, 1987. *Bull. Seismol. Soc. Am.* **79,** 252–281.

Shennan, I. (1989). Holocene crustal movements and sea-level change in Great Britain. *J. Quat. Sci.* **4,** 77–90.

Sheppard, J. C. (1975). *A Radiocarbon Dating Primer.* Bull. No. 338. Washington State University, Coll. Eng. Res., Pullman.

Sheppard, P. R., and Jacoby, G. C. (1989). Application of tree ring analysis to paleoseismology-2 case studies. *Geology* **17,** 226–229.

Sheppard, P. R., and White, L. O. (1995). Tree-ring responses to the 1978 earthquake at Stephens Pass, northeastern California. *Geology* **23,** 109–112.

Sherburn, S. (1992a). Characteristics of earthquake sequences in the Central Volcanic Region New Zealand. *N. Z. J. Geol. Geophys.* **35,** 57–68.

Sherburn, S. (1992b). Seismicity of the Lake Taupo region New Zealand. *N. Z. J. Geol. Geophys.* **35,** 331–335.

Shimazaki, K., and Nakata, T. (1980). Time-predictable recurrence model for large earthquakes. *Geophys. Res. Lett.* **7,** 279–282.

Shimozuru, D., and Kagiyama, T. (1989). Some significant features of pre-eruption volcanic earthquakes. In *Volcanic Hazards* (J. H. Latter, ed.), *IAVCEI Proc. Volcanology,* Vol. **1,** pp. 504–512. Springer-Verlag, Berlin.

Shlemon, R. J. (1985). Application of soil-stratigraphic techniques to engineering geology. *Bull. Assoc. Eng. Geol.* **22,** 129–142.

Sibson, R. H. (1982). Fault zone models, heat flow, and depth distribution of earthquakes in the continental crust of the United States. *Bull. Seismol. Soc. Am.* **72,** 151–163.

Sibson, R. H. (1985). A note on fault reactivation. *J. Struct. Geol.* **7,** 751–754.

Sibson, R. H. (1986). Earthquakes and rock deformation in crustal fault zones. *Ann. Rev. Earth Planet. Sci.* **14,** 149–175.

Siebert, L. (1984). Large volcanic debris avalanches: Characteristics of source areas, deposits and associated eruptions. *J. Volcanol. Geotherm. Res.* **22,** 163–197.

Siegel, R. A. (1978). *STABL User Manual.* Purdue University, West Lafayette, IN.

Sieh, K. E. (1977). A study of late Holocene displacement history along the south-central reach of the San Andreas fault. Ph.D. Dissertation, Stanford University, Stanford, CA.

Sieh, K. E. (1978a). Prehistoric large earthquakes produced by slip on the San Andreas fault at Pallet Creek, California. *J. Geophys. Res.* **83,** 3907–3939.

Sieh, K. E. (1978b). Slip along the San Andreas fault associated with the great 1857 earthquake. *Bull. Seismol. Soc. Am.* **68,** 1421–1448.

Sieh, K. E. (1981). A review of geological evidence for recurrence times for large earthquakes. In *Earthquake Prediction, An International Review* (D. W. Simpson and P. G. Richards, eds.), Maurice Ewing Ser., Vol. **4,** pp. 181–207. Am. Geophys. Union, Washington, DC.

Sieh, K. E. (1984). Lateral offsets and revised dates of large prehistoric earthquakes at Pallett Creek, southern California. *J. Geophys. Res.* **89,** 7641–7670.

Sieh, K. E., and Bursik, M. (1986). Most recent eruption of the Mono Craters, eastern central California. *J. Geophys. Res.* **91,** 12539–12571.

Sieh, K. E., and Jahns, R. H. (1984). Holocene activity of the San Andreas fault at Wallace Creek, California. *Geol. Soc. Am. Bull.* **95,** 883–896.

Sieh, K. E., Stuiver, M., and Brillinger, D. (1989). A more precise chronology of earthquakes produced by the San Andreas fault in southern California. *J. Geophys. Res.* **94,** 603–623.

Sieh, K. E., Jones, L., Hauksson, E., Hudnut, K., Eberhart-Phillips, D., Heaton, T., Hough, S., Hutton, K., Kanamori, H., Lilje, A., Lindvall, S., McGill, S. F.; Mori, J., Rubin, C., Spotila, J. A., Stock, J., Thio, H.-K., Treiman, J., Wernicke, B., and Zachariasen, Z. (1993). Near-field investigations of the Landers earthquake sequence, April to July 1992. *Science* **260,** 171–176.

Sigurdsson, H. (1980). Surface deformation of the Krafla fissure swarm in two rifting events. *J. Geophys.* **47,** 154–159.

Sims, J. D. (1973). Earthquake-induced structures in sediments of Van Norman Lake, San Fernando, California. *Science* **182,** 161–163.

Sims, J. D. (1975). Determining earthquake recurrence intervals from deformational structures in young lacustrine sediments. *Tectonophysics* **29,** 141–152.

Sims, J. D. (1978). Annotated bibliography of penecontemporaneous deformational structures in sediments. *U.S. Geol. Surv. Open File Rept.* **78-510,** 1–79.

Sims, J. D., and Garvin, C. D. (1995). Recurrent liquefaction induced by the 1989 Loma Prieta earthquake and 1990 and 1991 aftershocks: Implications for paleoseismicity studies. *Bull. Seismol. Soc. Am.* **85,** 51–65.

Slemmons, D. B. (1957). Geological effects of the Dixie Valley- Fairview Peak, Nevada, earthquakes of December 16, 1954. *Bull. Seismol. Soc. Am.* **47,** 353–375.

Slemmons, D. B. (1977). State-of-the-Art for Assessing Earthquake Hazards in the US, Rep. No. 6, *Misc. Pap.* **S-73-1.** U.S. Army Corps of Engineers, Waterways Exp. Stn., Vicksburg, MS.

Slemmons, D. B. (1981). A procedure for analyzing fault-controlled lineaments and the activity of faults. In *Basement Tectonics.* (D. W. O'Leary and J. L. Earle, eds.), *Basement Tect. Comm. Publ.* **3,** 33–49.

Slemmons, D. B. (1982). Determination of design earthquakes magnitudes for microzonation. In Proc. Third Int. Earthquake Microzon. Conf., Seattle, WA; *Earthquake Eng. Res. Inst.* **1,** 110–130.

Slemmons, D. B. (1995). Complications in making paleoseismic evaluations in the Basin and Range province, western United States. In Perspectives in Paleoseismology (L. Serva and D. B. Slemmons, eds.), *Assoc. Eng. Geol. Spec. Publ.* **6,** 19–34.

Slemmons, D. B., and dePolo, C. M. (1986). Evaluation of active faulting and related hazards. In Active Tectonics. Studies in Geophysics (R. E. Wallace, chairman), pp. 45–62. Natl. Acad. Press, Washington, DC.

Slemmons, D. B., Engdahl, E. R., Zoback, M. D., and Blackwell, D. D., eds. (1991). Neotectonics of North America- Decade Map Volume to Accompany the Neotectonic Maps, Part of the Continent-Scale Maps of North America. Geol. Soc. Am., Boulder, CO.

Small, R. J., and Clark, M. J. (1982). *Slopes and Weathering.* Cambridge Univ. Press, Cambridge, UK.

Smart, P. L., and Frances, P. D. (1991). *Quaternary Dating Methods-A User's Guide,* Tech. Guide 4. Quaternary Research Association, Cambridge, UK.

Smirnova, T. Y., and Nikonov, A. A. (1990). A revised lichenometric method and its application dating great past earthquakes. *Arct. Alp. Res.* **22,** 375–388.

Smith, D. G., and Jol, H. M. (1995), Wasatch fault (Utah), detected and displacement characterized by ground penetrating radar. *Environ. Eng. Geosci.* **1** (4), 489–496.

Smith, E. G. C., and Oppenheimer, C. M. M. (1989). The Edgecumbe earthquake sequence: 1987 February 21 to March 18. *N. Z. J. Geol. Geophys.* **32,** 31–42.

Smith, R. B., and Braile, L. W. (1994). The Yellowstone hotspot. *J. Volcanol. Geotherm. Res.* **61,** 121–187.

Smith, R. B., and Bruhn, R. L. (1984). Intraplate extensional tectonics of the eastern Basin and Range: Inferences on structural style from seismic reflection data, regional tectonics, and thermal-mechanical models of brittle-ductile deformation. *J. Geophys. Res.* **89,** 5733–5769.

Smith, R. P., Hackett, W. R., and Rogers, D. W. (1989). Geological Aspects of seismic hazards assessments at the INEL, Southeastern Idaho. *Proc. DOE Natl. Hazards Mit. Conf., 2nd,* Knoxville, TN. pp. 282–289.

Smith, R. P., Jackson, S. M., and Hackett, W. R. (1996). Paleoseismology and seismic hazards evaluations in extensional volcanic terrains. *J. Geophys. Res.* **101**(B3), 6277–6292.

Smith, T. E. (1967). Aeromagnetic measurements in Dixie Valley, Nevada; implications regarding Basin-and-Range structure. *J. Geophy. Res.* **73,** 1321–1331.

Soiltest, Inc. (1977). Sampling and drilling soil and rock. In *Subsurface Geology- Petroleum, Mining, and Construction* (L. W. Leroy, D. O. Leroy, and J. W. Raese, eds.), pp. 647–651. Colorado School Mines Press, Golden, CO.

Solonenko, V. P. (1962). Identification of epicentral zones of earthquakes by geological features. *Izv. Acad. Sci. USSR, Ser. Geophys.* **11,** 38–74 (in Russian).

Solonenko, V. P. (1970). The paleoseismogeological method. In Large Earthquakes in Soviet Central Asia and Khazakstan, Vol. **1**, pp. 83–93. Donish, Dushanbe, USSR, (in Russian).

Solonenko, V. P. (1973). Paleoseismogeology. *Izv. Acad. Sci. USSR, Phys. Solid Earth* **9,** 3–16 (in Russian).

Solonenko, V. P. (1977a). Seismogenic deformations and the paleoseismogeological method, in Solonenko, V. P., ed., Seismic Zonation of Eastern Siberia and its Geological and Geophysical Basis: Nauka Publ. House, Novosibirsk, p. 5–47.

Solonenko, V. P. (1977b'). Landslides and collapses in seismic zones and their prediction. *Bull. Int. Assoc. Eng. Geol.* **15,** 4–8.

Soule, C. H. (1978). Paleoseismicity as deduced from studies of stream terraces of tectonic origin. *Geol. Soc. Am., Abtsr. Prog.* **3,** 495–496.

Spalletta, C., and Vai, G. B. (1984). Upper Devonian intraclast parabreccias interpreted as seismites. *Mar. Geol.* **55,** 133–144.

Speight, R. (1938). Recent faulting in the Southern Alps. *N. Z. J. Sci. Technol. Sect. B* **19,** 701–708.

Stafford, T. W., Jr., and Forman, S. L. (1993). Radiocarbon and thermoluminescence dating of Wasatch faulting events, Garner Canyon, Utah. *Utah Geol. Surv. Contract Rep.* **93-4,** 1–15.

Stafford, T. W., Jr., Hare, P. E., Jull, A. J. T., and Donahue, D. J. (1991). Accelerator radiocarbon dating at the molecular level. *J. Archaeol. Sci.* **18,** 35–72.

Stahle, D. W., VanArsdale, R. B., and Cleaveland, M. K. (1992). Tectonic signal in bald-cypress trees at Reelfoot Lake, Tennessee. *Seismol. Res. Lett.* **63,** 439–447.

Stearns, H. T. (1985). *Geology of the State of Hawaii,* 2nd ed. Pacific Books, Palo Alto, CA.

Steele, F., Daniels, R. B., Gamble, E. E., and Nelson, L. A. (1969). Fragipan horizons and Be masses in the middle coastal plain of north central North Carolina. *Soil Sci. Soc. Am. Proc.* **33,** 752–755.

Stein, R. S. (1983). Reverse slip on a buried fault during the 2 May 1983 Coalinga earthquake; Evidence from geodetic elevation changes. In The 1983 Coalinga, California Earthquakes (J. H. Bennett and R. W. Sherburne, eds)., *Spec. Publ.- Calif. Div. Mines Geol.* **66,** 151–163.

Stein, R. S., and Barrientos, S. E. (1985). Planar high-angle faulting in the Basin and Range: Geodetic analysis of the 1983 Borah Peak, Idaho, earthquake. *J. Geophys. Res.* **90,** 11,355–11,366.

Stein, R. S., and King, G. C. P. (1984). Seismic potential revealed by surface folding; 1983 Coalinga, California, earthquake. *Science* **224,** 867–872.

Stein, R. S., and Yeats, R. S. (1989). Hidden earthquakes. *Sci. Am.* **260**(6), 48–57.

Stein, R. S., King, G. C., and Rundle, J. B. (1988). The growth of geological structures by repeated earthquakes. 2 Field examples of continental dip-slip faults. *J. Geophys. Res.* **93,** 13,319–13,331.

Stein, R. S., Briole, P., Ruegg, J. C., Tapponnier, P., and Gasse, F. (1991). Contemporary, Holocene, and Quaternary deformation of the Asal rift, Djibouti: Implications for the mechanics of slow-spreading ridges. *J. Geophys. Res.* **96,** 21,789–21,806.

Stephenson, W. J., Smith, R. B., and Pelton, J. R. (1993). A high-resolution seismic reflection and gravity survey of Quaternary deformation across the Wasatch fault, Utah. *J. Geophys. Res.* **98,** 8211–8223.

Stewart, I. S., and Hancock, P. L. (1988). Normal fault zone evolution and fault scarp degradation in the Aegean region. *Basin Res.* **1,** 139–153.

Stewart, I. S., and Hancock, P. L. (1990). What is a fault scarp? *Episodes* **13,** 256–263.

Stiros, S. C. (1988a). Earthquake effects on ancient constructions. In *New Aspects of Archaeological Science in Greece* (R. E. Jones, and H. W. Catling, eds.), Occas. Pap. No. 3, pp. 1–6. Fitch Lab., British School at Athens, Athens, Greece.

Stiros, S. C. (1988b). Archeology- a tool to study active tectonics. *EOS, Trans. Am. Geophys. Union* **69**(50), 1633, 1639.

Stiros, S. C. (1996) Identification of earthquakes from archaeological data: Methodology, criteria, and limitations. In Stiros, S. C., and Jones, R. E., eds. (1996). *Archaeoseismology.* Fitch Lab. Occas. Pap. 7, British School at Athens and Inst. Geol. Min. Explor., Oxbow Books, Oxford, UK, 129–152.

Stiros, S. C., and Jones, R. E. (1996). *Archaeoseismology.* Fitch Lab. Occas. Pap. 7, British School at Athens and Inst. Geol. Min. Explor., Oxbow Books, Oxford, UK.

Stone, J. R., and Ashley, G. M. (1992). Ice-wedge casts, pingo scars, and the drainage of glacial Lake Hitchcock. In *Guidebook for Field Trips in the Connecticut Valley Region of Massachusetts and Adjacent States* (P. Robinson, and J. B. Brady, eds.), Vol. **2,** Contrib. 66, pp. 305–331. Dep. Geol. Geogr., University Massachusetts, Amherst.

Stout, M. L. (1969). Radiocarbon dating of landslides in southern California and engineering geology implications. In *United States Contributions to Quaternary Research* (S. A. Schumm, and W. C. Bradley, eds.), *Spec. Pap.- Geol. Soc. Am.* **123,** 167–179.

Stout, M. L. (1977). Radiocarbon dating of landslides in southern California. Calif. Div. Mines Geol., *Calif. Geol.,* May, pp. 99–105.

Stover, C. W., and Coffman, J. L. (1993). Seismicity of the United States, 1568-1989 (revised). *U.S. Geol. Surv. Prof. Pap.* **1527,** 1–418.

Stuiver, M., and Kra, R. (1986). Calibration issue-Proceedings of the 12th International Radiocarbon Conference, Trondheim, Norway. *Radiocarbon:* **28**(2B), 1–225.

Stuiver, M., and Polach, H. A. (1977). Discussion: reporting of ^{14}C data. *Radiocarbon* **19,** 355–363.

Stuiver, M., and Reimer, P. J. (1993). Extended ^{14}C data base and revised CALIB 3.0 ^{14}C age calibration program. *Radiocarbon* **35,** 215–230.

Suggate, R. P. (1960). The interpretation of progressive fault displacement by flights of terraces. *N. Z. J. Geol. Geophys.* **3,** 364–374.

Suggate, R. P., Stevens, G. R., and Te Punga, M. T., eds. (1978). *The Geology of New Zealand,* 2 vols. New Zealand Geol. Surv., Wellington.

Sugimura, A., and Matsuda, T. (1965). Atera fault and its displacement vectors. *Geol. Soc. Am. Bull.* **76,** 509–522.

Sugimura, A., and Naruse, Y. (1954). Changes in sea-level, seismic upheavals and coastal terraces in southern Kanto region, Japan. *Jpn. J. Geol. Geophys.* **24,** 101–113.

Sullivan, J. T., and Nelson, A. R. (1983). Late Cenozoic faulting in Heber and Keetley Valleys, northeastern Utah. In *Geologic Excursions in Neotectonics and Engineering Geology in Utah* (K. D. Gurgel, ed.), *Spec. Stud.- Utah Geol. Miner Surv.* **62,** 55–62.

Summerfield, M. A. (1989). Tectonic geomorphology: Convergent plate boundries, passive continental margins, and supercontinent cycles. *Prog. Phys. Geogr.* **13,** 431–441.

Summerfield, M. A. (1991a). Tectonic geomorphology. *Prog. Phys. Geogr.* **15,** 193–205.

Summerfield, M. A. (1991b). *Global Geomorphology.* Longman, London.

Suppe, J. (1983). Geometry and kinematics of fault-bend folding. *Am. J. Sci.* **283,** 684–721.

Suppe, J. (1985). *Principals of Structural Geology.* Prentice-Hall, New York.

Swan, F. H., III (1988). Temporal clustering of paleoseismic events on the Oued Fodda fault, Algeria. *Geology* **16,** 1092–1095.

Swan, F. H., III, Schwartz, D. P., and Cluff, L. S. (1980). Recurrence of moderate to large magnitude earthquakes produced by surface faulting on the Wasatch fault, Utah. *Bull. Seismol. Soc. Am.* **70,** 1431–1462.

Swan, F. H., III, Schwartz, D. P., Hanson, K. L., Knuepfer, P. L., and Cluff, L. S. (1981). Study of earthquake recurrence intervals on the Wasatch fault at the Kaysville site, Utah. *U.S. Geol. Surv. Open File Rept.* **81-228,** 1–30.

Swanson, D. A., Jackson, D. B., Koyanagi, R. Y., and Wright, T. L. (1976a). The February 1969 East Rift eruption of Kilauea volcano, Hawaii. *U.S. Geol. Surv. Prof. Pap.* **891,** 1–30.

Swanson, D. A., Duffield, W. A., and Fiske, R. S. (1976b). Displacement of the south flank of Kilauea volcano: The result of forceful intrusion of magma into the rift zones. *U.S. Geol. Surv. Prof. Pap.* **963,** 1-39.

Swanson, D. A., Wright, T. L., and Zeitz, I. (1979). Aeromagnetic map and geologic interpretation of the west-central Columbia Plateau, Washington and adjacent Oregon. *U.S. Geol. Surv. Geophys. Invest. Map* **GP-917.**

Sykes, L. R., and Nishenko, S. P. (1984). Probabilities of occurrence of large plate rupturing earthquakes for the San Andreas, San Jacinto, and Imperial faults, California, 1983-2003. *J. Geophys. Res.* **89,** 5905-5927.

Sykes, L. R., and Quittmeyer, R. C. (1981). Repeat times of great earthquakes along simple plate boundaries. In *Earthquake Prediction: An International Review* (D. W. Simpson and P. G. Richards, eds.), Maurice Ewing Ser., Vol. **4**. pp. 217-247. Am. Geophys. Union, Washington, DC.

Sylvester, A. G. (1988). Strike-slip faults. *Geol. Soc. Am. Bull.* **100,** 1666-1703.

Taber, S. (1914). Seismic activity in the Atlantic Coastal Plain near Charleston, S. C. *Bull. Seismol. Soc. Am.* **4,** 108-160.

Tabor, R. W. (1971). Origin of ridge-top depressions by large-scale creep in the Olympic Mountains, Washington. *Geol. Soc. Am. Bull.* **82,** 1811-1822.

Takeo, M. (1992). The rupture process of the 1989 offshore Ito earthquake preceding a submarine volcanic eruption. *J. Geophys. Res.* **97,** 6613-6628.

Tallis, J. H., and Johnson, R. H. (1980). The dating of landslides in Longdendale, north Derbyshire, using pollen-analytical techniques. In *Timescales in Geomorphology* (R. A. Cullingford, D. A. Davidson, and J. Lewin, eds.), pp. 189-205. Wiley, New York.

Tanigawa, W. R., Nakata, J. S., and Klein, F. W. (1981). Hawaiian Volcano Observatory Summary 80. Part 1. Seismic data, January to December 1980. Unpublished. *U.S. Geol. Surv. Rep.*, Hilo, HI.

Tanigawa, W. R., Nakata, J. S., and Klein, F. W. (1983). Hawaiian Volcano Observatory Summary 82. Part 1. Seismic data, January to December 1980. Unpublished. *U.S. Geol. Surv. Rep.*, Hilo, HI.

Tarantola, A., Ruegg, J. C., and Lepine, J. P. (1979). Geodetic evidence for rifting in Afar: A brittle-elastic model of the behavior of the lithosphere. *Earth Planet. Sci. Lett.* **45,** 435-444.

Tarantola, A., Ruegg, J .C., and Lepine, J. P. (1980). Geodetic evidence for rifting in Afar: 2. Vertical displacements. *Earth Planet. Sci. Lett.* **48,** 363-370.

Taylor, R. E. (1987). *Radiocarbon Dating- An Archaeological Perspective.* Academic Press, Orlando, FL.

Taylor, R. E., Long, A., and Kra, R. S. (1992). *Radiocarbon After Four Decades-An Interdisciplinary Perspective.* Springer-Verlag, New York.

Tchalenko, J. S., and Ambraseys, N. N. (1970). Structural analysis of the Dasht-e-Bayaz (Iran) earthquake fractures. *Geol. Soc. Am. Bull.* **81,** 41-60.

Telford, W. M., Geldart, L. P., and Sheriff, R. E. (1990). *Applied Geophysics,* 2nd ed. Cambridge Univ. Press, New York.

Terasmae, J. (1975). Dating of landslides in the Ottawa River valley by dendrochronologyA brief comment. In *Mass Wasting* (E. Yatsu, A. J. Ward, and Adams, F., eds.), Proc. 4th Guelph Symp. Geomorphol., pp. 153-158. Norwich, GeoAbstracts, Norwich, UK.

Terzaghi, K., and Peck, R. B. (1967). *Soil Mechanics in Engineering Practice.* Wiley, New York.

Thatcher, W. (1984). The earthquake deformation cycle, recurrence, and the time-predictable model. *J. Geophys. Res.* **89,** 5674-5680.

Thatcher, W. (1986a). Cyclic deformation related to great earthquakes at plate boundaries. In Recent Crustal Movements of the Pacific Region (W. I. Reilly and B. E. Harford, eds.), *Bull.-R. Soc. N. Z.* **24,** 245-272.

Thatcher, W. (1986b). Geodetic measurement of active-tectonic processes. In Active Tectonics: Studies in Geophysics (R. E. Wallace, chairman), pp. 155-163. Natl. Acad. Sci., Washington, DC.

Thatcher, W. (1990). Order and diversity in the modes of circum-Pacific earthquake recurrence. *J. Geophys. Res.* **95,** 2609-2624.

Thatcher, W., and Bonilla, M. G. (1989). Earthquake fault slip estimation from geologic, geodetic, and seismologic observations; implications for earthquake mechanics and fault segmentation. In *Fault Segmentation and Controls on Rupture Initiation and Termination* (D. P. Schwartz and R. H. Sibson, eds.), U. S. Geol. Surv. Open File Rep. **89-315,** 386-399.

Thatcher, W., and Lisowski, M. (1987). Long-term seismic potential of the San Andreas fault southeast of San Francisco. *J. Geophys. Res.* **92,** 4771-4784.

Thompson, L. J., and Tannenbaum, R. J. (1977). Survey of construction related trench cave-ins. *J. Struct. Div., Am. Soc. Civ. Eng.* **103,** 501-512.

Tibaldi, A., Ferrari, L., and Pasquarè, G. (1995). Landslides triggered by earthquakes and their relations with faults and mountain slope geometry: An example from Ecuador. *Geomorphology* **11,** 215-226.

Tilling, R. I., and Dvorak, J. J. (1993). Anatomy of a basaltic volcano. *Nature* (*London*) **363,** 125-133.

Tokimatsu, K., and Seed, H. B. (1987). Evaluation of settlements in sands due to earthquake shaking. *J. Geotech. Eng., Am. Soc. Civ. Eng.* **113,** 861-878.

Treadway, J. A., Steeples, D. W., and Miller, R. D. (1988). Shallow seismic study of a fault scarp near Borah Peak, Idaho. *J. Geophys. Res.* **93,** 6325-6337.

Tricart, J. (1965). La cartographie geomorphologique detailee. In *Principe et Méthodes de la Géomorphologie,* pp. 182-215. Maisson, Paris.

Trifonov, V. G., Makarov, V. I., and Skobelev, S. F. (1992). The Talas-Fergana active right-lateral fault. *Ann. Tectonicae* **6,** suppl. 224-237.

Tryggvason, E. (1983). The widening of the Krafla fissure swarm during the 1975-1981 volcano-tectonic episode. *Nor. Volcanol. Inst. Rep.* **8304,** 1-48.

Tsukuda, E., and Yamazaki, H. (1984). Excavation survey of active faults for earthquake prediction in Japan-with special reference to the Ukihashi Central fault and the Atera Fault. *Geol. Surv. Jpn. Rep.* **263,** 349-361.

Tsukuda, E., Awata, Y., Yamazaki, H., Sugiyama, Y., Shimokawa, K., and Mizuno, K. (1993). Strip map of the Atera fault system. *Geol. Surv. Jpn. Tect. Map Ser.* **7,** Scale 1:25,000.

Tuttle, M. P. (1994). The liquefaction method for assessing paleoseismicity: *U.S. Nucl. Regul. Comm., NUREG/CR* **6258,** 1-38.

Tuttle, M. P., and Schweig, E. C. (1995). Archeological and pedological evidence for large prehistoric earthquakes in the New Madrid seismic zone, central United States. *Geology* **23,** 253-256.

Tuttle, M. P., and Seeber, L. (1991). Historic and prehistoric earthquake-induced liquefaction in Newbury, Massachusetts. *Geology* **19,** 594-597.

Tuttle, M. P., Cowie, P., and Wolf, L. (1992). Liquefaction induced by modern earthquakes as a key to paleoseismicity: A case study of the 1988 Saguenay event. *U.S. Nucl. Regul. Comm., NUREG/CP* **0119(3),** 437-462.

U.S. Geological Survey Staff (USGS) (1971). Surface faulting, in the San Fernando, California, earthquake of February 9, 1971. *U.S. Geol. Surv. Prof. Pap.* **733,** 55-76.

U.S. Geological Survey Staff (USGS) (1994). The magnitude 6.7 Northridge, California, earthquake of 17 January, 1994. *Science* **266,** 389-397.

U.S. Occupational Safety and Health Administration (OSHA) (1989). Occupational safety and health standards- Excavations; Final Rule. *Fed. Reg.,* **29 CFR 1926, 54**(209), 45894-45991 (also reprinted by the Assoc. Eng. Firms Pract. Geosci., Silver Springs, MD).

Utah Section, Association of Engineering Geologists (1987). Guidelines for evaluating surface fault rupture hazard in Utah. *Misc. Publ.- Utah Geol. Miner. Surv.* **N,** 1-2.

Valera, J. E., Traubenik, M. L., Egan, J. A., and Kaneshiro, J. Y. (1994). A practical perspective on liquefaction of gravels. In *Ground Failures Under Seismic Conditions* (S. Prakash and Dakoulas eds.), *Am. Soc. Civil Eng., Geotech. Spec. Publ.* **44,** 241-257.

Vandenberghe, J. (1988). Cryoturbations. In *Advances in Periglacial Geomorphology* (M. J. Clark, ed.), pp. 179–198. Wiley, New York.

van de Plassche, O., ed. (1986). *Sea-Level Research; A Manual for the Collection and Evaluation of Data.* Geo Books, Norwich, UK.

Van Dissen, R. J., Berryman, K. R., Pettinga, J. R., and Hill, N. L. (1992). Paleoseismicity of the Wellington-Hutt Valley segment of the Wellington Fault, North Island, New Zealand. *N. Z. J. Geology Geophys.* **35,** 165–176.

van Loon, A. J. (1992). The recognition of soft-sediment deformations as early-diagenetic features—A literature review. In K. H. Wolf and G. V. Chilingarian, eds., *Developments in Sedimentology,* **47,** 135–189, Elsevier.

Varnes, D. J. (1978). Slope movement types and processes. In *Landslides—Analysis and Control* (R. L. Schuster and R. J. Krizek eds.), Spec. Rep. **176,** pp. 11–33. Transp. Res. Board, Natl. Acad. Sci., Washington, DC.

Varnes, D. J., Radbruch-Hall, D. H., and Savage, W. Z. (1989). Topographic and structural conditions in areas of gravitational spreading of ridges in the western United States. *U.S. Geol. Surv. Prof. Pap.* **1496,** 1–28.

Varnes, D. J., Radbruch-Hall, D. H., and Savage, W. Z. (1989). Topographic and structural conditions in areas of gravitational spreading of ridges in the western United States. *U.S. Geol. Surv. Prof. Pap.* **1496,** 1–28.

Vendeville, B., and Cobbold, P. R. (1988). How normal faulting and sedimentation interact to produce listric fault profiles and stratigraphic wedges. *J. Struct. Geol.* **10,** 649–659.

Verstappen, H. Th., and van Zuidam (1968). *ITC System of Geomorphological Survey.* ITC Textbook of Photointerpretation, Delft, The Netherlands.

Vick, G. S. (1988). Late Holocene paleoseismicity and relative sea level changes of the Mad River Slough, northern Humboldt Bay, California. M. S. Thesis, Humboldt State University, Arcata, CA.

Vincent, K. R. (1985). Measurement of vertical tectonic offset using longitudinal profiles of faulted geomorphic surfaces near Borah Peak, Idaho: A preliminary report. *U.S. Geol. Surv. Open File Rep.* **85-290,** 76–96.

Vita-Finzi, C. (1986). *Recent Earth Movements-An Introduction to Neotectonics.* Academic Press, Orlando, FL.

Vittori, E., Labini, S. S., and Serva, L. (1991). Palaeoseismology; review of the state-of-the-art. *Tectonophysics* **193,** 9–32.

Walker, G. P. L. (1987). The dike complex of Koolau Volcano, Oahu: Internal structure of a Hawaiian rift zone. In Volcanism in Hawaii (R. W. Decker, T. L. Wright, and P. H. Stauffer, eds.), *U.S. Geol. Surv. Prof. Pap.* **1350,** 961–993.

Wallace, R. E. (1968a). Notes on stream channels offset by the San Andreas fault, southern Coast ranges, California. In *Geological Problems of the San Andreas Fault System* (W. R. Dickinson and A. Grantz, eds.), *Stanford Univ. Publ. Geol. Sci.* **11,** 6–21.

Wallace, R. E. (1968b). Earthquake of August 19, 1966, Varto area, eastern Turkey. *Bull. Seismol. Soc. Am.* **58,** 11–45.

Wallace, R. E. (1970). Earthquake recurrence intervals on the San Andreas fault. *Geol. Soc. Am. Bull.* **81,** 2875–2890.

Wallace, R. E. (1973). Surface fracture patterns along the San Andreas fault. *Stanford Univ. Publ. Geol. Sci.* **13,** 248–250.

Wallace, R. E. (1977). Profiles and ages of young fault scarps, north-central Nevada. *Geol. Soc. Am. Bull.* **88,** 1267–1281.

Wallace, R. E. (1980a). Degradation of the Hebgen Lake fault scarps of 1959. *Geology* **8,** 225–229.

Wallace, R. E. (1980b). Gilbert's studies of faults, scarps, and earthquakes. In The Scientific Ideas of G. K. Gilbert (Yochelson, E. L. ed.), *Spec. Pap.- Geol. Soc. Am.* **183,** 35–44.

Wallace, R. E. (1981). Active faults, paleoseismology, and earthquake hazards in the western United States. In *Earthquake Prediction: An International Review* (D. W. Simpson and P. G. Richards, eds.), Maurice Ewing Ser. **4,** 209–216. Am. Geophys. Union, Washington, DC.

Wallace, R. E. (1984). Faulting related to the 1915 earthquakes in Pleasant Valley, Nevada. *U.S. Geol. Surv. Prof. Pap.* **1274-A,** 1–33.

Wallace, R. E., chairman (1986). *Active Tectonics*: Studies in Geophysics. Natl. Acad. Sci., Washington, DC.

Wallace, R. E. (1987). A perspective of paleoseismology. In Directions in Paleoseismology (A. J. Crone and E. M. Omdahl, eds.), *U.S. Geol. Surv. Open File Rep.* **87-673,** 7–16.

Wallace, R. E. (1989). Fault-plane segmentation in brittle crust and anisotropy in loading system. *U.S. Geol. Surv. Open File Rep.* **89-315,** 400–408.

Wallace, R. E., ed. (1990). The San Andreas fault system, California. *U.S. Geol. Surv. Prof. Pap.* **1515,** 283 pp.

Wallace, R. E., and LaMarche, V. C. (1979). Trees as indicators of past movements on the San Andreas fault. *Earthquake Info. Bull.* **2**(4), 127–131.

Wallace, R. E., and Moxham, R. M. (1967). Use of infrared imagery in the study of the San Andreas fault system, California. *U.S. Geol. Surv. Prof. Pap.* **575-D,** D147–D156.

Wallace, R. E., and Whitney, R. A. (1984). Late Quaternary history of the Stillwater seismic gap, Nevada. *Bull. Seismol. Soc. Am.* **74,** 301–314.

Ward, S. N., and Goes, S. D. B. (1993). How regularly do earthquakes recur: A synthetic seismicity model for the San Andreas fault. *Geophys. Res. Lett.* **20,** 2131–2134.

Warren, G. A., and McCalpin, J. P. (1992). Quaternary faulting on the southern Star Valley fault, western Wyoming. *Geol. Soc. Am., Abtsr. Prog.* **24**(6), 67.

Waterbolk, H. T. (1983). Ten guidelines for the archaeological interpretation of radiocarbon dating, In ^{14}C Dating and Archaeology, W. G. Mook and H. T. Waterbolk, eds., *PACT* **8,** 57–70.

Watters, R. J., and Prokop, C. (1990). Fault-scarp dating utilizing soil strength behavior techniques. *Bull. Assoc. Eng. Geol.* **27,** 291–301.

Weber, G. E., and Cotton, W. R. (1980). Geologic Investigation and Recurrence Intervals and Recency of Faulting Along the San Gregorio Fault Zone, San Mateo County, California, *Unpublished Final Tech. Rep. to U.S. Geol. Surv., Contract No.* **14-08-0001-16822.** Wm. Cotton & Assoc., Los Gatos, CA.

Weldon, R. J., III (1991). Active tectonic studies in the United States, 1987-1990. In U. S. National Report to International Union of Geodesy and Geophysics 1987-1990. *Rev. Geophys., Suppl.* pp. 890–906.

Wellman, H. W. (1952). The Alpine Fault in detail; river terrace displacement at Maruia River. *N. Z. J. Sci. Technol. Sect. B* **33,** 409–414.

Wellman, H. W. (1953). Data for the study of Recent and late Pleistocene faulting in the South Island of New Zealand. *N. Z. J. Sci. Technol. Sect. B* **34,** 270–288.

Wellman, H. W. (1955). New Zealand Quaternary tectonics. *Geol. Rundsch.* **43,** 248–257.

Wells, D. L., and Coppersmith, K. J. (1994). Empirical relationships among magnitude, rupture length, rupture area, and surface displacement. *Bull. Seismol. Soc. Am.* **84,** 974–1002.

Wesnousky, S. G. (1986). Earthquakes, Quaternary faults, and seismic hazard in California. *J. Geophys. Res.* **91,** 12,587–12,631.

Wesnousky, S. G., and Leffler, L. M. (1992). The repeat time of the 1811 and 12 New Madrid earthquakes; a geological perspective *Bull. Seismol. Soc. Am.* **82,** 1756–1784.

Wesnousky, S. G., and Leffler, L. M. (1994). A search for paleoliquefaction and evidence bearing on the recurrence behavior of the great 1811-12 New Madrid earthquakes. *U.S. Geol. Surv. Prof. Pap.* **1538-H,** H1–H42.

Wesnousky, S. G., Scholz, C. H., Shimazaki, K., and Matsuda, T. (1984). Integration of geological and seismological data for the analysis of seismic hazard; a case study of Japan. *Bull. Seismol. Soc. Am.* **74,** 687–708.

Wesnousky, S. G., Prentice, C. S., and Sieh, K. E. (1991). An offset Holocene stream channel and the rate of slip along the northern reach of the San Jacinto fault zone, San Bernadino Valley, California. *Geol. Soc. Am. Bull.* **103,** 700–709.

West, M. W. (1992). An integrated model for seismogenesis in the Intermountain Seismic Belt. *Bull. Seismol. Soc. Am.* **82,** 1350–1372.

West, M. W. (1993). Extensional reactivation of thrust faults accompanied by coseismic surface rupture, southwestern Wyoming and north-central Utah. *Geol. Soc. Am. Bull.* **105,** 1137–1150.

West, M. W. (1994). Seismotectonics of north-central Utah and southwestern Wyoming. *Spec. Stud.- Utah Geol. Miner. Surv.* **82,** 1–93.

Wheeler, R. L. (1989). Persistent segment boundaries on basin-range normal faults. In *Fault Segmentation and Controls of Rupture Initiation and Termination* (D. P. Schwartz and R. H. Sibson, eds.), *U.S. Geol. Surv. Open File Rep.* **89-315,** 432–444.

Wheeler, R. L., and Krystinik, K. B. (1992). Persistent and nonpersistent segmentation of the Wasatch fault zone, Utah- statistical analysis for evaluation of seismic hazard. In *Assessment of Regional Earthquake Hazards and Risk along the Wasatch Front, Utah* (P. L. Gori, and W. W. Hays, eds.), *U.S. Geol. Surv. Prof. Pap.* **1500-B,** B1-B47.

Whitehouse, I. E., and Griffiths, G. A. (1983). Frequency and hazard of large rock avalanches in the central Southern Alps, New Zealand. *Geology* **11,** 331–334.

Wieczorek, G. F. (1984). Preparing a detailed landslide-inventory map for hazard evaluation and reduction. *Bull. Assoc. Eng. Geol.* **21,** 337–342.

Wieczorek, G. F., Wilson, R. C., and Harp, E. L. (1985). Map showing slope stability during earthquakes of San Mateo County, California. *U.S. Geol. Surv. Misc. Geol. Invest. Map* **I-1257-E,** Scale 1:62,500.

Wiley, M. A., Rupert, G. B., Christy, J. J., Cochrane, C. L., and Buffington, N. L., Jr. (1991). Delineation of the New Madrid seismic zone using Landsat MSS data with insurance and tax implications of future fault movement. *Proc. Thematic Conf. Geol. Rem. Sens., 8th,* pp. 131–143. Earth Resour. Inst. Michigan, Ann Arbor.

Williams, P. L., and Ingram, L. (1994). Using the shallow marine record to detect the geometry and recurrence behavior of active faults. *U.S. Geol. Surv. Open File Rept.* **94-568,** 197–199.

Williams, P. L., Jacoby, G. C., and Buckley, B. (1992). Coincident ages of large landslides in Seattle's Lake Washington. *Geol. Soc. Am., Abtsr. Prog.* **24**(5), 90.

Wilson, R. C., and Keefer, D. K. (1983). Dynamic analysis of a slope failure from the 6 August 1979 Coyote Lake, California, earthquake. *Bull. Seismol. Soc. Am.* **73,** 863–877.

Wilson, R. C., and Keefer, D. K. (1985). Predicting areal limits of earthquake-induced landsliding. In *Evaluating Earthquake Hazards in the Los Angeles Region—An Earth-Science Perspective* (J. I. Ziony, ed.), *U.S. Geol. Surv. Prof. Pap.* **1360,** 316–345.

Wing, R. S. (1970). Cholame area, San Andreas fault zone, California; a study in SLAR. *Mod. Geol.* **1,** 173–186.

Witkind, I. J. (1964). Reactivated faults north of Hebgen Lake. *U.S. Geol. Surv. Prof. Pap.* **435,** 37–50.

Wood, H. O., and Neumann, F. (1931). Modified Mercalli intensity scale of 1931. *Bull. Seismol. Soc. Am.* **21,** 277–283.

Wood, S. H. (1985). Regional increase in groundwater discharge after the 1983 Idaho earthquake; coseismic strain release, tectonic and natural hydraulic fracturing. In Workshop XXVIII on the Borah Peak Earthquake (R. S. Stein and R. C. Bucknam, eds.), *U.S. Geol. Surv. Open File Rep.* **85–290,** 573–592.

Woodward-Clyde Consultants (1980). Evaluation of the potential for resolving the geologic and seismic issues at the Humboldt Bay Power Plant Unit No. 3. Unpublished report to Pacific Gas and Electric Co., from Woodward-Clyde Consultants, San Francisco, CA. C1–C129.

Working Group on California Earthquake Probabilities (1988). Probabilities of large earthquakes occurring in California on the San Andreas fault. *U.S. Geol. Surv. Open File Rep.* **88-398,** 1–62.

Working Group on California Earthquake Probabilities (1990). Probabilities of large earthquakes in the San Francisco Bay region, California. *U.S. Geol. Surv. Circ.* **1053,** 1–51.

Working Group on California Earthquake Probabilities (1995). Seismic hazards in southern California-Probable earthquakes, 1994-2024. *Bull. Seismol. Soc. Am.* **85,** 379–525.

Wyss, M. (1979). Estimating maximum expectable magnitude of earthquakes from fault dimensions. *Geology* **7,** 336–340.

Wyss, M. (1988). A proposed source model for the great Kau, Hawaii, earthquake of 1868. *Bull. Seismol. Soc. Am.* **78,** 1450–1462.

Yadav, R. R., and Kulieshius, P. (1992). Dating of earthquakes; tree ring responses to the catastrophic earthquake of 1887 in Alma-Ata, Kazakhstan. *Geogr. Jour.* **158,** 295–299.

Yamaguchi, D. K., Woodhouse, C. A., and Reid, M. S. (1989). Tree-ring evidence for synchronous rapid submergence of the southwestern Washington coast 300 years B. P. *EOS, Trans. Am. Geophys. Union* **70**(43), 1332 (abstr.).

Yamasaki, N., and Tada, F. (1928). The Oku-Tango earthquake of 1927. *Earthquake Res. Inst. Bull., Univ. Tokyo* **4,** 159–177.

Yarnold, J. C., and Lombard, J. P. (1989). A facies model for large rock-avalanche deposits formed in dry climates. In *Conglomerates in Basin Analysis*: A Symposium Dedicated to A. O. Woodford (I. P. Colburn, P. L. Abbott, and J. Minch, eds.), *Pac. Sect., Soc. Econ. Paleontol. Mineral.* **62,** 9–31.

Yeats, R. S. (1986a). Faults related to folding with examples from New Zealand. *Bull.- R. Soc. N. Z.* **24,** 273–292.

Yeats, R. S. (1986b). Active faults related to folding. In *Active Tectonics*: Studies in Geophysics (R. E. Wallace, chairman), pp. 63–79. Natl. Acad. of Sci., Washington, DC.

Yeats, R. S. (1987). Coseismic folding. In Directions in Paleoseismology (A. J. Crone and E. M. Omdahl, eds.), *U.S. Geol. Surv. Open-File Rep.* **87-673,** 163–172.

Yeats, R. S. (1994). Historical paleoseismology. In Proceedings of the Workshop on Paleoseismology, 18–22 September 1994, Marshall, California (C. S. Prentice, D. P. Schwartz, and R. S. Yeats, conveners), *U.S. Geol. Survey Open-File Rep.* **94-568,** 208–210.

Yeats, R. S., Allen, C. R., and Sieh, K. E. (1996). *Earthquake Geology.* Oxford Univ. Press, New York.

Yeh, H., Imamura, F., Synolakis, C., Tsuji, Y., Liu, P., and Shi, S. (1993). The Flores Island tsunami. *EOS, Trans. Am. Geophys. Union* **74,** 371–373.

Yielding, G., Jackson, J. A., King, G. C. P., Sinvhal, H., Vita-Finzi, C., and Wood, R. M. (1981). Relations between surface deformation, fault geometry, seismicity, and rupture characteristics during the El Asnam (Algeria) earthquake of 10 October 1980. *Earth Planet. Sci. Lett.* **26,** 287–304.

Yokoyama, I. (1974). Geomagnetic and gravity anomalies in volcanic areas. In *Physical Volcanology* (L. Civetta, P. Gasparini, G. Luongo, and A. Rapolla, eds.), pp. 167–194. Elsevier, New York.

Yonekura, N. (1975). Quaternary tectonic movements in the outer arc on southwest Japan with special reference to seismic crustal deformations. *Bull. Dep. Geogr., Univ. Tokyo* **7,** 19–71.

Yonekura, N., and Shimazaki, K. (1980). Uplifted marine terraces and seismic crustal deformation in arc-trench systems; A role of imbricated thrust faulting. *EOS, Trans. Am. Geophys. Union* **61,** 1111 (abstr.).

Yoshikawa, T., Kaizuka, S., and Ota, Y. (1964). Mode of crustal movement in the late Quaternary of the southeast coast of Shikoku, southwestern Japan. *Geogr. Rev. Jpn.* **37,** 627–648.

Yoshikawa, T., Kaizuka, S., and Ota, Y. (1981). *The Landforms of Japan.* Univ. of Tokyo Press, Tokyo.

Yoshioka, T., Okumura, K., and Kuscu, I. (1993). Trenching survey of the North Anatolian fault east of Erzincan. *Chishitsu News, Geol. Surv. Jpn.* **471,** 26–33 (in Japanese).

Youd, T. L. (1973). Liquefaction, flow, and associated ground failure. *U.S. Geol. Surv. Circ.* **688,** 1–12.

Youd, T. L. (1978). Major cause of earthquake damage is ground failure. *Civ. Eng.* **48,** 47–51.

Youd, T. L. (1984a). Geologic effects - liquefaction and associated ground failure. *U.S. Geol. Surv. Open File Rept.* **84-760,** 210–232.

Youd, T. L. (1984b). Recurrence of liquefaction at the same site. *Proc. World Conf. Earthquake Eng., 8th,* Vol. **3,** pp. 231–238.

Youd, T. L., and Bartlett, S. F. (1991). Case histories of lateral spreads from the 1964 Alaska earthquake. In *Proceedings of the Third Japan-U. S. Workshop on Earthquake Resistance to Design of Lifeline Facilities and Countermeasures for Soil Liquefaction,* Tech. Rep. NCEER-91-0001, pp. 175–189. State University of New York, Buffalo.

Youd, T. L., and Hoose, S. N. (1978). Historic ground failures in northern California triggered by earthquakes. *U.S. Geol. Surv. Prof. Pap.* **993,** 1–177.

Youd, T. L., and Keefer, D. K. (1994). Liquefaction during the 1977 San Jose Province earthquake (Ms 7.4). *Eng. Geol.* **37,** 211–233.

Youd, T. L., and Perkins, D. M. (1978). Mapping liquefaction-induced ground failure potential. *J. Geotech. Eng., Am. Soc. Civ. Eng.* **104,** 433–446.

Youd, T. L., and Perkins, D. M. (1987). Mapping of liquefaction severity index. *J. Geotech. Eng., Am. Soc. Civ. Eng.* **113,** 1374–1392.

Youd, T. L., Holzer, T. L., and Bennett., M. J. (1989). Liquefaction lessons learned from Imperial Valley, California. *Int. Conf. Soil Mech. Found. Eng., Proc. Discuss. Sess. Influence Local Cond. Seismic Response 12th,* Rio de Janeiro, pp. 47–54.

Yount, J. C., Shroba, R. R., McMasters, C. R., Huckins, H. E., and Rodriguez, E. A. (1987). Trench logs from a strand of the Rock Valley fault system, Nevada Test Site, Nye County, Nevada. *U.S. Geol. Surv. Misc. Field Stud. Map* **MF-1824,** Scale 1:20.

Záruba, Q., and Mencl, V. (1982). *Landslides and Their Control,* 2nd ed. Elsevier, Amsterdam.

Zhang, B., Yuhua, L., Shunmin, G., Wallace, R. E., Bucknam, R. C., and Hanks, T. C. (1986). Fault scarps related to the 1739 earthquake and seismicity of the Yinchuan graben, Ningxia Huizu Ziziqu, China. *Bull. Seismol. Soc. Am.* **76,** 1253–1288.

Zhang, W., Liao, Y., Pan, Z., and Song, F. (1982). On the piedmont scarp in alluvial fans of Mt. Helanshan. *Seismol. Geol.* **4,** 32–34 (in Chinese).

Zhang, W., Jiao, D., Zhang, P., Molnar, P., Burchfiel, B. C., and Deng, Q. (1987). Displacement along the Haiyuan fault associated with the great 1920 Haiyuan, China, earthquake. *Bull. Seismol. Soc. Am.* **77,** 117–131.

Zhang, Z., and Schwartz, S. Y. (1992). Depth distribution of moment release in underthrusting earthquakes at subduction zones. *J. Geophys. Res.* **97,** 537–544.

Ziony, J. I., and Yerkes, R. F. (1985). Evaluating earthquake and surface-faulting potential. In *Evaluating Earthquake Hazards in the Los Angeles Region- An Earth-Science Perspective* (J. I. Ziony, ed.), *U.S. Geol. Surv. Prof. Pap.* **1360,** 43–92.

Zoback, M. L., and Thompson, G. A. (1978). Basin and Range rifting in northern Nevada: Clues from a mid-Miocene rift and its subsequent offsets. *Geology* **6,** 111–116.

Zobin, V. M. (1990). Seismotectonic crustal deformation during the large Tolbachik fissure eruption in Kamchatka. *J. Volcanol. Geotherm. Res.* **43,** 271–278.

Zollweg, J. E. (1990). Seismicity following the 1985 eruption of Nevado del Ruiz, Columbia. *J. Volcanol. Geotherm. Res.* **41,** 355–367.

Zreda, M. G., Phillips, F. M., Kubik, P. W., Sharma, P., and Elmore, D. (1993). Cosmogenic ^{36}Cl dating of a young basaltic eruption complex, Lathrop Wells, Nevada. *Geology* **21,** 57–60.

Zuchiewicz, W. (1989). Morphotectonic phenomena in the Polish flysch Carpathians; a case study of the eastern Beskid Niski Mountains. *Quaest. Geogr., Spec. Issue* **2,** 155–167.

Index